Signal definition and resource management techniques for upcoming communication and broadcasting systems

Charbel Abdel Nour

Université de Bretagne-Sud

Ecole Doctorale – MathSTIC

Signal definition and resource management techniques for upcoming communication and broadcasting systems

---

Habilitation à Diriger des Recherches

HDR

Presented by

Charbel Abdel Nour

Prepared at

IMT Atlantique

Department : Electronics

Laboratory : Lab-STICC / IAS team

Defended online

30/11/2020

Defense committee :

Gianluigi Liva	Head of transmission group, DLR, Germany	Reviewer
Christophe Jego	Professor at INP/ENSEIRB-MATMECA, Bordeaux	Reviewer
Carlos Bader	Professor at ISEP, Paris	Reviewer
Charly Poulliat	Professor at INP/ENSEEIHT Toulouse	President
Emmanuel Boutillon	Professor at UBS, Lorient	Examiner
Catherine Douillard	Professor at IMT Atlantique, Brest	Examiner

Contents

List of Figures

Acronyms

2G 2nd Generation mobile networks

3GPP 3rd Generation Partnership Project

4G/LTE 4th Generation mobile networks / Long Term Evolution

5G 5th Generation mobile networks

ACLR adjacent channel leakage ratio

ACS Add-Compare-Select

ADC Analog-to-Digital Converter

AFB Analysis Filter Bank

AI Artificial Intelligence

API Application Programming Interface

ARP Almost Regular Permutation

AS Antenna Selection

ASIC Application-Specific Integrated Circuit

AWGN Additive White Gaussian Noise

BBU BaseBand Unit

BCH Bose Ray-Chaudhuri Hocquenghem

BCJR Bahl Cocke Jelinek Raviv

BE Best Effort

BER Bit-Error Rate

BF-OFDM Block-Filtered-Orthogonal Frequency-Division Multiplexing

BICM Bit-Interleaved Coded Modulation

BICM-ID Bit-Interleaved Coded Modulation with Iterative Demodulation

BLER BLock-Error Rate

BMI Bitwise Mutual Information

BPSK Binary Phase Shift Keying

BS Base Station

C-RAN Cloud Radio Access Network

CAS Centralized Antenna Systems

CC Convolutional Codes

CCDF Complementary Cumulative Distribution Function

CFO Carrier Frequency Offset

CFR Channel Frequency Response

CIR Channel Impulse Response

CM Complex Multiplier

CoMP Coordinated MultiPoint

CP Cyclic Prefix

CPE Common Phase Error

CSD Canonical Signed Digit

CSI Channel State Information

D2D Device-to-Device

DA Deferred Acceptance

DAC Digital-to-Analog Converter

DAS Distributed Antenna Systems

DCT Discrete Cosine Transform

DDR Double Data Rate

DFE Decision Feedback Equalizer

DIF Decimation In Frequency

DMA Direct Memory Access

DMSIC Double Mutual Successive Interference Cancellation

DMT Diversity-Multiplexing Tradeoff

DSP Digital Signal Processor

DRP Dithered Relative Prime

DRS Demodulation Reference Signal

DVB Digital Video Broadcasting

DVB-NGH Digital Video Broadcasting New Generation Handheld

DVB-RCS2 Digital Video Broadcasting Return Channel Satellite 2nd generation

DVB-T2 Digital Video Broadcasting Terrestrial 2nd generation

EIC Equalization with Interference Cancellation

eMBB enhanced Mobile BroadBand

EMCM Even Multiplierless Constant Multiplication

EPA Extended Pedestrian A

ETU Extended Typical Urban

EVA Extended Vehicular A

EVM Error Vector Magnitude

EXIT EXtrinsic Information Transfer

F-OFDM Filtered-Orthogonal Frequency-Division Multiplexing

FB Filter-Bank

FC-OFDM Flexible-Configuration Orthogonal Frequency-Division Multiplexing

FBMC Filter Bank Multi-Carrier

FD Full-Duplex

FDA Frequency Domain Approximation

FDC Frequency Domain Compensation

FEC Forward Error Correction

FFT Fast Fourier Transform

FIFO First-In First-Out

FIR Finite Impulse Response

FPA Fixed Power Allocation

FPGA Field-Programmable Gate Array

FS Frequency Spread

FSPA Full Search Power Allocation

FTN FasterThan-Nyquist

FTPA Fractional Transmit Power Allocation

GUI Graphical User interface

GFDM Generalized Frequency Division Multiplexing

HARQ Hybrid Automatic Repeat reQuest

HFS Half Frequency Shift

HPA High Power Amplifier

IAI Inter-Antenna-Interference

IAM Interference Approximation Method

IBC International Broadcasting Convention

IBFD In-band Backhaul Full-Duplex

ICeI Inter-Cell Interference

ICI Inter-Carrier Interference

IFFT Inverse Fast Fourier Transform

IIR Infinite Impulse Response

IMT2020 International Mobile Telecommunications-2020

IoT Internet-of-Things

IOTA4 Isotropic Orthogonal Transform Algorithm 4

IR Incremental Redundancy

ISI Inter-Symbol Interference

IUI Inter-User Interference

JFG Joint Factor Graph

JT Joint Transmission

LDM Layer Division Multiplexing

LDPC Low density Parity Check

LO Local Oscillator

LoS Line-of-Sight

LPR Linear Phase Rotation

LTE Long Term Evolution

LUT Look-Up Table

M2M Machine-to-Machine

MAB Multi-Armed Bandits

MAP Maximum A Posteriori

Max-Log-MAP Maximum A Posteriori with Max-Log approximation

MBB Mobile BroadBand

MBS Master Base Station

MCC Mission Critical Communication

MCM Multiplier-less Constant Multiplication

MI Mutual Information

MIMO Multiple-Input Multiple-Ouput

MISO Multiple-Input Single-Ouput

ML Maximum Likelihood

MMB4 Martin–Mirabassi–Bellanger 4

MMC Massive Machine Communication

mMIMO massive Multiple-Input Multiple-Output

MMSE Minimum Mean Square Error

MRC Maximum Ratio Combining

MTC Machine Type Communications

MTD Machine-Type-Devices

MUST MultiUser Superposition Transmission

NB Non-Binary

NB-CC Non-Binary Convolutional Codes

NLOS Non-Line-of-Sight

NMSE Normalized Mean Square Error

NN Neural Network

NOMA Non Orthogonal Multiple Access

NPR1 Near Perfect Reconstruction 1

NR New Radio

NUC Non-Uniform Constellation

OFDM Orthogonal Frequency-Division Multiplexing

OMA Orthogonal Multiple Access

OMCM Odd Multiplierless Constant Multiplication

OOBPL Out-Of-Band Power Leakage

OS Overlap-Save

OSB Overlap-Save-Block

OQAM Offset Quadrature Amplitude Modulation

P-OFDM Pulse-shaped Orthogonal Frequency-Division Multiplexing

PAM Pulse-Amplitude Modulation

PAPR Peak-to-Average Power Ratio

PAS Probabilistic Amplitude Shaping

PD PPower Domain

PER Packet Error Rate

PF Proportional Fairness

PHYDYAS Physical Layer For Dynamic Spectrum Access And Cognitive Radio

PPN PolyPhase Network

ProF Prototype Filter

PSD Power Spectral Density

PTC Precoded Turbo Code

PU Primary User

QAM Quadrature Amplitude Modulation

QMF1 Quadrature Mirror Filter 1

QoS Quality of Service

QPP Quadratic Permutation Polynomial

QPSK Quadrature phase-shift keying

RA Real Addition

RAM Random Access Memory

RB Resource Block

RF Radio Frequency

RI Roll-off Interval

RL Reinforcement Learning

RM Real Multiplication

RRH Remote Radio Head

RT Real Time

SBF Subband Prototype Filter

SCMA Sparse Code Multiple Access

SC Successive Cancellation

SC-OFDM Single-Carrier Orthogonal Frequency-Division Multiplexing

SeI Self Interference

SFN Single Frequency Network

SI Side Information

SIC Successive Interference Cancellation

SINR Signal-to-interference-plus-noise ratio

SISO Soft-Input Soft-Output

SIR Signal-to-Interference Ratio

SLM Selective Mapping

SMT Staggered Modulated Multitone

SNR Signal-to-Noise Ratio

SP-RAM Single-Port Random-Access Memory

SoC System on Chip

SOVA Soft Output Viterbi Algorithm

SQNR Signal-to-Quantization-Noise Ratio

SSD Signal Space Diversity

SU Secondary User

STBC Space-Time Block-Coding

TA Timing Advance

TC Turbo Code

TDD Time-Division Duplexing

TDW Time Domain Windowing

TFL1 Time Frequency Localization 1

TMSIC Triple Mutual Successive Interference Cancellation

TTI Time Transmission Interval

TUKL Technical University of Kaiserslautern

UAV Unmanned Aerial Vehicle

UE User Equipment

UF-OFDM Universal-Filtered Orthogonal Frequency-Division Multiplexing

UFMC Universal Filtered Multi-Carrier

UMTS Universal Mobile Telecommunications System

URLLC Ultra-Reliable Low Latency Communications

UXMAP Unrolled X Maximum A Posteriori

V2I Vehicular-to-Infrastructure

V2X Vehicular-to-Anything

V2V Vehicular-to-Vehicular

VHDL VHSIC (Very High Speed Integrated Circuit) Hardware Description Language

ZF Zero-Forcing

ZT-OFDM Zero-Tail Orthogonal Frequency-Division Multiplexing

Short introduction

This document represents my Habilitation thesis manuscript. It summarizes my academic and professional career including recent and future research activities. It is organized as follows:

- A first part includes my Curriculum Vitae;

- A second short part gives a high level view on my research activities and articulates the rest of the document into addressed topics;

- *Chapter 1* presents the first topic related to the study and proposal of algorithms for coded modulations with(out) MIMO;

- *Chapter 2* presents the second topic related to the study and proposal of algorithms for filtered waveforms;

- *Chapter 3* presents the third topic related to the study and proposal of algorithms for non-orthogonal multiple access systems;

- The final *Chapter 4* provides a brief review of planned short and long-term future works.

Curriculum Vitæ

Current professional address:

IMT Atlantique — Electronics department
Lab-STICC UMR CNRS 6285
Technopôle Brest-Iroise — CS 83818
29238 Brest Cedex 3
France

Phone : +33 2 29 00 15 94
Fax : +33 2 29 00 11 84
Email : Charbel.Abdelnour@imt-atlantique.fr
Web :

1 Strong points/Summary

- 15+ years in R&D in the fields of digital communications and broadcasting.
- Active participation (35+ technical contributions) to the technical groups of 3GPP and three different DVB standards.
- Contribution to 18+ different R&D projects.
- Participation to 5 different teaching modules in undergraduate engineering degree. The creation of new teaching courses including advanced ones for last year students.
- In charge of the teaching module related to Electronics for the second year engineering students from 2014 till 2019. Since 2019, in charge of the digital and analog integrated circuits course.
- Large experience in managing a R&D team and tutorship: 7 post-doctoral researchers, 14 PhD students (including 9 defended), 4 R&D engineers and several Master and undergraduate students.
- 18 patent filings including 8 extended to multiple countries and 1 patent adopted and recognized as essential in 3 different DVB standards.
- 24 journal publications, 2 book chapters, 5 invited talks and 65 publications in conferences including 2 articles attributed best paper awards.

- 5+ demonstrations in forums including the international Broadcasting Convention (IBC) in 2010 (250+ visitors) and at the Mobile World Congress (MWC) in 2015 (1000+ visitors including the EU commissioner in charge of the digital technology).

2 Education and career

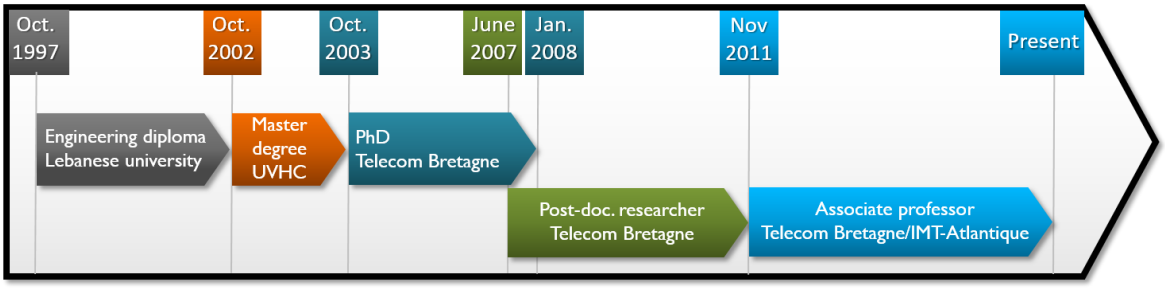

Figure 1: Education and career at a glance

2.1 Education

Oct. 1997-Oct. 2002 Engineering diploma in electronics, computer and communications. Lebanese university, faculty of engineering branch II, Roumieh, Lebanon.

Oct. 2002-Oct. 2003 Master Degree in electronics and image processing. Université de Valenciennes et du Haînaut Cambrésis (UVHC), Valenciennes, France.

Oct. 2003-Jan. 2008 PhD in electronics and communications: "Iterative methods for improving error correcting performance of spectrally efficient coded transmissions", Telecom Bretagne, Brest, France.

2.2 Career

Jun. 2007-Nov. 2011 Post-doctoral researcher in telecommunications. Telecom Bretagne, Brest, France.

Nov. 2011-Present Associate Professor in electronics and telecommunications. Telecom Bretagne/IMT Atlantique, Brest, France.

3 Research activities

My research activities take place in the *"Laboratoire des Sciences et Techniques de l'Information, Communication et Connaissance"* (Lab-STICC) within the team specialized in the Interaction between Algorithm and Silicon (IAS) where algorithms are designed while taking into account their future implementation. They target the elaboration of new algorithms in the field of digital communications and broadcasting. In particular, the study of:

- Binary and non-binary error correcting codes (turbo, LDPC, polar codes etc.) and their associated decoding.

- Digital modulations and Continuous Phase Modulation (CPM), etc.
- Multi-antennas or Multiple Input Multiple Output (MIMO) systems.
- Waveform design and multi-carrier modulations such as Filter-Bank MultiCarrier with Orthogonal Quadrature Amplitude Modulation (FBMC/OQAM), etc.
- Diversity techniques (signal space, interleaving, space-time codes, etc.).
- Resource and power allocation for (Non)-Orthogonal Multiple Access techniques ((N)OMA).
- Joint design of several physical layer components; system optimization for standards (LTE, DVB-T2, etc.); simulation methods of correlated fading.

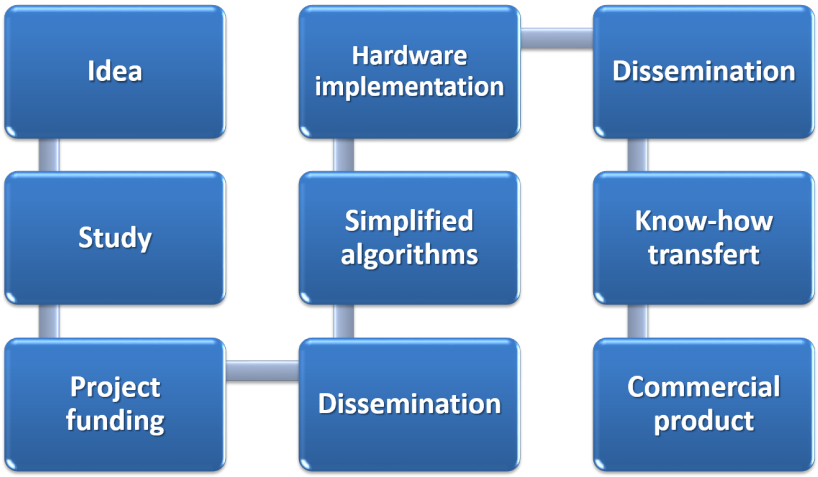

Figure 2: Guiding steps of research activity

These algorithmic studies have the particularity of following partially or totally, depending on the study at hand, an IAS approach summarized by the steps depicted in Fig. 2.

At the start of every study, there is an original idea that is often the fruit of an out-of-the-mainstream thinking. Deeper studies are needed hereafter to validate the originality of this idea and its positive impact on the obtained measurable results for the targeted application. If possible, implementation constraints would be already taken into consideration when elaborating corresponding algorithms following the IAS approach. In other words, choices would be made favouring hardware friendly functions. The work can be performed in the context of a collaborative/industrial project depending on the application. This allows providing the necessary funding to finance a Master degree student, a PhD student or a Post-doc fellow. Once validated via simulation results showing the superiority of the idea when compared to existing solutions in state of the art, the study can be the subject of a dissemination via one or more publications and potentially via patent filing.

A second phase can be initiated in collaboration with IAS team members specialized in hardware implementation where at first, fully hardware compliant algorithms are devised. Then architectural templates are explored depending on the translated application requirements into hardware constraints such as latency, complexity, throughput, etc. Once a suitable architecture is selected, implementation is performed leading to a prototype that can be demonstrated showing the benefits of the developed idea. The hardware architectures and the demonstrator can be the subject of a second dissemination step.

A third phase can take place where the know-how is transfered to an industrial partner to go one step further towards a commercial product. This widens the reach of these benefits to the general public.

4 Advisorship/Tutorship

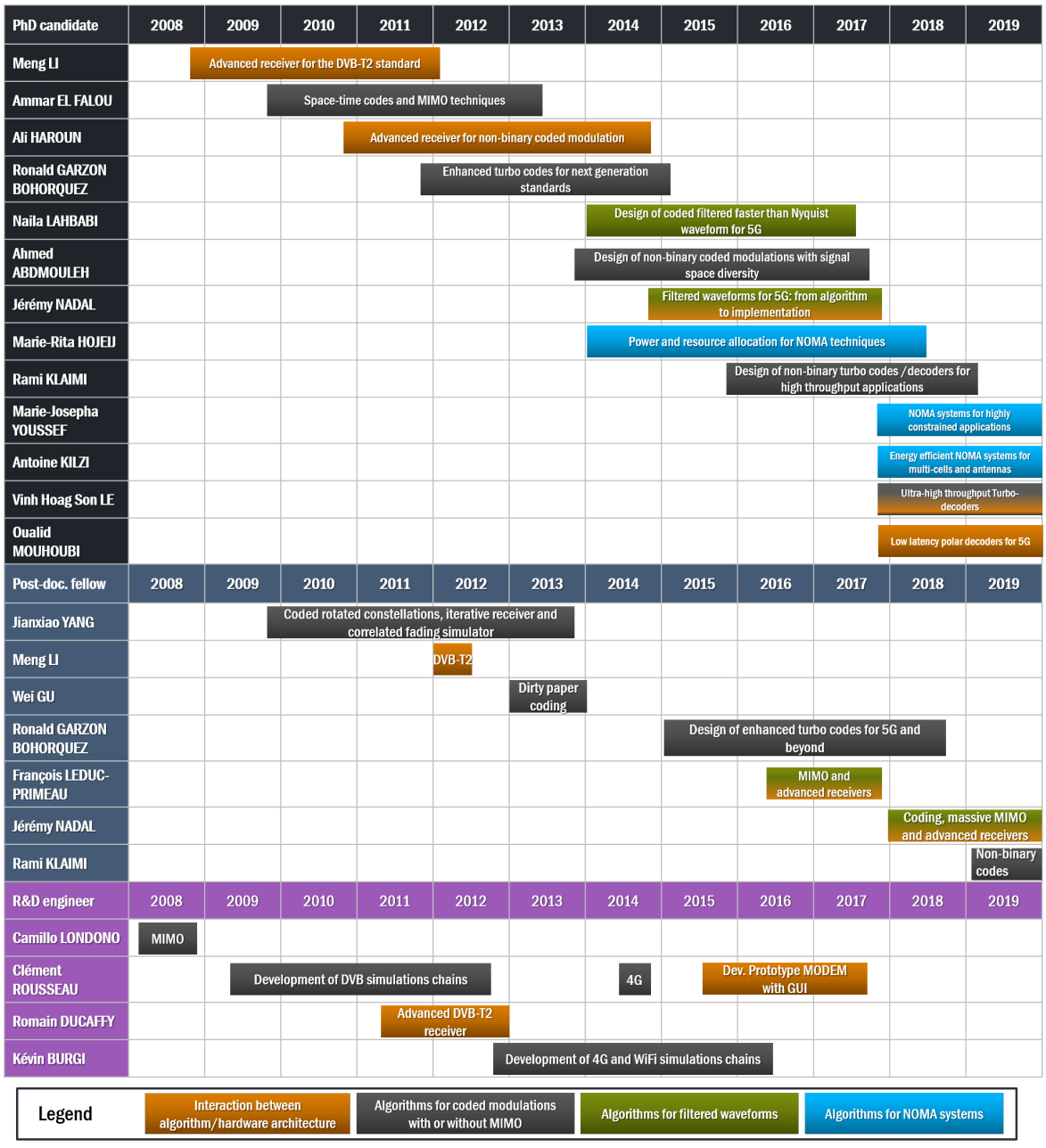

Figure 3: Summary of advisorship/tutorship activity

Since my PhD defense early 2008, I have been involved in the tutorship of 9 defended PhDs, 4 Master thesis students and 8 undergraduate student projects. I am currently the advisor of 5 PhDs with a scheduled defense date ranging between the end of 2020 and the end of 2022. In parallel, I have also collaborated closely with 7 post-doctoral fellows and 4 R&D engineers. The tutorship activity is summarized in Fig. 3 and falls within the 4 main research topics shown in the legend, namely:

- Interaction between algorithm/hardware architecture.
- Algorithms for coded modulations with or without MIMO.
- Algorithms for filtered waveforms.
- Algorithms for Non-Orthogonal Multiple Access (NOMA) systems.

5 Contribution to research projects

Since 2006, I have actively participated to numerous R&D projects as summarized in Table 1. Several projects received distinction and/or awards thanks to their impact on standardization and/or thanks to their innovative aspect.

Table 1: List of research projects.

Type of project	**Title**	**Role within IMT Atlantique**	**Budget**	**Period**
French national ANR	Quasi-Cyclic Small Packet (QCSP)	Technical manager	75k€	2019-2022
Industrial with Newtec	Design of improved turbo decoders	Technical and admin. manager	30k€	2019
EU H2020 beyond 5G	Enabling Practical Wireless Tb/s Communications with Next Generation Channel Coding (EPIC)	Setting up, WP leader and technical contribution	416k€	2017-2020
Industrial with Newtec	Design of improved turbo codes	Technical and admin. manager	30k€	2018
Industrial with Orange Labs and TCL	Implementation of a VLIW hardware accelerated 5G LDPC decoder	Admin. manager and technical contribution	80k€	2017-2018
PHC CEDRE Campus France	Green and robust digital communications	Setup, technical contribution	18k€	2017-2018
Patent factory with France brevets	Patent factory for non orthogonal multiple access schemes	Technical admin.	300k€	2016-2019
Patent factory with France brevets	Patent factory for filter bank multi-carrier modulation and demodulation	Technical admin.	150k€	2015-2018
Industrial with Orange Labs	Improving turbo codes for future standards	Technical and admin. manager	180k€	2015-2018
EU H2020 5G-PPP	Flexible air interface for scalable service delivery within wireless communication networks of the 5th Generation (FANTASTIC-5G)	Setup, technical contribution to several WPs	486k€	2015-2017
EU FP7	Mobile and wireless communications Enablers for Twenty-twenty (2020) Information Society (METIS)	Setup, technical contribution to several WPs	578k€	2012-2015
FUI GREENCoMM	GREEN Computing and CoMMunications	Technical contribution	280k€	2012-2015

Industrial with Orange Labs	Improved end-to-end 3G/4G simulator	Technical manager	25k€	2014
Bilateral with French space agency CNES	Rotated constellations for satellite to mobile communications	Technical and admin. manager	84k€	2012-2013
Bilateral with French space agency CNES	Development of a EMBMS simulation chain	Technical and admin. manager	32k€	2011
Industrial with SIMPULSE (SME)	Hardware implementation of a DVB-T2 receiver	Technical contribution	30k€	2011-2012
EU Eurostars	Enhanced wireless Technologies for News and Security Applications (ETNA)	Setup, technical contribution to several WPs	131k€	2011- 2013
French national ANR	Mobile MultiMedia (M3)	Setup, technical contribution to several WPs	289k€	2011- 2013
Celtic Plus EU	Enabling Next GeneratIon NEtworks for broadcast Services (ENGINES). **Received Celtic bronze award of excellence in 2014.**	Setup, technical contribution to several WPs	325k€	2010- 2012
EU Eurostars	Small and Medium Enterprise for T2 (SME42). **Ranked #1 among 113 accepted projects**.	Setup, technical contribution to several WPs	174k€	2008- 2011
Celtic EU	Broadcast for the 21st Century (B21C). **Received Celtic silver award of excellence in 2009**.	Setup, technical contribution to several WPs	286k€	2007- 2009
EU space agency ESA	Broadband Satellite Digital Transmissions	Technical contribution	80k€	2007- 2008
Internal IMT	Ultra Wide Band for Domotics (UWB-DOMO)	Technical contribution	30k€	2006- 2007

6 Collaborations

During my professional career, I have been able to build 3 types of collaborations:

- Strategic agreements/partnerships: recurrent collaborations within bilateral and collaborative projects that can lead to joint patent filing(s) and/or joint contributions to standards.
- Industrial collaborations: collaborations with industrial partners in the context of research projects or a joint vision regarding a particular technique in the context of standardization.
- Academic collaborations: repeated collaborations with academic partners leading to a strengthened relationship with common publications.

These collaborations span several countries as shown in Fig. 4. The corresponding details are as follows:

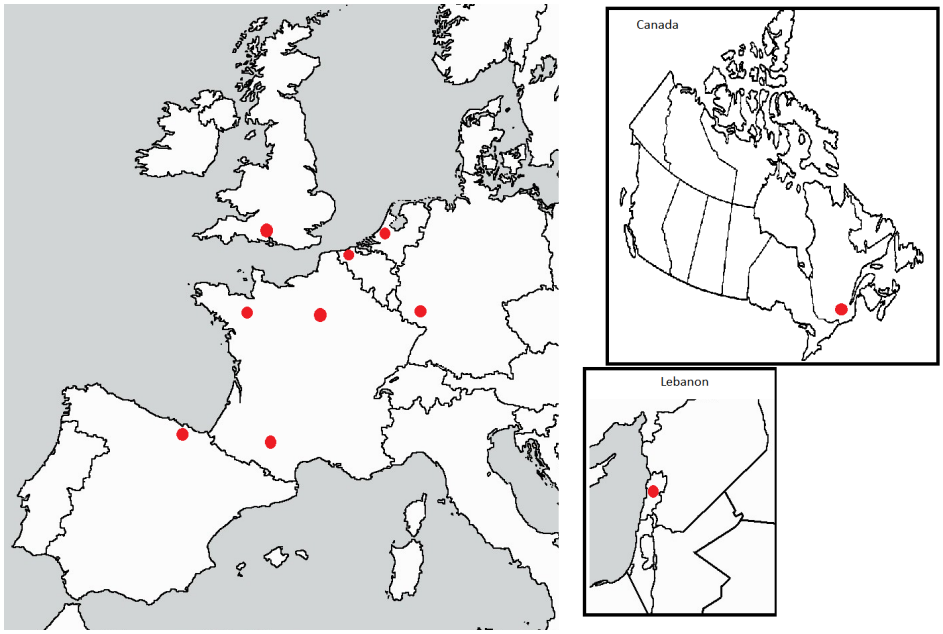

Figure 4: Collaboration map

- Strategic agreements/partnerships:
  - Orange Labs: Agreement on the design of enhanced turbo codes for next generation standards.
  - France Brevets: Agreement on financing research activity related to waveform and NOMA.
- Industrial collaborations:
  - Orange Labs: collaborations within more than 8 EU and bilateral projects.
  - TEAMCAST (Now ENENSYS group): collaboration within 3 EU and 1 French national projects.
  - Newtec: collaboration within 1 European Space Agency (ESA) project EU, 2 bilateral projects and one Cifre PhD.
  - Panasonic Germany: collaboration during DVB-T2 and DVB-NGH standardization.
  - European Space Agency (ESA): collaboration during DVB-RCS2 standardization and one bilateral project.
- Academic collaborations:
  - Lebanese university: Collaboration with Prof. Joumana Farah (associate researcher with IMT Atlantique): 4 common PhD students (2 defended). Execution of a joint CEDRE project (Campus France) and 11 common publications.
  - Holy Spirit University of Kaslik (USEK) Lebanon: collaboration with Associate professors Marie-Rita Hojeij and Charles Yaacoub: 1 PhD student and 2 Master students in common.
  - Basque Country University in Spain UPV/EHU: collaboration with Professor Pablo Angueira Buceta: 3 months visit of PhD student Jon Barrueco to Brest. 2 common publications.

- Technical University of Kaiserslautern (TUK) in Germany: collaboration with professor Norbert Wehn: 1 month visit of my PhD student Ahmed Abdmouleh to TUK. Two visits of two weeks each of postdoc Stefan Weithoffer to IMT Atlantique. Stefan participated to IMT teachings. 1 common publication with 2 planned submissions. Stefan was lately hired as an associate professor at IMT Atlantique.
- ENSTA Paristech: collaboration with Professor Benoît Geller and postdoc Jianxiao Yang: visit of 2 weeks of Jianxiao to IMT Atlantique. 3 common publications.
- Ecole Technique Supérieure and Polytech. Montréal: collaborations with Professor Georges Kaddoum and associate professor François Leduc-Primeau (associate researcher at IMT Atlantique) and visit of François for 2 weeks to IMT Atlantique. 2 common publications.
- University of Southampton: collaboration with Professor Rob Maunder: Multiple joint contributions to 3GPP technical group regarding coding for 5G.
- Concordia University: collaboration with Professor Walaa Hamouda: Visit of my PhD student Ammar el Falou to Québec for 3 months. 3 common publications.
- University of Illinois at Urbana-Champaign: Collaboration with Professor Venugopal V. Veeravalli: Visit of my PhD student Marie-Josepha Youssef to Urbana-Champaign for 6 months. 1 common publication and several under preparation.

7 Remarkable results

- In 2007, proposal of a coded Continuous Phase Modulation (CPM) scheme particularly suited for satellite transmissions. The proposal was implemented in Sat3Play modems of the company Newtec. This series of modems was successfully commercialized by the satellite operator SES Astra since 2009 using the service ASTRA2Connect.
- Adoption of 16-state double-binary turbo codes in 2009 (for the return channel), in 2012 (for the download channel) and of a variant of the coded CPM in the DVB-RCS2 standard.
- Delivered patent on rotated constellations technique in February 2009. Extension to Europe and Asia in 2010.
- Adoption of rotated constellations technique and acknowledgment of the essentiality of the patent to the DVB-T2 standard in June 2008 and to its mobile version in February 2011. This adoption was extended to include the hybrid terrestrial-satellite standard for mobile broadcasting DVB-NGH in September 2011.
- Implementation of the first published hardware prototype for a DVB-T2 receiver including rotated constellations. It was demonstrated at the International Broadcasting Convention (IBC) in 2010.
- The publication detailing an improved DVB-T2 receiver received the best PhD paper award at the IEEE International Workshop on Signal Processing Systems (SIPS) conference in 2011.
- Implementation of the first hardware prototype for a filtered multi-carrier waveform. The corresponding demonstrator was selected by the METIS project as one of its two contributions to the Mobile World Congress (MWC) in 2015. The corresponding booth received more than 1000 visitors including the European commissioner in charge of

the digital technologies and the director of research and strategy at Orange Labs. A following demonstration took place at the research forum of Orange Labs.

- In 2015-2016, agreement over 3 patent factories (2 with France brevets and 1 with Orange Labs) spanning 3 different technical topics: Filtered waveforms, NOMA and coding. These topics were considered of high importance for 5G and future communications standards.
- The publication addressing the association of NOMA techniques with single-user MIMO received the best paper award at the ISCC conference in 2017.
- The 2019 URSI Radioscience PhD Thesis Prize was awarded to Jérémy Nadal for his work entitled: "Filtered multicarrier waveforms in the context of 5G: novel algorithms and architecture optimizations". The PhD thesis was carried out within the IAS team under the direction of Amer Baghdadi and my supervision. The "Radioscience PhD Thesis Prize" is intended to reward annually excellent doctoral work in one or more of the URSI's scientific fields.

8 Teaching activities

8.1 Topics and courses

My teaching activities took place solely at Telecom Bretagne/IMT Atlantique premises with a total average volume of around 145 hours of equivalent tutorial classes. They are related to the following topics:

- Digital electronics.
- Components and architecture of transmission systems.
- System on chip.
- X86 processor architecture.
- Error correcting codes and coded modulations.

The following table details the type of courses, their level and the volume in number of hours annually:

Table 2: Detailed teaching activities

Course	**Level**	**Volume (eq. tut)**
Basic Electronics ELP203, ELP314, ELP213	1st and 2nd year	55 h/y
Architecture of transmission systems F14B201	3rd year, Master	27 h/y

... continued in the next page

TABLE 2 – Follow-up of the previous page

Course	**Level**	**Volume (eq. tut)**
Systems on chip	3rd year	18 h/y
Embedded systems	3rd year, Master	15 h/y
Introduction to engineering systems	1st and 2nd year	12 h/y
Discovering electronics project	1st year	18 h/y

8.2 Teaching and administrative responsabilities

a) I was attributed the following responsabilities at Telecom Bretagne/IMT Atlantique:

- Head of the digital and analog integrated circuit course since 2019 (40 face-to-face hours): Modification of the exercices and adaptation of the contents to the new cursus. This module takes place twice a year.
- Head of the basic Electronics course ELP203 from 2014 till 2019 (21 face-to-face hours): Modification of the exercices and the creation of a new course on memories. This module took place twice a year.
- Main contact for continuous courses at the Electronics department since 2012.
- In charge of the coding and modulation courses and exercices for 3rd year and Master degree students since 2015.

b) I have also managed student research projects of 1st and 3rd year/Master degree ($\approx$2 projects/year in average).

8.3 Other responsabilities, activities and distinctions

a) Active participation to the code selection group in 3GPP for 5G. More than 5 technical contributions in 5 different meetings.

b) Senior IEEE member since August 2019.

c) Member of the technical program committee of:

- The International Symposium on Turbo Codes (ISTC) initially planned in 2020 then postponed to 2021 due to Covid-19.
- The IEEE Symposium on Computers and Communications (ISCC) in 2020.
- ISTC in 2018.

- ISCC in 2017.
- *Colloque francophone de traitement du signal et des images* (GRETSI) 2017.
- ISTC in 2016.

d) Co-organiser of special sessions at:

- ISTC in 2018 on ultra-high throughput decoding.
- International Conference on Telecommunications (ICT) in 2018 on NOMA techniques.

e) Chairman of the following sessions:

- On the construction of LDPC codes at ISTC in 2018.
- On receiver design and sensor networks at the Workshop on Signal Processing Systems (SiPS) in 2011.

f) Regular reviewer for IEEE transactions on wireless communications, IEEE transactions on communications, IEEE transactions on vehicular technology, IEEE access, IEEE transactions on broadcasting, IEEE communications letters. Int. Conference on Telecommunications ICT, IEEE GLObal TeleCOMmunications conference GLOBECOM, Workshop on Signal Processing Systems SiPS, IEEE International Conference on Communications ICC.

g) Promoter of scientific progress and development through the participation to the researcher's night in Brest for several years.

9 Publications

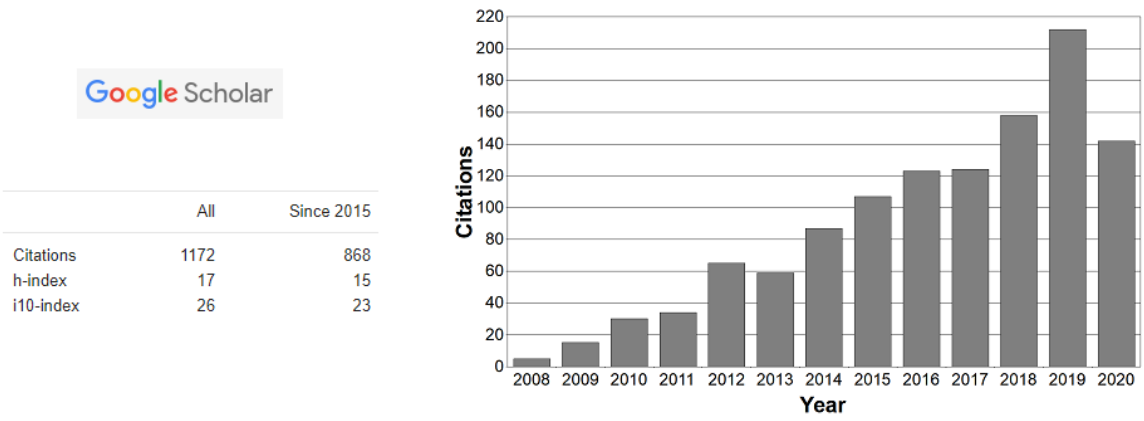

Figure 5: Google scholar citations and h-index

The results of my research activities generated **18** patent filings and were published in **24** journal publications, **2** book chapters, **65** conferences, **2** invited talks and **15** demonstration/exhibition/talk events. The performed work received **1172** citations with a h-index of **17** (ref. Google scholar, 08/09/2020) as shown in Fig. 5. In addition, I am also a co-author of **3** standardization documents:

- The ETSI specification document EN 302 755 of the DVB-T2 standard.
- The ETSI implementation guidelines document TS 102 831 for the DVB-T2 standard.
- The ETSI specification document EN 303 105 for the DVB-NGH standard.

Introduction to my research activities

The research activities since the beginning of my PhD have addressed the following 4 main topics as can be seen in Fig. 6:

- Algorithms for coded modulations with or without Multiple-Input Multiple-Output (MIMO) techniques. This activity represents the largest part of my research. It was the subject of 6 PhDs and one post-doctoral work. It spans the aspects of code design for binary and non-binary codes, the derivation of simplified decoding algorithms, the association of coding schemes with high order modulations, the increase of the diversity degree for coded modulations over fading and erasure channels, the association of coding schemes with multi-antenna systems and the design of coding/decoding schemes for high throughput applications.

- Algorithms for filtered waveforms. An important part of my research activity targets the study of post-OFDM filtered waveforms. This topic spans the design of such waveforms at the transmitter and the receiver side while addressing their penalizing drawbacks. This work was the subject of two PhDs and two post-doctoral fellowships.

- Algorithms for NOMA systems. This represents the newest topic of my research activity. It represents a shift in the type of treated topics addressing mainly the physical layer of communications and broadcasting systems to higher layers. Indeed, by studying the scheduling and the derivation of resource and power allocation schemes for complex systems with orthogonal and non-orthogonal multiple access, multiple antennas (centralized or distributed) with or without coordinated joint transmissions, we address MAC and crosslayer problems. This work is performed by 3 PhDs and is carried out in collaboration with Prof. Joumana Farah from the Lebanese university.

- Interaction between algorithm/hardware architecture. At the exception of resource allocation-based algorithms generally applied via software on general purpose processors, my research activity in the algorithmic domain is performed while taking into account potential future implementations. Therefore, it is natural to dedicate a considerable part of my research activity to the implementation of the derived algorithms. Indeed, in collaboration with colleagues specialized in hardware implementations, 4 PhDs took place on following the IAS approach on algorithms addressing coded modulations and waveform design.

In the following, for each topic a motivation for the performed work will be given, showing what is missing from the state-of-the-art, followed by the list of contributions through the performed technical work. Most important results are shown next followed by one or

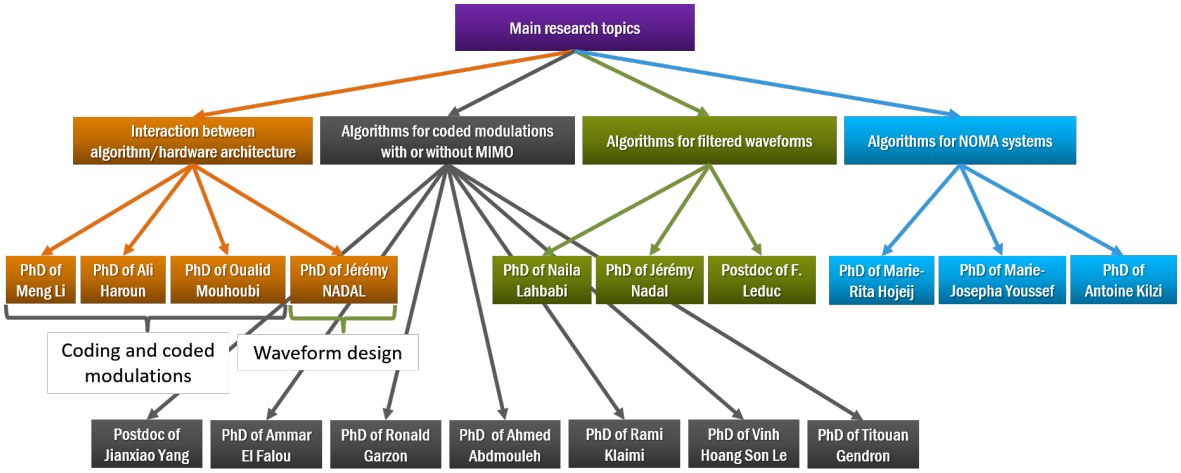

Figure 6: Map of the research activities since the beginning of my PhD

more impacting publications on the subject. Finally, the dissemination effort regarding the obtained results is provided.

Performed work on implementation targets algorithms proposed for one of the other topics as shown in Fig. 6. Therefore, the implementation work will be presented in the coding-related and waveform-related sections.

Chapter 1

Algorithms for coded modulations with(out) MIMO

1.1 Introduction and motivation

After my PhD defense in 2008, I have been deeply involved in the definition of Ffour different second-generation Digital Video Broadcasting (DVB) standards: the terrestrial fixed and mobile components DVB-T2 [1], DVB-T2 Lite [1] and DVB-NGH [2], in addition to the second generation of Return Channel Satellite DVB-RCS2 [3]. The work on the terrestrial fixed and mobile components was a direct extension of the second part of my PhD work, which focused on coded modulation schemes applying advanced constellation design and signal space diversity, or namely "rotated constellations", to approach capacity and improve robustness against severe channel conditions with deep fades. Through my extensive involvement in several Celtic EU (B21C and ENGINES), EU Eurostars (SME42 and ETNA), ANR (M3) projects and collaborations with other academic partners ranging from late 2007 to 2013 (until late 2017 for the collaborations) as detailed in Table 1, I had the chance to personally work on the refinement of the work done during my PhD and to co-supervise several PhD students and post-doctoral fellows as shown in Fig. 6.

To further increase throughput of real systems, the study of the introduction of multiple antenna schemes in the presence of channel coding complemented these studies at a later stage.

After the definition of second generation broadcasting standards, the focus shifted to the definition of 5G systems and beyond. Of a different type, the study items were naturally different from the ones for broadcasting standards with different sets of constraints. In concrete terms, the accent was put simultaneously on designing flexible (in frame size and coding rate) coding schemes, on achieving low error floors and on attaining high throughput with efficient hardware. In the context of the PhDs of Ronald, Rami, Vinh Hoang Son and Titouan, we have tried to achieve these multiple objectives by focusing on the design of binary and non-binary Turbo codes. Note that the non-binary variant may also be suitable for next generation broadcasting systems due to the increased capacity of symbol-based coded modulations when compared to their bit-based counterpart and to their improved asymptotic performance.

1.2 Diversity, constellation and mapping for broadcasting standards

1.2.1 Context and prior art

The emergence of new market driven services such as high definition television and 3DTV have offered unprecedented user experience creating a real need for improving transmission systems. A better use of the scarce spectrum resources became a must, leading to the development of the second generation broadcasting systems. Single Frequency Network (SFN) is a way to increase spectral efficiency. It consists of a broadcast network where several transmitters simultaneously send the same signal over the same frequency channel. While spectrally efficient, such a topology can lead to a severe form of multipath propagation. Indeed, the receiver sees several echoes of the same signal and the destructive interference among these echoes known as self-interference may result in additional fade events. This is problematic especially in wideband and high data rate digital communications, since the frequency-selective fading and the Inter-symbol Interference (ISI) caused by the time spreading of the echoes greatly deteriorate system performance in terms of Bit Error Rate (BER).

Spectral efficiency should not come at the price of reduced robustness. Therefore, numerous technical aspects are to be improved from first generation systems including source coding, channel coding, interleaving, modulation, diversity etc. In 2008, the work on the definition of the DVB-T2 standard was launched. This second generation introduced several enhancements to the transmission system including the 4th generation of the Moving Picture Experts Group (MPEG4) source coding, multiple physical layer pipes, and a state-of-the-art forward error correcting (FEC) code: Low Density Parity Check (LDPC) [4] + Bose Ray-Chaudhuri Hocquenghem (BCH) [5]. Incresed diversity was also introduced by a longer channel interleaver and the adoption of a diversity technique at the signal space level, a Multiple Input Single Output (MISO) Alamouti [6] based-scheme, etc.

The contributions related to this context are described in section 1.2.2, but as a first step, the following sub-sections describe the prior state of the art and/or the issues to be solved for each topic under consideration.

1.2.1.1 Coded modulation and diversity techniques

The work performed in this context focuses on signal-space diversity techniques and their association with the FEC decoder at the receiver side. Reliable transmissions over channels with deep fades require the increase of the diversity order. In 2008, the Bit-Interleaved Coded Modulation (BICM) principle [7] introduced by Zehavi in [8] represented the state of the art in coded modulations over fading channels. At the receiver side, an iterative exchange of information between the FEC decoder and the constellation demapper can be implemented in order to further improve the reliability of the transmission. This was first studied in [9] where a BICM scheme with Iterative Demodulation or Demapping (BICM-ID) was proposed, using a convolutional code with additional soft feedback from the Soft-Input Soft-Output (SISO) decoder to the constellation demapper. Later, in [10], the authors investigated different mapping techniques suited for BICM-ID and 16-QAM constellations. They proposed several mapping schemes providing large coding gains. In [11], the convolutional code classically used in BICM-ID schemes was replaced by a Turbo code, but only a small gain of 0.1 dB was observed. These findings suggested that BICM-ID was not appropriate for Turbo-like coding solutions even though the added complexity is relatively small.

On another note, the Signal Space Diversity (SSD) principle introduced in [12, 13] is a means of increasing the diversity order of BICM schemes over fading channels. While a known

concept since 1997, this principle had never been studied and published with advanced FEC code solutions such as Turbo or LDPC codes before our work [14].

1.2.1.2 Signal space diversity and receiver implementation

Thanks to our work and action in standardisation, SSD or more precisely rotated constellations were adopted in the DVB-T2 standard in 2011. Logically, the need for efficient hardware implementations followed. The main objective of a study we initiated on the topic was to design a DVB-T2 compliant receiver with an acceptable hardware complexity.

While improving performance, SSD introduces additional complexity especially for spectrally efficient constellation sizes. DVB-T2 was the first standard to adopt signal space diversity with high order constellations such as 256-QAM. In this case, the classical one dimensional Max-Log demapping algorithm applied on $log(M)$ Pulse Amplitude Modulation (PAM) based on de-coupling the I and Q components is not applicable. The quest for a hardware efficient SSD demapper was raised and not addressed before our study.

On the other hand, the implementation of the LDPC codes adopted in DVB-T2 is tricky, due to the double diagonal sub-matrices observed in their parity-check matrices. They induce memory update conflicts in the shuffled LDPC decoding architecture, which consequently causes inefficient message passing between the check nodes and bit nodes. These are crucial problems that have to be addressed when designing an LDPC decoder dedicated to the DVB-T2 standard.

A classical iterative receiver is frame-based, which induces large latency. The latency is introduced by the interleaving/de-interleaving block, which is based on memory writing and reading. The latency is also due to the state-of-the-art LDPC decoding algorithm (horizontal layered decoding algorithm). Indeed this algorithm provides the extrinsic information only after one complete iteration. Therefore, one iteration of a classical receiver consists of one complete iteration of LDPC decoding, de-interleaving memory writing and reading, demapping and interleaving memory writing and reading. The resulting large latency prohibits any efficient message exchange between the demapper and decoder, hence reducing the throughput.

All these issues were addressed in the context of the PhD thesis of Meng Li supported by the EU Eurostars SME-42 project. The designed receiver supports both non-iterative process and iterative process. The iterative receiver was studied even though practical applications are generally reluctant to mandate solutions based on iterative processes due to some challenges and constraints in terms of increased hardware complexity, memory access conflicts and additional latency.

1.2.1.3 Channel emulation/simulation

Achieved gains by SSD greatly depend upon the encountered channel. Therefore, special attention was put on the accurate simulation of correlated fading channels. State-of-the-art Rayleigh fading simulators can be divided into three main categories: the Sum of Sinusoids (SOS) method, the filtering white Gaussian variables method and the Inverse Fast Fourier Transform (IFFT) method.

The first method described in [15, 16] involves the superposition of a number of sinusoidal wave components. Each component is represented by a group of amplitude, frequency, and phase values related to the Doppler spectrum. Once the group of values is initialized at the beginning of each simulation trial, it is then kept constant during the whole duration of the trial. When an on-the-fly sample generation is required, the number of independent sinusoid functions needed to generate statistically accurate Doppler variables is too high to be supported by real-time implementations. In addition, the periodic nature of the underlying

sinusoidal function introduces an unexpected correlation between samples when a long interval of time has to be simulated. In order to reduce the number of sinusoidal components, a low-complexity channel simulator was proposed in [17] by using a truncated subspace representation of the Doppler spectrum based on discrete prolate spheroidal sequences. This technique is useful for a hardware emulator, but only if a limited numerical precision is required.

The second approach consists of filtering a white Gaussian sequence by using a Doppler filter in time domain. It can be divided into two different methods depending on the filter types. In [18], a Finite Impulse Response (FIR) filter is used whereas in [19], an Infinite Impulse Response (IIR) filter is proposed. FIR filter-based simulators do not suffer from any numerical instability. However, the number of Doppler filter taps required to meet statistical requirements leads to a high computational complexity when the ratio between the sampling frequency and Doppler frequency is high. Whereas the IIR filter-based simulators could provide a solution with lower complexity, they do suffer from numerical instabilities. Nevertheless, some solutions are provided in [19] in order to mitigate this risk.

The third approach, based on the IFFT method, is described in [20, 21]. The corresponding simulator first multiplies a series of independent complex Gaussian variables by a frequency mask corresponding to the square root of the Doppler spectrum. Then, it performs an IFFT over the frequency domain sequence and obtains the time domain Doppler variates. Thanks to the use of IFFT, this approach is the most computationally efficient of all previous methods while providing remarkable statistical properties. Unfortunately, one important drawback resides in its block-oriented nature requiring all Doppler variates to be generated by a single IFFT and stored in advance. Memory requirements exclude its application to continuous transmissions and high sampling frequency systems with long simulation periods.

To summarize this part, an efficient approach for simulating correlated fading was still lacking in literature. Here is why we decided to tackle this issue.

1.2.1.4 Non-uniform constellations and corresponding demappers

A collaboration with professor Pablo Angueira from the University of the Basque Country (UPV/EHU) was initiated in the context of the PhD of Jon Barrueco on the possible improvements of a DVB-T2-like system for the definition of the third generation US broadcasting standard, ATSC 3.0. In this new generation standard, Non-Uniform Constellations (NUCs) [22] were introduced to provide performance gains up to 1.8 dB compared to classical QAMs. NUCs are designed to maximize the BICM channel capacity [23, 24, 25].

There are two possible NUC families: 1-Dimensional NUC (1D-NUC) and 2-Dimensional NUC (2D-NUC). 1D-NUCs were already included in DVB-NGH [26]. For uniform constellations, the standard algorithms for searching the closest point to the received observation can usually be simplified for easy hardware implementation. However, for NUCs, these simplified algorithms cannot be applied directly, increasing demapping complexity. Most existing demappers resort to exhaustive search with a complexity in $O(\sqrt{(}M))$ where M is the order of the constellation.

Unlike 1D-NUCs, 2D-NUCs cannot be created using two non-uniform PAM signals. This implies that the in-phase (I) and quadrature (Q) components of the constellation symbols are no longer independent. As a consequence, a two-dimensional demapper (2D-demapper) must be applied to each received symbol. In addition, the number of Euclidean distances to be computed for Maximum Likelihood (ML) demapping of 2D-NUCs increases notably with respect to the one required for demapping 1D-NUCs [27]. This fact results into a significant increase in demapping complexity for 2D-NUCs when compared to 1D-NUCs. However, 2D-NUCs provide larger spectral efficiency gains, approaching closely Shannon channel capacity limit for higher constellation orders. Therefore, ATSC 3.0 includes 2D-NUCs up to 256

constellation points. Nevertheless, higher order 2D-NUCs (1K, 4K) were discarded during the standardization process due to their excessive hardware complexity.

A literature review showed abundant proposals for complexity reduction in demapping algorithms for MIMO [28, 29, 30] and rotated constellations [31, 32, 33, 34]. However, prior to our work, there was only one technical contribution addressing demapping techniques for 2D-NUCs [27]. Now adopted in a standard, simplified high order 1D and 2D-NUC demappers became a practical need.

1.2.1.5 Advanced interleaving for improved system performance

State-of-the-art FEC codes are now able to approach Shannon capacity [35, 36], especially for transmissions over memoryless channels where errors are randomly distributed and statistically independent. In contrast, when FEC codes are used in transmissions over channels in which the signal undergoes impulsive noise (i.e., error bursts in a short period of time) and/or selective fading (i.e., interference in a short frequency interval), the error rate performance can be greatly degraded. One possible solution to such a problem involves spreading error patterns arriving in bursts among several FEC frames. Therefore, channel interleaving [37] can be introduced to uniformly distribute codewords in time and frequency, in such a way that the transmitted symbols subject to impulsive noise and selective fading do not end up in the same coded frame. In other words, channel interleaving allows the overall system to take advantage of the available time and frequency diversities from the encountered channel.

Although DVB-T included the OFDM modulation technique, the lack of time interleaving made the broadcast system perform poorly in mobile environments [38]. To overcome this limitation, the next generation DVB-T2 includes more elaborate channel interleaving structures. Indeed, DVB-T2 advocates the use of three interleavers [1]: cell interleaver, time interleaver and frequency interleaver. The implementation of each of them introduces further system latency. On the other hand, since the implementation of each type of interleaver requires a specific part of the memory, the whole interleaving memory can represent a large part of the silicon area and of the power consumption of the receiver. In addition, from a diversity point of view, a bad interaction between channel interleavers can introduce a degradation of the overall system performance. To deal with these issues, a new technique to analyze and design channel interleavers was developed.

1.2.2 Performed work and contributions

1.2.2.1 Signal space diversity design and action in DVB standardization

The performed work in the context of the DVB-T2 standard addressed first the issue of properly designing and associating SSD with a powerful outer FEC codes in order to achieve a level of gains justifying the paid corresponding demapper complexity. This was done during my PhD and my postdoctoral fellowship. It focused on the choice of the design criteria that were used to define the rotation angle of the QAM contellation. Moreover, an iterative process between a FEC decoder and a soft MIMO detector [39] or a demapper or an interference canceller has proven to improve performance. The iterative process between a rotated QAM demapper and a LDPC decoder was shown to improve performance after a careful selection of the iterative process scheduling. A description of the work, the considered system model and studied channel models are summarized in the publication entitled “Improving BICM Performance of QAM constellations for broadcasting applications” included hereafter and published at the International Symposium on Turbo Codes and related topics (ISTC) in 2008, which received more than 60 citations in Google scholar. An extension of the results was also published in [40].

The work performed in the included publication was the subject of several technical contributions to the DVB-T2 standard. A specific working group led by the British Broadcasting Corporation (BBC) was created specifically to finalize the technical aspects related to the adoption of rotated constellations and the DVB-T2 recommendations. The choices made in the publication have shown gains reaching more than 5.0 dBs under some severe cases. Therefore, **they were adopted in the standard and the iterative process at the receiver side was recommended in their implementation guidelines** in order to improve the performance over fading channel without and with erasures. The fading channel with erasures represents the case of a severe fading in SFN networks. These choices were also the subject of a **patent filing in 2008** [41] **that was delivered and recognized as essential for the standard**. This adoption brought a wide spread recognition, indeed a simple Google search of both terms Télécom Bretagne and DVB-T2 results in more than 1500 technical and news articles online. We can say that rotated constellations became the destinguishing technique used to promote the DVB-T2 standard as attested by the DVB scene magazine cover from 28/02/2011 shown in Fig. 1.1.

Figure 1.1: DVB Scene magazine cover from 28/02/2011 with emphasis on rotated constellations.

Improving BICM Performance of QAM constellations for broadcasting applications

Charbel Abdel Nour and Catherine Douillard
TELECOM Bretagne (Institut TELECOM), Lab-STICC Laboratory
Brest, France
Email: charbel.abdelnour@telecom-bretagne.eu and catherine.douillard@telecom-bretagne.eu

***Abstract*— A technique intended to improve the performance of bit-interleaved coded modulations over non Gaussian channels is presented. It introduces signal space diversity by the means of modifications to the constellation mapper and to the corresponding demapper. A rotation of the constellation is followed by a signal space component interleaving. Iterative processing at the receiver side is shown to provide additional error correction. This method outperforms state-of-the-art systems over flat fading channels and substantial gains with respect to bit-interleaved coded modulation are obtained for severe channel conditions. It has been adopted by the Digital Video Broadcasting European consortium in the upcoming next generation of digital terrestrial television, DVB-T2, for the 4-, 16-, 64- and 256-QAM constellations. The resulting improvement in performance can vary from 0.2 dB to several dBs depending on the order of the constellation, the coding rate and the channel model.**

I. Introduction

Next generation broadcast systems should be designed to satisfy the need of high data rate transmissions through improving the robustness to severe channel conditions. Reliable transmissions over channels with deep fades require the increase of the diversity order. The Bit-Interleaved Coded Modulation (BICM) principle [1] introduced by Zehavi in [2] currently represents the state-of-the-art in coded modulations over fading channels. The Bit-Interleaved Coded Modulation with Iterative Demodulation or Demapping (BICM-ID) scheme proposed in [3] is based on BICM using a convolutional code with additional soft feedback from the Soft-Input Soft-Output (SISO) decoder to the constellation demapper. In [4], the authors investigated different mapping techniques suited for BICM-ID and 16-QAM constellations. They proposed several mapping schemes providing large coding gains. In [5], the convolutional code classically used in BICM-ID schemes was replaced by a turbo code. Only a small gain of 0.1 dB was observed. This result makes BICM-ID with turbo-like coding solutions unsatisfactory even though the added complexity is relatively small.

The Signal Space Diversity (SSD) principle introduced in [6-7] improves the diversity order of BICM schemes over fading channels. While a known concept since 1997, this principle had never been studied and published with advanced Forward Error Correcting (FEC) code solutions such as turbo or LDPC codes before [8]. In this paper, the authors investigated the impact of introducing the SSD principle with a 16-QAM constellation and the Digital Video Broadcasting Return Channel Satellite (DVB-RCS) turbo code over a flat fading Rayleigh channel. They have shown by means of Extrinsic Information Transfer (EXIT) charts [9] that an additional improvement in performance is achievable when iterative demapping is applied even in the case of using turbo codes.

In our work, modifications to the original proposal of [6-7] are made in order to adapt the principle to the outer code solution and to increase the robustness of the receiver to severe channel conditions. For this purpose, deep fades have been introduced into the channel model, that can be seen as erasure events at the receiver side.

In addition, another light is shed onto iterative demapping when associated with the SSD principle explaining the additional improvement in performance.

This paper is organized as follows:

In section 2, we present the channel model considered in this study.

In section 3, we start by a brief description of the BICM principle followed by a presentation of the studied SSD method. Introduced modifications to the mapper and its associated demapper are then detailed. We finally show that the proposed SSD technique can be viewed as the application of a repetition code, thus justifying the interest of iterative demapping at the receiver side.

Section 4 describes the adaptation of this SSD technique to actual transmissions systems, especially for broadcasting applications. In particular, it details the criteria adopted for the choice of the rotation angle.

Section 5 presents some simulation results corresponding to DVB-T2 transmission scenarios.

Section 6 concludes the paper.

II. The channel model

Two different channel types have been considered: the classical Rayleigh fading channel and a variation of this channel to which we have added additional deep fade events. Both are based on the fading channel model of [8]. The channel model with deep fades is representative for broadcasting applications over Single Frequency Networks

This work has been carried out in the framework of the CELTIC B21C European project.

(SFN). SFN, where several transmitters simultaneously send the same signal over the same frequency channel, is increasingly used in broadcasting applications due to the efficient usage of the radio spectrum. Consequently, in addition to multipath in the case of a single transmitter, several echoes of the same signal are also received due to presence of several transmitters. The constructive or destructive among these echoes, also known as self-interference, results in additional deep fades. This is problematic especially in wideband and high data-rate digital communications since the fading becomes frequency-selective and since the time spreading of the echoes may result in Inter-Symbol Interference (ISI).

One solution to selective fading is the introduction of Orthogonal Frequency-Division Multiplexing (OFDM) modulation. It divides the spectrum into several sub-channels each with a different frequency. Consequently, although the fading is frequency-selective over the whole frequency channel, it can be considered as flat within the narrowband sub-channel. In addition, the insertion of guard intervals between symbols is one way to eliminate ISI.

Although the resulting channel can be considered flat, some sub-channels are subject to such deep fades. Frequently, they have a dynamic range beyond the reach of a standard receiver due to quantization error. In this case, deep fades can be modeled by erasure events causing a significant performance penalty.

A. The classical Rayleigh fading channel model

The transmission channel under study is a frequency nonselective memoryless Rayleigh fading channel. The received discrete time baseband complex signal y_t can be written as:

$$y_t = \rho_t x_t + n_t \tag{1}$$

where x_t is the complex transmitted signal, ρ_t is a Rayleigh distributed fading coefficient with $E(\rho_t^2)=1$, and n_t is a complex white Gaussian noise with spectral density $N_0/2$ in each component axis. We assume coherent detection and perfect Channel State Information (CSI) knowledge so that ρ_t and the phase of the signal are perfectly estimated and available at the receiver.

B. The fading channel model with erasures

This channel model has been used to model the destructive interferences caused by SFN in the case of the upcoming DVB-T2 standard. In addition to the classical Rayleigh fading described above, additional erasure events affect the transmitted signal. If a properly designed time/frequency interleaver is inserted between the QAM mapper and the OFDM modulator, the erasure events can be modeled by a discrete random process e_t taking value 0 with a probability of P_e and value 1 with a probability of $1-P_e$. The received discrete time baseband complex signal y_t becomes:

$$y_t = \rho_t e_t x_t + n_t \tag{2}$$

Erasure ratios up to 15 % $(P_e = 0.15)$ have been considered in the context of DVB-T2. Note that, at the receiver side, the transmitted energy has to be normalized by a $\sqrt{1-P_e}$ factor in order to cope with the loss of transmitted power.

The occurrence of erasure events sets a bound on the coding rate R. In fact, with an erasure probability of P_e a reliable coded transmission cannot be ensured with a redundancy ratio lower than P_e, or in other words with a coding rate greater than $1-P_e$. This prevents the conventional system from operating at high coding rates in SFN.

III. SYSTEM DESCRIPTION

A. BICM system description

The BICM transmitter (cf. Fig. 1(a)) involves a serial concatenation of a FEC encoder, a bit interleaver π and a mapper.

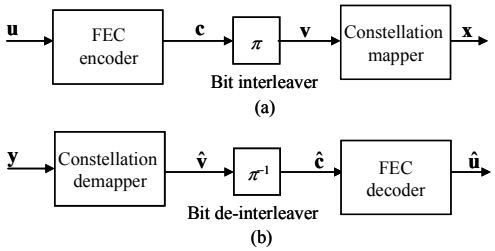

Fig. 1: the BICM structure (a) transmitter and (b) receiver

The information frame **u** goes through the FEC encoder to generate the codeword **c**. Afterwards, this sequence **c** is interleaved using the bit interleaver π to generate the mapper input sequence **v**. At time *t*, *m* consecutive bits of the interleaved sequence **v** are mapped to complex symbol x_t chosen from a 2^m-ary constellation χ by an *m*-bit signal label μ_m:

$$x_t = \{(x_t^I, x_t^Q) \in \chi\} \tag{3}$$

where x_t^I and x_t^Q represent the in-phase and quadrature components of $x_t = \mu_m(v_t)$. When Gray mapping is used, a QAM scheme is reduced to two independent Pulse Amplitude Modulations (PAM) signals, each carrying *m/2* bits.

At the receiver side (cf. Fig 1(b)), the demapper computes the Log Likelihood Ratio (LLR) $\hat{v}_t^i$ related to the i^{th} bit of v_t:

$$\hat{v}_t^i = \log\left(\frac{\sum_{x_t \in \chi_1^i} \frac{1}{\sigma\sqrt{2\pi}}.\exp\left(-\frac{(y_t-\rho_t x_t)^2}{2\sigma^2}\right).P(x_t)}{\sum_{x_t \in \chi_0^i} \frac{1}{\sigma\sqrt{2\pi}}.\exp\left(-\frac{(y_t-\rho_t x_t)^2}{2\sigma^2}\right).P(x_t)}\right) \tag{4}$$

where σ^2 is the channel noise variance and χ_b^i represents the subset of constellation symbols whose i^{th} bit is equal to

$b, b \in \{0,1\}$. When the *a priori* probability $P(x_t)$ is unavailable at the receiver, an equally likely assumption is made ($P(x_t) = 1/2^{m/2}$). After de-interleaving, the LLRs of (4) are used as inputs to the SISO decoder. When the received signal y_t is erased, the LLR computation is updated accordingly. The corresponding Euclidean distance $(y_t - \rho_t x_t)^2$ is replaced by zero in (4).

B. Application of SSD to BICM

When a constellation signal is submitted to a fading event, its I and Q coordinates fade identically. Thus, in case of severe fading, the information transmitted on I and Q channels suffers from an irreversible loss. A means of avoiding this loss involves making I and Q fade independently while each carrying all the information regarding the transmitted symbol.

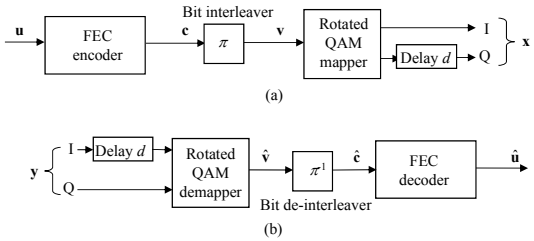

Fig. 2: the BICM-SSD structure (a) transmitter and (b) receiver

The SSD principle consists in introducing modifications to the mapper and demapper as shown in Fig 2. The QAM constellation is rotated by an angle α and the component axes are interleaved [7]. The rotation breaks the independence between the in-phase I and quadrature Q components of the constellation signal. In addition, the component interleaving results into sending the I and Q components of the same constellation signal in different symbol periods. Both transmitted components are threfore subject to two different fading coefficients, thus increasing the degree of diversity of the BICM scheme.

In the case of uncorrelated fading, the component interleaving can be reduced to a simple delay of one signal component with respect to the other. The delay value should be taken as a multiple of the symbol period. For memoryless channels, one symbol period is sufficient ($d = 1$).

The application of the SSD principle to BICM is straightforward. At the transmitter, the m-bit signal label $\mu_{r,m}(v_t)$ now takes into account the constellation rotation such that:

$$\chi_r = \left\{ \begin{array}{l} x_{r,t};\ x_{r,t} = \mu_{r,m}(v_t) = (x_{r,t}^I, x_{r,t}^Q) \\ \quad x_{r,t}^I = x_t^Q \cos\alpha + x_t^I \sin\alpha \\ \quad x_{r,t}^Q = x_t^I \cos\alpha - x_t^Q \sin\alpha \end{array} \right\} \quad (5)$$

After mapping, the quadrature component $x_{r,t}^Q$ of the rotated constellation signal $x_{r,t}$ is delayed of one symbol period with respect to $x_{r,t}^I$ before the transmission over the channel.

At the receiver side, the LLR computation has to take into account the introduced modifications. For Gray-mapped QAM constellations, the demapper now computes a two-dimensional Euclidean distance. The resulting $\hat{v}_t^i$ becomes:

$$\hat{v}_t^i = \log\left(\frac{\sum_{x_{r,t} \in \chi_{r,1}^i} F.\exp\left(-\frac{(y_t^I - \rho_{t-d} x_{r,t-d}^I)^2 + (y_t^Q - \rho_t x_{r,t}^Q)^2}{2\sigma^2} \right)}{\sum_{x_{r,t} \in \chi_{r,0}^i} F.\exp\left(-\frac{(y_t^I - \rho_{t-d} x_{r,t-d}^I)^2 + (y_t^Q - \rho_t x_{r,t}^Q)^2}{2\sigma^2} \right)} \right) \quad (6)$$

where $F = \dfrac{P(x_{r,t})}{\sigma\sqrt{2\pi}}$

If the received signal is erased, it is highly unlikely that both y_t^I or y_t^Q are erased due to the insertion of the delay d and only half of the corresponding Euclidean distance term is affected. For example, if y_t^I is erased, the corresponding term $\left(y_t^I - \rho_{t-d} x_{r,t-d}\right)^2$ should be replaced by zero in (6).

Without iterative demapping, an equally likely assumption is made for $P(x_{r,t})$. In the case of iterative demapping, the SISO FEC decoder computes extrinsic information on coded bits that are conveyed to the demapper after proper interleaving. The *a priori* symbol probabilities provided to the demapper are then obtained by combining the appropriate bit probabilities:

$$P(x_{r,t}) = P(\mu_{r,m}(v_t)) = \prod_{\substack{s=1 \\ s \neq i}}^{m} P(v_t^s) \quad (7)$$

C. Iterative demapping and SSD: another point of view

In this section, we provide an innovative point of view onto the introduction of iterative demapping when the SSD principle is used with BICM.

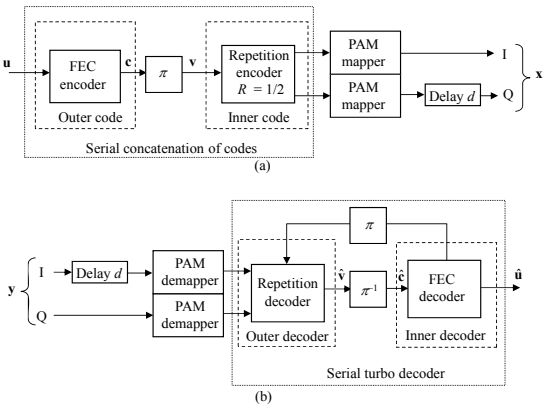

Fig. 3: an equivalent structure to BICM-SSD with a repetition code: (a) transmitter and (b) iterative receiver

Due to the rotation, the projection of the 2^m-ary QAM constellation on each signal component I or Q can be seen as a 2^m-ary PAM, carrying all the information regarding the m mapped bits. The insertion of the delay between I and Q leads to sending the same information twice over the channel at different symbol periods, as if an inner repetition code was used. The BICM-SSD structure can therefore be seen as a concatenation of an outer FEC code, a bit interleaver, an inner repetition code and a 2^m-ary PAM. In other words, the system is equivalent to a serially concatenated coded PAM as illustrated in Fig. 3(a).

At the receiver side, an additional improvement in error correcting performance can be seen if an extrinsic exchange of soft information is initiated between the outer and inner decoders as shown in Fig. 3(b). In other words, we end up with a serial turbo decoder.

IV. MODIFICATIONS TO IMPROVE SSD PERFORMANCE FOR BICM

The SSD principle for BICM was originally devised for fading channels. However this technique turns out to be also well adapted to channels with erasures. As mentioned in the previous section, the information related to a QAM constellation point is carried by two m-bit PAM symbols during two different symbol periods. Consequently, when an erasure event occurs, two PAM symbols are lost but they correspond to two different original QAM symbols. Therefore the transmitted bits can still be retrieved thanks to the added diversity.

In light of the presence of erasure events, some aspects of the original SSD principle have to be reconsidered. In previous studies, the choice of the rotation angle α was based on maximizing the so-called *product distance* [7] in order to minimize the pairwise error probability between two different transmitted sequences. This criterion was derived for fading channels. For the QAM modulations under study, it leads to $\alpha \approx 31.7°$. The second best value for 16-, 64-, and 256-QAM is $\alpha = 22.5°\,(\pi/8)$. Unfortunately, this criterion is only valid for asymptotical performance that is for high values of Signal-to-Noise Ratios (SNR). In practice, actual operating SNRs can be rather low, especially when powerful FEC coding is considered. Consequently, the product distance criterion turns out to be suboptimal for the SNR region of interest and the angle values mentioned above do not lead to the best actual coded performance. Moreover, for erased constellation signals, the distances are no longer two-dimensional because they are measured on the projection of the point on the non-erased axis, I or Q. In this case, a criterion based on a one-dimensional distance should be introduced.

For erasure channels without fading, the angle must be chosen such that the minimum distance between any two points of the constellation after projection over one of the component axes, $1D_{min}$, is maximized. This leads to having a uniform distribution for the projected constellation points. The corresponding angle value depends on the modulation order and is equal to $\alpha = \text{atan}\left(1/2^{m/2}\right)$ radians. Another advantage of this angle consists in having a quasi-Gray mapping for the projected constellation points.

To sum up, a properly chosen angle should try to cumulate the advantages of the angles designed for both fading and erasure channels.

A. Criteria for the choice of the rotation angle

The choice of the rotation angle should call for a compromise that suits a transmission over fading channels with and without erasure events. In order to satisfy this goal, the following design criteria are proposed:

- *The minimum product distance* (*PD)*: as already mentioned, this two dimensional distance should be maximized in order to minimize the asymptotical Bit Error Rate (BER) at the output of the demapper over fading channels without erasures.
- *The minimum 1-Dimensional Distance ($1D_{min}$):* in order to minimize the asymptotical BER at the output of the demapper in the presence of erasures, $1D_{min}$ should be maximized.
- *The average Hamming distance between any two adjacent constellation symbols ($d_{H,avg}$):* this is a mapping-related distance playing a role in the presence of erasures. In fact, when an erasure occurs, the projected constellation over a component axis no longer follows a Gray mapping. Depending on the rotation angle, the bit difference or in other words the Hamming distance between adjacent projected points varies. When the demapper is in error, the wrong symbol is chosen and respectively its projection. Since the mapping is different from a Gray mapping, a larger average number of bits will be in error. Consequently, in order to minimize the number of bits in error when a wrong constellation symbol is chosen, $d_{H,avg}$ should be kept as low as possible.
- *The Hamming distance between any two adjacent constellation symbols at distance $1D_{min}$ ($d_{H,1D}$):* it is based on a reasoning similar to $d_{H,avg}$. However, since at medium and high SNR regions the minimum distance $1D_{min}$ dominates error events, $d_{H,1D}$ should be chosen as low as possible in order to improve the BER at the output of the demapper in this region of interest.

As a summary, the "ideal" angle for fading channels with and without erasures would be the one that maximizes *PD* and $1D_{min}$ while minimizing $d_{H,avg}$ and $d_{H,1D}$. Unfortunately, in practice, these criteria are in conflict and their simultaneous application leads to different values of the angle. Thus, a compromise is inevitable.

Fig 4 shows a graphical representation of the distance measures as a function of the rotation angle in the case of 16-QAM. The results span only up to 45° due to symmetry. We have found $\alpha = 16.8°$ to be a good compromise angle.

Fig 5 compares the BER at the demapper output for

$\alpha = 16.8°$, $\alpha = 22.5°(\pi/8)$ and $\alpha = 14°$ (atan(1/4) rad) over fading channels with 15% of erasures.

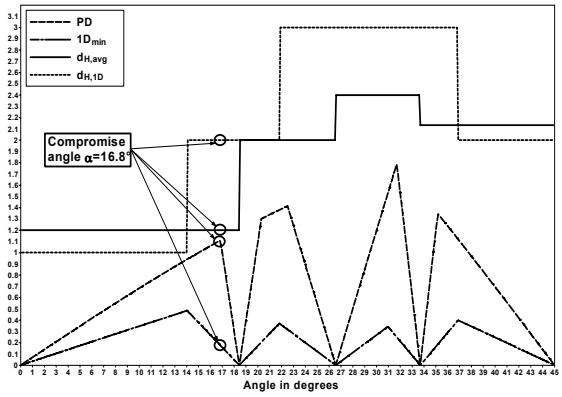

Fig. 4: graphical representation of the four distances used for the rotation angle selection for 16-QAM

Since the demapper output represents the input of the FEC decoder, the corresponding BER gives an insight into the behaviour of the coded system. In the context of DVB-T2, the DVB-S2 [11] LDPC code was adopted as FEC code. In the region of interest corresponding to the convergence threshold of this code for coding rates R lower than 9/10, the proposed angle $\alpha = 16.8°$ only suffers from a small penalty with respect to the optimum $\alpha = 14°$ angle. This penalty decreases with decreasing code rates (lower SNR regions).

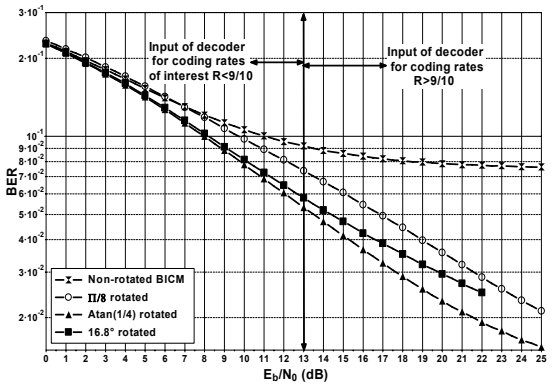

Fig. 5: BER at the output of the 16-QAM demapper respectively input of decoder for different angle values. Transmission over flat fading Rayleigh channel with 15% of erasures.

Fig 6 shows the BER at the demapper output for the angle values in Fig. 5 over a Rayleigh fading channel without erasures. At the operating point of the LDPC decoder for the typical code rate $R = 4/5$, the rotated system with the proposed $\alpha = 16.8°$ angle slightly outperforms all the other rotated systems. This remains true for a large range of coding rates.

The proposed approach has been extended to other modulation orders and the resulting angle values adopted in the DVB-T2 system are summarized in Table I.

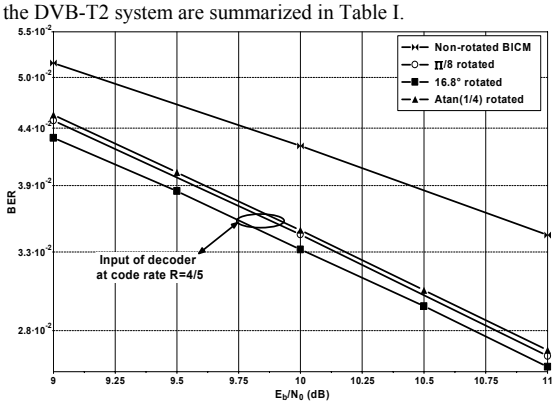

Fig. 6: BER at the output of the 16-QAM demapper for different angle values. Transmission over flat fading Rayleigh channel without erasures.

TABLE I
VALUES OF THE ROTATION ANGLE

Constellation	Rotation angle value in degree
QPSK	29.0
16-QAM	16.8
64-QAM	8.6
256-QAM	3.6

V. SIMULATION RESULTS

Simulations were carried out for the LDPC frame size of 64,800 bits. The decoder applies the sum-product algorithm [12] for a maximum of 50 iterations. When iterative demapping is used, feedback to the demapper is performed every LDPC decoder iteration. This choice keeps the same maximum number of decoder iterations as in the classical case. It has the advantage of offering the best error correcting performance while minimizing the impact on computation complexity. An S-random interleaver [13] was used as BICM interleaver.

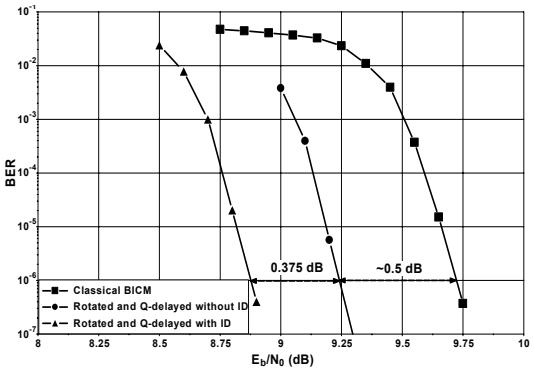

Fig. 7: BER at the output of the LDPC decoder for the proposed 16-QAM demapper with and without iterative demapping compared to the classical 16-QAM BICM scheme. Code rate $R = 4/5$ and 64,800-bit frames. Transmission over flat fading Rayleigh channel.

The curves of Fig. 7 show that the proposed system

outperforms the state-of-the-art BICM system over flat fading Rayleigh channel. It has around 0.5 dB gain at a BER of 10^{-6} when the rotation and the Q-delay are applied. It reaches nearly 0.9 dB when iterative demapping is introduced.

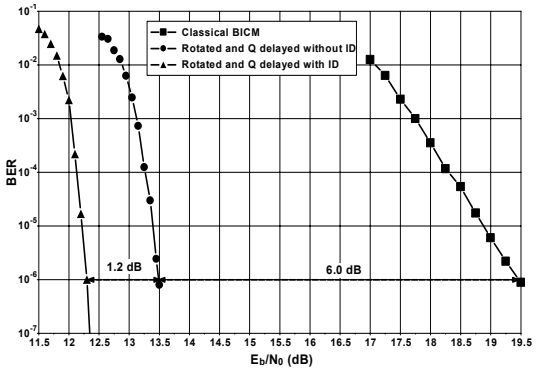

Fig. 8: BER at the output of the LDPC decoder for the proposed 16-QAM demapper with and without iterative demapping compared to the classical 16-QAM BICM scheme. Code rate $R = 4/5$ and 64,800-bit frames. Transmission over flat fading Rayleigh channel with 15% of erasures.

Fig. 8 extends the results of Fig. 7 to fading channels with 15% of erasures. In this case, we observe a substantial improvement in performance of 6.0 dB for the proposed system with respect to the classical BICM. It reaches 7.2 dB when iterative demapping is introduced. The steeper slopes predict a larger gain with increasing E_b/N_0.
Another important aspect to be noted is the robustness of the proposed system with respect to erasure events. In fact between Fig. 7 and Fig. 8, a penalty of only 3.2 dB is observed at 10^{-6} of BER when the erasure ratio reaches 15%. This loss reaches 9.7 dB for the classical BICM system.

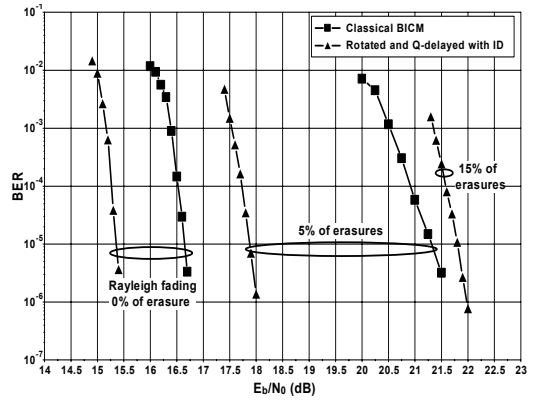

Fig. 9: BER at the output of the LDPC decoder for the proposed 64-QAM demapper with iterative demapping, compared to the classical 64-QAM BICM scheme. Code rate $R = 9/10$ and 64,800-bit frames. Transmission over flat fading Rayleigh channel with 0%, 5% and 15% of erasures.

Fig. 9 shows BER curves for a transmission over a flat fading Rayleigh channel without erasure, with 5% and 15% of erasures for a 64-QAM and a code rate of $R = 9/10$. Comments regarding simulation results of Fig. 8 apply as well for the curves of Fig. 9. Furthermore, we observe that the gain over BICM increases with the erasure ratio and that the proposed system is able to attain convergence with an erasure ratio of 15%. Note that this erasure ratio is beyond the theoretical value of $P_e = 1\text{-}R$, that is 10%. The curve related to the classical BICM system has been omitted for the case of 15% of erasures since the decoder does not attain convergence.

VI. CONCLUSION

In this paper we have proposed an approach to increase the diversity order of coded modulations over fading channels. It offers substantial gains with respect to classical BICM. This technique is well suited to severe channel conditions consequently improving the robustness of the receiver to deep fades and erasure events. It allows the reliable transmission of information for erasure ratios beyond the redundancy rate of the FEC code. Thanks to theses advantages, this technique has been adopted in the second generation Digital Video Broadcasting-Terrestrial standard.

REFERENCES

[1] G. Caire, G. Taricco, and E. Biglieri, "Bit-interleaved coded modulation," *IEEE Trans. Inform. Theory*, vol. 44, no. 3, pp. 927–946, May 1998.
[2] E. Zehavi, "8-PSK trellis codes for a Rayleigh channel," *IEEE Trans. Commun*., vol. 40, no. 5, pp. 873–884, May 1992.
[3] X. Li and J. Ritcey, "Bit-interleaved coded modulation with iterative decoding," *IEEE Commun. Lett*., vol. 1, no. 6, pp. 169–171, Nov. 1997.
[4] A. Chindapol and J. Ritcey, "Design, analysis, and performance evaluation for BICM-ID with square QAM constellations in Rayleigh fading channels," *IEEE J. Select. Areas Commun*., vol. 19, no. 5, pp. 944–957, May 2001.
[5] I. Abramovici and S. Shamai, "On turbo encoded BICM," Ann. Telecommun., vol. 54, no. 3, pp. 225-234, March 1999.
[6] X. Giraud, E. Boutillon, and J. C. Belfiore, "Algebraic tools to build modulation schemes for fading channels," *IEEE Trans. Commun.*, vol. 43, no. 3, pp. 938–952, May 1997.
[7] J. Boutros and E. Viterbo, "Signal space diversity: A power- and bandwidth-efficient diversity technique for the Rayleigh fading channel," *IEEE Trans. Inform. Theory*, vol. 44, no. 4, pp. 1453–1467, July 1998.
[8] C. Abdel Nour and C. Douillard, "On lowering the error floor of high order turbo BICM schemes over fading channels," in *IEEE Global Commun. Conf., GLOBECOM'06*, San Francisco, USA, Nov. 2006, pp. 1–5.
[9] S. ten Brink, "Convergence of iterative decoding, " *Electron. Lett*., vol. 35, no. 10, pp. 806–808, May 1999.
[10] W. C. Jakes, *Microwave Mobile Communications*, Wiley-Interscience, May 1994.
[11] DVB-S2, "Second generation framing structure, channel coding and modulation systems for broadcasting, interactive services, news gathering and other broadband satellite applications," *ETSI EN 302 307 V1.1.2*, 2006.
[12] N. Wiberg, H.-A. Loeliger, and R. KötterKotter, "Codes and iterative decoding on general graphs," *Eur. Trans. Telecomm*., vol. 6, pp. 513–525, Sept./Oct. 1995.
[13] C. Fragouli and R. D. Wesel, "Semi-random interleaver design criteria," *IEEE Global Telecommun. Conf., GLOBECOM'99*, Rio de Janeiro, Brazil, Dec. 1999, pp. 2352–2356.

1.2.2.2 Signal space diversity and receiver implementation

After the success of the adoption in DVB-T2, the next work during the PhD thesis of Meng Li focused on the design and implementation of a DVB-T2 BICM receiver with high hardware efficiency and implementing both non-iterative and iterative processing. The obtained results in algorithm design and hardware implementation demonstrated the potential of an iterative receiver as a practical and competitive solution for the DVB-T2 standard.

First, we have addressed the issue that the demapping algorithm for a rotated QAM constellation should be two-dimensional, which requires a large number of multiplications, especially for high-order constellations. In order to reduce the computational complexity, we proposed a Max-Log two-dimensional demapping algorithm based on sub-region detection. This algorithm reduces the number of required computations. The proposal of linear approximation of Euclidean distance further reduces the number of multiplications. This work was published in [34].

Based on these two contributions, a flexible demapper was implemented and tested. It supports the eight different DVB-T2 constellations over an AWGN channel, a fading channel with and without erasures. The demapper can be easily extended to higher order constellations, such as 1024-QAM constellation or 4096-QAM constellation adopted in the DVB-C2 standard.

Then, in order to reduce the latency of the message exchange between the demapper and the LDPC decoder in the case of an iterative receiver, a Min-Sum vertical shuffled LDPC decoding algorithm has been proposed to provide fast generation of extrinsic information. In addition, the methods to avoid memory access conflicts due to pipelining and message update conflicts due to double diagonal sub-matrices have been developed for the vertical shuffled LDPC decoder. This work was published in [42, 33].

A digital communication setup, including source generator, LDPC encoder, bit interleaver, mapper, channel emulator, equalizer, demapper, bit de-interleaver, LDPC decoder and BER calculator, was implemented onto one FPGA device (Xilinx Virtex 5) on an emulation board (DN9000K10PCI). We were able to verify the performance of the algorithm and architecture design of the demapper and LDPC decoder over an AWGN channel and a fading channel with and without erasures. The demapper and LDPC decoder have also been integrated onto a real DVB-T2 demodulator provided by the Teamcast company. The performance measures have been performed in a real environment provided by Teamcast and funded by the SME42 project, which included a real demodulator, a channel emulator and the demodulator. Measurement results have demonstrated the efficiency of the demapper and the LDPC decoder. The corresponding demonstrator shown in Fig. 1.2 represented the first published DVB-T2 receiver [33] and was exhibited at the International Broadcasting Convention (IBC) in 2010. A typical system configuration is selected in the developed Graphical User Interface (GUI) as shown in Fig. 1.3a. An example of the received rotated constellation is displayed in Fig. 1.3b.

Afterwards, we proposed a joint vertical shuffled iterative demapping and decoding algorithm to reduce the processing latency of an iterative receiver. The main idea of our proposal relies on dividing the whole frame into sub-frames and applying iterative processing on every sub-frame. This is achieved by using vertical shuffled LDPC decoding to provide a fast generation of extrinsic information and by using a Look-Up Table (LUT) based interleaving/deinterleaving to provide a fast routing of information between the demapper and the decoder. Several message exchange schedules were investigated. An efficient schedule that is suitable for hardware implementation was developed and the corresponding shuffled parallel iterative BICM receiver was designed and implemented onto an emulation board for QPSK constellation as a first step. This iterative receiver takes up around 50% of hardware resources in terms of RAM and logic slice of a Xilinx Virtex 5 LX330 device. The estimated maximum working frequency of the receiver is 80Mhz, which results in a throughput of 107 Mbps for

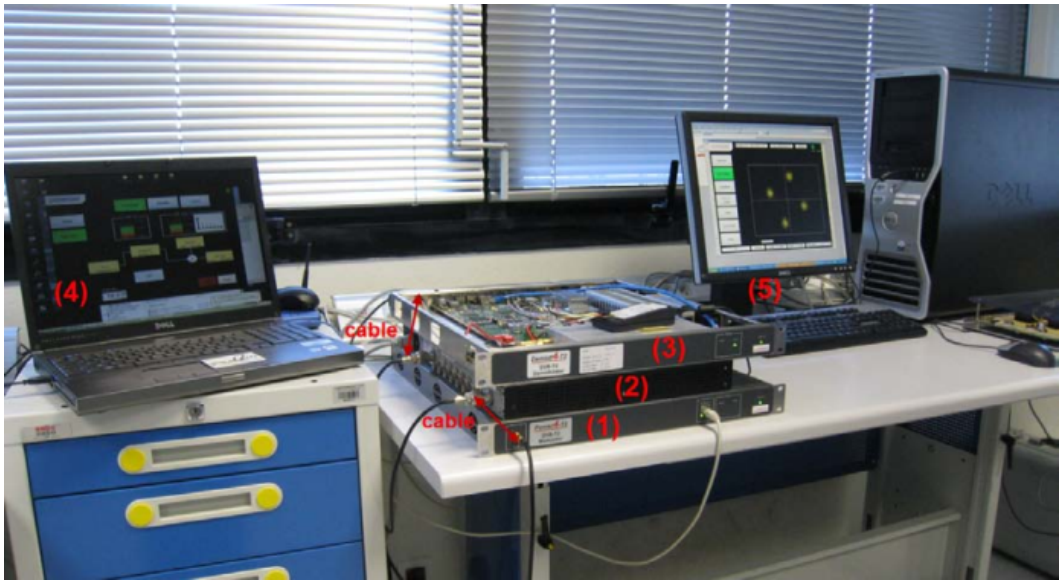

Figure 1.2: DVB-T2 transmitter, channel emulator and receiver of Teamcast integrating proposed BICM receiver demonstrated at IBC 2010.

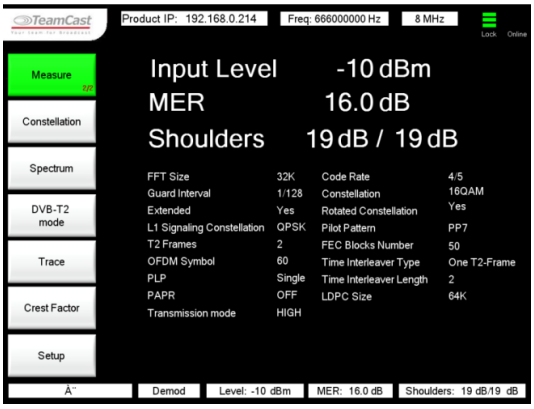

(a) Selection of system configuration.

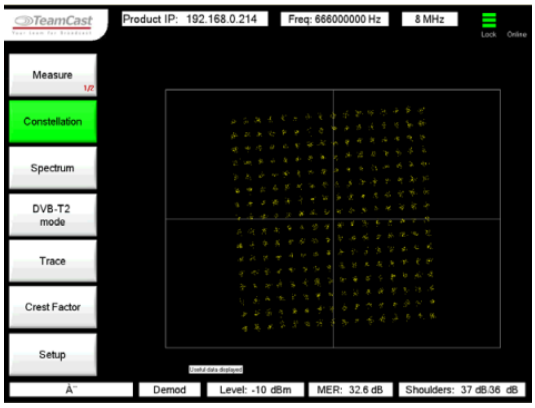

(b) Received rotated constellation.

Figure 1.3: The developed GUI for the demonstrator.

64K LDPC with a code rate of R=4/5. The measured performance achieved expected performance gains, which validated the efficiency of our proposal. To the best of our knowledge, this was the first hardware implementation of a BICM-ID receiver for the DVB-T2 standard. This work was published in [43, 44, 45, 46]. Morevoer, **the publication in the IEEE International Workshop on Signal Processing Systems (SIPS)** [46] **was attributed one of three best student paper awards in 2011**.

1.2.2.3 Channel emulation/simulation

Another part of the work focused on the efficient accurate simulation of elaborate multipath channel models suffering from correlated fading. This work was carried out in collaboration with Jianxiao Yang during his postdoctoral fellowship. A new fading channel simulator based on the Overlap-Save (OS) method was proposed. Based on Fast Fourier Transform (FFT) computations, this method improves the computation efficiency of direct filtering. In addition, overlapped sample processing overcomes the discontinuity problem of the classical IFFT method while retaining its advantages. Therefore, a real-time simulation of a contin-

uous transmission, meeting the statistical quality requirements, becomes of reasonable cost. Furthermore, by extending the application of the OS method to the interpolator, the resulting generator is capable of simulating very low Doppler frequencies with a practical sampling frequency. It is shown that simulated statistical qualities closely match theoretical predictions. Finally, the new simulator can be directly used to generate multiple uncorrelated stochastic fading processes (e.g., useful for multipath and multiple input multiple output channel simulation). This work was the subject of an IEEE Transactions on Wireless Communications journal publication in 2013 [47]. The corresponding hardware implementation is currently under submission at IEEE Transactions on Circuits and Systems II: Express Briefs for possible publication.

1.2.2.4 Non-uniform constellations and corresponding demappers

As a natural evolution, the study and proposal of innovative demapping techniques for NUCs was addressed in our collaboration with UPV/EHU during the visit of PhD candidate Jon Barrueco to our premises for 3 months.

- For 1D-NUC: We proposed a novel technique based on dividing the NUC into lattices of identical dimensions. The value of the received symbol is modified in order to provide an entry to a LUT where the closest point is stored. This solution provides low complexity for demodulation of the in-phase and quadrature PAMs of the NUC. The complexity is $O(2 + log(\sqrt{M}))$ while the exhaustive search is $O(\sqrt{M})$. The complexity implications in terms of memory, number of computations and system performance were analyzed. This work was published in [48].

- For 2D-NUC: A novel demapper combining two techniques based on condensation and adaptive sub-region for 2D-NUCs was proposed. It reduces latency when compared to state-of-the-art demappers [27]. Moreover, it shows a reduction in the number of Euclidean distances to be computed from 79.2% to 95.4% with respect to the ML demapper for 2D-256-NUCs, 2D-1024-NUCs and 2D-4096-NUCs. At the same time, error rate simulation results over AWGN, Rayleigh, DVBT-P1 and DVBT-F1 channels show comparable performance to ML demapping since the gap does not exceed 0.1 dB in all cases. This validation step includes ideal and non-ideal Channel State Information (CSI) conditions. The corresponding work was published in [49]. Since it represents our latests results on the subject, it is also included hereafter.

1.2.2.5 Advanced interleaving for improved system performance

Taking advantage of our experience in designing interleavers for Turbo codes in the context of the PhD thesis of Ronald Garzon-Bohorquez, we have presented a new method to design channel interleavers based on span properties and mutual information. It calls for a joint optimization of time and frequency span properties. A graphical representation of the span properties in a bi-dimensional L1 space can be used to efficiently parameterize interleavers. The Mutual Information (MI) distribution between FEC blocks was identified as a relevant selection criterion for channel interleavers. A suitable target is a homogeneous distribution of the MI in the FEC blocks. Thus, it is possible to select the best channel interleaver candidates according to the MI distribution variance, before running long BER simulations.

Improvements in the BER performance of the DVB-T2 chain can be achieved when using this approach, especially in poor channel conditions, such as in the presence of regular erasure patterns. Furthermore, the reduction in the number of channel interleaving components allows better control of the interleaver design parameters and provides reductions in system

latency and complexity. In transmission systems, it was shown that a good interaction between the bit interleaver and the channel interleaver can be achieved by using an appropriate constellation symbol mapping mask.

Resulting interleavers enjoy better burst error control and can mitigate the effect of regular error patterns. An application example based on DVB-T2 was elaborated. Four channel interleaving structures were generated, resulting from a joint optimization of the interleaver span properties in the time and frequency domains, while guaranteeing good interaction with the bit interleaver. Proposed solutions were compared to the standardized DVB-T2 channel interleaver in terms of performance, latency, and complexity. A significant improvement can be observed in severe channel conditions, especially over time and frequency selective channels with erasures. Moreover, the complexity and latency of the proposed channel interleavers are reduced compared to the original DVB-T2's. The corresponding results were reported in the ENGINES and M3 projects and were published in two conferences and in an IEEE Transactions on Broadcasting journal [50, 51, 52].

Low Complexity Adaptive Demapper for 2-D Non-Uniform Constellations

Jon Barrueco, *Member, IEEE*, Jon Montalban, *Member, IEEE*, Pablo Angueira, *Member, IEEE*, Charbel Abdel Nour, *Member, IEEE*, and Catherine Douillard, *Member, IEEE*

***Abstract*—In this paper, a novel demapper for 2-D non-uniform constellations (2D-NUCs) is proposed, exploiting the characteristics of these constellations. It represents the combination of two underlying demapping techniques targeting the ATSC 3.0 compliant OFDM transceiver. On the one hand, for low code rates, we define a metric to perform condensed demapping. On the other hand, for high code rates, adaptive sub-region demapping is proposed. In this paper, a combination of both demapping methods is designed showing comparable performance to the classical ML demapper. The gap does not exceed 0.1 dB for all code rates of the ATSC 3.0 standard. Higher complexity reduction, from 79.2% to 95.4%, than state of art 2D-NUC demappers is obtained for 2D-256NUCs. These results are validated for ideal and non-ideal channel state information over additive white noise Gaussian and Rayleigh independently and identically distributed channels. Results are extended to 2D-1kNUCs and 2D-4kNUCs showing demapping complexity reduction from 96% to 99.7% with a negligible impact on performance.**

***Index Terms*—ATSC 3.0, broadcasting, demapping complexity, non-uniform constellations.**

I. INTRODUCTION

INCREASING spectral efficiency of wireless broadcasting systems to get close to the channel capacity upper bound represents nowadays a major goal of many research projects worldwide. Techniques such as Multiple Input Multiple Output (MIMO) [1], Rotated Constellations (RC) [2] and Non-Uniform Constellations (NUC) [3] respond to this demand providing a good tradeoff between system capacity and bandwidth usage.

Manuscript received October 31, 2017; revised January 27, 2018; accepted February 2, 2018. Date of publication March 12, 2018; date of current version March 4, 2019. This work was supported in part by the Basque Government (PREDOC Program) under Grant IT-683-13, in part by the University of the Basque Country under Grant UFI 11/30, and in part by the Spanish Ministry of Economy and Competitiveness (Project 5G-newBROS) under Grant TEC2015-66153-P MINECO/FEDER, UE. *(Corresponding author: Jon Barrueco.)*

J. Barrueco and P. Angueira are with the Department of Communications Engineering, University of the Basque Country, 48013 Bilbao, Spain (e-mail: jon.barrueco@ehu.eus; pablo.angueira@ehu.eus).

J. Montalban is with the Department of Electronic Technology, University of the Basque Country, 20018 Donostia, Spain (e-mail: jon.montalban@ehu.eus).

C. Abdel Nour and C. Douillard are with the Institut Mines-Télécom/Télécom Bretagne, CNRS Lab-STICC, UMR 3192, 29238 Brest, France, and also with the Université Européenne de Bretagne, 29238 Brest, France (e-mail: charbel.abdelnour@imt-atlantique.fr; catherine.douillard@imt-atlantique.fr).

Color versions of one or more of the figures in this paper are available online at http://ieeexplore.ieee.org.

Digital Object Identifier 10.1109/TBC.2018.2811619

A paradigmatic standardization example is the newest digital terrestrial broadcasting system called ATSC 3.0 [4]. This standard adopts MIMO as an optional technology [5] and it also includes NUCs [6] to provide performance gains up to 1.8 dB (compared to classical Quadrature Amplitude Modulations (QAM)). NUCs are designed to maximize the Bit Interleaved-Coded Modulation (BICM) channel capacity [7]–[9].

There are two possible NUC families: 1-Dimensional NUC (1D-NUC) and 2-Dimensional NUC (2D-NUC). 1D-NUCs were already included in Digital Video Broadcasting Next Generation Handheld (DVB-NGH) [10] proposal. Unlike 1D-NUCs, 2D-NUCs cannot be created using two non-uniform Pulse Amplitude Modulation (PAM) signals. This implies that the in-phase (I) and quadrature (Q) components of the constellation symbols are no longer independent. As a consequence, a two-dimensional demapper (2D-demapper) must be applied to each received symbol. For 1D-NUCs, one-dimensional demapper [11], [12] can be applied significantly reducing the number of Euclidean Distances computed by Maximum Likelihood (ML) demapper with no system performance degradation. This fact results into a significant increase in demapping complexity for 2D-NUCs when compared to 1D-NUCs. However, 2D-NUCs provide larger spectral efficiency gains, approaching closely to Shannon's channel capacity limit for higher constellation orders. Therefore, ATSC 3.0 includes 2D-NUCs up to 256 constellation points. Nevertheless, higher order 2D-NUCs (1K, 4K) were discarded during the standardization process due to their excessive hardware complexity.

A literature review shows abundant proposals for complexity reduction in demapping algorithms for MIMO [13]–[15] and RCs [16]–[18]. However, to the best of our knowledge, there is only one technical contribution addressing demapping techniques for 2D-NUCs [19].

This work specifically targets low complexity demappers for 2D-NUCs. A novel demapper combining two techniques based on condensation and adaptive sub-region for 2D-NUCs is proposed. It reduces latency when compared to state of art demappers [19]. Moreover, it shows a reduction in the number of Euclidean distances to be computed from 79.2% to 95.4% with respect to the ML demapper for 2D-256NUCs, 2D-1kNUCs and 2D-4kNUCs. At the same time, error rate simulation results over AWGN, Rayleigh iid, DVBT-P1 and DVBT-F1 channels show comparable performance to ML demapping since the gap does not exceed 0.1 dB in all cases.

This validation step includes ideal and non-ideal channel state information (CSI) conditions.

The rest of the paper is organized as follows: Section II is a literature review of low complexity demapping techniques. Section III presents the characteristics of the 2D-NUCs. Section IV shows the proposed demapper analyzing its key parameters and the complexity reduction for each code rate. In Section V the system performance of the demapper is carried out using the BICM and OFDM platforms defined in ATSC 3.0 for ideal and non-ideal CSI. Finally, Section VI gathers the main conclusions of the paper.

II. Literature Review and Contribution

There are different families of demapping strategies depending on the following system features: the number of antennas, the application of signal space diversity techniques (SSD) and the specific constellation shape.

In the case of MIMO systems, three approaches have been explored. The first is based on the sphere decoder [20]–[23] while the second applies lattice reduction [24]–[26]. The third strategy focuses on using an approximation of the ED when looking for the minima in the LLRs computation [27], [28]. Although these demappers provide low complexity for MIMO systems, their use in SISO systems is not necessarily appealing since the number of operations associated to these demappers remains large with respect to the number of constellation points in the SISO system.

Another group of proposals are related to the specific shape of the constellation being demapped. Several algorithms have been specifically designed for systems using Amplitude Phase Shift Keying (APSK) modulation. A simplified soft demapper was created for this modulation in satellite systems [29]. This demapper decomposes the APSK into two different PAM signals which, again, is not directly applicable to 2D-NUCs. In [30] a simplified demapper was proposed for the Data Over Cable Service Interface Specification (DOCSIS) 3.1 [31] where non-square quadrature amplitude modulation schemes are used. In this case independence between several bits of the symbol is exploited to simplify the demapping process. Unfortunately, this approach is not applicable to 2D-NUCs where all the bits are dependent.

On a different research thread, the inclusion of the RC technique in DVB-T2 and DVB-NGH led to several studies of low complexity demappers. Kim *et al.* [32] reformulate the received rotated QAM as two PAM signals applying MMSE decorrelation. This technique is not applicable to 2D-NUCs because it is not possible to decorrelate I/Q components without high performance losses. Another family of demapping approaches reduces the area where Euclidean distances are evaluated. The latest proposal in this direction is a fixed sub-region demapper proposed in [33] and [34]. The result is a reduction in complexity ranging from 25% to 50% with variable performance losses. Another interesting result can be found in [19] where a sub-region demapper applicable to 2D-NUCs was proposed, following the foundations set by the previous results in [34]. This demapper provides low demapping complexity and low system performance losses when compared to the ML demapper for high code rates.

The authors of this paper have empathized contributions in three specific areas of demapping. First, there is still room for further optimization techniques in fixed region demappers targeting the invariable nature of the region size. The parameter defining the size of the region of interest is key in their performance. In previous works this parameter is kept constant for all the transmission/reception scenarios, no matter the SNR and the propagation channel scenario. Indeed, the dimension of the region is defined empirically and it will be a fixed feature of the modulation and the coding (MODCOD) choice at the design stage. The size of the area is calculated statistically from the system performance results around the vicinity of the Low Density Parity Check (LDPC) code waterfall region. In terms of network planning, this corresponds to tweaking the broadcast system depending on LDPC code threshold for the worst supported transmission channel scenario. In particular, the available SNR for most users will be significantly higher than the threshold SNR. Therefore due to high SNR users, the sub-region will be often too wide in terms of possible computation volume reduction. While this has been the use in traditional broadcast system design, an improved approach is feasible using our demapping proposal.

An additional limitation is associated to the propagation channel variations: the sub-region size optimization is carried out for a static situation and does not adapt to the channel type. This fact will result into system performance losses for some channel scenarios. Therefore, we propose a novel solution called adaptive sub-region demapper for 2D-NUCs with lower complexity and better system performance than constant sub-region demappers. The dimension of the region varies for each received symbol through adaptation to the characteristics of the MODCOD, perceived Signal to Noise ratio (SNR) and channel conditions.

Sub-region demappers do not provide any reduction in latency for low code rates, where they provide negligible complexity reduction. Authors in [19] and [35]–[37] propose to complement sub-region demapping with symbol condensation techniques to further reduce latency in these corresponding regions. Inspired by this proposal, we define a metric to appropriately condensate 2D-NUCs providing low demapping complexity with negligible performance losses. We propose to go one step further and limit the subregion algorithm to high SNR values, apply subregion plus condensation in the mid SNR range and keep simple condensation demapping on the low SNR range. Consequently, the demapper switches between these techniques depending on the corresponding system parameters.

III. Characteristics of 2D-NUCs

2D-NUCs are characterized by the complete freedom of movement of the constellation points during the design procedure. The number of degrees of freedom (DOF) when designing a M-ary 2D-NUC, where M is the constellation order, is $2M$. Already designed 2D-NUCs [3] present quadrant symmetry reducing the number of DOFs in the optimization

process to $\frac{M}{2}$. This full flexibility in the design process implies higher complexity at the demapping stage. The I and Q components are mutually dependent and a 1D-demapper is no longer valid. 2D-NUCs make use of the 2D-demapper, which presents higher complexity than the 1D-demapper in terms of the number of Euclidean distances to be computed. While ML-based 1D-demapper computes $\sqrt{M}$ Euclidean distances, the ML-based 2D-demapper computes M Euclidean distances.

The shaping of 2D-NUCs depends basically on the SNR value and channel model. The design factor with the largest impact of 2D-NUCs is the SNR value at which the NUC is designed. This value is directly related to the code rate at the waterfall region of the code as stated in [3]. The influence of the channel model slightly shifts the positions of the constellation points without modifying the overall shape of the constellation. Low SNR values correspond to low code rates and vice versa. 2D-NUCs designed for low code rates present several constellation symbols situated at the same position in the constellation diagram. This sort of constellations is called condensed 2D-NUCs [38], [39]. Condensation maximizes BICM channel capacity by favoring the capacity of the most significant bits (MSB) while sacrificing the capacity associated to the least significant bits (LSB), which in any case will be degraded by high noise values. Condensation with imperceptible capacity loss in 2D-NUCs is feasible in the low and mid code rate region.

2D-NUCs designed for the mid code rate region present circular shaping due to the maximization of the BICM channel capacity and to the application of quadrant symmetry. For high code rates, the constellation points are uniformly distributed along the constellation diagram. The shaping of 2D-NUCs for high code rates is similar to the uniform QAM.

IV. Proposed Demapper

In this section we define a condensation metric and present a study of the most appropriate value to provide low demapping complexity with negligible impact on performance for low code rates. For mid and high code rates, we propose an adaptive sub-region demapper. The combination of the two demapping techniques called Switched Condensed and Adaptive Sub-Region (SCASR) demapper is proposed providing lower demapping complexity than state of art 2D-NUC demappers with negligible impact on performance for all the code rate range. All the results shown in this section have been obtained using a fully compliant ATSC 3.0 BICM transceiver with 300 FEC blocks of length 64,800 bits [40]. Low density parity check (LDPC) code options ($R = 2/15$ to $R = 13/15$) included in ATSC 3.0 [41] are used. All the simulation results are obtained for BER $= 10^{-7}$.

A. Condensed Demapper Optimization

The condensed demapper takes advantage of the condensation applied to the 2D-NUCs designed for low and mid code rates [19], [35]. When designing a condensed demapper, the most important parameter is the condensation degree (or number of merged points) to be applied to the 2D-NUCs. Most of the 2D-NUCs included in ATSC 3.0 do not present complete condensation. Indeed, points are not merged, but close to each other.

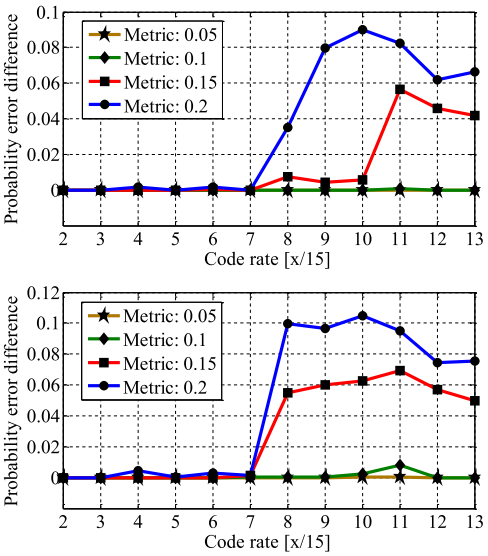

Fig. 1. Probability error difference between the ML and condensed demapper for ATSC 3.0 code rates for the AWGN channel (above) and Rayleigh iid channel (below).

The Euclidean distance between adjacent points is used as metric for condensation. Fig. 1 shows the bit error probability difference between the ML and the condensed demapper for different metric values (0.05, 0.1, 0.15 and 0.2). The bit error probability is calculated for the SNR threshold at LDPC waterfall region. ATSC 3.0 2D-256NUCs are analyzed for all code rates over AWGN and Rayleigh iid channels using the ATSC 3.0 BICM chain.

The condensed demapper presents similar bit error probability to the ML demapper for the four metric values and low code rates up to $R = 7/15$. In this region, 2D-256NUCs present the highest condensation degree. From $R = 8/15$ to $R = 13/15$ code rates the bit error probability for 0.15 and 0.2 metrics increases significantly. Condensation applied to 2D-256NUCs within this code rate range behaves poorly. The bit error probability penalty is even higher in the case of the Rayleigh iid channel. For both channels, the metrics 0.05 and 0.1 present similar error probability to the ML demapper (except for 0.1 at $R = 11/15$ code rate for Rayleigh iid channel).

Fig. 2 shows the reduction in terms of percentage of the number of Euclidean distances to be computed in the condensed demapper with respect to the ML demapper for all code rates. The complexity reduction increases with the value of the condensation metric. However, as shown in Fig. 1, the system performance gets worse as the metric increases. We propose to use a metric value of 0.05 as the best tradeoff between demapping complexity and system performance.

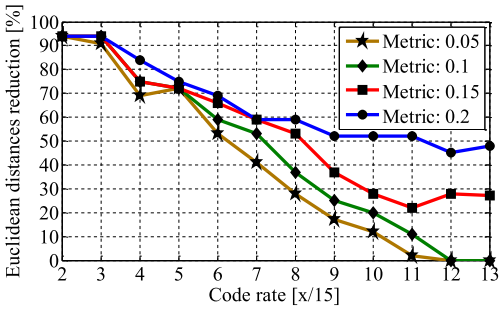

Fig. 2. Percentage of the Euclidean distances reduction between the ML and condensed demapper for ATSC 3.0 code rates.

B. Adaptive Sub-Region Demapper

The second demapper submodule makes use of the design methodology of 2D-NUCs [3]. As shown in Section III, 2D-NUCs are obtained as a function of the operating SNR and the considered channel model. An adaptive sub-region demapper with a variable region size depending on these two parameters is proposed. The size varies for each received constellation symbol.

1) Concept and Functional Diagram of Adaptive Sub-Region Demapper: The adaptive sub-region demapper is based on computing the Euclidean distances between the received symbol and the symbols inside a square sub-region of the constellation diagram with a determined length. In the case of 2D-NUCs, we propose a square sub-region varying with the operating SNR and considered channel model. In this way, the length of the sub-region closely fits the design conditions of each 2D-NUC, providing an efficient demapping process.

Fig. 3c depicts the functional diagram of the adaptive sub-region demapper. The first demapping step consists of calculating the length d of the sub-region (Section IV-B2) for each received symbol. In parallel, in order to calculate the closest constellation symbol to the received symbol, two processes are considered. First, a sign check of each component of the received symbol will determine the quadrant choice. The sign check is stored in K_I (in-phase) and K_Q (quadrature). Then, the I and Q components of the closest constellation symbol to the received symbol are obtained (C_I and C_Q) following the procedure described in Section IV-B4.

In the second step, using the I and Q components of the closest symbols (C_I and C_Q), the I and Q components of the symbols inside the sub-region are obtained and stored in arrays $\mathbf{S_I}$ and $\mathbf{S_Q}$, respectively (Section IV-B4).

The final step consists of merging the I and Q components of the symbols inside the sub-region, obtaining the constellation symbol set to calculate LLR values. These symbols are stored in the array $\mathbf{S}$.

A graphical description behind the idea of the adaptive sub-region demapper is shown in Fig. 3a and Fig. 3b. For simplicity, the optimal 2D-16NUC for 8 dB of SNR is considered. This constellation is composed of 16 symbols S_i where $i = 1 \dots 16$. Each symbol has one I and Q component associated S_{Ii} and S_{Qi}. Fig. 3a shows a graphical representation of the sub-region demapper for components I and Q. For the I component, the sub-region is limited by the I components of the constellation symbols inside the sub-region of length $2d$ centered at ry, where ry is the real part of the received symbol. In this case, these components are S_{I1}, S_{I2} and S_{I3}. The real part of the transmitted symbol is represented as rx. The same applies for the Q components, being S_{Q1},S_{Q2} and S_{Q6} the Q components of the symbols inside the sub-region. Fig. 3b shows the sub-region in the constellation diagram and the symbols inside it. The transmitted symbol is represented as x and the received symbol as y. Symbols S_1, S_2 and S_6 are inside the sub-region for the particular x and y symbols.

2) Length of the Square Adaptive Sub-Region Demapper: The value of the length of the sub-region is based on having, at least, the transmitted symbol inside the sub-region. Constellation symbols situated at the limit of the sub-region are also included. Equation (1) shows the calculation of the received symbol in a communication system with Gaussian noise for a determined channel.

$$y = hx + n \tag{1}$$

where y is the received symbol, x the transmitted symbol, n the noise value (in this case Gaussian noise is assumed) and h the fading coefficients of the channel. All the parameters are complex values. Manipulating (1), the position of the transmitted symbol x is obtained as:

$$x = \frac{y}{h} - \frac{n}{h} \tag{2}$$

The first term $\frac{y}{h}$ refers to a zero forcing equalization. Manipulating the second term in (2), we derive the length of the sub-region d in (3). This length is calculated for each received symbol, i.e., it adapts to the channel and noise variations.

$$d = \left| \frac{(l + jl)\sigma}{h} \right| \tag{3}$$

where σ is the standard deviation of the Gaussian distribution and l is the maximum random value which determines the percentage of values that lie within a band around the mean in a normal distribution. As shown in (3), the value of the length is directly proportional to the noise value. The higher the noise value the higher the length value and vice versa.

3) Design of Adaptive Sub-Region Demapper: The adaptive sub-region demapper presents a series of special cases. The first case is considered when there is no symbol inside the sub-region. In this case, the length of the sub-region is increased until at least, two symbols are inside. Second, in the calculation of the log-likelihood ratio (LLR) values for each transmitted bit, the conditional probability of receiving y given that the b_i transmitted is 0 $p(y|b_i \text{ is } 0)$ and the conditional probability of receiving y given that b_i transmitted is 1 $p(y|b_i \text{ is } 1)$ are needed. However, it can occur that for a determined b_i all the symbol values inside the sub-region are 0 or 1 for that particular bit. In this case, taking into account that a FEC soft decoder performs better under pessimistic assumptions (consider one symbol as if it was closer than its real position) the conditional probability of the missing bit value is calculated

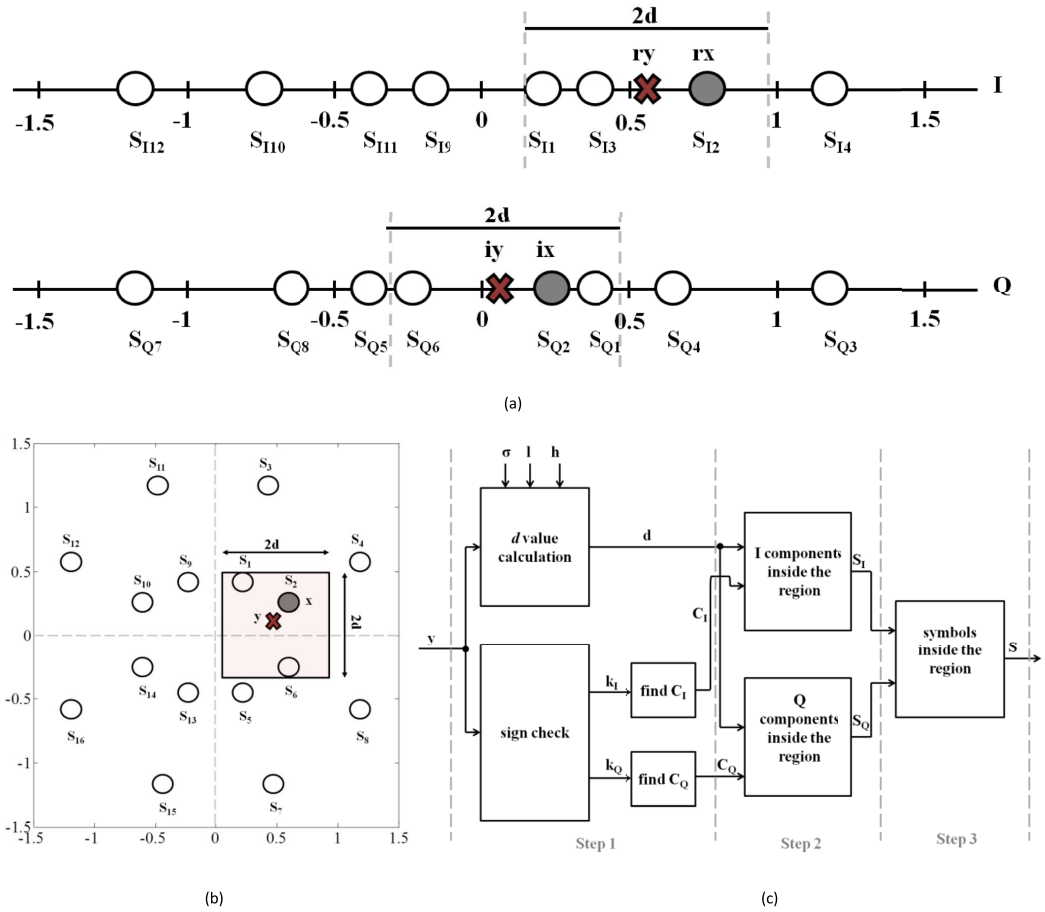

Fig. 3. a) In-phase and quadrature representation of the adaptive sub-region demapper for 2D-16NUC at 8 dB. b) Constellation diagram representation of the adaptive sub-region demapper for 2D-16NUC at 8 dB. c) Functional diagram of the adaptive sub-region demapper.

for the furthest symbol inside the sub-region. This can derive into both conditional probabilities with the same value if the Euclidean distances are the same for both bit values. This is solved by increasing the length value and forcing that there are, at least, two symbols with different Euclidean distances.

This solution performs efficiently for low and mid code rates (up to $R = 9/15$). However, for higher code rates, system performance gets worse. For low code rates, the sub-region covers mainly the totality of constellation points and this demapper does not reduce complexity. For high code rates the sub-region only covers part of the constellation diagram and the case explained above in which one bit value is not inside the sub-region commonly happens for the two MSBs. In this case, another approach is proposed: compute the Euclidean distance from the received point y to the origin of the constellation diagram (0+0j) since it represents the intersection of the four quadrants. This option requires only one Euclidean distance to be computed. As shown in Section V, this solution has negligible impact on the demapping complexity and system performance.

Fig. 4 shows the percentage reduction in the number of Euclidean distances to be computed w.r.t. ML demapper. For low code rates, limited reduction is observed. In this zone, where the noise components are high, the length of the sub-region is highly increased gathering almost all the constellation points. In the region of mid code rates, as the noise value is lower, the number of points inside the sub-region is lower and the number of Euclidean distances to be computed is reduced. High code rates present the highest complexity reduction as the length of the sub-region is highly reduced.

The adaptive sub-region demapper proposed in this section provides high demapping complexity reduction in the region of mid and high code rates with negligible performance loss. A complexity reduction from 60% for $R = 7/15$ to 95% for

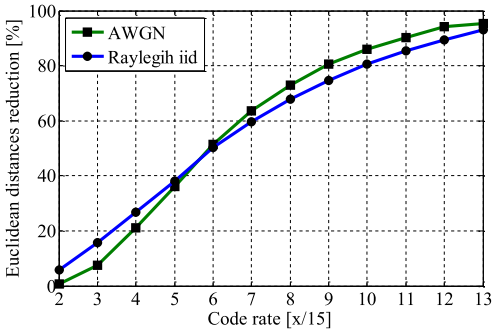

Fig. 4. Percentage of the Euclidean distances reduction between the ML and adaptive sub-region demapper for ATSC 3.0 code rates for the AWGN and Rayleigh iid channels.

$R = 13/15$ is achieved. In order to decrease the complexity for low and mid code rates, a combination of the adaptive sub-region and condensed demapper is proposed (Section IV-C).

4) Determination of Points Inside the Adaptive Sub-Region: The efficient determination of the points inside the sub-region is a key aspect. We propose a methodology based on finding the closest constellation symbol to the received symbol. Then, a comparison process starting from this symbol is performed in order to determine the first point outside the sub-region.

The procedure is explained for one axis (I) and the methodology is then repeated for the other axis (Q). First, a sign check of the I component of the received symbol is performed in order to determine the quadrant. Next, dichotomy process is applied to the real part of the constellation points in order to determine the closest constellation point to the received point. The dichotomy process consists of dividing the set of I components into two subsets with equal number of components. The I component of the received symbol is compared with the limit value of the two subsets. A subset is chosen based on this comparison. An iterative procedure is performed until there is only one I component in the subset. This I component belongs to the closest symbol. Next, starting from the I component of the closest constellation point, comparisons are performed between the real part of the constellation symbols and the value of the length of the sub-region. In this way, the number of comparisons performed is reduced, i.e., the number of the points inside the sub-region plus the first one outside the region having a larger value than the considered length.

5) Determination of l Value: The next step consists of determining the most suitable value of l. We approximate (3) to a normal distribution to set $l = 3$ as initial value. In this way, we assume that the transmitted symbol will be inside the sub-region in a high percentage of time. Then, an iterative procedure is performed to obtain the optimal value of l. Table I shows the study carried out to determine the optimal value of l with the lowest demapping complexity jointly with system performance losses below 0.1 dB. Steps of 0.1 are considered for the determination of the l value. Results from Table I show that for $\mathrm{l} = 3.6$, the performance penalty of the adaptive sub-region demapper w.r.t. the ML demapper is below 0.1 dB

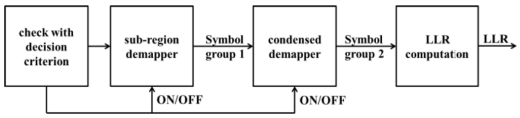

Fig. 5. Functional diagram of the SCASR demapper.

for all code rates. For $R = 2/15$ and $R = 6/15$ a value of $\mathrm{l} = 3$ also provides a negligible performance penalty and the same applies for $R = 10/15$ code rate with $\mathrm{l} = 3.3$. These values imply lower demapping complexity than for $\mathrm{l} = 3.6$ (in the range of 2 - 5% lower demapping complexity). For simplicity and targeting a hardware implementation, we take $l = 3.6$.

It is important to note that the value $l = 3.6$ is also valid for the ATSC 3.0 OFDM platform under ideal CSI. However, for non-ideal CSI the same study has been done obtaining a new value of $l = 5$.

C. Switched Condensed and Adaptive Sub-Region Demapper

Being a combination of the two proposed demapping techniques, the combined SCASR demapper applies the metric value of 0.05 for the underlying condensed demapper and $l = 3.6$ for the adaptive sub-region demapper. For these parameters, observed performance remains within 0.1 dB from the ML demapper. Fig. 5 shows the functional diagram of the SCASR demapper. The first block corresponds to the decision block where, depending on the code rate, either one or both demappers are switched on. The criteria depend on the code rate range: for the code rates of $R = 2/15$ and $R = 3/15$ only the condensed demapper is applied. From code rates $R = 4/15$ to $R = 10/15$, both demappers (condensed and adaptive sub-region) are used. From code rates of $R = 11/15$ to $R = 13/15$, only the adaptive sub-region demapper is used.

Fig. 6 shows the reduction in terms of percentage of the number of Euclidean distances to be computed w.r.t. ML demapper. The SCASR demapper presents a demapping complexity reduction ranging from 77% to 95% for the AWGN channel. This reduction ranges between 79% and 93% in the case of the Rayleigh iid channel. For this latter channel type, the fading coefficients and the SNR value (higher than in the AWGN channel for error-free decoding) increase the length of the sub-region.

The influence of the condensed demapper is remarkable for low code rates as it provides low demapping complexity. The adaptive sub-region demapper performs at its best for high code rates. In the range of mid code rates, both demappers have similar influence in the complexity reduction.

D. Hardware Implications

The additional hardware complexity of the SCASR demapper w.r.t. the ML or Max-Log demappers is the calculation of the length of the sub-region and the constellation points inside the sub-region. Regarding the calculation of the parameter d, the remarkable operations in terms of hardware

TABLE I
SEARCH OF THE OPTIMAL L VALUE

Channel	Code rate [x/15]	l value						
		3	3.1	3.2	3.3	3.4	3.5	3.6
		System performance losses (dB) of the adaptive sub-region w.r.t. the ML demapper						
AWGN	R=2	<0.1	<0.1	<0.1	<0.1	<0.1	<0.1	<0.1
	R=6	<0.1	<0.1	<0.1	<0.1	<0.1	<0.1	<0.1
	R=10	<0.1	<0.1	<0.1	<0.1	<0.1	<0.1	<0.1
	R=13	3.3	3.3	1.9	1.7	0.5	0.3	<0.1
Rayleigh iid	R=2	<0.1	<0.1	<0.1	<0.1	<0.1	<0.1	<0.1
	R=6	<0.1	<0.1	<0.1	<0.1	<0.1	<0.1	<0.1
	R=10	1.1	1.1	1.1	<0.1	<0.1	<0.1	<0.1
	R=13	1.5	0.8	0.5	0.3	0.3	0.3	<0.1

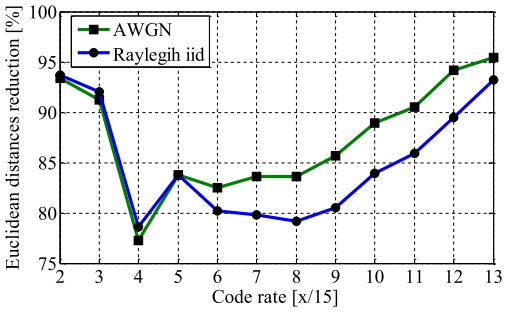

Fig. 6. Percentage of the Euclidean distances reduction between the ML and condensphere demapper for ATSC 3.0 code rates for the AWGN and Rayleigh iid channels.

requirements are one multiplication and one division. The multiplication can be easily implemented via an addition since the SNR is constant for all the received symbols. The division can be considered equivalent to an Euclidean distance computation and it is taken into account in the complexity analysis in Section V. The rest of operations are comparisons or additions which are negligible if compared with Euclidean distance computation.

The main source of simple operations is given by the dichotomy process. The maximum possible number of simple operations (and it does not occur) is M, where M is the number of constellation points, which is still negligible if compared with the computation of the Euclidean Distances needed to calculate the LLR of each bit of the symbol received.

V. PERFORMANCE EVALUATION

A. Demapping Complexity and System Performance

In this section, the system performance of the proposed SCASR demapper is analyzed. As a contribution, in this paper the results of a low complexity demapper for 2D-256NUCs are presented using, for the first time, a fully compliant ATSC 3.0 OFDM transmitter – receiver chain. The transmitted signal is composed of 300 FEC blocks with 64,800 bit length. Four different channel models are simulated: AWGN, Rayleigh iid for the BICM system and DVB-T P1 (Rayleigh) and DVB-T F1 (Rice) [42] for the OFDM system. Four different code rates are used ($R = 2/15$, $R = 6/15$, $R = 10/15$ and $R = 13/15$). In the OFDM system, all the interleavers defined in ATSC 3.0 for single Physical Layer Pipe (PLP) are used. Table II shows the results for ideal CSI. No pilots are used and perfect synchronization is considered.

Complexity results consider the maximum number of Euclidean distances used to compute an LLR among all the LLRs calculated during the simulations.

In all channel conditions, results from Table II show that the SCASR performance is comparable to the ML demapper with a negligible gap (under 0.1 dB). Meanwhile, complexity reduction from 6% to 27% w.r.t. the state of art demappers for 2D-NUCs [19] and from 79.2% to 95.4% w.r.t. the ML demapper is obtained.

Table III extends the results for non-ideal CSI. The value of l is 5 as explained in Section IV-B5. All the interleavers defined in ATSC 3.0 for single PLP are used, the pilot pattern is SP12_2, 16K FFT is used and the guard interval is 1024 samples. The pilot boosting is 4.7 dB. Two-dimensional channel estimation based on the Discrete Fourier Transform (DFT) method [43] is performed jointly with frequency and time filtering.

Results in Table III validate the proposed SCASR demapper under non-ideal CSI. The percentages of the demapping complexity reduction are quite similar to the ideal CSI case (from 8.7% to 23% w.r.t. [19] and from 71.8% to 93.7% w.r.t. the ML demapper). The corresponding performance penalties on DVB-T P1 channel conditions are 0.1 and 0.2 dB for $R = 10/15$ and $R = 13/15$ code rates respectively.

B. Extension to 2D-1kNUC and 2D-4kNUC

The main problem for high order 2D-NUCs (1k and 4k), is their design and demapping complexity. Indeed, proposed NUCs in ATSC 3.0 for these constellation orders are 1D-NUCs. As a contribution, the system performance and complexity reduction of the SCASR demapper for such high order constellations is presented. In a previous work, the authors

TABLE II
SYSTEM PERFORMANCE AND DEMAPPING COMPLEXITY REDUCTION OF THE SCASR DEMAPPER FOR IDEAL CSI

Channel	Parameter	Code rate [x/15]			
		R=2	R=6	R=10	R=13
AWGN	ML: SNR [dB]	1.7	10.6	17.2	22.3
	SCASR Losses [dB]	<0.1	<0.1	<0.1	<0.1
	Complexity Reduction [%]	93.4	82.5	88.9	95.4
Rayleigh iid	ML: SNR	2.9	12.9	20.1	26.7
	SCASR Losses [dB]	<0.1	<0.1	<0.1	<0.1
	Complexity Reduction [%]	93.7	80.2	83.9	93.2
P1	ML: SNR	2.3	12.5	19.7	26.6
	SCASR Losses [dB]	<0.1	<0.1	<0.1	<0.1
	Complexity Reduction [%]	93.7	79.2	81.5	92.2
F1	ML: SNR	1.3	10.5	17.1	22.3
	SCASR Losses [dB]	<0.1	<0.1	<0.1	<0.1
	Complexity Reduction [%]	93.7	80.1	86.7	94.6

TABLE III
SYSTEM PERFORMANCE AND DEMAPPING COMPLEXITY REDUCTION OF THE SCASR DEMAPPER FOR NON-IDEAL CSI

Channel	Parameter	Code rate [x/15]			
		R=2	R=6	R=10	R=13
P1	ML: SNR [dB]	3.4	13.3	20.3	27.7
	SCASR Losses [dB]	<0.1	<0.1	0.1	0.2
	Complexity Reduction [%]	93.7	74.2	75.2	90
F1	ML: SNR	2.2	11.1	17.5	22.8
	SCASR Losses [dB]	<0.1	<0.1	<0.1	<0.1
	Complexity Reduction [%]	93.7	71.8	78.7	91.1

proposed in [34] 2D-1kNUCs and 2D-4kNUCs. 2D-1kNUC for $R = 5/15$ code rate and 2D-4kNUC for $R = 3/15$ code rate are used in this study. Ideal CSI is considered.

Results in Table IV validate the use of the SCASR demapper for high order 2D-NUCs. Demapping complexity reduction ranges from 96.5% to 99.7% (AWGN) and from 96% to 99.1% (Rayleigh iid). In all cases, performance penalty remains within 0.1 dB from the ML demapper. High order 2D-NUCs could be taken into account in future communications systems

TABLE IV
SYSTEM PERFORMANCE AND DEMAPPING COMPLEXITY REDUCTION OF SCASR DEMAPPER FOR HIGH ORDER 2D-NUC

Channel	Parameter	Constellation order & code rate	
		2D-1kNUC & R=5/15	2D-4kNUC & R=3/15
AWGN	SCASR Losses [dB]	<0.1	<0.1
	Complexity Reduction [%]	96.5	99.7
Rayleigh iid	SCASR Losses [dB]	<0.1	<0.1
	Complexity Reduction [%]	96	99.1

with the use of low complexity demappers such as the SCASR demapper.

VI. CONCLUSION

In this paper, a novel low complexity demapper switching between two different demapping techniques based on condensation and on adaptive sub-region (SCASR) is proposed for 2D-NUCs. First, the main characteristics of the 2D-NUCs are identified in order to design a demapper which adapts to these characteristics. Clear criteria are proposed for the switching between the two underlying demappers providing the best performance. The functional diagram of the SCASR demapper is shown and the configuration of the sub-modules is detailed for the code rates defined in ATSC 3.0.

The first contribution of the work is the design of an adaptive sub-region demapper closely suited to the shaping of 2D-NUCs. The dimension of the sub-region with best compromise between performance and complexity is proposed. The design and functional diagram of the demapper are also defined. This demapper presents high demapping complexity reduction for high and mid code rates.

For low code rates, the use of a condensed demapper is proposed. A metric to appropriately condense 2D-NUCs to provide low demapping complexity with negligible impact on performance represents the second contribution.

In order to validate the proposed SCASR demapper, simulation results are presented using a fully compliant ATSC 3.0 OFDM transceiver. Obtained performance remains within 0.1 dB from the ML demapper. Meanwhile, a significant reduction in the number of computed Euclidean distances ranging from 79.2% to 95.4% is obtained when compared to the ML demapper. When other 2D-NUC demapping proposals are considered, the SCASR demapper still shows lower complexity (from 6% to 27%) and performs better (degradation always below 0.1 dB).

For non-ideal CSI, similar performance results and complexity reductions as for ideal CSI are still obtained. An extension of this demapper is proposed for high order 2D-NUCs showing a complexity reduction of up to 99.7% with respect to ML demapping.

Thanks to this proposal, the design of broadcasting systems which closely match Shannon's channel capacity limit for high spectral efficiency ranges becomes within feasible reach.

REFERENCES

[1] A. Goldsmith, S. A. Jafar, N. Jindal, and S. Vishwanath, "Capacity limits of MIMO channels," *IEEE J. Sel. Areas Commun.*, vol. 21, no. 5, pp. 684–702, Jun. 2003.

[2] C. A. Nour and C. Douillard, "Rotated QAM constellations to improve BICM performance for DVB-T2," in *Proc. ISSSTA*, Bologna, Italy, Aug. 2008, pp. 354–359.

[3] J. Barrueco *et al.*, "Constellation design for bit-interleaved coded modulation (BICM) systems in advanced broadcast standards," *IEEE Trans. Broadcast.*, vol. 63, no. 4, pp. 603–614, Dec. 2017.

[4] *ATSC Standard: Physical Layer Protocol*, document A/322:2016, Adv. Television Syst. Committee, Washington, DC, USA, Sep. 2016.

[5] D. Gómez-Barquero *et al.*, "MIMO for ATSC 3.0," *IEEE Trans. Broadcast.*, vol. 62, no. 1, pp. 298–305, Mar. 2016.

[6] N. S. Loghin *et al.*, "Non-uniform constellations for ATSC 3.0," *IEEE Trans. Broadcast.*, vol. 62, no. 1, pp. 197–203, Mar. 2016.

[7] J. Zoellner and N. Loghin, "Optimization of high-order non-uniform QAM constellations," in *Proc. IEEE Int. Symp. Broadband Multimedia Syst. Broadcast.*, London, U.K., Jun. 2013, pp. 1–6.

[8] B. Mouhouche, D. Ansorregui, and A. Mourad, "High order non-uniform constellations for broadcasting UHDTV," in *Proc. IEEE Wireless Commun. Netw. Conf. (WCNC)*, Istanbul, Turkey, Apr. 2014, pp. 600–605.

[9] J. Barrueco *et al.*, "Combining advanced constellations and SSD techniques for optimal BICM capacity," in *Proc. IEEE Int. Symp. Broadband Multimedia Syst. Broadcast. (BMSB)*, Ghent, Belgium, Jun. 2015, pp. 1–4.

[10] D. Gómez-Barquero, C. Douillard, P. Moss, and V. Mignone, "DVB-NGH: The next generation of digital broadcast services to handheld devices," *IEEE Trans. Broadcast.*, vol. 60, no. 2, pp. 246–257, Jun. 2014.

[11] F. Tosato and P. Bisaglia, "Simplified soft-output demapper for binary interleaved COFDM with application to HIPERLAN/2," in *Proc. IEEE Int. Conf. Commun.*, New York, NY, USA, Aug. 2012, pp. 664–668.

[12] Q. Wang, Q. Xie, Z. Wang, S. Chen, and L. Hanzo, "A universal low-complexity symbol-to-bit soft demapper," *IEEE Trans. Veh. Technol.*, vol. 63, no. 1, pp. 119–130, Jan. 2013.

[13] T.-J. Hsieh and W.-H. Sheen, "A lattice-reduction-aided max-log list demapper for coded MIMO receivers," *IEEE Trans. Veh. Technol.*, vol. 63, no. 2, pp. 664–673, Feb. 2014.

[14] E. C. Y. Peh and Y.-C. Liang, "Power and modulo loss tradeoff with expanded soft demapper for LDPC coded GMD-THP MIMO systems," *IEEE Trans. Wireless Commun.*, vol. 8, no. 2, pp. 714–724, Feb. 2009.

[15] X.-F. Qi and K. Holt, "A lattice-reduction-aided soft demapper for high-rate coded MIMO-OFDM systems," *IEEE Signal Process. Lett.*, vol. 14, no. 5, pp. 305–308, May 2007.

[16] S. Tomasin and M. Butussi, "Low complexity demapping of rotated and cyclic Q delayed constellations for DVB-T2," *IEEE Wireless Commun. Lett.*, vol. 1, no. 2, pp. 81–84, Apr. 2012.

[17] M. Z. Saleh, M. Sadek, and S. H. El Ramly, "Novel hybrid soft-hard demodulation schemes for RQD constellation," in *Proc. Int. Conf. Telecommun. Signal Process.*, Prague, Czech Republic, Jul. 2012, pp. 684–688.

[18] A. R. Jafri, A. Baghdadi, M. Waqas, and M. Najam-Ul-Islam, "High-throughput and area-efficient rotated and cyclic Q delayed constellations demapper for future wireless standards," *IEEE Access*, vol. 5, pp. 3077–3084, 2017.

[19] M. Fuentes, D. Vargas, and D. Gómez-Barquero, "Low-complexity demapping algorithm for two-dimensional non-uniform constellations," *IEEE Trans. Broadcast.*, vol. 62, no. 2, pp. 375–383, Jun. 2016.

[20] E. Viterbo and J. Boutros, "A universal lattice code decoder for fading channels," *IEEE Trans. Inf. Theory*, vol. 45, no. 5, pp. 1639–1642, Jul. 1999.

[21] Z. Guo and P. Nilsson, "Algorithm and implementation of the K-best sphere decoding for MIMO detection," *IEEE J. Sel. Areas Commun.*, vol. 24, no. 3, pp. 491–503, Mar. 2006.

[22] C. Studer, A. Burg, and H. Bolcskei, "Soft-output sphere decoding: Algorithms and VLSI implementation," *IEEE J. Sel. Areas Commun.*, vol. 26, no. 2, pp. 684–702, Feb. 2008.

[23] C. Barjau, M. Fuentes, T. Shitomi, and D. Gómez-Barquero, "MIMO sphere decoding with successive interference cancellation for two-dimensional non-uniform constellations," *IEEE Commun. Lett.*, vol. 21, no. 5, pp. 1015–1018, May 2017, doi: 10.1109/LCOMM.2017.2653775.

[24] E. Agrell, T. Eriksson, A. Vardy, and K. Zeger, "Closest point search in lattices," *IEEE Trans. Inf. Theory*, vol. 48, no. 8, pp. 2201–2214, Aug. 2002.

[25] M. O. Damen, H. El Gamal, and G. Caire, "On maximum-likelihood detection and the search for the closest lattice point," *IEEE Trans. Inf. Theory*, vol. 49, no. 10, pp. 2389–2402, Oct. 2003.

[26] A. Haroun, C. A. Nour, M. Arzel, and C. Jego, "Low-complexity soft detection of QAM demapper for a MIMO system," *IEEE Commun. Lett.*, vol. 20, no. 4, pp. 732–735, Apr. 2016.

[27] D. Perez-Calderon, V. Baena-Lecuyer, J. Chavez, A. C. Oria, and J. G. Doblado, "Simplified detection for DVB-NGH MIMO decoders," *IEEE Trans. Broadcast.*, vol. 61, no. 1, pp. 84–90, Mar. 2015.

[28] D. Perez-Calderon, V. Baena-Lecuyer, J. G. Doblado, A. C. Oria, P. López, "Simplified metrics calculation for soft bit detection in DVB-T2," *Radioengineering*, vol. 23, no. 1, pp. 399–404, Apr. 2014.

[29] Q. Xie, Z. Wang, and Z. Yang, "Simplified soft demapper for APSK with product constellation labeling," *IEEE Trans. Wireless Commun.*, vol. 11, no. 7, pp. 2649–2657, Jul. 2012.

[30] J. Lee, J.-Y. Jung, and J. M. Ahn, "Simplified non-square quadrature amplitude modulation demapper for DOCSIS 3.1," *IEEE Trans. Broadcsat.*, vol. 63, no. 1, pp. 156–161, Mar. 2017.

[31] "Data-over-cable service interface specifications DOCSIS 3.1-physical layer specification," Cable Televis. Lab., Louisville, CO, USA, Rep. CM-SP-PHYv3.1-I09-160602, Jun. 2016.

[32] K. Kim, N. Basutkar, K. Bae, P. Xue, and H. Yang, "One-dimensional soft-demapping algorithms for rotated QAM and software implementation on DSP," *IEEE Trans. Signal Process.*, vol. 61, no. 15, pp. 3918–3930, Aug. 2013.

[33] D. Pérez-Calderón, V. Baena-Lecuyer, A. C. Oria, P. López, and J. G. Doblado, "Rotated constellation demapper for DVB-T2," *IEEE Electron. Lett.*, vol. 47, no. 1, pp. 31–32, Jan. 2011.

[34] D. Perez-Calderon, V. Baena-Lecuyer, A. C. Oria, P. Lopez, and J. G. Doblado, "Simplified rotated constellation demapper for second generation terrestrial digital video broadcasting," *IEEE Trans. Broadcast.*, vol. 59, no. 1, pp. 160–167, Mar. 2013.

[35] S. Kwon *et al.*, "Simplified non-uniform constellation demapping scheme for the next broadcasting system," in *Proc. IEEE Int. Symp. Broadband Multimedia Syst. Broadcast. (BMSB)*, Ghent, Belgium, Jun. 2015, pp. 1–3.

[36] Y. Tao, H.-J. Kim, S. Jeon, and J.-S. Seo, "Low-complexity switched soft demapper for rotated non-uniform constellation DVB-NGH systems," in *Proc. IEEE Int. Symp. Broadband Multimedia Syst. Broadcast. (BMSB)*, Beijing, China, Jun. 2014, pp. 1–6.

[37] Y. Tao, H.-J. Kim, S. Jeon, and J.-S. Seo, "Low complexity switched soft demapper for rotated QAM constellations," *IEEE Trans. Broadcast.*, vol. 62, no. 3, pp. 532–539, Sep. 2016.

[38] J. Barrueco *et al.*, "Low complexity and high order two-dimensional non-uniform constellations for high capacity broadcasting systems," in *Proc. IEEE Int. Symp. Broadband Multimedia Syst. Broadcast. (BMSB)*, Nara, Japan, Jun. 2016, pp. 1–5.

[39] J. Barrueco *et al.*, "Condensation methodologies for two-dimensional non-uniform constellations," in *Proc. IEEE Int. Symp. Broadband Multimedia Syst. Broadcast. (BMSB)*, Cagliari, Italy, Jun. 2017, pp. 1–5.

[40] L. Michael and D. Gómez-Barquero, "Bit-interleaved coded modulation (BICM) for ATSC 3.0," *IEEE Trans. Broadcast.*, vol. 62, no. 1, pp. 181–188, Mar. 2016.

[41] K.-J. Kim *et al.*, "Low-density parity-check codes for ATSC 3.0," *IEEE Trans. Broadcast.*, vol. 62, no. 1, pp. 189–196, Mar. 2016.

[42] *Digital Video Broadcasting (DVB); Implementation Guidelines for a Second Generation Digital Terrestrial Television Broadcasting System (DVB-T2)*, document ETSI TS 102 831 V1.2.1, ETSI, Sophia Antipolis, France, Aug. 2012.

[43] O. Edfors, M. Sandell, J.-J. van de Beek, S. K. Wilson, and P. O. Börjesson, "Analysis of DFT-based channel estimators for OFDM," Div. Signal Process., Luleå Univ. Technol., Luleå, Sweden, Rep. TULEA 1996:17, Sep. 1996.

Jon Barrueco received the M.S. degree in telecommunications engineering from the Bilbao Engineering College, University of the Basque Country, in 2013, where he is currently pursuing the Ph.D. degree involved in several research projects in the signal processing area for wireless communications. Since 2013, he has been part of the TSR (Radiocommunications and Signal Processing) Research Group with the University of the Basque Country. He has been an active participant in the standardization process of the next generation terrestrial broadcasting standard ATSC 3.0. His current research interests include digital communications and the design and development of new technologies for the physical layer of communication systems.

Jon Montalban received the M.S. and Ph.D. degrees in telecommunications engineering from the University of the Basque Country, Spain, in 2009 and 2014, respectively. Since 2009, he has been part of the TSR (Radiocommunications and Signal Processing) Research Group with the University of the Basque Country, where he is currently a Post-Doctoral Researcher involved in several projects in the digital terrestrial television broadcasting area. His current research interests include digital communications and digital signal processing for mobile reception of broadband wireless communications systems in 5G.

Pablo Angueira received the M.S. and Ph.D. degrees in telecommunication engineering from the University of the Basque Country, Spain, in 1997 and 2002, respectively, where he joined the Communications Engineering Department, in 1998. Within the TSR Research Group, he has been involved in several digital broadcasting research projects (DVB-T, DRM, T-DAB, DVB-T2, and ATSC 3.0). He has supervised several Ph.D. dissertations in this field and co-authored an extensive list of papers in international peer-reviewed journals, and a large number of conference presentations as well as contributions to the ITU-R working groups WP6 and WP3. His main research interests are network planning and spectrum management applied to digital terrestrial broadcast technologies. His current research interest focuses on broadcast modes and services in 5G network ecosystems. He is an Associate Editor of the IEEE TRANSACTIONS ON BROADCASTING and a member of the Administrative Committee of the IEEE Broadcast Technology Society.

Charbel Abdel Nour received the computer and communications engineering degree from the Lebanese University in 2002, the master's degree in digital communications from the University of Valenciennes, France, in 2003, and the Ph.D. degree in digital communications from Telecom Bretagne, France, in 2008. Since 2008, he has been with the Electronics Department, Telecom Bretagne, where he currently holds an Associate Professor position. His interests concern the radio mobile communications systems, broadcasting systems, coded modulations, error correcting codes, MIMO, and iterative receivers. He is involved in several research projects related to broadcasting and satellite communications. Since 2007, he has been active in the Digital Video Broadcasting consortium, where he had important contributions.

Catherine Douillard received the Engineering degree in telecommunications from Ecole Nationale Supérieure des Télécommunications de Bretagne, France, in 1988, the Ph.D. degree in electrical engineering from the University of Western Brittany, Brest, France, in 1992, and the H.D.R. degree from the University of Southern Brittany, Lorient, France, in 2004. She is currently a Professor with the Electronics Department, Telecom Bretagne, where she is in charge of the Algorithm-Silicon Interaction research team. Her main research interests are turbo codes and iterative decoding, iterative detection, the efficient combination of high-spectral efficiency modulation and turbo coding schemes, diversity techniques, and turbo processing for multicarrier, multiantenna, and multiple access transmission systems. He was a recipient of the SEE/IEEE Glavieux Award for her contribution to standards and related industrial impact in 2009.

1.3 MIMO related studies

1.3.1 Context and prior art

Most of the modern wireless communication systems such as WiMAX, DVB-NGH, WiFi, HSPA+ and LTE have adopted the use of multiple antennas at the transmitter and the receiver. Space time coding for MIMO systems is an efficient technology to increase the data rate and enhance the reliability of wireless communications. The Diversity-Multiplexing Tradeoff (DMT) [53] characterizes the interplay between date rate and reliability achieved by any transmission over MIMO channels. Space-time block codes (STBCs) [54] are commonly designed according to the rank-determinant criteria suitable at high SNRs. On the other hand, wireless communication standards employ MIMO technology with capacity-approaching FEC codes like Turbo codes and LDPC codes, ensuring low error rates even at low SNRs. It turns out in practice that this partly invalidates commonly used MIMO design criteria. Moreover, a design criteria that remains suitable when antenna correlation is considered still lacks in literature.

Furthermore, for MIMO systems with more than dual antennas, Antenna Selection (AS) [55] can performed where the transmission is only done via best antennas in order to limit the increase in system complexity. In the MIMO literature, the AS for MIMO systems has only been studied for the case of uncoded systems where it was shown that it provides large diversity and SNR gains.

Therefore, we have revisited the design criteria for MIMO with FEC coding, with or without considering antenna correlation and we have also covered the issue of AS.

1.3.2 Performed work and contributions

In the work performed in the context of the PhD of Ammar El Falou, we investigated the design of STBCs for MIMO systems with capacity approaching FEC codes. To this end, we derived new STBC structures as well as new design criteria. A first step was made consisting of optimizing a low complexity ML-detection STBC according to the trace criterion, accurate at low SNRs to improve suitability for an association with a powerful outer FEC code. The resulting STBC outperforms the original STBC in the context of a WiMAX system especially with low coding rates [56]. Afterwards, a non-asymptotic STBC design criterion based on the Bitwise Mutual Information (BMI) maximization between transmitted and soft estimated bits at a specific target SNR was proposed. When applied, this criterion is able to provide SNR-dependent STBC codes leading to the proposal of adaptive STBCs [57]. Finally in this context, a proposed trace-orthonormal-based STBC shows identical or better performance than standard WiMAX profiles for all coding rates. Moreover, the main proposed structure reveals to be adaptive from the performance and the complexity viewpoints [58, 59]. After a first step assuming uncorrelated antennas, we investigated the effect of spatial correlation between antennas on the performance of coded MIMO systems. We showed that the BMI criterion can always be used to classify and select the suitable MIMO code depending on the communication environment [60].

At a later stage, we examined MIMO systems using more than dual transmit antennas applying AS. Once again, with a focus on a practical use in a real system, we extended these studies to the case of coded MIMO systems. The work started by designing adaptive STBCs for MIMO systems employing the AS. We showed that, although no additional diversity gain is observed in this context, a substantial SNR gain of more than 3 dB is obtained with respect to a conventional WiMAX system [60].

Finally, in more recent works in that period of time, the finite-SNR DMT was proposed as a novel framework to characterize the DMT at finite SNRs. Our last contribution consisted

of the derivation of the exact finite-SNR DMT for MIMO channels with dual antennas at the transmitter ($2 \times N_r$) and/or the receiver ($N_t \times 2$). Both uncorrelated and correlated Rayleigh fading channels were considered. It was shown that, at realistic SNRs, achievable diversity gains are significantly lower than asymptotic values. This finite-SNR could provide new insights on the design of STBCs at operational SNRs [61, 62]. The corresponding publication in IEEE Communications letters is included hereafter.

IEEE COMMUNICATIONS LETTERS, VOL. 17, NO. 4, APRIL 2013 753

Finite-SNR Diversity-Multiplexing Tradeoff for Rayleigh MIMO Channels

Ammar El Falou, *Student Member, IEEE,* Walaa Hamouda, *Senior Member, IEEE,*
Charlotte Langlais, *Member, IEEE,* Charbel Abdel Nour, *Member, IEEE,* and Catherine Douillard, *Member, IEEE*

***Abstract*—In this paper, exact diversity-multiplexing tradeoff (DMT) at finite signal to noise ratio (SNR) for multiple-input multiple-output (MIMO) systems with dual antennas at the transmitter ($2 \times N_r$) and/or at the receiver ($N_t \times 2$) is derived over Rayleigh fading channels. We derive the outage probability of the mutual information between transmitted and received signals versus SNR. It is shown that at realistic SNRs, achievable diversity gains are significantly lower than asymptotic values. While space-time codes (STCs) for MIMO systems are conventionally designed to achieve the asymptotic DMT frontier, this finite-SNR DMT could provide a new insight to design STCs for practical MIMO systems optimized at operational SNRs.**

***Index Terms*—MIMO systems, diversity multiplexing tradeoff.**

I. INTRODUCTION

MULTIPLE-input multiple-output (MIMO) systems have been adopted in most of the recently developed wireless communication systems, e.g., WiMAX, Wi-Fi, LTE, etc. Indeed, their potential benefits are data rate increase and better reliability. Spatial multiplexing techniques [1] have been incorporated for data rate increase, while space-time codes (STCs) [2] have been designed to improve the channel reliability through spatial diversity. Zheng and Tse in [3] have shown that both gains can be simultaneously delivered with a fundamental tradeoff between them. The diversity-multiplexing tradeoff (DMT) defines the optimal tradeoff between achievable diversity and multiplexing gains of any transmission over $N_t \times N_r$ MIMO channels.

The DMT formulated in [3], for uncorrelated Rayleigh MIMO channels, is an asymptotic framework as the signal to noise ratio (SNR) tends to infinity. In [2], asymptotic analysis was also used to obtain the well-known rank-determinant criteria for space-time block codes (STBCs) design. STBCs for MIMO systems are commonly designed according to these rank-determinant criteria e.g., [4]. A nonzero lower bound on the coding gain i.e., a nonzero minimum determinant is sufficient to reach the frontier of the asymptotic DMT [5]. Recently, several papers have noted that STBCs designed to perform better at high (asymptotic) SNRs are not effective at low to medium SNRs [6] (and references therein) where practical communication systems operate. Moreover, we have shown in [7] that STBCs design parameters are SNR-dependent and that adaptive STBCs are more effective for practical communication systems.

A novel framework has been proposed in [8–10] to characterize the tradeoff between diversity and multiplexing gains at finite-SNRs. This finite-SNR DMT could provide new insights to design MIMO systems optimized at operational SNRs. In [9, 10], Narasimhan has pointed out that exact form of the outage probability and therefore the finite-SNR DMT for any $N_t \times N_r$ MIMO channels are not tractable. Therefore, estimates of the finite-SNR DMT are given in [9–12] for uncorrelated, correlated Rayleigh and Rician fading $N_t \times N_r$ MIMO channels where $N_r \geq N_t$. In some cases, the exact expression of the outage probability and the finite-SNR DMT can be derived. To the best of our knowledge, exact expression of the finite-SNR DMT is derived only for 2×2 MIMO systems in [13] with uncorrelated Rayleigh fading and for both multiple-input single-output (MISO) and single-input multiple-output (SIMO) systems with uncorrelated [14] and correlated [12] Rayleigh fading. Inspired by the method in [13], we derive in this paper the exact finite-SNR DMT for any uncorrelated Rayleigh fading MIMO channels with dual antennas i.e., $N_t \times 2$ and $2 \times N_r$ MIMO systems.

II. SYSTEM MODEL AND DEFINITIONS

We consider a MIMO system with N_t transmit antennas, N_r receive antennas operating over a flat Rayleigh fading channel. A perfect channel state information (CSI) is assumed at the receiver, but not at the transmitter. A quasi-static fading is assumed where the channel remains constant over one space-time coding block of length T and changes independently across blocks. The MIMO channel is defined by the matrix $\mathbf{H}_{[N_r \times N_t]}$ where its entries are assumed to be independent and identically distributed (i.i.d.) circularly symmetric complex Gaussian random variables with probability density function (pdf) $\sim CN(0, 1)$.

The channel input-output relation is given by:

$$\mathbf{Y} = \mathbf{HX} + \mathbf{N} \tag{1}$$

where $\mathbf{X}_{[N_t \times T]}$ is the transmitted space-time block code, $\mathbf{Y}_{[N_r \times T]}$ is the matrix of received N_t noisy signals over T

Manuscript received January 2, 2013. The associate editor coordinating the review of this letter and approving it for publication was T. Oechtering.

A. El Falou, C. Langlais, A. Abdel Nour, and C. Douillard are with the Institut Mines-Telecom, Telecom Bretagne, UMR CNRS 3192 Lab-STICC, Electronics Department, Technopôle Brest Iroise CS 83818, 29238 Brest Cedex 3, Université européenne de Bretagne, France (e-mail: {ammar.elfalou, charlotte.langlais, charbel.abdelnour, catherine.douillard}@telecom-bretagne.eu). A. El Falou was a visiting Researcher at Concordia University from 01 April to 30 June 2012.

W. Hamouda is with Concordia University, Montreal, QC, Canada H3G 1M8 (e-mail: hamouda@ece.concordia.ca).

This work was partly funded by the French ANR Mobile MultiMedia project, ANR-10-VERS-0010.

Digital Object Identifier 10.1109/LCOMM.2013.022213.130007

channel uses and $\mathbf{N}_{[N_r \times T]}$ is the matrix of additive complex white Gaussian noise with i.i.d. entries and pdf $\sim CN(0, \sigma^2)$.

In [3], conventional asymptotic definitions of multiplexing and diversity gains for a MIMO channel are given by:

$$r_{\text{asymptotic}} = \lim_{\rho \to \infty} \frac{R}{\log \rho} \tag{2}$$

$$d_{\text{asymptotic}} = -\lim_{\rho \to \infty} \frac{\log P_{\text{out}}}{\log \rho} \tag{3}$$

where $r_{\text{asymptotic}}$ and $d_{\text{asymptotic}}$ represent the asymptotic multiplexing and diversity gains respectively, ρ is the average SNR per receive antenna, R is the MIMO system data rate and P_{out} is the outage probability. As no CSI is available at the transmitter, an equal power across transmit antennas is adopted and P_{out} is defined by:

$$P_{\text{out}} = \Pr\left[I \leq R\right], \tag{4}$$

where I is the mutual information between received and transmitted signals over the MIMO channel.

The asymptotic diversity-multiplexing or data rate-reliability tradeoff represents the upper bound achievable by any transmission over a $N_t \times N_r$ MIMO system. The asymptotic DMT has been established in [3] under the condition that $T \geq N_t + N_r - 1$, otherwise only upper and lower bounds on DMT exist. These bounds match at high multiplexing gains and they do not when r is small. Later, [5] has noted that $T \geq N_t$ is a sufficient condition. The asymptotic DMT is given by the piece-wise linear function connecting the points $(k, d^*(k))$ where $d^*(k)$ is given by:

$$d^*(k) = (N_t - k)(N_r - k); k = 1, \cdots, \min(N_t, N_r) \tag{5}$$

At SNR ρ, the multiplexing gain r is defined as the ratio of the system data rate R to the capacity of an additive white Gaussian noise (AWGN) channel with array gain G [10]:

$$r = \frac{R}{\log(1 + G\rho)} \tag{6}$$

In order to have a fair comparison of diversity and outage performance across different N_t and N_r antennas at low to medium SNRs, the array gain is chosen such that $G = N_r$ [9]. However, in a real scenario, the receiver can always extract a processing gain $G = N_r$ as full CSI is available at the receiver.

Considering a capacity-approaching channel code in the communication chain, the probability of error is well approximated by the channel outage at finite-SNR [8–10]. Therefore, the diversity gain $d(r, \rho)$ of a system with a fixed multiplexing gain r at SNR ρ is defined by the negative slope of the log-log curve of the outage probability versus SNR, leading to:

$$d(r, \rho) = -\frac{\partial \log P_{\text{out}}(r, \rho)}{\partial \log \rho} = -\frac{\rho}{P_{\text{out}}(r, \rho)} \frac{\partial P_{\text{out}}(r, \rho)}{\partial \rho} \tag{7}$$

This definition is important for system design as the diversity gain at a particular operating SNR can be used to estimate the additional SNR required to reach a specified outage probability, for a given data rate represented by the multiplexing gain.

In the sequel, motivated by the work in [13], we derive the exact finite-SNR DMT for systems with dual transmit and/or receive antennas over uncorrelated Rayleigh fading channels.

III. COMPUTATION OF FINITE-SNR DMT

A. Mutual information pdf

In this section, we derive an analytical expression for the pdf of the mutual information between received and transmitted signals for $N_t \times 2$ and $2 \times N_r$ MIMO systems. By assuming that $\mathbf{X}$ is a zero-mean white complex Gaussian random variable, the MIMO mutual information I conditioned on the channel realization $\mathbf{H}$ is given by [15]:

$$\begin{aligned} I &= \log\det\left(\mathbf{I}_{N_r} + \tfrac{\rho}{N_t}\mathbf{H}\mathbf{H}^H\right) \\ &= \log\det\left(\mathbf{I}_{N_t} + \tfrac{\rho}{N_t}\mathbf{H}^H\mathbf{H}\right) \end{aligned} \tag{8}$$

where the superscript ^{H} stands for conjugate transpose.

It is known that when $\mathbf{H}$ is a complex normally distributed matrix, matrices $\mathbf{H}\mathbf{H}^H$ and $\mathbf{H}^H\mathbf{H}$ are central complex Wishart distributed [16]. We define $m \triangleq \min(N_t, N_r)$ and $n \triangleq \max(N_t, N_r)$. The joint pdf of the m nonzero ordered eigenvalues $\lambda_1, ..., \lambda_m$ of the complex Wishart matrix is given in [16]. For $m = 2$, the joint pdf of the two nonzero ordered eigenvalues λ_1 and λ_2 ($\lambda_1 \geq \lambda_2$) is given by:

$$f(\lambda_1, \lambda_2) = \frac{(\lambda_1\lambda_2)^{n-2}}{\Gamma(n)\Gamma(n-1)}(\lambda_1 - \lambda_2)^2 e^{-(\lambda_1+\lambda_2)} \tag{9}$$

where $\Gamma(x)$ is the gamma function defined by $\int_0^\infty t^{x-1}e^{-t}\mathrm{d}t$. Therefore, the mutual information is expressed by:

$$I = \log\left(1 + \lambda_1\frac{\rho}{N_t}\right) + \log\left(1 + \lambda_2\frac{\rho}{N_t}\right). \tag{10}$$

Let us define new variables x and y as:

$$x \triangleq \log\left(1 + \lambda_1\frac{\rho}{N_t}\right) \text{ and } y \triangleq \log\left(1 + \lambda_2\frac{\rho}{N_t}\right). \tag{11}$$

Using the rules in [17],

$$\begin{aligned} f(x, y) = &\left(\tfrac{N_t}{\rho}\right)^{2n} \tfrac{1}{\Gamma(n)\Gamma(n-1)} e^{x+y}\left(e^x - e^y\right)^2 \\ &\times (e^x - 1)^{n-2}(e^y - 1)^{n-2} e^{-\frac{N_t}{\rho}(e^x + e^y - 2)} \end{aligned} \tag{12}$$

where $x \geq y \geq 0$.

From the definition in (11) the mutual information between received and transmitted signals is $I = x + y$. The joint pdf of I and y is then given by:

$$\begin{aligned} f(I, y, \rho) = &\left(\tfrac{N_t}{\rho}\right)^{2n} \tfrac{1}{\Gamma(n)\Gamma(n-1)} e^I\left(e^{I-y} - e^y\right)^2 \\ &\times (e^y - 1)^{n-2}\left(e^{I-y} - 1\right)^{n-2} e^{-\frac{N_t}{\rho}\left(e^{I-y} + e^y - 2\right)} \end{aligned} \tag{13}$$

where $I/2 \geq y \geq 0$.

From (13), and after integration, one can show that:

$$\begin{aligned} f(I, \rho) = &\left(\tfrac{N_t}{\rho}\right)^{2n} \tfrac{1}{\Gamma(n)\Gamma(n-1)} e^I \\ &\times \textstyle\int_0^{I/2} g(y, I, \rho)\mathrm{d}y \end{aligned} \tag{14}$$

where $g(y, I, \rho)$ is expressed by:

$$\begin{aligned} g(y, I, \rho) = &\left(e^{I-y} - e^y\right)^2\left(e^{I-y} - 1\right)^{n-2} \\ &\times (e^y - 1)^{n-2} e^{-\frac{N_t}{\rho}\left(e^{I-y} + e^y - 2\right)}. \end{aligned} \tag{15}$$

For each value of I and ρ, the expression $\int_0^{I/2} g(y, I, \rho)\mathrm{d}y$ can be calculated by numerical integration.

B. Outage probability

From (14), and thanks to numerical integration, the outage probability $P_{\text{out}}(r,\rho)$ is computed for each ρ and r by:

$$\begin{array}{rcl} P_{\text{out}}(r,\rho) & = & \Pr\left[I \le r\log(1+G\rho)\right] \\ & = & \int_0^R f(I,\rho)\mathrm{d}I \\ & = & \left(\frac{N_t}{\rho}\right)^{2n}\frac{1}{\Gamma(n)\Gamma(n-1)} \\ \times\int_0^{r\log(1+G\rho)} e^I & & \left(\int_0^{I/2} g(y,I,\rho)\mathrm{d}y\right)\mathrm{d}I \end{array} \quad (16)$$

This outage probability describes the performance of MIMO systems and its slope defines the finite-SNR DMT. It is to be noted that $P_{\text{out}}(r,\rho)$ decreases with ρ^{-2n} and at high SNRs, the slope of outage probability curves defines the maximum achievable diversity equal to $2n$.

C. Analytical finite-SNR DMT

The finite-SNR DMT is computed using (7). Using the well-known Leibniz integral rule [17] in (16), $\frac{\partial P_{\text{out}}(r,\rho)}{\partial\rho}$ is given by:

$$\frac{\partial P_{\text{out}}(r,\rho)}{\partial\rho} = A_1(r,\rho) + A_2(r,\rho) + A_3(r,\rho) \quad (17)$$

where

$$\begin{array}{rcl} A_1(r,\rho) & = & -2n\left(N_t\right)^{2n}\frac{1}{\rho^{2n+1}}\frac{1}{\Gamma(n)\Gamma(n-1)} \\ \times\int_0^{r\log(1+G\rho)} e^I & & \left(\int_0^{I/2} g(y,I,\rho)\mathrm{d}y\right)\mathrm{d}I \\ & = & -\frac{2n}{\rho}P_{\text{out}}(r,\rho)\,, \end{array} \quad (18)$$

$$\begin{array}{l} A_2(r,\rho) = \left(\frac{N_t}{\rho}\right)^{2n}\frac{1}{\Gamma(n)\Gamma(n-1)}\frac{rG}{1+G\rho}e^{r\log(1+G\rho)} \\ \quad\times\left(\int_0^{r\log(1+G\rho)/2} g(y,r\log(1+G\rho),\rho)\mathrm{d}y\right), \end{array} \quad (19)$$

and

$$\begin{array}{l} A_3(r,\rho) = \left(\frac{N_t}{\rho}\right)^{2n}\frac{1}{\Gamma(n)\Gamma(n-1)} \\ \quad\times\int_0^{r\log(1+G\rho)} e^I\left(\int_0^{I/2}\frac{\partial g(y,I,\rho)}{\partial\rho}\mathrm{d}y\right)\mathrm{d}I \end{array} \quad (20)$$

where

$$\begin{array}{l} \frac{\partial g(y,I,\rho)}{\partial\rho} = \left(e^{I-y}-e^y\right)^2\left(e^{I-y}-1\right)^{n-2}\left(e^y-1\right)^{n-2} \\ \quad\times e^{-\frac{N_t}{\rho}\left(e^{I-y}+e^y-2\right)}\frac{N_t}{\rho^2}\left(e^{I-y}+e^y-2\right). \end{array} \quad (21)$$

The above expressions can also be calculated using numerical integration. After deriving $P_{\text{out}}(r,\rho)$ and $\frac{\partial P_{\text{out}}(r,\rho)}{\partial\rho}$, the finite-SNR DMT can be easily computed using (7).

IV. NUMERICAL RESULTS

In order to examine the derived finite-SNR DMT, in Fig. 1 we plot the derived exact finite-SNR DMT curves for $n=2$ at SNR $= 5, 10$ dB and the asymptotic DMT [3]. We noted that the obtained DMT curves are identical to the ones obtained in [9, 11] by Monte Carlo simulations, which validates the derived exact DMT. Furthermore, the finite-SNR DMT derived in [9, 11] overestimate the achievable DMT. In order to discuss the achievability of our exact finite-SNR DMT, we have plotted the exact finite-SNR DMT for Alamouti code derived in [8]. It is noted that the Alamouti code always benefits from all the available diversity of the system (when the multiplexing gain r approaches zero), not only at asymptotic SNRs, but also at realistic SNRs.

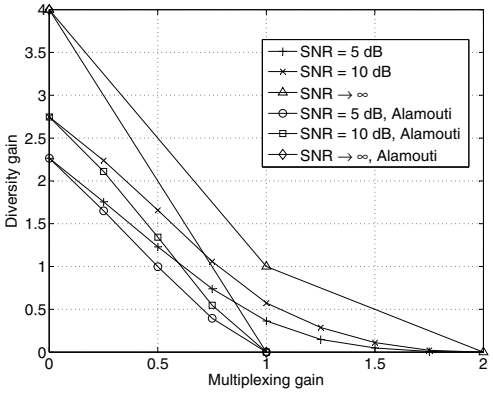

Fig. 1. Asymptotic and exact finite-SNR DMT curves for 2×2 MIMO channel and Alamouti code at various SNRs.

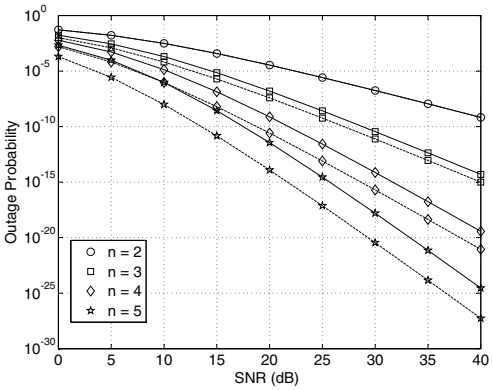

Fig. 2. Exact outage probability at a multiplexing gain $r=0.5$ for $n\times 2$ MIMO channel with solid lines and $2\times n$ MIMO channel with dashed lines, with $n=2,3,4$ and 5.

Fig. 2 plots the outage probability as a function of SNR at a multiplexing gain $r=0.5$ for $n\times 2$ MIMO channel with solid lines and $2\times n$ MIMO channel with dashed lines, with $n=2,3,4$ and 5. For $n=2$, the obtained curve is identical to the one obtained in [9, 11] by Monte Carlo simulations. Also the simulated outage probability values obtained by Monte Carlo simulations are relatively high e.g., up to 10^{-6} in [9, 11]. Our exact expression permits the assessment of very low values for the outage probability. In addition, Fig. 2 shows the superiority of $2\times N_r$ systems relative to $N_t\times 2$ systems. At high SNRs, both systems have the same slope and therefore the same diversity gain.

Fig. 3 and Fig. 4 show the asymptotic and exact finite-SNR DMT for $n\times 2$ MIMO system with solid lines and exact finite-SNR DMT for $2\times n$ MIMO system with dashed lines, for $n=3$ and $n=5$ respectively. Both figures show that the achievable diversity gains at finite-SNR are significantly lower than the asymptotic values. Furthermore, the results show that receive antennas provide higher diversity gain than transmit

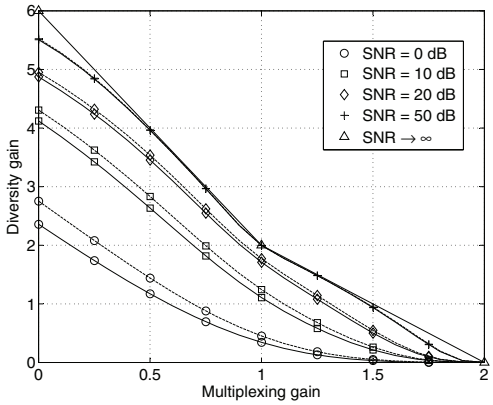

Fig. 3. Asymptotic and exact finite-SNR DMT for 3×2 MIMO channel with solid lines and 2×3 MIMO channel with dashed lines at various SNRs.

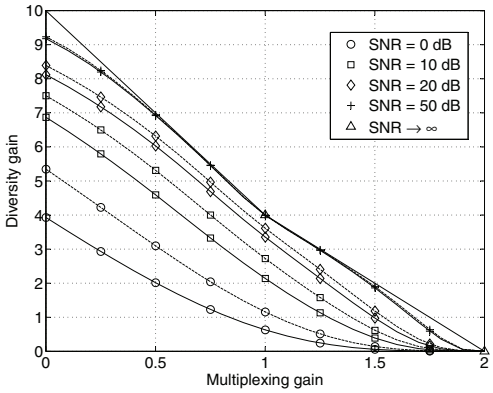

Fig. 4. Asymptotic and exact finite-SNR DMT for 5×2 MIMO channel with solid lines and 2×5 MIMO channel with dashed lines at various SNRs.

antennas especially at low to moderate SNRs. We recall that no CSI is available at the transmitter and an equal power across transmit antennas is adopted. Under this assumption, the outage probability is defined in (4) and the finite-SNR DMT in (7). Therefore, the superiority of $2 \times N_r$ with respect to $N_t \times 2$ can be explained by the fact that receive diversity is always obtained regardless of the transmission technique. On the other hand, a judicious transmission technique is required to benefit from transmit diversity, and an equal power across transmit antennas is not necessarily the best strategy at low to moderate SNRs. It is to be noted that the gap between $N_t \times 2$ and $2 \times N_r$ systems increases with the increase of n. Also, this gap decreases with the SNR increase where both systems converge to the asymptotic DMT [3] e.g. $\rho = 50$ dB where this convergence is not uniform. Unfortunately, an analytical proof of the convergence of the derived finite-SNR DMT to asymptotic DMT by letting $\rho \to \infty$ is not easily tractable.

V. CONCLUSIONS

In this paper, we have derived the exact finite-SNR diversity-multiplexing tradeoff for $N_t \times 2$ and $2 \times N_r$ Rayleigh MIMO channels. The finite-SNR DMT characterizes the system at operational SNRs where available diversity gains are computed. It has been shown that the Alamouti code benefits from all the available diversity at the operational SNR. Furthermore, we have shown that receive antennas provide higher diversity gains with respect to transmit antennas especially for low to moderate SNRs. Analysis on finite-SNR DMT shows that the achievable diversity gains are significantly lower than asymptotic values for SNR $\to \infty$. STCs for MIMO systems are conventionally designed to achieve the asymptotic DMT frontier and therefore are not efficient at realistic SNRs. This finite-SNR DMT could provide a new insight to design STCs for practical MIMO systems optimized at operational SNRs.

REFERENCES

[1] P. W. Wolniansky, G. J. Foschini, G. D. Golden, and R. A. Valenzuela, "V-blast: an architecture for realizing very high data rates over the rich-scattering wireless channel," in *Proc. 1998 IEEE Int. Symp. on Signals, Syst. and Electronics*.

[2] V. Tarokh, N. Seshadri, and A. R. Calderbank, "Space-time codes for high data rate wireless communications: performance criterion and code construction," *IEEE Trans. Inf. Theory*, vol. 44, no. 2, pp. 744–765, Mar. 1998.

[3] L. Zheng and D. N. C. Tse, "Diversity and multiplexing: a fundamental tradeoff in multiple-antenna channels," *IEEE Trans. Inf. Theory*, vol. 49, no. 5, pp. 1073–1096, May 2003.

[4] M. AlJerjawi and W. Hamouda, "Performance of space-time spreading in DS-CDMA systems over fast-fading channels," in *Proc. 2005 IEEE Global Telecommun. Conf.*

[5] P. Elia, K. Kumar, S. Pawar, P. Kumar, and H.-F. Lu, "Explicit space-time codes achieving the diversity-multiplexing gain tradeoff," *IEEE Trans. Inf. Theory*, vol. 52, no. 9, pp. 3869–3884, Sep. 2006.

[6] A. Lozano and N. Jindal, "Transmit diversity vs. spatial multiplexing in modern MIMO systems," *IEEE Trans. Wireless Commun.*, vol. 9, no. 1, pp. 186–197, Jan. 2010.

[7] A. El Falou, C. Langlais, C. Abdel Nour, and C. Douillard, "Adaptive trace-orthonormal STBC for MIMO system with capacity approaching FEC codes," in *Proc. 2012 IEEE Vehicular Technology Conference*.

[8] R. Narasimhan, A. Ekbal, and J. Cioffi, "Finite-SNR diversity-multiplexing tradeoff of space-time codes," in *Proc. 2005 IEEE Int. Conf. Commun.*, pp. 458–462.

[9] R. Narasimhan, "Finite-SNR diversity performance of rate-adaptive MIMO systems," in *Proc. 2005 IEEE Global Telecommun. Conf.*

[10] ——, "Finite-SNR diversity-multiplexing tradeoff for correlated Rayleigh and Rician MIMO channels," *IEEE Trans. Inf. Theory*, vol. 52, no. 9, pp. 3965–3979, 2006.

[11] Z. Rezki, D. Haccoun, F. Gagnon, and W. Ajib, "Impact of spatial correlation on the finite-SNR diversity-multiplexing tradeoff," *IEEE Trans. Wireless Commun.*, vol. 7, no. 4, pp. 1184–1189, Apr. 2008.

[12] ——, "Diversity-multiplexing tradeoff over correlated Rayleigh fading channels: a non-asymptotic analysis," *Wirel. Commun. Mob. Comput.*, vol. 10, no. 2, pp. 188–199, Feb. 2010.

[13] H. Ebrahimzad and A. Mohammadi, "Diversity-multiplexing tradeoff in MIMO system with finite SNR," in *Proc. 2007 European Conference on Wireless Technologies*, pp. 146–149.

[14] ——, "Diversity-multiplexing tradeoff in MISO/SIMO systems at finite SNR," in *Proc. 2007 IEEE Vehicular Technology Conference – Spring*, pp. 594–598.

[15] I. E. Telatar, "Capacity of multi-antenna gaussian channels," *Europ. Trans. Telecommun.*, vol. 10, pp. 585–595, 1999.

[16] A. T. James, "Distributions of matrix variates and latent roots derived from normal samples," *The Annals of Mathematical Statistics*, vol. 35, no. 2, pp. 475–501, Jun. 1964.

[17] A. Papoulis and S. U. Pillai, *Probability, Random Variable, and Stochastic Processes*, 4th edition. McGraw-Hill Press, 2002.

1.4 Improving binary Turbo codes

1.4.1 Context and prior art

The future generations of mobile networks (5G and beyond) [63] call for higher data rates and capacity, with an enhanced quality of service for different receiver scenarios [64] and applications. To meet such requirements, FEC codes able to guarantee low error rates (down to 10^{-5} of Frame Error Rate (FER)) need to be provided. A current communication system such as Long Term Evolution (LTE) [65] cannot guarantee such error rates. First of all, due to the hybrid automatic repeat request (HARQ) retransmission mechanism, the targeted error rate in LTE is around 10^{-2} of FER. In addition, the rate matching mechanism used to provide rate compatibility in LTE causes undesirable interactions between the code interleaver and the puncturing mechanism for some configurations of block sizes and coding rates, entailing a poor distance spectrum for the code and resulting in a pronounced error floor [66]. The LTE standard adopted a Turbo Code (TC) as channel code [65]. TCs, introduced by Berrou *et al.* [67], are certainly one of the most popular channel coding schemes in wireless systems since they reveal to be particularly flexible with respect to information frame length and coding rate. Indeed, encoding information frames of various lengths with different coding rates can be achieved with the same encoder just by modifying the interleaver parameters and the puncturing pattern. Provided that they are able to guarantee lower error rates when they are punctured, TCs remain promising channel coding candidates for future generation standards. The error rate performance of a TC is closely related to its internal interleaving function and applied puncturing pattern. Therefore, these two items represent the main study items that have been considered for potential improvement.

The interleaver is a key component of TCs. Its role is twofold. First, it has an important impact on the achievable minimum Hamming distance of the TC [68]. Second, due to its scattering properties, it also acts on the correlation of exchanged extrinsic information during the iterative decoding process [69]. In practical Turbo coded systems, algebraic permutations are preferred to random-based permutations. In this case, permuted addresses can be computed via the application of a mathematical expression avoiding the use of storage elements or a LUT. Therefore, they are easier to specify and implement. Three of the most popular interleavers with the above mentioned properties are Dithered Relative Prime (DRP) interleavers [70], Quadratic Permutation Polynomial (QPP) interleavers [71] adopted in LTE [65], and Almost Regular Permutation (ARP) interleavers [72] adopted in the DVB-RCS/RCS2 [73] and WiMAX standards. Despite the existence of different interleaver types, no generic permutation model for TCs has been established, yet. Therefore, any improvement to Turbo codes should start by addressing this point.

In the near future, the evolutions of LTE Advanced Pro will require Turbo decoders able to achieve throughputs as high as several tens of Gbit/s to complement the 5G New Radio (NR) deployments. To this end, the original BCJR algorithm and its derivatives are penalized by their inherent serial nature, thus leading to high latency and low throughput while requiring a large amount of memory to store the state metrics. Therefore, a number of techniques have been proposed as potential solutions to these issues, such as the sliding window technique [74], shuffled parallelism [75], sub-block parallelism [76], full parallelism [77] or high-order radix decoding [78]. Regarding the latter technique, previous works in the literature such as [79], [80] mainly tried to increase the throughput of SISO decoders, without specifically considering the complexity reduction of the studied algorithm. Only in [81], a low-complexity radix-16 SISO decoder was proposed, with the introduction of specific processing to limit the resulting error correction degradation at high signal-to-noise ratios. However, no general technique has yet been proposed on how to enable efficient high-order radix decoding schemes for SISO decoders. Therefore, this became one of our research items.

1.4.2 TC design: Performed work and contributions

The performed work started in the context of the H2020 FANTASTIC 5G project, continued within a bilateral project with Orange Labs and was mostly included in the PhD thesis of Ronald Garzon Bohorquez. It consists of several technical contributions addressing the improvement in performance first at low error rates and then for short frame sizes [82, 83].

As introduced by Berrou et al. [68, 67], the minimum Hamming distance (dmin) of a TC is not only defined by its constituent encoders but also fixed through the TC interleaver. For starting any potential improvement study, one should first choose the interleaver model. In [84], we showed that a relation exists among the three main algebraic families of interleavers. Indeed, we demonstrated that any DRP or QPP interleaver can be expressed as an ARP interleaver. In addition, QPP interleavers were found to be special cases of ARP interleavers in which the values of the periodic shifts follow the quadratic term of the QPP interleaver function. Thus, the same interleaving properties of DRP or QPP interleavers can be provided by ARP interleavers. In other words, this proves that ARP interleavers can achieve, at least, the same minimum Hamming distances as their DRP and QPP counterparts. Therefore, the ARP interleaver is a sufficient permutation model to design TCs with the achievable asymptotic performance from any of the three interleaver families. Furthermore, since TCs have found their way to several standards with a different interleaving structure in each, unifying the interleaving structure can have an advantage for implementation purposes. In fact, one can design an ARP interleaver that can support all standardized interleaver structures. Therefore, the overall complexity can be reduced when several interleaving structures have to be implemented in the same chip.

Among the various techniques to improve performance of TCs, it was shown that the prefixing of a rate-1 accumulator to a Turbo encoder can represent a suitable solution that does not alter its coding rate. In a first approach, we studied the application of this precoding technique to improve the performance of TCs in the context of the LTE standard. To efficiently select the best precoder parameters in terms of convergence, we proposed a design tool based on the real exchange of extrinsic information between the constituent SISO decoders. We also introduced two new precoding structures and we presented design criteria leading to good interleavers for Precoded TCs (PTCs). Three different precoding structures were analyzed. It was shown that convergence improvements are achieved with the reference precoding structure introduced in [85] compared to a classic TC. Furthermore, a significant asymptotic gain is attained with the proposed hybrid precoding structure [86]. It was observed that the composite precoding structure, representing a mix of the two previous structures, shows a performance level that can be considered as a compromise between the original structure with improved convergence threshold and the hybrid precoding structure with an improved error floor. It could not solve the convergence versus error floor tradeoff issue; however, it remains of interest for communication systems requiring the adaptation of channel coding to the encountered noise level. In addition to the proposal of two new precoding structures, we presented design criteria leading to good interleavers for PTCs. We showed that significant asymptotic performance improvements can be achieved with the proposed hybrid PTC scheme [86].

In a second context where the main code structure remains unaltered, we have first investigated the joint design of interleavers and puncturing patterns for TCs in order to guarantee low error floors and good convergence thresholds. As a result, a new puncturing constraint related to parity puncturing was proposed for the design of TC interleavers [83, 87]. The work focused on the ARP interleaver model [72]. Trellis termination was also modified to avoid the spectral efficiency loss due to tail bits. This puncturing constraint defined a connection strategy through the interleaver between bit positions in the natural order and the ones in the interleaved order. Taking full advantage of the periodic nature of ARP

interleavers, we proposed to generalise the connection strategy to all bits within a period, therefore fully defining a periodic connection strategy. This aspect greatly simplified the interleaver definition on the one hand and enabled highly parallel implementations with conflict free memory accesses on the other hand.

At a second phase, aspects related to flexibility were studied to propose efficient rate-compatible tail-biting TCs with 1-bit codeword flexibility and implementing the previously proposed interleaver and puncturing schemes. Its efficiency resides in the absence of any unexpected behavior such as the performance of a shorter frame size better than a larger one, as observed with the LTE code. The proposed techniques provided the necessary leap in TC error correcting performance required to put this code family at least on par with any other state-of-the-art capacity approaching/achieving code family in the context of 5G and beyond. The major part of the proposals/contributions was published as an article entitled "Protograph-Based Interleavers for Punctured Turbo Codes" in Transactions on Communications in 2018 [82] included hereafter. It was also the subject of two delivered patents [88, 89] in the framework of a patent filing collaboration program with Orange Labs.

IEEE TRANSACTIONS ON COMMUNICATIONS, VOL. 66, NO. 5, MAY 2018 1833

Protograph-Based Interleavers for Punctured Turbo Codes

Ronald Garzón-Bohórquez, *Member, IEEE*, Charbel Abdel Nour, *Member, IEEE*, and Catherine Douillard, *Senior Member, IEEE*

***Abstract*— A method to design efficient puncture-constrained interleavers for turbo codes (TCs) is introduced. Resulting TCs profit from a joint optimization of puncturing pattern and interleaver to achieve an improved error rate performance. First, the puncturing pattern is selected based on the constituent code Hamming distance spectrum and on the TC extrinsic information exchange under uniform interleaving. Then, the interleaver function is defined via a layered design process taking account of several design criteria, such as minimum span, correlation girth, and puncturing constraints. We show that applying interleaving with a periodic cross connection pattern that can be assimilated to a protograph improves error-correction performance when compared to the state-of-the-art TCs. An application example is elaborated and compared with the long-term evolution standard: a significant gain in performance can be observed. An additional benefit of the proposed technique resides in the important reduction of the search space for the different interleaver parameters.**

***Index Terms*— Turbo codes, protograph, puncturing pattern, interleaver, span, correlation girth.**

I. INTRODUCTION

IN RECENT years, interest in a large diversity of applications such as TV or multimedia content on demand [1], live streaming, or interactive gaming has been continuously growing due to the increased number of nomadic users. Accordingly, the future generations of mobile networks (5G and beyond) [2] call for higher data rates and capacity, with an enhanced quality of service for different receiver scenarios [3] and applications. To meet such requirements, error-correcting codes able to guarantee low error rates (down to 10^{-5} of frame error rate (FER)) need to be provided. A current communication system such as long term evolution (LTE) [4] cannot guarantee such error rates. First of all, due to the hybrid automatic repeat request (HARQ) retransmission mechanism, the targeted error rate in LTE is around 10^{-2} of FER. In addition, the rate matching mechanism used to provide rate compatibility in LTE causes undesirable interactions between the code interleaver and the puncturing mechanism for some configurations of block sizes and coding rates, entailing a poor distance spectrum for the code and resulting in a pronounced error floor [5].

The LTE standard adopted a turbo code (TC) as channel code [4]. TCs, introduced by Berrou *et al.* [6], are certainly one of the most popular channel coding schemes in wireless systems: besides LTE, they have been adopted in the IEEE 802.16 WiMAX (worldwide interoperability for microwave access) [7] and DVB-RCS2 (2^{nd} generation digital video broadcasting - return channel via satellite) [8] standards. In addition to their near-capacity performance, TCs are known to be particularly flexible with respect to information frame length and coding rate. Indeed, encoding information frames of various lengths with different coding rates can be achieved with the same encoder just by modifying the interleaver parameters and the puncturing pattern. Provided that they are able to guarantee lower error rates when they are punctured, TCs remain promising channel coding candidates for 5G and future generations.

The error rate performance of a TC is closely related to its internal interleaving function. As introduced by Berrou and Glavieux [9], the minimum Hamming distance ($d_{\min}$) of a TC is not only defined by its constituent encoders, but also affected by the TC interleaver. In the last decade, different interleaver structures have been proposed, particularly suited for practical implementation and for improving the asymptotic performance of TCs e.g., quadratic permutation polynomial (QPP) interleavers [10] adopted in LTE [4], dithered relative prime (DRP) interleavers [11], and almost regular permutation (ARP) interleavers [12], adopted in the DVB-RCS/RCS2 [8], [13] and IEEE 802.16 WiMAX [7] standards. The QPP interleaver coefficients are selected based on the maximization of the $d_{\min}$ value of a subset of low-weight input sequences with weights of the form $2n$, n being a small positive integer [10]. A similar criterion was used in [14] to select the DRP interleaver parameters. First, a regular interleaver with high scattering properties is identified. Then, the dither vectors of the DRP interleaver are selected in order to maximize the $d_{\min}$ value of a subset of low-weight input patterns. In the case of the ARP interleaver, a first strategy involves selecting the parameters from those providing the best scattering properties and leading to the highest $d_{\min}$ [12]. Another method, proposed in [15], is based on the maximization of the correlation girth. In [16], it was shown that introducing parity puncturing constraints into the interleaver design yields improved performance.

Manuscript received January 16, 2017; revised June 9, 2017, September 15, 2017, and December 8, 2017; accepted December 8, 2017. Date of publication December 15, 2017; date of current version May 15, 2018. This work was partially funded by the EPIC project of the European Union's Horizon 2020 research and innovation programme under grant agreement No. 760150. The associate editor coordinating the review of this paper and approving it for publication was A. Graell i Amat. *(Corresponding author: Ronald Garzón-Bohórquez.)*

The authors are with the Electronics Department, IMT Atlantique, CNRS UMR 6285 Lab-STICC, CS 83818-29238 Brest Cedex 3, France (e-mail: ronald.garzonbohorquez@imt-atlantique.fr; charbel.abdelnour@imt-atlantique.fr; catherine.douillard@imt-atlantique.fr).

Color versions of one or more of the figures in this paper are available online at http://ieeexplore.ieee.org.

Digital Object Identifier 10.1109/TCOMM.2017.2783971

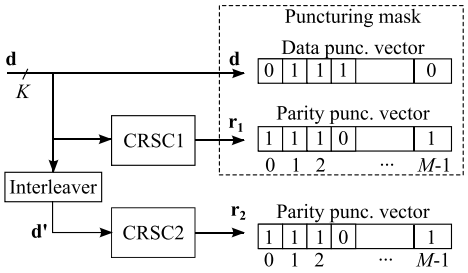

Fig. 1. Considered TC encoder structure with an example of puncturing mask.

In this study, we investigate the joint optimization of puncturing patterns and interleavers for TCs in order to guarantee low error floors and good convergence thresholds. As a result, a layered construction of TC interleaver is proposed, involving the introduction of connection patterns called protographs, named by analogy with protograph-based (PB) low-density parity-check (LDPC) codes [17]. This work focuses on the ARP interleaver model [12]. A significant reduction of the search space for the different interleaver parameters was achieved with an important improvement in TC error rate performance.

The rest of the paper is organized as follows. In Section II, a description of the considered encoder structure, code interleaver, and puncturing pattern is given. Section III introduces relevant interleaver design criteria. In Section IV, a puncturing pattern selection method is proposed. It is followed by the description of the constraints on the interleaver imposed by the puncturing patterns, leading to the concept of PB interleavers for TCs. Section V describes the proposed layered design method for TC interleavers. Afterwards, a summary of the puncture-constrained interleaver design method is given. Then, in Section VI, the proposed method is applied to design TC interleavers and puncturing patterns for a set of frame parameters included in LTE. Section VII shows the simulated error rate performance of the proposed code and its comparison with the original LTE code. Finally, Section VIII concludes the paper.

II. System Description

Among existing trellis termination techniques, tail-biting or circular termination [18] is well suited for TCs. This technique avoids the loss in spectral efficiency due to termination bits and the generation of truncated codewords. Furthermore, with tail-biting termination, the whole information sequence is protected in the same way avoiding any edge effect. Therefore, in this study we consider circular recursive systematic convolutional (CRSC) codes as constituent codes of the TC, since they apply tail-biting termination. The turbo encoder structure considered in this study is shown in Fig. 1. The information sequence $\mathbf{d}$ of size K is encoded by CRSC1, and the corresponding interleaved sequence $\mathbf{d}'$ is encoded by CRSC2. The vectors at the output of the TC, data ($\mathbf{d}$), parity 1 ($\mathbf{r_1}$), and parity 2 ($\mathbf{r_2}$), are punctured using a puncturing mask of period M before being transmitted.

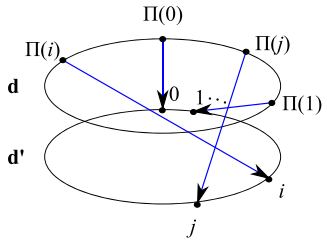

Fig. 2. A possible representation of the turbo code interleaver when using constituent CRSC codes.

A. Turbo Code Interleaver Model

The interleaver is a key component of TCs. Its role is twofold. First, it has a high impact on the achievable $d_{\min}$ of the TC [9]. Second, due to its scattering properties, it also affects the correlation of exchanged extrinsic information during the iterative decoding process [19]. In this paper, TC interleaving is defined as follows: the interleaver reads the symbols from the data vector $\mathbf{d} = (d_0, d_1, \ldots, d_{K-1})$ and writes them to the interleaved vector $\mathbf{d}' = (d_{\Pi(0)}, d_{\Pi(1)}, \ldots, d_{\Pi(K-1)})$, where Π denotes the interleaver function. A symbol read out from address $\Pi(i)$ in $\mathbf{d}$ is written to address i in $\mathbf{d}'$. When using CRSC codes as constituent codes of the TC, $\mathbf{d}$ and $\mathbf{d}'$ can be represented by circles, as shown in Fig. 2.

Three of the most popular interleaver families are the QPP interleavers [10], the DRP interleavers [11], and the ARP interleavers [12]. Our study only focuses on the ARP family. As shown in [20], the ARP interleaver can provide the same interleaving properties as the QPP or the DRP interleavers, guaranteeing $d_{\min}$ values *at least as high* as these two families of interleavers.

B. The ARP Interleaver

The ARP interleaver structure is derived from the regular interleaver (RI):

$$\Pi(i) = (P \cdot i) \bmod K \tag{1}$$

where P is the RI period that must be relatively prime to K. Rectangular return to zero (RTZ) error patterns cannot be efficiently avoided with this permutation due to its regular structure [12]. Therefore, a degree of disorder is introduced by a vector of shifts $\mathbf{S}$ into the permutation, leading to the ARP function:

$$\Pi(i) = (P \cdot i + S(i \bmod Q)) \bmod K. \tag{2}$$

The vector of shifts $\mathbf{S}$ has length Q. It represents the introduced disorder degree. Q is a divisor of K [15].

C. Puncturing Pattern

The TC coding rate, R, can be increased by puncturing some bits at the TC output. Periodic puncturing is widely used in practice because it can be easily implemented. In this study, a periodic puncturing pattern with period M is considered (see Fig. 1). CRSC codes with coding rate $1/2$ are used as constituent codes of the TC. Thus, for each constituent CRSC code, the puncturing mask or pattern is composed of two vectors of length M, corresponding to the puncturing positions

in the data ($\mathbf{d}$) and parity vectors ($\mathbf{r_1}$ and $\mathbf{r_2}$). In order to avoid edge effects when applying the puncturing mask, M is assumed to be divisor of K.

III. Interleaver Design Criteria

Two major target criteria have to be considered for the design of a TC interleaver: the Hamming distance spectrum of the resulting TC and the correlation between the channel information and the *a priori* information at the decoder input. The first terms of the distance spectrum have to be maximized, with multiplicities (i.e., the number of codewords at these distances) as low as possible, while the correlation between the channel and the *a priori* information should be minimized. Two measurable parameters related to these criteria have been considered in our work: mimimum span and correlation girth.

A. Minimum Span

The span value associated with a couple of symbols in positions i and j is defined according to [12] and [21] as:

$$S_p(i, j) = f(i, j) + f(\Pi(i), \Pi(j)) \tag{3}$$

where

$$f(u, v) = \min[|u - v|, K - |u - v|], \tag{4}$$

$f(u, v)$ evaluates the shortest distance between two symbols (u and v) in a circular vector of size K, also called Lee distance [22]. Then, the minimum value of span $S_{p\,\min}$ associated to the interleaver is defined as:

$$S_{p\,\min} = \min_{i \neq j}[S(i, j)]. \tag{5}$$

It was shown in [23] that the maximum achievable value for $S_{p\,\min}$ is upper bounded by:

$$S_{\text{ub}} = \left\lfloor \sqrt{2K} \right\rfloor \tag{6}$$

when using tail-biting termination.

The minimum span value affects the TC distance spectrum. In particular, for random-based interleavers, the increase of minimum span was shown to yield larger $d_{\min}$ values for the resulting TC [21]. Therefore, this value needs to be maximized.

B. Correlation Girth

In the turbo decoding process, the decoder output at position $\Pi(i)$ (i.e., corresponding to the symbol at address $\Pi(i)$ in $\mathbf{d}$) depends on the received symbol at the same position and, due to the recursive nature of the constituent code, it is also influenced by received symbols at positions in the vicinity of $\Pi(i)$. In addition, the decoder output at position $\Pi(i)$ also depends on the *a priori* information provided by the second decoder from position i (i.e., associated to the symbol at address i in $\mathbf{d}'$). The corresponding correlation properties depend on the recursive nature of the second decoder (i.e., positions in the vicinity of i in $\mathbf{d}'$) and on the interleaver [24]. This latter should be designed to reduce the level of correlation between the *a priori* information and the data sequence of each constituent code [25]. To this end, a correlation graph

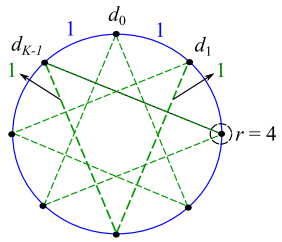

Fig. 3. Example of proposed correlation graph representation for TCs with $r = 4$ and $g = 4$.

can be established in the design of TC interleavers. The resulting interleaver should maximize the correlation girth g (i.e., minimum correlation cycle).

An example of the proposed correlation graph for a TC is shown in Fig. 3. The vertices are the bits of the information sequence. The connections between neighbor bits in the non-interleaved sequence $\mathbf{d}$ are represented by blue edges (outer circle). The green dotted edges are the connections between neighbor bits in the interleaved sequence $\mathbf{d}'$, for a given interleaver Π. This graph shows the different correlation cycles in the turbo decoding process. Note that the correlation graph for TCs is a regular graph of degree $r = 4$ (i.e., each vertex has exactly 4 neighbors) with a number of vertices $x = K$.

An upper bound on the girth value g of a regular graph of degree r can be deduced, based on the Moore bound [26]. Let $x(r, g)$ be the lowest number of vertices in a r-regular graph with girth g. The Moore bound implies that g can be at most proportional to the logarithm of $x(r, g)$:

$$g \leq 2 \log_{r-1}(x(r, g)) + O(1) \tag{7}$$

where $O(1)$ is the error term of the approximation. For the information block sizes considered in this paper, $K = 1504$ and 4000 bits, the upper bounds on the correlation girth obtained from (7) are 13 and 15.

IV. Interleaving With Puncturing Constraints

As shown in [27] and [28], the puncturing of well-chosen systematic bits can increase the $d_{\min}$ value and reduce the convergence threshold of high coding rate TCs. Thus, in this work, we consider the design of puncturing masks including data puncturing. The proposed puncturing mask selection and puncturing constraints on the interleaver design are described in the following sections.

A. Puncturing Mask Selection

The puncturing mask configuration is defined according to the target code rate R of the TC and to the puncturing period M. The target code rate R is computed as:

$$R = \frac{M}{M(1 - D_p) + 2U_p} \tag{8}$$

where the data puncturing rate D_p corresponds to the ratio between the number of punctured data bits (systematic bits) and the total number of data bits. It is illustrated by the puncturing mask applied on vector $\mathbf{d}$ in Fig. 1. U_p is the

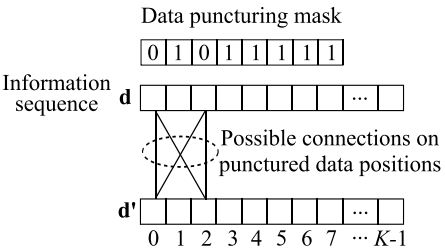

Fig. 4. Example of possible connections between $\mathbf{d}$ and $\mathbf{d}'$ on punctured data positions via a DPC interleaver.

number of unpunctured parity bits per constituent CRSC code in a puncturing period. For given R and M, D_p can take $M+1$ different values:

$$D_p = \frac{m}{M}, m = 0, \ldots, M. \tag{9}$$

However, in practice, the values of D_p are restricted to those ensuring a constituent CRSC code rate R_c smaller than 1, to be able to reconstruct the information sequence from the encoded sequence. From (8), U_p is given by:

$$U_p = \frac{M}{2}\left(\frac{1}{R} + D_p - 1\right). \tag{10}$$

In this study, U_p is an integer value and the same value applies for both CRSC codes, since only symmetric puncturing masks (i.e., same puncturing pattern for both constituent CRSC codes) are considered.

The puncturing mask design proposed in this work involves the following steps:

1) **Find the best puncturing pattern for each D_p value**: The "fast algorithm for searching trees" (FAST) was introduced in [29] to evaluate the Hamming distance spectrum of unpuctured convolutional codes. In practice, only the first terms of the distance spectrum, i.e., a truncated distance spectrum, are needed. When the CRSC code is punctured by a periodic pattern of period M, the FAST algorithm have to be run M times, each time starting from a different position in the mask, from 0 to $M-1$, and the resulting M distance spectra are accumulated to obtain the Hamming distance spectrum of the punctured CRSC code. The best puncturing mask for each D_p value is identified as the one generating the best CRSC Hamming distance spectrum (i.e., highest distance values in the first spectrum terms and minimal number of codewords at these distances). Note that the truncated distance spectrum of convolutional codes is independent of K, provided that K is large enough (in practice, if K is greater than the longest return to zero (RTZ) sequence at the maximum Hamming distance considered in the truncated spectrum). For CRSC codes, an RTZ sequence is defined as any finite input sequence which makes the code leave a given state and return back to the same state.
2) **Carry out a mutual information exchange analysis to select a restricted set of puncturing masks**: In [28], the distribution of the extrinsic information in terms of log-likelihood ratios at the output of a soft-zin soft-out (SISO) decoder was plotted and analyzed. It was shown that the distribution of the extrinsic information related to punctured data positions is different from the one related to unpunctured data positions. Thus, in the considered extrinsic information transfer (EXIT) chart [30] analysis, we do not rely on a Gaussian approximation of the *a priori* message. Rather, we measure the iterative evolution of the *a priori* mutual information, within actual turbo decoding iterations via Monte Carlo simulations. Uniform TC permutations [31] are used to average the effect of the interleaver on the extrinsic information exchange. A similar analysis was used in the past to identify efficient precoding structures for TCs [32]. The average mutual information between the *a posteriori* log-likelihood ratios L of each constituent SISO decoder and the data frame X is computed as in [33] by:

$$I(L; X) = 1 - \frac{1}{K}\sum_{i=1}^{K} \log_2(1 + e^{-x_i L_i}). \tag{11}$$

However, at each decoding iteration, the *a priori* information at the input of one SISO decoder is taken from the other SISO decoder, not from a virtual AWGN channel. In this modified EXIT chart, the best puncturing mask in terms of convergence performance is the one providing the closest crossing point (IA, IE) to $(1, 1)$. Actually, in the selection process, we keep the restricted set of puncturing masks providing crossing points closer to $(1, 1)$ than the mask corresponding to the systematic code ($D_p = 0$).

Afterwards, the error rate performance of the TC is evaluated for the remaining puncturing masks with uniform interleaving. The puncturing mask providing the best tradeoff between performance in the waterfall and error floor regions is finally selected.

B. Data Puncture-Constrained Interleavers

Designing a non-catastrophic puncturing mask with punctured data bits is an easy task for the first (non-interleaved) CRSC code of the TC [34], using for instance the above-mentioned FAST algorithm. However, when designing TC interleavers, data puncturing constraints must be considered to avoid semi-catastrophic or catastrophic puncturing masks in the second (interleaved) CRSC code [5], [34]. Indeed, due to such poor puncturing patterns, the Hamming distance spectrum of the CRSC code can contain a $d_{\min}$ value equal to one or even zero. To avoid poor puncturing patterns in the second CRSC code, a data puncture-constrained (DPC) interleaver must guarantee the same data puncturing pattern in both constituent CRSC codes [34]. For instance, the possible connections made by a DPC interleaver between punctured data positions from $\mathbf{d}$ to $\mathbf{d}'$ are shown in Fig. 4, for a data puncturing mask with period $M = 8$. Note that only the first puncturing period is shown in the figure, but connections between different periods are also admitted.

C. Protograph-Based Interleavers

The following analysis aims to identify additional useful puncturing constraints for the design of TC interleavers.

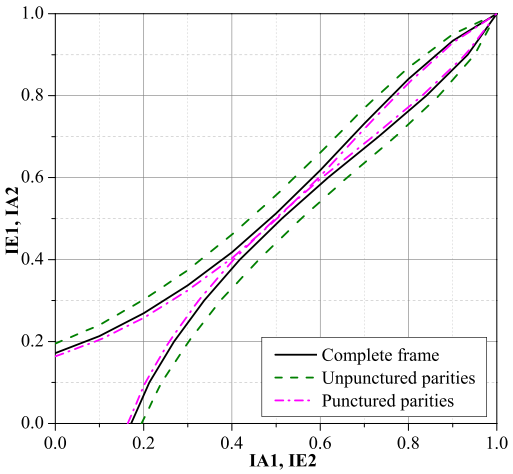

Fig. 5. Comparison of EXIT charts computed from the complete data frame and from punctured and unpunctured parity positions at the signal-to-noise (SNR) decoding threshold of the TC over the AWGN channel.

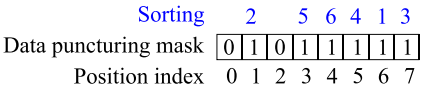

Fig. 6. Example of sorting result of unpunctured data positions by increasing error-prone level (1 = least error-prone position, 6 = most error-prone position).

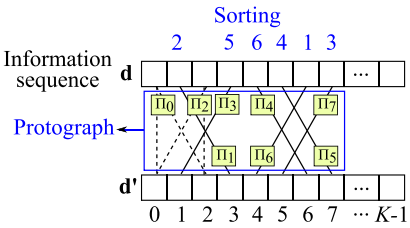

Fig. 7. Example of protograph for $M = 8$ according to the sorting of unpunctured data positions from Fig. 6.

Our approach is based on the observation that, for a punctured code, the reliability of extrinsic information related to an information symbol depends on different parameters such as the position of considered symbol in the puncturing period, the puncturing or not of the corresponding parity, and the number of punctured parities in the case of constituent codes with several parities per information symbol.

During the turbo decoding process, extrinsic information from a given constituent decoder is generated based on its received parity sequence and is sent to the other constituent decoder via the interleaver/deinterleaver as *a priori* information on data. The extrinsic information computed from unpunctured parity positions is expected to be more reliable than the one generated from punctured parity positions. In order to illustrate this conjecture, we have plotted a conventional EXIT chart for a TC only on positions with punctured parities, only on positions with unpunctured parities and on the complete frame. As shown in Fig. 5, the EXIT curve obtained from data at unpunctured parity positions shows a wider tunnel opening between the EXIT curves than the one obtained from data at punctured parity positions.

Since extrinsic information is used as *a priori* information on data, a possible strategy for the interleaver construction involves *connecting the positions with highly reliable extrinsic information to the positions with unreliable extrinsic information, which are more prone to errors*. This connection strategy aims to spread the correction capability of the TC over the whole data block. A particular case involves sorting the data positions in a puncturing period M by increasing order of reliability and connecting via the interleaver the least error-prone data positions of one CRSC code to the most error-prone data positions of the other one. We named the resulting connection graph *protograph*, refering to protograph-based LDPC codes [17], since the proposed protograph defines a set of inter-period permutations. The protograph will be then defined as follows:

1) **Sorting of unpunctured data positions by error-prone level in a puncturing period M**: To this end, the unpunctured data positions are punctured in turn with an associated evaluation of the distance spectrum of the resulting CRSC code. They are then sorted according to their distance spectrum: the *least error-prone data position* is the one with the best distance spectrum (i.e., the highest $d_{\min}$ and the lowest multiplicity; in the case of equal $d_{\min}$ values and multiplicities the next higher distance is considered) for the resulting CRSC code when punctured and the *most error-prone data position* is the one with the poorest distance spectrum (i.e., the lowest $d_{\min}$ and the highest multiplicity) for the resulting CRSC code when punctured. Note that additional data puncturing is only introduced to evaluate the error-prone level of unpunctured data positions and is then removed from the puncturing mask. An example of sorting of unpunctured data positions via this procedure is shown in Fig. 6 for a puncturing period $M = 8$.
2) **Cross connection of unpunctured data positions**: The protograph involves connecting via the interleaver the least error-prone data position of one CRSC code to the most error-prone data position of the other one, the second least error-prone data position to the second most error-prone data position, and so on. Fig. 7 shows an example of protograph for $M = 8$ considering the sorting of unpunctured data positions from Fig. 6. Dotted lines correspond to possible connections between punctured data positions due to the data puncturing constraint. The protograph is periodically applied via the interleaver to the information sequence $\mathbf{d}$. For $M = 8$, the protograph is represented as in Fig. 7 by 8 different sub-interleavers $(\Pi_0, \ldots, \Pi_7)$, where for example Π_1 ensures that symbols at position 2 within a puncturing period in $\mathbf{d}$ are interleaved to position 3 within a puncturing period in $\mathbf{d}'$.

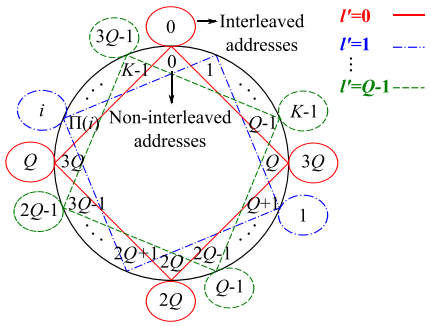

Fig. 8. Example of division of the ARP structure into Q layers, in the case $S(0), \ldots, S(Q-1) = 0$ and $K = 4Q$. Non-interleaved addresses, $\Pi(i)$, are placed in the inner part of the circle, and their corresponding interleaved addresses, i, in the outer part.

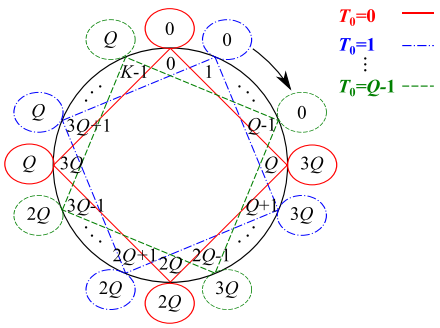

Fig. 9. Example of possible inter-layer shifts for layer $l' = 0$, with $K = 4Q$.

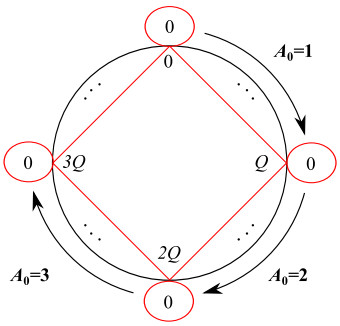

Fig. 10. Example of possible intra-layer shifts for layer $l' = 0$, with $T_0 = 0$ and $K = 4Q$.

V. LAYERED CONSTRUCTION OF ARP INTERLEAVERS

Different methods to select ARP interleaver parameters have been investigated, e.g., [12], [15]. However, the high coding rate TCs derived from these codes are still subject to error floors detrimental to applications with high reliability requirements. In this paper, we propose an alternative construction method, based on a layered approach, that helps to design TCs with high $d_{\min}$ values. In addition, the proposed approach facilitates the introduction of the above-mentioned puncturing constraints into the interleaver design, as well as the verification of other design criteria such as minimum span $S_{p\,\min}$ and minimum girth g targets.

In order to simplify the interleaver parameters selection, the interleaver addresses, $\Pi(i)$, are divided into different groups that are incrementally defined. Let us consider equation (2), it can be shown that (see Appendix A for the proof):

$$\Pi(i+Q) \bmod Q = \Pi(i) \bmod Q. \tag{12}$$

Therefore, Q groups of permutation addresses are identified, each corresponding to a given modulo Q value. The sequences $\mathbf{d}$ and $\mathbf{d}'$ are divided into these Q different layers of K/Q bits. The layer index l for the bit $\Pi(i)$ in sequence $\mathbf{d}$ and the layer index l' for the bit i in sequence $\mathbf{d}'$ are defined by:

$$l = \Pi(i) \bmod Q \tag{13}$$

$$l' = i \bmod Q \tag{14}$$

The interleaver is defined by a group of Q different regular permutations, each linking a layer l in the non-interleaved sequence $\mathbf{d}$ to its corresponding layer l' in the interleaved sequence $\mathbf{d}'$. It can be represented on a circle, as shown in Fig. 8, where each layer is identified by a color (and a line type) and a layer index. The addresses in the non-interleaved order, denoted by $\Pi(i)$, are at the inner part of the circle, and their corresponding addresses i, in the interleaved order, are at the outer part of the circle.

For a bit of layer l' at address i, the proposed interleaver chooses the shift value $S(l')$ decomposed into inter-layer shift $T_{l'}$ and intra-layer shift $A_{l'}$ such as:

$$S(l') = T_{l'} + A_{l'} Q \tag{15}$$

where $T_{l'} = 0, \ldots, Q-1$ and $A_{l'} = 0, \ldots, (K/Q)-1$. The inter-layer shift $T_{l'}$ defines the value of the layer position l (or equivalently the position within the period Q) of the non-interleaved sequence $\mathbf{d}$ that will be connected to layer position l' of the interleaved sequence $\mathbf{d}'$ as shown in Fig. 9. The intra-layer shift $A_{l'}$ defines which position, from of the K/Q possible ones within layer l (or equivalently which period), to be connected to address i as illustrated in Fig. 10.

This layered construction simplifies the validation of $S_{p\,\min}$ and g targets in the interleaver design step, since these criteria are verified each time a new layer is placed or equivalently its corresponding $S(l')$ value is defined.

In order to simplify the introduction of puncturing constraints into the interleaver design, the disorder degree Q of the ARP interleaver is set as a multiple of the puncturing period M. In this study, Q is set equal to M. In other words, the periodic disorder degree of the interleaver and puncturing period are identical. Since the PB interleaver constraints define a Q-periodic connection strategy for unpunctured data bits on one side and since the proposed ARP interleaver is defined by a group of Q different regular permutations on the other side, the $T_{l'}$ values are chosen to apply these constraints. Indeed, the validation of puncturing constraints within a puncturing period $M = Q$ is a sufficient condition for their validation

in the whole data sequence. Note that for a given layer l' in $\mathbf{d}'$ the corresponding layer position l in $\mathbf{d}$ is obtained by $l = (P \cdot l' + T_{l'}) \bmod Q$. Thus, a periodic connection pattern, with period Q, is established by the inter-layer shifts $T_{l'}$ between $\mathbf{d}$ and $\mathbf{d}'$, for a given P.

The Q layers of the interleaver structure can be defined incrementally by choosing their corresponding value $S(l')$. Note that the initial position of each layer (i.e., before the introduction of the described shifts) is defined by the value of P.

A. Overall Interleaver Construction Method

For a given set of design parameters ($S_{p\,\min}$ and g targets, K, R, polynomial generators, and puncturing mask), the proposed interleaver design strategy involves the following steps:

1) **Select the candidate values for P**: The set of admissible values for P is the group of integers from 1 to $K-1$ relatively prime to K. In this set, only the C candidate values for P ensuring a $S_{p\,\min}$ value (5) greater than or equal to $S_{p\,\min}$ target, considering a RI structure (1), are selected.
2) **Select the Q shift values for each candidate value for P**: A detailed description of the different steps of the shifts selection, for the C candidates for P, is presented in Appendix B. To summarize, for each candidate value for P, layer l' is placed by computing a value for $S(l')$ from (15), fulfilling puncturing constraints if any (see Section IV). For this value, $S_{p\,\min}$ and g are evaluated. If they are equal to or higher than $S_{p\,\min}$ and g targets, one can move on to layer $l'+1$. If the $S_{p\,\min}$ and g targets are not met, another value for $S(l')$ has to be evaluated. This process is performed until the whole group of Q shift values are determined.
3) **Select the best ARP interleaver candidate**: As a last phase of design, the best candidate for TC interleaver is selected from the group of candidates previously generated by comparing their Hamming distance spectra. The truncated TC Hamming distance spectrum can be estimated by different methods as proposed in [35]. The ARP interleaver candidate with the best TC Hamming distance spectrum is chosen.

Determining a suitable couple of $S_{p\,\min}$ and g targets for obtaining good ARP interleaver candidates is not trivial. However, a possible selection strategy involves the following steps: first, evaluate the convergence of the algorithm in Appendix B for values of $S_{p\,\min}$ and g set to their corresponding upper bounds (see Sections III-A and III-B). Then, if the algorithm does not converge, progressively reduce $S_{p\,\min}$ and g until the algorithm converges to a group of ARP candidate interleavers.

B. Summary of Puncture-Constrained Interleaver Design Method

This section summarizes the proposed method to jointly optimize the TC interleaver with the puncturing pattern:

1) **Select the puncturing mask:** The best puncturing mask for the constituent CRSC code of the TC, in terms of constituent code distance spectrum and TC extrinsic information exchange, is identified according to Section IV-A.
2) **Define the puncturing constraints:** The corresponding puncturing constraints that must be fulfilled by the interleaver are determined according to Sections IV-B and IV-C.
3) **Generate the candidate interleavers:** A group of candidate interleavers validating the different design criteria (e.g., $S_{p\,\min}$ and g targets, and proposed puncturing constraints) is generated via the method described in Section V-A. Finally, the candidate interleaver with the best TC Hamming distance spectrum is selected.

TABLE I

BEST CRSC DISTANCE SPECTRUM FOR EACH D_p, CORRESPONDING CODEWORD MULTIPLICITIES AT DISTANCE d, $\alpha(d)$, AND PUNCTURING MASKS (0 = PUNCTURED, 1 = UNPUNCTURED). $R = 2/3$, $M = 8, 16$

D_p	R_c	$\alpha(0)$	$\alpha(1)$	$\alpha(2)$	$\alpha(3)$	$\alpha(4)$	$\frac{\text{Data}}{\text{Parity}}$
0	0.8	0	0	0	15	89	$\frac{11111111}{10100000}$
2/16	0.84	0	0	2	49	344	$\binom{11111111}{10111011}$ $\binom{01000001}{01001100}$
2/8	0.88	0	0	3	62	566	$\frac{01111110}{11000001}$
6/16	0.94	0	0	21	424	7490	$\binom{11101011}{10101010}$ $\binom{00010100}{01110101}$
4/8	1	0	8	64	482	3616	$\frac{11110000}{11100001}$
6/8	1.14	1	36	670	12122	219196	$\frac{01000100}{11011100}$

VI. APPLICATION EXAMPLES

We have applied the previous design guidelines to two coding rates, $R = 2/3$ and $4/5$, for $K = 1504$ bits, available in the LTE standard. The constituent code is the CRSC code with feedback and feedforward polynomials 13 and 15 (expressed in octal format) CRSC$(1, 15/13)_8$. Only the design for code rate $2/3$ is detailed hereafter.

A. Puncturing Mask Selection

We consider puncturing periods M of 8 and 16. Table I lists the distance spectrum of the constituent CRSC code for the best puncturing masks at each D_p value. The analysis of the distance spectra shows that D_p values higher or equal to $6/8$ should be avoided, since the puncturing mask becomes catastrophic for the CRSC code.

The TC convergence behavior with the different puncturing masks is then analyzed, using uniform interleaving. Fig. 11 shows the modified EXIT chart of the TC evaluated at its signal-to-noise ratio (SNR) decoding threshold for $D_p = 0$. The puncturing masks providing better TC convergence performance than the $D_p = 0$ mask correspond to $D_p = 2/16$ and $2/8$. We finally choose the puncturing mask with $D_p = 2/8$, which displays the best error floor performance in the error rate evaluation.

B. Protograph Construction

For the selected mask, the unpunctured data positions are sorted as explained in Section IV-C. Table II lists the different

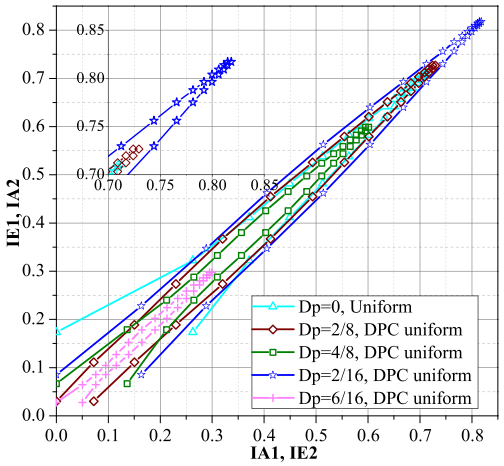

Fig. 11. Extrinsic information exchange between constituent codes of the TC at $E_b/N_0 = 1.6$ dB, 16 decoding iterations with the maximum *a posteriori* probability (MAP) algorithm, $K = 1504$, and $R = 2/3$ under uniform interleaving over the AWGN channel (DPC uniform: uniform interleaving including data puncturing constraint).

TABLE II

CRSC DISTANCE SPECTRUM OF THE D_p-2/8 MASK WHEN ONE ADDITIONAL DATA BIT IS PUNCTURED. $\alpha(d)$ IS THE MULTIPLICITY OF CODEWORDS AT DISTANCE d. CONSIDERED PARITY PUNCTURING MASK = 11000001 (0 = PUNCTURED, 1 = UNPUNCTURED)

$\alpha(0)$	$\alpha(1)$	$\alpha(2)$	$\alpha(3)$	$\alpha(4)$	Data Punc. Mask
0	0	1880	1060320	465121494	00111110
0	0	4000	2003510	671273377	01011110
0	4	3015	1151175	294778989	01101110
0	8	140	2229	35176	01110110
0	2	2256	1275364	320347391	01111010
0	4	3019	1152688	148963135	01111100

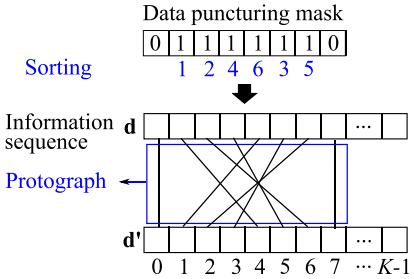

Fig. 12. Sorting of unpuntured data positions inferred from Table II and resulting protograph for the D_p-2/8 mask, $R = 2/3$ and $M = 8$.

distance spectra, truncated to distance 4, obtained including one additional punctured data symbol from positions 1 to 6 in the mask. Fig. 12 shows the corresponding sorting of unpunctured data positions and the resulting protograph for the D_p-2/8 mask, $R = 2/3$ and $M = 8$.

C. Puncture-Constrained Interleaver Design

For $K = 1504$, $S_{p\,\min}$ has an upper bound of 54 as defined in (6). Following the strategy introduced in Section V-A, a $S_{p\,\min}$ goal of 80-85% of the $S_{p\,\min}$ upper bound and a g goal of 8 were selected to guarantee the convergence of the algorithm described in Appendix B.

TABLE III

BEST CANDIDATES FOR ARP INTERLEAVER WITH THE DIFFERENT PUNCTURING CONSTRAINTS, $S_{p\,\min} = 45$, $g = 8$, $S(0) = 0$, $R = 2/3$ AND $K = 1504$

ARP	P	$S(1)$	$S(2)$	$S(3)$	$S(4)$	$S(5)$	$S(6)$	$S(7)$
NDP	399	792	630	829	1010	90	1471	658
DPC	227	495	998	280	1090	734	361	362
PB	651	89	528	852	1501	1396	688	490

TABLE IV

ESTIMATED DISTANCE SPECTRUM, TRUNCATED TO THREE TERMS, OF THE RESULTING TC FOR THE BEST ARP INTERLEAVERS IN AWGN CHANNEL WITH CORRESPONDING MULTIPLICITIES $\alpha(d)$ AND CUMULATED INPUT WEIGHT AT $d_{\min} = d_0$, w_{d_0}. $R = 2/3$ AND $K = 1504$

ARP	w_{d_0}	d_0	d_1	d_2	$\alpha(d_0)$	$\alpha(d_1)$	$\alpha(d_2)$
NDP	5640	15	16	17	1128	4512	7708
DPC	4324	19	20	21	752	1880	5264
PB	10716	20	21	22	1504	3008	6016

1) **Selection of the candidate values for *P***: The maximum achievable value of $S_{p\,\min}$ obtained when testing all the admissible candidate values for P considering a RI structure is 52. Thus, we limited the search to candidates for P leading to $S_{p\,\min}$ values between 45 and 52.
2) **Selection of the *Q* shift values for each candidate for *P***: The parameters for the ARP interleaver candidates are determined by the algorithm in Appendix B. Three different design configurations have been studied. In the first one (NDP), no data bits are punctured ($D_p = 0$). In the other two, DPC, and PB ARP interleavers are considered for the D_p-2/8 mask. DPC interleavers have already been studied in the past [34]. In this study, DPC interleavers are designed based on the ARP model for comparison purposes. In order to compare the efficiency of the different configurations in finding large $d_{\min}$ values, the same number of ARP candidates $(64,000)$ is generated by each configuration.
3) **Selection of the best ARP interleaver candidate**: Table III lists the best ARP interleavers generated for each design configuration. All candidates achieve a $S_{p\,\min}$ value of 45 and a g value of 8. Their respective distance spectrum, truncated to three terms, is estimated and given in Table IV. It is observed that the use of data puncturing allows a larger $d_{\min}$ value to be reached. Furthermore, the PB ARP interleaver achieves the largest $d_{\min}$.

Finally, the statistics on the search efficiency of the different configurations for large $d_{\min}$ values is provided in Table V. The configurations are compared in terms of the number of obtained candidates meeting the $S_{p\,\min}$ and g targets. Note that the more the constraints included into the interleaver design (e.g., DPC, PB), the larger the number of candidates validating these criteria. Actually, the introduction of these constraints reduces the randomness of the interleaver design

TABLE V

STATISTICS ON THE EFFICIENCY OF THE SEARCH AMONG 64,000 INITIAL CANDIDATES FOR EACH ARP CONFIGURATION. FIGURES OBTAINED FOR $R = 2/3$, $K = 1504$, USING CPU INTEL CORE I5 3.3 GHZ WITH RAM 8 GB

ARP	NDP	DPC	PB
Candidates found meeting $S_{p\,\min}$ and g targets	3873	6803	11026
Total time (day)	0.81	1.27	3.65
Percentage of candidates with $d_{\min} \geqslant 18$ (%)	0	1.95	4.53
Average time to find a candidate with $d_{\min} \geqslant 18$ (min)	-	13.67	10.53
Number of candidates with $d_{\min} = 19$	0	7	40
Number of candidates with $d_{\min} = 20$	0	0	1

TABLE VI

BEST CANDIDATES FOR ARP INTERLEAVER WITH THE DIFFERENT PUNCTURING CONSTRAINTS, $S_{p\,\min} = 39$, $g = 8$, $R = 4/5$ AND $K = 1504$

ARP	P	$(S(0), ..., S(15))$
NDP	725	(0, 250, 1224, 239, 931, 48, 236, 449, 30, 856, 1487, 1228, 1440, 1372, 293, 93)
DPC	267	(0, 1436, 521, 1492, 1048, 1142, 1337, 957, 57, 1125, 740, 189, 56, 650, 852, 158)
PB	365	(0, 1261, 1374, 1279, 417, 867, 549, 514, 730, 474, 1359, 285, 927, 670, 1176, 1078)

TABLE VII

ESTIMATED DISTANCE SPECTRUM FOR THE BEST ARP INTERLEAVERS IN AWGN CHANNEL WITH CORRESPONDING MULTIPLICITIES $\alpha(d)$ AND CUMULATED INPUT WEIGHT AT $d_{\min} = d_0$, w_{d_0}. $R = 4/5$ AND $K = 1504$

ARP	w_{d_0}	d_0	d_1	d_2	$\alpha(d_0)$	$\alpha(d_1)$	$\alpha(d_2)$
NDP	12220	9	10	11	2350	8554	29516
DPC	10434	11	12	13	1880	5358	16732
PB	4324	11	12	13	752	4794	15134

process and facilitates the validation of the span and girth criteria. Furthermore, the addition of the different constraints to the interleaver design allows the percentage of candidates with a $d_{\min}$ of at least 18 to be increased and the average time to find such candidates to be reduced. Thus, the search becomes more efficient due to the introduction of the design constraints. Note that PB candidates are the best in terms of $d_{\min}$ value.

The proposed design guidelines were also applied to a code rate $R = 4/5$. Table VI lists the best ARP interleavers generated for each design configuration. All candidates achieve a $S_{p\,\min}$ value of 39 and a g value of 8. Their respective distance spectrum is estimated and given in Table VII.

VII. SIMULATED PERFORMANCE RESULTS

The error rate performance of TCs using the interleaver parameters of Tables III and VI is evaluated in AWGN channel with BPSK modulation and a maximum of 16 decoding iterations with the maximum *a posteriori* probability (MAP) algorithm. The estimated truncated distance spectra listed in Tables IV and VII are used to compute the truncated union upper bounds (TUBs) [36]. In addition, error rate simulation results for the original LTE [4] TC are included for comparison.

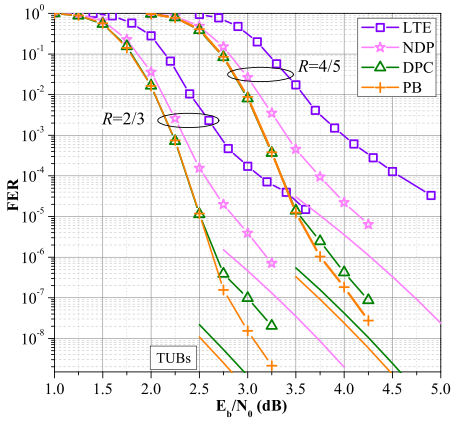

Fig. 13. Frame error rate performance comparison between the different ARP interleaver configurations and the LTE in AWGN channel with a maximum of 16 decoding iterations of the MAP algorithm for $R = 2/3$, $R = 4/5$, $K = 1504$ bits, and constituent CRSC codes with generator polynomials $(1, 15/13)_8$.

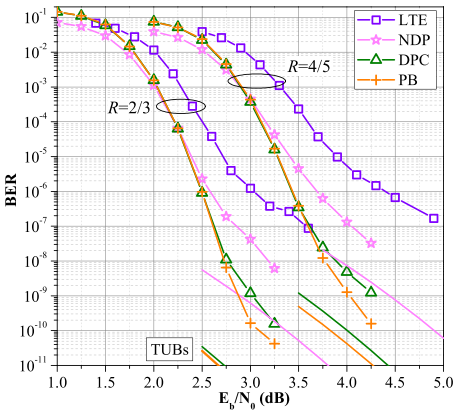

Fig. 14. Bit error rate performance comparison between the different ARP interleaver configurations and the LTE in AWGN channel with a maximum of 16 decoding iterations of the MAP algorithm for $R = 2/3$, $R = 4/5$, $K = 1504$ bits, and constituent CRSC codes with generator polynomials $(1, 15/13)_8$.

Figs. 13 and 14 show the FER and BER performance of the 8-state CRSC$(1, 15/13)_8$ TC for $K = 1504$ bits, $R = 2/3$ and $4/5$. We observe that DPC and PB interleavers achieve a substantial asymptotic performance gain compared to the NDP interleaver. The proposed PB interleaver achieves a slightly better asymptotic performance than the DPC interleaver for both code rates. Compared to the LTE TC, the proposed PB

interleaver provides a gain of about 0.5 and 0.7 dB at $2{\cdot}10^{-3}$ of FER for $R = 2/3$ and $4/5$, respectively and almost 4 decades in error floor in both cases (see Fig. 13).

Fig. 15 shows a comparison of the required SNR at 10^{-3} of FER evaluated over AWGN channel with QPSK modulation, between the proposed TCs, parity-check (PC) polar codes, and low-density parity-check (LDPC) codes considered during the 3GPP standardization process. The proposed TCs perform a maximum of 8 decoding iterations of the scaled max-log MAP algorithm, PC polar codes use the successive cancellation list-8 decoding algorithm, and LDPC codes use the layered offset min-sum algorithm with 20 decoding iterations. The three families of codes allow the same level of flexibility in terms of coding rate and frame size. The corresponding performance results are taken from [37] for the proposed TCs, from [38] ($R = 1/5$) and [39] for PC polar codes, and from [40] and [41] for LDPC codes. For short information block sizes (K around 100 bits) TCs and PC polar codes show similar error rates, while LDPC codes suffer of short correlation cycles leading to a degraded performance. As the information frame size increases, the error rate shown by the three family of codes becomes equivalent. Note that as the coding rate decreases the proposed TCs start to exhibit best performance. Additionally, performance results of LDPC codes finally adopted for 5G (from [42]) performing 50 iterations of the sum-product algorithm are included. As can be expected, obtained performance is better than the one obtained with the layered offset min-sum algorithm, especially for the largest frame size. However, even if the proposed TCs use the scaled max-log MAP decoding algorithm, the proposed TCs remain competitive when compared to these codes. Please note that these results do not necessarily provide a fair comparison due to large disparities in the levels of required decoding complexity. They have been included for information purposes.

As we can observe in the presented application examples, the proposed approach brings a gain both in convergence and in the error floor compared to the LTE code, showing that the association between the rate matching and the QPP interleaver of LTE is sub-optimal. Furthermore, the proposed TCs are competitive in terms of performance against considered PC polar and LDPC codes for the 5G.

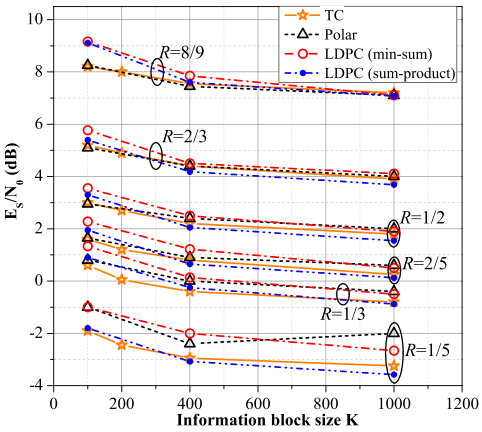

Fig. 15. Comparison of required SNR at 10^{-3} of frame error rate, for QPSK modulation, between the proposed TC with 8 decoding iterations of the scaled max-log MAP algorithm, parity-check polar code of [38] and [39] with the successive cancellation list-8 decoding algorithm, LDPC code of [40] and [41] with 20 decoding iterations of the layered offset min-sum algorithm, and LDPC code of [42] with 50 decoding iterations of the sum-product algorithm.

VIII. CONCLUSION

A new method to design TC interleavers is proposed, which calls for a joint optimization of puncturing patterns and interleaver function. Catastrophic puncturing masks for the constituent codes of the TC are early identified in the selection process by evaluating their respective distance spectrum. Then, a modified EXIT chart analysis allows identifying a suitable puncturing mask for the TC in terms of convergence performance, with data puncturing.

It was shown that significant improvements in the waterfall and error floor regions can be achieved by including puncturing constraints into the interleaver design. The best candidates in terms of $d_{\min}$ are obtained by using the proposed PB interleaver.

Finally, the presented method allows an easy introduction of puncturing constraints as well as the validation of other design criteria such as span and correlation girth into the interleaver design. The generation of ARP interleavers validating the different design criteria is greatly simplified in comparison to previous methods, since the proposed layered construction suitably limits the search space for the different interleaver parameters.

Thanks to the proposed method, enhanced turbo codes were designed and submitted to the 3GPP standardization process for 5G. They are currently being considered for the ultra-reliable and machine type communication scenarios.

APPENDIX A
PROOF OF $\Pi(i+Q)\bmod Q = \Pi(i)\bmod Q$

Considering (2), $\Pi(i+Q)$ can be written:

$$\begin{aligned}\Pi(i+Q) &= (P(i+Q) + S((i+Q) \bmod Q))\bmod K \\ &= (P\cdot i + S(i \bmod Q) + QP)\bmod K \\ &= (\Pi(i) + QP)\bmod K\end{aligned}$$

Then, noting that K is a multiple of Q:

$$\begin{aligned}\Pi(i+Q)\bmod Q &= ((\Pi(i) + QP)\bmod K)\bmod Q \\ &= (\Pi(i) + QP)\bmod Q \\ &= \Pi(i)\bmod Q\end{aligned}$$

APPENDIX B

Algorithm 1 Selection of the ARP Interleaver Parameters

Initialization : K, puncturing mask, $S_{p\,\min}$ and g targets, C candidate values for P, and $Q \leftarrow M$.
for $j := 0$ to $C-1$ **do**
  $CurrentLayer \leftarrow 0$, $Stay \leftarrow 1$, $flag \leftarrow 0$.
  while $Stay = 1$ **do**
    switch $(flag)$
    case 0**:**
      $l' := CurrentLayer$.
      Select a value for $T_{l'}$ at random from its possible values fulfilling puncturing constraints, if any.
      if there are no more possible values for $T_{l'}$ **then**
        $flag := 2$.
      else
        $flag := 1$.
      end if
    case 1**:**
      Select a value for $A_{l'}$ at random from its possible values.
      if there are no more possible values for $A_{l'}$ **then**
        $flag := 2$.
      else
        $flag := 3$.
      end if
    case 2**:**
      $CurrentLayer := CurrentLayer - 1$.
      if $CurrentLayer \leqslant 0$ **then**
        $Stay := 0$.
      else
        $flag := 0$.
      end if
    case 3**:**
      Obtain $S(l')$ by (15) and the interleaved addresses from (2) with $P := P(j)$, evaluate $S_{p\,\min}$ (5) and g.
      if $S_{p\,\min}$ and g targets are met **then**
        Save the value of $S(l')$.
        if $CurrentLayer < Q-1$ **then**
          $CurrentLayer := CurrentLayer + 1$.
          $flag := 0$.
        else
          A valid ARP interleaver candidate is found: $Stay := 0$.
        end if
      else
        $flag := 1$.
      end if
    end switch
  end while
end for

REFERENCES

[1] P. Marques *et al.*, "Broadcasting-Broadband convergence," CRS-I White Paper, Jun. 2013. [Online]. Available: http://www.ict-crsi.eu/index.php?option=com_content&view=article&id=9&Itemid=112&jsmallfib=1&dir=JSROOT/CRS-I+White+Papers

[2] E. Dahlman, G. Mildh, S. Parkvall, J. Peisa, J. Sachs, and Y. Selen. (Jun. 2014). 5G Radio Access. Ericsson Review. [Online]. Available: http://www.ericsson.com/res/thecompany/docs/publications/ericsson_review/2014/er-5g-radio-access.pdf

[3] "Evolution, convergence, and innovation," Datang Wireless Mobile Innov. Center Datang Telecom Technol. Ind. Group, Beijing, China, 5G White Paper, Dec. 2013. [Online]. Available: http://www.datanggroup.cn/upload/accessory/201312/2013129194455265372.pdf

[4] *LTE Envolved Universal Terrestrial Radio Access (E-UTRA): Multiplexing and Channel Coding*, document TS 136 212 (V10.0.0), ETSI, Jan. 2011.

[5] J. F. Cheng, A. Nimbalker, Y. Blankenship, B. Classon, and T. K. Blankenship, "Analysis of circular buffer rate matching for LTE Turbo code," in *Proc. IEEE 68th Veh. Technol. Conf. (VTC-Fall)*, Sep. 2008, pp. 1–5.

[6] C. Berrou, A. Glavieux, and P. Thitimajshima, "Near Shannon limit error-correcting coding and decoding: Turbo-codes," in *Proc. IEEE Int. Conf. Commun. (ICC)*, vol. 2. Geneva, Switzerland, May 1993, pp. 1064–1070.

[7] *IEEE Standard for Local and Metropolitan Area Networks, Part 16: Air Interface for Fixed and Mobile Broadband Wireless Access Systems*, IEEE Standard 802.16-2004/Cor 1-2005, Feb. 2006.

[8] *Digital Video Broadcasting (DVB): Second Generation DVB Interactive Satellite System (DVB-RCS2): Part 2: Lower Layers for Satellite Standard*, document EN 301 545-2 (V1.1.1), ETSI, Jan. 2012.

[9] C. Berrou and A. Glavieux, "Near optimum error correcting coding and decoding: Turbo-codes," *IEEE Trans. Commun.*, vol. 44, no. 10, pp. 1261–1271, Oct. 1996.

[10] J. Sun and O. Y. Takeshita, "Interleavers for Turbo codes using permutation polynomials over integer rings," *IEEE Trans. Inf. Theory*, vol. 51, no. 1, pp. 101–119, Jan. 2005.

[11] S. Crozier and P. Guinand, "Distance upper bounds and true minimum distance results for Turbo-codes designed with DRP interleavers," *Ann. Télécommun.*, vol. 60, nos. 1–2, pp. 10–28, 2005.

[12] C. Berrou, Y. Saouter, C. Douillard, S. Kerouedan, and M. Jezequel, "Designing good permutations for Turbo codes: Towards a single model," in *Proc. IEEE Int. Conf. Commun., (ICC)*, vol. 1. Paris, France, Jun. 2004, pp. 341–345.

[13] *Digital Video Broadcasting (DVB): Interaction Channel for Satellite Distribution Systems*, document EN 301 790 (V1.3.1), ETSI, Mar. 2003.

[14] S. Crozier and P. Guinand, "High-performance low-memory interleaver banks for Turbo-codes," in *Proc. IEEE 54th Veh. Technol. Conf. (VTC-Fall),* vol. 4. Atlantic City, NJ, USA, Oct. 2001, pp. 2394–2398.

[15] Y. Saouter, "Selection procedure of Turbocode parameters by combinatorial optimization," in *Proc. 6th Int. Symp. Turbo Codes Iterative Inf. Process. (ISTC)*, Brest, France, Sep. 2010, pp. 156–160.

[16] R. Garzón-Bohórquez, C. A. Nour, and C. Douillard, "Improving Turbo codes for 5G with parity puncture-constrained interleavers," in *Proc. 9th Int. Symp. Turbo Codes Iterative Inf. Process. (ISTC)*, Brest, France, Sep. 2016, pp. 151–155.

[17] J. Thorpe, "Low-density parity-check (LDPC) codes constructed from protographs," Jet Propulsion Lab., Pasadena, CA, USA, IPN Progr. Rep. 42-154, Aug. 2003, vol. 42.

[18] C. Weiss, C. Bettstetter, and S. Riedel, "Code construction and decoding of parallel concatenated tail-biting codes," *IEEE Trans. Inf. Theory*, vol. 47, no. 1, pp. 366–386, Jan. 2001.

[19] J. Hokfelt, O. Edfors, and T. Maseng, "Interleaver design for Turbo codes based on the performance of iterative decoding," in *Proc. IEEE Int. Conf. Commun. (ICC)*, vol. 1. Vancouver, BC, Canada, Jun. 1999, pp. 93–97.

[20] R. Garzón-Bohórquez, C. A. Nour, and C. Douillard, "On the equivalence of interleavers for Turbo codes," *IEEE Wireless Commun. Lett.*, vol. 4, no. 1, pp. 58–61, Feb. 2015.

[21] S. Crozier, "New high-spread high-distance interleavers for Turbo-codes," in *Proc. 20th Biennial Symp. Commun.*, Kingston, ON, Canada, May 2000, pp. 3–7.

[22] D. V. Truhachev, M. Lentmaier, and K. S. Zigangirov, "Some results concerning the design and decoding of Turbo-codes," *Problems Inf. Transmiss.*, vol. 37, no. 3, pp. 190–205, 2001.

[23] E. Boutillon and D. Gnaedig, "Maximum spread of D-dimensional multiple Turbo codes," *IEEE Trans. Commun.*, vol. 53, no. 8, pp. 1237–1242, Aug. 2005.

[24] J. Hokfelt, O. Edfors, and T. Maseng, "Turbo codes: Correlated extrinsic information and its impact on iterative decoding performance," in *Proc. IEEE 49th Veh. Technol. Conf. (VTC-Spring)*, vol. 3. Houston, TX, USA, May 1999, pp. 1871–1875.

[25] H. R. Sadjadpour, M. Salehi, N. J. A. Sloane, and G. Nebe, "Interleaver design for short block length Turbo codes," in *Proc. IEEE Int. Conf. Commun. (ICC)*, vol. 2. New Orleans, LA, USA, Jun. 2000, pp. 628–632.

[26] N. Biggs, "Minimal regular graphs with given girth," in *Algebraic Graph Theory*. New York, NY, USA: Cambridge Univ. Press, 1974, pp. 180–190.

[27] S. Crozier and K. Gracie, "On the error-rate performance of 4-state Turbo codes with puncture-constrained DRP interleavers," in *Proc. IEEE Int. Conf. Commun. (ICC)*, Jun. 2012, pp. 2601–2605.

[28] K. Gracie and S. Crozier, "Convergence performance and EXIT analysis of 4-state partially-systematic Turbo codes," in *Proc. 5th Int. Symp. Turbo Codes Rel. Topics*, Sep. 2008, pp. 414–419.

[29] M. L. Cedervall and R. Johannesson, "A fast algorithm for computing distance spectrum of convolutional codes," *IEEE Trans. Inf. Theory*, vol. 35, no. 6, pp. 1146–1159, Nov. 1989.

[30] S. ten Brink, "Convergence behavior of iteratively decoded parallel concatenated codes," *IEEE Trans. Commun.*, vol. 49, no. 10, pp. 1727–1737, Oct. 2001.

[31] S. Benedetto and G. Montorsi, "Unveiling Turbo codes: Some results on parallel concatenated coding schemes," *IEEE Trans. Inf. Theory*, vol. 42, no. 2, pp. 409–428, Mar. 1996.

[32] R. Garzón-Bohórquez, C. A. Nour, and C. Douillard, "Precoding techniques for Turbo codes," in *Proc. 21th Eur. Wireless Conf. (EW)*, Budapest, Hungary, May 2015, pp. 1–6.

[33] J. Hagenauer, "The EXIT chart—Introduction to extrinsic information transfer in iterative processing," in *Proc. 12th Europ. Signal Process. Conf (EUSIPCO)*, Sep. 2004, pp. 1541–1548.

[34] S. Crozier, P. Guinand, and A. Hunt, "On designing Turbo-codes with data puncturing," in *Proc. 9th Canadian Workshop Inf. Theory (CWIT)*, Montreal, QC, Canada, Jun. 2005, pp. 1–4.

[35] S. Crozier, P. Guinand, and A. Hunt, "Estimating the minimum distance of large-block Turbo codes using iterative multiple-impulse methods," in *Proc. 4th Int. Symp. Turbo Codes Rel. Topics*, Munich, Germany, Apr. 2006, pp. 1–6.

[36] L. C. Perez, J. Seghers, and D. J. Costello, "A distance spectrum interpretation of Turbo codes," *IEEE Trans. Inf. Theory*, vol. 42, no. 6, pp. 1698–1709, Nov. 1996.

[37] *Enhanced Turbo Codes for NR: Performance Evaluation for eMBB and URLLC*, document R1-1613029, 3GPP, Orange, Intitut Mines-Telecom, RAN1 Meeting 87, Reno, USA, Nov. 2016.

[38] *Performance Comparison of Channel Coding Candidates for Short Block Sizes*, document R1-1611316, Ericsson, RAN1 Meeting 87, Reno, USA, Nov. 2016.

[39] *HARQ Scheme for Polar Codes*, document R1-1611255, Huawei, HiSilicon, RAN1 Meeting 87, Reno, USA, Nov. 2016.

[40] *Performance Evaluation for NR Channel Coding*, document R1-1608864, Huawei, HiSilicon, RAN1 Meeting 86bis, Lisbon, Portugal, Oct. 2016.

[41] *Design of Flexible LDPC Codes*, document R1-167889, Samsung, RAN1 Meeting 86, Gothenburg, Sweden, Aug. 2016.

[42] *Performance Evaluation of LDPC Codes for NR eMBB Data*, document R1-1713740, Huawei, HiSilicon, RAN1 Meeting 90, Prague, Czech Republic, Aug. 2017.

Ronald Garzón-Bohórquez was born in Zipaquirá, Colombia, in 1985. He received the Engineering degree in electronics from the Escuela Colombiana de Ingeniería Julio Garavito, Bogotá, Colombia, the Engineering degree in mechatronics and the master's degree in telecommunications and networks from the Ecole Nationale d'Ingénieurs de Brest, Brest, France, in 2010 and 2011, respectively, and the Ph.D. degree in digital communications from Telecom Bretagne, Brest, France. Since 2014, he has been a Post-Doctoral Researcher at the Electronics Department, IMT Atlantique, Brest. His main research interests are forward error correction, diversity, and interleaving techniques. Recently, in the context of the FANTASTIC5G and EPIC European projects, he has been involved in the design of enhanced turbo codes that have been proposed to the 3GPP standardization group for the future 5G.

Charbel Abdel Nour received the degree in computer and communications engineering from Lebanese University in 2002, the master's degree in digital communications from the University of Valenciennes, France, in 2003, and the Ph.D. degree in digital communications from Telecom Bretagne, France, in 2008. From 2007 to 2011, he was a Post-Doctoral Fellow at the Electronics Department, Telecom Bretagne. He was involved in several research projects related to broadcasting and satellite communications. Additionally during the same period, he was active in the Digital Video Broadcasting DVB Consortium, where he had important contributions. In 2011, he was an Associate Professor at the Electronics Department, Telecom Bretagne. His interests concern radio mobile communications systems, broadcasting systems, coded modulations, error correcting codes, resource and power allocation for NOMA, waveform design, MIMO, and iterative receivers. Lately, he presented several contributions to the H2020 METIS and FANTASTIC5G projects and to the 3GPP consortium related to coding solutions for 5G.

Catherine Douillard received the Engineering degree in telecommunications from the École Nationale Supérieure des Télécommunications de Bretagne, France, in 1988, the Ph.D. degree in electrical engineering from the University of Western Brittany, Brest, France, in 1992, and the accreditation to supervise research from the University of Southern Brittany, Lorient, France, in 2004. She is currently a Full Professor with the Electronics Department, Telecom Bretagne, where she is in charge of the Algorithm-Silicon Interaction Research Team. Her main research interests are turbo codes and iterative decoding, iterative detection, the efficient combination of high-spectral efficiency modulation and turbo coding schemes, diversity techniques, and turbo processing for multi-carrier, multi-antenna, and multiple access transmission systems. In 2009, she received the SEE/IEEE Glavieux Award for her contribution to standards and related industrial impact. She was active in the Digital Video Broadcasting (DVB) Technical Modules for the definition of DVB-T2, DVB-NGH as chairperson of the Coding, Constellations and Interleaving task force, and DVB-RCS NG standards. Since 2015, she has had several contributions in the FANTASTIC-5G and EPIC H2020 European projects intended for the definition of new techniques for 5G and beyond.

1.4.3 Actions in the 3GPP consortium

Several technical contributions were submitted and presented during the attendance of 6 meetings of the coding group of the 3GPP RAN1. In [90], an enhanced TC based on the technical improvements detailed in the previous section was proposed. In [91], the details of the design (interleaver model, parameters, puncturing mechanism and patterns) and implementation of the enhanced TC for the agreed simulation conditions are provided. In [92], the corresponding simulation results and comparisons with respect to the LTE TC were presented. These contributions have shown large performance improvements, especially for short frames and for high coding rates, while requiring mild modifications with limited additional complexity to support both LTE and 5G's NR proposal. In [93], it was shown that the proposed enhanced TCs matched the performance of the best LDPC codes of [94] for large frame sizes while largely outperforming these LDPC codes for the short frame sizes. Indeed, a gain exceeding 1.5 dB was observed for the 100-bit frame size and coding rate of $R = 8/9$, as shown in Fig. 1.4. In addition, the improvements in the high SNR region were confirmed for the enhanced TC since error rates as low as 10^{-6} of BLock Error Rate (BLER) were attained without any change in the slope of the error rate curves.

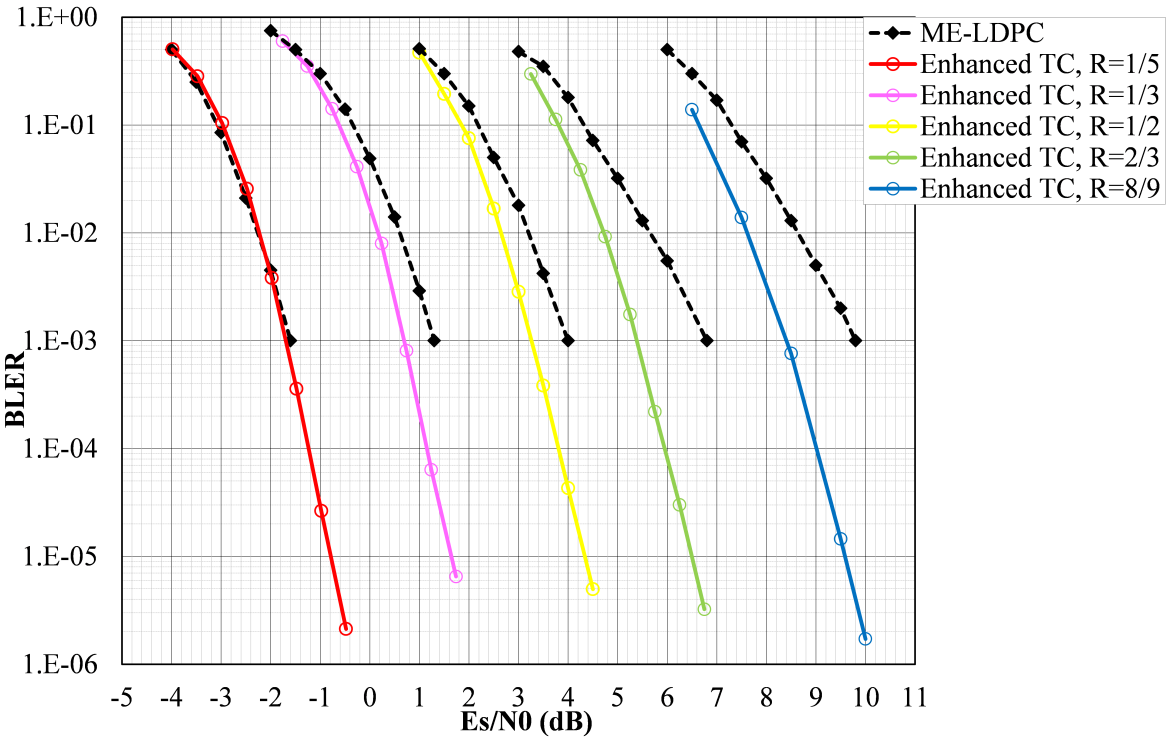

Figure 1.4: Performance comparison of the enhanced TC with the Multi-Edge LDPC code in AWGN channel for coding rates ranging from 1/5 to 8/9 in terms of BLock Error Rate vs Es/N0. QPSK modulation, block size K around 100 bits.

In [95], a rate-compatible version of the enhanced TC was proposed for both eMBB and URLLC scenarios and their corresponding simulation conditions. It was also shown that additional gains (0.6 to 0.8 dB) can be achieved when performing list-like decoding for TCs. Further improvements (up to 2.0 dB) are also possible, especially for short frame sizes when combining the list-like decoding of TCs with an outer CRC code. In [96], performance comparisons for short frame sizes ($K < 1024$bits) with the proposed polar codes were performed for the first and successive transmissions. It was shown that enhanced TC with Max-Log-

MAP decoding and 8 iterations offers BLER performance comparable to the polar code with list-8 decoding for rates $R > 2/3$ and slightly better performance for lower rates at the first transmission as shown in Fig. 1.5.

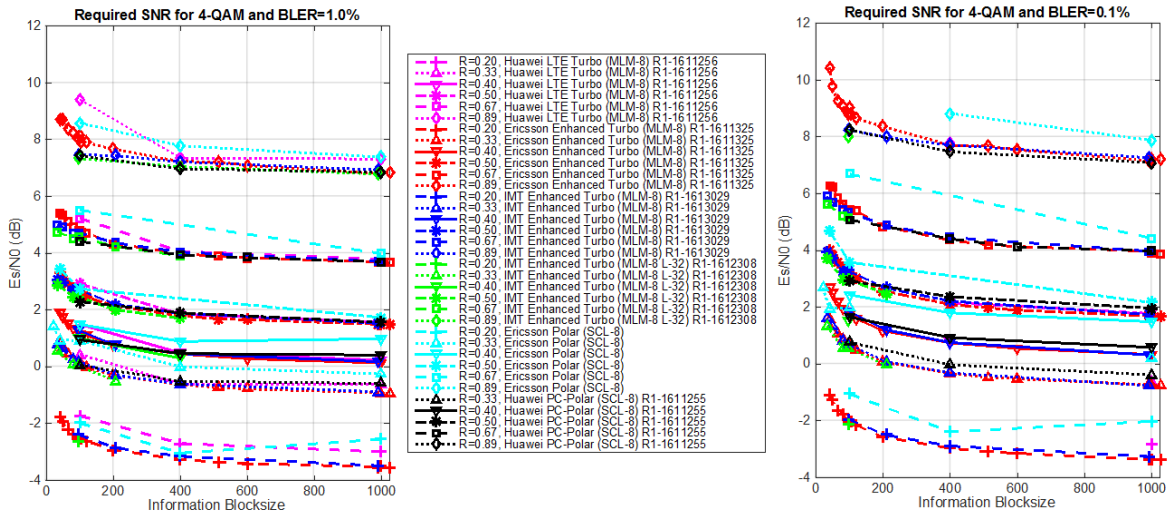

Figure 1.5: Performance comparison for the first transmission of the enhanced TC with the polar code in AWGN channel for coding rates ranging from 1/5 to 8/9 in terms of required Es/N0 to achieve 1% and 0.1% of BLER. QPSK modulation, block size K ranging from 32 to 1024 bits.

In subsequent transmissions for HARQ support, the enhanced TC offers better performance than the proposed rate-compatible polar code. Gains exceeding 0.5 dB can be observed in this case, as shown in Fig. 1.6. In addition, steeper BLER curves were seen for the enhanced TC, predicting larger gains if lower error rates would be targeted. In [97], the excellent performance of the proposed TCs was confirmed for the all simulation conditions of URLLC. Target BLER of 10^{-5} was achieved without any change in the slope of the curves for the simulation conditions agreed for URLLC, including the association with QAM modulations.

1.4.4 3GPP standardization discussions and conclusions

Binary Turbo (LTE and the proposed enhanced version), LDPC and concatenated polar codes were the main considered candidates proposed for adoption in 3GPP RAN1 for NR eMBB data channel. Agreed technical observations regarding the 3 families were drawn and captured in [98].

Performance results were collected in [99]. However, it has not been possible to draw conclusions directly from these results, owing to different views on the implementation complexities and possible enhancements. Technical concerns were raised regarding the efficient and performant support of IR-HARQ for the LDPC and polar codes whereas the ability of TCs to support IR-HARQ is considered as well established.

The following is a summary of the agreed observations about complexity, performance, maturity, flexibility, strengths and weaknesses for each family of codes captured in the NR chairman's notes [98].

Regarding complexity, it was agreed that computational complexity is far from being an accurate representative of final hardware complexity and power efficiency. Indeed, it was acknowledged that memory requirements and accesses have a large impact on chip area and power consumption respectively.

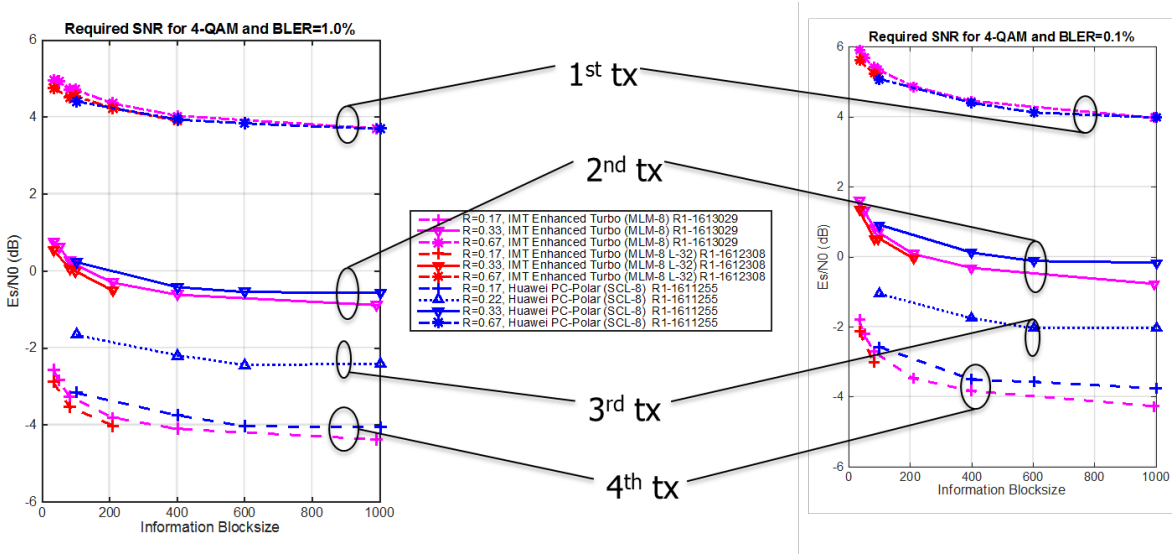

Figure 1.6: Performance comparison for up to four retransmissions of the enhanced TC with the polar code in AWGN channel for coding rates ranging from 1/12 to 2/3 in terms of required Es/N0 to achieve 1% and 0.1% of BLER. QPSK modulation, block size K ranging from 32 to 1024 bits.

LDPC codes are considered as widely implemented in commercial hardware supporting several Gbps throughput with attractive area and energy efficiency while supporting flexibility and features that are largely limited when compared to the corresponding requirements for NR. Actually, the area efficiency reduces for lower coding rates and the complexity increases with increasing flexibility for this family of codes. Moreover, despite the ability of achieving large parallel decoding degrees, some of this parallelism may not be exploited for all code block lengths and code rates for NR, resulting into a penalizing impact on energy and area efficiency. To conclude, hardware implementation with attractive area and energy efficiency is considered challenging when simultaneously targeting the peak throughput and flexibility requirements of NR.

Polar codes were considered implementable, although there were at that time no commercial implementations, and in relation to NR, there were some concerns linked to the maturity and the availability of decoding hardware. In addition, most existing work in literature was related to successive interference cancellation decoders and not list-based decoders that enable the excellent performance of this family of codes. For list decoders, the implementation complexity increases with increasing list size, especially with larger block sizes. Moreover, the area efficiency reduces for shorter block lengths and lower coding rates. List-4 decoder was agreed as implementable for all codeword sizes. However, in practice, most simulations considered list-8 decoders that could be argued implementable for short frame sizes. To conclude, for decoding hardware that can achieve acceptable latency, performance and flexibility, there were some concerns about the area efficiency and energy efficiency that are achievable with polar codes and about the maturity of the technology.

TCs are widely implemented in commercial hardware, supporting HARQ and flexibility similar to what is required for NR, but not at the high data rates or low latencies required for NR. In fact, TCs meet the flexibility requirements of NR with the most attractive area and energy efficiency except at higher throughputs, and particularly at lower code rates and lower block lengths. Generally, the area and energy efficiency is constant when varying the puncturing and repetition rate. Another advantage resides in the fact that the decoding complexity increases linearly with the information block size for a given mother code rate.

However, there were concerns that implementation with attractive area and energy efficiency is challenging when targeting the highest throughput requirements of NR. Therefore, two proposals were put forward by the proponents of TCs: the first one considered using TCs as a single solution in NR. The second considered designing a Turbo decoder capable of decoding both LTE and, at least, lower information block sizes ($K < 6144$ bits) of NR. For the high throughput case of NR, a LDPC code can be designed with a limited flexibility or equivalently for few combinations of code rates ($R > 1/2$) and frame sizes ($K > 6144$ bits). This proposal would have the benefit of combining the advantages of each family (Turbo and LDPC) of codes without bearing the burden of their drawbacks.

As a conclusion to the NR chairman's notes in [98], we can state that each family of codes presents its challenges when trying to satisfy simultaneously all the requirements of NR. Therefore, it was quite difficult to clearly identify an all-around favorite without performing a joint thorough analysis of performance and complexity/latency taking into account real implementations and not estimates of it.

Due to timing constraints, the framework for such a comparison was not agreed and individual technical contributions were used as a basis for the selection process. At a later stage, a proposal of combining polar codes for short frame sizes and LDPC codes for longer frame sizes was also put forward. It was motivated by the fact that the decoding complexity of list decoding increases with larger frame sizes. The willingness to accept the use of LDPC codes for larger frame sizes by the proponents of both polar and TCs, was used to adopt LDPC codes for large frame sizes spanning an interval of values and supporting a flexibility level well beyond what was foreseen at the start. Afterwards, it was proven in [100] that there is no LDPC code with the minimum cycle length or girth greater than or equal to 6 for the smallest info block lengths and high rates of NR. This results into a large performance penalty when using iterative decoding based on belief propagation. Consequently, the promising candidates for short frame sizes were limited to Turbo and polar codes.

Performance comparisons between the proposed enhanced TC and the polar code proposals taking into account IR-HARQ support were provided in [96]. The corresponding observations showed that enhanced TC with Max-Log-MAP decoding and 8 iterations offers comparable BLER performance to the polar code with list-8 decoding for rates $R > 2/3$ and slightly better performance for lower rates at the first transmission. In subsequent transmissions for HARQ support, enhanced TC offers better performance than rate-compatible polar code. Gains exceeding 0.5 dB can be observed in this case. In addition, steeper BLER curves were observed for the enhanced TC predicting larger gains if lower error rates were to be targeted.

Complexity assessment on the hardware implementation of channel decoders for short block lengths was presented in [101] for the three families of codes. It was shown that despite having lower computational complexity at many coding rates R, flexible list-4 polar decoder ASICs have inferior area-efficiency compared to state-of-the-art Turbo decoder ASICs. On the other hand, flexible LDPC decoder ASICs suffer from degraded area- and energy-efficiency at low coding rates and short block lengths. Turbo decoder ASICs have superior area- and energy efficiency.

Finally, regardless of potential technical drawbacks, a compromise was found that led to the adoption of LDPC codes for eMBB data channel and polar codes for the control channel.

1.4.5 Performed work and contributions in designing beyond 5G high throughput Turbo codes/decoders

Thanks to the proposed protograph-based interleavers, high regularity and periodicity were introduced in the structure of the TC permutation while improving performance. These

two new introduced features highly facilitate the proposal of highly parallel architectures to achieve yet higher throughputs.

In the context of the H2020 EPIC project, we were able to closely collaborate with the Technical University of Kaiserslautern (TUKL) to propose Turbo code/decoders able to demonstrate a throughput level well beyond 100 Gb/s without major impact on performance. The newly developed structure would get compared to similar structures for LDPC and polar codes.

A first step where the design space including all design and runtime parameters of TCs were listed and their impact on key performance indicators including communications performance, hardware efficiency, throughput, latency, etc., were identified. Then, an exploration of the design space pinpointed the parameters of relevance to the targeted increase in throughput, the main objective in EPIC project.

The road to Tb/s goes through the proposal of an improved TC, simplified decoding algorithms and optimized architectures. By the reuse of the protograph-based structure to design hardware-oriented interleavers, frame size flexibility becomes feasible. By exploiting the protograph, flexibility is supported via a simplified incremental increase in the number of connections. This leads into a large reduction in the number of required multiplexers for a hardware implementation. The new interleaver coupled with an original fully pipelined decoder architecture proposed in collaboration with TUKL were able to achieve a leap by around two orders of magnitude in throughput when compared to the latest published architectures. Indeed, 100 Gb/s was achieved with an unparalleled hardware efficiency as shown in [102]. This work represents a major milestone on the road to Tb/s.

Two main leads were investigated in the context of the PhD thesis of Vinh Hoang Son Le, regarding the simplified decoding algorithms:

- For the classical flexible decoder, a complete reformulation of the Max-Log-MAP [103] decoding algorithm was performed, leading to what we called the local SOVA decoding algorithm. It shows that major simplifications can be introduced especially for high radix orders.

- With a reduced emphasis on code rate flexibility while aiming for higher coding rates, dual-trellis decoding can represent a potential solution.

The first lead is detailed in the journal publication entitled “Revisiting the Max-Log-Map algorithm with SOVA update rules: new simplifications for high-radix SISO decoders” in IEEE Transactions on Communications included hereafter.

Revisiting the Max-Log-Map algorithm with SOVA update rules: new simplifications for high-radix SISO decoders

Vinh Hoang Son Le, *Student Member, IEEE,* Charbel Abdel Nour, *Member, IEEE,*
Emmanuel Boutillon, *Senior Member, IEEE* and Catherine Douillard, *Senior Member, IEEE*

***Abstract*—This paper proposes a new soft-input soft-output decoding algorithm particularly suited for low-complexity high-radix turbo decoding, called local soft-output Viterbi algorithm (local SOVA). The local SOVA uses the forward and backward state metric recursions just as the conventional Max-Log-MAP algorithm does, and produces soft outputs using the SOVA update rules. The proposed local SOVA exhibits a lower computational complexity than the Max-Log-MAP algorithm when employed for high-radix decoding in order to increase throughput, while having the same error correction performance even when used in a turbo decoding process. Furthermore, with some simplifications, it offers various trade-offs between error correction performance and computational complexity. For instance, employing the local SOVA algorithm for radix-8 decoding of the LTE turbo code reduces the complexity by 33% without any performance degradation and by 36% with a slight penalty of only 0.05 dB. Moreover, the local SOVA algorithm opens the door for the practical implementation of turbo decoders for radix-16 and higher.**

***Index Terms*—convolutional codes, soft-input soft-ouput decoding, soft-ouput Viterbi algorithm, high-radix decoding, turbo codes, high throughput.**

I. INTRODUCTION

TURBO codes were first proposed by Berrou *et al.* in 1993 [1]. A turbo encoder consists of two binary recursive systematic convolutional (RSC) encoders separated by an interleaver. At the receiver, each component decoder uses a soft-input soft-output (SISO) decoding algorithm to compute extrinsic estimates for every systematic bit. Extrinsic information is exchanged between the component decoders through an iterative process, until convergence is achieved. The Bahl-Cocke-Jelinek-Raviv (BCJR) algorithm [2] is usually employed to compute the maximum a posteriori (MAP) estimate of the bits. However, in practice, applying the BCJR algorithm in the logarithmic domain (Log-MAP algorithm) and possibly simplifying it using the max-log approximation (Max-Log-MAP or MLM algorithm), makes it more suitable for hardware implementations [3].

For the past two decades, binary turbo codes have been adopted as forward error correcting (FEC) codes in several wireless communication standards, such as the third and fourth generations (3G and 4G) of wireless mobile telecommunications and WiMAX, but also in digital video broadcasting standards such as DVB-RCS/RCS2 and DVB-SH [4]. In the near future, the evolutions of LTE Advanced Pro will require turbo codes able to achieve throughputs as high as several tens of Gbit/s, so as to complement the 5G New Radio deployments. To this end, the original BCJR algorithm and its derivatives are penalized by their inherent serial nature, thus leading to high latency and low throughput while requiring a large amount of memory to store the state metrics. Therefore, a number of techniques have been proposed as potential solutions to these issues, such as the sliding window technique [5], shuffled parallelism [6], sub-block parallelism [7], full parallelism [8] or high-order radix decoding [9]. In this work, we mainly focus on how to enable high-order radix decoding schemes for turbo decoders. Previous works in the literature, such as [10], [11], mainly tried to increase the throughput of BCJR-based SISO decoders, without specifically considering the complexity reduction of the studied algorithm. Only in [12], a low-complexity radix-16 SISO decoder for the MLM algorithm was proposed, with the introduction of specific processing to limit the resulting error correction degradation at high signal-to-noise ratios.

On the other hand, the soft-output Viterbi algorithm (SOVA) [13] has been recently reconsidered as an efficient SISO candidate for turbo decoding [14], [15]. However, the interest in this algorithm remains limited. This is because, first of all, the MLM algorithm outperforms the SOVA by about 0.75 dB when used for turbo decoding [3] and, second, the serial nature of the SOVA is even more pronounced when compared to the MLM algorithm due to the involved traceback and the soft output update procedures. Nevertheless, the SOVA provides an alternative way to perform the soft output computation for SISO decoding. In [16], the authors proposed the *modified SOVA* that combines two update rules, the Hagenauer rule [13] and the Battail rule [17], [18]. This modified algorithm performs better than the classical SOVA [13] where only the Hagenauer rule is employed. Nonetheless, the decoder in [16] is a SOVA-like decoder involving the soft output update procedure, which is a serial process in nature. The modified SOVA is able to achieve the same performance as the MLM algorithm but the decoder has then to perform the soft output update for each bit in each path every time it calculates the metric difference in the trellis. Consequently, it exhibits higher complexity and memory consumption than the classical SOVA.

In this paper, we propose the *local SOVA*, a combination between the MLM algorithm and the two above-mentioned update rules, the Hagenauer rule and the Battail rule. More specifically, the proposed algorithm first performs the forward and backward state metric recursions as in the MLM algo-

rithm. Then, for each trellis section, while the MLM generates the soft output as the difference between the maximum cumulated metric corresponding to the value 1 of the considered bit and the maximum cumulated metric corresponding to the value 0 of the considered bit, the proposed local SOVA applies a different computational process using both update rules. Note that both methods result into the same soft output value. In fact, we will show that the MLM generation of soft output appears to be a particular case of the local SOVA method. Moreover, the proposed algorithm does not involve either the traceback nor the soft output update of the classical SOVA and it applies computation steps closer to the MLM algorithm except for the soft output calculation. When applied to high-radix orders, the algorithm reveals to be quite different from the MLM and SOVA algorithms. Indeed, it performs high-radix decoding of convolutional codes in an efficient way, simplifying the high-throughput implementations of turbo decoders.

The rest of this paper is organized as follows. Section II recalls the MLM algorithm and analyzes it from the SOVA perspective. Section III describes the local SOVA and shows that the MLM algorithm is an instance of the proposed algorithm. High-radix turbo decoders using local SOVA are then considered with new simplifications in Section IV and simulation results and a computational complexity analysis are provided to illustrate the advantages of the local SOVA. Finally, Section V concludes the paper.

II. REVISITING THE MAX-LOG-MAP ALGORITHM

Let us assume a binary convolutional encoder with rate $1/m$ and memory length ν. Considering an input message sequence of length K, $\mathbf{u} = (u_0, \ldots, u_{K-1}) \in \{0,1\}^K$, the encoder produces codeword $\mathbf{x} = (x_0, \ldots, u_{M-1}) \in \{0,1\}^M$, where $M = m \times K$. A common representation of a convolutional code is the trellis diagram. With K message bits, the trellis diagram consists of $K+1$ *time indexes*, ranging from 0 to K. At time index k, the state of the convolutional code can take 2^ν values. The interval between a time index k and $k+1$ is considered as *trellis section* k. In a trellis section k, there are branches connecting states at time index k to states at time index $k+1$. Since the considered convolutional code is binary, two branches come out of any state s at time index k, each being connected to a state at time index $k+1$. Of the two branches, one is associated with input bit $u_k = 0$ and the other with input bit $u_k = 1$.

Assuming a transmission using BPSK modulation, the received sequence is $\mathbf{y} = \{y_1, \ldots, y_M\}$. The BCJR algorithm and its derivatives estimate the log-likelihood ratio (LLR) for each systematic bit as [3]:

$$L_{\text{BCJR}}(u_k) = \ln \frac{\sum_{s,s'|u_k=1} Pr\{s_k = s, s_{k+1} = s', \mathbf{y}\}}{\sum_{s,s'|u_k=0} Pr\{s_k = s, s_{k+1} = s', \mathbf{y}\}}. \quad (1)$$

Based on the max-log approximation, $\ln(\sum_{i=1}^{N} x_i) \approx \max_{i=1,\ldots,N}\{\ln(x_i)\}$, (1) can be rewritten so as to derive the MLM LLR estimate, which is the soft output of the decoder [3]:

$$\begin{aligned} L_{\text{MLM}}(u_k) &= \max_{(s,s')|u_k=1} \ln Pr\{s_k = s, s_{k+1} = s'|\mathbf{y}\} \\ &\quad - \max_{(s,s')|u_k=0} \ln Pr\{s_k = s, s_{k+1} = s'|\mathbf{y}\} \\ &= \max_{(s,s')|u_k=1} \big(A_k(s) + \Gamma_k(s,s') + B_{k+1}(s')\big) \\ &\quad - \max_{(s,s')|u_k=0} \big(A_k(s) + \Gamma_k(s,s') + B_{k+1}(s')\big), \end{aligned} \quad (2)$$

where $\Gamma_k(s,s')$ is the branch metric from state $s_k = s$ to state $s_{k+1} = s'$ at trellis section k, $A_k(s)$ is the forward state metric for $s_k = s$ at time index k and $B_{k+1}(s')$ is the backward state metric for $s_{k+1} = s'$ at time index $k+1$.

The forward (respectively backward) state metrics from time index 0 to K (respectively K to 0) are recursively calculated using (3a) (respectively (3b)):

$$A_{k+1}(s) = \max_{s'} \big\{A_k(s') + \Gamma_k(s',s)\big\}, \quad (3a)$$

$$B_k(s) = \max_{s'} \big\{B_{k+1}(s') + \Gamma_k(s,s')\big\}. \quad (3b)$$

The procedure of recursively calculating the forward state metrics is referred to as *forward propagation* and the procedure of recursively calculating the backward state metrics as *backward propagation*.

Let us take as an example the estimation of the soft output related to u_k at trellis section k in Fig. 1, using the MLM algorithm. The forward and backward propagations provide all the values for $A_k(s)$, $s = 0, \ldots, 3$ and $B_{k+1}(s')$, $s' = 0, \ldots, 3$. Then, assuming that $(s,s') = (0,0)$ is the most likely trellis branch for $u_k = 0$ (bold, dashed line) and that $(s,s') = (2,1)$ is the most likely trellis branch for $u_k = 1$ (bold, solid line), $L_{\text{MLM}}(u_k)$ can be written as:

$$\begin{aligned} L_{\text{MLM}}(u_k) =& (A_k(2) + \Gamma_k(2,1) + B_{k+1}(1)) - \\ & (A_k(0,0) + \Gamma_k(0,0) + B_{k+1}(0)). \end{aligned} \quad (4)$$

On the other hand, the LLR provided by the MLM algorithm can also be seen in a different way, involving *paths* in the trellis diagram. Assuming that the trellis begins and ends at known states s_0 and s_K, then there are 2^K possible state sequences connecting s_0 and s_K. Each state sequence corresponds to a distinct input bit sequence and is associated with a *path* in the trellis. Given the received codeword $\mathbf{y}$, the path or state sequence $\mathbf{s}$ has a *path metric* equal to

$$\ln Pr(\mathbf{y}|\mathbf{s}) = \sum_{k=0}^{K-1} \ln Pr(y_k|s_k, s_{k+1}). \quad (5)$$

In other words, for a given path going through a series of branches, the path metric is the sum of all the involved branch metrics. The Viterbi algorithm (VA) [19] employs a recursive selection of paths in the trellis from state s_0 to state s_K in order to find the state sequence with the highest path metric and provides the associated bit sequence as the output of the decoder. In fact, the forward propagation of the MLM algorithm is identical to the path recursion in the VA, as already reported in [20]. The backward propagation from state s_K to state s_0 could likewise be used for the same purpose.

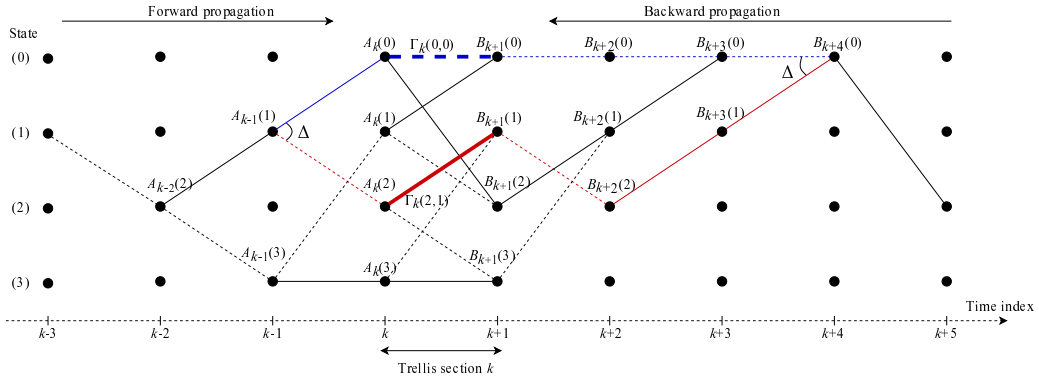

Fig. 1. Trellis representation of a convolutional code with $\nu = 2$. Dashed branches correspond to data bits equal to 0 and solid branches to data bits equal to 1.

For a binary convolutional code with rate $r = 1/m$, there are two branches in the trellis arriving at each state s_k at time index k. In the (forward) path recursion, the VA adds each of the two branch metrics to the path metric associated with the preceding state at time index $k-1$. It then selects the path with the larger metric as the *surviving path* and stores it. Therefore, at time index k, there are 2^ν surviving paths left, one for each state. Similarly, using the backward propagation, one can identify another set of 2^ν surviving paths at each time index and, in particular, at time index $k+1$.

Furthermore, thanks to the path convergence property of convolutional codes [19], the surviving paths can be truncated to some manageable length $\mathcal{L}$ to limit the amount of memory necessary for their storage, without any noticeable impact on the error correction performance. For a truncation length of $\mathcal{L}$ trellis sections, the VA needs to process the trellis paths until time index k to take the decision on the information bit at time index $(k-\mathcal{L})$. The value of $\mathcal{L}$ should be chosen large enough so that the 2^ν surviving paths from the forward propagation originate from a single state at time index $(k-\mathcal{L})$ with sufficiently high probability [21]. The same rule applies if a backward propagation is carried out: in this case, the VA needs to process the trellis paths until time index k' to take the decision on the information bit at time index $(k'+\mathcal{L})$.

Now, let us consider that both forward and backward propagations are carried out through the trellis. Then, for trellis section k, there are 2^ν surviving paths at time index k resulting from the forward propagation and 2^ν surviving paths at time index $k+1$ resulting from the backward propagation. Connecting these two sets of paths with the $2^{\nu+1}$ trellis branches yields a total number of $2^{\nu+1}$ surviving paths for trellis section k. The path going through state s at time index k and through state s' at time index $k+1$ has its path metric equal to $A_k(s)+\Gamma_k(s,s')+B_{k+1}(s')$. Moreover, because of the path convergence property, all $2^{\nu+1}$ paths originate from a single state at time index k' such that $\max(0,k-\mathcal{L}) \leq k' < k$ in the forward propagation and from a single state at time index k'' such that $k+1 < k'' \leq \min(k+\mathcal{L}+1, K)$ in the backward propagation. So, these $2^{\nu+1}$ paths merge together at times indexes k' and k''.

Many readers will recognize the concept of path merging exploited in the SOVA [13]. Therefore, for each pair of merging paths, we can obtain the metric difference between these two paths by subtracting the lower path metric from the higher one. Then, we can manipulate these resulting metric differences between paths to get the soft estimate of bit u_k for trellis section k.

Taking the example in Fig. 1, the forward propagation and the backward propagation provide us with four forward surviving paths at time index k and four backward surviving paths at time index $k+1$, respectively. So, eight paths have to be considered for trellis section k, and as shown in Fig. 1, these paths merge in state 2 at time index $k' = k-2$ and in state 0 at time index $k'' = k+4$. Furthermore, if we denote by P_0 the path going through the branch (0,0) and by P_1 the path going through the branch (2,1) in trellis section k, the LLR of bit u_k can be estimated as the metric difference Δ between these two paths where the path metric M_0 of P_0 is $M_0 = (A_k(0)+\Gamma_k(0,0)+B_{k+1}(0))$ and the path metric M_1 of P_1 is $M_1 = (A_k(2)+\Gamma_k(2,1)+B_{k+1}(1))$. The result is equal to the LLR estimated by the MLM algorithm in (4).

Based on this equivalence, we can reformulate the MLM algorithm. In the trellis diagram, each trellis section k involves $2^{\nu+1}$ paths going through $2^{\nu+1}$ branches and merging together. If a path goes through the branch (s,s'), its path metric M_k is then expressed as

$$M_k = A_k(s) + \Gamma_k(s,s') + B_{k+1}(s'). \tag{6}$$

The soft output related to bit u_k is then equal to the metric difference between the path with the largest path metric carrying $u_k = 1$ and the path with the largest path metric carrying $u_k = 0$. In the next section, we define the path merge operation, present its properties and show how it can be used to reformulate the MLM algorithm.

III. THE LOCAL SOVA

Conventionally, a path in a trellis diagram is defined as a sequence of states and is associated with an input bit

sequence and a path metric. From this section, we will adopt an alternative mathematical definition of a path, with a more local sense, that focuses on a particular trellis section k. In the following, all the derivations focus on trellis section k. Therefore, for sake of simplicity, we will omit k in the notations.

We define a path P as a 3-tuple consisting of a path metric denoted by M, a hard decision denoted by u and a reliability value related to u, denoted by L:

$$P = \{M, u, L\} \in \mathbb{R} \times \{0,1\} \times \mathbb{R}^+, \tag{7}$$

where $\mathbb{R}$ is the set of real numbers and $\mathbb{R}^+$ is the set of positive real numbers.

As stated in the previous section, if path P goes through branch (s, s') at trellis section k, its path metric M is given by (6). Moreover, the hard decision u is the data bit carried by the corresponding branch in the trellis diagram (0 for a dashed line or 1 for a solid line in Fig. 1). The reliability of the hard decision, L, is initialized to $+\infty$ or to the largest possible value achievable with the used quantization.

We further define the *merge operation*

$$\mathcal{M} \ : \ \{\mathbb{R} \times \{0,1\} \times \mathbb{R}^+\}^2 \rightarrow \mathbb{R} \times \{0,1\} \times \mathbb{R}^+, \tag{8}$$

taking two paths as arguments and producing one path as output. $P_a = \{M_a, u_a, L_a\}$ and $P_b = \{M_b, u_b, L_b\}$ being two paths, determining path P_c such that $P_c = \mathcal{M}(P_a, P_b)$ involves three procedures: finding M_c, u_c and L_c. The output path metric M_c and hard decision u_c can be obtained by comparing the path metrics M_a and M_b. Let $p = \arg\max_{a,b}(M_a, M_b)$, then $M_c = M_p$ and $u_c = u_p$. Through that mechanism, if several paths merge at a trellis stage, the resulting output path will be assigned the largest path metric and will be considered as the *maximum likelihood* (ML) path. The hard decision carried by the ML path is also the hard decision provided by the decoder. Furthermore, in order to find L_c, we employ two well-known reliability update rules: the Hagenauer rule (HR) [13] and the Battail rule (BR) [17], [18]. Both rules were proposed independently in the late 80's for SOVA decoders.

A. Reliability Update Rules

Let P_a and P_b be two paths to be merged and let us define p and p' as

$$p = \arg\max_{a,b}(M_a, M_b); \quad p' = \arg\min_{a,b}(M_a, M_b), \tag{9}$$

and the metric difference between P_a and P_b as $\Delta_{p,p'} = M_p - M_{p'}$. Note that the metric difference between two paths is always positive. Then, if $P_c = \mathcal{M}(P_a, P_b)$, L_c is calculated as follows:

1) If $u_a \neq u_b$, apply HR

$$L_c = \min\left(L_p, \Delta_{p,p'}\right) \tag{10}$$

2) If $u_a = u_b$, apply BR

$$L_c = \min\left(L_p, \Delta_{p,p'} + L_{p'}\right) \tag{11}$$

These two update rules can be summarized using the following update function ϕ:

$$\begin{aligned} L_c &= \phi\big(L_p, L_{p'}, \Delta_{p,p'}, u_p, u_{p'}\big) \\ &= \min\left(L_p, \Delta_{p,p'} + \delta(u_p, u_{p'})L_{p'}\right) \end{aligned} \tag{12}$$

where

$$\delta(u_p, u_{p'}) = \begin{cases} 1, & \text{if } u_p = u_{p'} \\ 0, & \text{otherwise.} \end{cases}$$

The combination of these two rules for SOVA decoding was already proposed in [16] and the authors proved the equivalence with the MLM algorithm. However, in [16], the authors only considered forward propagation. To estimate the reliability of the hardware decision at trellis section k, the algorithm carries out a forward propagation up to trellis stage $k + L$ and then performs a traceback procedure. Thus, a large number of paths should be considered, which translates into a massive use of function ϕ and also into large memory for storing the reliability values after each update.

We propose an alternative algorithm that uses both forward propagation and backward propagation and hence limits the number of paths considered for trellis section k to $2^{\nu+1}$, thus reducing the use of function ϕ.

B. Commutative and associative properties of the merge operation

As already mentioned earlier, the merge path operation described above involves three procedures: 1) selecting the output path metric 2) selecting the related hard decision and 3) updating the related reliability value using function ϕ in (12). We show in this section that the merge operation has the commutative and associative properties.

Theorem 1. *The merge operation is commutative and associative.*

- *Commutative property*
  Let P_a, P_b be two merging paths:

$$\mathcal{M}(P_a, P_b) = \mathcal{M}(P_b, P_a), \tag{13}$$

- *Associative property*
  Let P_a, P_b, and P_c be three merging paths:

$$\mathcal{M}(\mathcal{M}(P_a, P_b), P_c) = \mathcal{M}(P_a, \mathcal{M}(P_b, P_c)). \tag{14}$$

The "=" operator between two paths is defined as the equality between all the elements in their tuples.

Proof. We will prove that the three above-mentioned procedures are commutative and associative.

For the commutative property, let us define p and p' as in (9). The path metric of the output path is then M_p, the hard decision is u_p and according to (12), the reliability value is then equal to

$$\min(L_p, \delta(u_p, u_{p'})L_{p'} + \Delta_{p,p'}). \tag{15}$$

Since p and p' do not depend on the order of P_a and P_b, the merge operation is commutative.

Similarly, we can easily show that selecting a path metric and providing a hard decision are associative procedures

$$L_{\mathcal{M}(P_a,\mathcal{M}(P_b,P_c))} = \min\Big(\min\big(L_c, \delta(u_c,u_b)L_b + \Delta_{c,b}\big), \delta(u_c,u_a)L_a + \Delta_{c,a}\Big)$$
$$= \min\big(L_c, \delta(u_c,u_b)L_b + \Delta_{c,b}, \delta(u_c,u_a)L_a + \Delta_{c,a}\big), \quad (16)$$
$$L_{\mathcal{M}(\mathcal{M}(P_a,P_b),P_c)} = \min\Big(L_c, \delta(u_c,u_p)\min\big(L_p, \delta(u_p,u_{p'})L_{p'} + \Delta_{p,p'}\big) + \Delta_{c,p}\Big)$$
$$= \min(L_c, \delta(u_c,u_p)L_p + \Delta_{c,p}, \delta(u_c,u_p)\delta(u_p,u_{p'})L_{p'} + \delta(u_c,u_p)\Delta_{p,p'} + \Delta_{c,p}). \quad (17)$$

because they get the values of the path with the largest metric and the maximum function is associative since

$$\max(M_a, \max(M_b, M_c)) = \max(\max(M_a, M_b), M_c).$$

Concerning the reliability update procedure, without loss of generality, we assume that M_c is the largest path metric and we define p and p' as in (9). The updated reliability values of $\mathcal{M}(P_a, \mathcal{M}(P_b, P_c))$ and $\mathcal{M}(\mathcal{M}(P_a, P_b), P_c)$ in (14) are respectively derived in (16) and (17) using function ϕ. The proof is then divided into two parts, corresponding to two cases: 1) $u_c = u_p$ and 2) $u_c \neq u_p$.

1) $\delta(u_c, u_p) = 1$, then (17) becomes:

$$\min\big(L_c, \delta(u_c,u_p)L_p + \Delta_{c,p}, \delta(u_c,u_{p'})L_{p'} + \Delta_{c,p'}\big). \quad (18)$$

Since $\Delta_{c,p'} = \Delta_{c,p} + \Delta_{p,p'}$, (18) coincides with (16).

2) $\delta(u_c, u_p) = 0$, then (17) becomes:

$$\min(L_c, \Delta_{c,p}). \quad (19)$$

Assuming $p = b$, (16) becomes:

$$\min\big(L_c, \Delta_{c,b}, \delta(u_c,u_a)L_a + \Delta_{c,b} + \Delta_{b,a}\big). \quad (20)$$

Since L_a and $\Delta_{b,a}$ are always positive, (20) becomes $\min(L_c, \Delta_{c,b})$ which coincides with (19).

Therefore, the associative property is proved for both cases. □

Remark. Based on the commutative and associative properties of the merge operation, two important statements can be inferred:

- We can extend the merge operation to more than two paths. For instance, for four paths P_a, P_b, P_c and P_d, we can write $\mathcal{M}(P_a, P_b, P_c, P_d)$ to refer to the output path obtained by merging the four paths.
- The merge operation can be processed in a *dichotomous* fashion:

$$\mathcal{M}(P_a, P_b, P_c, P_d) = \mathcal{M}\big(\mathcal{M}(P_a, P_b), \mathcal{M}(P_d, P_c)\big),$$

where $\mathcal{M}(P_a, P_b)$ and $\mathcal{M}(P_c, P_d)$ can be processed in parallel and then the resulting paths are merged to yield the output path.

C. The MLM algorithm as an instance of the merge operation

Referring back to Section II, let us consider the $2^{\nu+1}$ paths going through trellis stage k and merging together. Among them, $n = 2^{\nu}$ paths, denoted by $\{P_{p_1^0}, P_{p_2^0}, \ldots, P_{p_n^0}\}$, carry hard decision $u = 0$ at trellis section k and the remaining n, denoted by $\{P_{p_1^1}, P_{p_2^1}, \ldots, P_{p_n^1}\}$, carry hard decision $u = 1$.

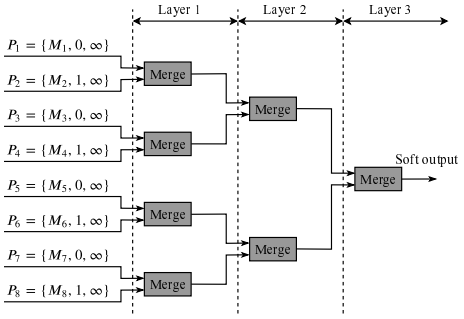

Fig. 2. Binary tree architecture used for the soft output computation in the local SOVA decoder for the code of Fig.1.

The reliability value related to bit u provided by the MLM algorithm is

$$L_{\text{MLM}}(u) = \max_{i=1,\ldots,n}\{M_{p_i^1}\} - \max_{j=1,\ldots,n}\{M_{p_j^0}\}. \quad (21)$$

Let us consider the operation merging all the paths with hard decision $u = 1$: $\mathcal{M}(P_{p_1^1}, \ldots, P_{p_n^1})$. The resulting output hard decision is obviously 1 and the output path metric is $M_1 = \max_{i=1,\ldots,n}\{M_{p_i^1}\}$. For the output reliability, merging paths with the same hard decision value requires the application of BR (11). Since the reliability values are all initialized at $+\infty$, applying (11) yields an output reliability also equal to $+\infty$. Similarly, merging together all the paths carrying hard decision $u = 0$ applying $\mathcal{M}(P_{p_1^0}, \ldots, P_{p_n^0})$ results in an output hard decision 0, an output path metric equal to $M_0 = \max_{i=1,\ldots,n}\{M_{p_i^0}\}$ and an output reliability at $+\infty$.

Then, if we merge the two resulting paths:

$$\mathcal{M}\big(\mathcal{M}(P_{p_1^1}, \ldots, P_{p_n^1}), \mathcal{M}(P_{p_1^0}, \ldots, P_{p_n^0})\big), \quad (22)$$

the computation of the output reliability amounts to the application of HR (10):

$$L_{\mathcal{M}} = \min\Big(+\infty, \big|M_1 - M_0\big|\Big) = \big|M_1 - M_0\big|, \quad (23)$$

which is the absolute value of the expression of L_{MLM} in (21). If we denote by $u_{\mathcal{M}}$ the output hard decision deriving from (22), then L_{MLM} is equal to

$$L_{\text{MLM}}(u_k) = (2u_{\mathcal{M}} - 1) \times L_{\mathcal{M}}. \quad (24)$$

Therefore, the result of the MLM algorithm can be interpreted as the outcome of a merge operation applied to all the paths.

On another note, thanks to the commutative and associative properties of the merge operation stated in (13) and (14),

the operation merging all the paths (22) can be performed in a different order for a better match with efficient software or hardware implementations. In particular, instead of first merging the paths with the same hard decision, one can start by merging pairs of paths with different hard decisions $(P_{p_i^1}, P_{p_i^0})$, $i = 1, \ldots, n$:

$$\mathcal{M}\big(\mathcal{M}(P_{p_1^1}, P_{p_1^0}), \ldots, \mathcal{M}(P_{p_n^1}, P_{p_n^0})\big). \tag{25}$$

Moreover, if $P_{p_i^1}$ and $P_{p_i^0}$ are chosen in such a way that the corresponding trellis branches at trellis section k, $(s_{p_i^1}, s'_{p_i^1})$ and $(s_{p_i^0}, s'_{p_i^0})$ verify $s'_{p_i^1} = s'_{p_i^0} = s'$, the merge operation of the pair of paths yields the following path metric:

$$\begin{aligned} M_{p_i} &= \max(M_{p_i^1}, M_{p_i^0}) && (26)\\ &= \max\big(A_k(s_{p_i^1}) + \Gamma_k(s_{p_i^1}, s') + B_{k+1}(s'),\\ &\qquad A_k(s_{p_i^0}) + \Gamma_k(s_{p_i^0}, s') + B_{k+1}(s')\big)\\ &= \max\big(A_k(s_{p_i^1}) + \Gamma_k(s_{p_i^1}, s'), A_k(s_{p_i^0}) + \Gamma_k(s_{p_i^0}, s')\big)\\ &\qquad + B_{k+1}(s') && (27)\\ &= A_{k+1}(s') + B_{k+1}(s'), && (28) \end{aligned}$$

and since $u_{p_i^1} \neq u_{p_i^0}$, the updated reliability with HR is

$$L_{p_i} = \min\big(+\infty, \Delta_{p_i^1, p_i^0}\big) = \Delta_{p_i^1, p_i^0} \tag{29}$$

where

$$\begin{aligned} \Delta_{p_i^1, p_i^0} &= \left| M_{p_i^1} - M_{p_i^0} \right|\\ &= \Big| \big(A_k(s_{p_i^1}) + \Gamma_k(s_{p_i^1}, s')\big) -\\ &\qquad \big(A_k(s_{p_i^0}) + \Gamma_k(s_{p_i^0}, s')\big) \Big|. \end{aligned} \tag{30}$$

The output hard decision u_{p_i} is provided by the path, $P_{p_i^0}$ or $P_{p_i^1}$, with the higher path metric.

We can see from (27) and (28) that, with the proposed merge ordering, the calculation of the output path metric for this scheduling proposal $\mathcal{M}(P_{p_i^1}, P_{p_i^0})$ includes the derivation of the forward state metric $A_{k+1}(s')$ as in the forward recursion (3a). Therefore, there is no need to perform a preliminary calculation of the forward state metrics. Only the backward state metrics need to be computed in advance. Similarly, one can show that if the paths $P_{p_i^1}$ and $P_{p_i^0}$ are chosen in such a way that the corresponding trellis branches at trellis section k are stemming from the same state ($s_{p_i^1} = s_{p_i^0} = s$), the calculation of the output path metric includes the same derivation of the backward state metric $B_k(s)$ as in the backward recursion (3b). Then, there is no need to perform a preliminary calculation of the backward state metrics and only the forward state metrics need to be computed in advance.

For a convolutional code with memory length ν, the overall merge operation for the computation of the soft output for the decoder can be carried out in a dichotomous fashion : the merge operation then requires a binary tree of $2^{\nu+1} - 1$ elementary merge operators organized in $\nu + 1$ layers. Taking Fig. 1 as an example, $\nu = 2$ and the soft output related to bit u_k is obtained by a binary tree consisting of $\nu + 1 = 3$ layers of merge operators, as shown in Fig. 2.

The next section describes the overall algorithm implementing this particular arrangement for the merge operations.

D. Soft output computation algorithm

The soft output calculation in a dichotomous fashion can be performed according to Algorithm 1.

Algorithm 1 The local SOVA

Initalization: $\mathbf{T} = [T(1) \ \ldots \ T(2^{\nu+1})]$ is the set of $2^{\nu+1}$ transitions of the trellis section defined by the pairs of states (s, s');
for each trellis stage $k = 1, \ldots, K$ **do**
  for each path $p = 1, \ldots, 2^{\nu+1}$ **do**
    $(s_p, s'_p) = T(p)$
    $M_p(0) = A_k(s_p) + \Gamma_k(s_p, s'_p) + B_{k+1}(s'_p)$;
    $u_p(0) =$ data bit on transition (s_p, s'_p);
    $L_p(0) = +\infty$;
  end for
  for each layer $l = 1, \ldots, \nu + 1$ **do**
    for each path $p = 1, \ldots, 2^{(\nu-l+1)}$ in layer l **do**
      $a = \arg\max_{j \in \{2p-1, 2p\}} \{M_j(l-1)\}$;
      $b = \arg\min_{j \in \{2p-1, 2p\}} \{M_j(l-1)\}$;
      $\Delta_{a,b} = M_a(l-1) - M_b(l-1)$;
      $M_p(l) = M_a(l-1)$;
      $u_p(l) = u_a(l-1)$;
      $L_p(l) = \phi\big(L_a(l-1), L_b(l-1), \Delta_{a,b}, u_a(l-1), u_b(l-1)\big)$;
    end for
  end for
  Hard output: $\hat{u}_k = u_1(\nu + 1)$;
  Soft output: $\hat{L}(u_k) = (2\hat{u}_k - 1) \times L_1(\nu + 1)$;
end for

Note that this algorithm is a generic version that assumes that all the forward and backward state metrics are pre-computed and stored in a memory. In practice, in order to reduce the state metric memory, sliding window techniques [5] are usually employed. Moreover, different schedules can be applied for the recursive computation of the state metrics, including the well known backward-forward (BF) and butterfly schedules [7], [22]. When compared, the former takes twice the time to decode a frame while the latter requires twice the hardware resources. Nevertheless, both these schedules have the same overall computational complexity. The only difference between the proposed local SOVA and the MLM algorithm is the way the soft output is calculated. Therefore, any sliding window technique or scheduling scheme for the computation of the state metrics applicable to the MLM algorithm is also directly applicable to the local SOVA. Also, the memory usage for the state metric of the local SOVA is the same as for the MLM algorithm. For the rest of the paper, we only consider the BF schedule without sliding window, the application of the results to other schedules and with sliding window being straightforward.

With the BF schedule, the backward state metrics are pre-computed and stored in a memory. Then, the algorithm recursively calculates the forward state metric and derives the soft output. As discussed in the previous section, specific simplifications can be made for the local SOVA at layer $l = 1$. First, at the initialization step, we can organize the set of transitions $\mathbf{T}$ so that two adjacent transitions have the same

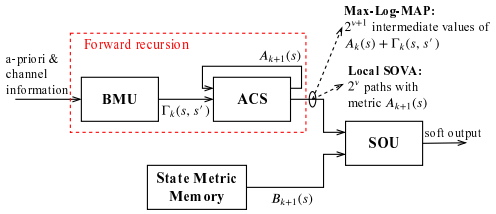

Fig. 3. Basic architecture considered for the local SOVA and MLM algorithms. With the BF scheduling, the backward recursion is firstly performed and the backward state metrics are stored in the state metric memory. Then, the forward recursion and the soft output computation are performed.

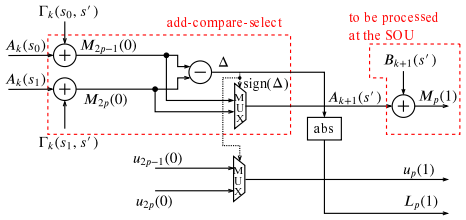

Fig. 4. Hardware architecture of Algorithm 1 for layer $l = 1$.

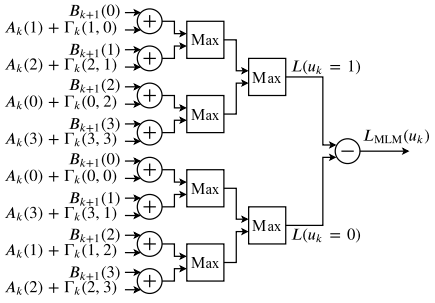

Fig. 5. SOU of a MLM decoder for $\nu = 2$.

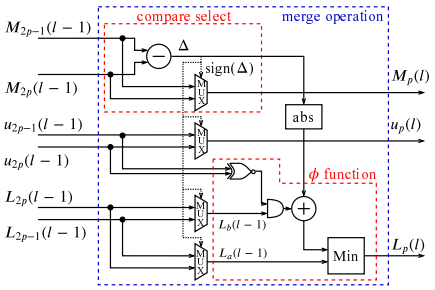

Fig. 6. Generic hardware architecture of a merge operation $\mathcal{M}$ of two paths indexed $2p$ and $2p-1$ at layer $l > 1$.

state s', i.e., $s'_{2i-1} = s'_{2i}$, for $i = 1, \ldots, 2^{\nu}$. Then, in line 5, we can initialize path metrics $M_p(0)$ to be $A_k(s) + \Gamma_k(s, s')$ instead of $A_k(s) + \Gamma_k(s, s') + B_{k+1}(s, s')$. The resulting path metric $M_a(1)$ at layer $l = 1$ is equal to $A_{k+1}(s')$, thus allowing the forward recursion to be incorporated into the soft output computation. To compensate for omitting $B_{k+1}(s')$ in the expression of $M_p(0)$, in line 14, the output path metric $M_p(1)$ should be taken equal to

$$M_p(1) = M_a(1) + B_{k+1}(s'). \tag{31}$$

Furthermore, in line 16, output reliability $L_p(1)$ can be directly assigned $\Delta_{a,b}$ and the calculation of the reliability value at the first layer can be replaced by a simple assignment operation, making the initial assignment in line 7 unnecessary. After layer $l = 1$, the subsequent layers should be carried out following Algorithm 1 without any modification.

To complete this algorithmic description, the next sections provide some details about possible hardware architectures for a local SOVA decoder. To this end, we first focus on a radix-2 trellis in Section III-E and highlight the differences with a conventional MLM decoder. Section IV will later describe higher radix architectures.

E. Radix-2 local SOVA decoder architecture

Since the proposed algorithm only differs from the MLM algorithm in the soft output calculation, its global architecture is composed of the same blocks as the architecture of a MLM decoder [23]: in the case of a BF decoding schedule, *branch metric units* (BMU) and *add-compare-select units* (ACSU) recursively compute the backward and forward state matrics, a *state metric memory* stores the backward state metrics and a *soft-output unit* (SOU) computes the extrinsic information and the soft decision during the forward recursion. Fig. 3 shows the corresponding basic architecture for the forward recursion; the backward BMU and ACSU are not shown. If a symmetric forward-backward scheduling is applied, the roles of forward and backward units are just swapped.

At trellis stage k, the BMU calculates all possible values of $\Gamma_k(s, s')$ and forwards them to the ACSU. The ACSU calculates $A_k(s) + \Gamma_k(s, s')$ for each branch in the trellis stage and computes (3a) for each state s' at time index $k + 1$. For the local SOVA architecture, the first layer of Algorithm 1, depicted in Fig. 4, performs the forward state metric recursion as well as it produces the hard decision, the reliability value and the path metric for subsequent layers. Besides the right-hand side adder, the structure shown in Fig. 4 for $l = 1$ is very close to the ACSU structure of a conventional MLM decoder. Therefore, in order to make the local SOVA easy to compare with the MLM algorithm, we consider this sub-structure as the ACSU of the local SOVA decoder and the final adder plus the units processing the subsequent layers as its SOU.

The main difference between both architectures comes from the SOU. In the MLM architecture, $2^{\nu+1}$ intermediate values $A_k(s) + \Gamma_k(s, s')$ computed in the ACSU are added to $B_{k+1}(s')$. Then, the most reliable branch for bit $u_k = 1$ and for bit $u_k = 0$ are selected using two 2^{ν}-input maximum selection operators and the LLR is obtained by computing the difference between the terms $A_k(s) + \Gamma_k(s, s') + B_{k+1}(s')$ for these two branches as shown in Fig. 5 for $\nu = 2$. On the other hand, the local SOVA SOU takes the 2^{ν} values of $A_{k+1}(s')$,

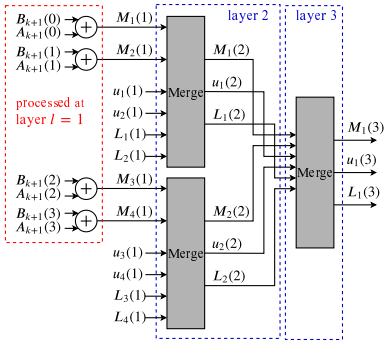

Fig. 7. SOU of a local SOVA decoder using merge operators for $\nu = 2$.

adds them to 2^ν corresponding values of $B_{k+1}(s')$ to provide the path metrics. The hard decisions and their reliability values computed by the ACSU are forwarded to the SOU. The SOU has then to process 2^ν paths using a binary tree of merge operators. The structure of merge operators used to process layers $l > 1$ is depicted in Fig. 6 and the overall structure of the tree is shown in Fig. 7 for $\nu = 2$ (including the adders actually part of layer $l = 1$).

In terms of computational complexity, with the convention that one adder is equivalent to one max or min operator and is accounted for as one computational unit and neglecting the multiplexers, the operator implementing function ϕ consists of one adder and one min operator and is therefore accounted for as two computational units. Consequently, the MLM SOU requires $(4\times 2^\nu - 1)$ computational units while the local SOVA SOU requires $(4\times 2^\nu - 3)$ computational units. Since the ACSU and the BMU of both architectures are similar, both algorithms have roughly the same computational complexity when a conventional radix-2 architecture is implemented. However, the proposed algorithm is mainly of interest when higher radix orders are considered, as explained in the following section.

IV. HIGH-RADIX DECODER ARCHITECTURES USING LOCAL SOVA

In the previous section, we have been considering the conventional radix-2 trellis diagram. In this section, we will concentrate on higher radix orders. In a radix-2^R trellis diagram, $R \in \mathbb{N}^*$, there are 2^R branches coming in and out of a state s at time index k. This is obtained by aggregating R consecutive radix-2 trellis stages. Hence, a branch in a radix-2^R trellis stage is now labeled with R systematic bits and we have to reconsider the definition of a path and its corresponding merge operation.

For a radix-2^R trellis diagram, we define a radix-2^R path P going through the branch (s, s') as

$$P = \{M, u^1, \ldots, u^R, L^1, \ldots, L^R\} \in \mathbb{R} \times \{0,1\}^R \times \{\mathbb{R}^+\}^R \tag{32}$$

where M is the path metric, $u^1, \ldots, u^R$ are the R hard decisions attached to branch (s, s'), and $L^1, \ldots, L^R$ are the reliability values for each hard decision and are initialized to $+\infty$.

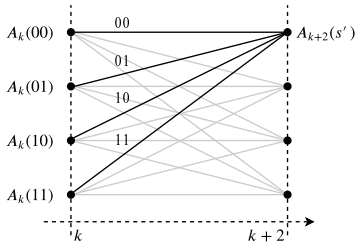

Fig. 8. A radix-4 stage for an convolutional code with $\nu = 2$.

We also define the radix-2^R merge operation $\mathcal{M}$ as in Section III with three procedures: path metric selection, hard decision selection and update of the reliability values. The selection of the path metric remains unchanged. The only difference is now that we have to select R hard decisions instead of one, and to update R reliability values using function ϕ, one for each hard decision. Note that the merge operation for high-radix paths is also commutative and associative, therefore, the order of the paths in the merge operation does not affect the output. To this end, if we arrange wisely the input paths, we can reduce complexity when compared to a straightforward implementation.

A. Radix-4 local SOVA decoder with minimum complexity ACSU

A branch in a radix-4 trellis diagram is the aggregation of two consecutive branches in a radix-2 diagram, as illustrated in Fig. 8 for an convolutional code with $\nu = 2$. From time index k to time index $k + 2$, four branches are leaving and merging into each trellis state, corresponding to the transmission of two systematic bits with possible values 00, 10, 01 and 11. Therefore, at time index $k + 2$, there are four radix-4 paths, denoted by $\{P_{00}, P_{01}, P_{10}, P_{11}\}$, merging into each state s'. Since these four paths have the same $B_{k+2}(s')$ value, as in section III-D we can initialize the corresponding path metrics with $A_k(s) + \Gamma_{k\to k+1}(s, s')$ instead of $A_k(s)+\Gamma_{k\to k+1}(s, s')+B_{k+2}(s')$, where $\Gamma_{k\to k+1}(s, s')$ is the sum of the two successive branch metrics at time indices k and $k+1$ in the equivalent radix-2 tellis diagram. Then, we perform the radix-4 merge operation:

$$\mathcal{M}\big(P_{00}, P_{01}, P_{10}, P_{11}\big). \tag{33}$$

The path metric resulting from this layer-1 merge operation is also the forward state metric of state s' at time index $k + 2$, $A_{k+2}(s')$. Hence, we can consider the operator implementing (33) as the radix-4 ACSU of the local SOVA decoder.

An important property of the radix-4 local SOVA ACSU is that its complexity depends on the processing order of the paths in the merge operation (33). If we implement (33) as

$$\mathcal{M}\big(\mathcal{M}(P_{00}, P_{01}), \mathcal{M}(P_{10}, P_{11})\big) \tag{34}$$

with the hardware architecture shown in Fig. 9, only one ϕ operator has to be implemented. Actually, we do not need

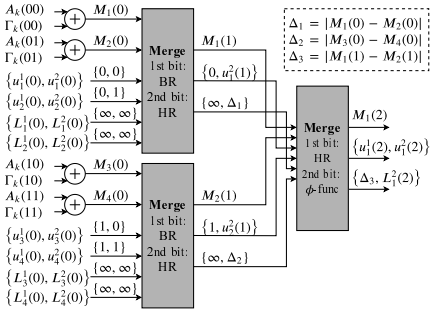

Fig. 9. Radix-4 local SOVA ACSU architecture implementing 2-bit merge operators according to (34).

to resort to function ϕ in the first layer since the output reliability is $+\infty$ or the metric difference between the two paths, depending whether BR or HR is employed.

On the other hand, if we implement (33) as

$$\mathcal{M}\big(\mathcal{M}(P_{00}, P_{11}), \mathcal{M}(P_{01}, P_{10})\big), \tag{35}$$

we can use HR for both bits at the first layer but have to use a ϕ operation for each bit at the second layer since we do not know *a priori* which hard decision will be selected. Therefore, the implementation of (34) is less complex than the one of (35) and it has minimum complexity. Note that (34) is not unique, since other processing orders of the paths can also yield the same complexity, such as $\mathcal{M}\big(\mathcal{M}(P_{00}, P_{10}), \mathcal{M}(P_{01}, P_{11})\big)$.

At the output of the radix-4 ACSU, 2^ν radix-4 paths are forwarded to the radix-4 SOU. First of all, each path metric is added to the appropriate $B_{k+2}(s')$ since it has been omitted in the ACSU. Then, a ν-layer tree of radix-4 merge operators is employed to produce the final hard decision along with its reliability value. Note that the radix-4 merge operation requires two ϕ operators for updating the reliability values, one for each bit.

When radix orders higher than 4 are considered, techniques for further reducing complexity can be considered, as explained in the following section.

B. Radix-8 local SOVA decoder using a simplified reliability update operator

In this section, we introduce a sub-optimal but less complex version of the function ϕ, called ω. Consequently, by combining the corresponding operator with the minimum complexity ACSU previously described in Section IV-A, we propose a number of local SOVA architectures with different complexity-performance tradeoffs.

A radix-8 trellis stage aggregates three consecutive radix-2 trellis stages. Each path is now composed of a path metric, three hard decisions and their three reliability values. From time index k to time index $k+3$, eight radix-8 branches are leaving and merging into each trellis state. Therefore, at time index $k+3$, there are eight radix-8 paths merging into each state s', denoted by $\{P_{000}, P_{001}, \ldots, P_{111}\}$, where the indices represent the hard decisions associated with each path. Similarly to the previous cases, when applying the radix-8 merge operation to this set of paths

$$\mathcal{M}\big(P_{000}, P_{001}, \ldots, P_{111}\big), \tag{36}$$

the resulting path metric is also the forward state metric of state s' at time index $k+3$, $A_{k+3}(s')$. This merging step can therefore be considered as the ACSU of the radix-8 local SOVA decoder. Then the output path is processed by the SOU to produce the soft decision.

The minimum complexity radix-8 ACSU can be obtained by implementing (36) as

$$\begin{aligned}\mathcal{M}\Big(&\mathcal{M}\big(\mathcal{M}(P_{000}, P_{001}), \mathcal{M}(P_{010}, P_{011})\big),\\ &\mathcal{M}\big(\mathcal{M}(P_{100}, P_{101}), \mathcal{M}(P_{110}, P_{111})\big)\Big).\end{aligned} \tag{37}$$

We can see from (37) that the first bit in $\mathcal{M}\big(\mathcal{M}(P_{000}, P_{001}), \mathcal{M}(P_{010}, P_{011})\big)$ is always zero, hence, we can resort to a radix-4 merge operation for the last two bits using only one ϕ operator. Similarly, the first bit in $\mathcal{M}\big(\mathcal{M}(P_{100}, P_{101}), \mathcal{M}(P_{110}, P_{111})\big)$ is always one, then again, only one ϕ operator is necessary. In the second stage, the first bit is always different in the two input paths, thus only the second and the third bits require the implementation of a ϕ operator. In total, four ϕ operators have to be implemented in a minimum complexity radix-8 ACSU.

However, employing ϕ operators has two main drawbacks. First of all, they consist of one adder and one min operator, therefore prohibitively increasing the complexity of the decoder if used excessively. Second and more importantly, the adder and the min operators are connected serially. This is not desirable since the ACSU dictates the critical path of the decoder [23]. Therefore, we propose a lower complexity, lower latency, sub-optimal update operator, based on new update function, called function ω.

1) The function ω: motivated by the the possibility of using only HR as in [13], one can substitute a simplified function ω for function ϕ. Assuming that paths P_{2p-1} and P_{2p} are to be merged at layer $l-1$, the output reliability is then computed as:

$$\begin{aligned}L_p(l) &= \omega\big(L_a, \Delta_{a,b}, u_{2p-1}(l-1), u_{2p}(l-1)\big)\\ &= \begin{cases}\min(L_a, \Delta_{a,b}), & \text{if } u_{2p-1}(l-1) \neq u_{2p}(l-1)\\ L_p, & \text{if } u_{2p-1}(l-1) = u_{2p}(l-1)\end{cases}\end{aligned} \tag{38}$$

where a, b and $\Delta_{a,b}$ are defined at lines 11, 12 and 13, respectively, in Algorithm 1. Fig. 10 shows the architecture of the elementary path merging operator using function ω. The ω operator is less complex than the ϕ operator since it uses only a min operation and a multiplexer resulting in a computational complexity of about one unit. However, the price to pay is a degradation of error correction performance. Indeed, a performance degradation of 0.5 dB is observed between the conventional SOVA that uses only functions ϕ [16] and the one that uses functions ω [13].

Unlike the classical SOVA, local SOVA can mix both types of functions. Therefore, this provides the flexibility of several complexity/correction performance trade-offs. However, care

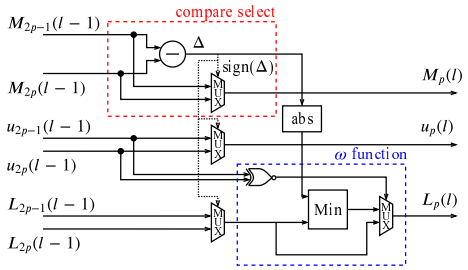

Fig. 10. Generic hardware architecture of path merging operation using function ω.

must be taken in making substitutions so that paths with high metrics are not eliminated from the selection process due to simplification. This is less likely to happen if the simplifications are made in the first layers of the tree, where the number of paths to be processed is high. Consequently, we observed that if we only substitute the ω operators for the ϕ operators in the first layers, we can significantly reduce complexity without degrading the performance of the decoder.

2) Radix-8 ACSU and SOU using ω operators: for a binary convolutional code with $\nu = 3$, the first 3 layers of the path merge binary tree are in the ACSU while the last 3 layers are processed by the SOU.

As already mentioned above, the radix-8 ACSU requires 4 ϕ operators to update the reliability values. Substituting the ω operators for the ϕ operators reduces the complexity by 4 computational units. For $\nu = 3$, the use of $2^\nu = 8$ ACSUs saves 32 computation units.

For the 3 layers of the binary tree implementing the radix-8 SOU, 7 radix-8 merge operations are required, resulting in the use of 21 ϕ operators (3 per merge operation). Replacing ϕ operators with ω operators reduces complexity but is expected to penalize the performance of the decoder.

C. Simulation results

Simulations were carried out to assess the error correcting performance of the radix-8 local SOVA and its variants for the LTE turbo code, in order to compare them with the radix-8 MLM algorithm. For radix-2 and radix-4 local SOVA, we proved in Section III-C that the LLR produced by the local SOVA is the same as with the MLM algorithm. Therefore, their performance should be identical. Nevertheless, we first simulated the radix-8 local SOVA with only ϕ operators to confirm this fact. Then, we gradually substituted ω operators for ϕ operators to observe the impact on error correction when simplifications are made to the radix-8 local SOVA. We use the notations ACSU-(i, j) and SOU-(i, j) to represent the different configurations, where i and j are the number of layers where ω and ϕ operators are employed, respectively. For example, ACSU-(2,1) means that ω operators and implemented in the two first layers of the ACSU and that ϕ operators are used in the last layer.

We simulated the following seven configurations for the SISO decoding algorithms, where L-SOVA is an abbreviation for local SOVA:

- DEC 1: MLM algorithm.
- DEC 2: L-SOVA with ACSU-(0,3) and SOU-(0,3).
- DEC 3: L-SOVA with ACSU-(3,0) and SOU-(0,3).
- DEC 4: L-SOVA with ACSU-(3,0) and SOU-(1,2).
- DEC 5: L-SOVA with ACSU-(3,0) and SOU-(2,1).
- DEC 6: L-SOVA with ACSU-(3,0) and SOU-(3,0).
- DEC 7: classical SOVA.

The simulations were carried out with information frames of $K = 1056$ bits, encoded with the non-punctured $r = 1/3$ LTE turbo code, modulated by BPSK and transmitted over the AWGN channel. A floating point representation of data is used in the decoder. The resulting bit error rate (BER) is measured after 5.5 decoding iterations. Fig. 11 shows that, as expected, the local SOVA with only ϕ operators (DEC 2) has the same performance as the MLM algorithm. Moreover, by substituting ω operators for ϕ operators in the ACSUs, i. e. in the first three layers, (DEC 3) the simulated curves confirm that the error correction performance of the decoder is not degraded, thus providing a low complexity alternative to the original local SOVA decoder. By gradually replacing the ϕ operators in the SOU, the performance is degraded by 0.05 dB at $BER = 10^{-6}$ when ω operators are used in the first two layers and by about 0.3 dB when only ω operators are implemented. Fig. 11 also shows that the classical SOVA (DEC 7) performs 0.1 dB worse than the local SOVA with only ω operators (DEC 6). According to [16], using ϕ operators instead of ω operators in the both the classical and local SOVAs would be equivalent to apply the MLM algorithm (DEC 1). However, contrary to the classical SOVA, the operations in the local SOVA are arranged so as to minimize the number of used ϕ operators. Therefore the performance gap between DEC 6 and DEC 7 is explained by the fact that the number of sub-optimal ω operators needed in DEC 7 is greater than in DEC 6.

D. Computational complexity analysis

In this section, we perform the comparison between the local SOVA and the MLM algorithm in terms of complexity for different radix orders. To quantify complexity, we calculate the number of additions and the number of compare select (CS) operations and consider one adder or CS operator as one computational unit. In this comparison, we do not take the memory requirements into account and only consider computational complexity. As aforementioned, the difference between the local SOVA decoder and the MLM decoder resides in the way it calculates the soft output. Therefore, the memory for the channel information, the state metrics and the extrinsic information is the same as in the MLM decoder. Moreover, sliding window techniques or different decoding schedules can also be applied to the local SOVA, hence, the memory consumption of the decoder depends on the hardware architecture. Readers may refer to [24] for a in-depth understanding of this matter.

In this analysis, we use a convolutional code with 8 states ($\nu = 3$). The decoding complexity, denoted by $\mathcal{C}$, is reported

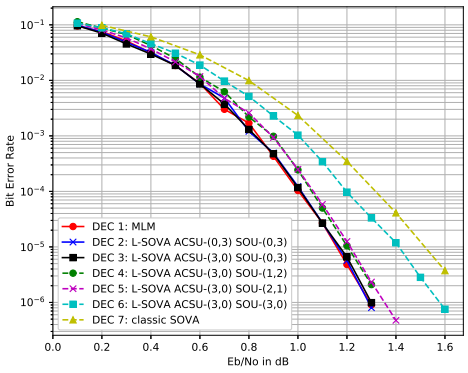

Fig. 11. BER performance of a LTE decoder using radix-8 MLM algorithm, local SOVA and its variant with $K = 1056$, $r = 1/3$ after 5.5 iterations. AWGN channel, BPSK modulation.

for one trellis section consisting of eight backward ACSUs, eight forward ACSUs, and one SOU as

$$\mathcal{C} = (8 \times \mathcal{C}_B) + (8 \times \mathcal{C}_F) + \mathcal{C}_S, \tag{39}$$

where $\mathcal{C}_B$, $\mathcal{C}_F$ and $\mathcal{C}_S$ denote the computational complexity of the backward ACSU, the forward ACSU, and the SOU, respectively. Note that we excluded the BMU in the expression since the calculation of branch metrics is the same for the local SOVA and the MLM algorithm. For the MLM algorithm, the backward and forward ACSUs have the same computational complexity. In contrast, since we are considering the BF schedule for the local SOVA, the backward ACSU is the same as in the MLM algorithm. However, the forward ACSUs not only calculate the state metrics but also take part in the soft output calculation with ϕ and ω operators. Therefore, there might be some difference compared to the forward ACSU of the MLM algorithm.

Firstly, we perform the complexity comparison between the local SOVA employing only ϕ operators and the MLM algorithm to observe the change of the complexity difference versus the radix order. Then, for radix-8, we perform further complexity analysis for cases where ϕ operators are gradually replaced by ω operators.

1) Radix-2 local SOVA and radix-2 MLM algorithm: As shown in Section III-E, the forward ACSUs of the local SOVA and the MLM algorithm are identical. Therefore, for both algorithms, the forward ACSU and the backward ACSU have the same complexity and consist of two adders and one CS operator. For the SOU, the structures are shown in Fig. 5 and Fig. 7 for the MLM algorithm and the local SOVA, respectively. With $\nu = 3$, the MLM SOU consists of 17 adders and 14 CS operators, whereas the SOU of the local SOVA requires 22 adders and 7 CS operators. In total, applying (39), the complexity of the MLM decoder is 79 computational units and the complexity of the local SOVA decoder is 77 computational units.

2) Radix-4 local SOVA and radix-4 MLM algorithm: For the MLM algorithm, the backward and the forward ACSUs have the same complexity and consist of 4 adders and 3 CS operators. Furthermore, the SOU of the MLM algorithm begins by adding 32 intermediate values of $A_k(s) + \Gamma_{k\to k+1}(s, s')$ to $B_{k+2}(s')$, using 32 adders. Next, two maximum selection trees for each systematic bit, each consisting of 15 CS operators, are needed. Finally, each LLR value is obtained by using one extra subtractor (adder). In total, MLM decoding requires 98 adders and 108 CS operators, i.e. 206 computational units. As for the local SOVA, the backward ACSU is the same as for the MLM algorithm. Apart from the calculation of the state metric, the forward ACSU requires one extra ϕ operator (one adder and one CS operator) to update the reliability values, as shown in Section IV-A. Therefore, the forward ACSU of the local SOVA consists of 5 adders and 4 CS operators. For the SOU, the $B_{k+2}(s')$ values are added to 8 path metrics using 8 adders. Then, a 3-layer tree of radix-4 merge operators is employed, which consists of 7 CS operators and (2×7) ϕ operators (to decode 2 bits). Therefore, the total complexity of the SOU for the local SOVA is 22 adders and 21 CS operators. Finally, from (39), the complexity of the radix-4 local SOVA is 151 computational units.

3) Radix-8 local SOVA and radix-8 MLM algorithm: For the MLM algorithm, the backward/forward ACSU requires 8 adders and 7 CS operators. The MLM SOU uses 64 adders to add $B_{k+3}(s')$ to the intermediate values provided by the forward ACSU. Then, two maximum selection trees, each consisting of 31 CS operators, are employed for each systematic bit. Finally, 3 extra subtractors are required to compute the LLR of the 3 bits. In total, the complexity of the radix-8 MLM decoder is 493 computational units. On the other hand, for the local SOVA, the forward ACSU requires 4 extra ϕ operators to update the reliability values. For the SOU, 8 adders are first required to add the values of $B_{k+2}(s')$ to the path metrics. Then, a 3-layer tree of radix-8 merge operators is employed, which consists of 7 CS operators and (3×7) ϕ operators (to decode 3 bits). Thus, in total, the complexity of the radix-8 local SOVA decoder is 361 computational units.

Table I summarizes the results of this complexity analysis. $\mathcal{C}_{\text{MLM}}$ and $\mathcal{C}_{\text{LSOVA}}$ denote the computational complexity of the MLM algorithm and the local SOVA, respectively. For radix 2, the MLM algorithm and the local SOVA have roughly the same complexity, while for radix-4 and radix-8 schemes, the local SOVA is less complex. For high-radix schemes (4 and 8), using the local SOVA reduces complexity by 27%.

Furthermore, the complexity per decoded bit of the MLM algorithm increases from 79 to 103 computational units when moving from radix 2 to radix 4. In contrast, it decreases from 77 to 75.5 computational units for the local SOVA. Therefore, using the local SOVA for radix-4 schemes can further increase the efficiency of the decoder. On the other hand, for radix-8 schemes, although the local SOVA is less complex than the MLM algorithm, its complexity per decoded bit is raised to 120.3 computational units. It is higher than for radix 4 but enables a throughput increase. Moreover, it can be significantly reduced by replacing the ϕ operators by ω operators, as shown in the following sub-section.

TABLE I
COMPARISON OF THE COMPUTATIONAL COMPLEXITY OF THE MLM ALGORITHM AND THE LOCAL SOVA FOR VARIOUS RADIX SCHEMES (CS: COMPARE-SELECT).

Radix schemes	Max-Log-MAP							local SOVA							
	$8\times\mathcal{C}_B$		$8\times\mathcal{C}_F$		$\mathcal{C}_S$		$\mathcal{C}_{\text{MLM}}$	$8\times\mathcal{C}_B$		$8\times\mathcal{C}_F$		$\mathcal{C}_S$		$\mathcal{C}_{\text{LSOVA}}$	$\frac{\mathcal{C}_{\text{LSOVA}}}{\mathcal{C}_{\text{MLM}}}$
	Adder	CS	Adder	CS	Adder	CS		Adder	CS	Adder	CS	Adder	CS		
Radix-2	16	8	16	8	17	14	**79**	16	8	16	8	22	7	**77**	**0.975**
Radix-4	32	24	32	24	34	60	**206**	32	24	40	32	22	21	**151**	**0.733**
Radix-8	64	56	64	56	67	186	**493**	64	56	96	88	29	28	**361**	**0.732**

TABLE II
COMPARISON OF THE COMPUTATIONAL COMPLEXITY OF VARIOUS RADIX-8 ALGORITHMS (CS: COMPARE-SELECT).

Algorithm	$8\times\mathcal{C}_B$		$8\times\mathcal{C}_F$		$\mathcal{C}_S$		Computational complexity $\mathcal{C}$	Complexity normalization	Performance loss at BER 10^{-6} (dB)
	Adder	CS	Adder	CS	Adder	CS			
MLM	64	56	64	56	67	186	493	1	–
L-SOVA ACSU-(0,3), SOU-(0,3)	64	56	96	88	29	28	361	0.73	0.0
L-SOVA ACSU-(3,0), SOU-(0,3)	64	56	64	88	29	28	329	0.67	< 0.01
L-SOVA ACSU-(3,0), SOU-(1,2)	64	56	64	88	17	28	317	0.64	0.05
L-SOVA ACSU-(3,0), SOU-(2,1)	64	56	64	88	11	28	311	0.63	0.05
L-SOVA ACSU-(3,0), SOU-(3,0)	64	56	64	88	8	28	308	0.62	0.3

4) Radix-8 local SOVA with ω operators: The complexity analysis of the local SOVA for a radix-8 scheme was reiterated by gradually replacing ϕ operators by ω operators in the forward ACSU and the SOU. We considered the same configurations as in Section IV-C and the computational complexity is still calculated based on (39). The complexity comparison is shown in Table II, where the MLM decoding complexity is taken as a reference for complexity normalization and performance comparison. We can observe that if we use ω operators instead of ϕ operators in the forward ACSUs, the resulting complexity is reduced to 67% of the complexity of the reference decoder compared to 73% if only ϕ operators are used, with no noticeable impact on the correction performance. If a lower complexity is desired, the local SOVA with ACSU-(3,0) and SOU-(2,1) can be employed to reach 63% of the reference complexity, at the cost of a performance degradation of 0.05 dB. Table II also shows that using only ω operators further reduces the complexity by 1% but the resulting 0.3 dB performance loss makes this configuration less attractive.

E. Radix-16 local SOVA decoder for convolutional codes with memory length $\nu = 3$: breaking the ACSU bottleneck

In this section, we only consider more practical convolutional codes with $\nu = 3$ (8 states) to show the advantage of the local SOVA compared to the conventional MLM algorithm. A section of a radix-16 trellis diagram is the aggregation of four consecutive sections in a radix-2 trellis diagram or, equivalently, of two consecutive sections in a radix-4 trellis diagram. With the latter representation, two branches are connecting any pair of states s and s' between time indices k and $k+4$, as illustrated in Fig. 12 between $s = 2$ and $s' = 4$.

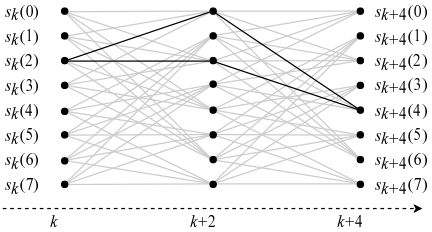

Fig. 12. A radix-16 trellis stage consisting of two radix-4 trellis stages.

Intuitively, one could decode the radix-16 turbo code with a radix-16 ACSU using 16-input max-select operations. However, increasing the number of inputs of the max-select operations results in a longer propagation path in the ACSU thus lengthening the critical path of the decoder. To get around this problem, the authors of [12] suggested that we can select the branch with larger branch metric among the two branches connecting two states at time indices k and $k+4$, and discard the other one. Since this task could be done in the BMU to reduce by half the number of branches, we can then use radix-8 ACSUs for the calculation of the state metrics.

However, the main drawback of this approach when applied to the MLM algorithm is that the branches selected after the BMU might carry either $u_j = 1$ or $u_j = 0$, for $j = k, \ldots, k+3$. This creates a non-static ratio between the number of branches having $u_j = 1$ and the number of branches having $u_j = 0$, consequently causing a major problem for the MLM SOU since it naturally employs max-select operations with a constant number of inputs referring to hard decisions 1 and 0.

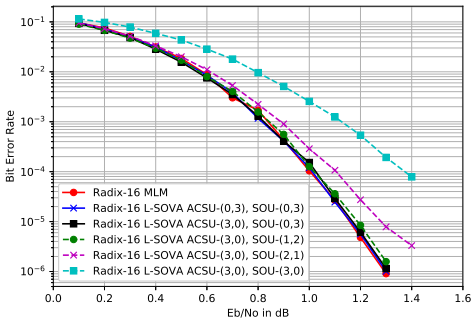

Fig. 13. BER performance of a LTE decoder using radix-16 MLM algorithm, local SOVA and its variant with $K = 1056$, $r = 1/3$ after 5.5 iterations. AWGN channel, BPSK modulation.

On the other hand, from the local SOVA perspective, the two branches processed by the BMU can be considered as two paths merging at time index $k+4$. Hence, we can use the path merging operation to produce one path carrying the selected hard decision and the updated reliability value. The BMU can then forward 64 paths to the radix-8 ACSUs and then the 8 output paths are sent to the SOU to finally compute the soft output. So, the BMU, the ACSU and the SOU constitute a path merging binary tree with 7 layers: the first layer is in the BMU, and thus not in the critical path, the three next layers are in the ACSU and the last three layers in the SOU. In addition, since the order of the path inputs does not affect the result of the merge operation, the local SOVA is immune to the problem of the non-static ratio of hard decision value mentioned above for the MLM algorithm.

Extensive simulations with the radix-16 local SOVA were also carried out. Similarly to the radix-8 case, we gradually substituted ω operators for ϕ operators in order to observe the behavior of the decoder. The results are shown in Fig. 13. We can observe that we can still replace ϕ operators by ω operators in the ACSU and in the first layer of the SOU with a negligible degradation in performance. However, further substitutions are not recommended since a penalty of 0.4 dB at 10^{-4} of BER can be observed if we use solely ω operators.

F. Convolutional codes with radix orders higher than 16

Similarly, for convolutional codes with 8 states, when considering higher radix orders such as 32 and 64, 4 and 8 parallel branches are respectively connecting two states in a trellis section. In this case, the BMU selects the path with the largest path metric among the 4 or 8 paths. Moreover, since the BMU does not involve a recursive loop as in the ACSU, it can be pipelined to ensure that the critical path always resides in the ACSU. However, since the complexity of the decoder increases exponentially with the number of bits decoded simultaneously, it is then necessary to find the processing order of the paths with the best compromise between throughput and complexity. Nonetheless, using local SOVA with high radix orders provides an ultra high throughput solution for turbo codes since the critical path of the decoder remains in the radix-8 ACSU while decoding an increasing number of systematic bits in a single clock cycle.

V. CONCLUSION

In this paper, we introduced a new SISO decoding algorithm for convolutional codes: local SOVA. The local SOVA architecture is shown to exhibit a more hierarchical structure and a lower computational complexity than the conventional Max-Log-MAP algorithm. We observed that using local SOVA in radix-8 LTE turbo decoders significantly reduces the complexity of the decoder compared to the respective radix-8 Max-Log-MAP architecture. Moreover, local SOVA makes it possible to increase the radix order without penalizing the error correction performance or the critical path of the decoder, but at the cost of added complexity. These advantages make local SOVA a first-choice algorithm for ultra-high throughput turbo decoders. Future work will include the investigation of very high radix orders, as well as the hardware implementation of merge operations for different radix orders.

ACKNOWLEDGEMENT

This work was partially funded by the EPIC project of the EU's Horizon 2020 research and innovation programme under grant agreement No. 760150.

REFERENCES

[1] C. Berrou, A. Glavieux, and P. Thitimajshima, "Near Shannon limit error-correcting coding and decoding: Turbo-codes," in *Proc. IEEE Int. Conf. Commun.*, vol. 2, May 1993, pp. 1064–1070.
[2] L. Bahl, J. Cocke, F. Jelinek, and J. Raviv, "Optimal decoding of linear codes for minimizing symbol error rate (corresp.)," *IEEE Trans. Inf. Theory*, vol. 20, no. 2, pp. 284–287, March 1974.
[3] P. Robertson, E. Villebrun, and P. Hoeher, "A comparison of optimal and sub-optimal MAP decoding algorithms operating in the log domain," in *Proc. IEEE Int. Conf. Commun.*, vol. 2, June 1995, pp. 1009–1013 vol.2.
[4] C. Douillard and M. Jézéquel, "Chapter 1. Turbo codes: from first principles to recent standards," in *Channel Coding: Theory, Algorithms, and Applications*. Academic Press, July 2014, pp. 1–53.
[5] S. Benedetto, D. Divsalar, G. Montorsi, and F. Pollara, "A soft-input soft-output maximum a posteriori (MAP) module to decode parallel and serial concatenated codes," *JPL TDA Progr. Rep.*, vol. 42, no. 127, pp. 1–20, 1996.
[6] J. Zhang and M. P. C. Fossorier, "Shuffled iterative decoding," *IEEE Trans. Commun.*, vol. 53, no. 2, pp. 209–213, Feb 2005.
[7] O. Muller, A. Baghdadi, and M. Jézéquel, "Exploring parallel processing levels for convolutional turbo decoding," in *Proc. 2nd ICTTA Conf.*, April 2006, pp. 2353–2358.
[8] R. G. Maunder, "A fully-parallel turbo decoding algorithm," *IEEE Trans. Commun.*, vol. 63, no. 8, pp. 2762–2775, Aug 2015.
[9] G. Fettweis and H. Meyr, "Parallel Viterbi algorithm implementation: breaking the ACS-bottleneck," *IEEE Trans. Commun.*, vol. 37, no. 8, pp. 785–790, Aug 1989.
[10] C. Tang, C. Wong, C. Chen, C. Lin, and H. Chang, "A 952ms/s Max-Log MAP decoder chip using radix-4× 4 ACS architecture," in *Proc. IEEE Asian Solid-State Circuits Conf.*, Nov 2006, pp. 79–82.
[11] K. Shr, Y. Chang, C. Lin, and Y. Huang, "A 6.6pj/bit/iter radix-16 modified log-MAP decoder using two-stage ACS architecture," in *Proc. IEEE Asian Solid-State Circuits Conf.*, Nov 2011, pp. 313–316.
[12] O. Sánchez, C. Jégo, M. Jézéquel, and Y. Saouter, "High speed low complexity radix-16 Max-Log-MAP SISO decoder," in *Proc. IEEE ICECS*, Dec 2012, pp. 400–403.
[13] J. Hagenauer and P. Hoeher, "A Viterbi algorithm with soft-decision outputs and its applications," in *Proc. IEEE GLOBECOM*, Nov 1989, pp. 1680–1686 vol.3.

[14] F. J. Martin-Vega, F. Blanquez-Casado, F. J. López-Martínez, G. Gomez, and J. T. Entrambasaguas, "Further improvements in SOVA for high-throughput parallel turbo decoding," *IEEE Commun. Lett.*, vol. 19, no. 1, pp. 6–9, Jan 2015.
[15] Q. Huang, Q. Xiao, L. Quan, Z. Wang, and S. Wang, "Trimming soft-input soft-output Viterbi algorithms," *IEEE Trans. Commun.*, vol. 64, no. 7, pp. 2952–2960, July 2016.
[16] M. P. C. Fossorier, F. Burkert, and J. Hagenauer, "On the equivalence between SOVA and Max-Log-MAP decodings," *IEEE Commun. Lett.*, vol. 2, no. 5, pp. 137–139, May 1998.
[17] G. Battail, "Pondération des symboles décodés par l'algorithme de Viterbi," *Ann. Telecommun.*, vol. 42, no. 1-2, pp. 31–38, Jan 1987.
[18] L. Lin and R. S. Cheng, "Improvements in SOVA-based decoding for turbocodes," in *Proc. IEEE Int. Conf. on Commun.*, vol. 3, June 1997, pp. 137–139.
[19] G. D. Forney, "The Viterbi algorithm," *Proc. IEEE*, vol. 61, no. 3, pp. 268–278, March 1973.
[20] A. J. Viterbi, "An intuitive justification and a simplified implementation of the map decoder for convolutional codes," *IEEE J. on Sel. Areas in Commun.*, vol. 16, no. 2, pp. 260–264, Feb 1998.
[21] F. Hemmati and D. Costello Jr, "Truncation error probability in Viterbi decoding," *IEEE Trans. Commun.*, vol. 25, pp. 530–532, 06 1977.
[22] E. Boutillon, W. J. Gross, and P. G. Gulak, "VLSI architectures for the MAP algorithm," *IEEE Trans. Comm.*, vol. 51, no. 2, pp. 175–185, Feb 2003.
[23] C. Benkeser, A. Burg, T. Cupaiuolo, and Q. Huang, "Design and optimization of an HSDPA turbo decoder ASIC," *IEEE J. Solid-State Circuits*, vol. 44, no. 1, pp. 98–106, Jan 2009.
[24] Zhongfeng Wang, Zhipei Chi, and K. K. Parhi, "Area-efficient high-speed decoding schemes for turbo decoders," *IEEE Trans. VLSI Systems*, vol. 10, no. 6, pp. 902–912, Dec 2002.

Vinh Hoang Son Le received the engineering degree in telecommunications from the Ho Chi Minh City University of Technology, in 2016, the Master's degree in Signal, Image, Embedded Systems, Automatism (SISEA) from the Université de Rennes 1, in 2017. He is currently working towards the Ph.D. degree in digital communications at IMT Atlantique. His current research interests are turbo codes and efficient high-throughput turbo decoders.

Charbel Abdel Nour obtained his computer and communications engineering degree in 2002 from the Lebanese University, his Masters degree in digital communications from the University of Valenciennes, France, in 2003 and his PhD in digital communications from Telecom Bretagne, France in 2008. From June 2007 till October 2011, he worked as a post-doctoral fellow at the Electronics Department of Telecom Bretagne. He was involved in several research projects related to broadcasting and satellite communications. Additionally during the same period, he was active in the Digital Video Broadcasting DVB consortium where he had important contributions. Starting November 2011, Charbel holds an associate professor position at the Electronics Department of Telecom Bretagne. His interests concern the radio mobile communications systems, broadcasting systems, coded modulations, error correcting codes, resource and power allocation for NOMA, waveform design, MIMO and iterative receivers. Lately, he presented several contributions to the H2020 METIS and FANTASTIC5G projects and to the 3GPP consortium related to coding solutions for 5G.

Emmanuel Boutillon was born in Chatou, France, in 1966. He received the Diploma degree in engineering from Télécom ParisTech, Paris, France, in 1990, and the the Ph.D. degree in 1995. In 1991, he was an Assistant Professor with the Ecole Multinationale Supérieure des Télécommunications, Dakar, Senegal. In 1992, he joined Télécom ParisTech as a Research Engineer, where he conducted the research in the field of VLSI for digital communications. In 1998, he spent a sabbatical year at the University of Toronto, Toronto, ON, Canada. In 2000, he joined Université Bretagne Sud as a Professor. He headed the LESTER Lab from 2005 to 2007 and the CACS Department from 2008 to 2015. He is currently the Scientific Advisor of the Lab-STICC. In 2011, he had a sabbatical year at INICTEL-UNI, Lima, Peru. His research interests are on the interactions between algorithm and architecture in the field of wireless communications and high-speed signal processing. In particular, he works on turbo codes and low-density parity-check decoders.

Catherine Douillard received the engineering degree in telecommunications from the Ecole Nationale Supérieure des Télécommunications de Bretagne, France, in 1988, the Ph.D. degree in electrical engineering from the University of Western Brittany, France, in 1992, and the accreditation to supervise research from the University of Southern Brittany, France, in 2004. She is currently a full Professor in the Electronics Department of IMT Atlantique where she is in charge of the Algorithm-Silicon Interaction research team of the Lab-STICC laboratory. Her main research interests are error correcting codes, iterative decoding, iterative detection, coded modulations and diversity techniques for multi-carrier, multi-antenna and multiple access transmission systems. Between 2007 and 2012, she participated in DVB (Digital Video Broadcasting) Technical Modules for the definition of DVB-T2, DVB-NGH and DVB-RCS2 standards. She also served as the technical program committee (co-)chair of ISTC 2010 and ISTC 2018 (International Symposium on Turbo Codes and Iterative Information Processing), as the general chair of ISTC 2016 and she will serve as the general co-chair of ISTC 2020. In 2009, she received the SEE/IEEE Glavieux Award for her contribution to standards and related industrial impact.

For the second and final lead already investigated, generating a high-rate code through puncturing a low-rate convolutional code has some drawbacks in terms of hardware implementation. In fact, a MAP decoder based on the original trellis will then have a decoding throughput close to the decoding throughput of the mother non-punctured code. A solution to overcome this limitation is to perform MAP decoding on the dual trellis of a high-rate equivalent convolutional code. In the literature, dual trellis construction is only reported for specific punctured codes with rate $k/(k+1)$. In our work in the context of the PhD of Vinh Hoang Son Le, we proposed a multi-step method to construct the equivalent dual code defined by the corresponding dual trellis for any punctured code. First, the equivalent non-systematic generator matrix of the high-rate punctured code is derived. Then, the reciprocal parity-check matrix for the construction of the dual trellis is deduced. As a result, we show that the dual-MAP algorithm applied on the newly constructed dual trellis yields the same performance as the original MAP algorithm while allowing the decoder to achieve a higher throughput. This work was published in [104].

The dual Log-MAP algorithm suffers from a high decoding complexity. More specifically, the source of complexity comes from the soft-output unit, which has to handle a high number of extrinsic values in parallel. To overcome this issue, we derived a new low-complexity sub-optimal decoding algorithm using the dual trellis, namely the dual Max-Log-MAP algorithm, for high coding rate convolutional codes. We showed that the state metric recursions and the extrinsic information calculations can then be reformulated using the max-log approximation and can be implemented with the local SOVA architecture. A complexity analysis was conducted, showing that the number of LUTs employed in the decoder can then be considerably reduced compared to the dual Log-MAP algorithm. Also, based on numerical simulations, we observed that dual Max-Log-MAP decoding yields only a minor loss of about 0.2 dB in performance at 10^{-6} of bit error rate compared to dual Log-MAP decoding. Therefore, it can be considered as a viable and practical low complexity sub-optimal decoding algorithm. Moreover, as a decoding algorithm on the dual trellis, when high coding rates are considered, the dual Max-Log-MAP decoder inherits the high-throughput property from the dual LogMAP decoder [105]. This makes it a first-choice algorithm for high-throughput high-rate decoding of convolutional and Turbo codes. This work was published in IEEE WCNC 2020 [106].

1.5 Study of non-binary codes and non-binary coded modulations

1.5.1 Context and prior art

1.5.1.1 Non-binary LDPC codes and coded modulation

Non-Binary (NB) FEC codes represent strong candidates for next generation communication standards. First, coded modulation capacity is always greater than or equal to BICM capacity [7]. This gain can be up to 1.0 dB in AWGN channels. Second, NB codes have been shown to perform better than binary codes for small block lengths [107, 108]. The transmission of short frames is of high importance for URLLC scenarios [109] in the upcoming standards.

On another note, Probabilistic Amplitude Shaping (PAS) [110] was recently proposed to close the shaping gap between constrained capacity and unconstrained capacity, by adjusting the channel input distribution. BICM schemes based on binary FEC codes and using PAS were then able to approach the unconstrained channel capacity limits. Further performance improvements of PAS with NB FEC codes were reported in [111, 112] where coding gains between 0.35 dB and 0.63 dB were reported for short block sizes, compared to binary FEC codes designed with the same PAS settings.

NB-LDPC codes were one of the first NB code families that were considered lately. Indeed, for moderate or small lengths, error performance can be improved by extending LDPC codes to high-order Galois Fields GF(q), $q > 2$ [113]. These NB-LDPC codes retain the benefits of steep waterfall region and low error floor. Compared to their binary counterparts, NB-LDPC codes generally present higher girths, which leads to better decoding performance. Different works have also revealed the interest of NB-LDPC in MIMO systems ([114, 115, 116]). Another advantage of NB-LDPC codes concerns their association with high-order q-ary modulations: by encoding directly over the q-ary constellation alphabet, binary-to-NB mapping and demapping operations are not needed, unlike for binary codes. In other words, NB symbol likelihoods are calculated directly and input to the NB decoder, without any marginalization [117]. Note that the demapping operation is costly in terms of complexity and introduces performance loss that would have to be partially countered by a proper choice of mapping or fully recovered by costly iterations over the demapper and decoder. For these reasons, NB-LDPC codes constitute a promising solution for high spectral efficiency coding, even if they present the drawback of high decoding complexity [118].

Classically, the design of NB codes relies on the maximization of the Hamming distance of the binary image of the code. However, when associated with high-order constellations, the maximization of the cumulated Euclidean distance represents a more accurate design criteria. Therefore, we have focused our studies in this direction.

1.5.1.2 Non-binary LDPC codes and MIMO

Moreover, similar advantages to their association with high order constellations can be obtained when NB codes are associated with MIMO schemes. A detection based on the belief propagation (BP) algorithm provides error rate performance comparable to ML detection while allowing a greater flexibility in coded system design. It becomes particularly appealing when the MIMO scheme is concatenated with an outer LDPC code. In order to improve performance, extrinsic information can be exchanged between the MIMO detector and the FEC decoder, i.e., the so-called "Turbo framework". In this context, the exchanged information between the FEC decoder and the MIMO STBC decoder is only provided after the end of the local decoding process of each of these blocks over the whole frame. The resulting latency of such a schedule can be prohibitively high outweighting the increase in throughput provided by the introduction of MIMO. We have investigated these schemes in order to address their main issues.

1.5.1.3 Non-binary convolutional and Turbo codes

The first attempt to approach coded modulation capacity dates back to the Turbo trellis-coded modulation schemes [119], based on Ungerboeck's trellis-coded modulations. More recently, several studies have targeted the design of NB Turbo codes (NB-TC). In [107], a NB-TC structure was derived from a protograph subensemble of a NB-LDPC code. In [120], NB-TCs over GF(q) were designed based on their EXIT charts and an estimate of their truncated union bounds. Both studies report significant gains in the short-to-moderate block size regime compared to state-of-the-art binary FEC codes. However, these studies do not provide a complete framework for the design of NB-TC. Indeed, a clear design criteria and choice of the component codes was still missing in literature. Interleaver and puncturing design criteria were also missing. Therefore, efforts have been made to provide answers to these lackings.

1.5.2 Performed work and contributions

1.5.2.1 Design of non-binary LDPC codes

In a first effort, we proposed to design NB-LDPC coded modulations by using a new criterion for devising the parity-check matrix. This criterion does not consider the Hamming distance of the binary image of the code as in [121, 122], but the Euclidean distance of the modulated codewords. To the best of our knowledge, this problem has never been considered in the literature for NB-LDPC codes. Our approach assumes that the positions of nonzero entries in the parity-check matrix have already been defined and we focused on the determination of the values of non-zero entries when the NB-LDPC code over GF(q) is directly associated to a q-ary QAM. We considered high-order NB-LDPC coded modulations where the order of the Galois Field and modulation order coincide. We based the NB-LDPC parity-check matrix optimisation on the analysis of a single parity-check node for a given modulation mapping. To show the good agreement between the theoretical analysis and the simulation results, we calculated and compared the union bound with the ML decoding curves. Finally, we presented simulation results to show how the NB-LDPC coded modulation designed with the proposed method outperforms the state of the art [123].

1.5.2.2 SSD and non-binary LDPC codes: Study of an association

The extension of the work performed on SSD and rotated constellations was also performed for NB-LDPC codes. In this work, we considered the SSD technique applied to coded modulation schemes with the novelty of selecting the rotation angle from the analysis of the mutual information variations. It is known that coded modulation outperforms bit-interleaved coded modulation, but we showed that coded modulation has also an extra advantage: the optimal rotation angle is only marginally impacted by the signal-to-noise ratio and the erasure rate of the fast Rayleigh fading channel. This opens the door to a robust coded modulation scheme particularly suited for broadcasting applications. Simulation results confirm the theoretical study with a gain of up to 1.2 dB when comparing to the DVB-T2 standard [124].

1.5.2.3 Non-binary LDPC codes and MIMO: Proposal of a joint framework

We have elaborated a new framework for a Joint Factor Graph (JFG) including the MIMO detector and an LDPC code. The case of a NB-LDPC code (see Fig. 1.7) was addressed in the work done by Jianxiao Yang during his post-doctoral fellowship and the case of a binary LDPC code by Ali Haroun during his PhD thesis. First, we proposed to apply a joint channel decoding and MIMO detection based on the BP shuffled algorithm over the JFG. A modified EXIT chart-based analysis introducing decoding trajectories has been used to assess decoding efficiency in terms of receiver iterations. Results show that the proposed algorithm offers a decoding schedule superior to the Turbo schedule in both performance and complexity. Moreover, the shuffle scheduling has shown high tolerance for simplified detection while being particularly appealing for a hardware implementation [125].

The extension of the work to different number of antennas while focusing on the reduction of receiver complexity and improving performance was performed in the context of the PhD thesis of Ali Haroun. Applying the proposed low-complexity BP-based detection greatly reduces the number of operations per iteration with a negligible performance penalty [126, 127]. In addition, EXIT chart analysis was used to reveal the best parameters for the low complexity detector and the best profile of iterations for the receiver [116, 128, 129]. Results show a division by a factor of ten of the number of operations in the detector for each inter-iteration between the detector and the decoder when compared to full-complexity BP [130, 131, 128]. This profile-based message passing proves to be efficient in terms of perfor-

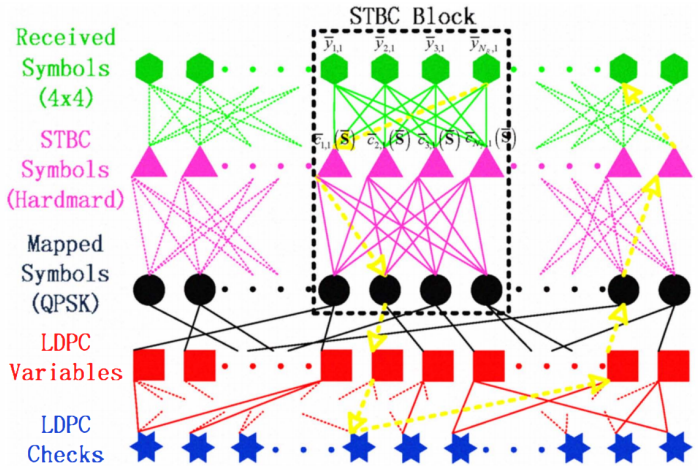

Figure 1.7: The joint Factor Graph representation of the detector and the decoder (example given for $NT = NR = 4$, $D = 1$, Hadamard STBC).

mance, complexity and latency. The paper entitled "Low-Complexity Soft Detection of QAM Demapper for a MIMO System" dedicated to the low complexity demapper was published in IEEE Communications letters and is included hereafter [132].

To sum up the work on the subject done in the context of Ali Haroun's PhD thesis, a geometric approach is applied on the BP algorithm similarly as a sphere decoding. The proposed approach is based on the principle of the conditioned detection to limit the search space of the number of candidate symbols. This makes it possible to avoid the decomposition of the channel matrix as in a sphere decoding [133], [134]. Indeed, the second difference compared to the sphere decoding is that the radius of the considered signal space sub-region is not only related to the SNR but also to the reliability of the detected symbol. Thus, for a particular SNR value, different sizes of sub-regions are obtained depending on the reliability of the detected symbol. This may improve the performance while reducing the computational complexity. In other words, one of the aims of this work was to propose algorithmic solutions to reduce the computational complexity of Euclidean distance computation during MIMO processing.

To do this, a dynamic approach was introduced to calculate the candidate symbols in a sub-region that surrounds the received symbol. In a first phase, this method is based on the identification of the point closest to the received symbol which makes it possible to avoid the computation of all Euclidean distances of candidate symbols. In a second phase, a recursive computation is proposed to provide a limited number of Euclidean distances corresponding to the points that surround the identified closest point or ML decision. Consequently, the resulting algorithm offers an appealing trade-off between performance and computational complexity.

This favorable tradeoff motivated the following work targeting the proposal of hardware architectural solutions for the constituent modules of the iterative receiver. The first part corresponds to the MIMO detector followed by the one of the NB-LDPC code. The MIMO detector applies the novel dynamic signal space sub-region-based simplified algorithm. An architectural representation, a timing organisation and the total number of required arithmetic computation and memory usage resources were provided for each elementary component. Moreover, a hardware architecture for the NB-LDPC decoder was devised, largely inspired from the work in [135, 136]. Finally, a study of a scheduling for the extrinsic information exchange between the detector and the decoder was performed. The corresponding results led to the definition of the global iterative receiver architecture applying an efficient ex-

change of information while supporting different levels of parallelism that favour targeting high throughputs and low latency applications.

732 IEEE COMMUNICATIONS LETTERS, VOL. 20, NO. 4, APRIL 2016

Low-Complexity Soft Detection of QAM Demapper for a MIMO System

Ali Haroun, Charbel Abdel Nour, *Member, IEEE*, Matthieu Arzel, and Christophe Jego, *Member, IEEE*

***Abstract*—MIMO systems exploit multipath propagation to improve throughput and performance of digital communication systems. However, at the receiver side, the computation of Euclidean distances requires prohibitive computational complexity particularly when combined with a high-order constellation. Conventionally, it is necessary to calculate all the Euclidean distances to find the maximum likelihood solution. In this letter, we propose a novel approach based on the principle of conditioned detection combined with lattice-reduction techniques to estimate the closest point to the received symbol without the computation of all the Euclidean distances. Thanks to this approach, a reduction up to 95% of the required number of multiplications is achieved without any degradation in terms of performance by comparison with a conventional BP technique.**

***Index Terms*—MIMO systems, BP algorithm, soft detection.**

I. INTRODUCTION

MULTIPLE-input multiple-output (MIMO) systems have become an essential element of wireless communication standards including IEEE 802.11n (Wi-Fi), IEEE 802.16 (WiMAX), and Long Term Evolution (LTE). This technique stands as an efficient way to increase data rates and reliability through the exploitation of spatial diversity and full rate schemes such as Spatial Multiplexing (SM) and some Space Time Block Codes (STBC) [1]. Despite the existence of several benefits to the application of an iterative MIMO processing at the receiver side, the computational complexity and the latency of this approach still represent a challenging task. In the literature, some proposals tried to solve these drawbacks. For example, the Minimum Mean Square Error (MMSE) detectors [2] require relatively low complexity at the price of a degraded performance. In parallel, studies on MIMO detections have mainly focused on the so-called Sphere Decoding (SD) [3]. These studies were dedicated to the application of SD detector to MIMO systems, by exploiting the incursion order in the search tree and sphere radius update [4]. Since the full tree search has a prohibitive computational complexity, a reduced search algorithm is applied by limiting the search space of the candidate symbols at each tree search stage [4]. However, to compute soft decisions required for channel decoding, an important reduction of the search space cannot be applied in order to conserve an acceptable level of performance when soft output information is provided [4]. In addition, a sphere decoder is not easy to implement due to the tree search step. It has a variable complexity, depending on the noise level and channel conditions, that hinders its integration into a digital communication system.

Meanwhile, another type of MIMO detection is based on Belief Propagation (BP) principle [5]. The BP algorithm has also been extensively studied for the decoding of channel codes with a sparse parity matrix, such as Low Density Parity Check (LDPC) codes [6]. Further studies on MIMO detector based on the BP algorithm have been proposed in [6]–[7]. In recent works [8]–[10], a BP-based layered detection and decoding for NB-LDPC Coded MIMO system is investigated such that the receiver works on a large Joint Factor Graph (JFG) [10]. This joint detection and decoding algorithm involves a shuffle schedule to reduce the processing latency and also introduces a greater flexibility. This flexibility should facilitate the soft information exchange between the decoder and the detector in contrast to a turbo scheduling.

In this letter, we propose an algorithmic solution that reduces the computational complexity of Euclidean distance estimation. This approach avoids computing all the Euclidean distances of the different candidate symbols in order to identify the ML solution. Indeed, once the ML solution is found, we restrict the computation of distances to the constellation points closest to this solution. We show that the resulting algorithm offers a very good trade-off between performance and computational complexity. This letter is organized as follows. Section II introduces the MIMO system and some definitions. Section III explains the proposed simplified detection of the point closest to the received observation. In section IV, a complexity analysis and simulation results are discussed.

II. SYSTEM MODEL AND DEFINITIONS

We consider a MIMO system with $N_t = 2$ transmit antennas, $N_r = 2$ receive antennas operating over a flat Rayleigh fading channel. The source information is encoded by a Non-Binary Low-Density Parity-Check (NB-LDPC) code which is conveniently combined with high-order modulation and multiple antenna schemes to process high data rate transmissions [11]. Indeed, $log(2^q)$ bits are mapped to a complex symbol of a Quadrature Amplitude Modulation (QAM) constellation. Thus, these symbols are Spatially Multiplexed onto a multiple antenna system and then transmitted over a MIMO channel. The channel input-output relation is given by:

$$y = Hx + n \tag{1}$$

where $x_{[N_t \times 1]}$ and $y_{[N_r \times 1]}$ are the transmitted and the received symbol vectors, respectively. The MIMO channel is defined by the matrix $H_{[N_r \times N_t]}$ whose entries are assumed to be independent and identically distributed Rayleigh faded with unit mean. n is a vector of complex Additive White Gaussian Noise (AWGN) with i.i.d entries and dimension N_r. At the receiver side, a MIMO detection based on the BP algorithm (BP-MIMO) computes soft information for all symbols. In order to improve

Manuscript received October 15, 2015; revised January 24, 2016; accepted January 28, 2016. Date of publication February 3, 2016; date of current version April 7, 2016. The associate editor coordinating the review of this paper and approving it for publication was M. Wigger.

A. Haroun and C. Jego are with Bordeaux INP, CNRS IMS, UMR 5218, Talence 33405, France, and also with the Université de Bordeaux, Talence, France (e-mail: firstname.lastname@ims-bordeaux.fr).

C. A. Nour and M. Arzel are with the Institut Mines-Télécom/Télécom Bretagne, CNRS Lab-STICC, UMR 3192, Brest 29238, France, and also with the Université Européenne de Bretagne, Brest, France (e-mail: firstname.lastname@telecom-bretagne.eu).

Digital Object Identifier 10.1109/LCOMM.2016.2525722

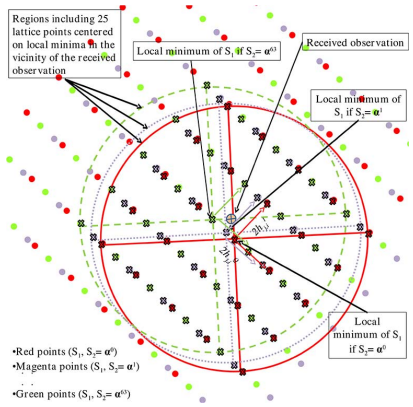

Fig. 1. Illustration of the proposed detection in the case of 64-QAM.

performance, extrinsic information can be exchanged between the NB-LDPC decoder and the BP-MIMO detector thanks to an iterative process [8]. In this letter, a regular NB-LDPC code defined over a Galois Field $GF(64)$ associated with a 64-QAM constellation has been considered. A frame size of $N = 384$ symbols was chosen. The regular NB-LDPC code with code rate $R = 1/2$ has variable and check node degrees $d_v = 2$ and $d_c = 4$, respectively. More information about this Forward Error Correction (FEC) code can be found in [12].

III. Simplified Detection of the Closest Point to the Received Observation

The main objective of this work is to reduce the complexity of Euclidean distance computation in the soft MIMO detector. We will first start by describing the required steps for such a detection. Then, we will detail each of these steps. In our 2×2 MIMO system where two symbols S_1 and S_2 have to be detected, we propose an original approach that starts by performing the detection of the first transmitted symbol S_1 (resp. S_2) conditioned by the assumption of the knowledge of the second symbol S_2 (resp. S_1). In other words, we replace the value of S_2 symbol (resp. S_1) in the expression of the Euclidean distance by a chosen value from the 64 possible values of the constellation symbols. In the following, we detect the S_1 symbol closest to the received observation that we call conditioned local minimum. Then, this detection applies a technique inspired by lattice reduction [13] to find the closest symbol value (for S_1 conditioned by the value of S_2) to the received observation by avoiding the computation and the comparison of Euclidean distances. This process is repeated in order to span all the possible values of S_2. The zoomed window of the set ensemble created by the 64 candidate solutions (one for each value of S_2) represented by the values of (S_1, S_2) couples is shown by cross points in Fig. 1. Denoted by local minima, they represent the set of points closest to the observation for each value of symbol S_2. The ML solution is the particular couple of the 64 candidates that minimizes the Euclidean distance.

In order to efficiently provide soft output information, the detector has to generate symbol Log Likelihood Ratio (LLRs) for a larger number of (S_1, S_2) combinations. Based on ML detection, these combinations that represent lattice points should be chosen within from the close vicinity of the received observation. To achieve this task at the lowest cost, we propose to span an additional region in signal space around each local minimum. Actually, the computation of Euclidean distances between the received observation and the lattice points in each of these regions can be recursively computed by the addition of a constant term to the Euclidean distance of the local minimum in this region. Indeed, by observing Fig. 1, starting from one local minimum (with a cross point) we can deduce all the possible lattice points conditioned by the value of S_2 in the vicinity of the received observation (points represented by a particular color in Fig. 1) by a shift operation of a constant term [14] . Repeating the process for all local minima results into considering all possible lattice points in a particular region closest to the received observation, similarly to a sphere decoder.

1-) First step: In-phase and Quadrature estimations

In the considered case ($N_t = N_r = 2$) , the symbol received by the first antenna can be expressed as:

$$\begin{aligned} y_1^I &= h_{1,1}^I.S_1^I - h_{1,1}^Q.S_1^Q + h_{1,2}^I.S_2^I - h_{1,2}^Q.S_2^Q + n_1^I \\ y_1^Q &= h_{1,1}^Q.S_1^I + h_{1,1}^I.S_1^Q + h_{1,2}^Q.S_2^I + h_{1,2}^I.S_2^Q + n_1^Q \end{aligned} \quad (2)$$

where $n_1 = n_1^I + jn_1^Q$ is a vector of AWGN. $h_{j,i}^I$ (resp. $h_{j,i}^Q$) represents the coefficient of the non-frequency-selective channel with Rayleigh fading of the i^{th} transmitting antenna to the j^{th} receiving antenna on the in-phase I (resp. quadrature Q) axis of the constellation with $j = 1, ..N_r$ and $i = 1, ..N_t$. S_1 and S_2 are two symbol candidates of a 64-QAM constellation. Their values have to be detected for each received MIMO symbol. From equation (2), the Euclidean distance between the received observation and a possible value of the two candidate symbols can be expressed as:

$$\mathrm{D}_{\mathrm{E(S1,S2)}} = \frac{\left|D_E^I\right|^2 + \left|D_E^Q\right|^2}{{\sigma_w}^2} \text{ such as}$$

$$\begin{aligned} D_E^I &= \overbrace{\left(y_1^I\right)}^{A} - \overbrace{\left(h_{1,1}^I.S_1^I - h_{1,1}^Q.S_1^Q + h_{1,2}^I.S_2^I - h_{1,2}^Q.S_2^Q\right)}^{B} \\ D_E^Q &= \overbrace{\left(y_1^Q\right)}^{A'} - \overbrace{\left(h_{1,1}^Q.S_1^I + h_{1,1}^I.S_1^Q + h_{1,2}^Q.S_2^I + h_{1,2}^I.S_2^Q\right)}^{B'} \end{aligned} \quad (3)$$

where ${\sigma_w}^2$ denotes the variance of the AWGN. From this equation, the difference between terms A and B (resp. A' and B') has to be minimized to detect the point closest to the received observation. By applying conditioned detection on symbol S_2, its value is fixed to α^k where the latter is composed of two components I and Q $\in$ 64-QAM constellation, $k = 0, 1, .., 63$. Then, we detect the real part S_1^I of symbol S_1 conditioned by the S_2 value $[S_1^I | S_2 = \alpha^k]$ thanks to the following equations:

$$\min_{\substack{S_1 \in 64QAM \\ S_2 = \alpha^k}} \left\{ h_{1,1}^I.S_1^I - \left(y_1^I + h_{1,1}^Q.S_1^Q - h_{1,2}^I.S_2^I + h_{1,2}^Q.S_2^Q \right) \right\} \quad (4a)$$

$$\min_{\substack{S_1 \in 64QAM \\ S_2 = \alpha^k}} \left\{ h_{1,1}^Q.S_1^I - \left(y_1^Q - h_{1,1}^I.S_1^Q - h_{1,2}^Q.S_2^I - h_{1,2}^I.S_2^Q \right) \right\} \quad (4b)$$

Then, an approximation between the two terms is applied. Actually, equations 4a and 4b are multiplied by the channel coefficients $h_{1,1}^I$ and $h_{1,1}^Q$, respectively. The results are added such as:

$$S_1^I \approx \overbrace{h_{1,1}^{I\,\prime}.y_1^I + h_{1,1}^{Q\,\prime}.y_1^Q}^{C} - \overbrace{\left(h_{1,1}^{I\,\prime}.h_{1,2}^I + h_{1,1}^{Q\,\prime}.h_{1,2}^Q\right)}^{D}.S_2^I + \overbrace{\left(h_{1,1}^{I\,\prime}.h_{1,2}^Q - h_{1,1}^{Q\,\prime}.h_{1,2}^I\right)}^{E}.S_2^Q \quad (5)$$

with $h_{1,1}^{I\,\prime} = \frac{h_{1,1}^I}{h_{1,1}^{I\,2} + h_{1,1}^{Q\,2}}$, $h_{1,1}^{Q\,\prime} = \frac{h_{1,1}^Q}{h_{1,1}^{I\,2} + h_{1,1}^{Q\,2}}$.

This expression for S_1^I is computed for each of the 64 possible values of symbol S_2. The calculation of the terms C, D and E requires 6 Real Multiplications (RMs) and 5 Real Additions (RAs) per received MIMO symbol. Furthermore, the calculations of the terms $D \times S_2^I$ and $E \times S_2^Q$ require 16 RMs since S_2^I and S_2^Q are in the interval $\{-7.0, -5.0, .., +5.0, +7.0\} \in$ 64-QAM constellation. In total, this step requires 22 RMs and 67 RAs to detect S_1^I symbols when S_2 spans all possible values $\{S_2 = \alpha^0, \alpha^1, .., \alpha^{63}\}$. Finally, comparison operations required in order to find the minimum can be avoided by applying a transformation to S_1^I values to positive integer domain P_1^I defined by:

$$P_1^I = \left\{ \frac{\sigma_s \times S_1^I + \sqrt{M} - 1}{2} \right\} | P = 0, 1, .., \sqrt{M} - 1 \quad (6)$$

where σ_s is a normalization factor equal to $\sqrt{42}$ and M is equal to 64 when the constellation is a 64-QAM. Indeed, rounding the value of P_1^I to the closest integer is equivalent to finding the value of S_1^I that minimizes equation (5) due to the equivalence between the particular integer value and the real I value of a 64-QAM constellation.

Similarly to the computation of the in-phase component, the quadrature component S_1^Q can be approximated by:

$$S_1^Q \approx \overbrace{h_{1,1}^{I\,\prime}.y_1^Q - h_{1,1}^{Q\,\prime}.y_1^I}^{F} + \overbrace{\left(h_{1,1}^{Q\,\prime}.h_{1,2}^I - h_{1,1}^{I\,\prime}.h_{1,2}^Q\right)}^{G}.S_2^I - \overbrace{\left(h_{1,1}^{Q\,\prime}.h_{1,2}^Q + h_{1,1}^{I\,\prime}.h_{1,2}^I\right)}^{H}.S_2^Q \quad (7)$$

This step requires 22 RMs and 67 RAs to estimate the S_1^Q symbols when S_2 spans all possible values $\{S_2 = \alpha^0, \alpha^1, .., \alpha^{63}\}$. Then, the same type of transformation to integer domain followed by a rounding operation to P_1^Q can be performed to find the quadrature part S_1^Q of the local minimum. In total, 44 RMs and 134 RAs are necessary to detect the 64 values of S_1^I and S_1^Q parts of the symbols S_1 such as $\{S_2 = \alpha^0, \alpha^1, .., \alpha^{63}\}$. Afterwards, the Euclidean distances of detected symbols can be calculated.

2-) Second step: computation of the Euclidean distance between received observation and local minima when $S_2 = \alpha^k$

Note that, only 8 values are possible for S_1^I and S_1^Q $\{S_i^I, S_i^Q \in -7.0, -5.0, ... + 5.0, + 7.0\}$. Therefore, computations of the multiplications of $h_{j,i}$ by S_i^I and S_i^Q requires 32 RMs to cover all possible values of the detected symbols S_1 if $\{S_2 = \alpha^0, \alpha^1, .., \alpha^{63}\}$. Furthermore, 9 RAs and 2 additional RMs are required to obtain the square of the two terms D_E^I and D_E^Q.

TABLE I
OPERATION COMPLEXITY COMPARISON BETWEEN DETECTION ALGORITHMS

$D_{E(S_1,S_2)}$	Real Mutl.	Real Add.
Proposed method based on BP {64 × 25}	[204+(64 × 25)] = 1804	[710+(64 × 25)] = 2310
Conventional SD [13]	≈ 3000	——
Conventional method based on BP {64 × 64} [10]	[10 × 64 × 64] = 40960	[9 × 64 × 64] = 36864
Recursive method based on BP {64 × 25} [14]	[(10 + 25) × 64)] = 2240	[(14 + 25) × 64)] = 2496

Overall, this second step requires {(9 RAs + 2 RMs) × 64 + 32 RMs}. Thenafter, a vector of Euclidean distances from D_{E0} to D_{E63} is obtained. This vector represents all the Euclidean distances of local minima or equivalently the symbols S_1 closest to the received symbol for each value $\{S_2 = \alpha^0, \alpha^1, .., \alpha^{63}\}$.

3-) Third step: recursive computation of the Euclidean distances for lattice points in close vicinity of the local minimum

Starting from each one of the 64 local minima, we propose to limit the computation of Euclidean distances to a region in signal space containing only 24 other points. This choice is based on EXtrinsic Information Transfer chart analysis of the resulting SISO detector confirmed by Bit Error Rate Monte Carlo simulations as described in [14]. Indeed, this choice provides an excellent compromise in terms of performance/complexity since almost no performance degradation is observed especially in an iterative receiver context. Moreover, under conditioned detection (a chosen value of symbol S_2) and based on equation (3), the difference between two Euclidean distances of two adjacent points of the lattice located on the same axis I (resp. Q) is equal to $2 \times h_{j,i}^I$ (resp. $2 \times h_{j,i}^Q$) as illustrated in Fig. 1. Therefore, it is possible to find by a recursive computation all the 24 remaining Euclidean distances in each region surrounding a local minimum from the Euclidean distance between the received observation and this local minimum. Circles in Fig. 1 delimit considered regions that include 25 lattice points. One color is attributed to the circle and the points for each conditioned S_2 value and equivalently for each local minimum value. Consequently, equation (3) is only applied to calculate the Euclidean distance of the local minimum as performed in step 2. Then, the 24 Euclidean distances around this local minimum are recursively deduced. This proposal greatly simplifies the computational complexity of this step. Indeed, only one addition and one multiplication are required for the square of one of the two terms D_E^I or D_E^Q.

IV. COMPLEXITY ANALYSIS AND SIMULATION RESULTS

The computational complexities of the 3 steps detailed in the previous section are summarized in Table I. The proposal is first compared with a 2 × 2 sphere decoding [13]. Then, it is compared with the conventional method based on BP as explained in [10]. Moreover, a simplified version called recursive method based on BP [14] is also considered in Table I. Considering conventional SD given in [13], the required number of real multiplications is approximately 3000. This value is obtained for SNR values between 14 and 16 dB. It represents the convergence threshold of our proposed algorithm. It appears that a reduction by a factor of 1.6 of the number of multiplications is obtained by applying the proposed method when compared

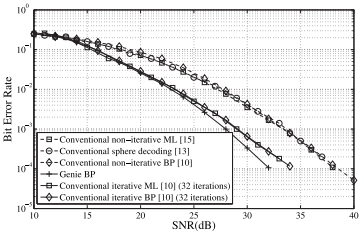

Fig. 2. BER Performance of detection algorithms for 2x2 MIMO system.

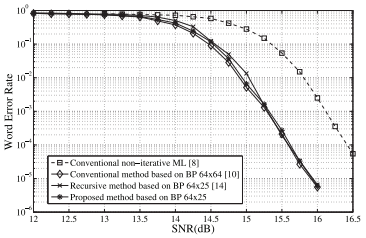

Fig. 3. WER performance of detection algorithms for 2x2 MIMO system with 32 iterations between the detector and the decoder.

to the conventional sphere decoding [13]. However, in comparison with the conventional method based on BP, the proposal achieves a reduction by 22 in the number of multiplications and a reduction by 16 in the number of additions. Finally, it also needs a lower number of multiplications and additions than the previous recursive methods.

The performance of uncoded MIMO systems for several detection algorithms is discussed. The performance is measured in terms of Bit Error Rate (BER) over a flat fading Rayleigh channel. In Fig. 2, the performance of the conventional BP detection [10] is compared with a conventional ML detection [15].

Comparisons with a conventional sphere decoding [13] are also given. For a non-iterative process, the conventional BP algorithm achieves the same performance as a conventional sphere decoding and a conventional ML detection. In order to evaluate the impact of the iterations during the detection process, an iterative ML detection and a genie BP algorithm are taken as references. Note that the genie curve is obtained by providing error-free *a priori* information at the input of the detector. The corresponding performance represents a lower bound on the best possible performance in a SISO context by applying an iterative process. In this case, 32 iterations within the detectors are applied. Comparisons are done for BER values between 10^{-3} and 10^{-4}. A conventional iterative BP detection achieves the same performance as the iterative ML algorithm [10]. A gain of more than 4 dB is observed by comparison with conventional sphere decoding. In addition, the performance of the conventional BP algorithm is closest to the genie bound.

Moreover, the performance of the proposal for an iterative reception 2×2 MIMO system with 32 iterations between the NB-LDPC decoder and the BP-MIMO detector is given in Fig. 3 where the performance is measured in terms of Word Error Rate (WER) over a flat fading Rayleigh channel. We observe that the proposal has almost the same performance as previous BP-based detection with a lower computational complexity. Moreover, a gain of 0.85 dB is observed by comparison with the non-iterative conventional ML [8].

V. CONCLUSION

In this letter, an geometric approach based on the principle of the conditioned detection to find the closest point to the received symbol without computing all the Euclidean distances of candidate symbols is proposed. Euclidean distances are computed by applying a method that reduces their number of Euclidean distances on one side and the complexity of the computation itself on the other side. A reduction of 95% of the number of multiplications that are required to estimate the Euclidean distances is achieved without any degradation in terms of performance when compared to the conventional BP detection. Moreover, the proposed technique needs a smaller number of real multiplications when compared to other algorithms and especially to a sphere decoding [13]. These results are achieved with a gain in terms of WER performance if an iterative process is applied to the receiver.

REFERENCES

[1] E. Telatar, "Capacity of multi-antenna Gaussian channels," *Eur. Trans. Telecommun.*, vol. 10, pp. 585–595, 1999.
[2] D. Wübben, R. Böhnke, V. Kühn, and K. Kammeyer, "MMSE extension of V-BLAST based on sorted QR decomposition," in *Proc. IEEE Veh. Technol. Conf. (VTC)*, 2003, pp. 508–512.
[3] A. Burg *et al.*, "VLSI implementation of MIMO detection using the sphere decoding algorithm," *IEEE J. Solid-State Circuits*, vol. 40, no. 7, pp. 1566–1577, Jul. 2005.
[4] S. Wang *et al.*, "A radius choice algorithm for MIMO sphere decoding based on the noise statistics," *J. Comput. Inf. Syst.*, vol. 52, pp. 2401–2408, 2012.
[5] M. Kaynak, T. Duman, and E. Kurtas, "Belief propagation over MIMO frequency selective fading channels," in *Proc. IEEE Int. Conf. Netw. Serv.*, 2005, vol. 34, pp. 564–570.
[6] F. R. Kschischang *et al.*, "Factor graphs and the sum-product algorithm," *IEEE Trans. Inf. Theory*, vol. 47, no. 2, pp. 498–519, Feb. 2001.
[7] X. Yang, Y. Xiong, and F. Wang, "An adaptive MIMO system based on unified belief propagation detection," in *Proc. IEEE Int. Conf. Commun. (ICC)*, 2007, pp. 209–213.
[8] A. Haroun, C. Abdel Nour, M. Arzel, and C. Jégo, "Symbol-based BP detection for MIMO systems associated with non-binary LDPC codes," in *Proc. IEEE Wireless Commun. Netw. Conf. (WCNC)*, 2014, pp. 212–217.
[9] A. Haroun, C. Abdel Nour, M. Arzel, and C. Jégo, "An efficient MIMO receiver based on BP algorithm with truncated message-passing," in *9ème Colloque GDR SoC-SiP*. du CNRS, Paris, France, Jun. 2014, pp. 1–12.
[10] A. Haroun, C. Abdel Nour, M. Arzel, and C. Jégo, "Low-complexity layered BP-based detection and decoding for a NB-LDPC coded MIMO system," in *Proc. IEEE Int. Conf. Commun. (ICC)*, 2014, pp. 5107–5112.
[11] L. Hanzo, T. H. Liew, B. L. Yeap, and S. X. Ng, *Turbo Coding, Turbo Equalisation and Space-Time Coding for Transmission Over Fading Channels*. Hoboken, NJ, USA: Wiley/IEEE Press, 2002, vol. 9, pp. 317–390.
[12] A. Voicila, D. Declercq, F. Verdier, M. Fossorier, and P. Urard, "Low complexity decoding algorithm for non-binary LDPC codes in high order fields," *IEEE Trans. Commun.*, vol. 58, no. 5, pp. 1365–1375, May 2010.
[13] L. Azzam and E. Ayanoglu, "Reduced complexity sphere decoding via a reordered lattice representation," *IEEE Trans. Commun.*, vol. 57, no. 9, pp. 2564–2569, Sep. 2009.
[14] A. Haroun, C. Abdel Nour, M. Arzel, and C. Jégo, "Low-complexity LDPC-coded iterative MIMO receiver based on belief propagation algorithm for detection," in *Proc. IEEE Int. Symp. Turbo Codes Iterative Inf. Process. (ISTC)*, 2014, pp. 213–217, 2014.
[15] S. Sezginer and H. Sari, "A high-rate full-diversity 2×2 space-time code with simple maximum likelihood decoding," in *Proc. IEEE Int. Symp. Signal Process. Inf. Technol.*, 2007, pp. 1132–1136.

1.5.2.4 Design and proposal of non-binary convolutional and Turbo codes

The final part of the work performed in this context addresses the lackings for the design of efficient NB-TCs. This work was carried out in the context of Rami Klaimi's PhD thesis and the H2020 EPIC project. The aim of this thesis was to start to provide the framework and tools for the design of NB-TCs. To this end, we addressed each of the building blocks one by one.

First, a design of low-complexity Non-Binary Convolutional Codes (NB-CCs) was proposed based on a new encoding template using an updated structure of an accumulator. This structure improves the minimum Euclidean distance by at least 25% when compared to the accumulator structure used in literature as shown in Fig. 1.8.

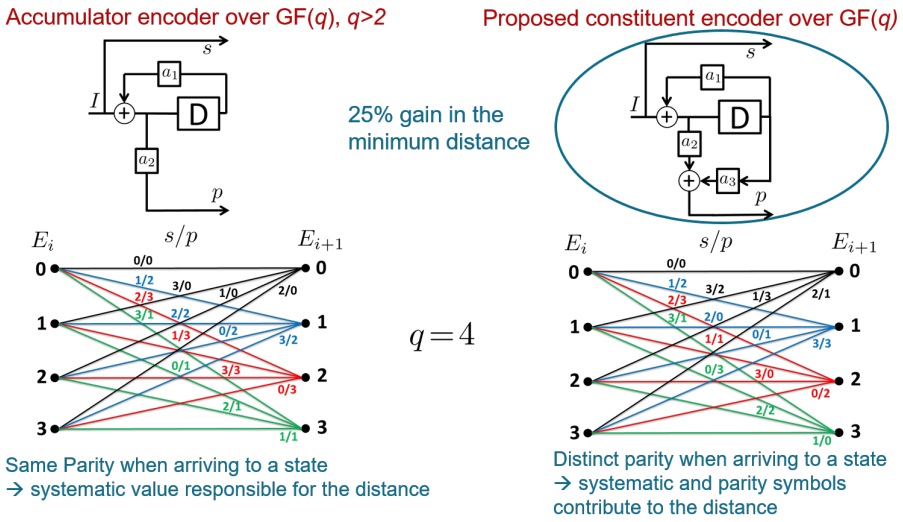

Figure 1.8: Comparison between the two template structures of a classical accumulator and the proposed one. The corresponding trellises are represented for q=4.

Next, a method to calculate the distance spectrum of the NB-CCs was proposed: sequences creating low cumulated Euclidean distances were identified, and a simple algorithm was presented that enumerates the lowest two Euclidean distances with their corresponding multiplicities. Then, we discussed the impact of the constellation mapping on the distance spectrum of the code. After having presented the error correction performance of several examples of NB-CCs designed over GF(4), GF(16) and GF(64), two additional techniques were proposed in order to enhance the performance of these codes when mapped to modulations of lower order than the Galois field of the code. Obtained codes outperfom all existing binary and NB-CC in literature with the same amount of states as shown in Fig. 1.9 and published in [137].

The subsequent work began by studying the effect of different interleaving techniques on NB-TCs and a method was proposed, that targeted the mitigation of the correlation problems in the short correlation cycles when short frame sizes are considered. Resulting ARP-based interleavers can achieve extremely low error rates without any change in the slope of the curves as shown in [138]. Next, two puncturing techniques were introduced: symbol-based and bit-based puncturing. It was shown that under particular design constraints, bit puncturing can largely outperform symbol-based one. A patent was filed on this technique in March 2020. The next part of this work was dedicated to the practical computation of the union bounds for NB-TCs. A method was derived to estimate a truncated cumulated Euclidean distance spectrum of NB-TCs by identifying the structure of competing sequences in the code trellis with low cumulated Euclidean distances. Indeed, the truncated Euclidean distance of

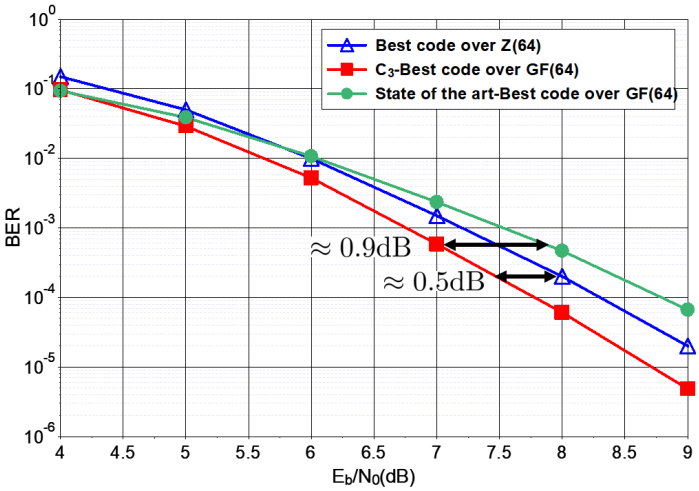

Figure 1.9: Performance comparison between the best state-of-the-art codeover Z(64), the best code over GF(64) and the proposed code – named C3 – over GF(64) from the application of the new design procedure. 64-QAM constellation, $R = 1/2$ over an AWGN channel.

the particular association of a NB-TC with a high order constellation was missing from the literature. The detailed description of the method and the derivation of the truncated union bound is provided in [139].

The insertion of a symbol transformation before one of the NB component encoders was also investigated. The design criterion to define the transformation connections was identified, and we derived an algorithm to define good transformation connections when a q-QAM constellation is used with NB-TCs over GF(q) as well as when a 4-QAM constellation is considered. Next, different application examples were investigated to assess the performance of the resulting NB-TCs, and comparisons were conducted with state-of-the-art binary and NB codes. The insertion of this symbol transformation has proven to considerably lower error floors by increasing the coding gain by avoiding the repetition of error-prone competing sequences at both decoders. Indeed, 10^{-10} of BLER can be achieved without any change in the slope of the curves as seen in Fig. 1.10. This work was subject to patent filing in 2018 [140].

The final part of the work studied a new low-complexity decoding algorithm for the proposed NB-TCs. A simplified algorithm to decode NB-TCs was proposed, which lowers the storage requirements as well as the computational complexity. In particular, the number of performed Add-Compare-Select (ACS) operations was reduced using a technique inspired from the bubble check sorter previously proposed for NB-LDPC codes. Different application examples were presented and our proposal was shown to offer high complexity reduction, at the price of a limited performance penalty still keeping most of the superior performance of the NB-TCs. Indeed, a division by a factor of 7 in number of ACS units can be achieved at the cost of a 0.15 dB in performance compared to the classical scaled Max-Log MAP algorithm as shown in [141]. This simplifed decoding algorithm can be seen as the first step towards possible hardware implementations of the proposed structure of NB-TCs.

Performance comparisons with LTE TC, enhanced TC codes, NB-LDPC codes, 5G-LDPC codes and 5G-polar codes were performed for different frame sizes and coding rates. Results show that NB-TCs are at least on-par with these codes in all cases. In most cases, a noticeable gain can be observed for NB-TCs as shown in Fig. 1.11 when compared to the 5G polar code with different list size types for SC-List decoding.

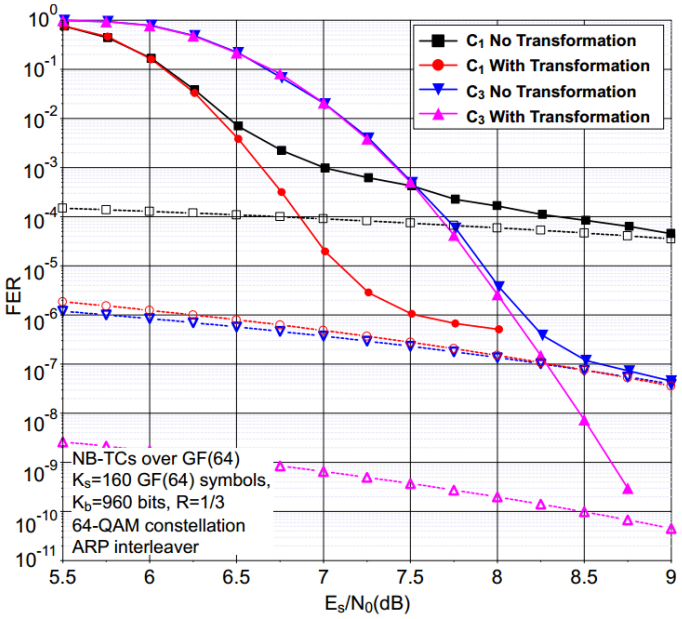

Figure 1.10: Frame error rate performance comparison with ARP interleaver over an AWGN channel with 64-QAM modulation, $K_s = 160$ GF(64) symbols and $R = 1/3$ for two convolutional codes, C1 and C3, in GF(64) with and without symbol transformation.

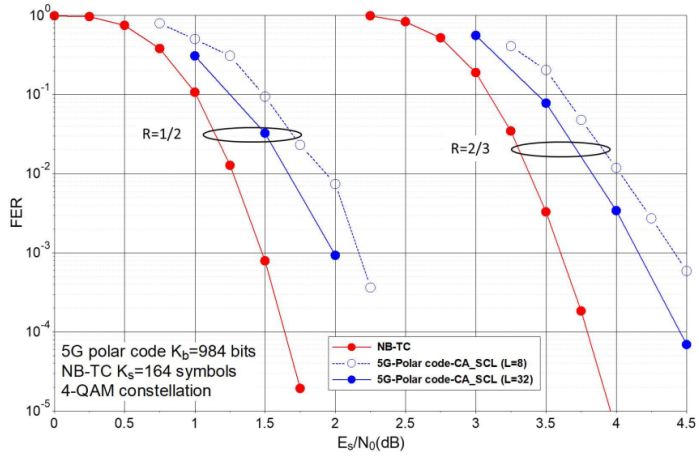

Figure 1.11: Frame error rate performance comparison of NB-TC defined over GF(64), $K_s = 164$ GF(64) symbols, and 5G-polar code, $K_b = 984$ bits with different coding rates, AWGN channel and 4-QAM constellation.

1.6 Summary

In addition to the work performed during my own PhD and post-doctoral fellowship, the studies on this topic were performed in the context of 8 PhDs and 2 post-doctoral fellowships. They were supported by a total of 2 EU H2020 projects, 2 EU Celtic projects, 2 EU Eurostars projects, 1 ANR project, 1 FUI project, 1 European Space Agency project and 8 industrial projects. The results were presented in 12 journal and 53 conference articles, 5 invited talks, 3 poster and 1 demonstration (IBC with more than 150 visitors) events. One article was attributed a best paper award. Moreover, 2 book chapters were written on the topic and 6 patents were filed including 1 patent recognized as essential in 3 different DVB standards.

It is also worth to note my strong involvement in the definition of communications and

broadcasting standards. These include 5 DVB standards with more than 30 contributions and the 3GPP consortium for the definition of 5G with 6 technical contributions. I am also the co-author of 3 DVB standards especially the part related to the adopted rotated constellation technique.

Chapter 2

Algorithms for filtered waveforms

2.1 Introduction and motivation

The multitude of services that are expected to be launched with the advent of the 5G standard set a major constraint on system design. Indeed, these services would have to coexist in the same wireless environment. This introduces new challenges, requiring investigation on new techniques to fulfill network constraints, from the application layer to the physical layer. For the latter, the current Orthogonal Frequency-Division Multiplexing (OFDM) waveform used in 4G/LTE may not be adapted to support all these demanding constraints. In fact, OFDM was an attractive solution in 4G/LTE due to its high robustness against multipath channel thanks to its Cyclic Prefix (CP), its orthogonality in both the time and frequency plane, its straightforward implementation with a FFT, and the simple per-subcarrier equalizer. OFDM is also known to efficiently support multiple MIMO schemes [142], such as spatial multiplexing and MIMO diversity scheme employing Alamouti code [6].

However, the high Out-Of-Band Power Leakage (OOBPL) of OFDM compromises the coexistence of multiple services in the same carrier as foreseen in 5G. In addition, it requires strict synchronization with the Base Station (BS) in time and frequency for each user, which adds important signalling overhead. Consequently, the latency and the energy consumption are highly impacted.

2.1.1 Post-OFDM waveforms: Improvement by filtering

In this context, multiple candidate waveforms for 5G have been investigated, such as FBMC/OQAM [143], UF-OFDM [144], F-OFDM [145], FC-OFDM [146], ZT-OFDM [147], GFDM [148], and BF-OFDM [149]. These candidate waveforms are mainly based on multicarrier modulation with specific filtering scheme used on the top of the OFDM basis. The filtering operation is applied in the digital domain, before transmitting the baseband discrete signal to the Digital-to-Analog Converter (DAC). This filtering step enables to greatly reduce the OOBPL, as shown in Fig. 2.1, thus increasing the coexistence capability and relaxing the synchronization constraint.

The difference between these waveforms mainly lies in the type of the filtering operation, per subcarrier or per group of subcarriers (subband), and in the orthogonality feature. For example, FBMC/OQAM applies per subcarrier filtering and it preserves the orthogonality in the real field as shown in Fig. 2.2.

GFDM also applies per subcarrier filtering, however it is not orthogonal. Both UF-OFDM and F-OFDM propose subband filtering, however the latter is not orthogonal.

Most of the new waveforms are studied and analyzed at the algorithmic level considering mainly the quality of the communication link. Although this remains as one of the most

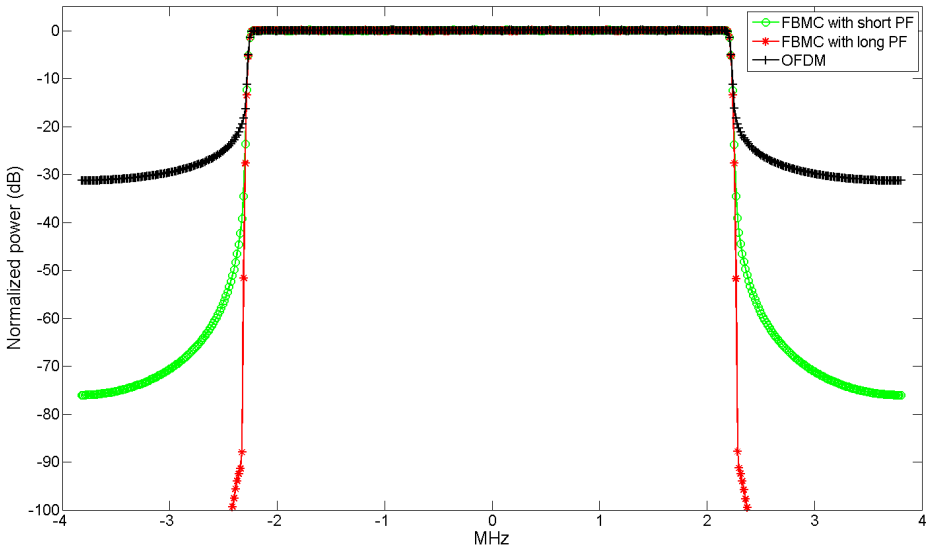

Figure 2.1: PSD comparison of OFDM and FBMC/OQAM using a short and a long prototype filter.

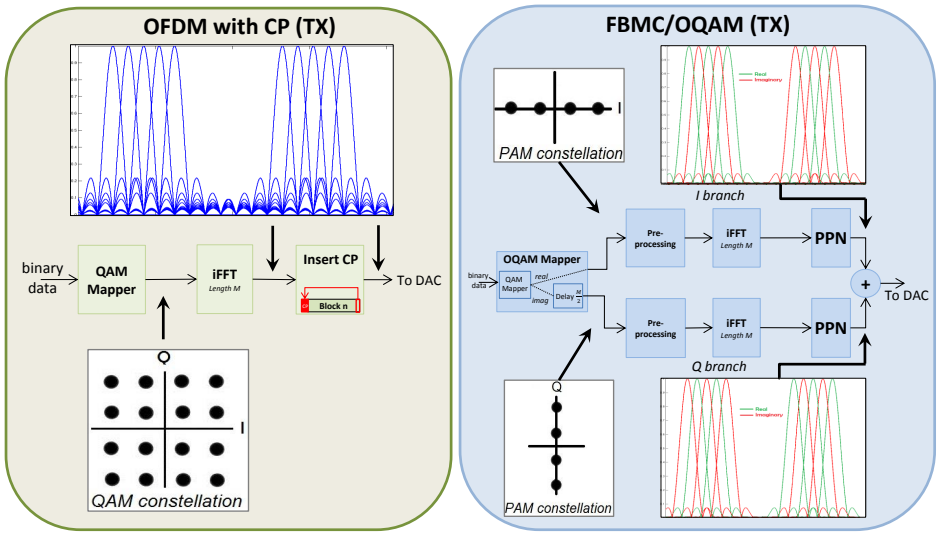

Figure 2.2: OFDM transmitter and PPN implementation of the FBMC/OQAM transmitter.

important assessment measure, the related hardware complexity and energy efficiency are becoming increasingly of relevance, especially for any adoption in future standards. Therefore, the elaboration of low-complexity implementations and the availability of real hardware prototypes are starting to become of interest for wide acceptance since they provide validation and proof-of-concept of the diverse proposed communication techniques.

One major drawback of the proposed 5G candidate waveforms such as FBMC/OQAM and UF-OFDM is their associated complexity. Indeed, their typical transmitters are considered to be several times more complex than the state-of-the-art OFDM transmitter. In particular, a straightforward implementation of the UF-OFDM transmitter is estimated to be up to 200 times more computationally complex than OFDM [150]. Some recent techniques have been proposed to reduce this computational complexity [150, 151]. Despite these efforts, these techniques still require up to 10 times the complexity of OFDM [150] while calling for an approximated signal implying a penalty in bit error rate and in spectral confinement.

Concerning FBMC, the use of the OQAM scheme requires to duplicate the processing units (or to double the processing rate) when compared to OFDM. In addition, the filtering stage may introduce a non-negligible complexity increase.

Therefore, more work was still needed to improve on that front, to investigate novel algorithms and hardware optimizations in order to reduce the complexity and the energy consumption of these waveforms.

In addition, despite several interesting advantages with respect to OFDM, FBMC had few important issues that still needed to be addressed. To start, the filtering operation introduces ramp-up and ramp-down transitions at the beginning and the end of each transmitted frame. To avoid significant spectral efficiency loss, the frame duration must be increased. However, 5G aims to use short frame sizes for several communication scenarios in order to reduce the latency. Moreover, certain techniques designed for OFDM are not directly applicable to FBMC due to the OQAM scheme. Among these techniques, there are the pilot structure for channel estimation, the FFT-spread to reduce the Peak-to-Average Power Ratio (PAPR), and the compatibility with MIMO Alamouti scheme [6]. Finding appropriate solutions to these technical issues is crucial if FBMC is to have any chance in getting adopted for certain services in future communication systems. It is worth noting in this regard that UF-OFDM is compliant with most of the techniques designed for OFDM, which can be re-used with minimal adaptations.

Addressing these issues was performed in the PhD thesis of Jérémy Nadal under the context of two European projects, namely FP7 METIS and H2020 FANTASTIC-5G.

2.1.2 Post-OFDM waveforms: Faster than Nyquist signalling

On another front, the Nyquist criterion ensures pulses orthogonality to avoid Inter-Symbol Interference (ISI). However, bandwidth efficiency is sacrificed to guarantee the orthogonality. Faster-Than-Nyquist (FTN) systems allow the transmission of data beyond the Nyquist rate, provided that ISI is tolerated. Even if this interference is intentionally introduced to the transmitted signal, sophisticated algorithms should be used at the receiver to deal with it. Actually, the question of whether signaling faster than the Nyquist rate is of any merit has attracted many researchers in the past years: [152, 153, 154]. In the meanwhile, the concept was not deemed to be an attractive technique until nowadays where we bare witness to the explosion of throughput requirements. This was mainly attributed to the complex processing necessary to deal with the interference introduced by FTN.

The declining cost of processing units, the importance of bandwidth resources and the emergence of spectrally efficient solutions overcame the importance of the amount of required processing. In fact, advances in semiconductor technology allows the number of transistors in integrated circuits to double every 18 months (a phenomenon referred to as the Moore's law [155]). Additionally, the density of the memory storage has been observed to increase at even a faster rate (known as the Kryder's law [156]). Moreover, important advancement in signal processing and coding have been achieved in the past years. Consequently, the available data and signal processing ability enables to practically implement advanced channel coding and equalization techniques to deal with the interference caused by FTN signaling. Hence, the concept of FTN transmissions has been recently re-investigated and is nowadays deemed being worthy of further investigation.

Performed work focuses on the combination of FTN signaling with multi-carrier modulations. FTN systems using OFDM modulation were discussed in [157]. Although this modulation is widely used in modern digital communication systems, our work carried out during the PhD thesis of Naila Lahbabi in the context of a collaboration with Orange Labs within the H2020 FANTASTIC-5G project focused on an attractive alternative to OFDM, namely FBMC/OQAM [158]. This is mainly because FBMC/OQAM modulation does not

necessitate the insertion of a CP, reaching therefore the full Nyquist rate. Further, FBMC/OQAM modulation can use different Prototype Filters (ProFs) having different time-frequency localization properties. However, the findings of our work are not exclusive to FBMC/OQAM waveform. Instead, they can be well extended to other waveforms including OFDM. The FTN concept was originally introduced to pack the transmitted signals closer in time domain, with respect to the Nyquist rate [159]. The extension of the FTN concept to multi-carrier modulations was discussed in [160], where the authors showed that the signals can be packed closer both in time and frequency domains. The concept is referred to as the two-dimensional Mazo limit.

Under this context, new efficient FTN implementations of the FBMC/OQAM system which allows to switch flexibly from Nyquist to FTN mode with limited complexity increase compared to FBMC/OQAM systems, while approaching very closely the theoretical rate growth promised by the FTN concept remained a challenge. This means that both ISI and Inter-Carrier Interference (ICI) are intentionally added to the transmitted signals, which calls for more complex algorithms at the receiver end. The FTN transceiver was originally based on the non-linear Maximum A Posteriori (MAP) sequence detection algorithm [161, 162] which achieves good performance. However the complexity is exponentially proportional to the constellation order. Supporting higher order constellations is an important request for high throughput transmission. But in the state of the art, only low constellations, basically BPSK or QPSK, are assumed. Therefore, supporting high constellations with a manageable complexity and appealing performance in FTN systems was still an open issue.

2.2 Performed work and contributions

2.2.1 Design of filtered waveforms

The performed work targeting the lackings of the considered waveforms aimed at:

- Analyzing and simplifying algorithms for FBMC and UF-OFDM waveforms from an implementation perspective towards low complexity and efficient transceiver design;
- Exploring hardware architectures for the devised low-complexity algorithms. The target objective was to propose a hardware implementation comparable in complexity to OFDM;
- Implementating and integrating the proposed transceiver architectures in a real hardware platform with a Radio Frequency (RF) interface. This platform should serve as a proof-of-concept with realistic conditions for the proposed hardware architectures. It should also illustrate the waveform performance in relevant 5G scenarios.

In the pursuit of these objectives, several original contributions have been proposed. These contributions related to both algorithmic domain and hardware design domain.

2.2.1.1 Design and algorithmic contributions

While FBMC/OQAM systems using long ProFs such as the MMB4 ProF [163] have been extensively studied in the literature, FBMC with short ProFs provides interesting advantages. For instance, the corresponding lower duration enables:

- The support of shorter frame lengths,
- The introduction of efficient block-type pilot structure for channel estimation,

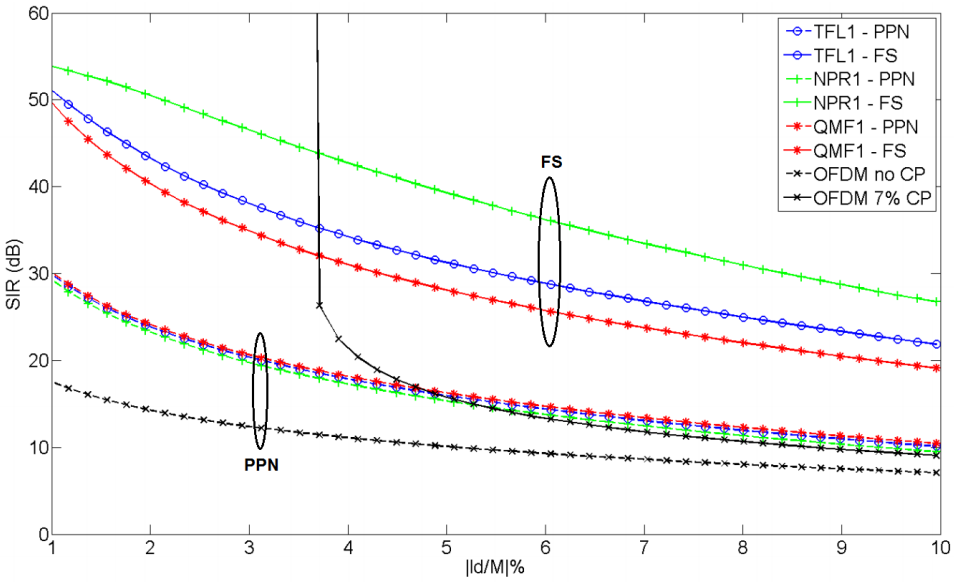

Figure 2.3: Timing offset evaluation in terms of measured SIR for OFDM and FBMC with the considered short ProFs. The effect of different implementations is also evaluated.

- The robustness improvement against Carrier Frequency Offset (CFO) or Doppler shift.

In addition, short ProFs present the following features when compared to long ProFs:

- Lower PAPR using precoding techniques,
- Reduced complexity of the transmitter.

Consequently, a FBMC system employing a short ProF can potentially be more energy-efficient. In this context, a novel short ProF for FBMC, referred to as NPR1, was designed and published in IEEE Access [164]. The original filter design approach involved reversing the time and frequency axes of the filter-bank impulse response generated by the MMB4 long ProF, and deducing the related prototype filter. Indeed, the impulse response of the MMB4 filter is highly localized in frequency since interference is limited only to one adjacent subcarrier in the frequency plane. Therefore, reversing the axis generates a prototype filter highly localized in time, with an overlapping factor equal to 1. The NPR1 shows improved performance for multiple channel impairments when compared to the other existing short ProFs. In presence of timing offset due to imperfect synchronization, the NPR1 ProF combined with the Frequency Spread (FS) implementation exhibits a gain of more than 8 dB of Signal-to-Interference Ratio (SIR) when compared to state-of-the-art short ProFs (TFL1 [165] and QMF1 [166]) as seen in Fig. 2.3. It largely outperforms OFDM, where a gap of 20 dB of SIR can be observed. The NPR1 ProF is also the most robust filter to combat CFO. In the case of 4G/LTE multipath channel models, the NPR1 ProF is even better than OFDM for the Extended Pedestrian A (EPA) channel model, due to the absence of CP.

2.2.1.2 Architecture, implementation and system aspects

In addition to its design, an efficient hardware architecture of the corresponding FS filtering stage is proposed also in [164]. Hardware complexity evaluation shows that the proposed FS-FBMC receiver, using the NPR1 ProF, requires 11% less hardware resources than a FBMC receiver using a PolyPhase Network (PPN) ProF, since the proposed ProF is more robust against truncation as seen in Fig. 2.4. Therefore, combining the proposed NPR1 filter and FS-FBMC receiver architecture provides an original solution that combines complexity reduction

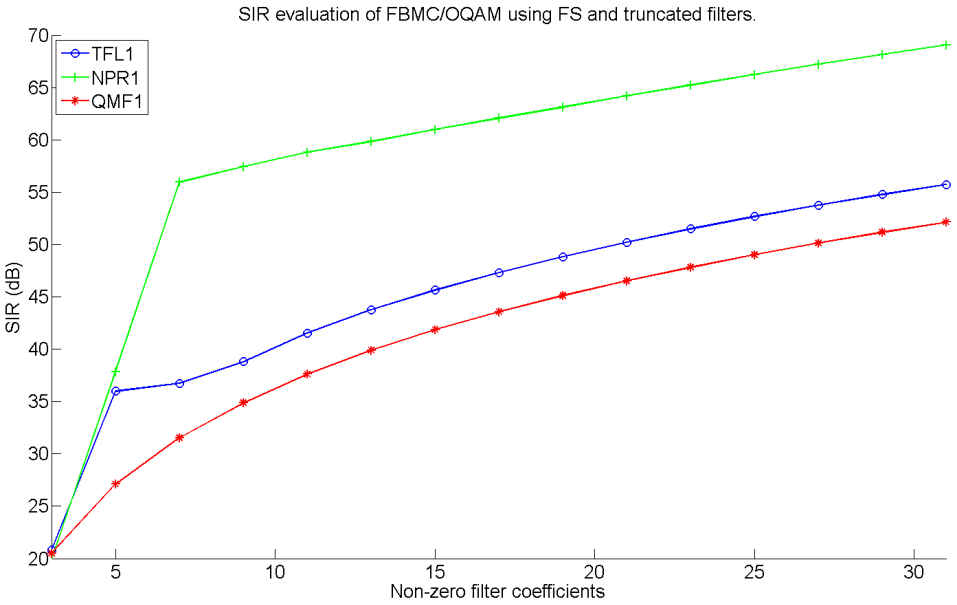

Figure 2.4: Evaluation of the impact of N_G (number of non-zero filter coefficients) on the SIR for different ProFs.

and performance improvement with respect to a typical PPN-FBMC receiver. More details can be found in [164].

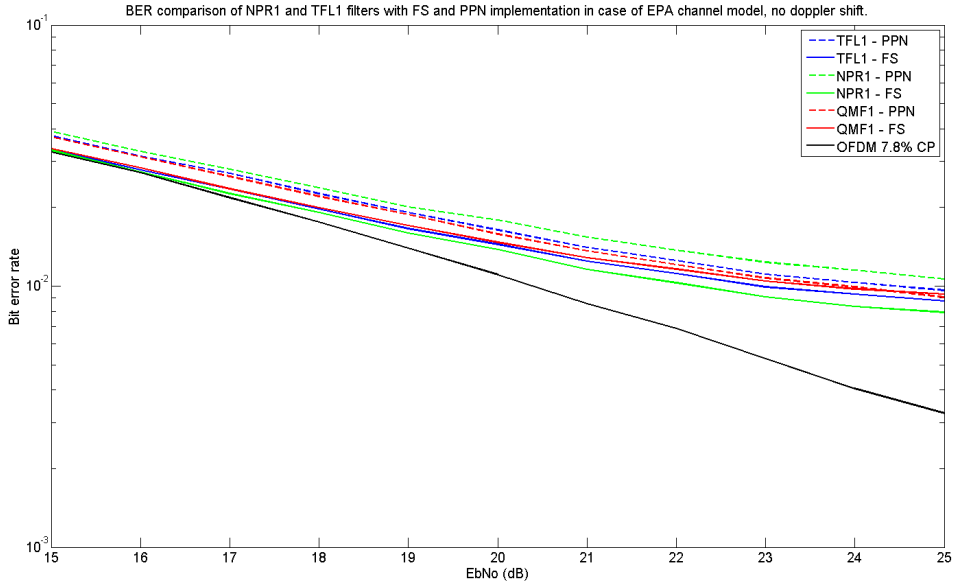

Figure 2.5: BER evaluation of OFDM and FBMC with different ProFs and implementations in presence of AWGN, for ETU static channel.

However, the conventional FS-FBMC receiver architecture fails to efficiently support long delay spread such as encountered in the Extended Typical Urban (ETU) channel model when short ProFs are considered as seen in Fig. 2.5.

Furthermore, it cannot support asynchronous communications, unlike the case where it is combined with a long filter such as the MMB4 ProF. In order to overcome these two limi-

tations, a novel FBMC receiver adapted for short ProFs has been investigated and proposed as a viable solution. This work was published in IEEE Transactions on Wireless Communications [167] included hereafter. This FBMC receiver, referred to as OS-FBMC, consists of merging the structure of a typical FS-FBMC receiver with a time-domain equalizer based on the OS algorithm.

A second FBMC receiver is derived, referred to as OSB-FBMC, where the OS-FBMC is adapted to process a block of transmitted FBMC symbols. Consequently, the FFT is only computed once per block, instead of once per FBMC symbol, enabling to reduce the complexity.

The NPR1 ProF appears to be the best adapted ProF for these receivers since it achieves the lowest residual interference, due to the filter coefficients truncation (see Fig. 2.4). When facing a timing offset, the proposed receivers offer improved SIR performance compared to the conventional FS-FBMC receiver. For a SIR target of 30 dB, the later can tolerate a timing offset up to 8% of the FBMC symbol duration, while the OSB-FBMC can reach up to 21%. Furthermore, the OS-FBMC receiver can support any timing offset value, making it perfectly suited for asynchronous communications. The robustness against multipath channels with Doppler spread was evaluated. It was shown that the OS-FBMC and OSB-FBMC receivers achieve similar BER than the FS-FBMC receiver with a MMB4 ProF. This shows that short ProFs can reach similar robustness against doubly dispersive channels when compared to long ProFs like MMB4, at similar receiver complexity.

A drawback of FBMC/OQAM systems when compared with OFDM systems is the difficulty of efficiently supporting MIMO schemes at low complexity. Particularly, the use of the popular Alamouti space-time code is more challenging than for OFDM because of the lack of orthogonality in the complex plane between neighboring OQAM symbols. In our work, we showed how the 2×2 Alamouti scheme can be supported with a block FBMC receiver. Moreover, two different equalizer schemes have been proposed for providing different complexity/performance tradeoffs depending on the required level of support for mobility.

Overlap-Save FBMC Receivers

Jérémy Nadal *Member IEEE*, François Leduc-Primeau *Member IEEE*,
Charbel Abdel Nour *Senior Member IEEE*, Amer Baghdadi *Senior Member IEEE*

***Abstract*—Future communication systems are foreseen to support several services with different requirements. Waveform designs based on filter-bank multi-carrier with offset quadrature amplitude modulation (FBMC/OQAM) can offer interesting advantages in this context, such as low out-of-band power leakage and high spectral efficiency due to the lack of guard intervals. However, downsides of FBMC/OQAM with respect to a typical orthogonal frequency-division multiplexing (OFDM) solution include higher latency, higher complexity and difficulties in adapting some existing OFDM techniques such as MIMO Alamouti. To address these issues, novel FBMC receivers suitable for short prototype filters are proposed. Based on the Overlap-Save algorithm, the proposed receivers improve error-rate performance on multipath channels and support asynchronous communication. We show that complexity can be further reduced by efficiently processing blocks of FBMC symbols jointly, and that user mobility support can be traded off for additional complexity reductions in a flexible way through polynomial decomposition of the equalizer stage. Finally, we show that a block-Alamouti scheme can be applied, and we propose a MIMO equalizer with improved error-rate performance on time-varying channels, compared to the typical FBMC block-Alamouti equalizer.**

I. INTRODUCTION

New communication systems are foreseen to support multiple types of services, each having different system parameters optimized for specific requirements, such as latency, data rate and energy consumption. For instance, in 5G, massive machine communication (MMC) and ultra-reliable low-latency communication (URLLC) services are introduced, respectively targeting low power consumption and low latency. To partly answer these new challenges, novel waveforms have been designed and proposed for future wireless communication systems.

Filter-bank multi-carrier with offset quadrature amplitude modulation (FBMC/OQAM, shortened to FBMC for simplicity) is a promising waveform for future communication standards. It consists of filtering the sub-carriers by a synthesis filterbank derived from a prototype filter (PF). The orthogonality is ensured in the real field thanks to the OQAM scheme. One of its remarkable feature is that it does not require a cyclic prefix as in OFDM: the time and frequency localization of the PF makes it naturally robust against channel impairments like multiple paths, timing offsets, carrier frequency offset (CFO) and Doppler spread.

Instead of employing a PF with a long impulse response such as PHYDYAS [1], [2], it can be interesting to consider the use of a shorter filter to reduce the latency and the complexity of the transceiver [3]. Additional benefits of a short PF include high robustness against CFO and Doppler spread, and easier channel estimation based on block-type pilots [4]. However, the use of short PFs makes the system more sensitive to multipath channels with long delay spreads, even when using a *frequency-spread* (FS) receiver [5]: an error floor appears for such channels due to inter-symbol interference [5], [6].

Therefore, a novel FBMC receiver design suitable for short filters is proposed. It is inspired by the idea proposed in [7] where a time-domain equalizer based on the overlap-save (OS) algorithm is employed before a FBMC receiver. This technique is however complex to implement. Thankfully, we show that the time-domain equalizer and the FBMC receiver can be merged into a unique structure due to the frequency localization of the filter, allowing to greatly reduce the computational complexity. Based on this novel receiver structure, alternative FBMC receivers and equalization techniques are proposed for both single-input single-output (SISO) and multiple-input multiple-output (MIMO) systems. The specific contributions presented in this paper can be summarized as follows:

1) A novel FBMC receiver is proposed based on the OS algorithm, robust against timing offset and multipath impairments even when using short filters.
2) A new block-based receiver is derived to reduce complexity at the cost of a reduction of the robustness against time-varying channel impairments.
3) Alternative equalization techniques are proposed to enable different trade-offs between complexity and robustness against time-varying channel impairments.
4) The MIMO Alamouti space-time code is shown to be efficiently supported by the proposed block-based receiver when combined with dedicated equalizer techniques.
5) The robustness to timing offset impairments of the proposed receivers is studied analytically, demonstrating their superiority.
6) The performance of the proposed receivers is evaluated using bit error rate (BER) simulations over 4G time-varying multipath channels, and the results are compared to typical FBMC and OFDM receivers.

The remainder of the paper is organized as follows. We start in Section II with a brief review of existing FBMC receivers. Then, Section III describes the proposed Overlap-Save receivers. Several techniques to reduce their complexity are proposed and detailed. In Section IV, the proposed receivers are adapted to efficiently support Alamouti-coded MIMO schemes. Particularly, a new block-Alamouti equalized is proposed, allowing to support time-varying channel with reduced computational complexity. The performance of the

J. Nadal, F. Leduc-Primeau are with the Department of Electrical Engineering, Polytechnique Montreal, QC H3T 1J4, Canada (e-mail: *firstname.lastname*@polymtl.ca).

C. Abdel Nour and A. Baghdadi are with the Electronics Department, IMT Atlantique, CNRS UMR 6285 Lab-STICC, Brest, France (e-mail: *firstname.lastname*@imt-atlantique.fr).

proposed receivers in the presence of synchronization errors are analyzed in Section V. Finally, Section VI compares the performance of all FBMC schemes discussed in the paper under realistic channel impairments, and Section VII concludes the paper.

II. Review of Existing FBMC Receivers

In the literature, two types of implementation of the FBMC modulation exist, which differ in complexity and performance. The *polyphase network* (PPN) implementation [8] performs the transmission using one inverse fast Fourier transform (IFFT) followed by a PPN that implements the filtering. An OQAM scheme is introduced to support orthogonality in the real domain. It first consists of separating the real and imaginary components of the transmitted QAM symbols. Then, each component is phase rotated and the imaginary component is time delayed by half the FBMC symbol duration. Finally, they are processed by 2 independent IFFT-PPN chains, the output being summed and the obtained samples transmitted to the channel. The PPN implementation is interesting at the transmitter side as it is possible to avoid duplicating the IFFT [3].

The second type of implementation is the FS implementation which was first proposed in [9] for the PHYDYAS filter [1], [2]. The original idea was to shift the filtering stage into the frequency domain, to enable the use of a low-complexity per-subcarrier (*one-tap*) equalizer at the receiver side. The FS implementation is generally more complex than the PPN implementation, since it requires fast Fourier transform (FFT) of size qM per FBMC symbol, where M is the total number of available subcarriers and q is the overlapping factor of the PF, compared to one FFT of size M for a PPN receiver. However, in the case of short filters ($q = 1$), the size of the FFT is the same in both implementations. In fact, the PPN-FBMC receiver offers comparatively a degraded performance while being as complex as the FS-FBMC receiver when considering an adapted short filter [5]. Therefore, it is not discussed further in this article, and the rest of the section reviews the FS-FBMC receiver only.

A. Transmitted Signal

We consider that a number N_s of FBMC symbols are transmitted, each composed of M OQAM symbols. An OQAM symbol at subcarrier m within FBMC symbol n can be expressed as $d_n(m) = a_n(m)\phi_n(m)$, with $a_n(m)$ the real or imaginary part of a QAM symbol, and $\phi_n(m) = i^{n+m}$. Each FBMC symbol is processed with a PF with impulse response $g(k)$, where $g(k) = 0$ if $k \notin [\![0, qM-1]\!]$. The transmitted signal $s(k)$ is thus given by

$$s(k) = \sum_{n=0}^{N_s-1} g\left(k - n\frac{M}{2}\right) \sum_{m=0}^{M-1} (-1)^{nm} d_n(m) e^{i\frac{2\pi km}{M}} . \quad (1)$$

B. FS-FBMC Receiver Description

We assume that the transmitted signal $s(k)$ is corrupted by a multi-path channel and by additive noise $w(k)$. The received signal $r(k)$ is therefore given by

$$r(k) = \sum_{\ell=0}^{L_{\text{DS}}-1} s(k-\ell)h_k(\ell) + w(k)\,, \quad (2)$$

where $h_k(\ell)$ is the impulse response of the channel at time k, and L_{DS} is the delay spread of the channel.

To compensate the effect of the channel, a single-tap linear equalizer stage is introduced in the frequency domain. The signal at its output can be expressed as

$$R_n(m) = C_n(m) \sum_{k=0}^{qM-1} r(k + n\frac{M}{2})\, e^{i\frac{-2\pi}{qM}km}\,, \quad (3)$$

where $C_n(m)$ are the equalization coefficients. For zero-forcing equalization, $C_n(m) = \frac{1}{\hat{H}_n(m)}$, where $\hat{H}_n$ is the estimated frequency response of the channel at symbol index n. Then, the filtering is applied by performing a convolution of the equalized signal with the frequency response G of the PF, followed by a down-sampling stage by a factor q. The obtained signal corresponds to the output of the analysis filter bank (AFB), and is expressed as

$$Y_n(m) = \sum_{\ell=-\Delta}^{\Delta} R_n(qm-\ell)G(\ell)\,, \quad (4)$$

where Δ is the number of significant coefficients of G and is a design choice [5]. Finally, OQAM demapping must be performed by first multiplying the output of the AFB by a linear phase rotation (LPR) term $\phi_n(m) = i^{n+m}$, then by extracting the real part of the signal to obtain the recovered real or imaginary part $\hat{a}_n(m)$ of the transmitted QAM symbols:

$$\hat{a}_n(m) = \Re(\phi_n^*(m)\, Y_n(m))\,. \quad (5)$$

In practice, only a subset N_c of the M available subcarriers are allocated. Therefore, only N_c samples of the a_n signal contain useful data and are sent to the OQAM demapper, the remaining $M - N_c$ samples being discarded. Figure 1 illustrates the processing steps applied by a FS-FBMC receiver, as described above.

When a short filter is considered ($q = 1$), the FFT size becomes equal to M, and there is no down-sampling step after the filtering stage. In this case, compared to a PPN receiver, the added complexity of the FS receiver can be attributed to the convolution operation, whose complexity can be greatly reduced by truncating the number of coefficients to $\Delta = 3$ while maintaining an acceptable signal-to-interference ratio (SIR) level of 55 dB [5]. However, an error floor is observed for channels having large delay spreads. In addition, machine-type communication scenarios in which users transmit data without a common time base, referred to as *asynchronous communications* in this paper, are not supported by typical FBMC receivers using short filters without a large performance penalty. Therefore, there is a need for more efficient FBMC receivers to address these issues.

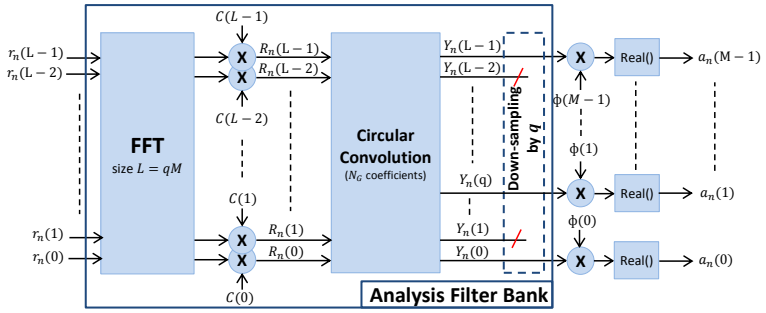

Fig. 1. System description of the FS-FBMC receiver.

III. OVERLAP-SAVE RECEIVERS

A possible way to improve the equalization in FBMC receivers was proposed in [7] and consists in adding a time-domain equalizer before the FBMC receiver. This approach can be adapted to any FBMC scheme. The time-domain equalizer can be implemented using the well known overlap-save (OS) algorithm to efficiently perform a fast convolution by the inverse of the channel response [8]. However, despite a performance improvement when compared to a typical FS-FBMC receiver, the complexity is highly increased due to the need to perform multiple FFTs, reducing the interest of this method for practical systems.

In this section, we show that an important complexity reduction can be obtained by exploiting the frequency localization of the filter. As a result, the time-domain equalizer and the FBMC receiver can be merged into a novel FBMC receiver that we call the OS-FBMC receiver. Optimization techniques are also presented to further reduce the complexity, including an alternative block-based OS-FBMC receiver. For the sake of generality, the proposed OS receivers are described for any filter overlapping factor q, but they are particularly interesting when combined with short filters ($q = 1$).

A. Time-Domain Equalization

To illustrate the principle behind the proposed receiver, we first discuss the time-domain equalization separately from the FBMC receiver. We consider that for each FBMC symbol n, the receiver processes a window of samples of size N that is larger than a FBMC symbol by an integer oversampling factor N_{UF}, such that $N = N_{\text{UF}}qM$. First, a FFT of size N is applied to that window, followed by a single-tap linear equalizer. For $m \in [\![0, N-1]\!]$, the resulting frequency-domain equalized signal is given by

$$X_n(m) = C_n(m) \sum_{k=0}^{N-1} r\left(k + n\frac{M}{2} - \ell_o\right) e^{-i\frac{2\pi km}{N}}, \quad (6)$$

where ℓ_o is used to position the window around the n-th received symbol. It is interesting to center the current symbol within the window, hence we choose $\ell_o = (N - qM)/2 = (N_{\text{UF}} - 1)qM/2$. After equalization, an IFFT of size N is immediately applied, but the samples that do not correspond to FBMC symbol n are discarded. For $k \in [\![0, qM-1]\!]$, the resulting time-domain signal can be expressed as

$$x_n(k) = \sum_{m=0}^{N-1} X_n(m) e^{i\frac{2m\pi(k+\ell_o)}{N}}. \quad (7)$$

The time-domain equalized samples must now be demodulated by a FBMC receiver, for instance by one based on the FS technique presented in Section II-B. As noted in [7], interference occurs at the edge of the IFFT since the channel impairment is compensated by a convolution, whereas the FBMC receiver signal does not exhibit any cyclostationarity due to the time overlapping of successive OQAM symbols. However, by choosing a sufficiently large N while retaining only the samples in the middle of the window, this interference can be suppressed.

At this stage, the OS time-domain equalizer technique offers improved robustness against channels with large delay spreads and against timing offsets, but at the cost of a significant increase in computational complexity. Indeed, the receiver now requires computing two FFTs of size N for each FBMC symbol in addition to the FFT already required by the standard FBMC receiver.

B. The Overlap-Save Receiver

The complexity of the receiver can be greatly reduced by taking advantage of the frequency localization of the PF while merging the time-domain equalizer with a FS-FBMC receiver. The first step consists in applying the "decimation in time" decomposition of the FFT to decompose the equalizer IFFT into N_{UF} IFFTs of size qM. Omitting the normalization terms, the equalizer output samples can then be expressed as

$$x_n(k) = \sum_{\ell=0}^{N_{\text{UF}}-1} \sum_{m=0}^{qM-1} X_n(N_{\text{UF}}m + \ell) e^{i2\pi\frac{(N_{\text{UF}}m+\ell)(k+\ell_o)}{N}}. \quad (8)$$

By defining the LPR term $z_\ell(k) \triangleq e^{i\frac{2\pi\ell(k-qM/2)}{N}}$, (8) can be rewritten as

$$x_n(k) = \sum_{\ell=0}^{N_{\text{UF}}-1} e^{i\frac{\pi\ell}{N_{\text{UF}}}} x_{n,\ell}(k) z_\ell(k), \quad (9)$$

with $x_{n,\ell}(k)$ defined as

$$x_{n,\ell}(k) = \sum_{m=0}^{qM-1} X_n(N_{\mathrm{UF}}m+\ell)e^{i\frac{2\pi(N_{\mathrm{UF}}m+\ell)\ell_o}{N}}e^{i2\pi\frac{km}{qM}}. \quad (10)$$

Instead of directly processing $x_n(k)$ using a single AFB as done in FS-FBMC receivers, each $x_{n,\ell}$ can be processed by a separate AFB. The output $Y_{n,\ell}$ of the ℓ-th AFB is then given by

$$Y_{n,\ell}(m) = e^{i\frac{\pi\ell}{N_{\mathrm{UF}}}}\sum_{k=0}^{qM-1} g(k)x_{n,\ell}(k)z_\ell(k)e^{-i2\pi\frac{mk}{qM}}. \quad (11)$$

The LPR term z_ℓ can be seen as a CFO by a fraction $\frac{\ell}{N_{\mathrm{UF}}}$ of the subcarrier spacing. By using the frequency-domain compensation (FDC) technique proposed in [10], the PF of each AFB can be adapted to directly incorporate the corresponding CFO. In our case, the FDC technique is used backwards to generate the required CFOs. Thus, moving the filter stage to the frequency domain, (11) becomes

$$Y_{n,\ell}(m) = \sum_{p=-\Delta}^{\Delta} G_\ell(p)\sum_{k=0}^{qM-1} x_{n,\ell}(k)e^{i\frac{\pi\ell}{N_{\mathrm{UF}}}}e^{-i2\pi\frac{(qm-p)k}{qM}}, \quad (12)$$

where G_ℓ is the shifted frequency response of the PF, given by

$$G_\ell(p) = \sum_{k=0}^{qM-1} g(k)z_\ell(k)e^{-i2\pi\frac{pk}{qM}}. \quad (13)$$

Noting that the time-domain signals $x_{n,\ell}\, exp[i\pi\ell/N_{\mathrm{UF}}]$ are obtained after an IFFT of size qM in (10), which is followed by a FFT of the same size in (12), Therefore, both transforms can be removed, and we can express the decomposed AFB outputs in terms of the equalized samples. Let us first define the equalized samples corresponding to part ℓ of the receiver as

$$\begin{aligned} X_{n,\ell}(m) &= X_n(N_{UF}m+\ell)e^{\frac{i\pi\ell}{N_{\mathrm{UF}}}}e^{\frac{i2\pi(N_{\mathrm{UF}}m+\ell)\ell_o}{N}} \\ &= C_{n,\ell}(m)R_{n,\ell}(m)\,, \end{aligned} \quad (14)$$

with

$$R_{n,\ell}(m) = \sum_{k=0}^{N-1} r(k+n\frac{M}{2}-\ell_o)e^{-i2\pi\frac{k(N_{\mathrm{UF}}m+\ell)}{N}}, \quad (15)$$

$$C_{n,\ell}(m) = C_n(N_{\mathrm{UF}}m+\ell)e^{\frac{i\pi\ell}{N_{\mathrm{UF}}}}e^{\frac{i2\pi(N_{\mathrm{UF}}m+\ell)\ell_o}{N}}. \quad (16)$$

Note that for $\ell_o = (N-qM)/2$, the two exponential terms in (16) simplify to $(-1)^{(N_{\mathrm{UF}}-1)m+\ell}$, which can be computed easily. We can then rewrite (12) as

$$Y_{n,\ell}(m) = \sum_{p=-\Delta}^{\Delta} G_\ell(p)X_{n,\ell}(qm-p)\,, \quad (17)$$

and the AFB output is obtained by simply summing the decomposed AFB outputs:

$$Y_n(m) = \sum_{\ell=0}^{N_{\mathrm{UF}}-1} Y_{n,\ell}(m)\,. \quad (18)$$

Finally, the transmitted symbols are recovered in the usual way, as given by (5). It should be noted that if $q > 1$, an additional downsampling step is necessary beforehand.

With these simplifications, only one FFT of size N (equation (15)) is now required to demodulate one FBMC symbol, followed by the single-tap linear equalizer stage and N_{UF} stages of convolution by the frequency shifted responses of the PF, as illustrated in Figure 2. The proposed OS receiver allows to trade-off complexity for performance using the parameter N_{UF}. Compared to a FS receiver, the complexity of the OS receiver is increased due to the need of computing a FFT that is larger by a factor N_{UF}, and by the need to apply N_{UF} convolutions instead of one. While a convolution operation is generally considered highly complex, the frequency localization of the PF causes it to have only a small number of coefficients in the frequency domain. For instance, it is shown in [5] that a SIR of ≈ 42 dB is obtained to compensate the worst CFO case when the Near-Perfect Reconstruction 1 (NPR1) filter is used with $\Delta = 3$. Therefore, the main complexity issue comes from the FFT processing, which is addressed in the next subsection by proposing an alternative OS-FBMC receiver technique.

C. The Overlap-Save Block Receiver

To further reduce complexity, we can adapt the OS receiver to process several symbols at once, by considering a larger window of samples. We can then think of the demodulation of a given symbol within that window as using the OS receiver with a window position ℓ_o that depends on the position of the current symbol. However, as discussed in Section III-A, this approach would cause a performance penalty for symbols located at the edges of the window, due to the lack of cyclostationarity in the received signal. While it is difficult to obtain strict cyclostationarity for a FBMC signal, it can be approximated by transmitting blocks of symbols isolated by guard intervals. Since the guard intervals prevent symbol overlapping for the first and last symbols in the block, the ramp-up and ramp-down of the PF causes the samples on each side of the block to have an amplitude close to zero.

We denote by N_s the number of symbols in a block. Due to the need for guard intervals between blocks, this number can be linked with spectral efficiency. The number of samples occupied by a block of N_s symbols is given by $L_B = M\left((N_s-1)/2+q\right)$. As a result, it can be shown that the spectral efficiency of the block scheme is $N_s/(N_s+2q-1)$. As can be expected, spectral efficiency is improved by placing more symbols in each block and by using a short filter ($q = 1$).

Similarly to the previous definition, we denote by N the size of the sample window. In order to process all the symbols in the block at once, we require $N \geq L_B$, and the decomposition used in the OS receiver requires $N_{\mathrm{UF}} = N/(qM)$ to be an integer. We therefore choose $N_{\mathrm{UF}} = \lceil\frac{L_B}{qM}\rceil = \lceil 1+\frac{N_s-1}{2q}\rceil$, where $\lceil x\rceil$ denotes the smallest integer greater or equal to x. As in the OS receiver, we start by taking the FFT of a sample window of size N, which now corresponds to a received block, and applying single-tap equalization. Let $r_b(k)$ denote the part of the received signal corresponding to a block b. When N is strictly greater than L_B, $r_b(k)$ is zero-padded to a length of

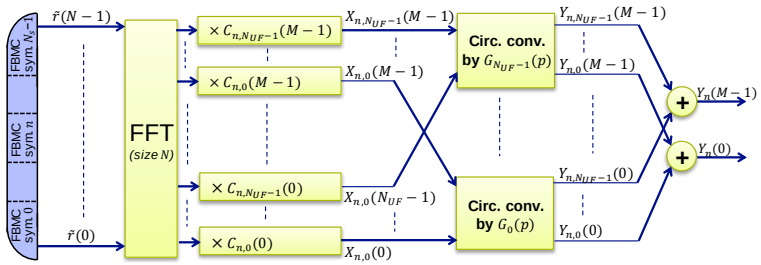

Fig. 2. System description of the proposed OS-FBMC receiver.

N before applying the FFT. The frequency-domain equalized signal for symbol n within block b is thus given by

$$X_{b,n}(m) = C_{b,n}(m) \sum_{k=0}^{L_B-1} r_b(k) e^{-i\frac{2\pi km}{N}}, \quad (19)$$

where $C_{b,n}(m)$ corresponds to the equalizer coefficients at block b and symbol n, and the sum corresponds to a FFT of size N of the zero-padded received block. Letting $\ell_n \triangleq n\frac{M}{2}$ be the window position associated with symbol n, the time-domain signal after equalization, previously given by (7) for the OS receiver, becomes

$$x_{b,n}(k) = \sum_{m=0}^{N-1} X_{b,n}(m) e^{i\frac{2m\pi(k+\ell_n)}{N}}. \quad (20)$$

Through similar steps as in Section III-B, the AFB output is obtained as

$$Y_n(m) = \sum_{\ell=0}^{N_{\mathrm{UF}}-1} \sum_{p=-\Delta}^{\Delta} G_\ell(p) X_{b,n,\ell}(qm-p), \quad (21)$$

with

$$X_{b,n,\ell}(m) = C_{b,n,\ell}(m) R_{b,\ell}(m), \quad (22)$$

$$R_{b,\ell}(m) = \sum_{k=0}^{L_B-1} r_b(k) e^{-i\frac{2\pi k(N_{\mathrm{UF}}m+\ell)}{N}}, \quad (23)$$

$$C_{b,n,\ell}(m) = C_{b,n}(N_{\mathrm{UF}}m+\ell) e^{i\frac{\pi mn}{q}} e^{i\frac{\pi\ell(n+q)}{qN_{\mathrm{UF}}}}. \quad (24)$$

As described in Section III-B, the transmitted symbols are recovered from $Y_n(m)$ using (5). In this receiver, only one FFT of size N (in (23)) is computed to process N_s FBMC symbols.

D. Complexity Reduction Using Equalizer Approximations

In the Overlap-Save Block (OSB) receiver described above, single-tap equalization is performed on a frequency-domain signal of length N for each FBMC symbol. This allows to accurately compensate fast varying channels, but increases the equalization complexity compared to the single-tap equalization of a CP-OFDM signal.

In the special case of low mobility, it can be sufficiently accurate to assume that the channel response remains constant over a block of N_s symbols. In that case, the equalization coefficients $C_{b,n}(m)$ in (24) do not depend on n, and $C_{b,n}(m)$ can be set to $C_{b,0}(m)$. Assuming $q = 1$, and by separating the even ($\epsilon = 0$) and odd ($\epsilon = 1$) FBMC symbol indexes, we can rewrite (21) as

$$Y_{b,2n+\epsilon}(m) = (-1)^{m\epsilon} \sum_{\ell=0}^{N_{\mathrm{UF}}-1} U_{b,\epsilon}(m,\ell) e^{2i\pi\frac{\ell(n+1)}{N_{\mathrm{UF}}}}, \quad (25)$$

with

$$U_{b,\epsilon}(m,\ell) = e^{i\pi\frac{\epsilon\ell}{N_{\mathrm{UF}}}} \sum_{p=-\Delta}^{\Delta} \Big[(-1)^{p\epsilon} G_\ell(p) R_{b,\ell}(m-p) \times C_{b,0}(N_{\mathrm{UF}}(m-p)+\ell)\Big]. \quad (26)$$

It can be inferred from (25) that all the FBMC symbols in a block can be recovered by applying two IFFTs of size N_{UF} on $U_{b,\epsilon}$ for each allocated subcarrier. Furthermore, the multiplications by the equalizer and the filter coefficients in (26) are applied once per block and per subcarrier. Therefore, a significant complexity reduction is obtained. However, performance degradation is expected for high mobility.

To support different tradeoffs between complexity and mobility robustness, the equalizer coefficients can be approximated by a polynomial in n given by

$$\hat{C}_{b,n}(m) = \sum_{d=0}^{D} W_{b,d}(m)\, n^d, \quad (27)$$

where the coefficients $W_{b,d}(m)$ are parameters to be optimized and D is the degree of the polynomial. Thus, (25) becomes

$$Y_{b,2n+\epsilon}(m) = \sum_{d=0}^{D} n^d\, Y_{b,2n+\epsilon}(m,d), \quad (28)$$

where $Y_{b,2n+\epsilon}(m,d)$ is the AFB output employing $W_{b,d}(m)$ as equalizer coefficients. As a result, all the FBMC symbols can be recovered by applying $2(D+1)$ IFFTs of size N_{UF} and by applying the multiplications by the equalizer and the filter coefficients $D+1$ times per block and per subcarrier.

As an example, we now derive a possible approximation for $D = 2$. Without loss of generality, the N_s symbols in the block occupy positions $-B, -B+1, \ldots, B$, with $B = (N_s-1)/2$. The optimal coefficients in the least-squares sense can be found by minimizing

$$\sum_{n\in\mathcal{P}} \left| \hat{C}_{b,n}(m) - \frac{1}{H_n(m)} \right|^2 \quad (29)$$

for $\mathcal{P} = \{-B, -B+1, \ldots, B\}$. Simpler coefficients can be found instead by minimizing (29) for $\mathcal{P} = \{-\mathcal{B}, 0, \mathcal{B}\}$, $\mathcal{B}$ being the time index of the equalizer coefficient $\hat{C}_{b,\mathcal{B}}(m)$ considered in the simplified optimization function. Omitting the subcarrier index m, we obtain

$$W_{b,d} = \begin{cases} C_{b,0} & \text{if } d = 0, \\ \frac{1}{2\mathcal{B}}\Big(C_{b,\mathcal{B}} - C_{b,-\mathcal{B}}\Big) & \text{if } d = 1, \\ \frac{1}{2\mathcal{B}^2}\Big(C_{b,\mathcal{B}} - 2C_{b,0} + C_{b,-\mathcal{B}}\Big) & \text{if } d = 2. \end{cases}$$

When considering $D = 1$ and $\mathcal{P} = \{-\mathcal{B}, \mathcal{B}\}$, we obtain

$$W_{b,d} = \begin{cases} \frac{1}{2}\Big(C_{b,\mathcal{B}} + C_{b,-\mathcal{B}}\Big) & \text{if } d = 0, \\ \frac{1}{2\mathcal{B}}\Big(C_{b,\mathcal{B}} - C_{b,-\mathcal{B}}\Big) & \text{if } d = 1. \end{cases}$$

If $\mathcal{B}$ is chosen to be a power of 2, then $W_{b,d}(m)$ can be computed without using any multiplication.

It is worth noting that the type of equalizer applied to a group of subcarriers (a subband) can be adapted to the channel condition of this subband. Therefore, the equalizer stage adapted for Doppler spread can be applied to all users that are in a high-mobility situation, while the simplified equalizer stage ($D = 0$) can be used for low-mobility users.

E. Complexity Analysis

In this subsection, the computational complexity of the proposed OS-FBMC techniques employing short filters are compared to FS-FBMC using short and long filters in terms of number of required real-valued multiplications (RMs) to demodulate one FBMC symbol. We denote by $C_{\text{RM}}(x)$ the number of RMs required for the operation x. It is assumed that one complex multiplier (CM) requires $C_{\text{RM}}(CM) = 3$ RMs. For an IFFT of size N, a well known and efficient computation algorithm is the split radix IFFT [11]. Its computational complexity, referred to as $C_{\text{RM}}(\text{FFT}_N)$, is given by [12]

$$C_{\text{RM}}(\text{FFT}_N) = N\log_2(N) - 3N + 4\,.$$

For clarity, the following notation is adopted in this subsection:

- FS_1-FBMC and FS_4-FBMC respectively refer to the FS-FBMC receiver with the NPR1 and PHYDYAS PFs,
- $\text{OS}_{N_{\text{UF}}}$-FBMC refers to the OS-FBMC receiver with an up-sampling factor of N_{UF},
- OSB_{N_s}-FBMC refers to the OSB-FBMC receiver with a block composed of N_s FBMC symbols.
- $\text{OSB}_{N_s,D}$-FBMC refers to a OSB_{N_s}-FBMC receiver employing the degree D polynomial approximation proposed in Section III-D.

The analytical expressions of the complexity of the considered receivers are given in Table I. The complexity of the OFDM receiver is scaled to take into account that two FBMC symbols must be processed to recover the transmitted QAM symbols, whereas only one OFDM symbol is processed to recover the same amount of QAM symbols for the OFDM case. For the OSB-FBMC receiver, several multiplications can be avoided when processing the LPR term in (24). Indeed, when $\text{mod}_{N_{\text{UF}}/2}\Big(\ell(n+1)\Big) = 0$, we have $\exp[i(\pi\ell(n+1))/N_{\text{UF}}] \in \{-1, 1, i, -i\}$. Therefore, the required number of multiplications to compute this LPR is

$$C_{\text{RM}}(\text{LPR OSB}_{N_s}) = \frac{3N_c}{Ns}\sum_{(\ell,n)\in\Lambda}\left\lceil\frac{\text{mod}_{\frac{N_{\text{UF}}}{2}}\Big(\ell(n+1)\Big)}{N_{\text{UF}}}\right\rceil, \tag{30}$$

with $\Lambda = [\![0, N_{\text{UF}}-1]\!] \times [\![0, N_s-1]\!]$. Furthermore, it is shown in Section III-D that the complexity of the equalizer stage can be significantly reduced in the OSB-FBMC receiver through the polynomial approximation of degree D of the equalizer coefficients. In this case, $D+1$ equalizer and filter stages are required to compute all the FBMC symbols in the block. In (25), the multiplications by the LPR terms can efficiently computed using two IFFTs of size N_{UF}. In (26), the LPR term $\exp[i\pi l\epsilon/N_{\text{UF}}]$ holds $N_{\text{UF}} - 2$ non trivial values when $\epsilon = 1$. Therefore, the required number of multiplications to compute these LPRs is

$$\begin{aligned} C_{\text{RM}}(\text{LPR OSB}_{N_s,D}) =& (2C_{\text{RM}}(\text{FFT}_{N_{UF}}) + N_{UF} - 2) \\ &\times \frac{(D+1)N_{UF}N_c}{N_s}. \end{aligned} \tag{31}$$

In addition, the multiplications by the polynomial power terms n^d in (28), which can be counted as part of the filter stage, requires $D(B - \lfloor\log_2(B)\rfloor - 1)$ RMs per subcarrier. In fact, only bit-shift operations are required when n is a power of two, and only the real part of the AFB output has to be computed due to the OQAM scheme.

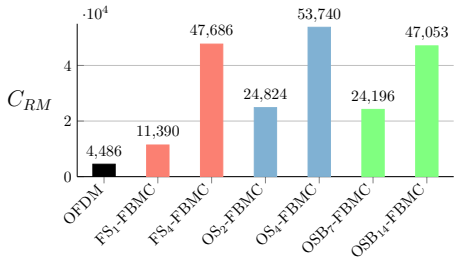

Fig. 3. Required number of real multiplications per processed FBMC symbol for each receiver.

Figure 3 shows the required number of real multiplications per processed FBMC symbol for each receiver. It is assumed that $M = 1024$, $N_c = 600$ and $\Delta = 3$. We see that the proposed OS_2-FBMC receiver has about half the complexity of the FS_4-FBMC receiver. Furthermore, the use of a short PF like NPR1 enables to also reduce the complexity at the transmitter side. The OS_4-FBMC receiver is 13% more complex than the FS_4-FBMC receiver, which can be explained by the slightly more complex filtering stage in the OS_4 receiver. However, this complexity increase concerns only the receiver and can be considered acceptable for the uplink MMC scenario.

While having the same N_{UF} value, the OSB_7-FBMC receiver has more than half (55%) the complexity of the OS_4-FBMC receiver. Even with higher N_{UF} value, the OSB_7-

TABLE I
NUMBER OF REAL MULTIPLICATIONS FOR EACH RECEIVER.

Receiver	FFT	Equalization	LPR	Filtering
OFDM	$C_{\mathrm{RM}}(FFT_M)/2$	$3N_c/2$	0	0
FS_1-FBMC	$C_{\mathrm{RM}}(FFT_M)$	$3N_c + 6\Delta$	0	$N_c(\Delta+1)$
FS_4-FBMC	$C_{\mathrm{RM}}(FFT_{4M})$	$12N_c + 18$	0	$6N_c$
$\mathrm{OS}_{N_{\mathrm{UF}}}$-FBMC	$C_{\mathrm{RM}}(FFT_N))$	$3N_{\mathrm{UF}}(N_c + 2\Delta)$	0	$N_{\mathrm{UF}}N_c(\Delta+1)$
OSB_{N_s}-FBMC	$C_{\mathrm{RM}}(FFT_N)/N_s$	$3N_{\mathrm{UF}}(N_c + 2\Delta)$	(30)	$N_{\mathrm{UF}}N_c(\Delta+1)$
$\mathrm{OSB}_{N_s,D}$-FBMC	$C_{\mathrm{RM}}(FFT_N)/N_s$	$3N_{\mathrm{UF}}(N_c + 2\Delta)\frac{D+1}{N_s}$	(31)	$\frac{N_c}{N_s}\Big(2N_{\mathrm{UF}}(\Delta+1)(D+1) + D(B - \lfloor \log_2(B) \rfloor - 1)\Big)$

FBMC receiver has about the same complexity as the OS_2-FBMC receiver and the OSB_{14}-FBMC receiver is 12% less complex than the OS_4-FBMC receiver. This complexity reduction can be explained by the fact than only one FFT of size N_{UF} is needed to process several FBMC symbols.

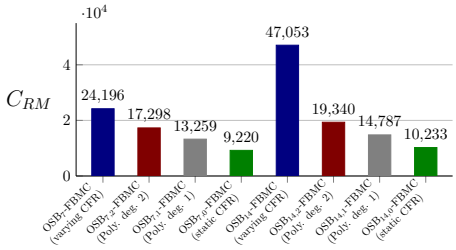

Fig. 4. Required number of real multiplications for the OSB-FBMC receivers using the polynomial approximation.

Furthermore, Figure 3 considers the OSB receivers without the proposed polynomial approximation. When considering this approximation, the complexity is significantly reduced, as shown in Figure 4. The OSB_{14} receiver greatly benefits from this approximation: the complexity with $D = 2$ is only 41% of the complexity of the original OSB_{14} receiver. With $D = 0$ (channel frequency response (CFR) considered constant in the FBMC block), the complexity of both the $\mathrm{OSB}_{7,0}$ and $\mathrm{OSB}_{14,0}$ is even lower than the complexity of the FS_1-FBMC receiver. It is expected that such approximation results in a marginal BER loss for channels having low Doppler frequencies. For high Doppler frequencies, BER degradation is expected at high E_b/N_o, and such performance impact will be evaluated in Section VI-A.

F. Latency Comparison

In a practical system, the transmission latency depends mainly on the frame duration rather than on the symbol duration, since a complete frame must be received before initiating the error-correction decoder. Furthermore, channel estimation techniques require to interpolate the CFR between two successive pilot symbols, which can be located in two successive frames.

As detailed in Section III-C, the spectral efficiency loss of different FBMC schemes depends on the number of FBMC symbols in a frame or block (N_s) and on the overlapping factor (q). To meet the same spectral efficiency loss requirement (for instance, 10%), an FBMC system with a PF having $q = 4$ requires a longer frame duration ($N_s = 63$) than a shorter PF ($N_s = 9$). It is worth noting that the latency of the OS-FBMC scheme is slightly larger than the latency of OSB-FBMC and FS_1-FBMC schemes. This is because with OS-FBMC, processing the last symbol in the frame requires $(N_{UF} - 1)M$ additional samples to be received.

IV. MIMO SUPPORT

A drawback of FBMC/OQAM systems when compared with OFDM systems is the difficulty of efficiently supporting MIMO schemes at low complexity. Particularly, the use of the popular Alamouti space-time code is more challenging than for OFDM because of the lack of orthogonality in the complex plane between neighboring OQAM symbols. In this section, we show how the 2×2 Alamouti scheme can be supported with a block FBMC receiver.

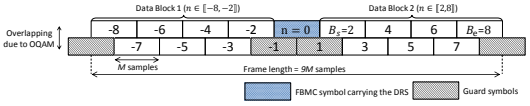

Fig. 5. Proposed frame structure for FBMC for $N_s = 7$.

To make the discussion more concrete, we consider a specific radio frame structure, illustrated in Figure 5, and assume that a short PF is used. The use of a short PF allows designing frame structures that occupy the same amount of radio resources as a 4G/LTE resource block (i.e. a bandwidth of 180 kHz and a duration of 0.5 ms). Some possible frame configurations are given in [13], with more details about the frame design. As shown in Figure 5, each frame contains two FBMC blocks. To simplify the notation in the remainder of this section, we let $n = 0$ be the index of the demodulation reference symbol in the middle of the frame. Furthermore, we use B_s and B_e to denote respectively the index of the first and last data symbol in the second block of the frame.

A. Block-Alamouti Scheme

The Alamouti space-time code is a well known diversity technique for systems with two transmit and two receive antennas. The code is usually formed over pairs of neighboring symbols, but the lack of orthogonality in the complex plane between neighboring OQAM symbols makes it challenging to directly use this coding approach with FBMC modulation. Instead, a *block-Alamouti* code can be used, which is formed by grouping symbols into two blocks and pairing the symbols in the first block with those in the second block [14]. A guard

interval is then inserted between the two blocks to preserve the orthogonality of all symbol pairs. This block-wise approach allows to isolate the symbol pairs with only a small impact on spectral efficiency, particularly when short PFs are used, since the length of the guard interval can then be limited to M samples.

In the block-Alamouti code, two blocks of FBMC symbols are transmitted using two antennas $n_T \in \{1,2\}$ and two block time slots $t_b \in \{1,2\}$. Since there are two FBMC blocks in the frame structure defined in Figure 5, the use of the block-Alamouti scheme is straightforward. The symbol indices $n \in [\![-B_e,-B_s]\!]$ correspond to the first block time slot, and $n \in [\![B_s,B_e]\!]$ to the second block time slot. Let $d_n^{(b_i)}(m) = \phi_n(m)a_n^{(b_i)}(m)$ be a sequence of FBMC information symbols indexed by $n \in [\![B_s,B_e]\!]$, with index $b_i \in \{1,2\}$ used to distinguish the two information blocks that form the block-Alamouti code. The code is formed by transmitting, in the first time slot $t_b = 1$, $d_{-n}^{(1)}$ on antenna 1 and $d_{-n}^{(2)}$ on antenna 2, and in the second time slot $t_b = 2$, $-(d_n^{(2)})^*$ on antenna 1 and $(d_n^{(1)})^*$ on antenna 2. We assume that the channel state information (CSI) is not available at the transmitter side and therefore no pre-equalization techniques are used. Since equalization is performed in the frequency domain, we consider the Alamouti-coded transmission in the frequency domain. We use $S^{(n_T)}(m)$ to refer to the frequency-domain vector (of size N) transmitted on antenna n_T. We denote the CFR associated with receive antenna n_R, transmit antenna n_T, and symbol position n by $H_n^{(n_R,n_T)}(m)$. Within each Alamouti time slot, we index the received vectors using the absolute value of the symbol position. We thus denote by $R_{n,\ell}^{(t,n_R)}(m)$ the frequency-domain received vector for time slot t_b, receive antenna n_R, and position $n \in [\![B_s,B_e]\!]$. This vector is defined similarly to (15), but first applying a time reversal to the time-domain received vector $r(k)$ when $t_b = 2$.

In the absence of additive noise and omitting the subcarrier index m, we can model the transmission as $\boldsymbol{R}_{n,\ell} = \boldsymbol{H}_n\boldsymbol{S}$, with $\boldsymbol{S} = [S^{(1)}S^{(2)}]^T$ and

$$\boldsymbol{R}_{n,\ell} = \begin{bmatrix} R_{n,\ell}^{(1,1)} \\ R_{n,\ell}^{(1,2)} \\ R_{n,\ell}^{(2,1)^*} \\ R_{n,\ell}^{(2,2)^*} \end{bmatrix}, \; \boldsymbol{H}_n = \begin{bmatrix} H_{-n}^{(1,1)} & H_{-n}^{(1,2)} \\ H_{-n}^{(2,1)} & H_{-n}^{(2,2)} \\ H_n^{(1,2)^*} & -H_n^{(1,1)^*} \\ H_n^{(2,2)^*} & -H_n^{(2,1)^*} \end{bmatrix}. \quad (32)$$

It is worth noting that the block-Alamouti scheme can also be used in the frequency dimension as proposed in [15]. In this case, groups of subcarriers must be defined. However, the main issue of this technique is that it assumes the channel frequency response is flat for two groups of subcarriers, which is not guaranteed for all the 4G/LTE channel models, especially if the group size is large. Furthermore, short PFs are less localized in frequency than the long PFs used in [16], and may require 1 or 2 additional guard-band subcarriers to suppress interference in successive groups of subcarriers, thus reducing the data rate. For these reasons, the space-time block code (STBC) technique is preferred for short PFs.

B. Constant-CFR Alamouti Equalizer

Typically, Alamouti equalization is performed by assuming that the channel response is the same for both symbols in the codeword, which simplifies the inversion of the channel matrix. In the case of the block-Alamouti code, this can be achieved by assuming that the CFR is constant over the entire Alamouti frame [14].

Let us denote by $\hat{H}^{(n_R,n_T)}$ the constant CFR approximation, and by $\hat{\boldsymbol{H}}$ the matrix obtained by substituting $H_n^{(n_R,n_T)}$ with $\hat{H}^{(n_R,n_T)}$ in $\boldsymbol{H}_n$. The matrix $\hat{\boldsymbol{H}}$ has the standard Alamouti form, and the zero-forcing equalizer, computed once per frame, is given by $\hat{\boldsymbol{H}}^+ = \frac{1}{\alpha}\hat{\boldsymbol{H}}^\dagger$, $\alpha = \sum_{n_R,n_T} |\hat{H}^{(n_R,n_T)}|^2$.

Given a frame structure, we can derive the optimal CFR approximation. Assuming that the CFR at each position n is obtained using linear interpolation, the CFR corresponding to the frame structure presented in Figure 5 would take the form

$$H_n^{(n_R,n_T)}(m) = \begin{cases} P_1^{(n_R,n_T)}(m)\, n + H_o^{(n_R,n_T)}(m), & n < 0, \\ P_2^{(n_R,n_T)}(m)\, n + H_o^{(n_R,n_T)}(m), & n \geq 0, \end{cases} \quad (33)$$

where H_o corresponds to the CFR in the current frame, P_1 is the slope of the linear interpolation between the current and previous CFRs, P_2 is the slope of the interpolation between the current and next CFRs. Dropping the subcarrier index m for clarity, the corresponding least-squares constant CFR approximation can be obtained by minimizing

$$\sum_{n=B_s}^{B_e} \left| \hat{H}^{(n_R,n_T)} + P_1^{(n_R,n_T)} n - H_o^{(n_R,n_T)} \right|^2 + \left| \hat{H}^{(n_R,n_T)} - P_2^{(n_R,n_T)} n - H_o^{(n_R,n_T)} \right|^2,$$

which yields

$$\hat{H}^{(n_R,n_T)} = H_o^{(n_R,n_T)} + \tfrac{1}{4}(B_s + B_e)(P_2^{(n_R,n_T)} - P_1^{(n_R,n_T)}). \quad (34)$$

When using an OSB receiver, this CFR approximation is used to obtain the Alamouti pseudo-inverse $\hat{\boldsymbol{H}}^+$, and the frequency-domain equalized vectors corresponding to each Alamouti block are then given by

$$\begin{bmatrix} X_{b,\ell}^{(1)}(m) \\ X_{b,\ell}^{(2)}(m) \end{bmatrix} = \hat{\boldsymbol{H}}^+(N_{\text{UF}}m + \ell)\, \boldsymbol{R}_{b,\ell}(m), \quad (35)$$

where $\boldsymbol{R}_{b,\ell}(m)$ is obtained by substituting $R_{n,\ell}^{(n_R,n_T)}$ with $R_{b,\ell}^{(n_R,n_T)}$ in $\boldsymbol{R}_{n,\ell}$, and $R_{b,\ell}^{(n_R,n_T)}$ is defined similarly to (23). For each $X_{b,\ell}^{(i)}$, the receiver is completed by evaluating (25).

C. Varying-CFR Alamouti Equalizer

In the presence of high mobility, the assumption that the CFR remains constant for the duration of two symbol blocks becomes unsuitable. In that case, the equalization can be improved by deriving a zero-forcing equalizer that takes the channel variation into account. For a given pair of symbols at positions n and $-n$, the channel matrix $\boldsymbol{H}_n$ takes the form in (32). The zero-forcing equalizer is obtained by taking the pseudo-inverse of $\boldsymbol{H}_n$, yielding

$$\boldsymbol{H}_n^+ = \left(\boldsymbol{H}_n^\dagger \boldsymbol{H}_n\right)^{-1} \boldsymbol{H}_n^\dagger = \frac{1}{ab - |c|^2} \begin{bmatrix} b & -c \\ -c^* & a \end{bmatrix} \boldsymbol{H}_n^\dagger, \quad (36)$$

where

$$a = |H_{-n}^{(1,1)}|^2 + |H_{-n}^{(2,1)}|^2 + |H_{n}^{(1,2)}|^2 + |H_{n}^{(2,2)}|^2$$
$$b = |H_{n}^{(1,1)}|^2 + |H_{n}^{(2,1)}|^2 + |H_{-n}^{(1,2)}|^2 + |H_{-n}^{(2,2)}|^2$$
$$c = H_{-n}^{(1,1)^*} H_{-n}^{(1,2)} + H_{-n}^{(2,1)^*} H_{-n}^{(2,2)} - \left(H_{n}^{(1,1)^*} H_{n}^{1,2} + H_{n}^{(2,1)^*} H_{n}^{(2,2)} \right) .$$

Computing (36) for each symbol would make the equalizer relatively complex. However, if we consider that the CFR takes the linear form

$$H_n^{(n_R,n_T)}(m) \approx \bar{P}^{(n_R,n_T)}(m)\, n + \bar{H}_o^{(n_R,n_T)}(m)\,, \quad (37)$$

the computation can be simplified by equalizing all the symbols in the frame jointly. In practice, the estimated CFRs at each pilot position within the frame are interpolated to obtain the CFRs for all the subcarriers and symbols. In such case, (37) simply corresponds to the CFR obtained through linear interpolation along the time axis. The linear interpolation is far from being optimal, but has the advantage of being simple, limiting the memory usage and the latency. Note that if we start with the linear interpolation given by (33), we must first convert the linear coefficients into the form of (37) using the least-squares approximation

$$\bar{P}^{(n_R,n_T)} = \tfrac{1}{2}(P_1^{(n_R,n_T)} + P_2^{(n_R,n_T)})\,,$$
$$\bar{H}_o^{(n_R,n_T)} = H_o^{(n_R,n_T)} + \tfrac{1}{4}(B_s + B_e)(P_2^{(n_R,n_T)} - P_1^{(n_R,n_T)})\,.$$

Using (37), we can express the channel model as $\boldsymbol{H}_n = \bar{\boldsymbol{P}} n + \bar{\boldsymbol{H}}_{\boldsymbol{o}}$, with

$$\bar{\boldsymbol{P}} = \begin{bmatrix} \bar{P}^{1,1} & \bar{P}^{1,2} \\ \bar{P}^{2,1} & \bar{P}^{2,2} \\ -(\bar{P}^{1,2})^* & (\bar{P}^{1,1})^* \\ -(\bar{P}^{2,2})^* & (\bar{P}^{2,1})^* \end{bmatrix}, \quad \bar{\boldsymbol{H}}_{\boldsymbol{o}} = \begin{bmatrix} \bar{H}_o^{(1,1)} & \bar{H}_o^{(1,2)} \\ \bar{H}_o^{(2,1)} & \bar{H}_o^{(2,2)} \\ (\bar{H}_o^{(1,2)})^* & -(\bar{H}_o^{(1,1)})^* \\ (\bar{H}_o^{(2,2)})^* & -(\bar{H}_o^{(2,1)})^* \end{bmatrix}$$

Let us first define $\sigma_P \triangleq \sum_{i,j} |\bar{P}^{(n_R,n_T)}|^2$, $\sigma_H \triangleq \sum_{i,j} |\bar{H}_o^{(n_R,n_T)}|^2$,

$$\alpha \triangleq \mathcal{R}\Big(\bar{P}^{(1,1)}(\bar{H}_o^{(1,1)})^* + \bar{P}^{(2,1)}(\bar{H}_o^{(2,1)})^* - \bar{P}^{(1,2)}(\bar{H}_o^{(1,2)})^* - \bar{P}^{(2,2)}(\bar{H}_o^{(2,2)})^* \Big)\,,$$
$$\beta \triangleq (\bar{P}^{(1,1)})^* \bar{H}_o^{(1,2)} + \bar{P}^{(1,2)}(\bar{H}_o^{(1,1)})^* + (\bar{P}^{(2,1)})^* \bar{H}_o^{(2,2)} + \bar{P}^{(2,2)}(\bar{H}_o^{(2,1)})^*\,,$$
$$\Gamma \triangleq \begin{bmatrix} -\alpha & -\beta \\ -\beta^* & \alpha \end{bmatrix}.$$

By developing the pseudo-inverse equation in (36), we obtain

$$\boldsymbol{H}_n^+ = \frac{W^{(1)} + W^{(2)} n + W^{(3)} n^2 + W^{(4)} n^3}{\sigma_H^2 - (4\alpha^2 + 4|\beta|^2 - 2\sigma_P\sigma_H)\, n^2 + \sigma_P^2 n^4}\,, \quad (38)$$

where

$$W^{(1)} = \sigma_H \bar{\boldsymbol{H}}_{\boldsymbol{o}}^\dagger \qquad W^{(2)} = \sigma_H \bar{\boldsymbol{P}}^\dagger + 2\Gamma \bar{\boldsymbol{H}}_{\boldsymbol{o}}^\dagger$$
$$W^{(3)} = 2\Gamma \bar{\boldsymbol{P}}^\dagger + \sigma_P \bar{\boldsymbol{H}}_{\boldsymbol{o}}^\dagger \qquad W^{(4)} = \sigma_P \bar{\boldsymbol{P}}^\dagger .$$

To perform the equalization efficiently in an OSB receiver, we can distribute the multiplication of $\boldsymbol{H}_n^+$ with $R_{b,\ell}(m)$ over the numerator. We first define $\boldsymbol{R}_P \triangleq \bar{\boldsymbol{P}}^\dagger \boldsymbol{R}_{b,\ell}$ and $\boldsymbol{R}_H \triangleq \bar{\boldsymbol{H}}_{\boldsymbol{o}}^\dagger \boldsymbol{R}_{b,\ell}$. We then have

$$W^{(1)}\boldsymbol{R}_{b,\ell} = \sigma_H \boldsymbol{R}_H \qquad W^{(2)}\boldsymbol{R}_{b,\ell} = \sigma_H \boldsymbol{R}_P + 2\Gamma \boldsymbol{R}_H$$
$$W^{(3)}\boldsymbol{R}_{b,\ell} = 2\Gamma \boldsymbol{R}_P + \sigma_P \boldsymbol{R}_H \qquad W^{(4)}\boldsymbol{R}_{b,\ell} = \sigma_P \boldsymbol{R}_P\,.$$

Note that $\boldsymbol{R}_P$ and $\boldsymbol{R}_H$ are length-2 vectors, and therefore the approach above reduces computational complexity compared to evaluating the coefficients and then performing the multiplication with $\boldsymbol{R}_{b,\ell}$. Finally, we obtain $[X_{b,n,\ell}^{(1)} X_{b,n,\ell}^{(2)}]^T$ by evaluating the numerator and denominator polynomials of $\boldsymbol{H}_n^+ \boldsymbol{R}_{b,\ell}$ at each symbol position $n \in [\![B_s, B_e]\!]$, and applying the phase rotation $e^{i\frac{\pi m n}{q}} e^{i\frac{\pi \ell (n+q)}{q N_{\mathrm{UF}}}}$ (as in (24)). For a given frame structure, this computation consists of constant multiplications by small integers, which have simple hardware implementations. The receiver processing is then completed by using (21) for each $X_{b,n,\ell}^{(i)}$.

TABLE II
PER-SUBCARRIER COMPUTATIONAL COMPLEXITY OF PROPOSED METHOD

Expression	Real multiplications
σ_H, σ_P	8×2
α, β	$8 + 12$
$\sigma_H \boldsymbol{R}_H, \sigma_P \boldsymbol{R}_P, \sigma_H \boldsymbol{R}_P, \sigma_P \boldsymbol{R}_H$	$24 \times 2 + 4 \times 4$
$\Gamma \boldsymbol{R}_P$, $\Gamma \boldsymbol{R}_H$	10×2
$\alpha^2, \sigma_H^2, \sigma_P^2, \sigma_H\sigma_P, \lvert\beta\rvert^2$	$1 \times 4 + 2$
$\times n, n^2, n^3, n^4$	$2(B - \lfloor \log_2(B) \rfloor - 1) \times 5$
$\times \frac{1}{\sigma_H^2 - (4\alpha^2 + 4\lvert\beta\rvert^2 - 2\sigma_P\sigma_H) n^2 + \sigma_P^2 n^4}$	$4(2B+1)^*$
Total	164 per subcarrier for $B = 3$

* Counting divisions as multiplications.

D. Complexity Analysis

In this subsection, the computational complexity of the different block-Alamouti techniques are compared in terms of number of required real-valued multiplications (RMs) to demodulate one FBMC symbol. The same notation and hypothesis as detailed in Section III-E regarding the complexity analysis will be considered.

The typical block-Alamouti scheme consider that the CFR does not vary in time over 2 successive FBMC blocks. In this case, only $\boldsymbol{R}_H/\sigma_H$ has to be computed, requiring 36 RMs per subcarrier. For time-varying CFRs, the expression (36) must be considered, requiring 81 RMs per subcarrier and per FBMC symbol. Assuming $N_s = 7$ ($B = 3$), this equalizer stage requires 567 RMs per subcarrier, which is 14.75 times more complex than the typical block-Alamouti scheme. To reduce this complexity, the simplified equalizer stage proposed in the previous section can be employed, where the per-subcarrier computational complexity analysis is detailed in Table II. It is shown that, for $N_s = 7$, only 164 RMs per subcarrier are required. Therefore, the complexity is divided by 3.46 when compared to a direct computation of (36).

This large complexity reduction can be explained by the fact that the number of 2×4 matrix multiplications to process is kept unvaried in our proposed method ($\boldsymbol{R}_P$ and $\boldsymbol{R}_H$), whereas it depends on N_s for the expression (36). In addition, the terms depending on the FBMC symbol index are simple to compute and are processed on length-2 vectors, greatly limiting the complexity.

V. PERFORMANCE UNDER TIMING OFFSETS

In this section, the performance of FS-FBMC and OS-based receivers using the NPR1 short PF is evaluated in the presence of timing offsets, for SISO transmissions. The results are compared with OFDM, and with an FS-FBMC receiver using the PHYDYAS PF ($q = 4$) [1], [2]. The notation introduced in Section III-E is considered in this section too.

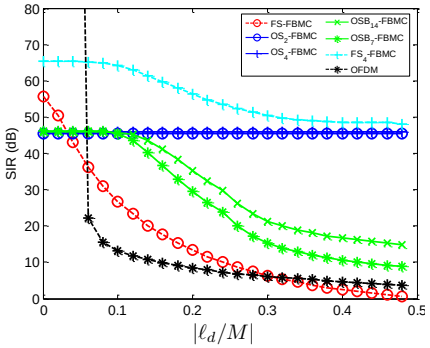

Fig. 6. Timing offset evaluation in terms of SIR for different FBMC receivers.

Timing offset impairments occur when the processing window of the receiver is not aligned in time with the transmitted signal. In an uplink mobile broadband scenario, the signals transmitted by each device are summed in the time domain at the base station receiver. Because the propagation delays vary for each user, different timing offset occurs for each signal when the synchronization is relaxed. To limit the complexity of the receiver, the timing offset must be compensated in the frequency domain. The equalizer coefficients are then set to $C_{\text{TO}}(m) = \exp[-i2\pi\ell_d m/N']$, where ℓ_d is the timing offset in number of samples and $N' = M$ for OFDM, $N' = qM$ for the FS-FBMC receivers and $N' = qN_{\text{UF}}M$ for the OS-based FBMC receivers. It is assumed that the ℓ_d is perfectly known. In a real system, data-aided techniques such as [17] can be employed to estimate ℓ_d. The frequency response of the NPR1 PF is truncated down to 7 coefficients ($\Delta = 3$) for the convolution operations. For the OFDM case, the CP length L_{CP} is set to 7% of the symbol duration, as in 4G. Furthermore, the receiver is considered perfectly time-aligned when the first sample processed by the FFT is the sample located at the middle of the CP length L_{CP}, so that both positive and negative timing offset values can be supported.

Figure 6 shows the SIR obtained by simulating the effect of the timing offset on the receivers. The FS_1-FBMC receiver is outperformed by all the other FBMC receivers when $|\ell_d/M| \geq 4\%$. For a SIR target of 30 dB, the FS_1-FBMC receiver can tolerate a timing offset of up to 8%, while the OSB_{14}-FBMC can reach 21% and the OSB_7-FBMC receiver 19%. Furthermore, the OS_2-FBMC and the FS_4-FBMC receivers can support any timing offset values, making them adequate for asynchronous communication.

Concerning the OSB-FBMC receivers, the SIR achieves a constant value up to a timing offset of 13% of the symbol duration, showing that the interference introduced is limited. For larger timing offset values, the SIR gradually decreases, showing that it is not as robust as the OS_2-FBMC receiver. Note that the OSB_{14}-FBMC receiver is more robust than the OSB_7-FBMC receiver for large timing offset values ($> 13\%$). This implies that the block size has an impact on the robustness against timing offset. Finally, OFDM is free from any interference when $|\ell_d| < L_{CP}/2$, but it is clearly outperformed by any FBMC receiver for larger timing offset values. The rest of this section provides an analytical study of the effect of timing offsets on the FBMC receivers.

A. OS-FBMC receivers

As shown in Figure 6, the OS_2-FBMC and OS_4-FBMC receivers are insensitive to timing offset impairments. In fact, this statement can be generalized for any $N_{\text{UF}} \geq 2$ and any PF. The particular case of $N_{\text{UF}} = 1$ corresponds to the case of the typical FS-FBMC receiver, which remains sensitive to timing offsets, even when using the PHYDYAS PF, as shown in Figure 6.

The time-domain OS equalizer presented in Section III-A combined with a time shift of ℓ_d samples can be equivalently seen as an OS equalizer having its ℓ_0 value replaced by $\ell_0' = \ell_0 - \ell_d$. The target FBMC symbol remains inside the FFT window of size N if $\ell_0 > \ell_d$ when ℓ_d has a positive value and if $\ell_0 - N < \ell_d$ when ℓ_d has a negative value. As defined in Section III-A, we have $\ell_0 = (N_{\text{UF}} - 1)qM/2$. Since $N_{\text{UF}} \geq 1$ and $q \geq 0$ are both integers, we have $\ell_0 \geq M/2$. In addition, we also have $\ell_0 - N = -\ell_0$. Therefore, the timing offset can be perfectly compensated if $-M/2 < \ell_d < M/2$. Furthermore, timing offsets larger than $M/2$ samples can also be perfectly compensated since this value is superior to the OQAM delay. Therefore, the data can be recovered at the next ($\ell_d > 0$) or the previous ($\ell_d < 0$) FBMC symbol.

B. OSB-FBMC receivers

For the OSB receiver, the interference is only introduced at the first and last FBMC symbol in the block if $|\ell_d| < M/2$. Indeed, the OSB-FBMC receiver can be seen as a special case of the OS-FBMC receiver, for which the FFT processes the same set of input samples r for each FBMC symbol within a given block. The first sample of the FBMC symbol number n is expected to be located at $r(nM/2)$. As demonstrated above, if $|\ell_d| < M/2$, then the timing offset does not introduce any interference for FBMC symbol indexes $n \in [\![1, N_s - 1]\!]$. When $n = 0$ and assuming $0 < \ell_d < M/2$, (19) becomes

$$\begin{aligned} X_{b,0}(m) &= C_{TO}(m) \sum_{k=0}^{N-1} \Pi_{L_B}(k) r_b(k+\ell_d) e^{-i\frac{2\pi km}{N}} \\ &= \sum_{k=0}^{N-1} \Big[\Big(1 - \Pi_{\ell_d}(k) - \Pi_{L_{ZP}-\ell_d}(k - L_B - \ell_d)\Big) r_b(k) \\ &\quad + \underbrace{\Pi_{\ell_d - L_{ZP}}(k) r_b(k+N)}_{\text{Interference term from the next block}} \Big] e^{-i\frac{2\pi km}{N}} \end{aligned} \tag{39}$$

where $\Pi_x(k)$ is the rectangular window of length x defined as:

$$\Pi_x(k) = \begin{cases} k, & k < x \text{ and } x > 0, \\ 0, & k \geq x \text{ or } x \leq 0\,. \end{cases}$$

First, let us consider that $L_B = N$ ($L_{ZP} = 0$). In this case, $\Pi_{L_{ZP}-\ell_d}(k) = 0$ in (39) for any k values. Then, after applying the FFT of size N on $X_{b,0}(m)$, (20) becomes, for $k \in [\![0, L_B - 1]\!]$ and $n = 0$:

$$x_{b,0}(k) = r_b(k) + \underbrace{\Pi_{\ell_d}(k)\Big(r_b(k+N) - r_b(k)\Big)}_{\text{interfering signal}}, \qquad (40)$$

Note that $\Pi_{\ell_d}(k) r_b(k+N) = \Pi_{\ell_d}(k) r_{b+1}(k)$, since this term corresponds to the first ℓ_d samples of the next transmitted block (indexed $b+1$) containing the first FBMC symbol of block $b+1$. When the received signal is zero-padded, the lowest value of L_{ZP} to ensure the use of a power of 2 FFT size is $M/2$ because L_B is a multiple of $M/2$ (and so is $N - L_B$). Therefore, we have $L_{ZP} > \ell_d$ and $\Pi_{\ell_d - L_{ZP}}(k) = 0$ in (39). Therefore (40) can be rewritten as follows when the received signal is zero-padded:

$$x_{b,0}(k) = r_b(k)\Big(1 - \Pi_{\ell_d}(k) + \underbrace{\Pi_{L_{ZP}-\ell_d}(k - (L_B + \ell_d))}_{=0 \text{ since } k < L_B}\Big),$$

It is interesting to note that the next FBMC block does not generate any interference when the received signal is zero-padded. Therefore, it is expected that the introduction of a zero-padding may improve the robustness of the receiver against timing offsets. To simplify the following development, (40) can be rewritten as follows:

$$x_{b,0}(k) = r_b(k) + \underbrace{\Pi_{\ell_d}(k)\Big(\gamma r_b(k+N) - r_b(k)\Big)}_{\triangleq j_b(k)}, \qquad (41)$$

where $j_b(k)$ represents the interfering signal in time domain, and γ identifies the presence or the absence of the zero-padding operation: $\gamma = 1$ if $L_{ZP} = 0$, else $\gamma = 0$. Assuming that $a_{b,0}(m)$ is the transmitted PAM symbol at the first FBMC symbol of the block number b, $j_b(k)$ can be rewritten as

$$j_b(k) = \Pi_{\ell_d}(k) g(k) \sum_{m=0}^{M-1} \phi_0(m)\Big(\gamma a_{b+1,0}(m) - a_{b,0}(m)\Big) e^{i\frac{2\pi km}{N}}.$$

At the output of the AFB and the OQAM demapper, the interference term $J_b(m)$ becomes

$$\begin{aligned} J_b(m) &= \Re\left[\phi_0^*(m) \sum_{k=0}^{M-1} g(k) j_b(k) e^{-i\frac{2\pi km}{N}}\right] \\ &= \Re\left[\phi_0^*(m) \sum_{p=-\frac{M}{2}}^{\frac{M}{2}-1} \Big(F_{g,ld}(p)\phi_0(m-p) \right. \\ &\quad \left. \times \Big(\gamma a_{b+1,0}(m-p) - a_{b,0}(m-p)\Big)\Big)\right], \end{aligned}$$

with

$$F_{g,ld}(p) = \sum_{k=0}^{\ell_d - 1} g^2(k) e^{-i\frac{2\pi km}{N}}.$$

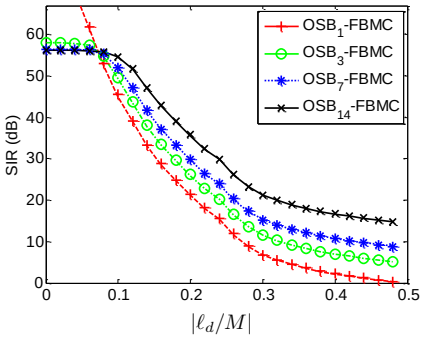

Fig. 7. OSB-FBMC: evaluation of the SIR for different block sizes.

It is worth noting that the above expression is obtained by considering that the effect of the filter coefficient truncation is negligible. Indeed, the interference term introduced by the timing offset is normally affected by this truncation. Finally, the recovered PAM symbol of block b and FBMC symbol $n \in [\![0, N_s - 1]\!]$ is expressed as

$$\hat{a}_{b,n}(m) \approx a_{b,n}(m) + e_{b,n}(m) + J_b(m)\delta(n)\,,$$

where $e_{b,n}(m)$ is the interference introduced by the filter coefficient truncation when $\ell_d = 0$, and δ is the Dirac function ($\delta(0) = 1$, else 0). If $a_n(m)$ are independent and identically distributed random variables of mean $\mathbb{E}(a_{b,n}(m)) = 0$ and of variance σ_a^2, $\mathbb{E}(x)$ being the mathematical expectation of the random variable x, then the SIR can be expressed as

$$\begin{aligned} \text{SIR}_{\text{OSB}}(\ell_d) &\approx \frac{\mathbb{E}\Big(a_{b,n}^2(m)\Big)}{\frac{1}{N_s}\sum_{n=0}^{N_s-1} \mathbb{E}\Big(\Big(a_{b,n}(m) - \hat{a}_{b,n}(m)\Big)^2\Big)} \\ &\approx \frac{\sigma_a^2}{\mathbb{E}\Big(e_{b,n}^2(m)\Big) + \frac{1}{N_s}\mathbb{E}\Big(j_b^2(m)\Big)}\,, \end{aligned} \qquad (42)$$

with

$$\mathbb{E}\Big(j_b^2(m)\Big) = 2^\gamma \sigma_a^2 \sum_{p=-\frac{M}{2}}^{\frac{M}{2}-1} \Re\Big(i^{-p} F_{g,ld}(p)\Big)^2.$$

The same SIR expression is obtained when $-M/2 < \ell_d < 0$. Figure 7 shows the SIR obtained by evaluating (42) and by simulation for different block sizes. As expected, higher robustness against timing offset is achieved when the block size is increased. Particularly, for large timing offset values, doubling the block size increases the SIR by 3 dB. It is also interesting to note that the zero-padding operation can asymptotically increase the SIR by 3 dB.

C. FS-FBMC receivers

The highest SIR values are obtained with the PHYDYAS PF using a typical FS-FBMC receiver. In this case, the SIR does not fall below 53 dB (at $\ell_d/M = 25$ %). This high

robustness against timing offset can be explained by examining the analytical SIR expression found in [18]:

$$\mathrm{SIR}_{\mathrm{PHY}}(\ell_d) = \frac{1}{3\times 10^{-7} + \frac{1}{8M}\sum_{l=0}^{\ell_d-1} g_{\mathrm{PHY}}^2(l)}, \qquad (43)$$

where g_{PHY} is the impulse response of the PHYDYAS PF. Due to its near-perfect reconstruction nature, this filter introduces a residual interference level of $10\cdot\log_{10}(\mathrm{SIR}_{\mathrm{PHY}}(0)) \approx 65$ dB. The interference level introduced by the timing offset is determined by the term $\sum_{l=0}^{\ell_d-1} g_{\mathrm{PHY}}^2(l)$ in (43). Since the power level of the PHYDYAS impulse response is almost null at its first $M/2$ samples, the interference is therefore limited. This also explains why there is such a performance gap between the NPR1 and the PHYDYAS PF when using the FS-FBMC receiver.

To outperform the PHYDYAS PF with FS-FBMC, we have observed that the OS-FBMC with NPR1 PF requires at least 21 filter coefficients ($\Delta = 10$), for a resulting SIR level of 65 dB. The complexity is however greatly increased. Furthermore, when hardware implementation is considered, quantization errors are introduced. Other channel impairments such as CFOs and imperfect channel estimation also greatly reduce the SIR. In the 4G standard, an error vector magnitude (EVM) of 3.5% is tolerated [19], corresponding to a SIR of ≈ 30 dB for the highest constellation order (256-QAM). Therefore, the proposed OS-FBMC still has a SIR margin of 15 dB when $\Delta = 3$ is chosen.

VI. PERFORMANCE ON MULTIPATH CHANNELS

To evaluate the robustness against multipath channels with Doppler spread, three multipath fading channel models, corresponding to the typical ones proposed in LTE, are considered [19]:

- Extended pedestrian A (EPA) model: $\tau = 410$ ns, $\mu = 5$ Hz,
- Extended vehicular A (EVA) model: $\tau = 2510$ ns, $\mu = 70$ Hz,
- Extended Typical Urban (ETU) model: $\tau = 5000$ ns, $\mu = 300$ Hz,

where τ corresponds to the delay spread of the multipath channel and μ is the Doppler spread frequency. The delay and power profiles of each channel model are detailed in [19].

A. Single-input/output case

To compensate the effect of the channel (in SISO case), the equalizer coefficients are set to $C_{\mathrm{n}}(m) = 1/(\sum_{l=0}^{N'-1} h_{\mathrm{idx}(n)}(l)\exp[-i2\pi kl/N'])$, where $\mathrm{idx}(n)$ is the sample index corresponding to the middle of the OFDM or FBMC symbol number n.

Figure 8 shows the uncoded BER in the presence of additive white Gaussian noise (AWGN) for the three considered channel models, assuming that the channel is known perfectly when a pilot symbol is available. In practice, the CSI can be estimated from the received block-type pilots [4]. These results are obtained by simulation, with the channels generated by the `comm.RayleighChannel` function of MATLAB's Communications System Toolbox. The 5 MHz bandwidth

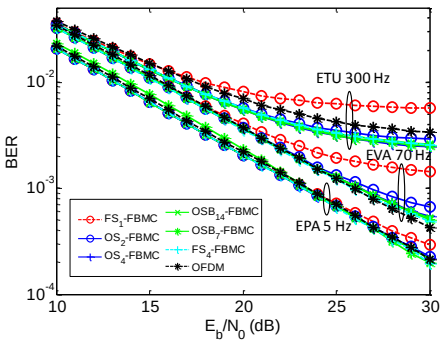

Fig. 8. BER evaluation of each receiver for different SISO channel models.

configuration of 4G/LTE is used for all waveforms, with 300 allocated subcarriers and a 16-QAM constellation. In the figure, the receivers are identified using the same notation as used in Section III-E.

The results for the EPA 5 Hz channel are presented in Figure 8. Similar BER levels are obtained for the OFDM, the OS_4-FBMC, the OSB-FBMC and the FS_4-FBMC receivers. The OS_2-FBMC performs slightly worse than the other OS-based configurations, while the FS_1-FBMC receiver offers the worst BER performance when we have $E_b/N_0 > 25$ dB. Similar observations can be made for the EVA 70 Hz channel model, presented in the same Figure 8. In this case, the OS_4-FBMC, FS_4-FBMC and the OSB-based FBMC receivers have a slight performance degradation at high E_b/N_0 values (> 25 dB) when compared to OFDM.

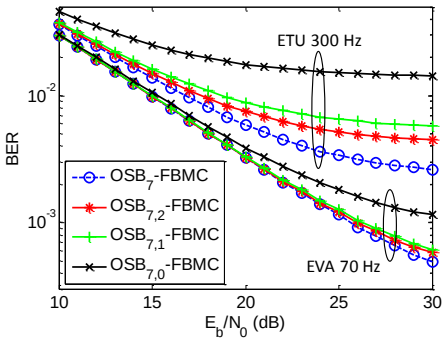

Fig. 9. BER evaluation of the OSB_7-FBMC receiver with different polynomial degrees and channel models.

For the ETU 300 Hz channel model case, the FS_1-FBMC is again outperformed by the other receivers. At $E_b/N_0 = 30$ dB, it exhibits a BER that is almost twice that of OFDM. However, all the proposed receivers achieve a lower BER than OFDM, demonstrating the high robustness of FBMC against doubly dispersive channels. It is worth noting that the delay spread (5 µs) of the channel is slightly larger than the CP duration (4.7 µs). Although this represents only a difference of 6%,

it is sufficient to increase OFDM's error floor compared to the proposed OS-FBMC receivers, which do not rely on any CP. Among the proposed receivers, the OS_2-FBMC receiver has the worst BER, while the OS_4 and OSB FBMC receivers achieve a BER similar to the FS_4-FBMC receiver. This shows that receivers with short PFs can achieve similar robustness against doubly dispersive channels compared to long PFs such as PHYDYAS.

To reduce the complexity, the polynomial approximation proposed in Section III-D can be employed for the OSB-FBMC receivers. Figure 9 shows the BER performance of the $OSB_{7,D}$-FBMC receivers using different polynomial degree D for the EVA 70 Hz and ETU 300 Hz channel models. We set $\mathcal{B} = 2$ for $D = 1$ and $\mathcal{B} = 3$ for $D = 2$ since the best BER performances are obtained when these values are considered. When $D = 0$, the BER is highly degraded for both EVA and ETU channel models. Particularly, the BER is degraded for all the E_b/N_0 values presented in Figure 9 for the ETU channel. For the EVA channel, acceptable performance are obtained for $D = 1$ and $D = 2$, with a slight error floor increase at high E_b/N_0 values (> 25 dB) when compared to the baseline OSB_7 receiver. When considering the ETU channel, the error floor for the $D = 2$ case is almost two times higher than the baseline OSB_7-FBMC receiver. However, acceptable BER performance is obtained at low E_b/N_0 values (< 15 dB). In any case, the degree 2 approximation provides the closest BER performance to the baseline receiver.

B. 2×2 MIMO Alamouti case

This subsection compares MIMO OFDM and MIMO FBMC systems with a numerology and a frame structure similar to that specified in 4G/5G standards. The two systems transmit frames of a duration of 0.5 ms and a RB bandwidth of 180 kHz. To support the MIMO Alamouti case with FBMC, the frame structure presented in Figure 5 is considered. This frame consists of 2 blocks, each composed of $N_s = 7$ FBMC symbols. Between each block, a FBMC pilot symbol is inserted corresponding to a Demodulation Reference Signal (DRS). It is assumed that the CFR is perfectly estimated at each DRS position. The CFR at the other symbol positions are obtained through linear interpolation. System parameters are chosen to be compliant with the OFDM frame format in LTE, with a frame duration of 0.5 ms and a RB bandwidth of 180 kHz. Therefore, the nunber of subcarriers per ressource block is set to 10, with a sampling frequency of 9.216 MHz and 18 kHz subcarrier spacing. This configuration has almost the same data rate as OFDM in 4G/LTE. Compared to 4G/LTE, the symbol duration is reduced by 20% and the subcarrier spacing is increased by the same amount. Transmitted data is modulated in 16-QAM over the entire band of 25 RBs. The simulated MIMO channel model is the low correlation model defined in the 3GPP standard [19].

For MIMO transmissions, the OFDM system implements the Alamouti code in the frequency domain, as prescribed in the 4G/LTE standard. Each Alamouti-coded symbol pair is equalized using the average channel response over the pair. For the FBMC receiver, the constant-CFR Alamouti equalizer presented in Section IV-B and the varying-CFR Alamouti equalizer proposed in Section IV-C are considered. The BER results are shown in Figure 10 for the EPA, EVA and ETU channel models. For FBMC systems, the proposed varying-CFR Alamouti equalizer outperforms the constant-CFR equalizer for all channel models, confirming its superiority. For the constant-CFR equalizer, no BER degradation is observed when considering the EPA channel model, as the Doppler spread is relatively low in this case (5 Hz). A slight BER degradation is observed for the EVA channel model (70 Hz), that becomes significant when the ETU channel model (300 Hz) is considered. This demonstrates the benefit of using the proposed varying-CFR Alamouti equalizer in such cases.

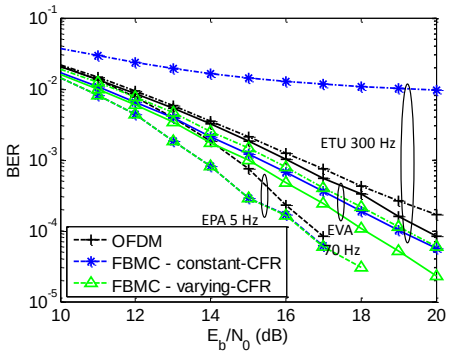

Fig. 10. BER evaluation of the FBMC receivers with different MIMO equalizers for the EPA, EVA and ETU channel models.

VII. CONCLUSION

This article proposed a new FBMC receiver based on the Overlap-Save algorithm. The obtained results related to robustness, complexity, latency and MIMO support are qualitatively summarized in Table III. One of the most remarkable features of this receiver is its support of asynchronous communications with short filters, demonstrated both by analytical studies and by simulations. Furthermore, it achieves a lower BER than OFDM for the ETU channel model and a comparable BER for the EPA and EVA channel models. However, the computational complexity is noticeably increased when compared to a typical FS or PPN FBMC receiver. Therefore, an alternative OSB-FBMC receiver is proposed, were several FBMC symbols are processed in blocks. This allows to keep the complexity similar to the FS-FBMC receiver for channels having low Doppler spread. For high Doppler spread channels, the equalizer stage can be decomposed into a polynomial form, allowing a trade-off between BER performance and complexity. Analytical and simulation studies show that increasing the block length improves the robustness against timing offsets and multipath channels. In addition, a block-Alamouti scheme free from any residual interference can be straightforwardly employed. As this technique can be sensitive to time-varying channel, a novel low complexity block-Alamouti equalizer stage is proposed. Simulations show that the BER performance

TABLE III
COMPARISON OF DIFFERENT FBMC SCHEMES.

FBMC scheme	FS_1-FBMC	FS_4-FBMC	**OS-FBMC**	**OSB-FBMC**
Low computational complexity (Section III-E)	$++$	$-$	$\sim$	$+$
Low latency support (Section III-F)	$++$	$--$	$+$	$++$
Robustness against timing offset (Section V)	$\sim$	$++$	$++$	$+$
Robustness against 4G channels (Section VI)	$-$	$+$	$+$	$+$
Block-Alamouti support (Section VI-B)	$\sim$	$--$	$-$	$++$

LEGEND: Worst: $--$ Worse: $-$ Acceptable: $\sim$ Better: $+$ Best: $++$

is greatly improved when facing high Doppler spreads. All these results suggest that the use of short filters can be a viable solution for future FBMC systems.

REFERENCES

[1] K. Martin, "Small Side-Lobe Filter Design for Multitone Data-comm. Applications," *IEEE Trans. on Circuits and Syst. II: Analog and Digital Signal Process.*, vol. 45, no. 8, pp. 1155–1161, Aug. 1998.

[2] "PHYDYAS project," http://www.ict-phydyas.org.

[3] J. Nadal, C. Nour, and A. Baghdadi, "Low-Complexity Pipelined Architecture for FBMC/OQAM transmitter," *IEEE Trans. on Circuits and Syst. II: Express Briefs*, no. 99, pp. 1–1, 2015.

[4] C. Lele, P. Siohan, and R. Legouable, "2 dB Better Than CP-OFDM with OFDM/OQAM for Preamble-Based Channel Estimation," in *IEEE Int. Conf. on Commun., 2008. ICC '08*, May 2008, pp. 1302–1306.

[5] J. Nadal, C. A. Nour, and A. Baghdadi, "Design and Evaluation of a Novel Short Prototype Filter for FBMC/OQAM modulation," *IEEE Access*, vol. 6, pp. 19 610–19 625, 2018.

[6] D. Roque, C. Siclet, and P. Siohan, "A performance comparison of FBMC modulation schemes with short perfect reconstruction filters," in *Signal Process.*, apr 2012, pp. 1–6.

[7] D. Mattera, M. Tanda, and M. Bellanger, "Filter bank multicarrier with PAM modulation for future wireless systems," *Signal Process.*, vol. 120, pp. 594–606, Mar. 2016.

[8] B. Hirosaki, "An Orthogonally Multiplexed QAM System Using the Discrete Fourier Transform," *IEEE Trans. on Commun.*, vol. 29, no. 7, pp. 982–989, Jul. 1981.

[9] M. Bellanger, "FS-FBMC: An alternative scheme for filter bank based multicarrier transmission," in *2012 5th Int. Symp. on Commun. Control and Signal Process. (ISCCSP)*, May 2012, pp. 1–4.

[10] D. Mattera, M. Tanda, and M. Bellanger, "Frequency domain CFO compensation for FBMC systems," *Signal Process.*, vol. 114, pp. 183–197, Sep. 2015.

[11] P. Duhamel and H. Hollmann, "Split radix FFT algorithm," *Electronics Letters*, vol. 20, pp. 14–16, January 1984.

[12] H. Sorensen, M. Heideman, and C. Burrus, "On computing the split-radix FFT," *IEEE Transactions on Acoustics, Speech, and Signal Process.*, vol. 34, no. 1, pp. 152–156, Feb 1986.

[13] J. Nadal, F. Leduc-Primeau, C. A. Nour, and A. Baghdadi, "A block FBMC receiver designed for short filters," in *2018 IEEE Int. Conf. on Comm. (ICC)*, 2018.

[14] M. Renfors, T. Ihalainen, and T. Stitz, "A Block-Alamouti Scheme for Filter Bank Based Multicarrier Transmission," in *Wireless Conf. (EW), 2010 European*, Apr. 2010, pp. 1031–1037.

[15] K. Choi, "Alamouti Coding for DFT Spreading-Based Low PAPR FBMC," *IEEE Transactions on Wireless Comm.*, vol. 18, no. 2, pp. 926–941, Feb 2019.

[16] D. Na and K. Choi, "Intrinsic ICI-free Alamouti coded FBMC," *IEEE Comm. Letters*, vol. 20, no. 10, pp. 1971–1974, Oct 2016.

[17] T. Fusco, A. Petrella, and M. Tanda, "Data-aided symbol timing and CFO synchronization for filter bank multicarrier systems," *IEEE Transactions on Wireless Comm.*, vol. 8, no. 5, pp. 2705–2715, May 2009.

[18] D. Mattera, M. Tanda, and M. Bellanger, "Performance analysis of some timing offset equalizers for FBMC/OQAM systems," *Signal Process.*, vol. 108, pp. 167 – 182, 2015.

[19] 3GPP 36.104, "3rd Generation Partnership Project; Technical Specification Group RAN4; E-UTRA Base Station (BS) radio transmission and reception," v13.8.0 (Release 14).

2.2.1.3 Implementation of FBMC-OQAM and OFDM transmitters

Still targeting FBMC, we proposed a novel low-complexity pipelined hardware architecture for the transmitter published in [168, 169]. It is based on the use of a pruned IFFT algorithm (Fig. 2.6) and on the proposal of novel architectures related to all constituent blocks.

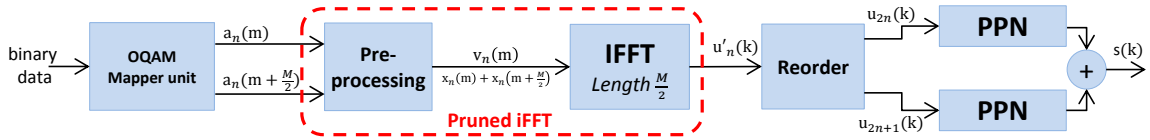

Figure 2.6: Optimized FBMC/OQAM hardware architecture using pruned IFFT algorithm

For comparison purposes, typical FBMC and OFDM transmitters have also been developed with similar architectural choices for the common blocks. The architectures of the three transmitters have been described in VHDL and synthesized targeting the XC7z020-1 Xilinx Zynq System on Chip (SoC) device. Obtained results are summarized in Table 2.1. These results correspond to an IFFT size of $M = 512$ and two different prototype filters (NPR1 and MMB4). The LUTs include, in addition to the synthesized combinational logic, the different coefficients related to the pre-processing unit, the twiddle factors, and the PPN filters. Note that all memories and First-In First-Out (FIFO) buffers used in all the developed transmitters use Random Access Memories (RAM), however they are synthetized as LUTs (distributed RAM) rather than block RAMs for more accurate comparisons.

Analytical and post-synthesis FPGA results of the proposed transmitter demonstrate significant complexity reduction. For a short ProF like NPR1, complexity scales down 40 to 50% when compared to a typical FBMC design and becomes comparable to OFDM. For longer ProF lengths such as MMB4, the PPN unit represents the main bottleneck in terms of hardware complexity. Moreover, on-board dynamic power consumption is measured for the corresponding designs. Results with a short filter indicate an increase of only 27% for the proposed optimized implementation with respect to OFDM. This increase reaches up to 126% for the typical FBMC implementation. In addition, the energy consumption is reduced by 45% when a short ProF is used instead of a long ProF. For accurate values, see Table 2.1. See our publications [168, 169] for more details.

Table 2.1: FPGA-based implementation results with $M = 512$ and NPR1/MMB4 prototype filters, for a maximum clock speed of 220 MHz

Unit	**Transmitter architecture**	**Registers**	**s**	**RAM** (as LUTs)	**DSP** multiplier	**Power** (mW)	**Latency** (clock cycles)
QAM mapper	OFDM	20	109	16	0	1	1
	FBMC/OQAM (typical)	51	254	104	0	6	1
	FBMC/OQAM (proposed)	108	300	192	0	6	257
Pre-processing	FBMC/OQAM (typical)	172	546	0	4	11	4
	FBMC/OQAM (proposed)	106	426	0	4	11	4
IFFTs	OFDM	2833	3343	544	16	97	549
	FBMC/OQAM (typical)	5666	6686	1088	32	194	549
	FBMC/OQAM (proposed)	2218	2534	348	12	88	278
Reorder	OFDM	111	141	352	0	12	514
	FBMC/OQAM (typical)	222	282	704	0	24	514
	FBMC/OQAM (proposed)	180	420	528	0	20	258
PPN NPR1	FBMC/OQAM (typical and proposed)	135	300	0	4	11	5
PPN MMB4	FBMC/OQAM (typical and proposed)	1095	1846	2112	16	124	8
TOTAL	OFDM	3006	3599	912	16	109	1064
	FBMC/OQAM NPR1 (typical)	5687	7385	1632	40	246	1073
	FBMC/OQAM NPR1 (proposed)	**2828**	**4011**	**1068**	**20**	**139**	**802**
	FBMC/OQAM MMB4 (typical)	6641	8952	3744	52	359	1076
	FBMC/OQAM MMB4 (proposed)	**3788**	**5585**	**3180**	**32**	**252**	**805**

2.2.1.4 Novel UF-OFDM transmitter

Always on the hardware side, another contribution concerns the proposal of a novel UF-OFDM transmitter. The proposed technique exploits two main ideas in order to reduce the computational complexity of the UF-OFDM baseline implementation. First, the processing of each subband and each subcarrier is separated, avoiding redundant operations. The subband processing requires an IFFT for each subband, reducing computational complexity. The second idea of the proposed technique consists of decomposing the UF-OFDM symbol into 3 parts as shown in Fig. 2.7:

- The prefix part, corresponding to the ramp-up transition of the UF-OFDM symbol.
- The suffix part, corresponding to the ramp-down transition of the UF-OFDM symbol.
- The core part, corresponding to the remaining samples of the UF-OFDM symbol.

By using the proposed decomposition into subband and subcarrier processing, it can be shown that the core part of the UF-OFDM symbol can be computed using a windowing operation followed by an IFFT for each decomposed subband. The samples corresponding to the prefix part of the UF-OFDM symbol are obtained by using a windowing operation and an accumulator for each sample of the prefix part. Finally, the suffix part is deduced by subtracting the prefix part from the core part.

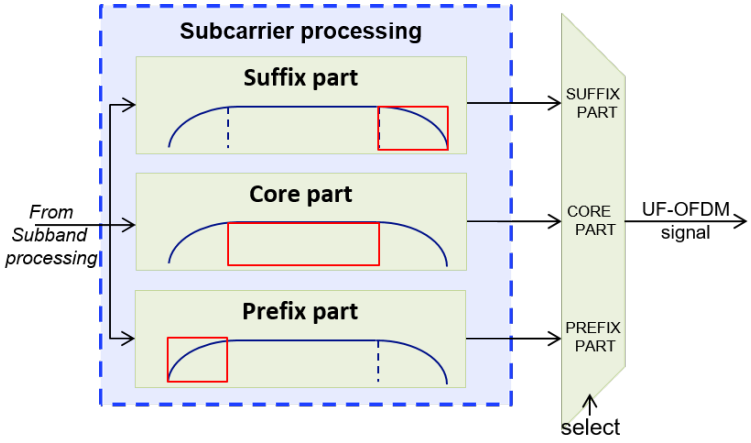

Figure 2.7: 3-way Decomposition of the UF-OFDM symbol

When compared to state-of-the-art solutions, a considerable complexity reduction is achieved for several configurations corresponding to the extreme cases where a user occupies the totality of the available bandwidth to achieve high data rates. Particularly, under these extreme conditions, the existing state-of-the-art Frequency Domain Approximation (FDA) [170] from the inventors of the UF-OFDM technique requires up to 4.18 times more Real Multiplications (RM) and 5.51 times more Real Additions (RA) than the proposed UF-OFDM technique. In addition, the proposed transmitter does not rely on any signal approximation, contrary to the state-of-the-art techniques. Therefore, the spectral confinement of the UF-OFDM signal is preserved. Obtained results represent a major contribution to the work on UF-OFDM, answering complexity concerns that were undermining its adoption in communications standards. The description of the performed work and obtained results were published in [171, 172]. Due to its major impact, our publication of [172] in IEEE Transactions on Vehicular Technology is included hereafter.

IEEE TRANSACTIONS ON VEHICULAR TECHNOLOGY, VOL. 67, NO. 3, MARCH 2018 2141

Novel UF-OFDM Transmitter: Significant Complexity Reduction Without Signal Approximation

Jérémy Nadal, *Student Member, IEEE*, Charbel Abdel Nour, *Member, IEEE*, and Amer Baghdadi, *Senior Member, IEEE*

***Abstract*—The upcoming fifth generation (5G) of mobile communication system aims to support multiple new services and use cases toward a flexible and unified connectivity. In order to meet the corresponding requirements, Universal-Filtered Orthogonal Frequency-Division Multiplexing (UF-OFDM) was proposed to replace the existing waveform since it combines the advantages related to OFDM with better spectral properties and with improved robustness against time-frequency misalignments. However, its main drawback resides in the computational complexity of the transmitter reaching up to 200 times that of OFDM if no simplification is applied. While still of high complexity, most efficient simplification techniques significantly compromise the achieved spectral confinement through signal approximations. In this context, a novel low-complexity UF-OFDM transmitter without any signal quality loss is proposed. For small subband sizes, the complexity becomes comparable to OFDM regardless of the number of allocated subbands. Furthermore, the proposed transmitter architecture is flexible and can be easily adapted to support OFDM modulation.**

***Index Terms*—OFDM, UF-OFDM, multicarrier modulation, 5G.**

I. INTRODUCTION

THE 5th generation (5G) of mobile communication systems is foreseen to support multiple new services while coexisting with the typical mobile broadband service of 4G/Long Term Evolution (LTE). For internet-of-things applications, massive Machine-Type Communication (mMTC) service is introduced, adding specific requirements such as the support of imperfect synchronization. Other applications, like Mission Critical Communication (MCC), may require the support of low-latency communication, which can be achieved by reducing the time transmission interval. Therefore, multiple waveform parameters on the same carrier (often referred to as numerology) may be required to support all types of applications, which raises the issue of their coexistence. To partly answer these new challenges, novel waveforms have been designed and proposed for the upcoming 5G standard.

Universal-Filtered Orthogonal Frequency-Division Multiplexing (UF-OFDM) is one of the key 5G candidate waveforms and was originally proposed in [1]. The original idea of this waveform consists in grouping multiple allocated subcarriers into subbands, independently filtered in the time domain. Thus, the filtering is realized subband-wise and not subcarrier-wise as in the Filter-Bank Multi-Carrier with Offset-Quadrature Amplitude Modulation (FBMC/OQAM) [2]. UF-OFDM shows advantages for low-latency communications (MCC services) and enables the use of open-loop synchronization to save bandwidth and energy [3]. In addition, unlike other 5G candidate waveforms such as FBMC/OQAM, the majority of the techniques employed in OFDM can be reused without significant modifications. For instance, the techniques presented in [4] are applicable to UF-OFDM.

However, the main drawback of the UF-OFDM modulation resides in the complexity of the transmitter. The baseline implementation is estimated to be up to 200 times more computationally complex than OFDM [5]. Some recent techniques have been proposed to reduce the computational complexity [5], [6]. However, these still require up to 10 times the complexity of OFDM [5], while calling for an approximated signal implying a penalty in bit error rate and in spectral confinement.

In this work, we propose a novel and significantly simplified UF-OFDM transmitter able to generate a signal exempt from any approximation when compared to the baseline solution. The complexity reduction is obtained by exploiting two main ideas:

1) First, the processing related to the subbands and the processing related to the subcarriers are separated. The subband processing can be performed at a low complexity by computing multiple Inverse Fast Fourier Transforms (IFFTs) of a small size.
2) Second, the subcarrier processing is subdivided into 3 parts corresponding to the generation of the prefix, the core and the suffix parts of the UF-OFDM symbol. The core part of the signal can be efficiently generated using multiple IFFTs of small size, and the suffix part can be simply deduced from the prefix and core parts of the signal, which further lowers the complexity.

Manuscript received April 10, 2017; revised July 19, 2017; accepted September 18, 2017. Date of publication October 18, 2017; date of current version March 15, 2018. This work has been performed in the framework of the Horizon 2020 Project FANTASTIC-5G (ICT-671660), which is partly funded by the European Union. The review of this paper was coordinated by Dr. J.-C. Chen. *(Corresponding author: Jeremy Nadal.)*

The authors are with the IMT Atlantique, CNRS Lab-STICC, UBL, F-29238, Brest, France (e-mail: jeremy.nadal@telecom-bretagne.eu; charbel.abdelnour@telecom-bretagne.eu; amer.baghdadi@telecom-bretagne.eu).

Color versions of one or more of the figures in this paper are available online at http://ieeexplore.ieee.org.

Digital Object Identifier 10.1109/TVT.2017.2764379

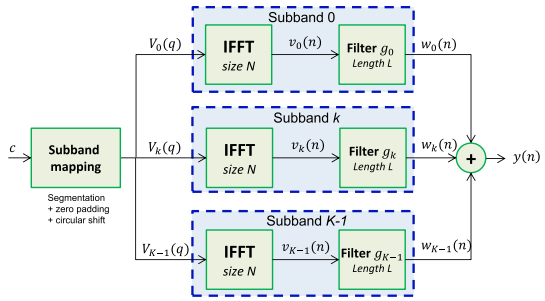

Fig. 1. Baseline UF-OFDM transmitter.

The originality of the proposed technique resides in avoiding redundant operations performed by the baseline technique without altering the original signal. Thus, being mathematically identical to the baseline solution, the proposed technique does not have any impact on the Out-Of-Band Power Leakage (OOBPL) with respect to the baseline solution. To the best of our knowledge, this is the first time that such UF-OFDM technique is proposed in the literature. Furthermore, the technique can be easily adapted to perform OFDM modulation and thus enables direct compatibility with 4G/LTE.

The rest of the paper is organized as follows. Section II gives a technical description of the UF-OFDM baseline transmitter and the solutions provided in the literature to reduce the computational complexity. Section III details the proposed UF-OFDM technique. Section IV provides computational complexity analysis and comparisons with the existing techniques in the literature. Finally, Section V concludes the paper.

II. UF-OFDM Technical Description and Existing Solutions

A. Baseline UF-OFDM Transmitter

The principle of the UF-OFDM modulation is to group the complex samples carrying information into several subbands, each composed of Q subcarriers. These complex samples can be, for instance, symbols from a Quadrature Amplitude Modulation (QAM) constellation. A maximum of $K = \lfloor N/Q \rfloor$ subbands carrying Q subcarriers can be used, where N is the total number of subcarriers, and $\lfloor x \rfloor$ represents the largest integer less than or equal to x (floor operator). The secondary sidelobes (residual power outside the subbands) of each subband are attenuated by independent subband-wise filtering of length L samples. The resulting discrete time signal represents the sum of the signals emanating from the filtered subbands. It forms the UF-OFDM symbol, composed of $N + L - 1$ samples. The baseline UF-OFDM transmitter is represented in Fig. 1.

Let c be a vector of length BQ containing the complex symbols to be transmitted. To map each symbol in c to the allocated subbands, we first group the symbols into B subsets $c_i(q)$, for $q \in [\![0, Q-1]\!] (= \{0, 1, ..., Q-1\})$, such that $c_i(q) = c(q + Qk)$. In order to support an arbitrary assignment of symbol groups to subbands, we define a bijective function $i = \phi(k)$ that maps the index $k \in \Omega_B$ of an allocated subband to a symbol group i, where Ω_B is the set of the B allocated subband indexes. The segmented samples $s_k(q)$ for subcarrier index q of subband $k \in [\![0, K-1]\!]$ can then be expressed as

$$s_k(q) = \begin{cases} c_{\phi(k)}(q), & k \in \Omega_B, \\ 0, & k \notin \Omega_B. \end{cases} \quad (1)$$

In the frequency domain, a total of N subcarriers are defined. Thus, the samples $s_k(q)$ must be zero padded with $N - Q$ zeros:

$$s'_k(q) = \begin{cases} s_k(q), & q \in [\![0, Q-1]\!] \\ 0, & q \in [\![Q, N-1]\!], \end{cases}$$

where $s'_k(q)$ represents the zero padded version of s_k. Then, a circular shift of $kQ + k_0$ samples is applied, to move each subband into its respective subband position in the frequency domain. The obtained signal $V_k(q)$ is expressed as

$$V_k(q) = s'_k(\mathrm{mod}_N(q - (kQ + k_0))),$$

where mod_N corresponds to the modulo N operator, $k_0 \in [\![0, Q-1]\!]$ corresponds to the value of the shift in number of subcarriers. This shift at subcarrier level can be used to move each subband to the center of the allocated bandwidth. For each index k, the $V_k(q)$ signal for subband k contains N samples, one for each subcarrier. However, only Q subcarriers, defining the subband number k, carry the information to transmit. The remaining subcarriers are not used (zero padded). Thus, each subband is isolated from the others, and can be processed independently. The subband mapping block represented in Fig. 1 corresponds to the segmentation, the zero padding and the circular shift operations detailed above.

Next, the $V_k(q)$ samples are transformed to the time domain using an IFFT of size N for each subband k:

$$v_k(n) = R_N(n) \sum_{q=0}^{N-1} V_k(q) e^{j2\pi \frac{qn}{N}}, n \in [\![0, N+L-2]\!], \quad (2)$$

where L is the length of the impulse response of the subband filter and $R_N(n)$ represents the rectangular window of length N: $R_N(n) = 1, n \in [\![0, N-1]\!]$ else 0. The windowing operation has negligible complexity and is omitted from Fig. 1 for clarity.

Then, as shown in Fig. 1, each subband is filtered separately using a linear convolution by the impulse response of the subband filter g_k:

$$w_k(n) = \sum_{l=0}^{L-1} g_k(l) v_k(n-l), n \in [\![0, N+L-2]\!],$$

where $w_k(n)$ represents the result of the filtering operation. The impulse response of these filters can be obtained from the impulse response of a common filter $f_Q(n)$, that we refer to as the subband prototype filter, as

$$g_k(n) = f_Q(n) e^{j2\pi \frac{kQn}{N}}, n \in [\![0, L-1]\!].$$

In fact, the impulse response of the subband filter number k corresponds to the impulse response of the subband prototype filter, shifted in frequency by kQ subcarriers. This frequency

shift aligns the frequency response of the filter to the subband position k. Furthermore, the frequency response of the subband prototype filter f_Q is centered around the subcarrier index $Q/2$ if Q is even (or around $(Q-1)/2$ if Q is odd), corresponding to the center of a subband. If $f(n)$ is the impulse response of the subband prototype filter, then, for $n \in [\![0, L-1]\!]$, we have

$$f_Q(n) = \begin{cases} \frac{Q}{2} & Q \text{ even}, \\ \frac{Q-1}{2} & Q \text{ odd}. \end{cases} \tag{3}$$

In the literature, a typical choice for the subband prototype filter is the Dolph-Chebyshev filter [7]. More recently, a specific filter design has been studied to reduce the out-of-band power spectral leakage for UF-OFDM [8] and to improve robustness against frequency/timing-offset errors [9].

Finally, the $N+L-1$ time domain samples of the filtered subbands are summed together to form the UF-OFDM symbol $y(n)$, implicitly sampled at the frequency f_s:

$$y(n) = \sum_{k=0}^{K-1} w_k(n), n \in [\![0, N+L-2]\!]. \tag{4}$$

In a practical implementation, only the B allocated subbands are considered to calculate the UF-OFDM symbol, since the $B-K$ other subbands correspond to zero-valued samples in the time domain:

$$y(n) = \sum_{k \in \Omega_B} w_k(n), n \in [\![0, N+L-2]\!].$$

While this solution has an acceptable computational complexity for a limited number of allocated subbands, it becomes computationally expensive when the number of allocated subbands increases. Indeed, the computation of one subband requires the use of an IFFT of size N (complexity in $\mathcal{O}(N \log_2 N)$) and a linear convolution operation (complexity in $\mathcal{O}(L^2 + LN)$)). Therefore, the computation of only one subband already requires a larger number of operations than needed to compute one OFDM symbol (one IFFT of size N), due to the complexity overhead introduced by the linear convolution of the subband filtering stage. These operations have to be repeated for each allocated subband. For $B = 100$, which corresponds to the maximum number of resource blocks ($Q = 12$) that can be allocated in 4G/LTE, the computational complexity exceeds 200 times the computational complexity of the OFDM transmitter [5].

Few techniques with lower computational complexity have been investigated in the literature. Among existing techniques, one applies the subband filtering in the frequency domain instead of the time domain, and a second approximates the UF-OFDM signal by decomposing it into multiple windowed OFDM signals that are then summed. These approaches are reviewed in the following subsections. They reduce the computational complexity of the UF-OFDM transmitter, but at the cost of a degradation of the original signal.

B. Frequency Domain UF-OFDM Transmitter

In this approach [5], the filtering stage and the summation of all subbands are computed in the oversampled frequency domain (FD), i.e. before the IFFT. We refer to this technique as FD UF-OFDM in this paper. The IFFT size is multiplied by N_{OS} which corresponds to a chosen oversampling factor. In general, this parameter is set to $N_{\mathrm{OS}} = 2$ since this value provides the best compromise between approximation errors and computational complexity [5]. Additionally, the computation of the filtering stage in the frequency domain requires an IFFT of size N_0 and an FFT of size $N_{\mathrm{OS}} N_0$ for each subband, where $N_0 \geq Q$ is a design parameter. Note that the computational complexity increases with the value of N_0. However, the impact on the OOBPL is reduced with respect to the baseline solution. Finally, only $N+L-1$ samples, corresponding to the length of one UF-OFDM symbol, are kept after the computation of the IFFT of size $N_{\mathrm{OS}} N$.

Since this technique uses a smaller IFFT size per processed subband than the baseline solution presented in Subsection II-A, the computational complexity is significantly reduced. However, it is still higher than that of OFDM, due to the use of an IFFT of size $N_{\mathrm{OS}} N$ instead of N, and due to the additionnal small IFFT/FFT of size N_0 and $N_{\mathrm{OS}} N_0$ for each allocated subband. According to [5], the required number of multipliers and adders can be up to 10 times higher than in the case of OFDM.

C. Time Domain Windowed UF-OFDM Transmitter

The second simplified UF-OFDM transmitter is based on a time-domain processing without oversampling [6]. We refer to it as Time-Domain-Windowed (TDW) UF-OFDM in this paper. It consists of subdividing each subband into small groups of subcarriers, each group being subcarrier-wise filtered by a dedicated filter. This subcarrier-wise filtering can be efficiently implemented by using a windowing operation in the time domain (after IFFT). The impulse response of the common group filter is used as window coefficients. It results into an approximated UF-OFDM signal. This results in an approximation of the UF-OFDM signal, which is obtained by summing multiple windowed OFDM symbols as

$$y(n) \approx \sum_{i=0}^{N_w - 1} w_i(n) u_i(n), n \in [\![0, N+L-2]\!].$$

The computational complexity increases linearly with the number of windows being employed (in $\mathcal{O}(N_W N \log_2 N)$) comparable to N_W times the complexity of a typical OFDM transmitter. However, increasing the number of windows decreases the approximation errors and reduces the OOBPL. Similarly to the FD UF-OFDM technique, a trade-off between approximation errors and computational complexity must be considered.

III. PROPOSED LOW-COMPLEXITY UF-OFDM TRANSMITTER

For all simplified UF-OFDM transmitters, a compromise must be found between performance and complexity. Thus, a novel UF-OFDM technique that reduces the computational complexity to an acceptable level without altering the original

signal is of high interest. The proposed approach achieves this goal by exploiting a specific decomposition into subband and subcarrier processing.

A. Description of the Proposed Technique

The proposed technique exploits two main ideas to reduce the computational complexity of the UF-OFDM baseline implementation. First, the required UF-OFDM processing is divided into subband-wise and subcarrier-wise computations in such a way to avoid redundant operations, especially when a high number of subbands is allocated. The second core idea is to divide the UF-OFDM symbol into prefix, core and suffix parts, which are efficiently processed by exploiting the previous decomposition into subband-wise and subcarrier-wise processing. The suffix part is deduced from the core part and the prefix part by a simple subtraction. These two core ideas exploit the UF-OFDM baseline equation. Therefore the resulting signal is not altered when compared to this baseline solution.

By using the circular shift property of the IFFT, (2) can be rewritten as

$$v_k(n) = R_N(n) e^{j2\pi \frac{(kQ+k_0)n}{N}} \sum_{q=0}^{N-1} s'_k(q) e^{j2\pi \frac{qn}{N}}$$

$$= e^{j2\pi \frac{k_0 n}{N}} R_N(n) \sum_{q=0}^{Q-1} s_k(q) e^{j2\pi \frac{(q+kQ)n}{N}}. \quad (5)$$

To simplify the development of the following equations, the number of shifted subcarriers is assumed to be equal to zero ($k_0 = 0$). This constraint does not alter the following demonstration, since the frequency shifted UF-OFDM symbol can be recovered by applying a simple linear phase rotation to the unshifted UF-OFDM symbol. Thus, expression (4) of the UF-OFDM symbol combined with (5) becomes, for $n \in [\![0, N + L - 1]\!]$,

$$y(n) = \sum_{k=0}^{K-1} \sum_{l=0}^{L-1} \left(f_Q(l) e^{j2\pi \frac{kQl}{N}} R_N(n-l) \times \sum_{q=0}^{Q-1} s_k(q) e^{j2\pi \frac{q+kQ}{N}(n-l)} \right).$$

It is possible to simplify this equation by rearranging the order of the three summations as

$$y(n) = \sum_{q=0}^{Q-1} \sum_{l=0}^{L-1} \left(f_Q(l) R_N(n-l) \times \sum_{k=0}^{K-1} s_k(q) e^{j2\pi \frac{q(n-l)+kQ(n-l)+kQl}{N}} \right)$$

$$= \sum_{q=0}^{Q-1} \left(f_q(n) \sum_{k=0}^{K-1} s_k(q) e^{j2\pi \frac{kQn}{N}} \right), \quad (6)$$

with

$$f_q(n) = \sum_{l=0}^{L-1} f_Q(l) R_N(n-l) e^{j2\pi \frac{q(n-l)}{N}}. \quad (7)$$

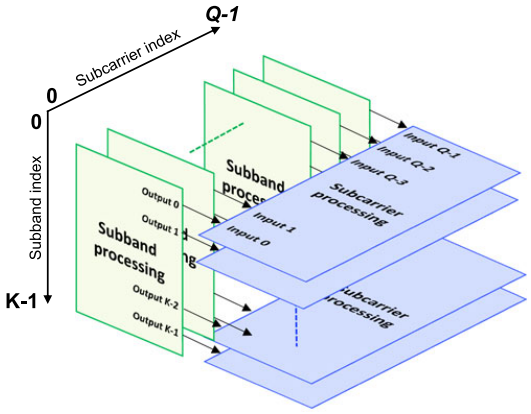

Fig. 2. Separation of the subband processing and the subcarrier processing.

These equations are further developed, by assuming that the total number of subcarriers across all the subbands (N) can be decomposed into an integer number of subbands ($\text{mod}_Q(N) = 0$). Then we have $K = N/Q$, and (6) can be rewritten as

$$y(n) = \sum_{q=0}^{Q-1} f_q(n) x_q(n), \quad (8)$$

with

$$x_q(n) = \sum_{k=0}^{K-1} s_k(q) e^{j2\pi \frac{kn}{K}}, \quad (9)$$

where $x_q(n)$ corresponds to the IFFT of size K of the samples related to the subcarrier number q of each of the K subbands. Then, by exploiting the fact that the IFFT of size K is a periodic function of K samples, the first N samples of the UF-OFDM symbol ($y(n)$) can be decomposed into Q fragments of K samples ($N = K \times Q$). The fragmented symbol $y_p(n') = y(n' + pK)$, for $n' \in [\![0, K-1]\!]$ and $p \in [\![0, Q-1]\!]$, its expression can be written as

$$y_p(n') = \sum_{q=0}^{Q-1} f_q(n' + pK) x_q(n'). \quad (10)$$

Thus, it is possible to separate the processing of each subband (for a given subcarrier index) and the processing of each subcarrier (for a given subband index), as illustrated in Fig. 2. The subband processing consists of calculating the $x_q(n')$ samples from (9) using an IFFT of size K. This processing must be repeated for all the Q subcarrier indexes, and K samples are generated per subband processing to obtain a total of N samples. Then, the UF-OFDM symbol is generated by the subcarrier processing that computes the $y_p(n')$ samples (for each subcarrier index q) from the subband processing according to (10).

This separation between subband processing and subcarrier processing is the first core idea of the proposed technique and enables to reduce the computational complexity to process the first N samples of the UF-OFDM symbol. Indeed, the required number of operations scales in $\mathcal{O}(N \log_2(K))$ which is less

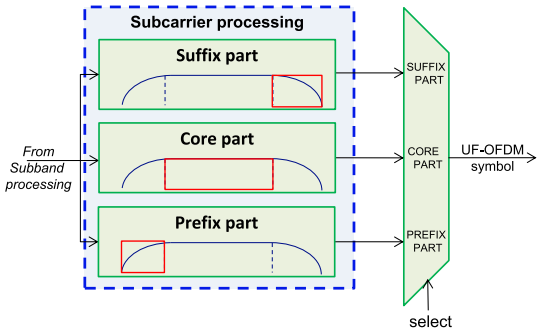

Fig. 3. Decomposition of the subcarrier processing into a prefix, core, and suffix parts.

computationally demanding than the processing of one IFFT of size N (in $\mathcal{O}(N\log_2(N))$). Furthermore, the computational complexity does not depend anymore on the number of allocated subbands B. However, the corresponding overhead introduced by the subcarrier processing (complexity in $\mathcal{O}(Q(N+L))$) is not negligible.

In fact, it is possible to further simplify the subcarrier processing by decomposing the UF-OFDM symbol into 3 distinct parts, as shown in Fig. 3:

1) The first part of the UF-OFDM symbol corresponds to the first L samples processed by the linear convolution operation (subband filtering). This part of the UF-OFDM symbol has a signal envelope that corresponds to the shape of the first half of the impulse response of the subband prototype filter. We refer to this part as the prefix part of the UF-OFDM symbol.
2) The second part of the UF-OFDM symbol, which we call the core part, is composed of $N-L$ samples and corresponds to the samples in the interval $n \in [\![L, N-1]\!]$. This part of the symbol can be seen as the result of a circular convolution applied to the output of the IFFTs of size N of the UF-OFDM baseline solution.
3) Finally, the last part of the UF-OFDM symbol corresponds to the last $L-1$ samples processed by the linear convolution operation. This part of the UF-OFDM symbol has a signal envelope that corresponds to the shape of the second half of the impulse response of the subband prototype filter. We refer to this part as the suffix part of the UF-OFDM symbol.

The core part of the UF-OFDM symbol can be efficiently computed by noting that (7) can be simplified when $n \in [\![L, N-1]\!]$ as

$$f_q(n) = e^{j2\pi\frac{qn}{N}} \sum_{l=0}^{L-1} f_Q(l) e^{-j2\pi\frac{ql}{N}}.$$

Furthermore, these coefficients can be segmented as

$$f_q(n'+pK) = e^{j2\pi\frac{qp}{Q}} F_q(n'),\ (n'+pK) \in [\![L, N-1]\!], \tag{11}$$

with

$$F_q(n') = e^{j2\pi\frac{qn'}{N}} \sum_{l=0}^{L-1} f_Q(l) e^{-j2\pi\frac{ql}{N}}. \tag{12}$$

The coefficients $F_q(n')$ can be obtained by applying an FFT of size N on the impulse response of the subband prototype filter $f_Q(l)$. From the result of this FFT, only the first Q coefficients are useful (since $q \in [\![0, Q-1]\!]$). Then, a linear phase rotation is applied (the exponential term) for each subcarrier index q. In total, $Q \times K = N$ coefficients are generated. These coefficients constitute the filter core coefficients.

By combining the equation of the segmented samples (10) with the equation of the segmented filter coefficients (11), we obtain

$$y_p(n') = \sum_{q=0}^{Q-1} z_q(n') e^{j2\pi\frac{qp}{Q}},\ (n'+pK) \in [\![L, N-1]\!], \tag{13}$$

with

$$z_q(n') = F_q(n') x_q(n'). \tag{14}$$

The $z_q(n')$ samples are obtained after multiplication of the $x_q(n')$ samples by the filter core coefficients $F_q(n')$ defined in (12), and can be seen as a windowing operation. Then, the n'-th samples of each of the Q fragments are calculated using an IFFT of size Q of the windowed samples $z_q(n')$ across the Q subcarriers. With the proposed separation between subband and subcarrier processing, it is then possible to efficiently compute the core part of the UF-OFDM symbol by using K IFFTs of size Q, reducing the computational complexity to $\mathcal{O}(N\log_2(Q))$. As shown in Fig. 2, the Q input samples of the subcarrier processing number $n' \in [\![0, K-1]\!]$ corresponds to the output samples number n' of the Q subbands processing. Thus, for the subcarrier processing, the order in which the subcarrier and subband samples are processed is interleaved when compared to the subband processing. Each subcarrier processing requires one windowing stage and one IFFT of size Q to generate Q samples of the segmented core part. Then, the core part is recovered using the following equation:

$$y_{\text{core}}(n) = y_{\lfloor n/K \rfloor}(\text{mod}_K(n)). \tag{15}$$

After the computation of the core part ($n \in [\![L, N-1]\!]$), the prefix ($n \in [\![0, L-1]\!]$) and suffix ($n \in [\![N, N+L-2]\!]$) parts of the UF-OFDM symbol must be calculated. When $n_p \in [\![0, L-1]\!]$, n_p being the sample index of the prefix part, (7) becomes

$$\begin{aligned} f_q(n_p) &= e^{j2\pi\frac{qn_p}{N}} \sum_{l=0}^{n_p} f_Q(l) e^{-j2\pi\frac{ql}{N}} \\ &= P_q(n_p). \end{aligned} \tag{16}$$

The $P_q(n_p)$ coefficients constitute the prefix tail coefficients. An efficient way to calculate these coefficients is by exploiting the

following:

$$P_q(n_p+1) = e^{j2\pi\frac{q(n_p+1)}{N}} \sum_{l=0}^{n_p+1} f_Q(l) e^{-j2\pi\frac{ql}{N}} = f_Q(n_p+1) + P_q(n_p) e^{j2\pi\frac{q\,n_p}{N}}.$$

Thus, the prefix tail coefficient number n_p+1 can be recursively calculated by adding the sample number n_p+1 of the impulse response of the subband prototype filter to the previously calculated prefix tail coefficients (number n_p), after multiplication by a linear phase rotation term. This efficient way to compute the prefix tail coefficients is interesting if there is a requirement to generate these filters in real time, for instance to support multiple types of filter coefficients and/or filter lengths. Otherwise, such coefficients can be simply pre-computed and stored in a Look-Up-Table (LUT).

Then, the prefix part of the UF-OFDM symbol $y_{\text{prefix}}(n_p)$ can be deduced from (8)

$$y_{\text{prefix}}(n_p) = \sum_{q=0}^{Q-1} P_q(n_p) x_q(n_p), n_p \in [\![0, L-1]\!]. \quad (17)$$

The samples corresponding to the prefix part of the UF-OFDM symbol are obtained by:

1) Multiplying the $x_q(n_p)$ samples by the prefix tail coefficients $P_q(n_p)$, which can be seen as a windowing operation.
2) Summing over the subcarrier index q all the Q windowed samples for each sample n of the prefix part.

The generation of the prefix part can be included in the subcarrier processing of Fig. 2 since the interconnections between the subband and the subcarrier processing are unchanged. The sample number n of the prefix part is generated from the output number n of each of the Q subband processing blocks.

For the suffix part of the UF-OFDM symbol, we have $n_s \in [\![N, N+L-2]\!]$, and in that case (7) becomes

$$f_q(n_s) = e^{j2\pi\frac{qn}{N}} \sum_{l=n_s-N+1}^{L-1} f_Q(l) e^{-j2\pi\frac{ql}{N}}, = S_q(n_s).$$

The coefficients $S_q(n_s)$ denote the suffix tail coefficients. These coefficients can be deduced by subtracting the filter core coefficients from the prefix tail coefficients as

$$S_q(n_s) = e^{j2\pi\frac{qn}{N}} \left(\sum_{l=0}^{L-1} f_Q(l) e^{-j2\pi\frac{ql}{N}} - \sum_{l=0}^{n_s-N} f_Q(l) e^{-j2\pi\frac{ql}{N}} \right), = F_q(n_s) - P_q(n_s-N).$$

Then, the suffix part of the UF-OFDM symbol can be deduced from (8)

$$y(n_s) = \sum_{q=0}^{Q-1} \Big(F_q(n_s) - P_q(n_s-N) \Big) x_q(n_s),\ n_s \in [\![N, N+L-2]\!].$$

Due to the periodicity of $x_q(n_s)$ and $F_q(n_s)$, the above equation is equivalent to

$$y(n_s) = \sum_{q=0}^{Q-1} \Big(F_q(n_s-N) - P_q(n_s-N) \Big) x_q(n_s-N).$$

Thus, the suffix part $y_{\text{suffix}}(n_s)$ can be expressed as follows for $n_s \in [\![0, L-2]\!]$:

$$\begin{aligned} y_{\text{suffix}}(n_s) &= y(n_s+N) \\ &= \sum_{q=0}^{Q-1} \Big(F_q(n_s) - P_q(n_s) \Big) x_q(n_s) \\ &= y_{\text{core}}(n_s) - y_{\text{suffix}}(n_s), \end{aligned} \quad (18)$$

where the support of $y_{\text{core}}(n)$ is extended to $n \in [\![0, N-1]\!]$ instead of $[\![L, N-1]\!]$ as in (13). The samples in the interval $n \in [\![0, L-1]\!]$ are only generated to compute the suffix part of the UF-OFDM symbol. This shows that the suffix part of the UF-OFDM symbol can be simply deduced by subtracting the core part of the UF-OFDM symbol from its prefix part, avoiding additional computational complexity overhead.

Finally, the complete UF-OFDM symbol is obtained by the concatenation of the prefix part, the core part and the suffix part:

$$y(n) = \begin{cases} y_{\text{prefix}}(n), & n \in [\![0, L-1]\!] \\ y_{\text{core}}(n), & n \in [\![L, N-1]\!] \\ y_{\text{suffix}}(n-N), & n \in [\![N, N+L-2]\!]. \end{cases} \quad (19)$$

The proposed UF-OFDM transmitter is illustrated in detail in Fig. 4 and can be summarized by the 8 steps:

Step 1: Segment the complex source symbols c into B subbands of Q subcarriers.

Step 2: Compute the IFFT of size K of the segmented samples (from step 1) corresponding to the qth subcarrier of each of the K subbands. This IFFT has to be computed Q times, for each subcarrier $q \in [\![0, Q-1]\!]$ to obtain the $x_q(n)$ samples.

Step 3: Multiply the $x_q(n')$ samples (from step 2) by the subband prototype filter coefficients $F_q(n')$ to obtain the windowed samples $z_q(n')$.

Step 4: Compute the IFFT of size Q of the windowed sample $z_q(n')$ for the n-th sample index of each of the Q subcarriers. This IFFT has to be computed K times, for each sample, to obtain the fragmented samples $y_p(n')$.

Step 5: Recover the core part of the UF-OFDM symbol from the fragmented samples $y_p(n')$.

Step 6: Calculate the prefix part of the UF-OFDM symbol by multiplying the $x_q(n_p)$ samples by the prefix tail coefficients $P_q(n_p)$, and by summing them over each subcarrier index $q \in [\![0, Q-1]\!]$.

Step 7: Calculate the suffix part of the UF-OFDM symbol ($y_{\text{suffix}}(n_s)$) by subtracting the samples of the core part ($y_{\text{core}}(n_s)$) from the samples of the prefix part ($y_{\text{prefix}}(n_s)$) for $n_s \in [\![0, L-2]\!]$.

Step 8: Concatenate the prefix part, the core part and the suffix part to obtain the UF-OFDM symbol.

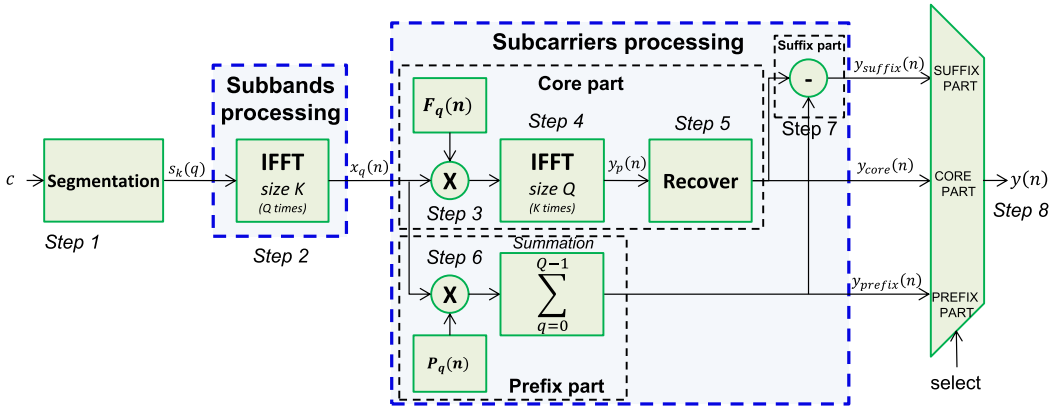

Fig. 4. Proposed low-complexity UF-OFDM transmitter.

Note that the generation of the prefix and the core parts being independent, step 4/5 and step 6 can be processed in any order. Only the generation of the suffix part (step 7) requires to first compute the prefix part and the core part of the UF-OFDM symbol.

The proposed UF-OFDM technique generates the UF-OFDM symbol without frequency shift, since it was assumed to be equal to 0 to simplify the development of the equations. When the frequency shift by (k_0 subcarriers) is taken into account, the equation of the frequency shifted UF-OFDM symbol is given by

$$y'(n) = e^{j2\pi \frac{k_0 n}{N}} y(n), n \in [\![0, N+L-2]\!].$$

This additional linear phase rotation would increase the complexity of the transmitter by adding $N+L-1$ complex multipliers. It is however possible to calculate the frequency shifted UF-OFDM symbol more efficiently. Indeed, for the prefix part of the UF-OFDM symbol ($y_{\text{prefix}}(n)$), the linear phase rotation term can be included in the prefix tail coefficients:

$$P_q(n_p) = e^{j2\pi \frac{(q+k_0)n_p}{N}} \sum_{l=0}^{n_p} f_Q(l) e^{-j2\pi \frac{ql}{N}}.$$

Concerning the core part of the UF-OFDM symbol $y_{\text{core}}(n)$, the fragmented samples $y_p(n')$ can be expressed as

$$y_p(n') = e^{j2\pi \frac{k_0 p}{Q}} \sum_{l=0}^{Q-1} (z_q(n') e^{j2\pi \frac{k_0 n'}{N}} e^{j2\pi \frac{qp}{Q}}).$$

The term $\exp[j2\pi(k_0 n')/N]$ can be included in the core filter coefficients $F_q(n)$ and the term $\exp[j2\pi(k_0 p)/Q]$ is equivalent to a circular shift of k_0 samples applied to the inputs of the IFFT of size Q (on the windowed samples $z_q(n)$):

$$y_p(n') = \sum_{q=0}^{Q-1} z_{q-k_0}(n') e^{j2\pi \frac{qp}{Q}},$$

with the filter core coefficients given by

$$F_q(n') = e^{j2\pi \frac{(q+k_0)n'}{N}} \sum_{l=0}^{L-1} (f_Q(l) e^{-j2\pi \frac{ql}{N}}).$$

Therefore, the frequency shift of k_0 subcarriers does not introduce any computational complexity overhead.

B. Adaptation of the Proposed Technique for any Subband Size

The technique detailed in Section III-A assumes that the total number of subcarriers across all the subbands N can be divided into an integer number of subbands ($\text{mod}_Q(N) = 0$). However, in the particular case of 4G/LTE systems, the minimum allocation size, called a Resource Block (RB), corresponds to 12 subcarriers (frequency) and 7 OFDM symbols (time). Thus, the subband size Q must be equal to a multiple of 12, whereas the IFFT size in 4G/LTE is defined to be a power of 2 in most cases. The only exception concerns the numerology related to the 15 MHz bandwidth case, where the IFFT size is equal to 1536 and the proposed technique can be directly applied for this case since $\text{mod}_{12}(1536) = 0$.

One straightforward solution is to adapt the subband size to satisfy both the simplification constraints and the LTE allocation size. Such condition is satisfied if $Q = 4$, implying that each allocated RB is divided into 3 subbands. However, the spectral confinement and system performance would be negatively affected for such values.

A second solution is to use a subband size that is a power of 2, allocate the information-carrying symbols to the center of the corresponding allocated subbands, and pad with zero-valued samples the edge of the first and last allocated subbands to complete the subband allocation. As an example, if 1 RB must be allocated, then $Q = 16$ and $B = 1$ can be chosen, and $(Q - 12)/2 = 2$ zeros must be inserted at the beginning and end of the allocated subbands. More generally, if P corresponds to the minimum allocation size (in number of subcarriers) supported by the communication system ($P = 12$ in 4G/LTE) and N_P is the number of groups of P subcarriers, then, if the subband size

Q is fixed, we have

$$B = \left\lceil \frac{N_P \times P}{Q} \right\rceil,$$
$$N_{\mathrm{ZP}} = \frac{B \times Q - N_P \times P}{2},$$

where N_{ZP} corresponds to the number of zero valued samples which must be padded at each edge of the allocated subbands. If the number of allocated subbands B is equal to 1, any subband size superior to P can be used and leads to the same spectral confinement as the baseline solution with $Q = P$, since the subband prototype filter coefficients ($f(n)$) do not depend on the subband size Q. However, for a higher number of allocated subbands, the presence of zero-padded samples at the edges of the allocated subbands can impact the spectral confinement and the performance of the system. Thankfully, this solution can be used without performance degradation when $N_{\mathrm{ZP}} = 0$, namely when $\mathrm{mod}_Q(N_P \times P) = 0$, but this does not cover all the 4G/LTE RB allocation possibilities.

A third solution is to increase, at the transmitter side, the total number of subcarriers and the frequency sampling by a factor β such that

$$\mathrm{mod}_P(\beta N) = 0, 1 \leq \beta < 2,$$

with $\beta = 1.5$ to support 4G/LTE numerology. The subcarrier spacing being equal to the ratio between the frequency sampling and the total number of subcarriers ($\Delta f = f_s/N$), it remains unchanged (15 kHz for 4G/LTE). The subband size is now a multiple of P, satisfying the condition to employ the proposed technique. Note that this solution does not require changing the frequency sampling and the total number of subcarriers at the receiver side, since it is an oversampling technique. Thus, such solution is transparent for the receiver and is totally compatible with 4G/LTE numerology. Using an IFFT size which is not a power of 2 can be seen as a drawback, but as mentioned in the beginning of this subsection, 4G/LTE numerology requires the support of an IFFT of size 1536 ($= \beta \times 2^{10}$), and the FFT precoder of the Single Carrier (SC) OFDM modulation used in LTE uplink already requires a size that is a multiple of 12 (more precisely, FFT of size $N = 2^a 3^b 5^c \leq 1200$). Furthermore, if $Q \neq 2^n$ can be decomposed into a product such that $Q = Q_N \times R$, with $Q_N = 2^n$ and n, R integers, then it is possible to calculate an IFFT of size Q from R IFFTs of size Q_N as

$$\begin{aligned} x(n) &= \sum_{k=0}^{RQ_N-1} X(k) e^{j2\pi \frac{kn}{RQ_N}} \\ &= \sum_{k=0}^{R-1} e^{j2\pi \frac{kn}{R}} \sum_{l=0}^{Q_N-1} X(kQ_N + l) e^{j2\pi \frac{ln}{Q_N}}. \end{aligned} \quad (20)$$

As an example, if the subband size is set to the 4G/LTE RB size composed of 12 subcarriers, then the IFFT of the subcarrier processing part can be calculated using 3 IFFTs of size 4. The main issue with this solution is that the computational complexity is increased due to the oversampling.

C. Flexibility to Support Classical OFDM Modulation

With the increasing number of scenarios supported in 5G, some applications may require the reuse of the classical OFDM modulation of 4G/LTE in addition to the support of novel multicarrier waveforms such as UF-OFDM. This implies that the transmitter should be able to switch between UF-OFDM and OFDM modulations without major modifications to the computation core, to avoid the duplication of the processing units when considering hardware implementation issues.

In fact, the signal decomposition presented in Section III-A can be applied for OFDM. Indeed, the OFDM symbol with the extension of a cyclic prefix of length L can be generated as

$$y(n) = \sum_{k=0}^{N-1} c(k) e^{j2\pi \frac{kn}{N}}, n \in [\![-L, N-1]\!].$$

The signal $y(n)$ can be decomposed into virtual (non-filtered) subbands as

$$\begin{aligned} y(n) &= \sum_{q=0}^{Q-1} \sum_{k=0}^{K-1} c(q + Qk) e^{j2\pi \frac{(q+Qk)n}{N}} \\ &= \sum_{q=0}^{Q-1} e^{j2\pi \frac{qn}{N}} \sum_{k=0}^{K-1} s_k(q) e^{j2\pi \frac{kn}{K}} \\ &= \sum_{q=0}^{Q-1} x_q(n) e^{j2\pi \frac{qn}{K}}. \end{aligned}$$

Similarly to an UF-OFDM symbol, the OFDM symbol can be segmented as

$$y_p(n') = \sum_{q=0}^{Q-1} F'_q(n') x_q(n') e^{j2\pi \frac{qp}{Q}},$$

with

$$F'_q(n') = e^{j2\pi \frac{qn'}{N}},$$

Therefore, the OFDM symbol without the cyclic prefix can be generated by using the equation of the UF-OFDM core part and changing the filter core coefficients to $F'_q(n')$. The cyclic prefix part can be generated by using (17) (step 6 of the method), and is given by

$$\begin{aligned} y_{\mathrm{prefix}}(n_p) = y(n_p - L) &= \sum_{q=0}^{Q-1} x_q(n_p - L) P'_q(n_p), n_p \\ &\in [\![0, L-1]\!], \end{aligned}$$

with

$$P'_q(n_p) = e^{j2\pi \frac{q(n_p - L))}{N}}.$$

The prefix tail coefficients of the UF-OFDM modulation (16) must be replaced by the $P'_q(n)$ coefficients defined above.

An alternative way to generate the cyclic prefix is simply by copying the last L samples of the core part. This can be done during the recover step (step 5) since it is a concatenation operation. The cyclic prefix can be inserted at the same time,

without any complexity increase. Note that, for the two proposed cyclic-prefix insertion methods, the cyclic prefix length in OFDM mode can be different from the filter length in UF-OFDM mode. The related processing unit just has to be adapted to process the corresponding length.

IV. Computational Complexity Analysis and Comparisons

A. Complexity Analysis

We evaluate the computational complexity of the proposed technique in terms of the number of real-valued additions (RAs) and real-valued multiplications (RMs) required to compute one UF-OFDM symbol, and compare it with state-of-the-art approaches for UF-OFDM modulation. We distinguish RAs and RMs because their impact on implementation complexity can differ depending on the type of implementation. For instance, when considering a dedicated hardware implementation, a RM requires more hardware resources (more logic gates) than a RA.

For complex-valued operations, it is necessary to define the number of RMs and RAs required to compute one complex multiplication (CM). We denote by $C_{\text{RM}}(x)$ and $C_{\text{RA}}(x)$ respectively the number of RMs and RAs required for the operation x. Typically, a complex multiplication requires $C_{\text{RM}}(\text{CM}) = 4$ RMs and $C_{\text{RA}}(\text{CM}) = 2$ RAs. But a complex multiplication can be also be counted as $C_{\text{RM}}(\text{CM}) = 3$ RMs and $C_{\text{RA}}(\text{CM}) = 5$ RAs by using the following development:

$$(a+jb)(c+jd) = c(a+b) - b(c+d) + j(c(a+b) + a(d-c)).$$

Furthermore, if a complex sample is multiplied by pre-computed complex coefficients (for instance, filter coefficients), 2 RAs can be removed and $C_{RA}(\text{complexMultiplier}) = 3$. Indeed, if $c+jd$ is the pre-computed complex coefficient, then $c+d$ and $d-c$ can also be pre-computed instead of directly calculated. Since all the complex multiplications of the UF-OFDM techniques involve a pre-computed coefficient, only 3 RAs are required for any complex multiplication. Thus, $C_{\text{RM}}(\text{CM}) = 3$ RMs and $C_{\text{RA}}(\text{CM}) = 3$ are considered in this paper.

In addition, the choice of the IFFT computation technique is another critical aspect when considering complexity, since this choice has a significant impact on the required number of RMs and RAs. A well-known and efficient IFFT computation technique is the split radix IFFT [10], which can be used when the IFFT size is a power of 2 ($N = 2^n$). The computational complexity of the split radix IFFT of size N, referred as $C_{\text{RA/RM}}(\text{IFFT}_N)$, is given by [11]

$$C_{\text{RM}}(\text{IFFT}_N) = N\log_2(N) - 3N + 4,$$
$$C_{\text{RA}}(\text{IFFT}_N) = 3N\log_2(N) - 3N + 4.$$

The computational complexity of the baseline UF-OFDM technique is not considered in this section due to its relatively high complexity when compared to the other presented techniques. This baseline solution is generally presented for understanding and illustrating the UF-OFDM modulation and its specific per-subband filtering. On the other hand, computational complexity analysis of the FD UF-OFDM, the TDW UF-OFDM and the proposed UF-OFDM techniques are derived in the rest of this section.

TABLE I
CHOICE OF N_0 DEPENDING ON THE SUBBAND SIZE FOR THE FD UF-OFDM TECHNIQUE

Subband size	N_0	NMSE (dB)
12	64	−25.8
16	64	−25.6
48	128	−29.3
64	128	−28

1) FD UF-OFDM complexity analysis: As explained in Section II-B, the FD UF-OFDM technique employs multiple small IFFTs of size proportional to N_0 in the oversampled frequency domain (by an oversampling factor N_{OS}) to efficiently process the subband filter. In this section, the oversampling factor N_{OS} is fixed to 2 since this value provides a good trade-off between the signal approximation error and the computational complexity. Thus, the computational complexity of the FD UF-OFDM technique is given by

$$C_{\text{RM}}(\text{FD UF-OFDM}) = B\Big(C_{RM}(\text{FFT}_{N_0}) + C_{\text{RM}}(\text{IFFT}_{2N_0}) + 6N_0\Big) + C_{RM}(\text{IFFT}_{2N}),$$

$$C_{\text{RA}}(\text{FD UF-OFDM}) = B\Big(C_{\text{RA}}(\text{FFT}_{N_0}) + C_{\text{RA}}(\text{IFFT}_{2N_0}) + 6N_0\Big) + C_{\text{RA}}(\text{IFFT}_{2N}) + 4(B-1)N_0.$$

Due to the IFFT of size $2N$, the FD UF-OFDM is in any case more computational complex than an OFDM transmitter which only requires an IFFT of size N. Furthermore, the complexity is dependent on the number of allocated subbands and the chosen small IFFT size N_0. For each allocated subband, one FFT of size N_0, one IFFT of size $2N_0$ and $2N_0$ complex multiplications (subband filtering) have to be computed. Thus, the computational complexity increases linearly with the number of allocated subbands. Additionally, when the subband size changes, the choice of N_0 must be reconsidered such that the approximation errors are kept within an acceptable level. The choice of $N_0 = 64$ determined in [8] is applicable for $Q = 12$. However, for other subband sizes, no analysis has been performed in the literature. In order to fairly evaluate the computational complexity, the Normalized Mean Square Error (NMSE) of the approximated UF-OFDM symbol has been evaluated for the subband size of 12, 16, 48 and 64 subcarriers for different N_0 values. Table I shows the N_0 values corresponding to each of these subband sizes for an NMSE inferior to −25 dB, assuming a Dolph-Chebyshev filter [7] with a sidelobe level of 70 dB. This value was chosen to obtain an NMSE level comparable to the one obtained for the case where $Q = 12$ and $N_0 = 64$, to keep an acceptable approximation error. It can be seen from Table I that the N_0 value is only doubled if the subband size is

TABLE II
NUMBER OF REQUIRED RMS AND RAS PER STEP FOR THE PROPOSED UF-OFDM TECHNIQUE

Step	Operation	C_{RM}	C_{RA}
1	Segmentation	0	0
2	IFFTs of size K	$Q \times C_{\text{RM}}(\text{IFFT}_K)$	$Q \times C_{\text{RA}}(\text{IFFT}_K)$
3	Core windowing	$3Q \times K = 3N$	$3Q \times K = 3N$
4	IFFTs of size Q	$K \times C_{\text{RM}}(\text{IFFT}_Q)$	$K \times C_{\text{RA}}(\text{IFFT}_Q)$
5	Reconstruction	0	0
6	Prefix calculation	$Q \times 3L$	$Q \times 3L$
7	Suffix calculation	0	$2(L-1)$
8	Concatenation	0	0

multiplied by 4. This implies that the computational complexity does not increase linearly with the subband size, contrary to the number of allocated subbands. Thus, it is preferable to use few subbands of large size instead of multiple subbands of short size when considering this technique.

2) TDW UF-OFDM complexity analysis: The complexity of this method mainly depends on the number of windows N_w. A TDW UF-OFDM transmitter using N_w windows will be denoted by TDW_{N_w} UF-OFDM in this section. According to [6], the computational complexity of this technique in terms of number of required RMs and RAs is

$$C_{\text{RM}}(\text{TDW}_{N_w}\text{ UF-OFDM}) = N_w\Big(C_{RM}(\text{IFFT}_N) + 3(N+L-1)\Big),$$

$$C_{\text{RA}}(\text{TDW}_{N_w}\text{ UF-OFDM}) = N_w\Big(C_{RA}(\text{IFFT}_N) + 3(N+L-1)\Big) + (N_w-1)(N+L-1).$$

Contrary to the FD UF-OFDM technique, the computational complexity does not increase with the number of allocated subbands B. However, it increases linearly with the number of windows N_w. When only 1 window is used ($N_w = 1$), the computational complexity is close to the one of an IFFT of size N. Thus, the computational complexity is at least N_w times larger than the computational complexity required to compute an OFDM symbol. In the original paper [6], the number of windows N_w considered was set to:

1) $N_w = 1$ for the lowest computational complexity, but at the cost of higher approximation errors leading to lower spectral confinement.
2) $N_w = 3$ for a good compromise between computational complexity and approximation errors.

In this section, TDW_1 UF-OFDM and TDW_3 UF-OFDM techniques are considered, since $N_w > 3$ leads to a high computational complexity largely undermining the interest of using this technique.

3) Proposed UF-OFDM complexity analysis: Table II shows the number of required RMs and RAs per step (see Subsection III-A for the details of each step) to compute one UF-OFDM symbol using the proposed technique, assuming $\text{mod}_Q(N) = 0$. The total computational complexity in number of RMs and RAs to calculate one UF-OFDM symbol is given by

$$C_{\text{RM/RA}}(\text{UF-OFDM}) = \sum_{i=1}^{8} C_{\text{RM/RA}}(\text{step}_i),$$

$$C_{\text{RM}}(\text{UF-OFDM}) = C_{\text{RM}}(\text{IFFT}_N) + 4(Q+K-1) + 3N\frac{L}{K},$$

$$C_{\text{RA}}(\text{UF-OFDM}) = C_{\text{RA}}(\text{IFFT}_N) + 4(Q+K-1) + 3N\frac{L}{K} + 2L - 1.$$

Similarly to the TDW UF-OFDM technique, the computational complexity does not depend on B, the number of allocated subbands. Furthermore, the computational complexity is equivalent to the one required to compute an OFDM symbol (IFFT of size N) plus an overhead term. This overhead term depends on the ratio between the filter length L and the total number of subbands K ($\alpha = L/K$). In other words, the proposed technique has a computational complexity almost equivalent to OFDM for short subband sizes (for any number of allocated subbands), and the complexity increases with the subband size Q.

When considering any subband size, the oversampling techniques presented inSection III-B can be used at the cost of an increase in the computational complexity, as the total number of subcarriers must be multiplied by a factor β (= 1.5 for 4G/LTE). Since the IFFT of the subcarrier processing part is no longer a power 2, the split radix FFT technique cannot be directly applied, except if this IFFT is computed using (20) which mostly requires R IFFTs of size Q_N and $(R-1)RQ_N$ complex multiplications by the $\exp[j2\pi(kn)/R]$ terms (for $k \in [\![1, R-1]\!]$). The computational complexity related to the multiplication by the exponential terms can be greatly reduced by noting that $\exp[j2\pi(kn)/R] = 1$ when $\text{mod}_R(n) = 0$, for any $k \in [\![1, R-1]\!]$ values. Thus, $Q/R = Q_N$ complex multiplications can be avoided per k values. In this case, the computation complexity of an IFFT of size $Q = R \times Q_N$ becomes

$$C_{\text{RM}}(\text{IFFT}_{R,Q_N}) = RC_{\text{RM}}(\text{IFFT}_{Q_N}) + 3Q_N(R-1)^2,$$

$$C_{\text{RA}}(\text{IFFT}_{R,Q_N}) = RC_{\text{RA}}(\text{IFFT}_{Q_N}) + 3Q_N(R-1)^2 + 2(R-1)RQ_N.$$

In this section, only the oversampled solution is considered, as it enables to support any subband size without any restriction, while being less computationally complex than the solution based on multiple intermediate UF-OFDM symbols.

B. Complexity Comparison

The computational complexity of the FD UF-OFDM, TDW UF-OFDM and the proposed UF-OFDM are compared with respect to OFDM using the following ratio:

$$\text{Ratio-to-OFDM}_{\text{RM/RA}} = \frac{C_{\text{RM/RA}}(\text{UF-OFDM})}{C_{\text{RM/RA}}(\text{OFDM})},$$

TABLE III
ANALYTICAL EXPRESSION OF THE COMPUTATIONAL COMPLEXITY FOR EACH CONSIDERED UF-OFDM TRANSMITTER

Transmitter	C_{RM}	C_{RA}
OFDM	$N\log_2(N) - 3N + 4$	$3N\log_2(N) - 3N + 4$
FD UF-OFDM	$B\left(3N_0\log_2(N_0) - N_0 + 8\right)$ $+ 2N\log_2(2N) - 6N + 4$	$B\left(9N_0\log_2(N_0) + 7N_0 + 8\right)$ $+ 6N\log_2(2N) - 6N - 4N_0 + 4$
TDW_{N_w} UF-OFDM	$N_w\left(N\log_N + 3L + 1\right)$	$N_w\left(3N\log_N + N + 4L\right) - N - L + 1$
Proposed UF-OFDM ($\text{mod}_Q(N) = 0$)	$N\log_2(N) - 3N + 4(Q+K) + 3N\frac{L}{K}$	$3N\log_2(N) - 3N + 4(Q+K) + 3N\frac{L}{K} + 2L - 1$
Proposed UF-OFDM ($\text{mod}_Q(N) \neq 0$)	$\beta N\left(\log_2(\frac{\beta N}{R}) + 3\left(\frac{(R-1)^2}{R} + \frac{\beta L}{K} - 1\right)\right)$ $+ 4(Q + KR)$	$\beta N\left(3(\log_2\left(\frac{\beta N}{R}\right) + 3\beta\frac{L}{K} + 5R + \frac{3}{R} - 11\right)$ $+ 4(Q + KR) + 2(\beta L - 1)$

TABLE IV
SELECTED CONFIGURATIONS FOR COMPLEXITY COMPARISON

	Number of subband allocated B	Subband size Q
Configuration A	1	16
Configuration B	1	64
Configuration C	37	16
Configuration D	9	64
Configuration E	50	12
Configuration F	12	48

where the required numbers of RMs and RAs $C_{\text{RM/RA}}$ (UF-OFDM) are analytically evaluated in the previous subsection for each technique and summarized in Table III. Note that $C_{\text{RM/RA}}(\text{OFDM}) = C_{\text{RM/RA}}(\text{IFFT}_N)$ since an OFDM transmitter only requires an IFFT of size N. Several representative sets of subband sizes and number of allocated subbands must be considered to fairly compare the different UF-OFDM techniques. For this purpose, 6 different configurations are considered. They are detailed in Table IV. For all these configurations, the total number of subcarriers is fixed to 1024 and the length of the subband prototype filter is equal to $L = 73$ samples. Short and large subband sizes are considered to evaluate their impact on the complexity. In addition, subband sizes compatible with a 4G/LTE system are considered for configuration E and F. Configuration A and B represent the cases where only 1 subband is allocated, which is adequate for low data rate services like massive machine communications. Configurations C to F represent the cases where multiple subbands are allocated: the number of allocated subbands is determined such that the entire bandwidth that can be allocated in 4G/LTE is occupied (at most 600 active subcarriers from the total 1024 subcarriers). This corresponds to the extreme cases where a user occupies the totality of the available bandwidth to achieve high date rates.

The computational complexity results are illustrated in Fig. 5(a) for configuration A. The proposed UF-OFDM technique requires almost the same number of RMs and RAs when compared to the TDW_1 UF-OFDM technique, and only 53% more RMs and 14% more RAs when compared to OFDM. Furthermore, the proposed technique requires 37% less RM and 51% less RAs than the FD UF-OFDM technique. The TDW_3 UF-OFDM technique has the highest computational complexity for this configuration, and is therefore the least interesting technique. When considering configuration B, the proposed UF-OFDM technique requires 13% more RMs when compared to the FD UF-OFDM technique, as shown in Fig. 5(b). However, the number of RAs being reduced by 40%, the proposed UF-OFDM technique is still less complex than the FD UF-OFDM technique if the total number of operations is considered (28% less number of RMs and RAs).

Concerning the TDW1 UF-OFDM technique, its complexity reduction comes at the price of an accuracy loss. Thus, the effect of the approximation errors must be considered for a fair comparison. For this purpose, the power spectral densities of the considered UF-OFDM techniques are presented in Fig. 6 for the following parameters:

1) allocation of 1 subband of 48 subcarriers,
2) use of 1024 subcarriers in total, for a sampling frequency of 15.36 MHz as defined in 4G/LTE,
3) application of the Dolph-Chebyshev filter with a sidelobe level of 70 dB.

The OOBPL located outside the allocated subband is higher in the case of the FD UF-OFDM technique by around 5 dB when compared to the proposed technique. As mentioned in [8], this part of the spectrum is not as important as the OOBPL located at each edge of the allocated subband. Indeed, in a practical system, such low OOBPL is never achieved due to the imperfection of the front end components, for instance due to the non-linearity of the power amplifier. Therefore, the approximation errors introduced by the FD UF-OFDM technique do not degrade much the spectral confinement. When considering the TDW UF-OFDM technique, the number of windows has a great impact on the signal approximation and the resulting OOBPL. This is illustrated in Fig. 6, which shows the Power Spectral Density (PSD) of each UF-OFDM transmitter, assuming that the subbands are normalized: the distortion caused by the subband filter is compensated by readjusting the power of each sub-carrier. It can be seen that the use of only 1 window greatly degrades the OOBPL at the edges of the allocated subband. When 3 windows are used, the spectral confinement is improved, but not as much as with the proposed technique: at

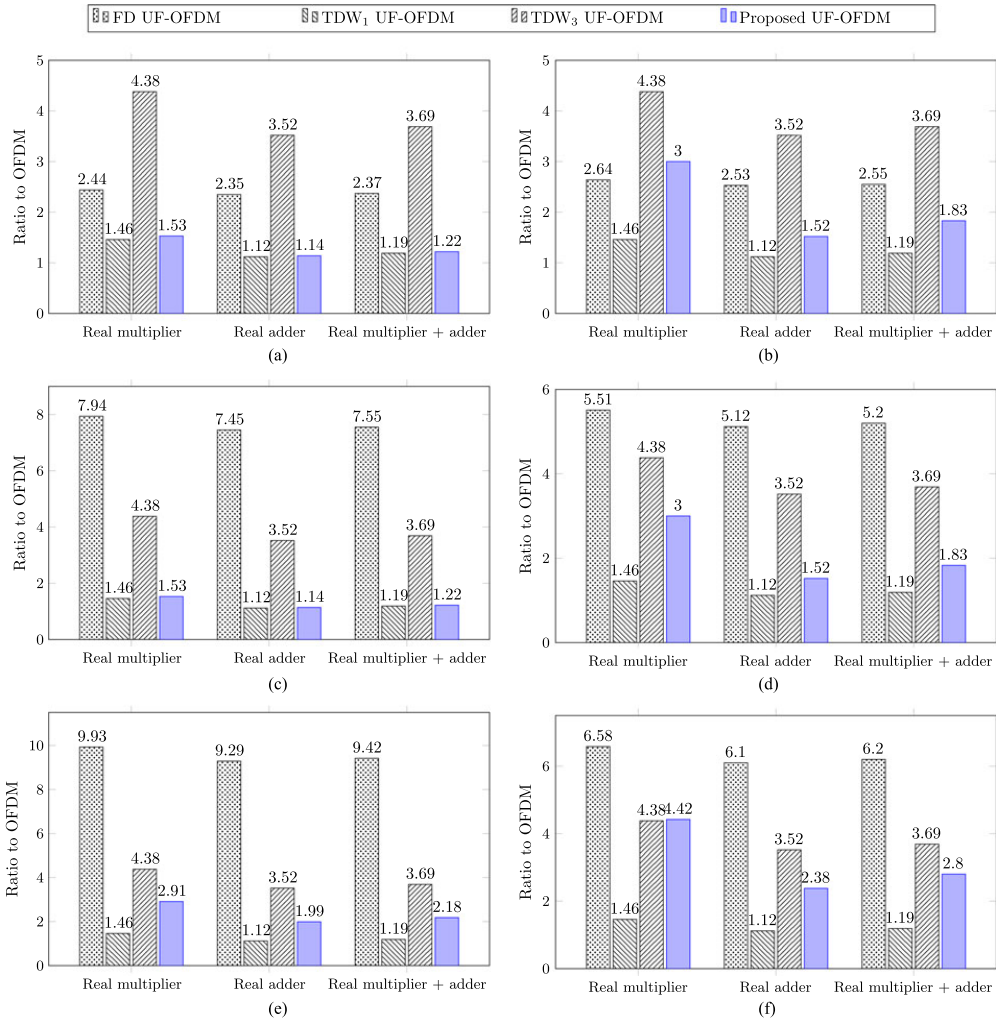

Fig. 5. Computational complexity of the FD UF-OFDM, TDW UF-OFDM, and proposed UF-OFDM for different subband configurations. (a) 1 subband of size 16. (b) 1 subband of size 64. (c) 37 subbands of size 16. (d) 9 subbands of size 64. (e) 50 subbands of size 12. (f) 12 subbands of size 48.

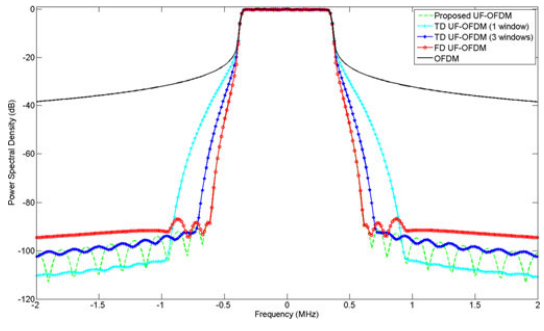

Fig. 6. Power spectral density of the UF-OFDM techniques.

−40 dB, the frequency difference between the TDW_3 UF-OFDM and the proposed UF-OFDM techniques is around 50 kHz, which is not negligible since it corresponds to more than 3 subcarriers. Thus, a larger guard interval may be required between users to offer the same spectral isolation as the proposed UF-OFDM technique, leading to a data rate loss. A larger number of windows can be employed to reduce the approximation errors, at the cost of an increased computational complexity. Concerning the TDW_1 UF-OFDM technique, the original signal is highly degraded along with the OOBPL. In fact, the TDW_1 UF-OFDM is closer to windowed-OFDM than UF-OFDM.

When considering a subband size of 12 subcarriers for configuration A and a subband of size of 48 subcarriers for configuration B, the same complexity results are obtained. Indeed,

Subsection III-B shows that the proposed technique is compatible with any subband size when $B = 1$: the active carriers can be allocated at the middle of the subband, and zero-valued samples can be padded at its extremities. Thus, the proposed UF-OFDM technique is the most interesting technique for $B = 1$, since it has the lowest computational complexity while preserving the signal quality.

Concerning configuration C, the proposed UF-OFDM technique is employed without any oversampling since the total number of subcarriers can be divided into an integer number of subbands. It can be shown in Fig. 5(c) shows that the proposed technique has a lower complexity than the FD UF-OFDM and the TDW_3 UF-OFDM techniques. Particularly, the FD UF-OFDM technique requires 4.18 times more RMs and 5.51 times more RA than the proposed UF-OFDM technique. Thus, the FD UF-OFDM loses its appeal when a large number of subbands is employed. When considering a larger subband size with configuration D (Fig. 5(d)), the proposed UF-OFDM still has a lower complexity than the other techniques, with the exception of the TDW_1 UF-OFDM, which has an unacceptable spectral confinement.

Next, configuration E and F represent cases where multiple subbands are allocated, but the subband size is not a multiple of the total number of subcarriers ($\text{mod}_Q(N) > 0$). In this context, the oversampling technique described in Subsection III-B must be employed for the proposed technique. While this increases the complexity, our proposal still offers reduced complexity when compared to the FD UF-OFDM and to the TDW UF-OFDM techniques, as shown in Fig. 5(e) and in (f).

Therefore, for all the configurations considered, the proposed technique offers significant reductions in computational complexity while preserving the signal accuracy. Note also that the complexity is close to OFDM for a subband size $Q = 16$, regardless of the number of allocated subbands. Finally, our proposed transmitter architecture can be easily adapted to generate an OFDM symbol as demonstrated in Section III-C, which is more difficult for techniques like FD UF-OFDM where the IFFT size must be doubled (assuming $N_{\text{OS}} = 2$). This is particularly interesting from a hardware implementation perspective, where resources must be shared to reduce the hardware complexity.

Finally, the proposed technique assumes that each subband contains the same number of subcarriers. Therefore, the use of different subband sizes on the same carrier is not directly supported. In fact, for downlink communication, multiple communication services using different numerologies are considered in 5G. For instance, narrow subbands can be employed for mMTC, whereas wider subbands can be used for broadband communication. For the uplink, the user equipment being configured for a particular application, the subband size should be kept constant. Note that the TDW UF-OFDM technique suffers from the same drawback, and only the FD UF-OFDM transmitter can support multiple subband sizes in the same bandwidth. For the latter, the stage of IFFT/FFT (of size N_0) can simply be adapted for a given subband configuration, since subbands are processed separately and independently. In our case, the support of multiple subband sizes can be done by duplicating the transmitter. Assuming that the whole bandwidth is allocated and both subband sizes of 16 and 64 subcarriers must be supported, the proposed transmitter remains 18% to 43% less complex (in number of RM) than the FD UF-OFDM transmitter, despite the replication. These values are obtained by considering the lowest and highest complexity of the FD UF-OFDM transmitter, which correspond to 9 subbands of size 64 and 37 subbands of size 16 respectively. If subbands of size 12 and 48 are considered, the complexity of the proposed transmitter is comparable to the FD UF-OFDM transmitter (between 26% less and 11% more complex).

V. CONCLUSION

In this paper, a novel UF-OFDM technique with low computational complexity is proposed. One of the main features of this novel technique is that, contrary to the ones proposed in the literature, it does not introduce any approximation of the original signal. Additionally, appropriate solutions have been detailed to support any subband size as defined in 4G/LTE numerology. Comparisons were performed with the techniques presented in the literature using different set of subband allocations and subband sizes. The results show that the proposed UF-OFDM technique provides significant computational complexity reduction in most cases. Finally, power spectral density comparisons were conducted showing that the proposed technique preserves the spectral confinement of UF-OFDM, contrary to the TDW UF-OFDM technique. This demonstrates for the first time the possibility to design a low-complexity UF-OFDM transmitter without any signal degradation, making the UF-OFDM particularly appealing for adoption in upcoming wireless applications and standards.

REFERENCES

[1] V. Vakilian, T. Wild, F. Schaich, S. ten Brink, and J. F. Frigon, "Universal-filtered multi-carrier technique for wireless systems beyond LTE," in *Proc. 2013 IEEE Globecom Workshops*, Dec. 2013, pp. 223–228.
[2] P. Siohan, C. Siclet, and N. Lacaille, "Analysis and design of OFDM/OQAM systems based on filterbank theory," *IEEE Trans. Signal Process.*, vol. 50, no. 5, pp. 1170–1183, May 2002.
[3] F. Schaich and T. Wild, "Relaxed synchronization support of universal filtered multi-carrier including autonomous timing advance," in *Proc. 2014 11th Int. Symp. Wireless Commun. Syst.*, Aug. 2014, pp. 203–208.
[4] T. Hwang *et al.*, "OFDM and its wireless applications: A survey," *IEEE Trans. Veh. Technol.*, vol. 58, no. 4, pp. 1673–1694, May 2009.
[5] T. Wild and F. Schaich, "A reduced complexity transmitter for UF-OFDM," in *Proc. 2015 IEEE 81st Veh. Technol. Conf.*, May 2015, pp. 1–6.
[6] M. Matthe, D. Zhang, F. Schaich, T. Wild, R. Ahmed, and G. Fettweis, "A reduced complexity time-domain transmitter for UF-OFDM," in *Proc. 2016 IEEE 83rd Veh. Technol. Conf.*, May 2016, pp. 1–5.
[7] T. W. Parks and C. S. Burrus, *Digital Filter Design*. New York, NY, USA: Wiley, 1987, ch. 7.
[8] M. Mukherjee, L. Shu, V. Kumar, P. Kumar, and R. Matam, "Reduced out-of-band radiation-based filter optimization for UFMC systems in 5G," in *Proc. 2015 Int. Wireless Commun. Mobile Comput. Conf.*, Aug. 2015, pp. 1150–1155.
[9] X. Wang, T. Wild, and F. Schaich, "Filter optimization for carrier-frequency and timing-offset in universal filtered multi-carrier systems," in *Proc. 2015 IEEE 81st Veh. Technol. Conf.*, May 2015, pp. 1–6.
[10] P. Duhamel and H. Hollmann, "Split radix FFT algorithm," *Electron. Lett.*, vol. 20, pp. 14–16, Jan. 1984.
[11] H. Sorensen, M. Heideman, and C. Burrus, "On computing the split-radix FFT," *IEEE Trans. Acoust., Speech, Signal Process.*, vol. 34, no. 1, pp. 152–156, Feb. 1986.

Jérémy Nadal received the engineering degree from Telecom Bretagne, Brest, France, in 2013. He is currentlyworking toward the Ph.D. degree at IMT Atlantique/Lab-STICC Laboratory, Brest, France. He occupied the position of a Research Engineer from 2013 to 2014 at the Electronics Department. His general research interests include both algorithm development for 5G waveform candidates and corresponding efficient hardware architecture design. In this context, he proposed several original contributions for FBMC/OQAM, FC-OFDM, and UF-OFDM waveforms, associated with corresponding hardware proof-of-concept (Exhibition at Mobile World Congress 2015, European Conference on Networks and Communications EuCNC 2014 and 2017). He has actively participated in METIS and Fantastic-5G European research projects.

Charbel Abdel Nour received the degree in computer and communications engineering from Lebanese University, Beirut, Lebanon, the Master's degree in digital communications from the University of Valenciennes, Valenciennes, France, and the Ph.D. degree in digital communications from Telecom Bretagne, Brest, France, in 2002, 2003, and 2008, respectively. Since June 2007, he has been working as a Postdoctoral fellow at the Electronics Department, Telecom Bretagne. His research interests include the radio mobile communications systems, broadcasting systems, coded modulations, waveform design, error correcting codes, MIMO, and iterative receivers. He is involved in several research projects related to broadcasting and satellite communications. Since 2007, he is active in the Digital Video Broadcasting DVB consortium where he had important contributions. Starting November 2011, he has been an Associate Professor at the Electronics Department, IMT Atlantique.

Amer Baghdadi received the engineering and the Master of Science degrees in 1998, and the Ph.D. degree in 2002, all from Grenoble Institut National Polytechnique (INP), Grenoble, France. Furthermore, he received the accreditation to supervise research (HDR) in Sciences and Technologies of Information and Communication in 2012 from the University of Southern Brittany, Lorient, France. He is a Professor at IMT Atlantique/Lab-STICC Laboratory. His general technical area concerns both theoretical and practical aspects, and both algorithm development for digital baseband components and corresponding hardware/software implementations and digital circuit design. His research activities target mainly digital communication applications, in addition to other application domains, and more particularly the design of flexible digital physical layer for future wireless communication standards and terminals. He serves on the technical program committee for several international conferences. He coauthored more than 100 papers on scientific journals and proceedings of international conferences.

2.2.1.5 Complete demonstrator platform

The last contribution concerns one of the first flexible and efficient hardware platform for beyond 5G waveform design proof-of-concept. The proposed platform constitutes a complete hardware/software development environment that can emulate different communication scenarios foreseen in 5G and beyond. The developed environment is presented in Figure 2.8 where one board (Xilinx ZedBoard) emulates a User Equipment (UE) at the transmitter side, and a second board (Xilinx ZC706 evaluation board) is used to emulate the BS at the receiver side. These two digital processing boards are based on the recent Zynq-7000 SoC which integrates a dual-core ARM Cortex A9 processor and a reconfigurable logic fabric (FPGA). Both boards are extended by a RF board (Analog Devices AD-FMCOMMS1-EBZ) to enable radio transmissions. Each of these RF boards integrates one transmitter and one receiver interfaces. The transmit interface of the BS is optionally used to emulate a multi-user environment for demonstration purpose. On-board control and communication interfaces are ensured by the embedded dual-core Cortex A9 processor. The considered modulation techniques are implemented in hardware on the FPGA part of the Zynq-7000 SoC.

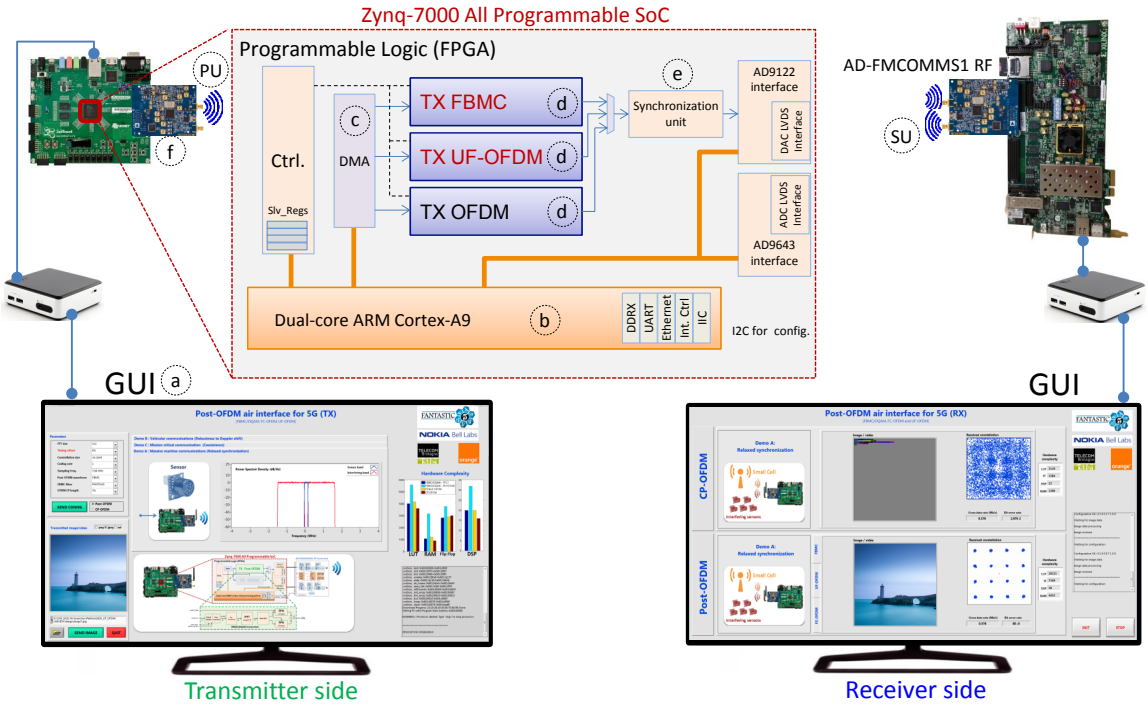

Figure 2.8: Demonstration setup with front-end interface.

In addition to these boards, two host computers are used for control and display results purpose. They run two dedicated LabVIEW GUIs. The GUI at the transmitter side is used to select the target scenario, the waveform parameters, and the image file to transmit. In addition, it displays the power spectral density corresponding to the selected waveform parameters. At the receiver side, the GUI displays relevant performance metrics, such as BER, received constellation and received image data. Furthermore, both GUIs display metrics related to the hardware complexity and throughput.

As illustrated in Figure 2.8 ⓐ multiple parameters can be selected using the GUI at the transmitter side (TX): target scenario, QAM constellation, type of waveform, type of filter for FBMC, etc. The user can also select between several images or between several videos to transmit.

The implemented FBMC/OQAM and UF-OFDM transceivers, in addition to OFDM,

have been integrated in the platform. Measured BER demonstrates how the candidate waveforms clearly outperform OFDM in the considered scenarios, confirming state-of-the-art theoretical results. For the Massive Machine Communication (MMC) scenario, the best results are obtained for FBMC/OQAM with the MMB4 filter, closely followed by the NPR1 short filter. The latter is the best adapted waveform for Vehicule-to-Anything (V2X) scenarios and it is also suitable for Mission Critical Communications (MCC). UF-OFDM outperforms OFDM for both MMC and MCC scenarios, and it is the most suitable waveform for MCC. Hardware synthesis results show that the required hardware resources for most of the candidate waveforms are close to that of OFDM at the transmitter side. Therefore, with the recently proposed optimizations and hardware proof-of-concept, the hardware complexity becomes no longer a discriminating factor for the considered beyond 5G candidate waveforms. For more details regarding the platform and/or the obtained results, the reader is refered to our conference publication of [173] and our journal publication of [174].

2.2.2 Performed work and contributions on FTN signalling for FBMC/OQAM

FTN transmissions introduced by Mazo can be seen as a means to trade processing complexity for improved spectral efficiency. Indeed, the transmission rate is not necessarily limited by the Nyquist rate. Faster transmission rate can be envisaged provided that interference is accepted. The main goal of this work performed in the context of Naila Lahbabi's PhD thesis was to define and evaluate a new transmission mode involving FTN signaling with FBMC/OQAM modulation to boost the transmission throughput. We considered only packing the multicarrier signals closer in time domain compared to the Nyquist rate. The major contributions of our work involved:

- An efficient implementation of an FTN transceiver using FBMC/OQAM modulation,
- A new precoding technique aiming at reducing FTN self interference at the transmitter side,
- The proposal of an enhanced design of FTN-OQAM transceiver.

The first promising work concerning FTN-OQAM transceivers was presented in [175]. However, the complexity of their solution increases considerably compared to traditional FBMC/OQAM systems due to the introduced FTN related blocks. Moreover, their receiver relies on the MAP algorithm meaning that its complexity increases with the modulation order.

In contrast, our work's objective was to propose a new FTN signaling system approaching closely the FTN theoretical rate improvement with a reasonable complexity increase when switching from Nyquist to FTN mode. Differently form the state-of-the-art solutions, we proposed a turbo-like receiver based on linear Minimum Mean Square Error (MMSE) equalization. The complexity of such equalizers only depends on the channel impulse response and is independent of the modulation order which makes them good candidates if high modulation orders are to be used. By reducing the equalization complexity, we quickly found out that it comes at the cost of more iterations to cancel the intrinsic interference, ending up increasing complexity again. We identified that the degradation was mainly due to the inefficient symbol detection from the MMSE equalizer at the first iteration. To improve this, we considered two directions:

- Apply MAP equalization for only the first iteration. However, the complexity for conducting MAP algorithm remains an issue as stated previously and this solution does not fully address our design target.

- Imbalance the interference level to make some of the symbols experience less interference than the others. Thus for those less affected symbols, the MMSE equalizer can provide a better estimation that can be used to improve the overall turbo-equalization efficiency.

Since FBMC/OQAM modulation employs various pulse shapes having different time-frequency localization properties, we showed that the MMSE equalizer should better operate along time axis when the prototype filter is well localized in time domain and vise-versa.

Furthermore, we proposed an algorithm based on EXtrinsic Information Transfer (EXIT) chart analysis to investigate the smallest packing factor the FTN-OQAM transceiver can achieve while providing a BER performance close to the Nyquist one.

Differently from the state-of-the-art solution, we targeted high modulation orders and showed that a rate improvement of 11% is achievable, in case of 64-QAM modulation, with a performance very close to the Nyquist one and after performing only 5 iterations at the receiver side. We also showed that the rate improvement can be up to 25% with 16-QAM modulation at the cost of 1 dB loss around a BER of 10^{-4} compared to the Nyquist performance while only 4 iterations are needed at the receiver side.

When signaling faster than the Nyquist rate, the pulses orthogonality is no longer valid and interferences are intentionally added to the transmitted signal even when transmitting over AWGN channel. As a first step to combat its penalizing effect, we provided an analytical expression of this interference and showed that it can be modeled by an equivalent interference channel. However, this interference is perfectly known by both the transmitter and the receiver which is similar to transmissions over multipath channels with perfect CSI at the transmitter. As a step further, we investigated a new precoding scheme we called Sparse Interference Pre-Cancellation to remove FTN-induced interference at the transmitter side. Given the nature of this interference, it is difficult to jointly precode all the transmitted symbols. Moreover, our analysis showed that FTN-induced interference is not evenly distributed among the transmitted symbols. Therefore, we proposed to remove interference from only a sub-group of the transmitted symbols, hence the sparse nature of our method.

To this end, we introduced three precoder families depending on whether ISI and/or ICI cancellation is prioritized. The corresponding receivers deal first with the precoded symbols and then with the non-precoded ones. Our main objective was to improve the decoding of the precoded symbols and to remove their contribution to interference with the non-precoded ones before decoding the latter. A significant gain was achieved thanks to the proposed precoding especially in case of high modulation orders and low packing factors, corresponding to the cases where FTN-self interference is severe. Since less interference is introduced to the transmitted symbols, EXIT chart analysis showed that the tunnel between the equalizer and the decoder is now wider, compared to the non-precoded FTN-OQAM scenario, meaning that the exchange of soft information between the soft equalizer and the decoder is improved. This is confirmed by the fact that less iterations are needed at the receiver side when the precoder is applied. Moreover, an important gain in terms of BER is obtained when considering high modulation orders and low packing factors τ (results were given for 16-QAM with $\tau = 0.7$ and 64-QAM with $\tau = 0.8$). This work was published in European Wireless Conference in 2016 and included hereafter [176].

As a final major part, the performed work aimed to enhance the different blocks of the FTN-OQAM transceiver by taking into account the interference introduced by FTN signaling. The proposed modifications concerned the channel encoder, the bit-to symbols mapping and the symbols to time and frequency positions mapping.

In the (partially) precoded FTN-OQAM transceiver, the precoded and non-precoded symbols exhibit different BER since they are affected differently by interference. Therefore, the channel coding could be jointly optimized with the interference imbalance pattern that we intentionally created through precoding. Thus, we proposed to adapt the channel encoder by

using different local coding rates, to encode the precoded and non-precoded symbols, while keeping the original (total) coding rate unchanged. We showed that an important gain is obtained in case of high modulation orders and low packing factors (16-QAM with $\tau = 0.7$ and 64-QAM with $\tau = 0.8$) when using a stronger code to encode the precoded symbols.

Moreover, we proposed to take advantage of the different bit level protections provided by the Gray mapping in case of high modulation orders. As the considered channel coding is based on convolutional codes, we proposed a reordering of the encoded bits in a way to place information bits at highly protected positions of the Gray mapping and redundancy bits at the less protected positions. This can also be an additional source of imbalance in the protection of transmitted bits that can be exploited for performance improvement. Indeed after a thorough investigation via EXIT charts, the new bits ordering enabled significant BER improvement for high packing factors: $0.8 \leq \tau$ for 16-QAM modulation and $\tau = 0.9$ for 64-QAM modulation.

Finally, we proposed a new mapping of symbols to time-frequency positions different from the classical mapping used by FBMC/OQAM modulation. This was motivated by the fact that in a time and frequency lattice, the transmitted symbols at different time instants are impacted differently by interference. Considering convolution channel codes, we proposed to map symbols made up of information bits to time and frequency positions which are less affected by interference and to place symbols made up of redundancy bits at the remaining positions. Our method enabled BER improvement when high modulation orders (16 and 64-QAM modulation) and low packing factors ($\tau = 0.7$ and 0.8, respectively) are considered. For more details, the reader is referred to our work published in ICC 2017 proceedings [177].

European Wireless 2016

Sparse Interference Pre-Cancellation for FTN-OQAM Systems

Naila Lahbabi*&, Hao Lin*, Charbel Abdel Nour&, Catherine Douillard&, Pierre Siohan†
* Orange Labs, Cesson Sévigné, France.
& Télécom Bretagne, Brest, France.
† retired from Orange Labs

***Abstract*—In this paper, we propose several precoding methods to reduce the interference caused by Faster-Than-Nyquist (FTN) signaling for Orthogonal Frequency Division Multiplexing Offset Quadrature Amplitude Modulation (OFDM/OQAM). The proposed precoders are combined with an FTN-OFDM/OQAM modulator to pre-cancel the interference at the transmitter side. An iterative receiver for each precoding scheme is also presented. With the simulations, we show that the convergence speed of the FTN-OFDM/OQAM transceiver increases with the proposed precoders.**

I. INTRODUCTION

Although OFDM has been widely used in radio communications, the issue of whether it should be the ultimate waveform for future radio systems such as 5G, has recently triggered many discussions [1] and is still open. The main drawbacks of OFDM have long been identified i.e., overhead wasting due to cyclic prefix (CP) insertion and weak robustness against frequency dispersive channels. Among the competing waveforms proposed to overcome these drawbacks, the offset signaling on the top of OFDM (known as OFDM/OQAM) is recognized as a good alternative candidate to OFDM [2] because of two advantages. First, OFDM/OQAM systems have the flexibility of applying efficient pulse shaping with different time-frequency localization properties thanks to the filter design. Actually this advantage is due to its offset signaling [3]. Second, due to the improved waveform, the use of CP is not always necessary, which keeps a full Nyquist rate [2], [4], [5]. Moreover, in [6], the link to the filter bank approach is first established, proving that the OFDM/OQAM, or OQAM in short, systems can efficiently be realized with Fast Fourier Transform (FFT) and polyphase filtering, which further justifies their practical feasibility. Thus, the OQAM is sometimes also called Filter Bank Multi-Carrier (FBMC) [5].

The continuous increasing mobile data volume constrains the future radio systems to include advanced modulations/waveforms offering higher data rates with more efficient bandwidth usage. One possibility is to violate the well-known Nyquist condition [7] by transmitting faster than the Nyquist rate, i.e. using a technique also known as FTN signaling. The original idea was raised by Mazo in 1975 [8]. He stated that the transmission rate is not necessarily limited by the Nyquist rate, meaning that faster transmission rate can be envisaged provided that interference is accepted. Mazo also showed that as long as the boosted transmission rate does not go beyond 1.25x[1], the resulted minimum sequence distance keeps constant, thus not entailing any performance degradation, provided the receiver uses Maximum Likelihood Sequence Estimation (MLSE) [9]. However, this scheme was not deemed attractive until the arrival of the mobile data tsunami became unavoidable. The combination of FTN with OFDM [10] made this scheme even more interesting.

The first work on the combination of OQAM and FTN, denoted here as FTN-OQAM, was reported in [12]. The authors modified the classical OQAM of [6] by inserting a block named *FTN mapper* between the OQAM modulator and the FFT. Due to this additional block, the complexity of their solution is higher than that of the classical OQAM system and depends on the block size. An iterative Maximum A Posteriori (MAP)-based receiver, whose complexity increases with the modulation order, is proposed in [13]. Later, the implementation of FTN-OQAM was revised in [14]. The proposed algorithm is able to approach very closely the promised performance of FTN systems without complexity increase compared to a classical OQAM system. At the receiver side, a Minimum Mean Square Error Linear Equalization and Interference Cancelation (MMSE LE-IC) was introduced. Unlike the MAP-based receiver, the MMSE LE-IC algorithm is independent of the modulation order which makes it a good candidate if high modulation orders are to be used.

In this paper, we consider an FTN-OQAM transmission system with iterative processing at the receiver side and aim to improve the iterative receiver convergence while keeping its complexity under an acceptable level. The proposed method involves combining a precoder with FTN-OQAM in order to pre-cancel the interference introduced by FTN signaling at the transmitter side. Given the nature of this interference, we propose a sparse precoding pattern. Actually, interference pre-cancellation is only applied to a group of symbols positions in the transmitted block while keeping the original OQAM symbols at the other positions. At the receiver side, we propose a two-step MMSE LE-IC algorithm. First, the precoded symbols are detected and used to reduce their interference with the non-precoded symbols. Then these latter symbols are detected and used, at the next iteration, to remove their interference with the precoded symbols.

The reminder of the paper is organized as follows. Sec-

[1]A ratio between Nyquist rate and FTN rate.

ISBN 978-3-8007-4221-9

European Wireless 2016

tion II introduces the background of FTN-OQAM as well as the transceiver presented in [14]. Section III describes our proposed precoding methods, while in Section IV, their performance is evaluated and compared to [14]. Conclusions are given in Section V.

II. OQAM AND FTN-OQAM

In this section, we briefly present the background of OQAM and its combination with FTN.

A. OQAM

For M subcarriers, the continuous-time OQAM signal in baseband is [6]:

$$s(t) = \sum_{m=0}^{M-1} \sum_{n=-\infty}^{+\infty} a_{m,n} \underbrace{g(t - \frac{nT_0}{2}) e^{j2\pi m F_0 t} e^{j\Phi_{m,n}}}_{g_{m,n}(t)}, \quad (1)$$

and the equivalent baseband discrete-time OQAM signal is [6]:

$$s[k] = \sum_{m=0}^{M-1} \sum_{n\in\mathbb{Z}} a_{m,n} g[k - nN] e^{\frac{j2\pi m(k-\frac{D}{2})}{M}} e^{j\Phi_{m,n}}. \quad (2)$$

The pulses $g_{m,n}$ are called basis functions and construct a Hilbert basis, with $T_0 F_0 = 1$, where T_0 is the symbol duration and F_0 is the subcarrier spacing. $g(t)$ is a prototype function of length L (without any restriction, we suppose $L = bM, b \in \mathbb{N}$), $N = \frac{M}{2}$ is the discrete time offset, $D = L - 1$ and $\Phi_{m,n}$ is a phase term often equal to $\frac{\pi}{2}(m+n) + \Phi_0$, where $\Phi_0 = 0$ or $\pm\pi mn$. The real-valued transmitted symbol $a_{m,n}$ on the m^{th} subcarrier at time instant n is obtained from taking the real and imaginary part of the complex-valued 2^{2K}-QAM constellation. The orthogonality constraint of OQAM is expressed using the real inner product as:

$$\Re\left\{\int_{-\infty}^{+\infty} g_{m,n}(t) g^*_{m',n'}(t) dt\right\} = \delta_{m,m'}\delta_{n,n'}, \quad (3)$$

where, δ is the Kronecker symbol. It is worthwhile noting that this orthogonality condition can only be satisfied at the Nyquist rate $T_0 F_0 = 1$ or above.

B. FTN-OQAM

The FTN-OQAM modulator consists in packing the pulses closer in time at a signaling rate faster than permitted by the Nyquist transmission criterion. The modulated baseband signal is expressed as [14]:

$$s(t) = \sum_{m=0}^{M-1} \sum_{n=-\infty}^{+\infty} a_{m,n} g(t - n\tau\frac{T_0}{2}) e^{j2\pi m F_0 t} e^{j\Phi_{m,n}}, \quad (4)$$

where $0 < \tau < 1$ is the FTN time packing factor. The discrete-time signal is obtained:

$$s[k] = \sum_{m=0}^{M-1} \sum_{n\in\mathbb{Z}} a_{m,n} g[k - nN_f] e^{\frac{j2\pi m(k-\frac{D}{2})}{M}} e^{j\Phi_{m,n}} \quad (5)$$

where, $T_s = \frac{T_0}{M}$ is the sampling rate, $F_0 = \frac{1}{MT_s}$ and M is the size of IFFT/FFT.

N_f is called the FTN factor and is defined as $N_f = \lfloor \tau . \frac{M}{2} \rfloor$, where $\lfloor . \rfloor$ denotes the floor function.

At the receiver side, the signal is detected using an MMSE LE-IC iterative based algorithm. The number of iterations for the system convergence depends on the FTN packing factor and on the modulation order. In order to reduce the number of iterations while keeping the same complexity as the FTN-OQAM system, we combine a precoder with the FTN-OQAM modulator. The idea behind is to pre-cancel the known interference at the transmitter side so that less iterations are needed.

III. SPARSE INTERFERENCE PRE-CANCELLATION (SIPC) METHOD

In this section, we present the SIPC method for pre-canceling the Inter-Symbol-Interference (ISI) and Inter-Carrier-Interference (ICI) at the transmitter side using the transceiver in [14].

At the demodulator output, the received signal at frequency m_0 and time instance n_0 is:

$$\begin{aligned} y_{m_0,n_0} &= \Re\Big(\sum_k s[k] g[k - n_0 N_f] e^{-j\Phi_{m_0,n_0}} e^{\frac{-j2\pi m_0(k-\frac{D}{2})}{M}}\Big) \\ &= a_{m_0,n_0} + \Re\Big(\sum_{(m,n\neq n_0)} a_{m,n} e^{j\frac{\pi}{2}(n-n_0+m-m_0)} \\ &\quad \times \sum_k g[k - nN_f] g[k - n_0 N_f] e^{\frac{j2\pi(k-\frac{D}{2})(m-m_0)}{M}}\Big) \end{aligned} \quad (6)$$

The first term of (6) is the useful signal and the second term represents the added interference composed of ISI and ICI, which are expressed as:

$$\begin{aligned} ISI &= \sum_{q=-l, q\neq 0}^{+l} a_{m_0,n_0+q} \\ &\quad \underbrace{\times \Re\Big(e^{j\frac{\pi}{2}q} \sum_k g[k - (n_0+q)N_f] g[k - n_0 N_f]\Big)}_{h_q} \end{aligned} \quad (7)$$

and

$$ICI_{n_0} = \sum_{p=-l', p\neq 0}^{+l'} \sum_{q=-l}^{l} a_{m_0+p,n_0+q} \times g^R_{p,q,n_0} \quad (8)$$

where h_q is the coefficient of the equivalent channel of ISI and

$$\begin{aligned} g^R_{p,q,n_0} &= \Re\Big(e^{j\pi\left(\frac{2p(k-\frac{D}{2})}{M} + \frac{p+q}{2}\right)} \\ &\quad \times \sum_k g[k - (n_0+q)N_f] g[k - n_0 N_f]\Big) \end{aligned} \quad (9)$$

is the ICI contribution of symbols at positions (m_0+p, n_0+q) to the symbol at (m_0, n_0), with $p, q \in \mathbb{Z}$. ICI depends on the time instance n. Factors l and l' represent the zone of symbols contributing to ISI and ICI, respectively. They depend on the prototype filter and on the packing factor τ.

ISBN 978-3-8007-4221-9

European Wireless 2016

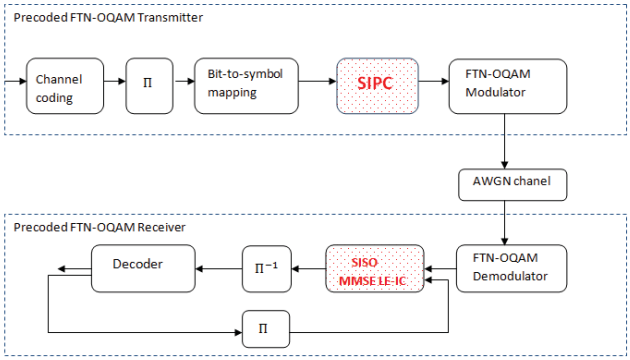

Fig. 1: The proposed precoded FTN-OQAM transceiver in the transmission chain of [14]. Dashed blocks are related to the SIPC method.

Since the ISI and ICI are known by the transmitter, they can be pre-canceled from OQAM symbols as follows:

$$c_{m,n} = a_{m,n} - ISI - ICI_n \tag{10}$$

Precoding the symbols at positions $(m+p, n+q)$ with $(p,q) \in [-l^{'}, l^{'}] \times [-l, l]$ creates a different interference from the one used to precode the symbol at position (m,n). To overcome this problem, we propose a SIPC method which aims at removing the interference from only a group of symbol positions in the transmitted block. This group is determined according to the packing factor τ and the prototype filter. Moreover, two factors α and β $(0 \leq \alpha, \beta \leq 1)$ are introduced in order to control the amount of interference to be pre-canceled.

In the following, we propose three variations of SIPC precoders.

A. SIPC at time axis

In this section, a technique aiming at pre-canceling ISI at the transmitter, named SIPC from time axis (SIPC-t) is detailed. As shown in figure 1, the information bits are first encoded, interleaved and then mapped to OQAM symbols. According to the value of l, the block SIPC precodes symbols in positions n, as follows:

$$c_{m,n} = a_{m,n} - \alpha \left(\sum_{k=-l, l\neq 0}^{l} h_k a_{m,n-k} \right), \tag{11}$$

if $(n = k \ mod \ (l+2))$ or $(n = (k+1) \ mod \ (l+2))$, with $(k \in \mathbb{N}, k \leq l+1)$ and mod is the modulo operator.

The other positions in the transmitted block are not pre-coded and contain OQAM symbols. The precoding pattern is illustrated in figure 2, in case of $l = 2$, using a time-frequency lattice of the transmitted block. Because OQAM extracts only the real part of the received signal, symbols at odd positions do not contribute to ISI. Therefore, we alternate two precoded symbols and two OQAM symbols.

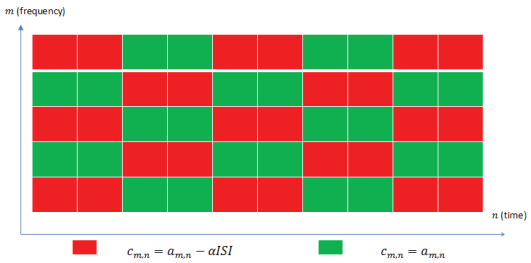

Fig. 2: The time-frequency lattice of the transmitted block. The red and green positions represent the precoded symbols and the non-precoded ones, respectively.

The two-step turbo-based MMSE-LE-IC receiver is illustrated in figure 3. At the first iteration, the precoded symbols are equalized using an MMSE-LE filter from the time axis (MMSE-t). Then, they are decoded by a Max-Log-MAP decoder. A soft estimation of these symbols, at the decoder's output, is used by the Soft-Interference-Cancellation (SIC 1) block to remove their interference with the non-precoded symbols. They are then equalized and decoded. At the next iteration, the soft estimation of the non-precoded symbols enables the block SIC 2 to cancel their interference with the precoded symbols and to update the MMSE-t coefficients. The soft mapping and demapping functions are used to translate the information from bit level to symbol level and vice-versa and thus exchange information between the symbol level filter and the bit level decoder.

B. SIPC at frequency axis

The SIPC-t precoder can be replaced by a precoder operating in the frequency axis, named SIPC from frequency axis

ISBN 978-3-8007-4221-9

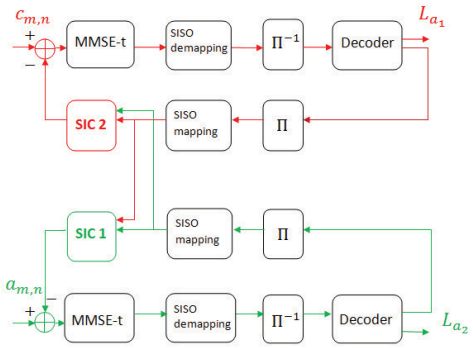

Fig. 3: Structure of the SISO MMSE LE-IC used for SIPC-t.

(SIPC-f), which pre-cancels ICI from symbols at frequency positions m, as follows:

$$c_{m,n} = a_{m,n} - \beta \left(\sum_{p=-l',p\neq 0}^{l'} \sum_{q=-l}^{l} a_{m+p,n+q} g_{p,q,n} \right), \quad (12)$$

if $(m = k \ mod \ (l^{'}+1)$, with $k \in \mathbb{N}, k \leq l^{'})$.

At the other positions, OQAM symbols are kept unchanged. Figure 4, presents an example of precoding pattern for $l^{'} = 1$. At the receiver side, we use a similar two-step turbo-based

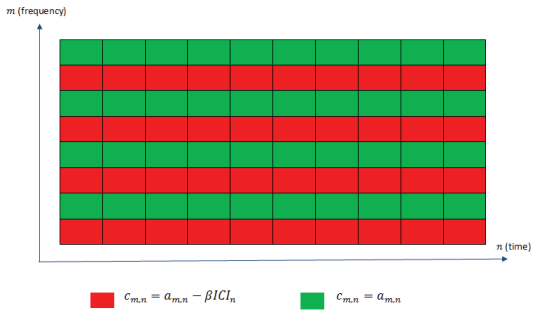

Fig. 4: The time-frequency lattice of the transmitted block. The red and green positions represent the precoded symbols and the non-precoded ones, respectively.

MMSE LE-IC algorithm as in the previous section. Since ICI depends on time, we choose to equalize the non-precoded symbols using a frequency domain MMSE LE (MMSE-f) equalization.

C. SIPC at both time-frequency axes

Now, we replace the SIPC block by a precoder to pre-cancel ISI and ICI from a group of symbol positions(m, n), named SIPC-tf, as follows:

$$c_{m,n} = a_{m,n} - \alpha \left(\sum_{k=-l,l\neq 0}^{l} h_k a_{m,n-k} \right) - \beta \left(\sum_{p=-l',p\neq 0}^{l'} \sum_{q=-l}^{l} a_{m+p,n+q} g_{p,q,n} \right), \quad (13)$$

if $(m = k \ mod \ (l^{'}+1)$, with $k \in \mathbb{N}, k \leq l)$ and $(n = k^{'} \ mod \ (l^{'}+2)$ or $n = (k+1) \ mod \ (l^{'}+2)$ with $k^{'} \in \mathbb{N}, k^{'} \leq l^{'}+1)$. Figure 5 shows the precoding pattern in case of $(l, l^{'}) = (1, 2)$.

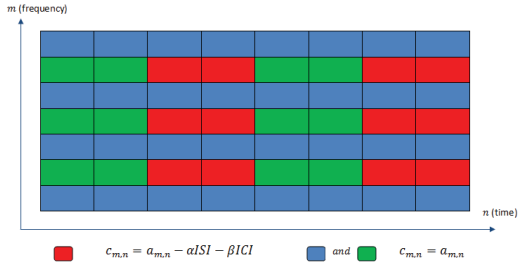

Fig. 5: The time-frequency lattice of the transmitted block. The red positions represent the precoded symbols while the green and blue positions represent the non-precoded symbols.

The turbo-based MMSE LE-IC receiver is illustrated in figure 6. At the first step, we equalize the precoded symbols in red positions using an MMSE-t filter. Then, their soft estimation at the decoder's output is used by block SIC2 to remove their interference with the non-precoded symbols in the green positions. At the second step, the symbols in the green positions are equalized using an MMSE-t filter. At the third step, the block SIC 3 uses the soft estimation of the red and green symbols to remove their interference with the blue ones. These symbols are then equalized using an MMSE-f filter. At the next iteration, the block SIC 1 uses the soft estimation of the blue and green symbols to remove their interference with the red ones.

IV. SIMULATIONS

In this section, we evaluate the Bit-Error-Rate (BER) of the proposed SIPC precoders using different pulse shapes, modulation orders and packing factors. Then, we compare the selected precoders to the FTN-OQAM system [14] in terms of BER performance.

A. SIPC precoders performance

We use a (1,5/7) Recursive Systematic Convolutional (RSC) code for channel coding with a size-15360 random interleaver, QPSK-Gray mapping, a MAP-based outer decoder and an MMSE filter of length 30 and delay 15. We compare the performance of the various SIPC precoders using different pulse shapes: PHYDYAS filter [15], Frequency Selective (FS) filter

ISBN 978-3-8007-4221-9

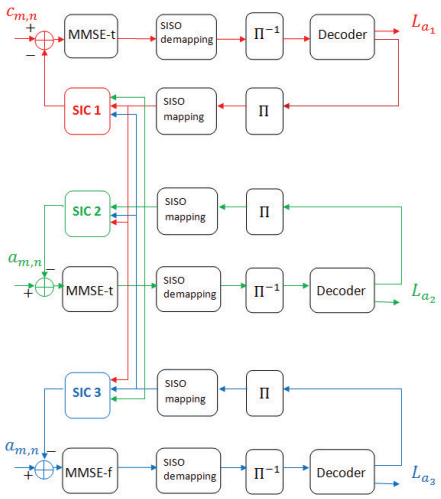

Fig. 6: Structure of the SISO MMSE LE-IC used for SIPC-tf.

[4], Time Frequency Localization (TFL) filter [4], Isotropic Orthogonal Transform Algorithm (IOTA) filter [2], Extended Gaussian Function (EGF) filter with a spreading factor of 2 [6], and Square Root Raised Cosine filter with a roll-of factor of 0.5 (SRRC05) and a roll-of factor of 0.3 (SRRC03).

Figure 7 gives the result for SIPC-t at iteration 9. In what follows, SIPC-t results are given for $l = 2$. We observe that, the IOTA, TFL and EGF pulses give the best performance in terms of BER .

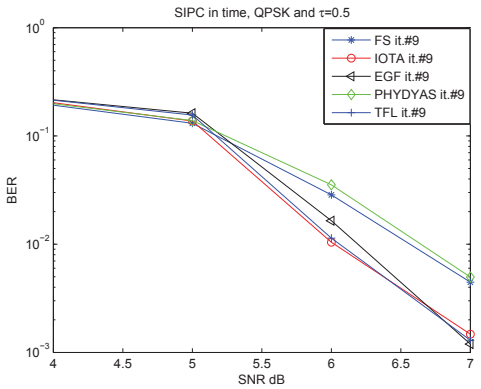

Fig. 7: BER evaluation for SIPC-t using different pulse shapes.

Table I summarizes the recommended pulse shapes for each SIPC precoder, modulation order and packing factor. SIPC-f-freq is similar to SIPC-f except that the MMSE-f filter is used for both the precoded and the non-precoded symbols. In the following, we choose $(l, l') = (2, 1)$ for SIPC-f, SIPC-tf and SIPC-f-freq.

Precoder	QPSK	16-QAM	16-QAM	64-QAM	64-QAM
Packing factor (τ)	0.5	0.7	0.8	0.8	0.9
SIPC-t	TFL IOTA EGF	FS Phydyas IOTA	FS Phydyas IOTA	FS Phydyas	FS Phydyas SRRC05
SIPC-f	EGF TFL	IOTA FS Phydyas	FS Phydyas IOTA	FS Phydyas SRRC05	FS Phydyas SRRC05
SIPC-tf	TFL EGF IOTA	TFL	FS Phydyas	FS Phydyas	FS Phydyas IOTA
SIPC-f -freq	IOTA	FS Phydyas SRRC05	FS Phydyas SRRC05 SRRC03	FS Phydyas SRRC05 SRRC03	SRRC05 FS Phydyas

TABLE I: Recommended pulse shapes for the SIPC precoders.

Modulation order	Recommended SIPC precoders	Recommended pulses
QPSK ($\tau = 0.5$)	SIPC-t SIPC-tf SIPC-f-freq	TFL TFL IOTA
16QAM ($\tau = 0.7$)	SIPC-f-freq	FS
16QAM ($\tau = 0.8$)	SIPC-t SIPC-t	FS Phydyas
64QAM ($\tau = 0.8$)	SIPC-t SIPC-f SIPC-tf	Phydyas Phydyas Phydyas
64QAM ($\tau = 0.9$)	SIPC-t SIPC-t SIPC-f-freq	FS Phydyas SRRC05

TABLE II: Recommended SIPC precoders and pulse shapes for different modulation orders and packing factors.

Table II gives the selected SIPC method for each modulation order and packing factor, obtained from the comparison of the BER performance of these precoders.

B. Study of the effect of SIPC precoding on the FTN-OQAM transmission scheme

In this section, we show the effect of SIPC method on the FTN-transceiver in [14]. We keep the same configuration as in the previous section. Figure 8 gives the BER performance of both systems using QPSK modulation and $\tau = 0.5$. We observe that SIPC precoding improves the convergence of the iterative receiver: at SNR of 7 dB, SIPC-t precoding permits convergence at iteration 5, while the FTN-OQAM system only converges at iteration 7.

Figure 9 gives the BER performance of both systems using 16QAM modulation and $\tau = 0.8$. We observe that SIPC precoding improves the convergence of the iterative receiver: SIPC-t precoding permits convergence at iteration 3 while the FTN-OQAM system only converges at iteration 7. We observe the same tendency in figure 10 for 64QAM modulation and $\tau = 0.9$: SIPC-f-freq precoding permits convergence at iteration 3 while the FTN-OQAM system only converges at iteration 5.

ISBN 978-3-8007-4221-9

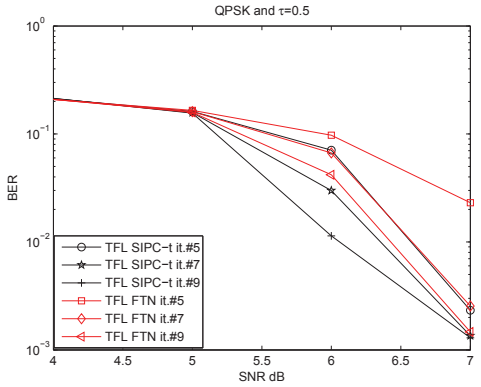

Fig. 8: BER evaluation for SIPC-t and the FTN-OQAM system using QPSK and $\tau = 0.5$.

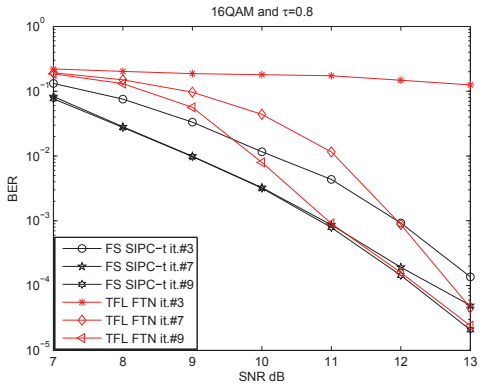

Fig. 9: BER evaluation for SIPC-t and the FTN-OQAM system using 16QAM and $\tau = 0.8$.

V. CONCLUSION

In this paper, we introduced a family of precoders, named SIPC, to deal with the interference caused by FTN signaling. Since this interference is known at the transmitter side, it can be pre-canceled before transmitting the signal. We introduced a precoding pattern depending on the used prototype filter and on the FTN packing factor. Monte Carlo simulations confirmed that the proposed method enables the FTN-OQAM system to converge with less iterations. The suitable pulse shapes for each SIPC method and modulation order were recommended. Furthermore, the best precoders, in terms of BER performance, and their corresponding pulse shapes were also reported for each modulation order.

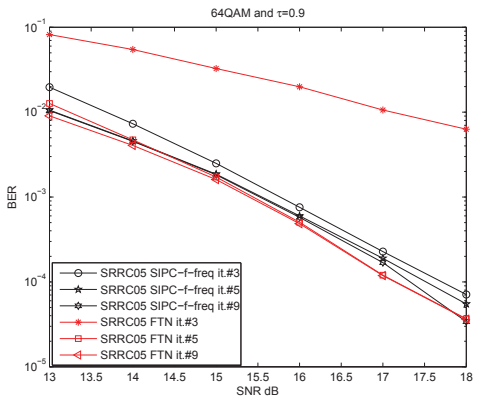

Fig. 10: BER evaluation for SIPC-f-freq and the FTN-OQAM system using 64QAM and $\tau = 0.9$.

REFERENCES

[1] *"Mobile and Wireless communications enablers for the twenty-twenty information society"*.https://metis2020.com/.

[2] B. Le Floch, M. Alard, and C. Berrou.*"Coded Orthogonal Frequency Division Multiplex"*.Proceedings of the IEEE, vol. 83, pp. 982-996, June 1995.

[3] H. Bölcskei,*"Advances in Gabor Analysis"*. Chapter Orthogonal frequency division multiplexing based on offset QAM, pp. 321-352, 2003.

[4] D. Pinchon, P. Siohan, and C. Siclet.*"Design techniques for orthogonal modulated filterbanks based on a compact representation"*. IEEE Trans. Signal Process, vol. 52, no. 6, pp. 1682-1692, 2004.

[5] *"Physical Layer for Dynamic Spectrum Access and Cognetive Radio"*. http://www.ict-phydyas.org/index.php/camax/page/view?id=21.

[6] P. Siohan, C. Siclet and N. Lacaille.*"Analysis and design of OFDM/OQAM systems based on filterbank theory"*. IEEE Trans. Signal Process, vol. 50, no. 5, pp. 1170-1183, 2002.

[7] H. Nyquist.*"Certain topics in teleraph transmission theory"*.Trans. AIEE, vol. 47, pp.617-644, Apr. 1928.

[8] E. Mazo. *"Faster-Than-Nyquist signaling"*. Bell. Syst. Tech. Journal, 54:1451-1462, 1975.

[9] G. Forney. *"Maximum-likelihood sequence estimation of digital sequences in the presence of ontersymbol interference"*. Information Theory, IEEE Trans, vol. 18, no. 3, pp. 363-378, 1972.

[10] J.B. Anderson and F. Rusek. *"Improving OFDM: Multistream Faster-Than-Nyquist Signaling"*. In Turbo Codes Related Topics; 6th International ITG-Conference on Source and Channel Coding (TURBOCODING), 2006 4th International Symposium, pp. 1-5, Apr. 2006.

[11] F. Rusek and J.B. Anderson.*"Constrained Capacities for Faster-Than-Nyquist Signaling"*. Information Theory, IEEE Trans, vol. 55, no. 2, pp. 764-775, Feb. 2009.

[12] D. Dasalukunte, F. Rusek and J.B. Anderson.*"Transmitter architecture for Faster-Than-Nyquist signaling systems"*. In Circuits and Systems, 2009. ISCAS 2009. IEEE International Symposium, pp. 1028-1031, May. 2009.

[13] D. Dasalukunte, F. Rusek, V. Owall. *"An Iterative Decoder for Multicarrier Faster-Than-Nyquist Signaling Systems"*. In Communication (ICC), 2010. IEEEE International Conference, pp. 1-5, May. 2010.

[14] H. Lin, N. Lahbabi, P. Siohan and X. Jiang. *"An efficient FTN Implementation of the OFDM/OQAM System"*. In Communication (ICC), 2015. IEEEE International Conference, pp. 4787-4792, June. 2015.

[15] M. Bellanger. *"Specification and design of a prototype filter for filter bank multicarrier transmission"*. ICASSP, 2001.

ISBN 978-3-8007-4221-9

2.3 Summary

The work on this topic was performed mainly in the context of two PhDs theses and two post-doctoral fellowships and was supported by two EU projects METIS and FANTASTIC-5G and a dedicated patent factory with France Brevets. A remarkable result was the development of the first FBMC/OQAM hardware demonstrator confirming predicted gains. Another remarkable result was the 2019 URSI Radioscience PhD thesis prize that was awarded to Jérémy Nadal for his work on the subject. The totality of algorithmic and hardware contributions led to 4 journal and 11 conference publications. In addition, 6 patents were filed and we participated to 9 demonstration events including the Mobile World Congress where we had more than 1000 visitors.

Chapter 3

Algorithms for NOMA systems

3.1 Introduction and motivation

Nowadays, human activities become highly dependent on the mobile internet services such as social media services, multimedia streaming and many real-time interactive services. According to the Cisco Visual Networking Index [178], a standard for broadband insights and trends related to spectrum, there will be 11.6 billion mobile connected devices by 2021, including Machine-to-Machine (M2M) modules and exceeding the worlds projected population at that time (7.8 billion). Furthermore, the global mobile data traffic will increase sevenfold between 2016 and 2021, reaching 49.0 exabytes per month by 2021. On the other side, with such a tremendous growth, the spectrum demanded by these devices is likely to outstrip capacity, resulting in spectrum congestion, which will lead to slower data speeds, dropped calls, and increased prices for both consumers and providers. However, the licensed frequency bands is a finite and scarce resource and making use of millimeter bands is a complex challenge. Therefore, in order to meet the increasing number of connected devices and their demands, an efficient use of the limited available spectrum has to be addressed in developing the next generation of mobile systems since the existing system is reaching its performance limits and is not able to address these challenges.

For an efficient use of the available spectrum, several Non-Orthogonal Multiple Access (NOMA) schemes were under evaluation for 5th generation of mobile communication systems requirements. 3GPP initiated a study on downlink MultiUser Superposition Transmission (MUST) for LTE [179]. Its main objective was to scrutinize different implementations of superposition coding and the proposal of advanced receivers. Another example of NOMA is the Sparse Code Multiple Access (SCMA) technique, which is regarded as a multicarrier form of NOMA [180]. Because of its superior spectral efficiency, NOMA has also been applied to other types of wireless networks. For example, a version of NOMA termed Layer Division Multiplexing (LDM), has been proposed for the next general digital TV standard ATSC 3.0 [181]. Our work focused on the Power Domain (PD) NOMA schemes, which will be usually simply denoted by NOMA throughout the rest of this chapter. The concept is proposed in [182, 183, 184] and shown in Fig. 3.1. NOMA exploits an additional degree of freedom, the power domain. Indeed, it allows users to be multiplexed in this new domain while sharing the same time/frequency resource. Signal separation is done by employing the Successive Interference Cancellation (SIC) which allows the separation and decoding of multi-user signals at the receiver side [185].

NOMA is shown to have the potential to increase system capacity making it a hot topic for many research activities [186]. Motivated by the importance and the arising challenges of spectrum efficiency in 5G and beyond systems, a work was initiated to address several radio resource allocation problems dedicated to communication systems using the PD-NOMA

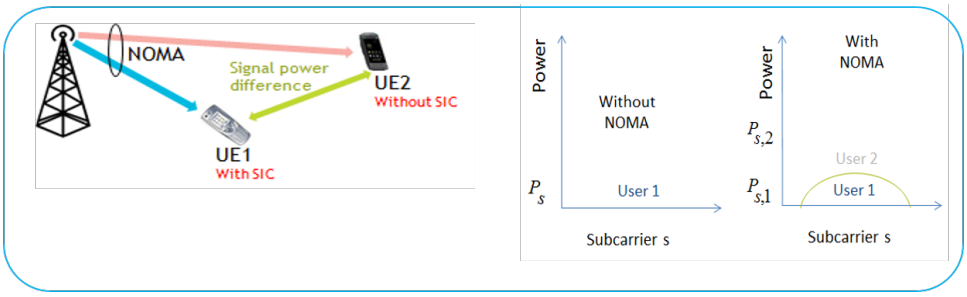

Figure 3.1: The principle of PD NOMA [182, 183, 184].

technique, which in some cases can also be applied to Orthogonal Multiple Access (OMA) schemes. In fact, we aim to meet the high number of connected devices, achieve users demands, and optimize several system performance metrics such as system capacity, user data rate, and user fairness. These objectives are met by providing theoretical and algorithmic solutions under multiple realistic constraints and deployment scenarios.

3.1.1 Resource allocation

The key function of performance improvement of a cellular network fundamentally involves radio resource allocation or scheduling. The main objective of resource allocation is the optimization of the limited frequency/power/time resources assignment in order to achieve desired performance while taking into account realistic constraints. A radio resource optimization problem consists of a utility function as the objective, and a set of constraints to be optimized. The utility can be selected from a range of performance metrics. Various physical limitations in cellular networks or Quality of Service (QoS) requirements are in practice the reasons behind setting the set of constraints. When combined with the optimization variables, a feasible solution region for the optimization problem can be then defined. At large, we aimed to find optimal solutions from the feasible region, or develop near-optimal solutions. In our work, we addressed several radio resource optimization problems in OMA and NOMA.

3.1.1.1 Resource allocation for OMA

In the context of multiuser OMA networks, subcarriers and power are assigned in such a way to optimize a chosen service utility function. The multiuser resource allocation can be performed using waterfilling-based techniques. In [187], an iterative waterfilling algorithm is proposed for the sake of maximizing the sum capacity of a Gaussian multiple access channel. In [188], the data rate maximization is performed otherwise; each subcarrier is attributed to its best user (i.e., the user with the highest channel gain), and then waterfilling is applied on subcarriers assigned to each user individually. The waterfilling-based technique aims at maximizing system capacity but does not guarantee fairness among users. In other words, the users that are away from the base station or with bad channel condition will be penalized. In this sense, several works have taken into account the individual rate or the QoS requirements. Some works tend to minimize the transmit power while guaranteeing a service data rate for each user [189, 190]. Other works, aims to maximize the throughput under a power constraint with some fairness criteria (e.g., proportional fairness among the users). For example, in [191] a rate maximization problem is considered with the objective of maximizing the minimum rate among the users, for a given power budget. The Proportional Fairness (PF) scheduler is also used in a huge number of existing works dealing with resource allocation for an OMA system. The PF scheduler allocates subbands to users in such a way to provide a fair balance

between throughput and fairness. In [192] the rate maximization is extended to include proportional fairness.

3.1.1.2 Resource allocation for NOMA

Unlike OMA, multiple users in NOMA are allowed to simultaneously share the same subband, and one user may need to be multiplexed on several subbands, with different cohabiting users and in various multiplexing orders within each subband. Even after SIC processing, co-channel interference in NOMA is non-negligible. Therefore, radio resource optimization in the case of NOMA is not straightforward. In this sense, several design aspects should be taken into consideration, such as user pairing and multiuser frequency scheduling, power allocation among subbands, power repartition between scheduled users within a subband, etc., as well as the interaction of these different design issues as shown in Fig. 3.2.

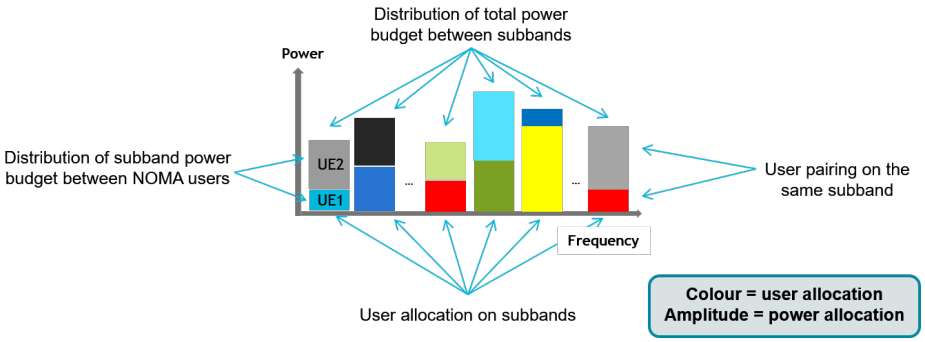

Figure 3.2: The problem of resource allocation for of PD NOMA.

Some algorithms and schemes are proposed to optimize the channel and power allocation for NOMA dowlink and uplink [183, 184, 193]. Most of the previous approaches address the radio resource optimization problems in NOMA by making assumptions to reduce the complexity of the optimization process, e.g., assuming uniform power allocation, predefining fixed groups of users or/and channels before the optimization process. Some researches also consider splitting the difficult optimization procedure into several problems considered easier to be solved. By doing so, the overall problem becomes tractable, however, the optimality is sacrificed, e.g., splitting the joint channel and power allocation into two separate steps: channel allocation and power allocation.

In a large number of works dealing with NOMA, the PF scheduler [194, 195] has been considered for user pairing and subband assignement due to the good tradeoff it provides between system capacity and user fairness. The total bandwidth granted to serve users is divided over a fixed number of subbands. Every subband is then attributed a fraction of the available transmit power that the base station is allowed to use. An equal repartition is the simplest way to divide the power among subbands since it reduces the complexity of the scheduling process; therefore, a great number of papers dealing with NOMA consider this repartition [182, 196].

In [197], the performance of downlink NOMA with wideband and subband frequency scheduling is evaluated under wide-area cellular system configurations. Power allocation is done such that the amount of power attributed to a subband is common to all subbands, and intra-subband power repartition between each pair of scheduled users is done as a subsequent stage. Some other works have proposed non-equal power allocation among subbands for NOMA [198, 199].

At this level, users are paired together on a subband that is attributed a certain amount of power. The last step to be accomplished is to divide this power among scheduled users,

in a way to respect the NOMA principle: the user with the highest channel gain must be attributed the lowest amount of power, and vice-versa. We can identify several intra-subband power allocation techniques. The less complex one is called Fixed Power Allocation (FPA) [184] where a coefficient controls linearly with respect to the total subband power the power attributed to every user. Another technique called Fractional Transmit Power Allocation (FTPA) [196] can be also used to divide the power allocated to a subband between paired users. This technique is quite more complex than FPA since the amount of power attributed non-linearly depends on the channel gains of scheduled users. Yet another intra-subband power allocation technique is called Full Search Power Allocation (FSPA) [184]. The complexity of this technique is very high compared to FPA and FTPA since it requires, in each intra-subband power allocation step, a search among all possible power repartitions and chooses the repartition that results in the highest achieved throughput. Even though FSPA imposes a high penalty in terms of complexity, it was found in [182] that its resulting throughput does not sufficiently surpass FPA's neither FTPA's achieved throughput.

This tour of state-of-the-art review of power and resource allocation techniques prior to our work for NOMA has motivated us to dig deeper in order to find the best NOMA-based resource and power allocation techniques. Most of the researches related to NOMA have considered improving system capacity but few of them have targeted a joint improvement of the capacity and the short-term fairness (fairness at every scheduling time instance). When dealing with user pairing, the majority of papers claim that users have to be chosen to allocate a subband such that the channel gain difference between them is maximized. Few are the papers that studied this issue carefully by evaluating how the user rate is affected by the channel gain difference. When it comes to power allocation, a lot of works have been done, but few of them have reached an optimal power repartition. For this sake, we have decided to work on several aspects of resource and power allocation in order to achieve high performance in NOMA systems.

3.2 Performed work and contributions for NOMA

Two different contexts were considered in the performed work: A cognitive radio-like scenario and a classical communications system scenario as shown in Fig. 3.3. NOMA work was supported by the H2020 FANTASTIC5G project and a patent factory in collaboration with France Brevets. This part was done in the context of the PhD thesis of Marie-Rita Hojeij.

3.2.1 Cognitive radio-like scenario

This first context addresses minimizing the spectrum usage while satisfying requested data rates by a set of users. The resource allocation problem was first formulated, then, several design issues were investigated: the choice of user pairing, optimum or sub-optimum power allocation, fixed and adaptive intra-subband power allocation, dynamic switching from NOMA to orthogonal signaling, weighting strategies for the optimized sum-rate function, etc. An algorithm taking into account all the mentioned design issues was proposed and evaluated. It begins with an initialization and priority assignment for each user based on users Channel State Information (CSI); user selection, subband assignment and user pairing are then detailed. Afterwards, several power allocation techniques are proposed: optimum and sub-optimum waterfilling-based power allocation, weighting strategies for the optimized waterfilling-based power allocation, power allocation according to the actual achieved throughput, and a static power allocation. In addition, we have also derived a decision metric that allows an adaptive switching to orthogonal signaling whenever it is needed; moreover, a data rate estimation for each user is carried out and we came up with a control mechanism to adjust its correspond-

ing power. For more details, the reader is refered to our conference [200] and our journal publications [201].

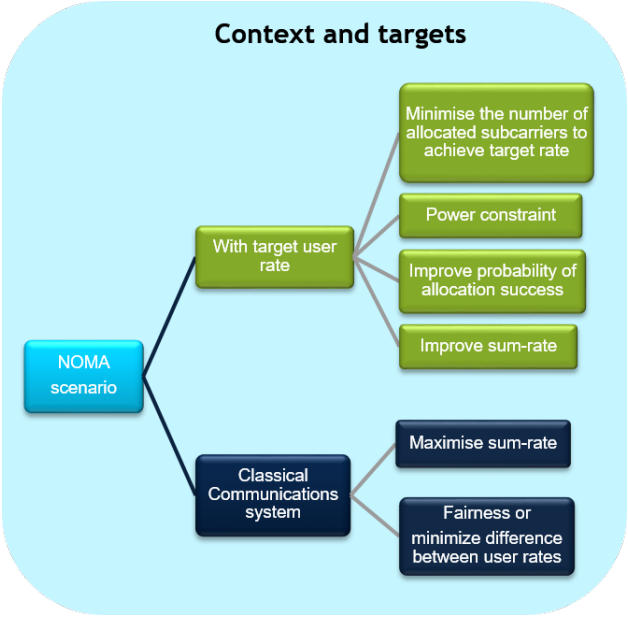

Figure 3.3: The different scenarios for resource allocation of of PD NOMA.

The initiated performance evaluation has shown a significant improvement in the spectral efficiency, and in the probability of success to meet each user requirements, when compared to a classical system purely based on either orthogonal or non-orthogonal signaling [200, 201]. In addition, the proposed optimum power allocation obtained by numerically solving an optimized allocation problem showed a substantial gain in performance when compared to the suboptimum solutions. Moreover, the proposed design for resource allocation allows different types of user prioritization by the adoption of appropriate weights in the considered optimized sum-rate metric [201].

3.2.2 Classical communications system scenario

This second context refers to a classical communications system management scenario were the whole system bandwidth can be used to satisfy all populations of users (cell center and cell edge) while trying simultaneoulsy to maximize the cell sum-rate on the one side and the fairness between users on the other side. To do so, the utility function used for power allocation should be modified. Two proposals to improve the conventional proportionally fair PF scheduler for a NOMA-based system were put forward. We started by investigating the PF scheduler, its advantages and drawbacks. Improvements were then included at the level of user scheduling by introducing adaptive weights to the PF metric with the aim of improving the user fairness while maximizing system capacity. This work was published in journal publication [202]. Then, modifications were implemented at the level of power allocation where a low-complexity waterfilling-based power allocation technique, incorporated within the proportional fairness scheduler, was proposed and published in IEEE Wireless Communications Letters [203] included hereafter.

Simulation results have shown an increased total user throughput, when compared to an orthogonal-based signaling and to the conventional NOMA-based PF scheduler. A comparison of the considered methods in terms of performance and complexity was also conducted [203].

Waterfilling-based Proportional Fairness Scheduler for Downlink Non-Orthogonal Multiple Access

Marie-Rita Hojeij, *Student Member, IEEE,* Charbel Abdel Nour, *Member, IEEE,* Joumana Farah, *Member, IEEE,* and Catherine Douillard, *Senior Member, IEEE*

***Abstract*—In this letter, a low-complexity waterfilling-based Power Allocation (PA) technique, incorporated within the Proportional Fairness (PF) scheduler, is proposed and applied to a Non-Orthogonal Multiple Access (NOMA) scheme in a cellular downlink system. The aim of the proposed joint PA and scheduling scheme is to maximize the achieved average throughput through a quasi-optimal repartition of the transmit power among subbands, while guaranteeing a high level of fairness in resource allocation. Extensive simulation results show that the proposed technique enhances both system capacity and user fairness, when compared to either orthogonal signaling (OS) or NOMA with static PA.**

***Index Terms*—Non-orthogonal multiple access, proportional fair scheduling, waterfilling, power allocation.**

I. INTRODUCTION

WITH the proliferation of smart and Machine-to-Machine devices, it is expected that by 2021 the mobile traffic volume will be almost 10 times larger than today's [1]. To satisfy such constraints, NOMA has recently emerged as a promising candidate for future radio access. NOMA allows the cohabitation of multiple users per subband at the transmitter side, on top of the Orthogonal Frequency Division Multiplexing (OFDM) layer, and relies on Successive Interference Cancellation (SIC) [2], [3] at the receiver side.

Most of the papers dealing with NOMA consider the proportional fairness (PF) scheduler as a multiuser scheduling scheme [4], due to the good tradeoff between total user throughput and user fairness it provides. Regarding PA algorithms, equal power repartition among subbands is adopted in most cases while different multiuser PA schemes are proposed in order to distribute power among users within a subband [2], [4]. There are a few exceptions such as in [5], where a mixed combinatorial non-convex optimization problem for the maximization of the weighted sum throughput was solved using monotonic optimization, and the resulting optimal power and subcarrier allocation policy has served as a performance benchmark due to its high computational complexity. The novelty of this letter resides in the low-complexity incorporation of an inter-subband waterfilling-based PA scheme within the PF scheduler. In [2], power is maintained constant for all subbands, but an optimal PA method based on iterative waterfilling (WF) is used to allocate power among scheduled users on each subband. However, the authors state that a degraded achievable throughput occurs since the WF principle is not considered for subband allocation.

The remainder of this letter is organized as follows. We present the system description in Section II. Our proposed multiuser scheduling and PA scheme is detailed in Section III. The performance of the proposed scheme is evaluated in Section IV, and conclusions are drawn in Section V.

M. Hojeij, C. Abdel Nour and C. Douillard are with Institut Mines-Telecom, CNRS UMR 6285 Lab-STICC, France (email: marie.hojeij@telecom-bretagne.eu; charbel.abdelnour@telecom-bretagne.eu; catherine.douillard@telecom-bretagne.eu) and M. Hojeij is also with the Faculty of Engineering, Holy Spirit University of Kaslik, Lebanon

J. Farah is with the Faculty of Engineering, Lebanese University, Lebanon email:joumana.farah@ul.edu.lb

Part of this work has been performed in the framework of the Horizon 2020 project FANTASTIC-5G (ICT-671660), which is partly funded by the European Union. The authors would like to acknowledge the contributions of their colleagues in FANTASTIC-5G. This work has also been funded with support from the Lebanese University.

II. SYSTEM DESCRIPTION

In this letter, a downlink system with a Single Input Single Output (SISO) antenna configuration is considered. It consists of K users per cell, with a total system bandwidth B divided into S subbands, and a maximum allowable transmit power P_{max} by the Base Station (BS). Among the K users, a set of users $U_s = \{k_1, k_2, ..., k_n, ..., k_{n(s)}\}$, is selected to be scheduled over each frequency subband s, $(1 \leq s \leq S)$. $n(s)$ indicates the number of users non-orthogonally scheduled on subband s. A SIC process is conducted at the receiver side, and the optimum order for user decoding is in the increasing order of the users' channel gains [4] normalized by the noise and inter-cell interference $h^2_{s,k_n}/n_{s,k_n}$, where h^2_{s,k_n} is the equivalent channel gain between user k_n and the BS, at subband s, and n_{s,k_n} the average power of the Gaussian noise plus inter-cell interference received by user k_n. Assuming successful decoding with no SIC error propagation and random inter-cell interference considered as white noise [2], the achievable throughput for user k_n, at subband s, R_{s,k_n}, is given by:

$$R_{s,k_n} = \frac{B}{S}\log_2\left(1 + \frac{h^2_{s,k_n}P_{s,k_n}}{\sum\limits_{j=1,\ h^2_{s,k_n}<h^2_{s,k_j}}^{n(s)} h^2_{s,k_n}P_{s,k_j} + n_{s,k_n}}\right) \quad (1)$$

The PA constraint is represented by the following equation, where P_s denotes the amount of power allocated to subband s.

$$\sum_{s=1}^{S} P_s = P_{\max},\ with\ P_s = \sum_{n=1}^{n(s)} P_{s,k_n} \quad (2)$$

III. MULTI-USER SCHEDULING AND POWER ALLOCATION

The adopted scheduling policy and PA algorithm affect system efficiency and user fairness. In our previous work [6], fairness was achieved by setting user target rates, in the context of bandwidth minimization. This could be inconvenient for certain services where users are not supposed to be granted fixed data rates. Therefore, in the current work, we use

the PF scheduler to achieve fairness. In the PF scheduler, the allocation of each subband requires the estimation of a scheduling metric for each possible user candidate (in OS) or candidate set (in NOMA). These estimations call for rate calculations which, in turn, require the power levels to be predicted on the considered subband, for each candidate. This becomes problematic as the number of subbands and/or users increases. To circumvent the power estimation problem, all previous works dealing with PF scheduling assumed equal power distribution between subbands, thus preventing inter-subband power optimization. Indeed, WF, in its classical formulation, cannot be directly used within the PF, since this would necessitate performing a separate WF procedure, for each attributed subband and each candidate set, leading to a prohibitive complexity. On the contrary, in [6], setting a priority scheme allowed us to avoid the high number of tests necessary to determine the best candidate for each subband, on the one hand, and allowed the incorporation of more elaborate power allocation schemes, on the other hand. The current work aims at introducing a low-complexity iterative WF technique that allows the incorporation of the WF sub-optimal solution proposed in [6], [7] within the PF, and therefore enhance its performance.

A. Proportional Fairness Scheduler

The objective of the PF scheduler [8] is to ensure balance between cell throughput and user fairness. This scheduling policy has been adopted in the majority of papers dealing with NOMA [2], [4]. The scheduler keeps track of the average throughput $T_k(t)$ of each user in a past window of length t_c, where t_c defines the throughput averaging time window (number of subframes). $T_k(t)$ is defined as:

$$T_k(t+1) = \left(1 - \frac{1}{t_c}\right) T_k(t) + \frac{1}{t_c} \sum_{s=1}^{S} R_{s,k}(t) \qquad (3)$$

where $R_{s,k}(t)$ represents the throughput of user k on subband s, at time instance t. It is calculated based on (1), and can amount to zero if user k is not scheduled on subband s.
For a subband s under consideration, the PF metric is estimated for each possible users' combination U, and the combination that maximizes the PF metric will be denoted by U_s:

$$U_s = \arg\max_{U} \sum_{k \in U} \frac{R_{s,k}(t)}{T_k(t)} \qquad (4)$$

Since the same combinations of candidate users are tested for each subband, a user might be selected more than once and attributed multiple subbands during the same time slot. However, it can also happen that a user will not be allocated any subband. In this case, its historical rate in the following time slots will tend to be low and hence, based on the PF metric, such user will have more chance to be selected for allocation afterwards.

B. Proposed Power Allocation Scheme

We propose in this section a new low-complexity waterfilling-based PA technique that predicts the waterline level recursively from the previous level (at the allocation stage i) and from the channel gain of the considered strongest user scheduled on the current subband.

Indeed, maximizing the achieved throughput through an optimal sharing of the total transmit power among subbands can be achieved if [9]:

$$P_s + \frac{N_0 B/S}{h^2_{s,k^*}} = W(S_A(i)),\ s \in S_A(i) \qquad (5)$$

where $S_A(i)$ is the set of allocated subbands at allocation stage i, $W(S_A(i))$ the corresponding waterline at stage i, and h^2_{s,k^*} the channel gain of user k^* showing the highest channel gain among scheduled users on subband s.
During the allocation process, the total transmit power P_{max} is distributed, at each stage, among allocated subbands based on (5), resulting in:

$$P_{\max} = \sum_{s \in S_A(i)} \left(W(S_A(i)) - \frac{N_0 B/S}{h^2_{s,k^*}} \right) \qquad (6)$$

Since the same amount of total power is redistributed each time the scheduler allocates a new subband denoted by s_{new}, the waterline level is updated by $W(S_A(i+1))$ only if $\frac{N_0 B/S}{h^2_{s_{new},k^*}} < W(S_A(i))$, otherwise it keeps its previous value $W(S_A(i))$. In case the waterline is updated, P_{max} is distributed at stage $i+1$ as follows:

$$\begin{aligned} P_{\max} = &\sum_{s \in S_A(i)} \left(W\left(S_A(i+1)\right) - \frac{N_0 B/S}{h^2_{s,k^*}} \right) \\ &+ \left(W\left(S_A(i+1)\right) - \frac{N_0 B/S}{h^2_{s_{new},k^*}} \right) \end{aligned} \qquad (7)$$

If we denote by $N(i)$ the number of subbands in the set $S_A(i)$, (6) can be re-written as:

$$P_{\max} = N(i).W(S_A(i)) - \sum_{s \in S_A(i)} \frac{(N_0 B/S)}{(h^2_{s,k^*})} \qquad (8)$$

Hence, by comparing (7) and (8), we obtain:

$$\begin{aligned} N(i)W(S_A(i)) - &\sum_{s \in S_A(i)} \frac{N_0 B/S}{h^2_{s,k^*}} = N(i)W(S_A(i+1)) \\ &- \sum_{s \in S_A(i)} \frac{N_0 B/S}{h^2_{s,k^*}} + \left(W(S_A(i+1)) - \frac{N_0 B/S}{h^2_{s_{new},k^*}} \right) \end{aligned} \qquad (9)$$

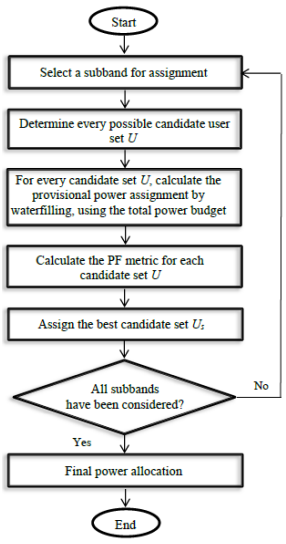

Fig. 1. Flow chart of the considered waterfilling-based allocation scheme.

Therefore, the waterline at stage $i+1$ can be formulated as:

$$W(S_A(i+1)) = \frac{1}{N(i)+1}\left(N(i).W(S_A(i)) + \frac{N_0B/S}{h^2_{s_{new},k^*}}\right) \quad (10)$$

Fig. 1 shows the main steps of the proposed resource allocation technique that incorporates the introduced waterfilling PA within the PF.

For each new subband s_{new} considered for allocation, Eq.(10) is applied for every possible candidate set of users, U, while taking into account user k^* showing the highest channel gain among users in the set U, over s_{new}. Once the waterline level at the current stage, $i+1$, is determined, power is then estimated for U as $P_{s_{new}|U}$ using:

$$P_{s_{new}|U} = W(S_A(i+1)) - \frac{N_0B/S}{h^2_{s_{new},k^*|U}} \quad (11)$$

Afterwards, $P_{s_{new}|U}$ is divided among scheduled users in the set U based on the chosen intra-subband PA technique, e.g. FTPA, the scheduling PF metric is calculated for each U and the best set U_s is selected based on (4). Note that, at each allocation step, the power estimation using (11) is performed only for subband s_{new} in order to choose the best candidate user set, i.e., there is no need to update the provisional powers on the previously allocated subbands. The complete PA is performed only at the end of the scheduling process, after all subbands have been attributed, using the final waterline level, to yield the final power levels on all subbands.

IV. NUMERICAL RESULTS

A. System Model Parameters

The performance of the proposed scheduling techniques are evaluated using the LTE/LTE-Advanced specifications [10]. The maximum BS transmission power is 46 dBm. The system bandwidth is 10 MHz divided into 8, 16, 32, 64, or 128 subbands, with a carrier frequency of 2 GHz. The noise power spectral density is 4.10^{-18} mW/Hz. Users are randomly deployed in a cell of radius 500 meters, with a minimum distance of 35 meters between users and BS. Distance-dependent path loss is considered with a decay factor of 3.76. The Extended Typical Urban (ETU) channel model is used, with a mobile velocity of 50 km/h. Perfect channel estimation is assumed. Without loss of generality, in our evaluations, the maximum number of scheduled users per subband is 2 ($n(s) = 2$).

B. Performance Evaluation

First, two system-level performance indicators are used for evaluation: achieved system capacity and user fairness. The latter is estimated using the Gini fairness index [11] defined as:

$$G = \frac{1}{2K^2\overline{r}}\sum_{x=1}^{K}\sum_{y=1}^{K}|r_x - r_y|, \text{ with } \overline{r} = \frac{1}{K}\sum_{k=1}^{K} r_k \quad (12)$$

where r_k is the total achieved throughput of user k averaged over a time-window length t_c. G takes values between 0 and 1, where $G = 0$ (resp. $G = 1$) corresponds to the maximum (resp. lowest) level of fairness among users.

In order to evaluate our proposed PA scheme for NOMA, we compared it with an OS-based system, and with a NOMA system using EP repartition among subbands followed by an intra-subband PA based on FTPA. OS system can be regarded as a special case of NOMA where $n(s) = 1$. Note that in the NOMA case, some subbands can also be assigned to single users, leading to a hybrid scheme, such as in [4], [7].

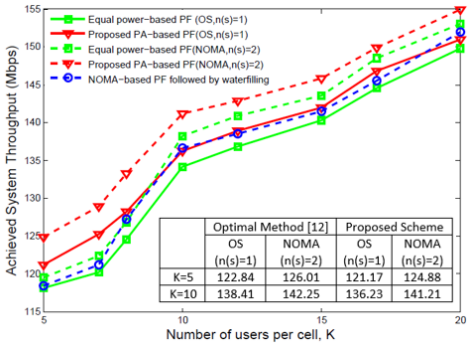

	Optimal Method [12]		Proposed Scheme	
	OS (n(s)=1)	NOMA (n(s)=2)	OS (n(s)=1)	NOMA (n(s)=2)
K=5	122.84	126.01	121.17	124.88
K=10	138.41	142.25	136.23	141.21

Fig. 2. Achieved system throughput in terms of K, for 128 subbands.

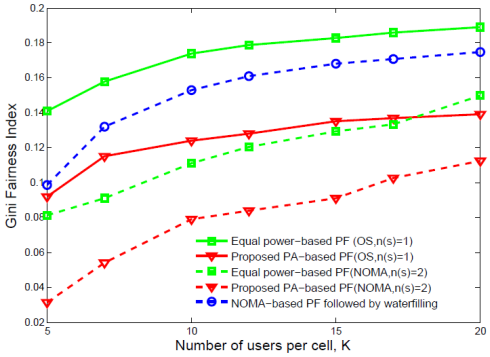

Fig. 3. Gini fairness index in terms of K, for 128 subbands.

Fig. 2 shows the achieved system throughput in terms of K, with a number of subbands equal to 128. The throughput increases with the number of users per cell, for all the simulated methods. In fact, when K increases, the scheduling schemes exploit the multi-user diversity more efficiently. Simulation results show that the proposed NOMA system always outperforms the OS-based system.

When compared to an equal inter-subband PA algorithm, our proposed PA scheme shows improved performance regardless of K, in the NOMA case as well as in the OS case. For the NOMA case, the gain in throughput can reach 5 Mbps for 5 users per cell, i.e. 1 Mbps per user.

A comparison of our proposed scheme with the optimal solution described in [6], and incorporated within the PF, shows that the gap between the two methods is generally 1%.

Fig. 3 shows the Gini metric as a function of K. Fairness is significantly improved when power is dynamically distributed among subbands, independently of the access technique (OS or NOMA). However, the fairness level of NOMA is better than that of OS case. In fact, in NOMA, users having a low channel gain are given the possibility of being paired (as second users) with other users on certain subbands, and are in this case attributed a power level higher than that of the

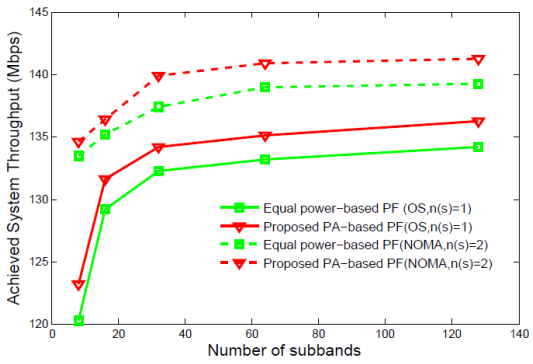

Fig. 4. Achieved system throughput in terms of S, for K = 10.

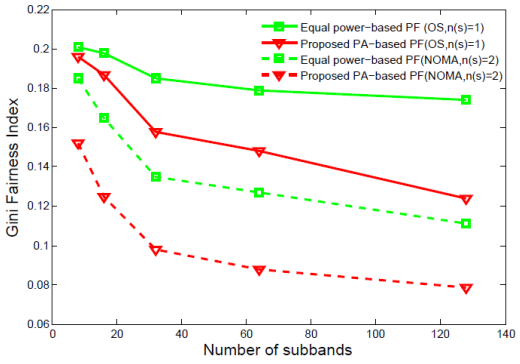

Fig. 5. Gini fairness index in terms of S, for K = 10.

users close to the center of the cell. On the contrary, when PF scheduling is used with OS, only one user is scheduled on each subband, therefore depriving cell-edge users from having access (as second users) to a significant number of subbands that can significantly increase their achieved data rate. From this perspective, we can see that NOMA is fairer to users than OS, since it compensates for the distance effects on the user channel quality by offering appropriate power levels.

The proposed PA scheme is also compared with an alternative method where equal inter-subband PA is considered within the PF scheduling process (to assign all subcarriers) and WF is only applied once at the end to determine the final power levels. This method (see Fig. 2 and Fig. 3) shows degraded performance with respect to the integrated WF process. This is due to the fact that users experiencing bad channel conditions but having low historical rates can be considered by the EP-based PF as having high priority on certain subbands. When applying WF at the end of the allocation, such users will be allocated a low level of power (depending on their channel gains), leading to a low spectral efficiency. The incorporation of WF within the PF allows avoiding such cases.

Fig. 4 shows the achieved system throughput as a function of S, for 10 users per cell. We can see that the proposed joint PA and scheduling scheme outperforms the classical NOMA PF even when the number of subbands is limited. As for the long-term fairness presented in Fig. 5, the gain of the proposed PA technique compared to the EP repartition is almost constant for NOMA, regardless of S.

From a complexity point of view, the proposed joint scheduling scheme differs from the classical PF in the waterline calculation and the power estimation step for each candidate user set. Our proposed technique increases the PF computational load by $2SK + 2S(C_K^2 + C_K^1)$ multiplications and $3S(C_K^2 + C_K^1)$ additions. As for classical NOMA PF, the calculation of the PF metric in (4) depends on the number of multiplexed users in the candidate user set. The classical NOMA PF requires a total of $3KS+C_K^1S(4+S)+C_K^2S(13+2S)$ multiplications and $C_K^1S(1 + 3S/2) + C_K^2S(6 + 3S)$ additions.

When it comes to the optimal solution [6], since it includes a numerical solver, it is not possible to compare its complexity towards that of the suboptimal method in terms of the number of additions and multiplications. Instead, a measure of the average execution time of one complete allocation cycle (i.e. in one timeslot), for the case of 10 users per cell and 8 subbands, yielded 182745 ms for the optimal solution and 68 ms for the proposed suboptimal scheme.

V. CONCLUSION

In this letter, we have proposed a low-complexity waterfilling-based PF scheduling scheme. Simulation results show that the proposed scheme allows an increase in the total user throughput and in the system fairness, when compared to an OS-based system and to a NOMA system considering an equal power repartition among subbands. The study conducted here with two scheduled users per subband can be easily adapted to a larger number of paired users.

REFERENCES

[1] https://www.ericsson.com/res/docs/2016/ericsson-mobility-report-2016.pdf
[2] N. Otao, Y. Kishiyama, and K. Higuchi, "Performance of non-orthogonal access with SIC in cellular downlink using proportional fair-based resource allocation", in *proc. Int. Symp. on Wireless Commun. Syst.*,2012, 476-480.
[3] Z. Ding, Z. Yang, P. Fan, and H. Poor, "On the performance of non-orthogonal multiple access in 5G systems with randomly deployed users", *IEEE Signal Process. Lett.*, 2014, 21(12), 1501-1505.
[4] Y. Saito, A. Benjebbour, Y. Kishiyama, and T. Nakamura, "System-level performance evaluation of downlink non-orthogonal multiple access (NOMA)", in *proc. IEEE PIMRC*, Sept. 2013.
[5] Sun, Yan, et al. "Optimal Joint Power and Subcarrier Allocation for Full-Duplex Multicarrier Non-Orthogonal Multiple Access Systems." arXiv preprint arXiv:1607.02668 (2016).
[6] M.R. Hojeij, J. Farah, C. Abdel Nour, and C. Douillard, "New Optimal and Suboptimal Resource Allocation Techniques for Downlink Non-orthogonal Multiple Access", *Wireless Pers. Commun.*, 2015, 1-31.
[7] M.R. Hojeij, J. Farah, C. AbdelNour, and C. Douillard, "Resource Allocation in Downlink Non-Orthogonal Multiple Access (NOMA) for Future Radio Access", in *proc. 81st IEEE VTC*, 2015.
[8] F.P. Kelly, a.K. Maulloo, and D.K.H. Tan, "Rate control for communication networks: shadow prices, proportional fairness and stability"', *J. of the Operational Research Soc*, 1998, 49(3), 237-252.
[9] S. Haykin, *Communications Systems*, 4th ed. Colorado: Wiley, ch.6, pp. 451-460.
[10] 3GPP, TR25-814 (V7.1.0), "Physical Layer Aspects for Evolved UTRA", 2006.
[11] M. Dianati, X. Shen, and S. Naik, "A new fairness index for radio resource allocation in wireless networks", in *Proc. IEEE Wireless Commun. and Netw. Conf.*, 2005.

In the next part of the work, new throughput and fairness allocation metrics were proposed and assessed. To do so, we began by analyzing the impact of the channel gain difference between multiplexed users on the achieved throughput for different intra-subband power allocation techniques. We have shown that the increase in the channel gain difference between multiplexed users is not always in favor of NOMA's achieved throughput, when different intra-subband power allocation techniques are considered. This observation that we published in [204] highlighted the importance of taking into account the throughput and channel gain dependency when pairing users together. Then, guided by it, we have designed several resource allocation techniques that aim to be fully adapted to NOMA. These techniques base the pairing of users on controllable metrics that aim to achieve a flexible throughput and/or fairness maximization. In addition to that, the new scheduling metrics published in [205, 206] were developed such that they can be easily associated with unequal power allocation techniques such as waterfilling. As a result, the designed techniques have shown an improvement at the level of user throughput, long-term and short-term fairness while being less complex to apply [205, 206].

3.2.3 Extension to single-user MIMO

In the context of the Master's degree project of Marie-Josepha Youssef, we extended the study of resource allocation techniques to allow the coupling of NOMA with MIMO systems. Once again as in most existing downlink NOMA systems prior to our work, the PF scheduler was used. As for power allocation, most previous works for MIMO assumed an equal repartition between antennas and subbands, which is sub-optimal. We first proposed a method to reduce the complexity of the conventional equal-power PF scheduling algorithm. Simulation results showed that the achieved reduction method does not incur any degradation in performance, compared to the conventional PF. We have also proposed a generalization of the iterative waterfilling-based power allocation to the case of single user MIMO NOMA, such that to incorporate a joint inter-antenna and inter-subband unequal power allocation. This method allows the user fairness to be increased by improving the data rates achieved by the cell-edge users, either when compared to OMA signaling or to equal-power NOMA. The waterfilling-PF technique was also shown to be more attractive for large cells. This work received the best paper award at the IEEE Symposium on Computers and Communications (ISCC) [207] in 2017.

3.2.4 Allocation dedicated to the reduction of BS power consumption

At a later stage, we have studied a hybrid context where we aimed to minimize the average downlink BS transmit power, under user rate constraints. We have provided several new methods for joint subcarrier and power allocation for this context under orthogonal and non-orthogonal multiple access. Particular care was taken to reduce the complexity of the corresponding algorithms. Simulation results showed substantial gains with NOMA compared to orthogonal multiplexing. An interesting additional result resides in the fact that it seems much more advantageous, from the power perspective, to apply user pairing at a subsequent stage to single-user assignment, i.e., after all subcarriers have been assigned first users, than to jointly assign first and second users. An alternative efficient solution was also proposed to further reduce the complexity of the algorithms, at the expense of a small increase in BS power. This work was performed in the context of the Master's degree project of Elie Sfeir and was published in [208, 209].

3.2.5 Joint broadcast-broadband operation

A hybrid broadcast and unicast system based on NOMA was proposed next. Indeed, we have used the principle of superposition provided by NOMA in order to allow the transmission of the broadband and broadcast messages on the same frequency platform, and to go further, we have proposed different techniques that allow the hybrid transmission to be done on the same subbands. The study starts with a formulation of the resource allocation problem. Then differently from the most previous works, we have considered broadcasting in an *a posteriori* allocation step, whereas OMA and NOMA-based multicasting schemes treat multicast messages in an *a priori* step. For more details see [210].

The proposed techniques are compared to benchmarking schemes from literature. The proposed hybrid system ensures better performance, at the level of achieved broadband throughput and long-term fairness, when compared to previous broadcasting schemes [210].

3.2.6 NOMA for distributed antenna systems

Recently, Distributed Antenna Systems (DAS) [211, 212] were predicted to be one of the main leveraging techniques in future mobile communication systems, since this technology offers several advantages over Centralized Antenna Systems (CAS). The concept of DAS (also known as distributed base stations) consists in deploying the base station antennas throughout the cell, instead of having multiple antennas installed on a single tower at the cell center. Each antenna is referred to as Remote Radio Head (RRH). The aim of this configuration is to reduce the mean distance (and the path-loss) between users and their serving antennas, thus enabling the system to achieve a better reception quality. In addition, it makes it possible to benefit from the advantages of small cell networks while avoiding the problem of excessive hand-offs inherent to cell sectoring. In that regard, the DAS concept emerges as a win-win trade-off between small cells and large sectored cells as it combines the best of both network architectures. Moreover, the spreading of antennas over each cell enables the system to better adapt to various user-network topologies, which strengthens the resilience to fading and provides a robust framework to combat inter-cell and intra-cell interference.

Inspired by previous results on NOMA, we decided to pursue the extension of the work to DAS systems. Several contributions of different natures were made on their association. This was done in the context of the PhD theses of Marie-Josepha Youssef and Antoine Kilzi.

An effort was put to propose new approaches for combining NOMA with distributed antenna systems. The study targeted a minimization of the total transmit power in each cell, under user rate and power multiplexing constraints. The context of 5G networks and beyond was targeted. Several enhancements to our previously developed method for CAS of [209] were introduced prior to extending it to the DAS context. Then, several new suboptimal power allocation techniques were proposed. They are shown to yield very close performance to an optimal power allocation scheme. Different techniques were designed for the joint allocation of subcarriers, antennas, and power, with a particular care given to maintain a moderate complexity. The coupling of NOMA with DAS is shown to greatly outperform any other combination of OMA/NOMA schemes with distributed or centralized deployment scenarios.

Furthermore, we unveiled some of the hidden potentials of DAS for NOMA systems and developed new techniques to make the most out of these advantages, while extracting their best characteristics and tradeoffs. Particularly, this study introduced NOMA systems with SIC decoding at both paired UE sides that we called mutual successive interference cancellation (mutual SIC), a remarkable outcome. Simulation results have shown the superiority of the proposed methods with respect to single SIC configurations. They also promoted mutual

SIC with suboptimal power adjustment to the best tradeoff between transmit power and complexity at both the BaseBand Unit (BBU) and the UE levels.

The importance of the proposed mutual SIC approach resides in its ability to cancel interference at both receivers, largely improving efficiency. For this reason, the corresponding work published in IEEE Transactions on Vehicular Technology [213] is included hereafter.

Several aspects of this work were further explored, since many additional challenges needed to be addressed to enhance the NOMA-DAS-specific resource allocation schemes. For instance, practical considerations were incorporated in the study, such as the introduction of power limitations to some of the antennas, as described in the next section.

Power Minimization in Distributed Antenna Systems using Non-Orthogonal Multiple Access and Mutual Successive Interference Cancellation

Joumana Farah, Antoine Kilzi, Charbel Abdel Nour, Catherine Douillard

***Abstract*—This paper introduces new approaches for combining non-orthogonal multiple access with distributed antenna systems. The study targets a minimization of the total transmit power in each cell, under user rate and power multiplexing constraints. Several new suboptimal power allocation techniques are proposed. They are shown to yield very close performance to an optimal power allocation scheme. Also, a new approach based on mutual successive interference cancellation of paired users is proposed. Different techniques are designed for the joint allocation of subcarriers, antennas, and power, with a particular care given to maintain a moderate complexity. The coupling of non-orthogonal multiple access to distributed antenna systems is shown to greatly outperform any other combination of orthogonal/non-orthogonal multiple access schemes with distributed or centralized deployment scenarios.**

***Index Terms*—Distributed Antenna Systems, Non Orthogonal Multiple Access, Power minimization, Resource allocation, Waterfilling, Mutual SIC.**

I. INTRODUCTION

THE concept of distributed antenna systems (DAS), also known as distributed base stations, [1], [2] was introduced in the past few years in mobile communication systems to increase the cell coverage in a cost effective way, and to strengthen the network infrastructure, particularly in saturated areas. It consists of deploying the base station (BS) antennas in a distributed manner throughout the cell, instead of having multiple antennas installed on a single tower at the cell center. The remote units, called remote radio heads (RRH), are connected to the baseband unit (BBU) through high capacity coaxial cables or fiber optics. By reducing the average distance of each mobile user to its transmitting/receiving antenna, the overall transmission power required to guarantee a certain quality of reception is reduced in comparison to the centralized configuration (centralized antenna system or CAS). Therefore, from an ecological standpoint, DAS can greatly reduce local electromagnetic radiation and CO_2 emissions of transmission systems. Alternatively, for the same overall transmission power as in CAS, DAS offers a higher capacity and a fairer throughput distribution between the active users of a cell. Moreover, it provides a better framework for improving the system robustness to fading, intra-cell and inter-cell interferences, shadowing, and path-loss. It also allows the system to better adapt to the varying user distribution. Moreover, the decoupled architecture will allow the deployment of small antennas in large scale and in discrete locations in urban areas, e.g. on building roofs, electric poles, traffic and street lights, where they can be almost invisible due to their small size. This will significantly simplify and reduce the cost of site installation, therefore lowering the capital expenditure (CAPEX) of mobile operators.

Efficient implementation is key in squeezing the achievable potentials out of DAS. For this purpose, the study in [3] explored the advantages of DAS and compared the achievable ergodic capacity for two different transmission scenarios: selection diversity and blanket transmission. In the first one, one of the RRHs is selected (based on a path-loss minimization criterion) for transmitting a given signal, whereas in the second, all antennas in the cell participate in each transmission, thus creating a macroscopic multiple antenna system. The results of [3] show that selection diversity achieves a better capacity in the DAS context, compared to blanket transmission. The same observations are made in [4]. In [5], RRH selection is also preconized as a mean to decrease the number of information streams that need to be assembled from or conveyed to the involved RRHs, as well as the signaling overhead.

A. Energy Efficiency Maximization in DAS

Several works target the optimization of system energy efficiency (EE) in the DAS context. In [6], two antenna selection techniques are proposed, either based on user path-loss information or on RRH energy consumption. Also, proportional fairness scheduling is considered for subband allocation with a utility function adapted to optimize the EE. In [7], subcarrier assignment and power allocation (PA) are done in two separate stages. In the first one, the number of subcarriers per RRH is determined, and subcarrier/RRH assignment is performed assuming initial equal power distribution. In the second stage, power allocation (PA) is performed by maximizing the EE under the constraints of the total transmit power per RRH, of the targeted bit error rate and of a proportionally-fair throughput distribution among active users. The optimization techniques proposed in [6], [7] for DAS are designed for the case of orthogonal multiple access (OMA). In other words, they allow the allocation of only one user per subcarrier.

J. Farah is with the Department of Electricity and Electronics, Faculty of Engineering, Lebanese University, Roumieh, Lebanon (joumanafarah@ul.edu.lb).

A. Kilzi, C. Abdel Nour and C. Douillard are with IMT Atlantique, Lab-STICC, UBL, F-29238 Brest, France, (email: antoine.kilzi@imt-atlantique.fr; charbel.abdelnour@imt- atlantique.fr; catherine.douillard@imt-atlantique.fr).

B. Power Domain Non-Orthogonal Multiple Access

Non-orthogonal multiple access (NOMA) has recently emerged as a promising multiple access technique to significantly improve the attainable spectral efficiency for fifth generation (5G) mobile networks. Power-domain NOMA enables the access of multiple users to the same frequency resource at the same time by taking advantage of the channel gain difference between users [8–12], through signal power multiplexing. At the receiver side, user separation is performed using successive interference cancellation (SIC). Applying power multiplexing on top of the orthogonal frequency division multiplexing (OFDM) layer has proven to significantly increase system throughput compared to orthogonal signaling, while also improving fairness and cell-edge user experience. A few previous works have studied the application of NOMA in the DAS context. An outage probability analysis for the case of two users in cloud radio access networks (C-RAN) is provided in [13] where all RRHs serve simultaneously both users. The results show the superiority of NOMA when compared to time division multiple access (TDMA), in the context of C-RANs. In [14], the study investigates the application of distributed NOMA for the uplink of C-RANs. The partially centralized C-RAN architecture allows the use of joint processing by distributed antennas, in which RRHs can exchange correctly decoded messages from other RRHs in order to perform SIC. In [15], an efficient end-to-end uplink transmission scheme is proposed where the wireless link between users and RRHs on one side, and the fronthaul links between the RRHs and BBU on the other side are studied. User grouping on blocks of subcarriers is proposed to mitigate the computational complexity, and a fronthaul adaptation for every user group is performed in order to strike a tradeoff between throughput and fronthaul usage.

C. State of the Art of Power Minimization in the NOMA Context

A few recent works tackle the power minimization problem in the NOMA context. In [16], a "relax-then-adjust" procedure is used to provide a suboptimal solution to the NP-hard problem: first, the problem is relaxed from the constraints relative to power domain multiplexing. Then, the obtained solution is iteratively adjusted using a bisection search, leading to a relatively high complexity. In [17], optimal PA is first conducted assuming a predefined fixed subcarrier assignment. Then, a deletion-based algorithm iteratively removes users from subcarriers until the constraints of the maximum number of multiplexed users are satisfied, thus necessitating a large number of iterations to converge. In [18], the authors propose an optimal and a suboptimal solution for determining the user scheduling, the SIC order, and the PA, for the case of a maximum of two users per subcarrier. However, the power multiplexing constraints are not taken into consideration. The power multiplexing constraints state that the signal that is to be decoded first must have a higher power level than the other received signals, so that it is detectable at the receiver side. Power minimization strategies are also proposed in [19] for multiple-input multiple-output NOMA (MIMO-NOMA), where PA and receive beamforming design are alternated in an iterative way. Constraints on the targeted SINR (signal to interference and noise ratio) are considered to guarantee successful SIC decoding. The subcarrier allocation problem is not included, i.e. all users have access to the whole spectrum. Results, provided for a moderate number of users (4 or 6), show an important gain in performance with respect to OMA.

In [20], we have introduced a set of techniques that allow the joint allocation of subcarriers and power, with the aim of minimizing the total power in NOMA-CAS. Particularly, we showed that the most efficient method, from the power perspective, consists of applying user pairing at a subsequent stage to single-user assignment, i.e. after applying OMA signaling at the first stage, instead of jointly assigning collocated users to subcarriers. To the best of our knowledge, no previous work has studied the downlink power minimization problem in a DAS configuration and using NOMA.

D. Contributions

The main objective of this work is to study the potentials of applying NOMA in the DAS configuration from a power minimization perspective. We investigate the resource allocation (RA) problem in downlink, seeking the minimization of the total transmit power at the RRHs under user rate constraints. The contributions of this paper are summarized in the following :

- We introduce several techniques that allow a significant complexity reduction of the waterfilling procedures used for PA in [20], for both orthogonal and non-orthogonal transmission, while adapting the allocation techniques to the DAS context.
- We propose a new PA scheme for user pairing that outperforms FTPA (fractional transmit power allocation) [9], [10], while taking into account the power multiplexing constraints.
- Unlike previous works, we investigate the use of different RRHs to power the multiplexed subcarriers in NOMA. This new setting gives rise to the concept of "mutual SIC" where paired users on a subcarrier can perform SIC at the same time, under well defined conditions.
- Finally, we propose new suboptimal algorithms to achieve joint subcarrier, RRH, and power allocation, in light of the newly uncovered potentials specific to the application of NOMA in the DAS context.

The rest of this paper is organized as follows: in Section II, a description of the system model is provided along with a formulation of the RA problem in the context of NOMA-DAS. Then, in Section III, several suboptimal solutions are investigated for the power minimization problem in the case of a single powering RRH per subcarrier. In Section IV, a novel approach allowing a mutual SIC implementation on certain subcarriers is introduced, followed by the proposal of several allocation techniques for exploiting such subcarriers. Section V provides a brief overview of the complexity of the proposed algorithms. Section VI presents a performance analysis of the different allocation strategies, while Section VII concludes the paper.

II. DESCRIPTION OF THE NOMA-DAS SYSTEM AND FORMULATION OF THE POWER MINIMIZATION PROBLEM

This study is conducted on a downlink system consisting of a total of R RRHs uniformly positioned over a cell where K mobile users are randomly deployed (Fig. 1). The RRHs are connected to the BBU through high capacity optical fibers. RRHs and users are assumed to be equipped with a single antenna. Users transmit their channel state information (CSI) to RRHs, and the BBU collects all the CSI from RRHs. The influence of imperfect channel estimation on the performance of DAS was studied in [21]. However, perfect CSI is assumed throughout this study (the influence of imperfect or outdated CSI is not the aim of this work). Alternatively, the BBU can benefit from channel reciprocity to perform the downlink channel estimation by exploiting the uplink transmissions. Based on these estimations, the BBU allocates subcarriers, powers, and RRHs to users in such a way to guarantee a transmission rate of $R_{k,req}$ [bps] for each user k. The system bandwidth B is equally divided into S subcarriers. Each user k is allocated a set $\mathcal{S}_k$ of subcarriers. From the set of K users, a maximum of $m(n)$ users $\{k_1, k_2, \ldots, k_{m(n)}\}$ are chosen to be collocated on the n^{th} subcarrier ($1 \leqslant n \leqslant S$). Classical OMA signaling corresponds to the special case of $m(n) = 1$. Let $h_{k_i,n,r}$ be the channel coefficient between user k_i and RRH r over subcarrier n, and H the three-dimensional channel gain matrix with elements $h_{k,n,r}$, $1 \leqslant k \leqslant K$, $1 \leqslant n \leqslant S$, $1 \leqslant r \leqslant R$. A user k_i on subcarrier n can remove the inter-user interference from any other user k_j, collocated on subcarrier n, whose channel gain verifies $h_{k_j,n} < h_{ki,n}$ [8], [9] and treats the received signals from other users as noise.

As shown in Fig. 1, NOMA subcarriers can be served by the same RRH or by different RRHs. For instance, one can consider serving User 1 and User 2 on the same subcarrier SC 1 by RRH 1, while User 2 and User 3 are paired on another subcarrier, SC 2, and served by RRH 1 and RRH 2 respectively.

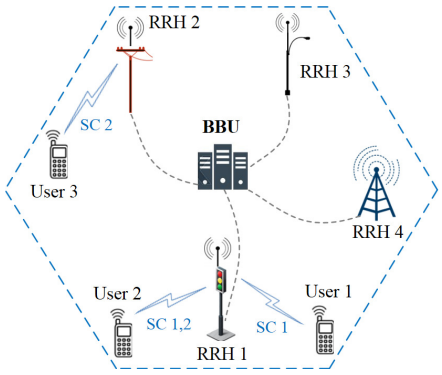

Fig. 1: DAS using NOMA

The capacity of the BBU-RRH links is assumed to be many orders of magnitude higher than the capacity of the RRH-users wireless links. This is due to the radical differences between the two channel media: interference immune, low loss, high bandwidth fibers with dedicated channels as opposed to the frequency selective, time varying, shared medium that is the wireless link. Clearly, the bottleneck of the system, in terms of capacity and power consumption, resides at the wireless link level, where large margins of improvement can be achieved.

In the rest of the study, and without loss of generality, we will consider a maximum number of collocated users per subcarrier of 2, i.e. $m(n)$= 1 or 2. On the one hand, it has been shown [9] that the gain in performance obtained with the collocation of 3 users per subcarrier, compared to 2, is minor. On the other hand, limiting the number of multiplexed users per subcarrier limits the SIC complexity at the receiver terminals. We will denote by first (resp. second) user on a subcarrier n the user which has the higher (resp. lower) channel gain on n between the two paired users. Let $P_{k_i,n,r}$ be the power of the i^{th} user on subcarrier n transmitted by RRH r. The theoretical throughputs $R_{k_i,n,r}, 1 \leqslant i \leqslant 2$, on n are given by the Shannon capacity limit as follows:

$$R_{k_1,n,r} = \frac{B}{S}\log_2\left(1 + \frac{P_{k_1,n,r}h^2_{k_1,n,r}}{\sigma^2}\right), \quad (1)$$

$$R_{k_2,n,r} = \frac{B}{S}\log_2\left(1 + \frac{P_{k_2,n,r}h^2_{k_2,n,r}}{P_{k_1,n,r}h^2_{k_2,n,r} + \sigma^2}\right), \quad (2)$$

where N_0 and $\sigma^2 = N_0 B/S$ are respectively the power spectral density and the power level (over a subcarrier) of additive white Gaussian noise, including randomized inter-cell interference, and assumed to be constant over all subcarriers.

Let $\mathcal{T}_k$ be the mapping set of RRHs corresponding to user k, such that the i^{th} element of $\mathcal{T}_k$ corresponds to the RRH selected for powering the i^{th} subcarrier from $\mathcal{S}_k$. Note that user k can be first, second, or sole user on any of its allocated subcarriers in $\mathcal{S}_k$. Taking into account the power multiplexing constraints proper to NOMA, the corresponding optimization problem can be formulated as:

$$\{\mathcal{S}_k, \mathcal{T}_k, P_{k,n,r}\}^* = \underset{\{\mathcal{S}_k,\mathcal{T}_k,P_{k,n,r}\}}{\arg\min} \sum_{k=1}^{K} \sum_{\substack{n\in\mathcal{S}_k \\ r=\mathcal{T}_k(i),\ \text{s.t. } \mathcal{S}_k(i)=n}} P_{k,n,r},$$

Subject to:

$$\begin{cases} \sum_{n\in\mathcal{S}_k} R_{k,n,r} = R_{k,req}, \forall k, 1 \leqslant k \leqslant K & (3) \\ P_{k,n,r} \geqslant 0, n \in \mathcal{S}_k, r \in \mathcal{T}_k, 1 \leqslant k \leqslant K & (4) \\ P_{k_2,n,r} \geqslant P_{k_1,n,r}, \forall n \in \mathcal{S}_k, 1 \leqslant k \leqslant K & (5) \end{cases}$$

The problem consists in finding the optimal subcarrier-RRH-user allocation, as well as the optimal power allocation over the allocated subcarriers, so as to minimize the objective function that is the total transmit power of the cell. This must be done under the rate constraints (3), positive power constraints (4), and power multiplexing constraints (5). The first constraint imposes a minimum rate requirement $R_{k,req}$ for every user k, that must be achieved over the subcarriers $\mathcal{S}_k$ allocated to k. The second condition ensures that all power variables remain non-negative (a null power variable corresponds to an

unallocated subcarrier). Finally, the last constraint accounts for the power multiplexing conditions where the power level of the signal of the weak user, $P_{k_2,n,r}$, must be greater than the power level of the signal of the strong user, $P_{k_1,n,r}$. Solving this optimization problem resides in determining the optimal allocation sets $\mathcal{S}_k$, $\mathcal{T}_k$ for every user k, as well as finding the optimal power allocation over the allocated subcarriers. Therefore, the optimization problem at hand is mixed combinatorial and non-convex, that is why we resort to suboptimal solutions for the joint subcarrier-RRH-user assignment and power allocation problem. Moreover, compared to the case of NOMA-CAS signaling, an additional dimension is added, corresponding to the determination of the best RRH to power each multiplexed subcarrier. Therefore, we study separately the cases of powering the multiplexed signals on a subcarrier by a common RRH (Section III), or by different RRHs (Section IV). We optimize the performance of both allocation schemes and then combine the RRH selection strategies into a unified algorithm which outperforms its predecessors.

III. Resource Allocation Techniques for the Case a Single Powering RRH per Subcarrier

A. Power minimization procedure

Given the intractability of the optimal subcarrier and power allocation solutions, a greedy approach was introduced in [20] for the CAS context, which aims at minimizing the power decrease resulting from every new subcarrier allocation: user-subcarrier assignment is determined by first selecting the most power consuming user and then allocating to it the available subcarrier that best reduces its requested transmit power from the base station. Note that in DAS, this step resides in the selection of the best subcarrier-RRH couple from the space of $S \times R$ subcarrier-antenna pairs.

In the OMA phase, power allocation is performed using a recursive low-complexity waterfilling technique. For this reason, we start by revisiting the waterfilling principle in order to introduce several procedures for reducing the complexity of both orthogonal and non-orthogonal RA phases. Then, we extend the obtained solution to the DAS context.

Given a user k allocated a total of N_k subcarriers and having a waterlevel $w_k(N_k)$, the addition of a subcarrier-RRH pair (n_a, r) in the OMA phase decreases the waterline if and only if its channel gain verifies [20]:

$$h^2_{k,n_a,r} > \frac{\sigma^2}{w_k(N_k)} \tag{6}$$

The new waterlevel, as well as the power incurred by the subcarrier assignment in the OMA phase, can be determined by means of the following equations:

$$w_k(N_k+1) = \frac{(w_k(N_k))^{N_k/(N_k+1)}}{(h^2_{k,n_a,r}/\sigma^2)^{1/(N_k+1)}} \tag{7}$$

$$\Delta P_{k,n_a,r} = (N_k+1)w_k(N_k+1) - N_k w_k(N_k) - \frac{\sigma^2}{h^2_{k,n_a,r}} \tag{8}$$

For more detailed information about (6), (7), and (8), the reader is referred to [20]. Note that when a CAS configuration is considered, r designates the central (unique) BS antenna.The subcarrier minimizing the power decrease for user k is also the subcarrier with the best channel for this user, as shown in Appendix A. This equivalence will allow us to decrease the complexity of the OMA phase with respect to [20].

Next, the user pairing phase is considered, i.e. the assignment of second users to subcarriers in the NOMA phase. As stated in [20], when allocating a subcarrier to user k as second user, the waterline of the solely occupied subcarriers by k must be decreased in order to avoid any excess in rate (compared to its required rate) and thus in power. In addition, the initial waterlevel for every user k in the NOMA phase is the final waterline obtained in the OMA phase. In [20], a dichotomy-based waterfilling technique [22] is used after each new pairing in the NOMA phase to determine the power level on each sole subcarrier of user k. For this purpose, we derive next an alternative iterative waterfilling calculation for the NOMA phase, with a significant complexity reduction compared to dichotomy-based waterfilling.

Let $\mathcal{S}_k^{sole}$ be the set of solely allocated subcarriers to user k, N_k^{sole} the cardinal of this set denoted by $N_k^{sole} = |\mathcal{S}_k^{sole}|$, and R_k^{sole} the total rate achieved by user k over its subcarriers in $\mathcal{S}_k^{sole}$. We have:

$$R_k^{sole} = \sum_{\substack{n\in\mathcal{S}_k \\ r=\mathcal{T}_k(i),\ \text{s.t. } \mathcal{S}_k(i)=n}} \frac{B}{S}\log_2\left(1+\frac{P_{k,n,r}h^2_{k,n,r}}{\sigma^2}\right),$$

with $P_{k,n,r} = w_k(N_k^{sole}) - \sigma^2/h^2_{k,n,r}$, where $w_k(N_k^{sole})$ is the waterline corresponding to $\mathcal{S}_k^{sole}$.
Therefore, R_k^{sole} can be rewritten as:

$$R_k^{sole} = \sum_{n\in\mathcal{S}_k^{sole}} \frac{B}{S}\log_2\left(\frac{w_k(N_k^{sole})h^2_{k,n,r}}{\sigma^2}\right), \text{ leading to:}$$

$$w_k(N_k^{sole}) = \left(2^{R_k^{sole}S/B}\prod_{n\in\mathcal{S}_k^{sole}}\frac{\sigma^2}{h^2_{k,n,r}}\right)^{\frac{1}{N_k^{sole}}} \tag{9}$$

On the other hand, R_k^{sole} is calculated by subtracting from $R_{k,req}$ the rates of user k on the subcarriers where k is either first or second user. When user k is assigned as a second user to a subcarrier n, the corresponding rate gain is calculated using (2), with a power level on n given by FTPA:

$$P_{k_2,n,r} = P_{k_1,n,r}h^{-2\alpha}_{k_2,n,r}/h^{-2\alpha}_{k_1,n,r}$$

where $P_{k_1,n,r}$ is the power of the first user previously allocated to subcarrier n in the OMA phase. This additional rate corresponds to the rate decrease $\Delta R_{k,n,r}$ that should be compensated for on the sole subcarriers of k, so as to ensure the global rate constraint $R_{k,req}$. In other words, the variation that the rate R_k^{sole} undergoes is opposite to the rate addition that comes along the new subcarrier assignment. We can write the new rate that must be achieved on $\mathcal{S}_k^{sole}$ as $R_k^{sole'} = R_k^{sole} + \Delta R_{k,n,r}$ where the rate decrease $\Delta R_{k,n,r}$

is negative. Using (9), the new waterline on the set $\mathcal{S}_k^{sole}$ can then be derived as follows:

$$w'_k(N_k^{sole}) = \left(2^{R_k^{sole\prime}S/B} \prod_{n\in\mathcal{S}_k^{sole}} \frac{\sigma^2}{h_{k,n,r}^2}\right)^{\frac{1}{N_k^{sole}}}$$

$$w'_k(N_k^{sole}) = 2^{\frac{\Delta R_{k,n,r}S}{BN_k^{sole}}} w_k(N_k^{sole}) \quad (10)$$

This expression of the waterline update in the NOMA phase enables the fast computation of the potential power decrease corresponding to any candidate subcarrier-RRH pair, using:

$$\Delta P_{k_2,n,r} = N_{k_2}^{sole}\left(w'_{k_2}(N_{k_2}^{sole}) - w_{k_2}(N_{k_2}^{sole}\right) + P_{k_2,n,r} \quad (11)$$

This reduced complexity algorithm can then be directly extended to the DAS context. In the OMA phase, the subcarrier selection in CAS turns into a subcarrier-RRH pair assignment in DAS. Therefore, the space of possible links to attribute to the user is enlarged by the factor R. However, in the NOMA phase, we restrict the transmission of the paired subcarrier to the same RRH serving the first user. Indeed, when different RRHs are chosen to power the multiplexed subcarrier, special features need to be addressed as will be shown in Section IV-A. This NOMA-DAS method will be referred to as SRRH (meaning Single RRH per subcarrier). The corresponding details are presented in Algorithm 1, where $\mathcal{U}_p$ is the set of users whose power level can still be decreased, $\mathcal{S}_p$ is the set of unallocated subcarriers, and $\mathcal{S}_f$ is the set of subcarriers assigned a first user without a second user.

Algorithm 1 SRRH

Initialization: $\mathcal{S}_p = [1:S]$
$\mathcal{U}_p = [1:K]$
$\mathcal{S}_f = \varnothing$

Phase 1: // Worst-Best-H phase
Take the user whose best subcarrier-RRH link is the lowest among users and assign it its best subcarrier-RRH pair with the needed power to reach $R_{k,req}$. Repeat until all users have one allocated subcarrier-RRH pair moved from $\mathcal{S}_p$ to $\mathcal{S}_f$.

Phase 2: // Orthogonal multiplexing (single-user assignment)
$k^* = \arg\max_k P_{k,tot}$//identify the most power-consuming user
$(n^*, r^*) = \underset{(n,r),\text{ s.t. } n\in\mathcal{S}_p \& (6)}{\arg\max} h_{k*,n,r}$ // identify its most favorable
// subcarrier-RRH pair
Calculate $w_{k*}(N_{k*}+1), \Delta P_{k*,n*,r*}$ using (7) and (8)
If $\Delta P_{k*,n*,r*} < -\rho$ // (n^*, r^*) allows a significant power
// decrease
Attribute (n^*, r^*) to k^*,
Remove n^* from $\mathcal{S}_p$,
Add n^* to $\mathcal{S}_f$,
Update $P_{k*,tot}$
Else remove k^* from $\mathcal{U}_p$ // k^*'s power can no longer be decreased
// in OMA

Repeat Phase 2 until no more subcarriers can be allocated

$\mathcal{U}_p = [1:K]$

Phase 3: // NOMA pairing

$k_2 = \arg\max_k P_{k,tot}$
For every $n \in \mathcal{S}_f$ s.t. $h_{k_2,n,r} < h_{k_1,n,r}$ // r is the RRH powering
// user k_1 on n
Calculate $P_{k_2,n,r}$ through FTPA
Calculate $w'_{k_2}(N_{k_2}^{sole})$ using (10)
Calculate $\Delta P_{k_2,n,r}$ using (11)
End for
$n^* = \arg\min_n \Delta P_{k_2,n,r}$
If $\Delta P_{k_2,n*,r} < -\rho$
Assign k_2 on n^* and remove n^* from $\mathcal{S}_f$
Fix $P_{k_1,n*,r*}$ and $P_{k_2,n*,r*}$, update $P_{k_2,n,r}, \forall n \in \mathcal{S}_{k_2}^{sole}$
Else remove k_2 from $\mathcal{U}_p$
Repeat Phase 3 until $\mathcal{S}_f = \varnothing \vee \mathcal{U}_p = \varnothing$

In Algorithm 1, we start by ensuring that all users reach their targeted rates in the Worst-Best-H phase. From that point onward, the total power of the system decreases with every subcarrier allocation (by at least ρ).

The threshold ρ is chosen in such a way to strike a balance between the power efficiency and the spectral efficiency of the system, since unused subcarriers are released for use by other users or systems. Each time a user k_2 is paired with a user k_1 on a subcarrier n^*, the powers of k_1 and k_2 on n^* are kept unvaried, i.e. they will no longer be updated at subsequent iterations. Actually, in both phases 2 and 3, an iteration results in either the allocation of a subcarrier-RRH pair, or the dismissing of a user from the set $\mathcal{U}_p$ of active users (in case of a negligible power decrease). Either ways, the total number of available subcarriers or active users is decreased by one in every iteration. Therefore, phases 2 and 3 involve at most $|\mathcal{S}_p| - K$ and $|\mathcal{S}_f|$ iterations respectively. In the worst case scenario, we have $|\mathcal{S}_f| = |\mathcal{S}_p| = S$. These considerations are central to the complexity analysis led in Section V, and they prove the stability of Algorithm 1.

B. Enhancement of the power minimization procedure through local power optimization (LPO)

The power decrease incurred by a candidate subcarrier n in the third phase of SRRH is greatly influenced by the amount of power $P_{k_2,n,r}$ allocated to user k_2 on n using FTPA. Indeed, the addition of a new subcarrier translates into an increase of the power level allocated to the user on the one hand, and conversely into a power decrease for the same user due to the subsequent waterline reduction on its sole subcarriers on the other hand. Therefore, we propose to optimize the value of $P_{k_2,n,r}$ in such a way that the resulting user power reduction is minimized:

$$\min_{P_{k_2,n,r}} \Delta P_{k_2}$$

Subject to:

$$P_{k_2,n,r} \geqslant P_{k_1,n,r}$$

By replacing (10) into (11), and expressing $R_{k_2,n,r}$ using (2), we can formulate the Lagrangian of this optimization problem as:

$$L(P_{k_2,n,r},\lambda) = P_{k_2,n,r} + N_{k_2}^{sole} w_{k_2}(N_{k_2}^{sole}) \left(\left(1 + \frac{P_{k_2,n,r} h_{k_2,n,r}^2}{P_{k_1,n,r} h_{k_2,n,r}^2 + \sigma^2} \right)^{-\frac{1}{N_{k_2}^{sole}}} - 1 \right) + \lambda (P_{k_2,n,r} - P_{k_1,n,r})$$

where λ is the Lagrange multiplier.
The corresponding Karush-Khun-Tucker (KKT) conditions are:

$$\begin{cases} 1+\lambda - \frac{w_{k_2}(N_{k_2}^{sole}) h_{k_2,n,r}^2}{P_{k_1,n,r} h_{k_2,n,r}^2 + \sigma^2} \left(1 + \frac{P_{k_2,n,r}^* h_{k_2,n,r}^2}{P_{k_1,n,r} h_{k_2,n,r}^2 + \sigma^2} \right)^{\frac{-N_{k_2}-1}{N_{k_2}}} = 0 \\ \lambda (P_{k_2,n,r}^* - P_{k_1,n,r}) = 0 \end{cases}$$

We can check that the second derivative of the Lagrangian is always positive, and therefore the corresponding solution is the global minimum. For $\lambda = 0$, this optimum is:

$$P_{k_2,n,r}^* = \left(\left(\frac{w_{k_2}(N_{k_2}^{sole}) h_{k_2,n,r}^2}{P_{k_1,n,r} h_{k_2,n,r}^2 + \sigma^2} \right)^{\frac{N_{k_2}^{sole}}{N_{k_2}^{sole}+1}} - 1 \right) \left(P_{k_1,n,r} + \frac{\sigma^2}{h_{k_2,n,r}^2} \right) \quad (12)$$

For $\lambda \neq 0$, $P_{k_2,n,r}^* = P_{k_1,n,r}$. However in such cases, with no power difference between the two paired users, successful SIC decoding is jeopardized at the receiver side for the first user. To overcome such a problem, we take:

$$P_{k_2,n,r}^* = P_{k_1,n,r}(1+\mu), \quad (13)$$

with μ a positive safety power margin that depends on practical SIC implementation. In other terms, if the obtained $P_{k_2,n,r}^*$ in (12) verifies the power constraint inequality, it is retained as the optimal solution, otherwise, it is taken as in (13). This method, referred to as "SRRH-LP", operates similarly to Algorithm 1, except for the FTPA power allocation which is replaced by either (12) or (13).

IV. RESOURCE ALLOCATION TECHNIQUES FOR THE CASE OF TWO POWERING RRHS PER SUBCARRIER

Having extended previous CAS RA schemes to the DAS context and enhanced the corresponding solutions, the rest of the paper aims at designing specific NOMA RA schemes capturing the unique properties that arise in DAS. We start by developing the theoretical foundation lying behind SIC implementations when different RRHs are used to power the multiplexed signals on a subcarrier. The results show that under some well defined conditions, both paired users can perform SIC on the subcarrier. Finally, we propose several RA schemes taking advantage of the capacity gains inherent to mutual SIC and combine them with single SIC techniques.

A. Theoretical foundation

In the case where the same RRH powers both multiplexed users on a subcarrier, there always exists one strong user at a given time which is the user having the best subcarrier-RRH link. However, this isn't necessarily the case when different RRHs are chosen to power the subcarrier, since the concept of weak and strong users is only valid relatively to a specific transmitting antenna. Indeed, the greater diversity provided by powering multiplexed subcarriers by different RRHs involves four instead of two different user-RRH links and thus opens the possibility of having more than one "strong" user at a time.

Theorem 1. *Two users k_1 and k_2, paired on subcarrier n and powered by two different RRHs, respectively r_1 and r_2, can both perform SIC if:*

$$h_{k_1,n,r_2} \geqslant h_{k_2,n,r_2} \quad (14)$$

$$h_{k_2,n,r_1} \geqslant h_{k_1,n,r_1} \quad (15)$$

Proof. Let s_1 be the signal of user k_1 emitted by RRH r_1 with a power P_{k_1,n,r_1}, and let s_2 be the signal of user k_2 emitted by RRH r_2 with a power P_{k_2,n,r_2}. Therefore, the channel conditions experienced by every signal arriving at a given user are different: at the level of k_1, the power levels of the signals s_1 and s_2 are $P_{k_1,n,r_1} h_{k_1,n,r_1}^2$ and $P_{k_2,n,r_2} h_{k_1,n,r_2}^2$ respectively. Similarly, at the level of k_2, the power levels of signals s_1 and s_2 are $P_{k_1,n,r_1} h_{k_2,n,r_1}^2$ and $P_{k_2,n,r_2} h_{k_2,n,r_2}^2$ respectively. Depending on their respective signal quality, users k_1 and k_2 can decode the signal s_2 at different rates. Let $R_{k_2}^{(k_1)}$ be the necessary rate at the level of user k_1 to decode the signal of user k_2 in the presence of the signal of user k_1. And let $R_{k_2}^{(k_2)}$ the necessary rate to decode the signal of user k_2 at the level of k_2 in the presence of the signal of user k_1. The capacity that can be achieved by k_1 and k_2 over the signal s_2 and in the presence of the interfering signal s_1 are given by the Shannon limit:

$$R_{k_2}^{(k_1)} = \frac{B}{S} \log_2 \left(1 + \frac{P_{k_2,n,r_2} h_{k_1,n,r_2}^2}{P_{k_1,n,r_1} h_{k_1,n,r_1}^2 + \sigma^2} \right) \quad (16)$$

$$R_{k_2}^{(k_2)} = \frac{B}{S} \log_2 \left(1 + \frac{P_{k_2,n,r_2} h_{k_2,n,r_2}^2}{P_{k_1,n,r_1} h_{k_2,n,r_1}^2 + \sigma^2} \right) \quad (17)$$

For k_1 to be able to perform SIC, the rates should satisfy the following condition:

$$R_{k_2}^{(k_1)} \geqslant R_{k_2}^{(k_2)} \quad (18)$$

By writing: $R_{k_2}^{(k_1)} - R_{k_2}^{(k_2)} = \frac{B}{S} \log_2 \left(\frac{X}{Y} \right)$, we can express $X - Y$ as:

$$X - Y = P_{k_1,n,r_1} P_{k_2,n,r_2} \left(h_{k_1,n,r_2}^2 h_{k_2,n,r_1}^2 - h_{k_2,n,r_2}^2 h_{k_1,n,r_1}^2 \right) + \sigma^2 P_{k_2,n,r_2} \left(h_{k_1,n,r_2}^2 - h_{k_2,n,r_2}^2 \right) \quad (19)$$

Similarly for user k_2, the rate condition that should be satisfied for the implementation of SIC at the level of k_2 is:

$$R_{k_1}^{(k_2)} \geqslant R_{k_1}^{(k_1)} \quad (20)$$

$R_{k_1}^{(k_2)}$ and $R_{k_1}^{(k_1)}$ can be obtained from (16) and (17) by interchanging indexes 1 and 2. Also, by writing: $R_{k_1}^{(k_2)} - R_{k_1}^{(k_1)} = \frac{B}{S}\log_2\left(\frac{Z}{T}\right)$, we get:

$$\begin{aligned} Z - T =& P_{k_2,n,r_2}P_{k_1,n,r_1}\left(h_{k_2,n,r_1}^2 h_{k_1,n,r_2}^2 - h_{k_1,n,r_1}^2 h_{k_2,n,r_2}^2\right) \\ &+\sigma^2 P_{k_1,n,r_1}\left(h_{k_2,n,r_1}^2 - h_{k_1,n,r_1}^2\right) \end{aligned} \quad (21)$$

Let us note that for the special case of $r_1 = r_2 = r$, we get:

$$X - Y = \sigma^2 P_{k_2,n,r}\left(h_{k_1,n,r}^2 - h_{k_2,n,r}^2\right)$$
$$Z - T = -\sigma^2 P_{k_1,n,r}\left(h_{k_1,n,r}^2 - h_{k_2,n,r}^2\right)$$

Therefore, either (19) or (21) is positive, not both, which justifies why only the stronger user, the one with the higher channel gain, is able to perform SIC as it has been stated in all previous works on NOMA [8–10], [16], [17].

For both users to perform SIC, the rate conditions (18) and (20) must be verified at the same time. By inspecting (19) and (21), we conclude that the following two conditions are sufficient to enable mutual SIC:

$$h_{k_1,n,r_2} \geqslant h_{k_2,n,r_2}$$
$$h_{k_2,n,r_1} \geqslant h_{k_1,n,r_1}$$

Indeed, these conditions ensure the positivity of each of the two terms in both $X - Y$ and $Z - T$. This concludes our proof. □

Regarding the power multiplexing constraints, the key is to design the power allocation scheme in such a way that the received power of the first signal to be decoded is larger than the power of the other signal. The resulting power conditions for users k_1 and k_2 respectively become:

$$P_{k_1,n,r_1}h_{k_1,n,r_1}^2 \leqslant P_{k_2,n,r_2}h_{k_1,n,r_2}^2$$
$$P_{k_2,n,r_2}h_{k_2,n,r_2}^2 \leqslant P_{k_1,n,r_1}h_{k_2,n,r_1}^2$$

They can be combined into the following condition:

$$\frac{h_{k_1,n,r_1}^2}{h_{k_1,n,r_2}^2} \leqslant \frac{P_{k_2,n,r_2}}{P_{k_1,n,r_1}} \leqslant \frac{h_{k_2,n,r_1}^2}{h_{k_2,n,r_2}^2} \quad (22)$$

Remark 1. *If (14) and (15) are true, then* $\frac{h_{k_1,n,r_1}^2}{h_{k_1,n,r_2}^2} \leqslant \frac{h_{k_2,n,r_1}^2}{h_{k_2,n,r_2}^2}$. *In this case, a PA scheme can be found to allow a mutual SIC, i.e. there exist* P_{k_1,n,r_1} *and* P_{k_2,n,r_2} *such that (22) is true.*

Finally, the conditions (14) and (15) are sufficient but not necessary for the application of mutual SIC. Actually, the conditions for the application of mutual SIC lie in the positivity of (19) and (21). If any of (14) or (15) is not valid, the power terms in (19) and (21) should be considered, since they affect the sign of both equations. However, a closer examination of (19) and (21) reveals that in practical systems, their numerical values are greatly dominated by their first common term, since in general $\sigma^2 << Ph_{k,n,r}^2$. In that regard, a simpler constraint is derived on the channel gains:

$$h_{k_1,n,r_1}h_{k_2,n,r_2} \leqslant h_{k_2,n,r_1}h_{k_2,n,r_1} \quad (23)$$

This constraint will be used instead of (14) and (15) in the sequel. Note that condition (23) also ensures the existence of a PA scheme that will allow a mutual SIC. When both users k_1 and k_2 perform SIC on a subcarrier n, their reachable rates on n are given by:

$$R_{k_1,n,r_1} = \frac{B}{S}\log_2\left(1 + \frac{P_{k_1,n,r_1}h_{k_1,n,r_1}^2}{\sigma^2}\right) \quad (24)$$

$$R_{k_2,n,r_2} = \frac{B}{S}\log_2\left(1 + \frac{P_{k_2n,r_2}h_{k_2,n,r_2}^2}{\sigma^2}\right) \quad (25)$$

Following the introduction of mutual SIC, the RA strategy should be modified accordingly. Therefore, the next sections describe the development of novel RA techniques that can benefit from this new potential of the NOMA-DAS combination.

B. Mutual SIC-based power minimization without power multiplexing constraints

The new RA problem in hand is still combinatorial, which motivates the proposal of suboptimal RA schemes in the following sections.

In addition to the selection of different antennas in the pairing phase of Algorithm 1, the key modifications that must be accounted for, when moving from single SIC to mutual SIC RA schemes, involve:

- Subcarrier subset selection: only the subcarrier-RRH links satisfying (23) are considered for potential assignment in mutual SIC configurations.
- Power assignment: the power multiplexing constraint (22) must be accounted for.

We first address a relaxed version of the problem where the power multiplexing constraints are disregarded. This consideration reverts the optimal PA scheme in the pairing phase to the user-specific waterfilling solution in OMA. Therefore, the pairing phase in mutual SIC becomes a simple extension of the OMA phase from Algorithm 1. This method referred to as MutSIC-UC will be used as a lower bound on the performance of mutual SIC algorithms (in terms of the total transmit power).

To compensate for the disregarded constraints, subcarrier assignment should be followed by a power optimization step as shown in Appendix B. However, the set of possible power corrections grows exponentially with the number of multiplexed subcarriers. Therefore, alternative suboptimal strategies accounting for the power multiplexing constraints at every subcarrier assignment are investigated in the following sections.

C. Mutual SIC power minimization with direct power adjustment (DPA)

From a power minimization perspective, the power distribution obtained through waterfilling is the best possible PA scheme. However, compliance with the power multiplexing conditions is not guaranteed; therefore, a power adjustment should occasionally be made on the multiplexed subcarriers.

When an adjustment is needed, the new value of P_{k_2,n,r_2} in (22) should fall between $P_{k_1,n,r_1}h_{k_1,n,r_1}^2/h_{k_1,n,r_2}^2$ and $P_{k_1,n,r_1}h_{k_2,n,r_1}^2/h_{k_2,n,r_2}^2$ (the value of P_{k_1,n,r_1} is fixed). However, since any deviation from the waterfilling procedure degrades the performance of the solution, this deviation must be

rendered minimal. Therefore, P_{k_2,n,r_2} is set at the nearest limit of the inequality (22), with some safety margin μ accounting for proper SIC decoding. After this adjustment, the powers on the multiplexed subcarrier are kept unvaried, as in Algorithm 1. This procedure will be referred to as MutSIC-DPA; its details are presented in Algorithm 2.

Algorithm 2 MutSIC-DPA

Phase 1:
Worst-Best-H followed by OMA single-user assignment

Phase 2: // NOMA MutSIC pairing

$k_2 = \arg\max_k P_{k,tot}$

$S_c = \{(n, r_2)$ s.t. (23) & (6) are verified$\}$

For every candidate couple $(n, r_2) \in S_c$
Calculate $P^*_{k_2,n,r_2}$ and $\Delta P_{k_2,n,r_2}$ using (7) and (8)

If $P^*_{k_2,n,r_2}$ verifies (22), set $P_{k_2,n,r_2} = P^*_{k_2,n,r_2}$

If $\frac{P_{k_2,n,r_2}}{P_{k_1,n,r_1}} < \frac{h^2_{k_1,n,r_1}}{h^2_{k_1,n,r_2}}$ set $P_{k_2,n,r_2} = (1+\mu) P_{k_1,n,r_1} \frac{h^2_{k_1,n,r_1}}{h^2_{k_1,n,r_2}}$
and estimate $\Delta P_{k_2,n,r_2}$ using (10) and (11)

If $\frac{P_{k_2,n,r_2}}{P_{k_1,n,r_1}} > \frac{h^2_{k_2,n,r_1}}{h^2_{k_2,n,r_2}}$ set $P_{k_2,n,r_2} = (1-\mu) P_{k_1,n,r_1} \frac{h^2_{k_2,n,r_1}}{h^2_{k_2,n,r_2}}$
and estimate $\Delta P_{k_2,n,r_2}$ using (10) and (11)

End for

$(n^*, r_2^*) = \arg\min_{(n,r_2)} \Delta P_{k_2,n,r_2}$

Continue similarly to SRRH

D. Mutual SIC power minimization with sequential optimization for power adjustment (SOPA)

In order to improve on the MutSIC-DPA technique, we propose to replace the adjustment and power estimation steps by a sequential power optimization. Instead of optimizing the choice of P_{k_2,n,r_2} over the candidate couple (n, r_2), we look for a wider optimization in which powers of both first and second users on the considered subcarrier are adjusted, in a way that their global power variation is minimal:

$$\{P_{k_1,n,r_1}, P_{k_2,n,r_2}\}^* = \underset{P_{k_1,n,r_1}, P_{k_2,n,r_2}}{\arg\max} \; (-\Delta P_{k_1,n,r_1} - \Delta P_{k_2,n,r_2})$$

subject to:

$$\frac{h^2_{k_1,n,r_1}}{h^2_{k_1,n,r_2}} \leqslant \frac{P_{k_2,n,r_2}}{P_{k_1,n,r_1}}$$
$$\frac{P_{k_2,n,r_2}}{P_{k_1,n,r_1}} \leqslant \frac{h^2_{k_2,n,r_1}}{h^2_{k_2,n,r_2}}$$

The power variations of users k_2 and k_1 are given by:

$$\Delta P_{k_2,n,r_2} = N^{sole}_{k_2} w_{k_2}(N^{sole}) \left(\left(1 + \frac{P_{k_2,n,r_2} h^2_{k_2,n,r_2}}{\sigma^2} \right)^{-\frac{1}{N^{sole}_{k_2}}} - 1 \right) + P_{k_2,n,r_2}$$

$$\Delta P_{k_1,n,r_1} = (N^{sole}_{k_1} - 1) W_{I,k_1} \left(2^{-\frac{\Delta R_{k_1} S}{(N^{sole}_{k_1}-1)B}} - 1 \right) + P_{k_1,n,r_1} - P^I_{k_1,n,r_1}$$

where $P^I_{k_1,n,r_1}$ is the initial power allocated on n to k_1 and W_{I,k_1} the initial waterline of k_1 (before pairing with user k_2). Also, the rate variation of user k_1 on n, due to the power adjustment on n, can be written as:

$$\Delta R_{k_1} = \frac{B}{S} \log_2 \left(\frac{\sigma^2 + P_{k_1,n,r_1} h^2_{k_1,n,r_1}}{\sigma^2 + P^I_{k_1,n,r_1} h^2_{k_1,n,r_1}} \right)$$

The Lagrangian of this problem is:

$$L(P_{k_1,n,r_1}, P_{k_2,n,r_2}, \lambda_1, \lambda_2) = -\lambda_1 \left(P_{k_1,n,r_1} \frac{h^2_{k_1,n,r_1}}{h^2_{k_1,n,r_2}} - P_{k_2,n,r_2} \right) - \lambda_2 \left(P_{k_2,n,r_2} - P_{k_1,n,r_1} \frac{h^2_{k_2,n,r_1}}{h^2_{k_2,n,r_2}} \right) - \Delta P_{k_1,n,r_1} - \Delta P_{k_2,n,r_2}$$

The solution of this problem must verify the following conditions:

$$\nabla L(P_{k_1,n,r_1}, P_{k_2,n,r_2}, \lambda_1, \lambda_2) = 0$$
$$\lambda_1 \left(P_{k_1,n,r_1} h^2_{k_1,n,r_1} / h^2_{k_1,n,r_2} - P_{k_2,n,r_2} \right) = 0$$
$$\lambda_2 \left(P_{k_2,n,r_2} - P_{k_1,n,r_1} h^2_{k_2,n,r_1} / h^2_{k_2,n,r_2} \right) = 0$$
$$\lambda_1, \lambda_2 \geqslant 0$$

Four cases are identified:

1. $\lambda_1 = 0, \lambda_2 = 0$
2. $\lambda_1 \neq 0, \lambda_2 = 0 \rightarrow P_{k_2,n,r_2} = P_{k_1,n,r_1} h^2_{k_1,n,r_1} / h^2_{k_1,n,r_2}$
3. $\lambda_1 = 0, \lambda_2 \neq 0 \rightarrow P_{k_2,n,r_2} = P_{k_1,n,r_1} h^2_{k_2,n,r_1} / h^2_{k_2,n,r_2}$
4. $\lambda_1 \neq 0, \lambda_2 \neq 0$

Case 1 corresponds to the unconstrained waterfilling solution applied separately to the two users. Case 4 is generally impossible, since the two boundaries of the inequality (22) would be equal. Considering case 2, by replacing P_{k_2,n,r_2} in terms of P_{k_1,n,r_1} in the Lagrangian and by taking the derivative with respect to P_{k_1,n,r_1}, we can verify that $P^*_{k_1,n,r_1}$ is the solution of the following nonlinear equation:

$$W_{I,k_2} \frac{h^2_{k_1,n,r_1} h^2_{k_2,n,r_2}}{h^2_{k_1,n,r_2} \sigma^2} \left(1 + \frac{P_{k_1,n,r_1} h^2_{k_2,n,r_2} h^2_{k_1,n,r_1}}{\sigma^2} \right)^{-\frac{1}{N^{sole}_{k_2}} - 1} + \frac{W_{I,k_1} h^2_{k_1,n,r_1}}{\sigma^2 + P^I_{k_1,n,r_1} h^2_{k_1,n,r_1}} \left(\frac{\sigma^2 + P_{k_1,n,r_1} h^2_{k_1,n,r_1}}{\sigma^2 + P^I_{k_1,n,r_1} h^2_{k_1,n,r_1}} \right)^{-\frac{1}{N^{sole}_{k_1}-1} - 1} - \frac{h^2_{k_1,n,r_1}}{h^2_{k_1,n,r_2}} - 1 = 0 \quad (26)$$

Note that in practice, we also take into consideration the safety power margin μ in the calculation of P_{k_1,n,r_1}. Similar calculations are performed for case 3. The solution that yields the lowest ΔP is retained. Also, if none of the cases provides positive power solutions, the current candidate couple (n, r_2) is discarded. This method of optimal power adjustment (OPAd) is employed both at the subcarrier allocation stage (for the selection of the best candidate couple (n, r_2) for

user k_2) and at the power allocation stage (following the selection of the subcarrier-RRH pair). It will be referred to as "MutSIC-OPAd".

Finally, in order to decrease the complexity of "MutSIC-OPAd", inherent to the resolution of a nonlinear equation for every subcarrier-RRH candidate, we consider a "semi-optimal" variant of this technique, called "MutSIC-SOPAd": at the stage where candidate couples (n, r_2) are considered for potential assignment to user k_2, DPA is used for power adjustment to determine the best candidate in a cost-effective way. Then, the preceding OPAd solution is applied to allocate power levels to users k_1 and k_2 on the retained candidate.

E. Combination of the allocation of mutual and single SIC subcarriers in DAS

To further exploit the space diversity inherent to DAS and minimize the system transmit power, single SIC and mutual SIC algorithms are combined to take advantage of the full potential of NOMA techniques. Given the superiority of mutual SIC over single SIC schemes, we prioritize the allocation of subcarriers allowing mutual SIC by first applying MutSIC-SOPAd. Then, the remaining set of solely assigned subcarriers is further examined for potential allocation of a second user in the single SIC context, using the same RRH as that of the first assigned user. LPO is used for power allocation in this second phase. This method will be referred to as "Mut&SingSIC".

V. COMPLEXITY ANALYSIS

In this section, we analyze the complexity of the different allocation techniques proposed in this study. The complexity of OMA-CAS, NOMA-CAS and OMA-DAS is also considered for comparison. It is studied by considering an implementation that includes the runtime enhancement procedures introduced in section III-A. In OMA-CAS and OMA-DAS scenarios, only phases 1 and 2 of Algorithm 1 are applied, with either R=1 (for OMA-CAS) or $R \neq 1$ (for OMA-DAS). In NOMA-CAS, Algorithm 1 is used with R=1.

For OMA-CAS, we consider that the channel matrix is reordered so that the subcarriers for each user are sorted by the decreasing order of channel gain. This step accelerates the subsequent subcarrier allocation stages and has a complexity of $O(KS\log(S))$. Following the Worst-Best-H phase, each iteration complexity is mainly dominated by the search of the most power consuming user with a cost $O(K)$. Assuming all the remaining $S-K$ subcarriers are allocated, the final complexity is $O(KS\log(S)+(S-K)K)$.

Each allocation step in the pairing phase of NOMA-CAS consists of the identification of the most power consuming user, followed by a search over the subcarrier space, and a power update over the set of sole subcarriers for the user, with an average number of S/K subcarriers. Assuming S paired subcarriers, the total complexity of NOMA-CAS is $O(KS\log(S)+(S-K)K+S(K+S+S/K))$.

In OMA-DAS, we consider an initial sorting of each user subcarrier gains, separately for each RRH, with a cost of $O(KSR\log(S))$. Then, an allocation cycle consists of user identification, followed by the search of the RRH providing the subcarrier with the highest channel gain. This corresponds to a complexity of $O(K+R)$. Therefore, the total complexity is: $O(KSR\log(S)+(S-K)(K+R))$. Consequently, the total complexity of SRRH and SRRH-LPO is $O(KSR\log(S)+(S-K)(K+R)+S(K+S+S/K))$. In order to assess the efficiency of SRRH-LPO, we compare our solution to the optimal power allocation technique developed in [16]. More specifically, we apply SRRH-LPO to determine the user-subcarrier-RRH assignment; then, in a second phase, we apply the optimal PA in [16]. This technique will be referred to as SRRH-OPA; its complexity analysis and comparison with SRRH-LPO is provided in appendix C.

Concerning MutSIC-UC, by following the same reasoning as for OMA-DAS, and accounting for the search of an eventual collocated user for at most S subcarriers, we get a total of $O(KSR\log(S)+(S-K)(K+R)+S(K+R-1))$.

As for MutSIC-DPA, the total complexity is $O(KSR\log(S)+(S-K)(K+R)+S(K+S(R-1)+S/K))$, where the $S(R-1)$ term stems from the fact that the search over the subcarrier space in the pairing phase is conducted over all combinations of subcarriers and RRHs, except for the RRH of the first user on the candidate subcarrier.

Regarding MutSIC-OPAd, let C be the complexity of solving the nonlinear equation (26). The total complexity is therefore $O(KSR\log(S)+(S-K)(K+R)+S(K+S(R-1)C+S/K))$. Given that MutSIC-SOPAd solves (26) only once per allocation step, its complexity is $O(KSR\log(S)+(S-K)(K+R)+S(K+S(R-1)+S/K+C))$. Consequently, the complexity of Mut&SingSIC is $O(KSR\log(S)+(S-K)(K+R))+S(K+S(R-1)+S/K+C)+S(K+S+S/K)$. The additional term corresponds to the Single SIC phase which is similar to the pairing phase in NOMA-CAS.

TABLE I: Approximate complexity of the different allocation techniques.

Technique	Complexity
OMA-CAS	$O(KS\log(S))$
NOMA-CAS	$O(S^2+KS\log(S))$
OMA-DAS	$O(KSR\log(S))$
SRRH	$O(S^2+KSR\log(S))$
SRRH-LPO	$O(S^2+KSR\log(S))$
MutSIC-UC	$O(KSR\log(S))$
MutSIC-DPA	$O(S^2R+KSR\log(S))$
MutSIC-OPAd	$O(S^2RC+KSR\log(S))$
MutSIC-SOPAd	$O(S^2R+SC+KSR\log(S))$
Mut&SingSIC	$O(S^2R+SC+KSR\log(S))$

To give an idea of the relative complexity orders, we present in Table I the approximate complexity of the different techniques. In fact, the complexity of the methods employing a numerical solver depends on the resolution cost C that is dependent on the closeness of the initial guess to the actual solution. In that regard, we note that MutSIC-SOPAd is roughly C times less complex than MutSIC-OPAd, and has a complexity comparable to MutSIC-DPA.

VI. PERFORMANCE RESULTS

The performance of the different allocation techniques are assessed through simulations in the LTE/LTE- Advanced context [23]. The cell is hexagonal with an outer radius R_d of 500 m. For DAS, we consider four RRHs ($R = 4$), unless specified otherwise. One antenna is located at the cell center, while the others are uniformly positioned on a circle of radius $2R_d/3$ centered at the cell center. The number of users in the cell is $K = 15$, except for Fig. 5. The system bandwidth B is 10 MHz, and it is divided into $S = 64$ subcarriers except for Fig. 5. The transmission medium is a frequency-selective Rayleigh fading channel with a root mean square delay spread of 500 ns. We consider distance-dependent path-loss with a decay factor of 3.76 and lognormal shadowing with an 8 dB variance. The noise power spectral density N_0 is 4.10^{-18} mW/Hz. In this study, we assume perfect knowledge of the user channel gains by the BBU. For typical system parameters, the system performance in terms of transmit power is mainly invariant with ρ, thus ρ is set to 10^{-3} W. A detailed analysis of the system behavior in terms of ρ can be found in [24] for OMA systems. The α decay factor in FTPA is taken equal to 0.5,and the safety power margin μ is set to 0.01. The performance results of OMA-CAS, NOMA-CAS and OMA-DAS are also shown for comparison.

Fig. 2 represents the total transmit power in the cell in terms of the requested rate considering only SRRH schemes for NOMA-based techniques.

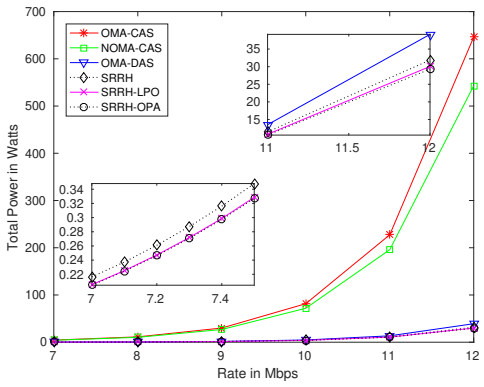

Fig. 2: Total power in terms of $R_{k,req}$ for DAS and CAS scenarios, with OMA and NOMA-SRRH schemes

The results show that the DAS configuration greatly outperforms CAS: a large leap in power with a factor around 16 is achieved with both OMA and NOMA signaling. At a target rate of 12 Mbps, the required total power using SRRH, SRRH-LPO and SRRH-OPA is respectively 17.6%, 24.5%, and 26.1% less than in OMA-DAS. This shows a clear advantage of NOMA over OMA in the DAS context. Besides, applying LPO allows a power reduction of 7.7% over FTPA, with a similar computational load. The penalty in performance of LPO with respect to optimal PA is only 2% at 12 Mbps, but with a greatly reduced complexity.

In Fig. 3, the results are focused on the evaluation of mutual SIC and single SIC configurations. It can be seen that all three constrained configurations based on pure mutual SIC (MutSIC-DPA, MutSIC-SOPAd and MutSIC-OPAd) largely outperform SRRH-LPO. Their gain towards the latter is respectively 56.1%, 63.9% and 72.9%, at a requested rate of 13 Mbps. The significant gain of optimal power adjustment towards its suboptimal counterpart comes at the cost of a significant complexity increase, as shown in Section V. The most power-efficient mutual SIC implementation is obviously MutSIC-UC, since it is designed to solve a relaxed version of the power minimization problem by dropping all power multiplexing constraints. Therefore, it only serves as a benchmark for assessing the other methods, because power multiplexing conditions are essential for allowing correct signal decoding at the receiver side.

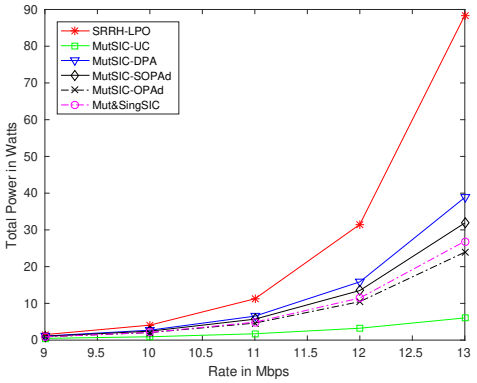

Fig. 3: Total power in terms of $R_{k,req}$ for the proposed NOMA-DAS schemes

Except for the OPAd solution, the best global strategy remains the combination of mutual and single SIC subcarriers, since it allows a power reduction of 15.2% and 15.6% at 12 and 13 Mbps respectively, when compared to MutSIC-SOPAd.

Fig. 4 shows the influence of increasing the number of RRHs on system performance. As expected, increasing the number of spread antennas greatly reduces the overall power, either with single SIC or combined mutual and single SIC configurations. A significant power reduction is observed when R is increased from 4 to 5, followed by a more moderate one when going from 5 to 7 antennas. The same behavior is expected for larger values of R. However, practical considerations like the overhead of CSI signaling exchange and the synchronization of the distributed RRHs, not to mention geographical deployment constraints, would suggest limiting the number of deployed antennas in the cell.

In Fig. 5, we show the performance for a varying number of users, for the case of 4 RRHs and 128 subcarriers. Results confirm that the allocation strategies based on mutual SIC, or

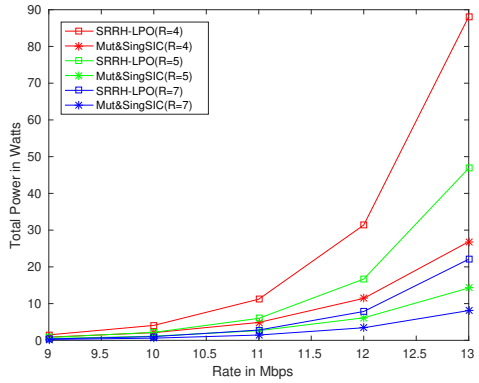

Fig. 4: Total power in terms of $R_{k,req}$ for NOMA-DAS schemes, with K=15, S=64, and R=4, 5 or 7

combined mutual and single SIC, scale much better to crowded areas, compared to single SIC solutions. The power reduction of Mut&SingSIC towards SRRH-LPO is 69.8% and 78.2% for 36 and 40 users respectively.

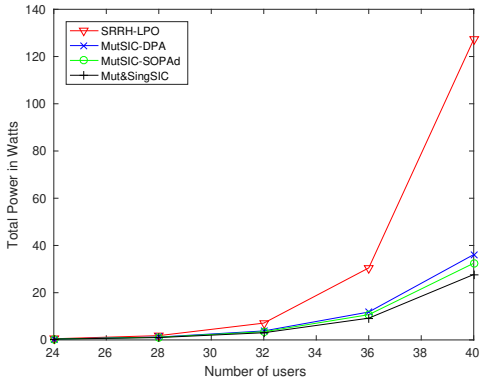

Fig. 5: Total power in terms of the number of users for the NOMA-DAS schemes, with $R_{k,req}$=5 Mbps, S=128, and R=4

Table II shows the statistics of the number of non-multiplexed subcarriers, the number of subcarriers where a mutual SIC is performed, and the number of subcarriers where a single SIC is performed. On average, SRRH-LPO uses single SIC NOMA on 25% (resp. 32%) of the subcarriers for $R_{k,req}$ = 9 Mbps (resp. 12 Mbps), while the rest of the subcarriers is solely allocated to users (a small proportion is not allocated at all, depending on the power threshold ρ). On the other hand, the proportions are respectively 17% and 23% with MutSIC-SOPAd. Therefore, in light of the results of Figs. 3 and 5, MutSIC-SOPAd not only outperforms SRRH-LPO from the requested transmit power perspective, but it also presents the advantage of yielding a reduced complexity at the User Equipment (UE) level, by requiring a smaller amount of SIC procedures at the receiver side. This shows the efficiency of the mutual SIC strategy, combined with appropriate power adjustment, over classical single SIC configurations.

TABLE II: Statistics of subcarrier multiplexing, for K=15, S=64, and R=4.

Resource allocation technique	Non Mux SC	SC MutSIC	SC SingSC
	$R_{k,req}$=9Mbps		
SRRH-LPO	48.1	-	15.9
MutSIC-SOPAd	53.4	10.6	-
Mut&SingSIC	39.2	10.6	14.2
	$R_{k,req}$=12Mbps		
SRRH-LPO	43.7	-	20.3
MutSIC-SOPAd	49.4	14.6	-
Mut&SingSIC	29	14.6	20.4

It can be noted that in Mut&SingSIC, 17% (resp. 23%) of the subcarriers are powered from different antennas. This shows the importance of exploiting the additional spatial diversity, combined with NOMA, inherent to DAS.

VII. CONCLUSION

In this paper, various RA techniques were presented for minimizing the total downlink transmit power in DAS for 5G and beyond networks. We first proposed several enhancements to a previously developed method for CAS, prior to extending it to the DAS context. Furthermore, we unveiled some of the hidden potentials of DAS for NOMA systems and developed new techniques to make the most out of these advantages, while extracting their best characteristics and tradeoffs. Particularly, this study has enabled the design of NOMA with SIC decoding at both paired UE sides. Simulation results have shown the superiority of the proposed methods with respect to single SIC configurations. They also promoted mutual SIC with suboptimal power adjustment to the best tradeoff between transmit power and complexity at both the BBU and the UE levels. Several aspects of this work can be further explored, since many additional challenges need to be addressed to enhance the NOMA-DAS-specific resource allocation schemes. For instance, practical considerations can be incorporated in the study, such as imperfect antenna synchronization and limited CSI exchange. Furthermore, the study can be enriched by the use of MIMO antenna systems in a distributed context.

VIII. ACKNOWLEDGMENT

This work has been funded with support from the Lebanese University and the PHC CEDRE program (research project between the Lebanese University and IMT Atlantique). Part of this work has been performed in the framework of the Horizon 2020 project FANTASTIC-5G (ICT-671660), which is partly funded by the European Union.

APPENDIX A

Proof. By inspecting (7) and (8), we see that a higher channel gain ensures a lower waterline, but also a lower inverse channel gain in the expression of $\Delta P_{k,n_a,r}$. In order to prove that the subcarrier which yields the lowest ΔP is indeed the one with the best channel gain, we start by combining (7) and (8), and we express the power decrease as:

$$\Delta P_{k,n_a,r} = (N_k+1)\left(\frac{(w_k(N_k))^{N_k}}{h^2_{k,n_a,r}/\sigma^2}\right)^{1/(N_k+1)} - N_k w_k(N_k) - \frac{\sigma^2}{h^2_{k,n_a,r}}$$

By taking the derivative of $\Delta P_{k,n,r}$ with respect to $h_{k,n_a,r}$, we get:

$$\frac{\partial \Delta P_{k,n,r}}{\partial h_{k,n_a,r}} = -2\frac{(\sigma^2)^{1/N_k+1}}{(h_{k,n_a,r})^{\frac{2}{N_k+1}+1}}\left(w_k(N_k)\right)^{N_k/(N_k+1)} + \frac{2\sigma^2}{h^3_{k,n_a,r}}$$

Therefore, we can verify that:

$$\frac{\partial \Delta P_{k,n,r}}{\partial h_{k,n_a,r}} \leqslant 0 \Longleftrightarrow \frac{\sigma^2}{h^2_{k,n_a,r}} \leqslant \left(\frac{\sigma^2}{h^2_{k,n_a,r}}\right)^{1/N_k+1}\left(w_k(N_k)\right)^{N_k/(N_k+1)}$$

which directly leads to (6).
We can deduce that, provided that (6) is verified by subcarrier n_a, $\Delta P_{k,n_a,r}$ is a monotonically decreasing function of $h_{k,n_a,r}$, which concludes the proof. □

APPENDIX B
FORMULATION OF THE POWER OPTIMIZATION PROBLEM FOR THE CONSTRAINED CASE IN MUTUAL SIC

For a predefined subcarrier-RRH-user assignment, the constrained power minimization problem for power assignment can be cast as the solution of the following optimization problem:

$$\max_{\{P_{k,n,r}\}}\left(-\sum_{k=1}^{K}\sum_{n=1}^{S}\sum_{r=1}^{R}P_{k,n,r}\right),$$

Subject to:

$$\sum_{n\in\mathcal{S}_k}\log_2\left(1+\frac{P_{k,n,r}h^2_{k,n,r}}{\sigma^2}\right) = R_{k,req}, 1\leqslant k\leqslant K$$

$$-\frac{P_{k_2,n,r_2}}{P_{k_1,n,r_1}} \leqslant -\frac{h^2_{k_1,n,r_1}}{h^2_{k_1,n,r_2}}, \forall n\in\mathcal{S}_{mSIC}$$

$$\frac{P_{k_2,n,r_2}}{P_{k_1,n,r_1}} \leqslant \frac{h^2_{k_2,n,r_1}}{h^2_{k_2,n,r_2}}, \forall n\in\mathcal{S}_{mSIC}$$

where $\mathcal{S}_{mSIC}$ is the set of subcarriers undergoing a mutual SIC. The corresponding Lagrangian with multipliers λ_k and $\beta_{i,n}$ is:

$$L(P,\lambda,\beta_1,\beta_2) = -\sum_{k=1}^{K}\sum_{n=1}^{S}\sum_{r=1}^{R}P_{k,n,r}$$
$$+\sum_{n\in\mathcal{S}_{mSIC}}\beta_{1,n}\left(\frac{h^2_{k_2,n,r_1}}{h^2_{k_2,n,r_2}}-\frac{P_{k_2,n,r_2}}{P_{k_1,n,r_1}}\right)$$
$$+\sum_{n\in\mathcal{S}_{mSIC}}\beta_{2,n}\left(\frac{h^2_{k_2,n,r_2}}{h^2_{k_1,n,r_1}}-\frac{P_{k_1,n,r_1}}{P_{k_1,n,r_2}}\right)$$
$$+\sum_{k=1}^{K}\lambda_k\left(R_{k,req}-\sum_{n\in\mathcal{S}_k}\log_2\left(1+\frac{P_{k,n,r}h^2_{k,n,r}}{\sigma^2}\right)\right)$$

Writing the KKT conditions (not presented here for the sake of concision) leads to a system of N_e non-linear equations with N_e variables, where $N_e = 3|S_{mSIC}| + K + S$ (taking into account the $S-|\mathcal{S}_{mSIC}|$ power variables on non-paired subcarriers). Knowing that $\beta_{1,n}$ and $\beta_{2,n}$ cannot be simultaneously non-zero, we have, for every subcarrier allocation scheme, a total of $3^{|\mathcal{S}_{mSIC}|}$ different possible combinations to solve, that is $3^{|\mathcal{S}_{mSIC}|}$ different variations of a square system of $2|\mathcal{S}_{mSIC}| + K + S$ equations (per subcarrier allocation).

APPENDIX C
COMPLEXITY ANALYSIS OF SRRH-OPA AND COMPARISON WITH SRRH-LPO

SRRH-OPA consists in successively applying SRRH-LPO to set the subcarrier-RRH assignment, and afterwards applying the optimal PA described in [16]. Therefore, the complexity of SRRH-OPA equals that of SSRH-LPO added to the complexity of optimal PA which is discussed next.

Following the optimal power formulation provided in [16], the relaxed version of the problem is as follows:
Let K_n be the set of multiplexed users on subcarrier n, $\mathcal{N}_M$ the set of multiplexed subcarriers, $\mathcal{S}^{sole}$ the set of sole subcarriers with $N^{sole} = |\mathcal{S}^{sole}|$, $k_1(n)$ the first user over the subcarrier n, where n is either a sole or a multiplexed subcarrier, $k_2(n)$ the second user over the subcarrier n, where n is a multiplexed subcarrier, $r(n)$ the RRH powering the signals on the subcarrier n, $R_{k,n,r}$ the rate achieved by user k on subcarrier n powered by RRH r. Using the same rate to power conversion procedure as in [16], the optimization problem can be expressed as follows:

$$\min_{R_{k,n,r}}\sum_{n\in\mathcal{N}_M\cup\mathcal{S}^{sole}}\frac{a(n)\sigma^2}{h_1(n)}+\frac{(b(n)-1)\sigma^2}{h_2(n)}\left[\frac{1}{h_2(n)}+\frac{a(n)-1}{h_1(n)}\right]$$

Subject to:

$$\sum_{n\in S_k}R_{k,n,r(n)} = R_{k,req}, \forall k\in 1:K$$

Where $h_1(n) = h^2_{k_1(n),n,r(n)}$, $h_2(n) = h^2_{k_2(n),n,r(n)}$, $\sigma^2 = N_0B/S$, $a(n) = 2^{R_{k_1(n),n,r(n)}S/B}$, and $b(n) = 2^{R_{k_2(n),n,r(n)}S/B}$. $R_{k_1(n),n,r(n)}$ is the rate achieved by the strong or sole user $k_1(n)$ on subcarrier n, and $R_{k_2(n),n,r(n)}$ is the rate delivered on the subcarrier n to the user $k_2(n)$. If

n happens to be a sole subcarrier, than $R_{k_2(n),n,r(n)}$ is null. The Lagrangian of this problem is given by:

$$L(R_{k,n,r},\lambda) = \left[\frac{(a(n)-1)\sigma^2}{h_1(n)} + \frac{\sigma^2}{h_2(n)}\right]\frac{b(n)-1}{h_2(n)} + \sum_{n\in\mathcal{N}_M\cup\mathcal{S}^{sole}}(a(n)-1)\frac{\sigma^2}{h_1(n)} - \sum_{k=1}^{K}\lambda_k\left(\sum_{n=1}^{N}R_{k,n,r(n)} - R_{k,req}\right)$$

After applying the KKT conditions, and including the K rate constraints, we obtain a system of $N_{sole} + 2card(\mathcal{N}_M) + K$ non-linear equations and unknowns ($N_{sole} + 2card(\mathcal{N}_M)$ rate variables and K Lagrangian multipliers). A numerical solver is used to determine the solution, namely the trust-region dogleg method. Since finding an exact expression of this method's complexity is cumbersome, we propose to provide instead the average execution time ratio of SRRH-OPA with respect to SRRH-LPO, measured over a total of 1000 simulations at a rate of 12Mbps, for $K = 15$ users, $S = 64$ subcarriers and $R = 4$ RRHs. We observed that the execution time of SRRH-OPA is more than the double the one of SRRH-LPO, while the performance improvement is of only 2%. This showcases the efficiency of our LPO procedure, both in terms of its global optimal-like performance and in terms of its cost effective implementation.

REFERENCES

[1] R. Heath, S. Peters, Y. Wang, and J. Zhang, "A Current Perspective on Distributed Antenna Systems for the Downlink of Cellular Systems," *IEEE Commun. Mag.*, vol. 51, no. 4, pp. 161–167, Apr 2013.

[2] Z. Liu and L. Dai, "A Comparative Study of Downlink MIMO Cellular Networks With Co-Located and Distributed Base-Station Antennas," *IEEE Trans. on Wireless Commun.*, vol. 13, no. 11, pp. 6259–6274, Nov 2014.

[3] W. Choi and J. G. Andrews, "Downlink Performance and Capacity of Distributed Antenna Systems in a Multicell Environment," *IEEE Trans. on Wireless Commun.*, vol. 6, no. 1, pp. 69–73, Jan 2007.

[4] R. W. H. Jr, T. Wu, Y. H. Kwon, and A. C. K. Soong, "Multiuser MIMO in Distributed Antenna Systems With Out-of-Cell Interference," *IEEE Trans. on Signal Process.*, vol. 59, no. 10, pp. 4885–4899, Oct 2011.

[5] F. Yuan, S. Jin, Y. Huang, K. k. Wong, Q. T. Zhang, and H. Zhu, "Joint Wireless Information and Energy Transfer in Massive Distributed Antenna Systems," *IEEE Commun. Mag.*, vol. 53, no. 6, pp. 109–116, Jun 2015.

[6] H. Li, G. P. Koudouridis, and J. Zhang, "Antenna Selection Schemes for Energy Efficiency in Distributed Antenna Systems," in *2012 IEEE Int. Conf. on Commun. (ICC)*, Jun 2012, pp. 5619–5623.

[7] C. He, G. Y. Li, F. C. Zheng, and X. You, "Energy-Efficient Resource Allocation in OFDM Systems with Distributed Antennas," *IEEE Trans. on Veh. Technol.*, vol. 63, no. 3, pp. 1223–1231, Mar 2014.

[8] Z. Ding, F. Adachi, and H. V. Poor, "Performance of MIMO-NOMA Downlink Transmissions," in *2015 IEEE Global Commun. Conf. (GLOBECOM)*, Dec 2015, pp. 1–6.

[9] Y. Saito, A. Benjebbour, Y. Kishiyama, and T. Nakamura, "System-Level Performance Evaluation of Downlink Non-Orthogonal Multiple Access (NOMA)," in *2013 IEEE 24th Annual Int. Symp. on Personal, Indoor, and Mobile Radio Comm. (PIMRC)*, Sep 2013, pp. 611–615.

[10] Y. Saito, Y. Kishiyama, A. Benjebbour, T. Nakamura, A. Li, and K. Higuchi, "Non-Orthogonal Multiple Access (NOMA) for Cellular Future Radio Access," in *2013 IEEE 77th Veh. Tech. Conf. (VTC Spring)*, June 2013, pp. 1–5.

[11] M.-R. Hojeij, J. Farah, C. A. Nour, and C. Douillard, "New Optimal and Suboptimal Resource Allocation Techniques for Downlink Non-Orthogonal Multiple Access," *Wireless Pers. Commun.*, vol. 87, no. 3, pp. 837–867, Apr 2016.

[12] M. R. Hojeij, C. A. Nour, J. Farah, and C. Douillard, "Waterfilling-Based Proportional Fairness Scheduler for Downlink Non-Orthogonal Multiple Access," *IEEE Wireless Commun. Lett.*, vol. 6, no. 2, pp. 230–233, Apr 2017.

[13] X. Gu, X. Ji, Z. Ding, W. Wu, and M. Peng, "Outage Probability Analysis of Non-Orthogonal Multiple Access in Cloud Radio Access Networks," *IEEE Commun. Lett.*, vol. 22, no. 1, pp. 149–152, Jan 2018.

[14] K. N. Pappi, P. D. Diamantoulakis, and G. K. Karagiannidis, "Distributed Uplink-NOMA for Cloud Radio Access Networks," *IEEE Commun. Lett.*, vol. 21, no. 10, pp. 2274–2277, Oct 2017.

[15] D. Boviz, C. S. Chen, and S. Yang, "Effective Design of Multi-User Reception and Fronthaul Rate Allocation in 5G Cloud RAN," *IEEE J. on Selected Areas in Commun.*, vol. 35, no. 8, pp. 1825–1836, Aug 2017.

[16] L. Lei, D. Yuan, and P. Värbrand, "On Power Minimization for Non-Orthogonal Multiple Access (NOMA)," *IEEE Commun. Lett.*, vol. 20, no. 12, pp. 2458–2461, Dec 2016.

[17] X. Li, C. Li, and Y. Jin, "Dynamic Resource Allocation for Transmit Power Minimization in OFDM-Based NOMA Systems," *IEEE Commun. Lett.*, vol. 20, no. 12, pp. 2558–2561, Dec 2016.

[18] Z. Wei, D. W. K. Ng, J. Yuan, and H. M. Wang, "Optimal Resource Allocation for Power-Efficient MC-NOMA With Imperfect Channel State Information," *IEEE Trans. on Commun.*, vol. 65, no. 9, pp. 3944–3961, Sep 2017.

[19] J. Cui, Z. Ding, and P. Fan, "Power Minimization Strategies in Downlink MIMO-NOMA Systems," in *2017 IEEE Int. Conf. on Commun. (ICC)*, May 2017, pp. 1–6.

[20] J. Farah, E. Sfeir, C. A. Nour, and C. Douillard, "New Resource Allocation Techniques for Base Station Power Reduction in Orthogonal and Non-Orthogonal Multiplexing Systems," in *2017 IEEE Int. Conf. on Commun. Workshops (ICC Workshops)*, May 2017, pp. 618–624.

[21] Z. Zhu, S. Huang, Z. Chu, F. Zhou, D. Zhang, and I. Lee, "Robust designs of beamforming and power splitting for distributed antenna systems with wireless energy harvesting," *IEEE Syst. J.*, pp. 1–12, 2018.

[22] J. Farah and F. Marx, "Combining Strategies for the Optimization of Resource Allocation in a Wireless Multiuser OFDM System," *AEU - Int. J. of Electronics and Commun.*, vol. 61, no. 10, pp. 665 – 677, 2007.

[23] 3GPP, TR25-814 (V7.1.0), Physical Layer Aspects for Evolved UTRA (2006).

[24] J. Farah, E. Sfeir, C. A. Nour, and C. Douillard, "New Efficient Energy-Saving Techniques for Resource Allocation in Downlink OFDMA Transmission Systems," in *2017 IEEE Symp. on Comput. and Commun. (ISCC)*, July 2017, pp. 1056–1062.

Joumana Farah Joumana Farah received the B.E. degree in Electrical Engineering from the Lebanese University, in 1998, the M.E. degree in Signal, Image, and Speech processing, in 1999, and the Ph.D. degree in mobile communication systems, in 2002, from the University of Grenoble, France. Since January 2010, she has held a Habilitation to Direct Research (HDR) from University Pierre and Marie Curie (Paris VI), France. She is currently a full-time professor with the Faculty of Engineering, Lebanese University, Lebanon. She has supervised a large number of Master and PhD theses. She has received several research grants from the Lebanese National Council for Scientific Research, the Franco-Lebanese CEDRE program, and the Lebanese University. She has nine registered patents and software and has coauthored a research book and more than 90 papers in international journals and conferences. Her current research interests include resource allocation techniques, channel coding, channel estimation, interference management, and distributed video coding. She was the General Chair of the 19th International Conference on Telecommunications (ICT 2012), and serves as a TPC member and a reviewer for several journals and conferences.

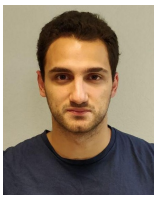

Antoine Kilzi Antoine Kilzi received his computer and communications engineering degree in 2017 from the Lebanese University. He is currently working towards the Ph.D. degree in information and communication engineering at IMT Atlantique. His current research interests include resource allocation, non-orthogonal multiple access and coordinated multipoint systems.

Charbel Abdel Nour Charbel Abdel Nour obtained his computer and communications engineering degree in 2002 from the Lebanese University, his Masters degree in digital communications from the University of Valenciennes, France, in 2003 and his PhD in digital communications from Telecom Bretagne, France in 2008. From June 2007 till October 2011, he worked as a post-doctoral fellow at the Electronics Department of Telecom Bretagne. He was involved in several research projects related to broadcasting and satellite communications. Additionally during the same period, he was active in the Digital Video Broadcasting DVB consortium where he had important contributions. Starting November 2011, Charbel holds an associate professor position at the Electronics Department of Telecom Bretagne. His interests concern the radio mobile communications systems, broadcasting systems, coded modulations, error correcting codes, resource and power allocation for NOMA, waveform design, MIMO and iterative receivers. Lately, he presented several contributions to the H2020 METIS and FANTASTIC5G projects and to the 3GPP consortium related to coding solutions for 5G.

Catherine Douillard Catherine Douillard received the engineering degree in telecommunications from the Ecole Nationale Supérieure des Télécommunications de Bretagne, France, in 1988, the Ph.D. degree in electrical engineering from the University of Western Brittany, Brest, France, in 1992, and the accreditation to supervise research from the University of Southern Brittany, Lorient, France, in 2004. She is currently a full Professor in the Electronics Department of Telecom Bretagne where she is in charge of the Algorithm-Silicon Interaction research team. Her main research interests are turbo codes and iterative decoding, iterative detection, the efficient combination of high spectral efficiency modulation and turbo coding schemes, diversity techniques and turbo processing for multi-carrier, multi-antenna and multiple access transmission systems. In 2009, she received the SEE/IEEE Glavieux Award for her contribution to standards and related industrial impact. She was active in the DVB (Digital Video Broadcasting) Technical Modules for the definition of DVB-T2, DVB-NGH as chairperson of the "Coding, Constellations and Interleaving" task force and DVB-RCS NG standards. Since 2015, she has had several contributions in the FANTASTIC-5G and EPIC H2020 European projects intended for the definition of new techniques for 5G and beyond.

3.2.6.1 New power minimization techniques for OMA and NOMA with power-constrained DAS

One of the main challenges posed by DAS configurations lies in the elaboration of efficient resource allocation schemes that take advantage of the embedded spatial diversity, while allowing the implementation of efficient solutions with an affordable runtime complexity. Moreover, the relative geographic proximity between the users and the antennas in DAS may give rise to more restrictive regulations on antenna power limits than before, in order to limit the electromagnetic field exposure, especially in sensitive locations in dense urban areas (e.g. around hospitals, police stations, etc.). Therefore, in such hybrid configurations, certain antennas in the cell may have restrictive transmit power constraints (due to their geographical position, their powering source or their small size), while others have access to a much higher amount of available power.

The development of procedures which can deal with such different restrictions goes along with the philosophy of beyond 5G communications in designing new smart networks that can dynamically adapt to various network demands and configurations. These procedures would also come in handy in situations where the operators use hybrid sources of energy to power the antennas deployed at different locations in the cell, including electric grids, local generators and various energy harvesting techniques.

To provide a potential answer, this work considers the power minimization problem in hybrid DAS where antennas are supplied by various - low power and high power - energy sources as shown in Fig. 3.4. Antenna-specific power limits were considered and the problem is reformulated in this new hybrid context. Moreover, to the best of our knowledge, the problem of downlink power minimization in DAS networks with RRH power limits using NOMA has not been addressed before.

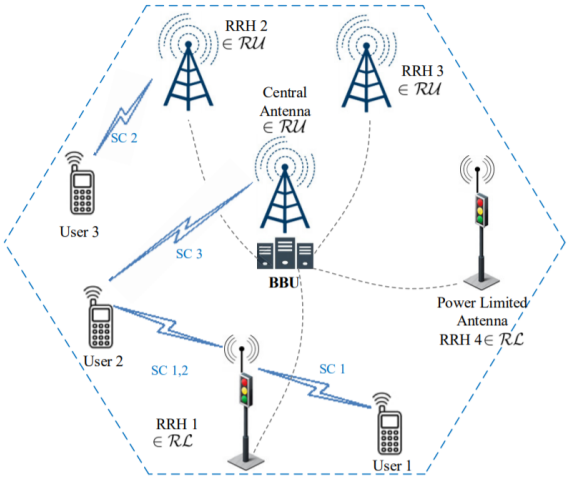

Figure 3.4: DAS cell with two power-limited RRHs (RRH 1 and RRH 4).

We have first formulated the optimal power allocation problem and then proceeded to providing a solution in the orthogonal multiplexing scenario. Different resource allocations schemes based on this optimal power allocation were then proposed for the orthogonal and nonorthogonal multiplexing contexts. The results suggest the use of different algorithms depending on system conditions:

- A first approach that takes into consideration the antenna power constraints at the end of the algorithm in a sort of an *a posteriori* correction. This proposal is favored in the

presence of low requested rate, high power limits and small numbers of served users and constrained antennas.

- A second approach that accounts for the loading of the constrained antennas throughout the algorithm. This proposal proves to be remarkably efficient in harsher system constraints, maintaining a significant advantage over the trivial solution of shutting down the constrained antennas. Thus, relying on a judicious antenna allocation in the first place is preferable over resorting systematically to the optimum power correction procedure.

Simulation results illustrate the efficiency of the proposed algorithms and show the importance of non-orthogonal multiplexing in the reduction of the total transmission power, especially in hybrid antenna systems. For more details, we refer to our publication in IEEE Transactions on Green Communications and Networking [214].

3.2.6.2 Resource allocation for mixed traffic types in DAS using NOMA

5G and beyond systems are expected to provide support to an increasingly growing number of diverse applications, while ensuring connectivity to a massive number of devices. In addition to traditional bandwidth-hungry applications (e.g. web browsing), some of the envisioned applications need relatively low throughput but demand strict latency and reliability (e.g. e-health, automated control, and autonomous vehicles), while others require both high throughput and low latency (e.g. video conferencing, augmented and virtual reality). As a result, mobile traffic is evolving into a more heterogeneous or mixed model. To cope with these requirements, 5G networks must benefit from new technologies and employ flexible and highly adaptable architectures.

All the previous work on mixed traffic types employ OMA for resource allocation. However, allocating a resource to a user running an application with low throughput and stringent latency constraints leads into a sub-optimal bandwidth distribution among users, penalizing system spectral efficiency as also noted by [215]. With its potential to serve a larger number of simultaneous users, NOMA seems particularly suited to this context.

The studied framework consists of users with mixed traffic types: Real-Time (RT) users having strict QoS requirements (in terms of amount of data and latency), and Best-Effort (BE) users aiming to maximize their throughput and fairness. To guarantee an efficient use of the spectrum, we propose to serve users by employing NOMA in the context of DAS. By doing so, whenever a RT user is allocated a resource exceeding its needs, the resource can be shared with another user (either RT or BE) to enhance system performance. Therefore, we target a new traffic-aware resource allocation technique employing NOMA in a downlink DAS. After formulating the resource and power optimization problem, we propose a low complexity sub-optimal algorithm that aims at guaranteeing the requirements of RT users while maximizing the utility function of BE users.

Simulation results showed that our method outperforms the PF scheduler, especially in terms of the number of satisfied RT users. Also, the proposed technique achieves near optimal fairness for BE users while maximizing their average throughput. We also showed the performance improvement obtained by NOMA over OMA, and DAS over CAS, in the mixed traffic context. This work can be directly used in the context of Cloud Radio Access Network (C-RAN) and heterogeneous networks. To the best of our knowledge, this is the first study that considered resource allocation for mixed traffic in a NOMA-DAS context. We published it in [216].

This work was extended through the support of OMA schemes on the one side and through the proposal of a new method based on matching theory on the other side. In fact, the method proposed in this extension is the first to provide a joint solution for the assignment problem at

hand while allowing each user to access any number of RRHs and subbands simultaneously. Our new contributions can be summarized as follows:

- After the choice of the performance measures for RT and BE user types, we formulated the corresponding optimization problem. Moreover, to ensure successful SIC decoding at the receiver side, it takes into account the NOMA power multiplexing constraints for users scheduled on each subband. These constraints state that the signal that is to be decoded first must have a higher power level than the other received signals, so that it is detectable at the receiver side. Note that the power multiplexing constraints were mostly neglected in previous works dealing with matching theory to simplify the analysis.
- Different system settings including OMA, NOMA, CAS, DAS and their combinations were investigated. For each setting, we formulated the channel allocation problem as a one-to-many matching game. We then proposed algorithms based on the Deferred Acceptance (DA) [217] method to solve the channel allocation problem. To the best of our knowledge, no previous study has considered the use of matching theory to solve the mixed traffic resource allocation problem, combining DAS and NOMA. It should also be noted that differently to our work, none of the previous works applying matching theory to solve the resource allocation problem for a NOMA system incorporated rate requirements into their analysis.
- A hybrid NOMA system was devised for the NOMA-CAS and NOMA-DAS system settings, using matching theory, where subbands are either allocated to single users or user-pairs in such a way to optimize system performance. Moreover, an algorithm, that overcomes the need for a swapping phase to deal with the interdependencies between the preferences of users, was introduced.
- Convergence of the proposed algorithm to a stable solution was proven to be achieved within a limited number of iterations.
- No *a priori* subband assignment was assumed nor restrictions on the choice and or on the number of the subbands or/and antennas were imposed on the assignment procedure to simplify the study as performed in all previous literature.
- Through simulation results, the proposed method was shown to achieve a better performance than our previous method introduced in [216], especially in terms of the percentage of RT users that meet their QoS requirements.

For more details about the results of this extention, our publication in Transactions on Communications [218] is included hereafter.

414 IEEE TRANSACTIONS ON COMMUNICATIONS, VOL. 68, NO. 1, JANUARY 2020

Resource Allocation in NOMA Systems for Centralized and Distributed Antennas With Mixed Traffic Using Matching Theory

Marie-Josepha Youssef, *Student Member, IEEE*, Joumana Farah, *Member, IEEE*, Charbel Abdel Nour, *Senior Member, IEEE*, and Catherine Douillard, *Senior Member, IEEE*

***Abstract*— In this paper, we study the traffic-aware resource allocation problem for a system with mixed traffic types. The considered framework encompasses real-time (RT) users having strict QoS requirements (in terms of amount of data and latency), and best-effort (BE) users for which the system tries to strike a balance between throughput and fairness. The resource allocation problem is studied in different contexts: orthogonal and non-orthogonal multiple access (OMA and NOMA respectively) in either centralized or distributed antenna systems (CAS and DAS respectively). Following the formulation of the resource optimization problem, we propose a low complexity suboptimal solution based on matching theory for each system context. We also propose an iterative approach to determine the number of subbands per antenna for the DAS contexts. The proposed techniques aim at guaranteeing the requirements of RT users while maximizing the utility function of BE users. Simulation results show that the proposed allocation method based on matching theory greatly outperforms a previously proposed greedy approach, especially in terms of RT users satisfaction.**

***Index Terms*— Mixed traffic types, latency, resource allocation, matching theory, NOMA, DAS.**

I. INTRODUCTION

THE explosive growth in connectivity and information sharing brought by the proliferation of IoT applications has been paving the way towards the 5th generation of cellular networks. 5G systems are expected to fulfill a certain set of diverse requirements [1]. In addition to increasing the achieved data rates, they are expected to accommodate a massive number of connected devices deployed to enable different applications. These span various sectors (e.g. autonomous vehicles, automated control, e-health, virtual reality, etc.) and should co-exist with traditional applications (e.g. file download, web browsing, etc.). However, the new envisioned applications have very different requirements, compared to traditional services, in terms of data rate, latency and reliability. As a result, 5G systems must adopt new technologies to cope with mixed or heterogeneous traffic models.

Resource allocation for mixed traffic types was previously investigated in the literature. In [2], the authors adopted utility theory for a system consisting of real-time (RT) and best-effort (BE) users, and proposed a heuristic algorithm to solve the resource allocation problem, based on Lagrange multipliers. In [3] and [4], after partitioning users among different classes based on their requirements, the priority of each user was calculated using fuzzy logic before scheduling the most urgent ones. In [5], the authors proposed a heuristic to perform QoS-based scheduling for small-cell users. They also developed an admission control algorithm to enhance the scheduling policy. Network coordination was employed to enhance the performance of RT users in [6] and minimize the amount of resources needed by RT users, increasing their availability for BE users. This minimization was also the target of [7] where a scalable transmission time interval (TTI) was adapted to the data and latency requirements of the users.

With the exception of [8] and [9], all previous studies on resource allocation for mixed traffic employed orthogonal multiple access (OMA) to enable different users to simultaneously access the spectrum. This orthogonality aims at limiting inter-user interference. Although OMA benefits from both, good system level performance and a simplified receiver design, it suffers from several drawbacks. First, the number of admitted users in OMA systems is limited by the number of available frequency subbands. Also, OMA restricts the allocation of each subband to one user only. This results in a poor overall spectral efficiency, as was also noted by [10], especially if the allocated resource exceeds the requirements of the scheduled user or if the latter suffers from poor channel conditions. Since 5G systems are expected to provide massive connectivity for users with very heterogeneous requirements, OMA is becoming a limiting factor for system design. Hence, there is a need to diverge towards new radio access technologies with better support for the changing needs of connected devices.

From an information-theoretical point of view, it is well-known that non-orthogonal user multiplexing using superposition coding at the transmitter and proper decoding techniques at the receiver not only outperforms orthogonal multiplexing, but is also optimal in the sense of achieving the capacity region of the downlink broadcast

Manuscript received February 18, 2019; revised June 19, 2019 and October 1, 2019; accepted October 5, 2019. Date of publication October 15, 2019; date of current version January 15, 2020. This work has been funded with support from the Lebanese University and IMT-Atlantique. The associate editor coordinating the review of this article and approving it for publication was Y. Liu. *(Corresponding author: Marie-Josepha Youssef.)*

M.-J. Youssef, C. Abdel Nour, and C. Douillard are with IMT Atlantique, LabSTICC, UBL, F-29238 Brest, France (e-mail: marie-josepha.youssef@imt-atlantique.fr; charbel.abdelnour@imt-atlantique.fr; catherine.douillard@imt-atlantique.fr).

J. Farah is with the Department of Electricity and Electronics, Faculty of Engineering, Lebanese University, El Metn, Lebanon (e-mail: joumanafarah@ul.edu.lb).

Color versions of one or more of the figures in this article are available online at http://ieeexplore.ieee.org.

Digital Object Identifier 10.1109/TCOMM.2019.2947429

channel [11]. As a result, non-orthogonal multiple access (NOMA) emerged as a promising multiple access technology for 5G systems [12]–[14]. NOMA allows multiple users to be scheduled on the same time-frequency resource by multiplexing them in the power domain. At the receiver side, successive interference cancellation (SIC) is performed to retrieve superimposed signals. By allowing multiple users to access the same resource, NOMA enhances spectral efficiency and increases the number of admitted users which is necessary to achieve massive connectivity, rendering NOMA a promising solution to support mixed traffic systems. In fact, in a mixed traffic system where some users have rate requirements and others aim to maximize theirs, NOMA enables the sharing of one subband between two users of the two categories. That way, if the rate requirement of a user is low, the system spectral efficiency is not penalized as in an OMA system as another user can benefit from the same subband. Moreover, NOMA enables the spectrum to be overloaded which ensures the accommodation and the satisfaction of a higher number of users when compared to OMA scheduling.

Resource allocation for NOMA systems has been extensively studied with different performance measures. To name a few, the weighted sum rate of a NOMA system was maximized in [15]; however the proposed method has exponential complexity. Maximizing system fairness was the target of [16], minimizing the used power subject to rate requirements was the target of the works in [17] and [18]. Considering a millimeter wave system with mixed traffic, [9] proposed an algorithm for user grouping, then determined the optimal power allocation to maximize the spectral efficiency of BE users while serving RT users with their rate requirements. However, [9] restricted RT users to be scheduled as second users in NOMA, i.e. users not performing SIC, which decreases the probability of satisfying their needs.

In addition to NOMA, distributed antenna systems (DAS) and their evolution to cloud radio access networks (C-RAN) were recently introduced as promising network architectures. By using multiple remote radio heads (RRHs) coordinated by a central controller, DAS enable higher capacities and increased coverage. To further enhance system performance, the combination of NOMA and DAS or C-RAN was given some attention in recent literature. In [19] and [20], the authors used NOMA in the transmission from the central controller to various RRHs. They proposed a power allocation scheme between the RRHs as well as an algorithm that finds the optimal number of BSs in order to guarantee the cell-edge user requirement in [19] or maximize the energy efficiency (EE) in [20]. [21] considered an uplink setting, where the RRHs cooperate to remove the interference brought by NOMA. In [22], the outage probability of a downlink two-user C-RAN system was derived using stochastic geometry. In [23], several joint subcarrier, RRH and power allocation techniques were proposed for reducing the total transmit power in each cell, using proper combinations of NOMA with DAS. However, none of these works investigated the use of NOMA and DAS to accommodate mixed traffic systems.

To achieve the full-potential of NOMA in the DAS settings, RRH and sub-channel assignment, as well as power allocation must be optimized jointly. However, this results in a mixed-integer optimization problem which is NP-hard and for which the optimal solution is found by exhaustive search. That said, exhaustive search has a prohibitive complexity for practical systems. Therefore, suboptimal but more efficient resource allocation techniques are preferred in practice.

In a previous work [8], we proposed a greedy algorithm to perform resource allocation for a mixed traffic system consisting of RT and BE users. In the current work, we study the resource allocation problem with a focus on antenna and subband assignment under different system configurations. To tackle the assignment problem in an efficient manner, the antenna and subband assignment problem is cast as a matching game. The primary goal of the proposed solution is to ensure the satisfaction of RT users through guaranteeing their rate requirements. Then, when possible, the introduced technique must maximize both the data rates and fairness of BE users. The study is conducted in different system settings combining DAS or centralized antenna systems (CAS) with different signaling technologies, namely OMA and NOMA, to compare their performance in the mixed traffic context.

Matching theory-based algorithms for resource allocation have recently gained significant attention. In [24], the authors considered a hybrid C-RAN system with D2D communications and adopted matching theory to perform the subband-RRH assignment. However, to simplify the problem, they supposed that the user-RRH association is done beforehand and restricted each user to be assigned to one antenna and access one subband only. Similarly, in the context of NOMA, [25] developed a user pairing technique based on matching theory. In [26] and [27], an algorithm based on matching theory was proposed to perform subband allocation for users and D2D pairs respectively. However, to the best of our knowledge, no previous work considered the application of matching theory to solve the subband assignment problem for mixed traffic in a NOMA-DAS system. More specifically, none of the previously proposed matching theory-based algorithms for NOMA systems ensured that rate requirements are met. Furthermore, in the DAS settings, the restrictions made by previous algorithms on antenna and subband assignment are unrealistic in practice, and are introduced only to simplify the resource allocation problem. Indeed, the work in [24] assumed that the assignment of users to the distributed antennas is done beforehand. In addition, almost all previous studies in this context restricted each user to be assigned to one antenna and to access one subband only, while others [28] considered that the spectrum consists of one subband to bypass the subband assignment step.

Contrary to previous works, the method proposed in this paper is the first to provide a joint solution for the assignment problem at hand while allowing each user to access any number of RRHs and subbands simultaneously. Our contributions can be summarized as follows:

- After formulating the performance measures for both RT and BE users, we propose an optimization problem to conduct resource allocation in the considered framework. To ensure successful SIC decoding at the receiver side, the optimization problem takes into account the NOMA

power multiplexing constraints for users scheduled on each subband. These constraints state that the signal that is to be decoded first must have a higher power level than the other received signals, so that it is detectable at the receiver side. Note that the power multiplexing constraints were mostly neglected in previous works dealing with matching theory to simplify the analysis.

- We consider different system settings, namely OMA-CAS, OMA-DAS, NOMA-CAS and NOMA-DAS for performance comparison. More precisely, OMA-CAS (NOMA-CAS resp.) corresponds to a CAS setting employing OMA signaling (NOMA signaling resp.), whereas OMA-DAS (NOMA-DAS resp.) corresponds to a DAS setting employing OMA signaling (NOMA signaling resp.). For each scenario, we formulate the channel allocation problem as a one-to-many matching game. We then propose algorithms based on the deferred acceptance (DA) [29] method to solve the channel allocation in each of the considered settings. To the best of our knowledge, no previous study has considered the use of matching theory to resolve the mixed traffic resource allocation problem, combining DAS and NOMA. It should also be noted that none of the previous works applying matching theory to solve the resource allocation problem for a NOMA system incorporated rate requirements into their analysis, which is not the case for the current work. Moreover, the proposed algorithms can be easily applied to solve other problems with different objectives in the different considered system settings. This can be done by modifying the preference relations of the users and, in the case of systems with one user type only, slightly adapting the different algorithms.
- For the NOMA-CAS and NOMA-DAS system settings, a hybrid NOMA system is devised using matching theory, where subbands are either allocated to single users or user-pairs in such a way to optimize system performance. Moreover, an algorithm that overcomes the need for a swapping phase to deal with the interdependencies between users' preferences is introduced.
- We prove that the proposed algorithm, for each of the considered system settings, converges to a stable solution within a limited number of iterations.
- For the DAS setting, no *a priori* information about the assignment of subbands or users to the different RRHs is assumed as was done in most previous works in the DAS context, such as [24], [30], [31]. Moreover, contrary to previous works, users are not restricted to be assigned to one predefined antenna and one subband only. Instead, an iterative approach is proposed to determine this assignment and its convergence is proved.
- Through simulation results, the proposed method is shown to achieve a better performance than a previous method introduced in [8], especially in terms of the percentage of RT users that meet their QoS requirements.

The rest of this paper is organized as follows. In section II, the system model is described. Sections III, IV, V present the proposed algorithms to solve the resource allocation problem in OMA-CAS, OMA-DAS, NOMA (CAS and DAS) respectively. The properties of the proposed algorithms are analyzed in Section VI. Finally, simulation results are presented in Section VII, before drawing the conclusion in Section VIII.

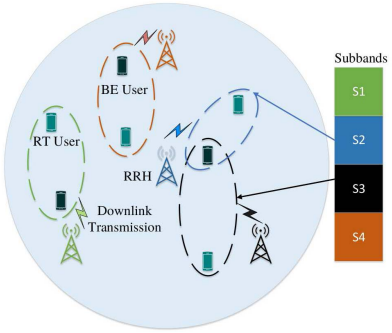

Fig. 1. System model.

II. SYSTEM MODEL AND PROBLEM FORMULATION

A. System Description

Consider a downlink system as shown in Fig. 1 with K single-antenna users uniformly deployed over a cell. The total system bandwidth B is divided into S subbands, leading to a bandwidth of $B_c = B/S$ per subband. In this work, different system configurations are studied. More precisely, we consider both CAS and DAS settings: CAS consists of one antenna located at the cell center, with a power budget P_{CAS}, whereas in DAS, A single-antenna RRHs are uniformly deployed over the cell. Each antenna has a total power budget of P_{DAS}. For multiple access, OMA as well as NOMA, which enables up to N_s users to be non-orthogonally multiplexed over a subband s, are considered. Hence, the different studied system configurations are OMA-CAS, OMA-DAS, NOMA-CAS and NOMA-DAS. The sets of users, subbands and RRHs will be respectively denoted by $\mathcal{K}, \mathcal{S}$ and $\mathcal{A}$.

When DAS is considered, a subband can only be assigned to one antenna during a scheduling slot to limit intra-cell interference. When NOMA is adopted for multiple access, the messages of up to N_s users are superposed and transmitted over subband s. This results in co-channel interference between the collocated users. Therefore, user k applies SIC [32] before demodulating its own signal, resulting in the following achieved rate:

$$R^t_{k,s,a}=B_c \log_2 \left(1+\frac{p^t_{k,s,a}(h^t_{k,s,a})^2}{\sum\limits_{k'\in\mathcal{I}^t_{k,s,a}} p^t_{k',s,a}(h^t_{k,s,a})^2+N_0B_c} \right). \quad (1)$$

In (1), $p^t_{k,s,a}$ and $h^t_{k,s,a}$ are respectively the transmit power and the channel gain of user k over subband s when assigned to antenna a at timeslot t. N_0 is the noise power spectral density. The first term in the denominator reflects the interference experienced by user k from users in $I^t_{k,s,a} = \{(k' \in \mathcal{S}_s \setminus \{k\}) \cap \left(h^t_{k',s,a} > h^t_{k,s,a}\right)\}$, i.e. users scheduled

on subband s and having a higher channel gain than k on s, when the latter is assigned to antenna a.

SIC results in a significant complexity increase at the receiver side; therefore, in this study, the maximum value of N_s is restricted to 2, $\forall s \in \mathcal{S}$.

B. User Characteristics

In this work, we differentiate between two user classes characterized by different requirements.

1) BE Users: This category includes users running delay-tolerant, rate-demanding applications such as file download or web browsing. The goal of these users is to maximize both achieved data rates and system fairness. The performance measure for BE users is therefore chosen to be:

$$M^t_{BE}(\boldsymbol{x^t}, \boldsymbol{p^t}) = \sum_{k=1}^{K_{BE}} \sum_{a=1}^{A} \sum_{s=1}^{S} x^t_{k_{BE},s,a} R^t_{k_{BE},s,a} f\left(T^t_{k_{BE}}\right), \quad (2)$$

where $x^t_{k_{BE},s,a} = 1$ if k_{BE} is scheduled on s when the latter is assigned to antenna a, and 0 otherwise. $\boldsymbol{p^t}$ is the power allocation vector and f is a measure of system fairness that depends on the average data rate $T^t_{k_{BE}}$ of each BE user until the beginning of timeslot t. $T^t_{k_{BE}}$ is updated at the beginning of each timeslot according to:

$$T^t_{k_{BE}} = \left(1 - \frac{1}{t_c}\right) T^{t-1}_{k_{BE}} + \frac{1}{t_c} R^{t-1}_{k_{BE}}. \quad (3)$$

In (3), t_c is the averaging window and $R^{t-1}_{k_{BE}}$ is the total rate of user k_{BE} at timeslot $(t-1)$.

The expression of (2) is a generic form that can enclose a wide range of specific performance metrics. A common trait of these metrics is the combination of the achieved rate and the system fairness in the scheduling decision. If the expression of (2) did not include the achieved throughput term, the scheduler would optimize system fairness, while penalizing the achieved sum rate. In contrast, if this expression did not include the fairness measure, the system throughput would be maximized by only scheduling users with a high channel gain, hence achieving a low system fairness. Therefore, to optimize performance, both the achieved throughput and the fairness measure need to be accounted for in the expression of (2). The maximum of (2) for BE users is reached when the product between their achieved rates and the fairness between them is maximized. Hence, by adopting this measure, a tradeoff between the maximization of the achieved rates and that of user fairness is reached. This tradeoff can be efficiently reached by the well known proportional fairness (PF) scheduler [12], known to achieve the best balance between rate and system fairness. In fact, the PF metric is one of the expressions embodied by (2), and will be adopted later on in the proposed solutions.

2) RT Users: This category includes users running latency-constrained applications. While some applications require only a small rate (e.g. autonomous cars or sensor applications), others are more bandwidth-hungry (e.g. virtual reality). Therefore, RT users are characterized by a strict latency limit $L_{k_{RT}}$ (expressed as an integer number of timeslots) as well as a requested amount of data bits $D^{\text{req}}_{k_{RT}}$. Their satisfaction depends upon receiving $D^{\text{req}}_{k_{RT}}$ prior to their latency limit. In this work, $D^{\text{req}}_{k_{RT}}$ is equally divided among the timeslots preceding the latency limit. Hence, from the start of the scheduling period till the end of timeslot t, each user k_{RT} needs to be allocated a number of bits equal to:

$$D^{\text{req},t}_{k_{RT}} = t D^{\text{req}}_{k_{RT}} / L_{k_{RT}}. \quad (4)$$

$D^{\text{req},t}_{k_{RT}}$ is an increasing function of the current timeslot index t and $D^{\text{req}}_{k_{RT}}$ and decreasing in $L_{k_{RT}}$. Hence, its value increases when the latency limit is small, the total required number of bits is large and when the current timeslot index approaches the latency limit.

Adopting $D^{\text{req},t}_{k_{RT}}$ as the number of required bits at timeslot t leads to the following required rate in timeslot t:

$$R^{\text{req},t}_{k_{RT}} = \frac{D^{\text{req},t}_{k_{RT}} - D^{\text{ach},t-1}_{k_{RT}}}{\tau}, \quad (5)$$

where τ is the timeslot duration and $D^{\text{ach},t-1}_{k_{RT}}$ denotes the received number of bits by k_{RT} at the end of the previous timeslot $(t-1)$.

Let $\mathbb{I}^t_{k_{RT}}(\boldsymbol{x^t}, \boldsymbol{p^t})$ be a measure of the satisfaction of k_{RT} defined by:

$$\mathbb{I}^t_{k_{RT}}(\boldsymbol{x^t}, \boldsymbol{p^t}) = \begin{cases} 1 & \text{if } \sum_{a=1}^{A} \sum_{s=1}^{S} x^t_{k_{RT},s,a} R^t_{k_{RT},s,a} \geq R^{\text{req},t}_{k_{RT}} \\ 0 & \text{otherwise.} \end{cases} \quad (6)$$

In (6), $\mathbb{I}^t_{k_{RT}}(\boldsymbol{x^t}, \boldsymbol{p^t}) = 1$, and hence user k_{RT} is satisfied if the current resource and power allocation scheme allows it to achieve a sum rate that is at least equal to its requested rate $R^{\text{req},t}_{k_{RT}}$, which is calculated to allow user k_{RT} to reach its requested number of data bits before its latency limit. In the opposite case, k_{RT} is not satisfied with the current allocation which reflects in having $\mathbb{I}^t_{k_{RT}}(\boldsymbol{x^t}, \boldsymbol{p^t}) = 0$.

Having (6) at hand, we propose to formulate the optimization function for all RT users as:

$$M^t_{RT}(\boldsymbol{x^t}, \boldsymbol{p^t}) = \sum_{k=1}^{K_{RT}} \mathbb{I}^t_{k_{RT}}(\boldsymbol{x^t}, \boldsymbol{p^t}). \quad (7)$$

Using the above formulation, (7) measures the number of RT users having received their requested data rate at each timeslot t. Hence, at the end of the latency period of all RT users, (7) finds the number of satisfied RT users, i.e. users having received the totality of requested data bits.

For concision purposes, the timeslot index t will be dropped in the following when there is no confusion. Table I contains the main notation used throughout this paper.

C. Optimization Problem

Having defined the performance measures to be maximized for both user types, the following optimization problem must be solved at each time slot:

$$\max_{\boldsymbol{a},\boldsymbol{p}} \quad (2), (7) \quad (8)$$

$$\text{such that} \sum_{a \in \mathcal{A}} x_{k,s,a} \leq 1, \ \forall (k,s) \in \mathcal{K} \times \mathcal{S} \quad (8a)$$

$$\sum_{k \in \mathcal{K}} x_{k,s,a} \leq 2, \ \forall (s,a) \in \mathcal{S} \times \mathcal{A} \quad (8b)$$

TABLE I
NOTATION TABLE

K	Total number of users	K_{RT}, K_{BE}	Number of RT and BE users resp.
S	Number of subbands	$\mathcal{S}_s$	Set of users scheduled on subband s
A	Number of distributed antennas	$\mathcal{N} = \{N_a, a \in \mathcal{A}\}$	Vector containing the number of subbands assigned to each antenna
N_0	Noise power spectral density	B_c	Subband bandwidth
P_{CAS}, P_{DAS}	Power per antenna in the CAS and DAS settings resp.	P_a	Power per subband on antenna a
t	Timeslot index	$\mathcal{K}_{\text{active}}$	Set of active users
$p^t_{k,s,a}$	Power allocated to user k on subband s and antenna a at timeslot t	$h^t_{k,s,a}$	Channel gain of user k on subband s and antenna a at timeslot t
$R^t_{k,s,a}$	Rate achieved by user k on subband s and antenna a at timeslot t	T^t_k	Average rate achieved by user k before reaching timeslot t
M^t_{RT}, M^t_{BE}	Satisfaction measure of RT and BE users resp. at timeslot t	$\mathcal{U}^t_{RT}(.,s)$, $\mathcal{U}^t_{BE}(.,s)$	Utility of RT and BE users resp. on subband s at timeslot t
L_k, D^{req}_k	Latency limit and number of requested data bits of user k	$R^{\text{req},t}_k$, $D^{\text{req},t}_k$	Required rate and required number of bits of user k at timeslot t
Ψ	Matching outcome	$\mathcal{PL}$	Preference list
$\mathcal{M}(s)$, $\mathcal{AS}(s)$	Matching set and applying user set of subband s resp.	$v^{k,a}_p$	Proposing virtual user relative to user k on antenna a

$$\sum_{k\in\mathcal{K}}\sum_{s\in\mathcal{S}} P_{s,a}x_{k,s,a} \leq P,\ \forall a \in \mathcal{A} \tag{8c}$$

$$p_{k_1,(s,a)} < p_{k_2,(s,a)}\ \forall (s,a), \in \mathcal{S}\times\mathcal{A} \tag{8d}$$

$$x_{k,s,a} \in \{0,1\}. \tag{8e}$$

Constraint (8a) restricts each subband to be assigned to one antenna only in the DAS case while (8b) limits the maximum number of users per subband to 2. (8c) is the power budget per antenna, where $P = P_{CAS}$ (resp. $P = P_{DAS}$) in the CAS setting (resp. DAS setting). Denoting by k_1 and k_2 the users scheduled on (s,a) s.t. $h_{k_1,s,a} > h_{k_2,s,a}$, k_2 must be allocated a higher power value than user k_1 as expressed in (8d) to guarantee SIC stability [8], [33], i.e. successful decoding at the user side. Indeed, as shown in [34], the power of the weak user must be strictly greater than that of the strong user. In the opposite case, the outage probabilities of the users will be always one. Note that (8) is formulated for the general case of a NOMA-DAS system, the other system configurations being special cases of it.

The optimization problem in (8) has two objectives. Since the applications of RT users are time sensitive and can be considered as "more urgent" than BE applications, satisfying RT users is given a higher priority in the proposed solutions. Moreover, (8) is a mixed-integer multi-objective optimization problem for which an optimal solution is computationally intractable. If equal power repartition between subbands assigned to the same antenna is assumed, solving (8) consists of finding the optimal subband and antenna assignment. Therefore, we invoke the two-sided matching theory framework to obtain a suboptimal solution for the formulated problem.

III. MATCHING THEORY IN THE OMA-CAS CONTEXT

A. Definition

To develop a low-complexity solution for (8), the subband assignment problem can be modeled as a two-sided one-to-many matching game. In this model, the set of subbands $\mathcal{S}$ and the set of users $\mathcal{K} = \mathcal{K}_{RT} \cup \mathcal{K}_{BE}$ form two disjoint sets of selfish and rational agents. In this first context, a subband s can be assigned to at most one user while a user k can be matched with more than one subband. If a user k is scheduled on subband s, (k,s) forms a *matching pair*. Note that, since only a single central base station is involved in the current CAS context, the antenna index a will be dropped from all involved variables.

A one-to-many matching Ψ is defined as a mapping from the set $\mathcal{K}\cup\mathcal{S}$ into the set of all subsets of $\mathcal{K}\cup\mathcal{S}$ such that for each $k \in \mathcal{K}$ and $s \in \mathcal{S}$:

1) $\Psi(k) \subseteq \mathcal{S}, \forall k \in \mathcal{K}$
2) $\Psi(s) \subseteq \mathcal{K}, \forall s \in \mathcal{S}$
3) $|\Psi(s)| = 1, \forall s \in \mathcal{S}$
4) $s \in \Psi(k) \Leftrightarrow k \in \Psi(s)$

To reach a final matching Ψ, each player p builds a preference relation $\succ_p$ over the players from the other set. Using these predefined preference relations, players dynamically interact with each other to reach a stable matching. Ψ is stable when there are no user k and subband s that are not matched together, but prefer each other over their partners $\Psi(k)$ and $\Psi(s)$, respectively. Hence, the subband assignment problem can be represented by the tuple $(\mathcal{S},\mathcal{K},\succ_s,\succ_k)$.

B. Preference Lists

To decide on the outcome of the game, each user k builds a preference list $\mathcal{PL}_k$ over the set of subbands. $\mathcal{PL}_k$ is sorted in a descending order based on the channel gain experienced by user k over all subbands in the set $\mathcal{S}$. In other words, $\mathcal{PL}_k$ is based on Definition 1.

Definition 1: Assuming equal inter-subband power allocation, users base their preferences on the channel gains over different subbands. Put differently, user k prefers subband s_i over s_j, i.e. $s_i \succ_k s_j$, where $s_i, s_j \in \mathcal{S}$, if $h_{k,s_i} > h_{k,s_j}$.

Similarly each subband s_i bases its preferences over the set of users based on Definition 2.

Definition 2: Subbands must account for the heterogeneity of users while building their preference lists by always preferring RT users over BE users, since they have the highest priority. Therefore, we define the preference relation of subband s_i as:

$$k_{RT} \succ_{s_i} k_{BE}, \forall s_i \in \mathcal{S}, k_{RT} \in \mathcal{K}_{RT} \text{ and } k_{BE} \in \mathcal{K}_{BE}.$$

In addition to preferring RT users, subbands must also be able to separately prioritize among the set of RT users and that of BE users. Therefore, at timeslot t, the following utility metric, inspired by the proposed metrics of [4], [5], is introduced for RT users:

$$\mathcal{U}^t_{RT}(k^l_{RT}, s_i) = \frac{R^t_{k^l_{RT},s_i}}{R^t_{k^l_{RT}}} \times \frac{t}{L_{k^l_{RT}}}. \tag{9}$$

In (9), $R^t_{k^l_{RT},s_i}$ denotes the achievable rate by k^l_{RT} over subband s_i if matched together at timeslot t and $R^t_{k^l_{RT}}$ is the rate already achieved by k^l_{RT} before reaching timeslot t. (9) is proportional to the achieved rate of user k_{RT} over subband s_i, and to the timeslot index t. Therefore, the users with the highest priorities are those who would benefit the most from subband s_i in terms of rate, and who have most approached their latency limit. Moreover, (9) is inversely proportional to $R^t_{k^l_{RT}}$ as well as to the latency limit of user k_{RT}. By considering t, $\mathcal{U}^t_{RT}(k^l_{RT}, s_i)$ grows larger as t increases. Also, by accounting for the latency limit $L_{k^l_{RT}}$, $\mathcal{U}^t_{RT}(k^l_{RT}, s_i)$ is increased for a more stringent latency requirement. In addition to considering the time and latency limits, (9) captures the transmission rate of k^l_{RT} if it were scheduled on s_i. Hence, this enables users with a better channel quality to have a higher priority during scheduling, therefore increasing spectral efficiency. Last, by also accounting for the achieved data rate of k^l_{RT} prior to reaching timeslot t, (9) achieves a certain fairness between RT users by prioritizing users that have not previously achieved a large enough throughput.

Each subband s_i bases its preferences over RT users according to the following definition.

Definition 3: At timeslot t, subband s_i prefers k^l_{RT} over k^m_{RT}, i.e. $k^l_{RT} \succ_{s_i} k^m_{RT}$, if $\mathcal{U}^t_{RT}\left(k^l_{RT}, s_i\right) > \mathcal{U}^t_{RT}\left(k^m_{RT}, s_i\right)$.

Similarly, subbands must differentiate between BE users, and the utility metric should strike a tradeoff between fairness and rate maximization. Hence, the PF scheduler metric [12] is adopted:

$$\mathcal{U}^t_{BE}\left(k^l_{BE}, s_i\right) = \frac{R^t_{k^l_{BE},s_i}}{T^t_{k^l_{BE}}}. \tag{10}$$

It should be noted that (10) aims to maximize the performance measure for BE users formulated in (2), as the fairness measure $f(T^t_{k_{BE}})$ in (2) is represented by the weight $1/T^t_{k_{BE}}$ in (10).

Each subband s_i bases its preferences over BE users at timeslot t according to Definition 4.

Definition 4: Subband s_i prefers k^l_{BE} over k^m_{BE}, i.e. $k^l_{BE} \succ_{s_i} k^m_{BE}$, if $\mathcal{U}^t_{BE}\left(k^l_{BE}, s_i\right) > \mathcal{U}^t_{BE}\left(k^m_{BE}, s_i\right)$.

Having defined the preference relations for both sets of players, the proposed algorithm to solve the formulated matching game is described next.

C. Proposed OMA-CAS DA Algorithm

Since users have different priority levels, the classical DA algorithm [35] cannot be directly used to solve the considered matching game. That is why, in Algorithm 1, a priority-aware version of the DA algorithm suitable for the studied context in the OMA-CAS setting is proposed.

Initially, the set of active users $\mathcal{K}_{\text{active}}$ is built; it includes all RT users that have not yet received their requested data rate and all BE users. Each user $k \in \mathcal{K}_{\text{active}}$ builds its preference list $\mathcal{PL}_k$, whereas each subband s_i initializes its matching set $\mathcal{M}(s_i)$ consisting of the user to which it is assigned throughout the algorithm. At the first iteration of the algorithm, $\mathcal{M}(s_i) = \emptyset, \forall s_i \in \mathcal{S}$. In the first phase of the algorithm, each user k applies to its most preferred subband, i.e. the very first element in $\mathcal{PL}_k$. Each subband s_i receiving proposals forms an applying user set $\mathcal{AS}(s_i)$, to which it adds all proposing users as well as the user to which it was matched at the previous iteration of the algorithm. Note that $\mathcal{AS}(s_i)$ can be empty if none of the users apply to s_i and $\mathcal{M}(s_i) = \emptyset$. Having a system with heterogeneous users, subband s_i must prioritize RT users in the decision phase. Therefore, for each subband s_i receiving user proposals, i.e. having $\mathcal{AS}(s_i) \neq \emptyset$, if RT users are among the applicants, the most preferred RT user according to (9), k^*_{RT}, is accepted by s_i. All users in $\mathcal{AS}(s_i) \setminus \{k^*_{RT}\}$ are rejected and $\mathcal{K}_{\text{active}}$ is updated to reflect the resulting rate requirement changes. However, if a subband receives applications from BE users only, it accepts the most preferred BE user according to (10) and rejects all others. At the end of the second phase of the algorithm, every user removes the subband that it proposed to at the current iteration from its preference list. This process continues until the preference lists of all active users are empty. Upon termination, the optimal matching result is obtained.

IV. MATCHING THEORY IN THE OMA-DAS CONTEXT

A. DAS Matching Game Model and Algorithm

In this section, we aim to apply matching theory to solve the subband allocation problem in the DAS context. However, the DAS layout brings a new dimension into the resource allocation problem: antenna association. In addition to the user-subband assignment of the CAS context, it is also necessary to decide on the serving antenna for each subband assigned to a user. This new dimension complicates the problem considerably and renders the application of matching theory challenging. In fact, since we have to associate each user with a subband and an antenna, we are faced with a three-dimensional matching problem for which a stable solution is not guaranteed to exist [36].

Most previous studies on resource allocation in distributed settings make some assumptions with the aim of making the problem tractable. For example, [28] focused on antenna selection and power allocation to maximize the EE of a DAS setting, where the spectrum was assumed to consist of one subband only. However, in practical systems, this assumption does not hold. Maximizing the EE was also the purpose of [31], where the authors associated the user with the antenna providing the best average SINR, before proceeding with the subband and power allocation steps. Although the antenna selection scheme may seem logical, it might result in an antenna being associated a large number of users. This decreases the power available to each user on that antenna and some users may benefit from being assigned to other, less congested antennas. Moreover, in [31], a user was constrained to be associated with one antenna only, and all RRHs have access to the whole spectrum which increases the interference. In [30], the subband and power allocation steps were separated. For the subband assignment, the number of subbands per antenna was estimated based on the average path-loss of the users, and the actual subband assignment was performed with the aim of maximizing proportional fairness.

In the current work, a user is not restricted to be assigned to a unique antenna. Moreover, a subband can be assigned to one

antenna only to limit interference. In addition to that, no *a priori* information about the distribution of subbands among RRHs is assumed. To overcome these challenges, the concept of virtual users is introduced, in which each user is duplicated into A virtual users, A being the number of antennas in the cell. This leads to a total of $K \times A$ virtual users with each virtual user representing the potential association of a real user and a serving antenna. This transformation recovers the two-dimensional aspect of the resource allocation problem, which makes it possible to find a solution using matching theory.

As in the CAS case, the sets of players in the matching game as well as the preference lists must be defined. In the DAS context, the sets participating in the matching game are the set of virtual users $\mathcal{KV}$, consisting of RT and BE virtual users, and the set of subbands $\mathcal{S}$. Virtual users and subbands also build their preference relations according to Definition 1 and 2 respectively. However, the algorithm conceived for the CAS case is revisited.

First, allowing each active virtual user to propose to its most preferred subband might result in a real user being allocated more than one subband at each iteration. Although inconsistent with the nature of the matching game, this variation was compared to a second one that restricts each real user to apply through one virtual user only. Simulations showed that the second variation yields better results. Therefore, at each iteration, among virtual users pertaining to the same real user, only one is allowed to propose to its most preferred subband. This virtual user is selected to guarantee the best performance among virtual users relative to the same real user. Put differently, each real user must aim to be assigned to the antenna guaranteeing the best performance. However, the choice should not only take into consideration the channel gains of the users. In fact, the power levels of the subbands generally differ between antennas, depending on the respective congestion levels of the antennas. Consequently, the power level per subband on each antenna should also be considered in the decision process. Assuming equal inter-subband power allocation on each antenna, the power allocated to each subband assigned to antenna a (hence to each virtual user associated with a) is given by: $P_a = \frac{P_{DAS}}{N_a}$. N_a is the number of subbands assigned to antenna a, the derivation of which will be detailed in section IV-B. Then, each real user chooses the proposing virtual user according to Definition 5.

Definition 5: Proposing virtual user $v_p^{k,a}$ representing the association of real user k with antenna a is the one satisfying:

$$v_p^{k,a} = \underset{\substack{v^{k,a'},\\ a'=1,\cdots,A}}{\operatorname{argmax}} \left(P_{a'} \times h^2_{v^{k,a'},s^*_{v^{k,a'}}} \right). \tag{11}$$

In (11), $v^{k,a'}$ represents the virtual user associated to antenna a' and relating to real user k. $s^*_{v^{k,a'}}$ is the preferred subband of virtual user $v^{k,a'}$, i.e. the very first one in its preference list $\mathcal{PL}_{v^{k,a'}}$. Choosing the proposing user following (11) ensures that real users are matched with their best subbands and antennas, in terms of rate maximization.

Algorithm 1 summarizes the proposed DA resource allocation algorithm in the OMA-DAS context, when $N_a, \forall a \in \mathcal{A}$, is known.

Algorithm 1 Priority-Aware OMA DA Algorithm

Input: $\mathcal{K}_{RT}, \mathcal{K}_{BE}, \boldsymbol{H_{RT}}, \boldsymbol{H_{BE}}, \boldsymbol{R^{\text{req}}_{RT}}, \boldsymbol{L_{RT}}, \boldsymbol{T_{BE}}, t, \boldsymbol{N}$

Output: $\boldsymbol{A_{RT}}, \boldsymbol{A_{BE}}, \boldsymbol{R_{RT}}, \boldsymbol{R_{BE}}$ // $\boldsymbol{A_{RT}}$ (resp. $\boldsymbol{A_{BE}}$) is the assignment matrix of RT users (resp. BE users) to subbands and antennas while $\boldsymbol{R_{RT}}$ (resp. $\boldsymbol{R_{BE}}$) denotes their achieved rates over each (subband, antenna) pair

Initialization:

if CAS setting **then**
  $\mathcal{K}^{RT}_{\text{active}} = \left\{k_{RT} \in \mathcal{K}_{RT} / R^{\text{req}}_{k_{RT}} > 0\right\}, \mathcal{K}_{\text{active}} = \mathcal{K}_{BE} \cup \mathcal{K}^{RT}_{\text{active}}$.
else if DAS setting **then**
  Construct virtual user sets $\mathcal{K}^{v}_{RT}$ and $\mathcal{K}^{v}_{BE}$.
  $\mathcal{K}^{RT,v}_{\text{active}} = \left\{v^{k_{RT},a}, a = 1, \ldots, A \ / R^{\text{req}}_{k_{RT}} > 0\right\}$,
  $\mathcal{K}_{\text{active}} = \mathcal{K}^{v}_{BE} \cup \mathcal{K}^{RT,v}_{\text{active}}$.
end if
Build the preference lists $\mathcal{PL}_k$ of users in $\mathcal{K}_{\text{active}}$.
Set $\mathcal{M}(s_i) = \emptyset, \forall s_i \in \mathcal{S}$.

Phase 1: Active users apply to subbands

if CAS setting **then**
  Each user $k \in \mathcal{K}_{\text{active}}$ proposes to the first subband in $\mathcal{PL}_k$.
else if DAS setting **then**
  Each real user $k \in \mathcal{K}_{\text{active}}$ chooses its proposing virtual user $v_p^{k,a}$ and proposes to the first subband in $\mathcal{PL}_{v_p^{k,a}}$.
end if
Find the applicant set $\mathcal{AS}(s_i)$ for each subband $s_i \in \mathcal{S}$, $\mathcal{AS}(s_i) = \mathcal{AS}(s_i) \cup \mathcal{M}(s_i), \ \forall s_i \in \mathcal{S}$.

Phase 2: Subbands make decisions

if $\mathcal{AS}(s_i) \neq \emptyset$ and $\mathcal{AS}(s_i) \cap \mathcal{K}^{RT}_{\text{active}} \neq \emptyset$ **then**
  $\mathcal{M}(s_i) = \{k^*_{RT}\}$,
  where $k^*_{RT} = \underset{k^l_{RT} \in \mathcal{AS}(s_i) \cap \mathcal{K}^{RT}_{\text{active}}}{\operatorname{argmax}} \mathcal{U}^t_{RT}(k^l_{RT}, s_i)$.
  Update $R^{\text{req}}_{k^*_{RT}}$, $\mathcal{K}^{RT}_{\text{active}}, \mathcal{K}^{RT,v}_{\text{active}}$ and $\mathcal{K}_{\text{active}}$.
else if $\mathcal{AS}(s_i) \neq \emptyset$ **then**
  $\mathcal{M}(s_i) = \{k^*_{BE}\}$, where $k^*_{BE} = \underset{k^l_{BE} \in \mathcal{AS}(s_i)}{\operatorname{argmax}} \mathcal{U}^t_{BE}(k^l_{BE}, s_i)$.
end if

Phase 3: Preference lists update

Each user k that proposed to $s_i, \forall s_i \in \mathcal{S}$, removes s_i from $\mathcal{PL}_k$.

Repeat Phases 1, 2 and 3 until $\mathcal{PL}_k = \emptyset, \ \forall k \in \mathcal{K}_{\text{active}}$

B. Estimation of the number of subbands per antenna

To find $N_a, \ \forall a \in \mathcal{A}$, we first use $w_{k,a}$, the large-scale fading parameter between user k and antenna a, as was done in [30]:

$$N_a = \left\lfloor \frac{S \times \sum_{k=1}^{K} w_{k,a}}{\sum_{a=1}^{A} \sum_{k=1}^{K} w_{k,a}} \right\rfloor, a \in \mathcal{A}. \tag{12}$$

However, contrary to [30], in our work, this estimation is only used for initial power approximation and does not dictate the number of assigned subbands to each antenna a in each timeslot.

Using this initial estimation of the number of subbands per antenna, Algorithm 2 provides the final assignment

of users and subbands to antennas. In each iteration of Algorithm 2, each antenna performs equal-power distribution using its estimated number of assigned subbands. Then, subband assignment is determined using Algorithm 1. The number of subbands per antenna is then updated, as well as P_a, $\forall a \in \mathcal{A}$. Algorithm 2 converges when the number of subbands per antenna remains unchanged between two successive iterations.

Algorithm 2 OMA-DAS Resource Allocation

Input: $\boldsymbol{N}, \mathcal{K}_{RT}, \mathcal{K}_{BE}, \boldsymbol{H_{RT}}, \boldsymbol{H_{BE}}, \boldsymbol{R}^{\text{req}}_{\boldsymbol{RT}}, \boldsymbol{L_{RT}}, \boldsymbol{T_{BE}}, t$
Output: $\boldsymbol{A_{RT}}, \boldsymbol{A_{BE}}, \boldsymbol{R_{RT}}, \boldsymbol{R_{BE}}, \boldsymbol{N}$ // $\boldsymbol{N}$ is the number of subbands per antenna

1: ***Repeat:***
2: $N^{\text{old}} = N$.
3: $P_a = P_{DAS}/N_a$.
4: Find the assignment of users and subbands to antennas according to Algorithm 1.
5: Using the resulting $\boldsymbol{A_{RT}}$ and $\boldsymbol{A_{BE}}$, re-calculate $\boldsymbol{N} \in \mathbb{N}^{A\times 1}$ and $\boldsymbol{P} \in \mathbb{R}_{+}^{A\times 1}$ as well as $\boldsymbol{R_{RT}}$ and $\boldsymbol{R_{BE}}$.
6: ***Until convergence***

V. MATCHING THEORY IN THE NOMA CONTEXT

Solving the resource allocation problem in the NOMA context using matching theory is not straightforward. On the one hand, the power multiplexing constraints, neglected in previous works like [26], must be respected to guarantee SIC stability. On the other hand, applying the methods proposed in previous works like [26] and [37] does not guarantee the rate requirements of RT users. Nor does applying the same algorithms proposed in sections III and IV, while allowing multiple users to be scheduled on the same subband. Moreover, because of the interdependencies between users' preferences, due to the inter-user interference between paired users on NOMA subbands, the outcome of these algorithms is not guaranteed to be optimal. That is why, in this section, we generalize the resource allocation techniques proposed in the previous sections to encompass the NOMA case, starting with the NOMA-CAS context.

The proposed solution to the resource allocation problem in the NOMA-CAS context is divided into two stages. The first one, consisting of the assignment of single RT users and NOMA BE users, aims at maximizing the number of satisfied RT users, as well as boosting the performance of BE users when possible. The second stage, where user pairings are performed on the subbands allocated to RT users, aims at further enhancing system performance.

A. Assignment of Subbands to Single RT Users and NOMA BE Users

To ensure that rate requirements of RT users are met, the allocation process starts by scheduling OMA RT users, as done in section III. The preference relations of RT users and subbands are formulated in the same way as in section III. If all RT users reach their rate requirements and free subbands remain in the system, BE users are scheduled on these subbands directly via NOMA.

NOMA Matching Game for BE Users: In [26], matching theory was used to solve the subband allocation problem in NOMA and a technique based on the DA algorithm was proposed. However, interdependencies between users' preferences exist in the NOMA case because of the interference brought by non-orthogonally scheduling different users on the same subband. This is why previous work as in [27] and [37] performed a swapping step at the end of the matching step to further enhance system performance. This step allows different users to swap their assigned subbands, conditioned by the approval of all involved players, and generally requires a significant number of additional iterations.

In this study, we follow a different direction by allowing single users as well as pairs of users to make proposals. By doing so, interdependencies between users are directly taken into account, without the need for an additional swap phase. Also, thanks to this new idea, a hybrid-NOMA system (where subbands are either allocated to sole or paired users) is enabled, which achieves a better performance than non-hybrid NOMA [38].

Similarly to the previous sections, the sets of players in the NOMA-CAS case are subbands and users. However, the user set, denoted by $\mathcal{US}$, now consists of both single users and pairs of users. It contains $|K_{BE}| + P(|K_{BE}|, 2)$ elements, where $|K_{BE}|$ accounts for single users and $P(|K_{BE}|, 2)$ for user pairs. Each user combination in $\mathcal{US}$ complies with the following definition to form its preference list.

Definition 6: Each user combination $us_n \in \mathcal{US}$ divides the available power per subband, P_s, among its members according to the fractional transmit power allocation (FTPA) [13] (Note that if $|us_n| = 1$, P_s is entirely allocated to the sole user in us_n). Then, us_n bases its preferences on (13), where R_{us_n,s_i} is the rate achieved by users in the set us_n on subband s_i.

$$s_i \succ_{us_n} s_j \text{ if } R_{us_n,s_i} > R_{us_n,s_j}. \tag{13}$$

For subbands, the utility achieved by scheduling us_n is defined in (14), with $\mathcal{U}^t_{BE}(k, s_i)$ given by (10). Then, subbands base their preferences on (15).

$$\mathcal{U}^t_{BE}(us_n, s_i) = \sum_{k\in us_n} \mathcal{U}^t_{BE}(k, s_i), \tag{14}$$

$$us_n \succ_{s_i} us_m \quad \text{if} \quad \mathcal{U}^t_{BE}(us_n, s_i) > \mathcal{U}^t_{BE}(us_m, s_i). \tag{15}$$

Phases 1 and 2 of Algorithm 3 describe the steps involved in the first stage of the resource allocation technique in the NOMA-CAS case.

B. NOMA Pairing on Subbands Assigned to RT Users

Since the first stage of the proposed solution in the NOMA-CAS context schedules RT users based on OMA and assuming equal inter-subband power repartition, some scheduled RT users exceed their required rates, while others may not have satisfied their requirements (because of system congestion or bad channel states). Consequently, in this second stage of the allocation process, NOMA pairing is performed on the subbands assigned to RT users in the first stage.

This second stage starts by finding the amount of power that satisfied RT users can spare, without jeopardizing their satisfaction. Therefore, for each RT user having exceeded its required rate, the following optimization problem is solved:

$$\min_{\boldsymbol{p}_{k_{RT}}} \sum_{s\in\mathcal{S}_{k_{RT}}} p_{k_{RT},s} \tag{16}$$

$$\text{such that} \sum_{s\in\mathcal{S}_{k_{RT}}} R_{k_{RT},s} = R^{\text{req}}_{k_{RT}} \tag{16a}$$

$$0 \le p_{k_{RT},s,a_s} \le P_s. \tag{16b}$$

In (16), $\mathcal{S}_{k_{RT}}$ is the set of subbands assigned to user k_{RT} in the first stage of the allocation process. Solving the above optimization problem leads to the well-known waterfilling solution:

$$p_{k_{RT},s} = \left[\frac{\lambda_{k_{RT}} B_c}{\log(2)} - \frac{N_0 B_c}{H^2_{k_{RT},s,a_s}}\right]^{P_s}_0. \tag{17}$$

In (17), $\lambda_{k_{RT}}$ is the Lagrange multiplier given by:

$$\lambda_{k_{RT}} = 2^{\frac{1}{S_{k_{RT}}}\left[\frac{R^{\text{req}}_{k_{RT}}}{B_c} - \sum\limits_{s\in\mathcal{S}_{k_{RT}}} \log_2\left(\frac{H^2_{k_{RT},s}}{\log(2)N_0}\right)\right]}. \tag{18}$$

The required rate on $s \in \mathcal{S}_{k_{RT}}$ is given by:

$$R^{\text{req}}_{k_{RT},s} = B_c \log_2\left(1 + \frac{p_{k_{RT},s} H^2_{k_{RT},s}}{N_0 B_c}\right). \tag{19}$$

This rate must be guaranteed regardless of the pairing order on s. Note that if the rate $R_{k_{RT},s}$ obtained on s at the end of the first allocation stage is lower than $R^{\text{req}}_{k_{RT},s}$, s is removed from $\mathcal{S}_{RT}$, the set of subbands available for NOMA pairing (given by step 7 of Algorithm 3). In the opposite case, s can be shared with another user. To guarantee $R^{\text{req}}_{k_{RT},s}$, two separate cases are considered concerning the channel gain of the candidate user for pairing, k':

1) $h_{k_{RT},s} > h_{k',s}$: In this case, k_{RT} is paired as first user on s with a required rate given by (19). However, to guarantee SIC stability, $p_{k_{RT},s} < p_{k',s}$ must hold. This translates into considering s for NOMA pairing if $p_{k_{RT},s} < P_s/2$. If this condition is verified, the available power for k' on s is: $p^{2,\text{av}}_s = P_s - p_{k_{RT},s}$.

2) $h_{k_{RT},s} < h_{k',s}$: In this case, k_{RT} is paired as second user on s. To guarantee $R^{\text{req}}_{k_{RT},s}$, k_{RT} needs to be assigned a power equal to:

$$p^{2,\text{req}}_{k_{RT},s} = \frac{(a-1)\left(P_s h^2_{k_{RT},s} + N_0 B_c\right)}{a h^2_{k_{RT},s}}, \tag{20}$$

where $a = 2^{R^{\text{req}}_{k_{RT},s}/B_c}$. SIC stability is guaranteed if $p^{2,\text{req}}_{k_{RT},s} > P_s/2$ which is warranted if $a \ge 2$. Hence, if being scheduled as second user, the required rate of k_{RT} to ensure SIC stability is chosen to be $R^{\text{req}}_{k_{RT},s} = \max\left(R^{\text{req}}_{k_{RT},s}, B_c\right)$. In the case where $R^{\text{req}}_{k_{RT},s}$ takes the value of B_c, $p^{2,\text{req}}_{k_{RT},s}$ is recalculated to reflect the change. Then, the power available for a potential first user k' is given by: $p^{1,\text{av}}_s = P_s - p^{2,\text{req}}_{k_{RT},s}$.

Having determined the amounts of power available for NOMA pairing, the matching algorithm proposed for the second allocation stage can now be described.

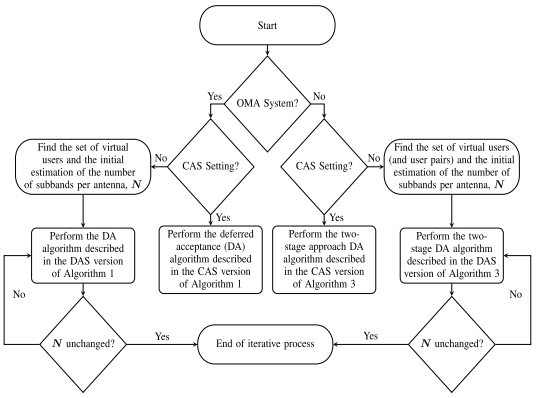

Fig. 2. Flowchart of the proposed matching technique in the studied settings.

The active users in this second stage are the unsatisfied RT users and the BE users, hence $\mathcal{K}_{\text{active}} = \{\mathcal{K}_{BE} \cup k_{RT} \in \mathcal{K}_{RT} / R^{\text{req}}_{k_{RT}} > 0\}$. First, the achievable rate of each candidate user $k \in \mathcal{K}_{\text{active}}$ over subband $s \in \mathcal{S}_{\text{rem}}$ (where k_{RT} is scheduled) is calculated using (21). Then, each active user builds its preference list according to the decreasing order of achievable rates.

$$R^{\text{av}}_{k,s} = \begin{cases} B_c \log_2\left(1 + \dfrac{p^{1,\text{av}}_s h^2_{k,s}}{N_0 B_c}\right), \text{ if } h_{k,s} > h_{k_{RT},s}, \\ B_c \log_2\left(1 + \dfrac{p^{2,\text{av}}_s h^2_{k,s}}{p_{k_{RT},s} h^2_{k,s} + N_0 B_c}\right), \text{ otherwise.} \end{cases} \tag{21}$$

Since only one additional user is to be scheduled on each subband allocated to RT users, Algorithm 1 can be used to solve the second stage of the allocation process. However, instead of considering all subbands in set $\mathcal{S}$ as done in Algorithm 1, only those assigned to RT users in the previous stage must be considered (i.e. subbands in $\mathcal{S}_{RT}$).

C. Matching Technique for NOMA-CAS

The complete algorithm used to solve the allocation problem in the NOMA-CAS setting is given in Algorithm 3.

D. Matching Technique in the NOMA-DAS Context

Resource allocation through matching theory in the NOMA-DAS case is conducted by incorporating the concepts from Section IV and subsections V-A, V-B and V-C. The proposed method is detailed in Algorithm 3.

To summarize, the flowchart in Fig. 2 shows how the matching technique is used in the different system settings.

VI. ANALYSIS OF STABILITY, CONVERGENCE AND COMPLEXITY

To analyze the properties of the proposed matching technique in all studied system settings (i.e. OMA-CAS, OMA-DAS, NOMA-CAS, NOMA-DAS), we separately consider the following two parts: 1) The matching algorithm, 2) The iterative approach proposed to find the number of subbands per antenna in the DAS case.

Algorithm 3 Priority-Aware NOMA DA Algorithm

Input: $\mathcal{K}_{RT}, \mathcal{K}_{BE}, \boldsymbol{H_{RT}}, \boldsymbol{H_{BE}}, \boldsymbol{R}^{\text{req}}_{\boldsymbol{RT}}, \boldsymbol{L_{RT}}, \boldsymbol{T_{BE}}, t$
Output: $\boldsymbol{A_{RT}}, \boldsymbol{A_{BE}}, \boldsymbol{R_{RT}}, \boldsymbol{R_{BE}}$
Initialization:
$\mathcal{K}^{RT}_{\text{active}} = \left\{ k_{RT} \in \mathcal{K}_{RT} / R^{\text{req}}_{k_{RT}} > 0 \right\}$ in the CAS setting and
$\mathcal{K}^{RT}_{\text{active}} = \left\{ v^{k_{RT},a}, a = 1, \ldots, A \ / R^{\text{req}}_{k_{RT}} > 0 \right\}$ in the DAS setting.
Build the preference lists $\mathcal{PL}_k$ of users in $\mathcal{K}^{RT}_{\text{active}}$.
Set $\mathcal{M}(s_i) = \emptyset, \ \forall s_i \in \mathcal{S}$.
$P_a = P_{DAS}/N_a, \ \forall a \in \mathcal{A}$. // Only in DAS setting
Repeat steps 5 to 27 in the DAS setting
$N^{\text{old}} = N$.
Phase 1: Scheduling RT users
Perform phases 1, 2 and 3 from Algorithm 1.
Repeat Phase 1 until $\mathcal{PL}_k = \emptyset, \ \forall k \in \mathcal{K}^{RT}_{\text{active}} \ || \ \mathcal{K}^{RT}_{\text{active}} = \emptyset$
$\mathcal{S}_{RT} \leftarrow$ Subbands used by RT users,
$\mathcal{S}_{\text{rem}} \leftarrow \mathcal{S} \setminus \mathcal{S}_{RT}$.
Phase 2: Scheduling BE users
if $\mathcal{S}_{\text{rem}} \neq \emptyset$ **then**
Initialization:
Construct user set $\mathcal{US}$ consisting of both single users and user pairs in the CAS setting (resp. virtual user set in the DAS setting consisting of virtual users and user sets).
Build the preference lists $\mathcal{PL}_{us_n}$ of user sets $us_n \in \mathcal{US}$.
Set $\mathcal{M}(s_i) = \emptyset, \ \forall s_i \in \mathcal{S}_{\text{rem}}$.
Phase 2.1: BE users and BE pairs apply to subbands
Each $us_n \in \mathcal{US}$ proposes to the first subband in $\mathcal{PL}_{us_n}$ in the CAS setting (In the DAS setting, each real user chooses its proposing virtual user us^v_n and proposes to the first subband in $\mathcal{PL}_{us^v_n}$).
Construct the applicant set $\mathcal{AS}(s_i)$ for each subband $s_i \in \mathcal{S}_{\text{rem}}$, $\mathcal{AS}(s_i) = \mathcal{AS}(s_i) \cup \mathcal{M}(s_i), \ \forall s_i \in \mathcal{S}_{\text{rem}}$.
Phase 2.2: Subbands make decisions
if $\mathcal{AS}(s_i) \neq \emptyset$ **then**
$\mathcal{M}(s_i) = \{us^*_n\}$, where
$us^*_n = \underset{us_n \in \mathcal{A}(s_i)}{\text{argmax}} \ \mathcal{U}^i_{BE}(us_n, s_i)$.
end if
Phase 2.3: Preference lists update
Each user set us_n that proposed to $s_i, \ \forall s_i \in \mathcal{S}_{\text{rem}}$, removes s_i from $\mathcal{PL}_{us_n}$.
Repeat Phases 2.1, 2.2 and 2.3 until $\mathcal{PL}_{us_n} = \emptyset, \ \forall \ us_n \in \mathcal{US}$
end if
Using the resulting $\boldsymbol{A_{RT}}$ and $\boldsymbol{A_{BE}}$, re-calculate $\boldsymbol{N} \in \mathbb{N}^{A \times 1}$ and $\boldsymbol{P} \in \mathbb{R}^{A \times 1}_{+}$ as well as $\boldsymbol{R_{RT}}$ and $\boldsymbol{R_{BE}}$.
Phase 3: NOMA pairing on subbands assigned to RT users
if $\mathcal{S}_{RT} \neq \emptyset$ **then**
Find RT users that exceed their required rates $\mathcal{K}^{\text{excess}}_{\text{RT}}$.
Solve (16) for $k \in \mathcal{K}^{\text{excess}}_{\text{RT}}$.
Find the available power on $s \in \mathcal{S}_{RT}$.
$\mathcal{K}_{\text{active}} = \{\mathcal{K}_{BE} \cup k_{RT} \in \mathcal{K}_{RT} / R^{\text{req}}_{k_{RT}} > 0\}$.
Build preference lists for users in $\mathcal{K}_{\text{active}}$.
Use Algorithm 1 to schedule additional users on subbands belonging to $\mathcal{S}_{RT}$.
end if
Until convergence

A. Properties of the Matching Technique

Before discussing the stability property of the matching technique, the definition of *blocking pair* [29] is first recalled.

Definition 7: Given a matching Ψ and a pair (k_n, s_i), where $k_n \in \mathcal{US} \ \cup \ \mathcal{K}_{RT}$ and $s_i \in \mathcal{S}$, with $k_n \notin \Psi(s_i)$ and $s_i \notin \Psi(k_n)$, (k_n, s_i) forms a blocking pair if:

1) $k_n \succ_{s_i} \Psi(s_i)$,
2) $s_i \succ_{k_n} s_j$, where $s_j \in \Psi(k_n)$.

With the definition above, it is now possible to define the concept of stability and prove that the proposed matching technique does indeed converge towards a stable matching.

Definition 8: If there is no blocking pair $(k_n, s_i) \in \Psi$, matching Ψ is considered *stable*.

Theorem 1: The proposed matching technique in all system settings is guaranteed to converge to a stable matching Ψ^*.

Proof: See Appendix A. ■

Theorem 2: The matching technique is guaranteed to converge after a limited number of iterations for all studied system settings.

Proof: See Appendix B. ■

Theorem 3: The maximum complexity of the proposed matching technique is $\mathcal{O}\left((K_{RT} + |\mathcal{US}|)AS^2\right)$, and is achieved in the NOMA-DAS setting.

Proof: See Appendix C. ■

B. Properties of the Iterative Approach

Theorem 4: The iterative approach introduced in Algorithm 2 is guaranteed to converge within a limited number of iterations.

Proof: See Appendix D. ■

Concerning the complexity of Algorithm 2, the number of iterations cannot be given in a closed form expression because it is not certain at which round the algorithm converges to the final solution. However, an upper bound on the complexity can be derived. Since system performance increases after each iteration, if ΔP denotes the performance gain yielded by the iterative approach and δ_{min} is the minimum increase in performance at each iteration, an upper bound on the complexity of this method is given by $\mathcal{O}(\frac{\Delta P}{\delta_{min}})$.

VII. NUMERICAL RESULTS

The performance of the proposed subband assignment technique based on matching theory, denoted by "MM", is evaluated in this section through simulations. The performance of MM is tested in the OMA-CAS, OMA-DAS, NOMA-CAS and NOMA-DAS settings. A variation of the MM method, denoted by MM-FA, in the DAS settings is also tested. MM-FA adopts the approach of [30] and determines the number of subbands per antenna, $N_a, \forall a \in \mathcal{A}$, at the beginning of the resource allocation algorithm based on the average path-loss experienced by all users. For fair comparison, each antenna a is assigned the N_a subbands having the highest average channel gain for all users. The performance achieved by the greedy method, denoted by "GM", that was formerly proposed in [8] is also shown for comparison.

The parameters used in the simulations are summarized in Table II [39]. When a CAS case is considered, one antenna is assumed to be located at the center of the cell. In the case of DAS, $A = 4$ RRHs are assumed to be deployed in the cell. In addition to the centrally located antenna, the other 3 antennas are equally distanced and positioned on a circle of radius $2R_d/3$, R_d being the cell radius, with an angular separation of $120°$. The power budget per cell is 40 W; when DAS is considered, this budget is equally partitioned between

TABLE II
SIMULATION PARAMETERS

Cell Radius R_d	500 m
Overall Transmission Bandwidth	10 MHz
Number of subbands	16
Cell Power Budget	40 Watts (46 dBm)
Number of RT users in the cell	5, 10, 15, 20, 25, 30
Number of BE users in the cell	20
Distance Dependent Path Loss	$128.1 + 37.6 \log_{10}(d)$(dB), d in Km
Receiver Noise Density	4.10^{-18} mW/Hz

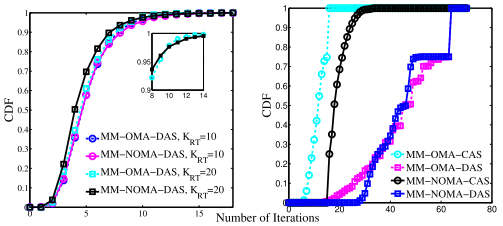

Fig. 3. CDF of the number of iterations needed: to find the number of subbands per antenna (left), for the matching method with $K_{RT} = 10$ (right).

antennas leading to 10 W per antenna. The number of RT users K_{RT}, is varied between 5 and 30 to depict different system congestion levels. To reflect different RT application requirements, RT users are partitioned among 3 classes (C1, C2 and C3). Users in all 3 classes request 10^5 bits. However, a user $k_{RT} \in$ C1 has a latency limit $L_{k_{RT}} = 6$ timeslots, whereas if $k_{RT} \in$ C2 (resp. $k_{RT} \in$ C3), $L_{k_{RT}} = 10$ timeslots (resp. $L_{k_{RT}} = 15$ timeslots). For all K_{RT} values, it is assumed that 20% of the users belong to each of C1 and C2 while the remaining 60% users belong to C3. The number of BE users K_{BE} is maintained at 20 throughout the simulations.

A. Convergence of the Proposed Method

First, the convergence of the iterative method that aims to find the number of subbands per antenna is observed. Fig. 3 (left) plots the cumulative distribution function (CDF) of the number of iterations needed for Algorithm 2 to converge for both the OMA and NOMA settings, when the number of RT users takes the values 10 and 20. The CDF shows that the proposed method converges within a small number of iterations (90% of the cases converge within 8 iterations) for both the OMA and the NOMA settings, as well as for both $K_{RT} = 10$ and $K_{RT} = 20$ users. The convergence of the NOMA settings is slightly slower than its OMA counterpart. Fig. 3 (left) shows that the convergence of the setting with $K_{RT} = 10$ users is slower than the one with 20 RT users. In fact, when $K_{RT} = 10$, BE users have a higher chance of being scheduled. Hence, all 30 users (10 RT users and 20 BE users) contribute to deciding on the assignment of subbands to the RRHs. However, when $K_{RT} = 20$, the system is more congested and BE users have a harder time getting resources. Therefore, the subband to antennas assignment is mostly decided upon by the 20 RT users in this case, which explains the faster convergence.

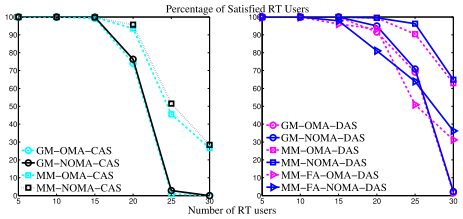

Fig. 4. Percentage of satisfied RT users for the CAS settings (left), and the DAS settings (right).

In Fig. 3 (right), the convergence of the MM technique is shown for the different settings, when $K_{RT} = 10$ users. As expected, the OMA settings converge faster than the NOMA ones. However, it can be seen that the maximum number of iterations needed for MM to converge is $AS = 64$ in the DAS settings, which is a relatively small number of iterations.

B. Performance of the MM Technique

In Fig. 4, the performance of the proposed technique in terms of RT users satisfaction is evaluated. It can be noted that, until $K_{RT} = 15$ users, MM and GM perform similarly regardless of the considered scenario. However, as the cell becomes more congested with a larger number of RT users, MM outperforms GM in all its variations. More concretely, when $K_{RT} = 30$, GM achieves almost no satisfaction for RT users. However, MM-OMA-CAS (resp. MM-OMA-DAS) outperforms its GM equivalent by almost 28% (resp. 62 %). Also, in the NOMA cases, MM-NOMA-CAS (resp. MM-NOMA-DAS) outperforms its GM equivalent by almost 30% (resp. 63%). Fig. 4 also shows the gains achieved by the iterative method to find the number of subbands per antenna introduced in Algorithm 2. For example, when $K_{RT} = 30$ users, MM-OMA-DAS (resp. MM-NOMA-DAS) outperforms MM-FA-OMA-DAS (resp. MM-FA-NOMA-DAS) by almost 30% (resp. 26%). Additionally, the results show the gain achieved by using a DAS setting, in comparison to CAS, as it can increase the performance by more than 30%.

Having observed the performance enhancement brought by the DAS settings, hereinafter, only the performance of MM-NOMA-CAS will be compared to the other methods as it has the best behavior in the CAS setting. Also, MM-FA-OMA-DAS will be dropped since it is outperformed by its NOMA version.

In Fig. 5, the percentage of satisfied RT users per class is shown. As previously stated, GM and MM both satisfy all RT users when $K_{RT} \leq 15$ users. However, when $K_{RT} \geq 20$, the performance of GM degrades and the satisfaction of RT users belonging to the strictest class, C1 (with a latency of 6 timeslots), is mostly affected. In fact, for $K_{RT} = 25$ for example, the GM technique achieves close to 10% satisfaction for users belonging to C1 in the case of a DAS system, while a CAS system cannot satisfy any user in C1. On the other hand, MM-OMA-DAS and MM-NOMA-DAS achieve both almost 96% satisfaction while the CAS versions achieve almost 70% satisfaction. For the more relaxed classes, the percentage of

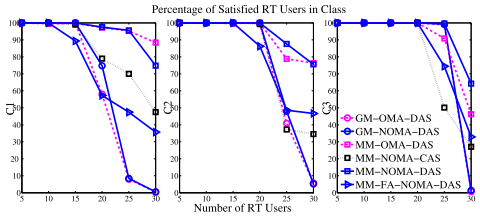

Fig. 5. Percentage of satisfied RT users per class.

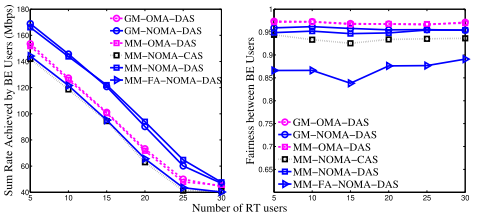

Fig. 6. Achieved rate for BE users as K_{RT} increases (left); System fairness in terms of K_{RT} (right).

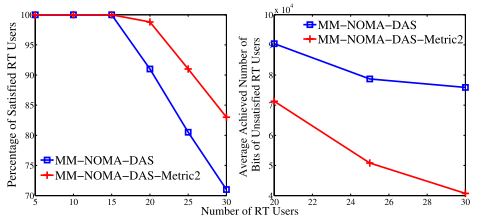

Fig. 7. Percentage of satisfied RT users as K_{RT} increases (left); Average number of bits received by unsatisfied RT users as K_{RT} increases (right).

satisfied RT users with the GM method is higher than for C1, since their requirements are more relaxed. Hence, even if the GM algorithm achieves an acceptable global percentage of satisfaction for $K_{RT} = 20$ and 25, this performance results from the satisfaction of the users in the most relaxed classes. This is not the case for the MM algorithm which prioritizes users having more strict requirements. Therefore, it achieves an acceptable performance in all classes.

Remark 1: In Fig. 5, for C1, we notice that MM-OMA-DAS outperforms MM-NOMA-DAS for a system consisting of 30 RT users. This results from the fact that at timeslot t, for NOMA pairing, all additional power allocated to a satisfied RT user k_{RT} is taken away from it to accommodate more users via NOMA. Hence, the rate achieved by k_{RT} at t is equal to its required rate, not more. At a subsequent timeslot t' ($t < t' \leq L_{k_{RT}}$), k_{RT} might not be able to reach its required rate (for example, because of a bad channel state). However, if k_{RT} was allowed to exceed its required rate at timeslot t, the required rate at t' would be reduced and hence k_{RT} could have been satisfied. A solution for this problem might be to allow RT users to keep a small amount of additional power during the NOMA pairing step.

Fig. 6 (left) shows the achieved rate of BE users as K_{RT} increases. As expected, the sum rate of BE users decreases for all methods as K_{RT} grows, as less resources are available for BE users. Both methods (GM and MM) perform similarly when it comes to the sum rate achieved by BE users. For example, for the NOMA-DAS case, GM-NOMA-DAS achieves almost 1 Mbps gain over MM-NOMA-DAS when $K_{RT} = 5$ or 10 users. However, for $K_{RT} = 20$ or 25 users, MM-NOMA-DAS achieves almost 3 Mbps gain over GM-NOMA-DAS. Therefore, while significantly enhancing the satisfaction of RT users, MM does not degrade the sum rate of BE users. Moreover, MM-NOMA-DAS greatly outperforms MM-FA-NOMA-DAS. Hence, the complexity added by the use of Algorithm 2 is justified by the enhanced performance for both RT and BE users.

In Fig. 6 (right), we show the fairness achieved by the different methods in terms of K_{RT}. System fairness is assessed through Jain's fairness index [40]: $J = \frac{\left(\sum_{k\in\mathcal{K}_{BE}} R_k\right)^2}{K_{BE}\sum_{k\in\mathcal{K}_{BE}} R_k^2}$, where R_k is the total rate achieved by user k. Jain's fairness index ranges between 0 and 1 with the maximum achieved in the case of optimal fairness. It can be seen that MM-NOMA-DAS outperforms its FA counterpart. Putting MM-FA apart, Fig. 6 (right) shows that all considered methods have a good performance in terms of fairness with a Jain index higher than 0.9, with an advantage for the DAS settings. Therefore, system fairness is not a deciding factor in the evaluation of the different methods. It should be noted that although the OMA versions slightly outperform the NOMA ones, NOMA increases the minimum individual rate of BE users. Hence, the slightly decreased fairness is due to some users having slightly more rate that others in the NOMA setting.

To show the adequacy of the proposed metrics in (9) and (10), their performance is compared against the unified metric proposed in [2], given by (22), where $\alpha_k = 1$ for BE users and $\alpha_k = 1 + t$ for RT users. $\theta_k(t)$ is the normalized delay.

$$\mathcal{UM}_{k,s}(t) = \alpha_k R_{k,s}^t \exp(\theta_k(t)). \tag{22}$$

To compare, a NOMA-DAS setting is considered and Algorithm 3 is employed. However, the preference relation of the subbands is modified depending on the tested metric. The performance of the unified metric is denoted by MM-NOMA-DAS-Metric 2 in the simulations.

Fig. 7 compares the performance of the two metrics for RT users. In terms of the percentage of satisfied RT users, Fig. 7 (left) shows that both metrics achieve a similar performance for $K_{RT} \leq 15$ users. As K_{RT} increases, (22) outperforms (9) by up to 10% for $K_{RT} = 30$. That is because (22) privileges users with a high rate. In contrast, (9) seeks to achieve a high fairness between RT users by accounting for the received rate before timeslot t. In other words, even if it were unable to satisfy all users, (9) aims at approaching most RT users to their requirements, as shown in Fig. 7 (right). Indeed, Fig. 7 (right) shows that (9) increases the amount of received data bits of unsatisfied RT users by up to 3.6×10^4 bits, when compared to (22).

Fig. 8 compares the performance of both metrics for BE users. As expected, (22) achieves a higher sum rate for BE users than (10). This is due to the fact that in (22), only the achievable rate of BE users is taken into account, without any

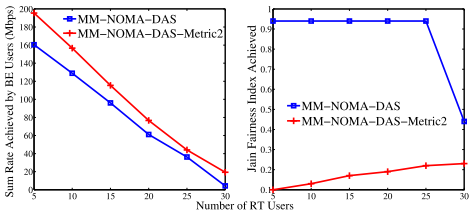

Fig. 8. Achieved sum rate of BE users in terms of K_{RT} (left); Achieved Jain fairness index in terms of K_{RT} (right).

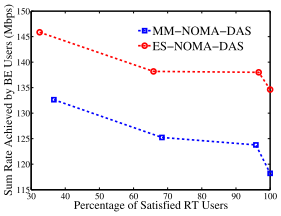

Fig. 9. Pareto frontier comparison between MM-NOMA-DAS and ES-NOMA-DAS.

fairness consideration. This is not the case of (10), which seeks to achieve a tradeoff between rate and fairness maximization. The superior performance of (10) in terms of fairness is shown in Fig. 8 (right).

Fig. 7 and 8 show the different tradeoffs existing between the used metrics and (22). In the current paper, our goal is to formulate a matching theory based solution for the resource allocation problem in CAS, DAS, OMA and NOMA settings, without necessarily focusing on the optimal scheduling metric. However, to find new metrics reaping the best of these compared ones, a possible future work could consider the formulation, analysis and comparison between multiple metrics. Then, the new metrics can be readily plugged into our proposed algorithms.

On a final note, the performance of the proposed matching-based technique was compared with the optimal solution found by exhaustive search in the NOMA-DAS setting and denoted by ES-NOMA-DAS. For moderate values of the system parameters ($S = 2$, and 4 subbands, $K_{RT} = 2$ users and K_{BE} ranging from 2 to 6 users), the matching-based technique was able to achieve more than 90% of the performance of ES-NOMA-DAS, albeit with a much lower complexity. More precisely, MM-NOMA-DAS requires 2.78% and $5.36\times10^{-4}\%$ of the complexity of ES-NOMA-DAS when $K_{BE} = 6$ users, for 2 and 4 subbands, respectively. Moreover, Fig. 9 shows a comparison of the Pareto Frontier (the achieved data rate of BE users vs. the minimum percentage of satisfied RT users) between ES-NOMA-DAS and MM-NOMA-DAS, for $K_{RT} = K_{BE} = 4$ users and $S = 2$ subbands. It can be clearly seen that the total throughput achieved by BE users decreases when the minimum percentage of satisfied RT users increases. This is due to RT users requiring more resources for a higher percentage of satisfied RT users, leaving fewer resources for BE users. Fig. 9 also shows that the slope of decrease of the exhaustive search method and the matching technique is relatively the same. Moreover, the matching technique achieves 90% of the performance of ES-NOMA-DAS on average, with a much lower complexity. As a conclusion, depending on the system requirements regarding the satisfaction of RT users, a different performance of BE users can be achieved.

VIII. CONCLUSION

In this paper, subband allocation for mixed traffic types was studied for different system settings. For all settings, a new subband allocation method based on matching theory was proposed in such a way to take into account the particularities of each traffic type. Additionally, an iterative approach to determine the number of subbands per antenna for the DAS cases was introduced. The proposed techniques aim at maximizing the satisfaction of RT users while preserving a good performance for BE users. Simulation results showed that the proposed method based on matching theory outperforms the previously introduced greedy method by up to 63% in terms of RT users satisfaction when $K_{RT} = 30$ users. Moreover, the use of DAS in combination with MM was shown to increase satisfaction by more than 30%, compared to its CAS counterpart.

APPENDIX A
PROOF OF THEOREM 1

Suppose that there exists a pair $(k_n, s_i) \notin \Psi^*$ such that (k_n, s_i) forms a blocking pair. According to phases 1 and 2 of Algorithm 1 (as well as Algorithm 3), k_n has already proposed to s_i and was rejected at a certain iteration q, meaning that $\Psi^q(s_i) \succ_{s_i} k_n$, where Ψ^q is the matching state at iteration q. Since $\Psi^*(s_i) \succ_{s_i} \Psi^q(s_i)$, s_i is matched to its final partner $\Psi^*(s_i)$ which it prefers to k_n. Hence, (k_n, s_i) does not form a blocking pair and the matching Ψ^* is stable. It should be noted that a stable matching is guaranteed to exist since the problem is modeled as a one-to-many matching game [29].

APPENDIX B
PROOF OF THEOREM 2

At the beginning of the algorithm, each active user k builds a preference list $\mathcal{PL}_k$ over the S subbands. Therefore, $\mathcal{PL}_k$, $\forall k \in \mathcal{K}$, has initially S elements, hence has a finite size. At each iteration of the algorithm, after subbands make decisions regarding accepted users (or user combinations in the NOMA case), each active user removes the subband it proposed to at the current iteration from its preference list. Hence, as the number of iterations increases, the preference lists of active users become smaller. When the maximum number of iterations is reached, the preference lists of active users become empty and the algorithm converges. Next, the maximum number of iterations needed by each setting is evaluated.

1) OMA-CAS: Each user can propose to, at most, S subbands, leading to a maximum number of iterations of S for OMA-CAS .
2) OMA-DAS: The DAS context involves duplicating each user A times. Hence, the system consists of $A\times K$ virtual

TABLE III
COMPLEXITY ANALYSIS

	OMA-CAS	OMA-DAS	NOMA-CAS	NOMA-DAS
Sorting Complexity	$\mathcal{O}(KS^2)$	$\mathcal{O}(KAS^2)$	$\mathcal{O}((K_{RT}+\lvert\mathcal{US}\rvert)S^2)$	$\mathcal{O}((K_{RT}+\lvert\mathcal{US}\rvert)AS^2)$
Matching Complexity	$\mathcal{O}(KS)$	$\mathcal{O}(KAS)$	$\mathcal{O}((K_{RT}+\lvert\mathcal{US}\rvert)S)$	$\mathcal{O}((K_{RT}+\lvert\mathcal{US}\rvert)AS)$
Overall Complexity	$\mathcal{O}(KS^2)$	$\mathcal{O}(KAS^2)$	$\mathcal{O}((K_{RT}+\lvert\mathcal{US}\rvert)S^2)$	$\mathcal{O}((K_{RT}+\lvert\mathcal{US}\rvert)AS^2)$
Exhaustive Search Complexity	$\mathcal{O}(K^S)$	$\mathcal{O}((K\times A)^S)$	$\mathcal{O}\left((K+P(K,2))^S\right)$	$\mathcal{O}\left(((K+P(K,2))\times A)^S\right)$

users, each having preferences over the S subbands. In addition to that, during each iteration, only one of the duplicated users is allowed to propose to its favorite subband. Therefore, at each iteration, K entries of the preference lists are removed, which leads to the maximum number of iterations being upper bounded by $A \times S$.

3) NOMA-CAS: For NOMA, the matching technique is divided into two stages: assignment of subbands followed by user pairing on the subbands assigned to RT users. In the first stage, since we have S subbands in the system, a user (or user pair) can propose to at most S subbands, meaning that the maximum number of iterations before reaching convergence is also S. For the second stage, the maximum number of iterations is given by the number of subbands assigned to RT users, which is upper bounded by S also. Hence, the maximum number of iterations before the CAS version of Algorithm 3 converges is $2 \times S$.
4) NOMA-DAS: The maximum number of iterations in this case is an extension of the OMA-DAS and NOMA-CAS ones. In the first step of the allocation technique, $A \times S$ is the maximum number of iterations followed by a maximum of S iterations for the second part. Hence, an upper bound for the maximum number of iterations is $S \times (A+1)$.

APPENDIX C
PROOF OF THEOREM 3

The complexity of the proposed matching technique in all system settings is dominated by two steps: 1. sorting the subbands to form the preference lists, 2. the matching step which involves making proposals and decisions. In Table III, the complexity of each system setting is evaluated. For comparison, the complexity of the optimal method based on exhaustive search is also given.

APPENDIX D
PROOF OF THEOREM 4

The number of subbands and antennas of the considered system is limited. Hence, the number of potential assignments of subbands to antennas is finite. Furthermore, system performance is evaluated in terms of RT users satisfaction and BE users sum rate. It can be shown that system performance is enhanced after each iteration. Since system performance has an upper bound because of the limited spectral resources, the iterative approach terminates when this upper bound is reached. Therefore, the number of subbands per antenna can be found in a limited number of iterations.

REFERENCES

[1] E. Dahlman *et al.*, "5G wireless access: Requirements and realization," *IEEE Commun. Mag.*, vol. 52, no. 12, pp. 42–47, Dec. 2014.
[2] M. Katoozian, K. Navaie, and H. Yanikomeroglu, "Utility-based adaptive radio resource allocation in OFDM wireless networks with traffic prioritization," *IEEE Trans. Wireless Commun.*, vol. 8, no. 1, pp. 66–71, Jan. 2009.
[3] W.-C. Chung, C.-J. Chang, and L.-C. Wang, "An intelligent priority resource allocation scheme for LTE-A downlink systems," *IEEE Wireless Commun. Lett.*, vol. 1, no. 3, pp. 241–244, Jun. 2012.
[4] Y.-H. Chung and C.-J. Chang, "A balanced resource scheduling scheme with adaptive priority thresholds for OFDMA downlink systems," *IEEE Trans. Veh. Technol.*, vol. 61, no. 3, pp. 1276–1286, Mar. 2012.
[5] R. Balakrishnan and B. Canberk, "Traffic-aware QoS provisioning and admission control in OFDMA hybrid small cells," *IEEE Trans. Veh. Technol.*, vol. 63, no. 2, pp. 802–810, Feb. 2014.
[6] M. Pischella and J. C. Belfiore, "Resource allocation for QoS-aware OFDMA using distributed network coordination," *IEEE Trans. Veh. Technol.*, vol. 58, no. 4, pp. 1766–1775, May 2009.
[7] Q. Liao, P. Baracca, D. Lopez-Perez, and L. G. Giordano, "Resource scheduling for mixed traffic types with scalable TTI in dynamic TDD systems," in *Proc. IEEE Globecom Workshops (GC Wkshps)*, Dec. 2016, pp. 1–7.
[8] M.-J. Youssef, J. Farah, C. A. Nour, and C. Douillard, "Resource allocation for mixed traffic types in distributed antenna systems using NOMA," in *Proc. IEEE 88th Veh. Technol. Conf. (VTC-Fall)*, Aug. 2018, pp. 1–7.
[9] A. Brighente and S. Tomasin, "Power allocation for non-orthogonal millimeter wave systems with mixed traffic," *IEEE Trans. Wireless Commun.*, vol. 18, no. 1, pp. 432–443, Jan. 2019.
[10] L. Song, Y. Li, Z. Ding, and H. V. Poor, "Resource management in non-orthogonal multiple access networks for 5G and beyond," *IEEE Netw.*, vol. 31, no. 4, pp. 8–14, Jul. 2017.
[11] D. Tse and P. Viswanath, *Fundamentals of Wireless Communication*. Cambridge, U.K.: Cambridge Univ. Press, 2005.
[12] Y. Saito, A. Benjebbour, Y. Kishiyama, and T. Nakamura, "System-level performance evaluation of downlink non-orthogonal multiple access (NOMA)," in *Proc. IEEE Int. Symp. Pers., Indoor Mobile Radio Commun. (PIMRC)*, Sep. 2013, pp. 611–615.
[13] A. Benjebbour, A. Li, Y. Saito, Y. Kishiyama, A. Harada, and T. Nakamura, "System-level performance of downlink NOMA for future LTE enhancements," in *Proc. IEEE Globecom Workshops (GC Wkshps)*, Dec. 2013, pp. 66–70.
[14] M.-Y. Youssef, J. Farah, C. A. Nour, and C. Douillard, "Waterfilling-based resource allocation techniques in downlink non-orthogonal multiple access (NOMA) with single-user MIMO," in *Proc. IEEE Symp. Comput. Commun. (ISCC)*, Jul. 2017, pp. 499–506.
[15] Y. Sun, D. W. K. Ng, Z. Ding, and R. Schober, "Optimal joint power and subcarrier allocation for full-duplex multicarrier non-orthogonal multiple access systems," *IEEE Trans. Commun.*, vol. 65, no. 3, pp. 1077–1091, Mar. 2017.
[16] S. Timotheou and I. Krikidis, "Fairness for non-orthogonal multiple access in 5G systems," *IEEE Signal Process. Lett.*, vol. 22, no. 10, pp. 1647–1651, Oct. 2015.
[17] L. Lei, D. Yuan, and P. Värbrand, "On power minimization for non-orthogonal multiple access (NOMA)," *IEEE Commun. Lett.*, vol. 20, no. 12, pp. 2458–2461, Dec. 2016.
[18] J. Farah, E. Sfeir, C. A. Nour, and C. Douillard, "New resource allocation techniques for base station power reduction in orthogonal and non-orthogonal multiplexing systems," in *Proc. IEEE Int. Conf. Commun. Workshops*, May 2017, pp. 618–624.
[19] Q.-T. Vien, N. Ogbonna, H. X. Nguyen, R. Trestian, and P. Shah, "Non-orthogonal multiple access for wireless downlink in cloud radio access networks," in *Proc. 21th Eur. Wireless Conf.*, May 2015, pp. 1–6.

[20] Q.-T. Vien, T. A. Le, C. V. Phan, and M. O. Agyeman, "An energy-efficient NOMA for small cells in heterogeneous CRAN under QoS constraints," in *Proc. 23th Eur. Wireless Conf.*, May 2017, pp. 1–6.

[21] K. N. Pappi, P. D. Diamantoulakis, and G. K. Karagiannidis, "Distributed uplink-NOMA for cloud radio access networks," *IEEE Commun. Lett.*, vol. 21, no. 10, pp. 2274–2277, Oct. 2017.

[22] X. Gu, X. Ji, Z. Ding, W. Wu, and M. Peng, "Outage probability analysis of non-orthogonal multiple access in cloud radio access networks," *IEEE Commun. Lett.*, vol. 22, no. 1, pp. 149–152, Jan. 2018.

[23] J. Farah, A. Kilzi, C. A. Nour, and C. Douillard, "Power minimization in distributed antenna systems using non-orthogonal multiple access and mutual successive interference cancellation," *IEEE Trans. Veh. Technol.*, vol. 67, no. 12, pp. 11873–11885, Dec. 2018.

[24] B. Zhang, X. Mao, and J.-L. Yu, "Resource allocation for 5G heterogeneous cloud radio access networks with D2D communication: A matching and coalition approach," *IEEE Trans. Veh. Technol.*, vol. 67, no. 7, pp. 5883–5894, Jul. 2018.

[25] W. Liang, Z. Ding, Y. Li, and L. Song, "User pairing for downlink non-orthogonal multiple access networks using matching algorithm," *IEEE Trans. Commun.*, vol. 65, no. 12, pp. 5319–5332, Dec. 2017.

[26] B. Di, S. Bayat, L. Song, and Y. Li, "Radio resource allocation for downlink non-orthogonal multiple access (NOMA) networks using matching theory," in *Proc. IEEE Global Commun. Conf. (GLOBECOM)*, Dec. 2015, pp. 1–6.

[27] J. Zhao, Y. Liu, K. K. Chai, Y. Chen, and M. Elkashlan, "Joint subchannel and power allocation for NOMA enhanced D2D communications," *IEEE Trans. Commun.*, vol. 65, no. 11, pp. 5081–5094, Nov. 2017.

[28] Y. Li, M. Sheng, X. Wang, Y. Shi, and Y. Zhang, "Globally optimal antenna selection and power allocation for energy efficiency maximization in downlink distributed antenna systems," in *Proc. IEEE Global Commun. Conf. (GLOBECOM)*, Dec. 2014, pp. 3856–3861.

[29] D. Gale and L. S. Shapley, "College admissions and the stability of marriage," *Amer. Math. Monthly*, vol. 69, no. 1, pp. 9–15, Jan. 1962.

[30] C. He, G. Y. Li, F. C. Zheng, and X. You, "Energy-efficient resource allocation in OFDM systems with distributed antennas," *IEEE Trans. Veh. Technol.*, vol. 63, no. 3, pp. 1223–1231, Mar. 2014.

[31] Y. L. Lee, L.-C. Wang, T. C. Chuah, and J. Loo, "Joint resource allocation and user association for heterogeneous cloud radio access networks," in *Proc. 28th Int. Teletraffic Congr. (ITC)*, vol. 1, Sep. 2016, pp. 87–93.

[32] J. G. Andrews, "Interference cancellation for cellular systems: A contemporary overview," *IEEE Wireless Commun*, vol. 12, no. 2, pp. 19–29, Apr. 2005.

[33] J. Zhu, J. Wang, Y. Huang, S. He, X. You, and L. Yang, "On optimal power allocation for downlink non-orthogonal multiple access systems," *IEEE J. Sel. Areas Commun.*, vol. 35, no. 12, pp. 2744–2757, Dec. 2017.

[34] Z. Ding, Z. Yang, P. Fan, and H. V. Poor, "On the performance of non-orthogonal multiple access in 5G systems with randomly deployed users," *IEEE Signal Process. Lett.*, vol. 21, no. 12, pp. 1501–1505, Dec. 2014.

[35] A. E. Roth and M. A. O. Sotomayor, "Two-sided matching: A study in game-theoretic modeling and analysis," *Econometric Society Monographs*. Cambridge, U.K.: Cambridge Univ. Press, 1990.

[36] T. Quint, "The core of an m-sided assignment game," *Games Econ. Behav.*, vol. 3, no. 4, 1991.

[37] B. Di, L. Song, and Y. Li, "Sub-channel assignment, power allocation, and user scheduling for non-orthogonal multiple access networks," *IEEE Trans. Wireless Commun.*, vol. 15, no. 11, pp. 7686–7698, Nov. 2016.

[38] M.-R. Hojeij, J. Farah, C. A. Nour, and C. Douillard, "Resource allocation in downlink non-orthogonal multiple access (NOMA) for future radio access," in *Proc. IEEE 81st Veh. Technol. Conf. (VTC Spring)*, May 2015, pp. 1–6.

[39] *Physical Layer Aspects for Evolved Universal Terrestrial Radio Access (UTRA)*, document 3GPP, TR25-814 (V7.1.0), 2006.

[40] R. Jain, D. Chiu, and W. Hawe, "A quantitative measure of fairness and discrimination for resource allocation in shared computer systems," DEC, New Delhi, India, Tech. Rep. 301, Sep. 1984.

Marie-Josepha Youssef received the B.E. and M.S. degrees in computer and communications engineering from Lebanese University, Lebanon, in 2016. She is currently pursuing the Ph.D. degree in information and communication engineering with IMT Atlantique, France. Her current research interests include resource allocation, non-orthogonal multiple access, matching theory, and unmanned aerial vehicles.

Joumana Farah received the B.E. degree in electrical engineering from Lebanese University, Lebanon, in 1998, the M.E. degree in signal, image, and speech processing, the Ph.D. degree in mobile communication systems from the University of Grenoble, France, in 1999 and 2002, respectively, and the Habilitation to Direct Research (HDR) from University Pierre and Marie Curie (Paris VI), France, in 2010. She is currently a full-time Professor with the Faculty of Engineering, Lebanese University. She has supervised a large number of master's and Ph.D. theses. She has nine registered patents and a software and has coauthored a research book and a hundred of articles in international journals and conferences. Her current research interests include resource allocation techniques, channel coding, channel estimation, interference management, and distributed video coding. She serves as a TPC member and a reviewer for several journals and conferences. She received several research grants from the Lebanese National Council for Scientific Research, the Franco-Lebanese CEDRE Program, and Lebanese University. She was the General Chair of the 19th International Conference on Telecommunications (ICT 2012).

Charbel Abdel Nour received the Computer and Communications Engineering degree from Lebanese University in 2002, the master's degree in digital communications from the University of Valenciennes, France, in 2003, and the Ph.D. degree in digital communications from Télécom Bretagne, France, in 2008. From June 2007 to October 2011, he was a Post-Doctoral Fellow with the Electronics Department, Télécom Bretagne. He was involved in several research projects related to broadcasting and satellite communications. He was active in the Digital Video Broadcasting DVB Consortium, where he had important contributions. Since November 2011, he has been an Associate Professor with the Electronics Department, IMT Atlantique. He presented several contributions to the H2020 METIS and FANTASTIC5G projects and to the 3GPP consortium related to coding solutions for 5G. His interests concern the radio mobile communications systems, broadcasting systems, coded modulations, error correcting codes, resource and power allocation for NOMA, waveform design, MIMO, and iterative receivers.

Catherine Douillard received the Engineering degree in telecommunications from the École Nationale Supérieure des Télécommunications de Bretagne, France, in 1988, the Ph.D. degree in electrical engineering from the University of Western Brittany, Brest, France, in 1992, and the accreditation to supervise research from the University of Southern Brittany, Lorient, France, in 2004. She is currently a Full Professor with the Electronics Department, IMT Atlantique, where she is in charge of the Algorithm-Silicon Interaction Research Team. She was active in the Digital Video Broadcasting (DVB) Technical Modules for the definition of DVB-T2, DVB-NGH, as the Chairperson of the Coding, Constellations and Interleaving task force, and DVB-RCS NG standards. Since 2015, she has several contributions in the FANTASTIC-5G and EPIC H2020 European projects intended for the definition of new techniques for 5G and beyond. Her main research interests are turbo codes and iterative decoding, iterative detection, the efficient combination of high spectral efficiency modulation and turbo coding schemes, diversity techniques, and turbo processing for multi-carrier, multi-antenna, and multiple access transmission systems. In 2009, she received the SEE/IEEE Glavieux Award for her contribution to standards and related industrial impact.

3.2.6.3 Mutual SIC strategies in NOMA to enhance the spectral efficiency of coordinated multi-point systems

The large scale deployment of small cells and distributed antenna systems in 5G heterogeneous environments will require more elaborate interference mitigating techniques to increase spectral efficiency and to help unlock the expected performance leaps from the new network topologies.

A direct result of conventional SIC ordering in conventional NOMA systems is that cell-edge users suffer from the intracell interference of other multiplexed users in the cell, and are more vulnerable to Inter-Cell Interference (ICeI) due to their location. To mitigate the ICeI of both OMA and NOMA systems, 3GPP proposed in release 9 [219] and then adopted in release 11 [220] Coordinated MultiPoint (CoMP) as the evolution of enhanced ICeI coordination to improve the performance of interference-prone users. With CoMP, cooperating cells can share the channel state information of users when scheduling is performed. This sharing makes joint scheduling possible. Different CoMP techniques have been proposed in [221, 222]. More elaborate CoMP techniques such as dynamic point selection and Joint Transmission (JT-CoMP) require enough backhaul capacity so that user information is available at every transmission point of the CoMP BSs. In JT-CoMP, signals are transmitted to the user from multiple points, therefore tighter synchronization between JT cells is required.

In all previous studies on NOMA-CoMP, only cell-edge users are considered as potential CoMP users. Also, cell-edge users are not considered able to decode and remove the signals of inner cell users. Finally, user-antenna association for non CoMP users is based on the sole criterion of maximizing channel gain.

During our first study on the use of NOMA in a DAS network described in section 3.2.6, we showed that, under some channel and transmit power conditions, when multiplexed signals are sent from different RRHs, paired users can both cancel the interference of each other, hence the name mutual SIC. Such a configuration corresponds in fact to an intra-site CoMP, behaving as inter-site CoMP [222]. This new concept of mutual SIC relying on CoMP systems makes the combination of NOMA and CoMP much more interesting than their combination using the single SIC approach. Indeed, a complete interference cancellation (intra-cell and inter-cell) among users from the same NOMA cluster (whether cell-edge or cell-center users) becomes possible. Therefore, in this work we studied the combination of NOMA and multicell-CoMP, establishing the conditions enabling a successful mutual SIC procedure at the level of all users, and assessing the performance by means of the system throughput metric.

Concretely, we considered the case of mutual SIC in a two-cell system and enlarge the scope of NOMA application to JT-CoMP. The key contributions of this work can be summarized as follows:

- We proposed to increase the cell-edge user rate and overall system throughput by introducing JT not only for cell-edge but also for cell-centered users. In practice, JT is not necessarily applied to all users on all sub-bands, but may be restricted to users signals transmitted on sub-bands including at least one cell-edge user.

- We studied the conditions for allowing interference cancellation in NOMA for several CoMP scenarios including JT, and showed that applying SIC to the signals of inner users is possible at the level of the cell-edge user.

- We rigorously defined the conditions allowing the feasibility of mutual SIC for any user and apply it to a three-user NOMA cluster.

- We showed that JT is more favorable for enabling interference cancellation than other CoMP scenarios without being a necessary condition for achieving mutual SIC.

- We challenged the common practice of max-received signal strength-based user-antenna association for achieving the highest system capacity, and we favored the associations allowing the much more profitable mutual SIC procedure.

Thanks to these contributions, a highly efficient inter-cell interference cancellation scheme was then devised, that can encompass several deployment configurations and coordination techniques. The obtained results in terms of system throughput and user fairness prove the superiority of this approach compared to conventional NOMA-CoMP systems. These noticeable performance enhancements published in IEEE Transactions on Communications [223] unleashed the potential of this technology in reaching current and future challenges imposed by 5G and beyond systems.

3.3 Summary

NOMA-related studies were intiated in the context of the H2020 FANTASTIC-5G project and were perfomed in collaboration with Joumana Farah, Professor at the Lebanese University. They were also supported by a dedicated patent factory with France Brevets. The results were obtained in the context of 3 PhD theses, the one of Marie-Rita Hojeij already defended followed by the ones of Marie-Josepha Youssef and Antoine Kilzi still running in parallel. They led to 7 journal and 9 conference publications in addition to the filing of 6 patents.

Chapter 4

Future works

4.1 Ongoing work

4.1.1 Coding and modulation-related: Towards Tb/s turbo decoders

4.1.1.1 Motivation and introduction

Wireless communication systems are a driving force for connecting our world. The *third* (3G) and *fourth* (4G) *generation wireless communication systems* brought forth the mobile internet which changed our society. 5G and beyond 5G systems will also bring their share of society changing technologies, like virtual and augmented reality [224] made possible through high-speed fixed wireless broadband connections [225]. Moreover, in the context of the 2020 pandemic crisis the interest in increased connectivity goes well beyond entertainment applications and towards population-wide distance learning and widespread home office programs.

This technological (r-)evolution goes along with a continued increase in demand for higher throughput, lower power consumption and more scalability for all parts of the system including the baseband signal processing on the physical layer. In terms of throughput for example, requirements that go far beyond the tens of Gb/s targeted in the 5G standardization are foreseen. A major source of complexity and power consumption in baseband signal processing for wireless communication systems is the Forward Error Correction. An efficient FEC is therefore crucial for reliable communications.

In 3G and 4G standards, Turbo codes [226] were adopted as FEC codes. Indeed, for standards like Universal Mobile Telecommunications System (UMTS), which only required a throughput of 1 Mb/s in its 1999 release, to LTE, which required 100 Mb/s in the 2008 release, Turbo codes with their excellent error correcting performance. for the targeted error rates, built-in code rate flexibility and ease of encoding were a perfect match. Turbo codes are also used in current and future releases of LTE-A Pro (4G+), which requires a throughput of several Gb/s and support for almost 200 different frame sizes and a wide range of code rates. In terms of error correcting performance, the performed work presented in section 1.4 greatly lowered the error floor of Turbo codes [82], known to be one of its weaknesses. Indeed, contributions to the 5G NR standardization presented in section 1.4.3 (see also [82]) showed Turbo codes at least on a par with the contending code families of LDPC codes [227] and Polar codes [228] in this regard.

Despite these improvements and their advantages, Turbo codes were not adopted in 5G NR in favor of LDPC and Polar codes. One contributing factor to this decision is that this family of codes has been seen at a disadvantage for high-throughput applications because of the inherently serial nature of their decoding algorithm as opposed to the inherently parallel Belief propagation decoding of LDPC codes and the low-complexity successive cancellation decoding of Polar codes [229]. Both LDPC and Polar codes can be decoded with several

hundred Gb/s at the cost of flexibility and coding gain, while most state-of-the-art implementations for Turbo decoders (inherently flexible w.r.t. code rate) achieve less than 10 Gb/s - a throughput-gap of several orders of magnitude [230, 231, 229, 102].

At the same time, the 3GPP standardization committee submitted its 5G solution to meet the International Mobile Telecommunications-2020 (IMT2020) requirements, based jointly on LTE evolution and on the first 5G NR specifications [232]. Being the FEC solution of LTE evolution, the need for high-throughput Turbo decoders (in the order of several Gb/s) becomes a short-term need. Moreover, B5G applications like large-scale virtual/augmented reality, holographic calls, etc, require throughputs even in the order of Tb/s. In summary, any serious FEC code contender for future standards should be able to achieve high throughputs efficiently.

4.1.1.2 Way forward and study items

The higher area efficiency of high-throuhghput LDPC and Polar decoders comes at the cost of a deficit in flexibility with respect to code rate and frame size. Most of the Turbo decoders either are highly flexible with respect to frame sizes, or can be made flexible (i.e. [233]). However, when supported with the classical BCJR decoding algorithm [234], this flexibility represents one of the main factors that lead to the reduced efficiency of Turbo decoders. The consequences are two-fold: first, there is a high potential for lowering Turbo decoder complexity for applications with limited flexibility requirements and second, for applications requiring high flexibility such as mobile broadband, Turbo codes can be clearly superior to LDPC or Polar codes if the factors limiting the achievable throughput for hardware implementations can be overcome.

The road to Tb/s Turbo decoders goes through the joint introduction of profound modifications to their decoding algorithm and to their code design while taking into account implementation and application constraints. In fact, the BCJR [234] or SOVA-based algorithm [235] offered excellent performance while being able to keep up with the throughput requirements up to a few Gb/s, which limited the need and the effort spent to propose viable alternatives. Meanwhile, major modifications were proposed for the other code families towards increasing throughput efficiency. We can clearly cite here the various simplifications of check-node processing for LDPC codes [236, 237, 238] in addition to the structural code design modifications towards more regularity and periodicity such as the introduction of the quasi-cyclic nature of their parity-check matrix.

More than 30 years after their inception, it was the work of Neal & MacKay[227] (and the advent of Turbo codes and iterative processing) that sparked academic interest in LDPC codes. On the other hand, it was not until the publication of the landmark paper of Tal & Vardy [239] and the subsequent addition of Cyclic Redundancy Checks (CRCs) to SC-list decoding [240], four years after the discovery of Polar codes, that they were put on equal footing with the previously unchallenged LDPC and Turbo codes in terms of error correcting performance. Moreover, despite the intensive academic interest following the above mentioned advancements, it took in both cases another 8 years before those codes made their way into standards. These examples illustrate that the age of a code family is not on its own a meaningful metric for potential. Therefore, revisiting 27-year-old Turbo codes, with nowadays advanced knowledge and techniques, in particular recent advances w.r.t. code and decoding algorithm design as well as decoder hardware architectures, can have the potential to transform this code family to appealing contenders for future standardization.

Promising results have been obtained lately for Turbo codes. These mainly include recent advancements made in the context of the B5G European project EPIC (that ends in August 2020) in code and decoding algorithm design [82, 235] as well as in hardware architecture [102, 241, 233] and show, that the factors limiting the achievable throughput for Turbo decoders are

of different nature (in relation to code design, decoding algorithm and hardware architecture), and they can be overcome only if investigated and considered jointly to make the leap across the throughput gap. This is one of the original factors of the proposed new approach that will build on the results obtained in EPIC.

Our recent proposal of Local SOVA algorithm [235] should enable further simplifications since it employs a forward and backward recursion like the conventional Max-Log-MAP algorithm, but features a new way of computing the extrinsic information. This new way is based upon a new path-merging operation which leads to a hierarchical structure and allows for a reduction in the computational complexity for high radix orders. Indeed in [235], a computational complexity reduction of around 30% w.r.t. addition and comparison operations is shown for radix orders 4 and 8 on the example of the (8-state) LTE code. We know that the reductions in computational complexity do not necessarily translate into similar levels of reductions in area for implementation. Therefore in collaboration with my colleaugue, associate professor Stefan Weithoffer, recent work is targeting the efficient implementation of Local SOVA.

	Max-Log-MAP	**Local-SOVA**	**Area Saving**
Recursion unit	Cell area [μm]		
Radix-2	1639	1777	-7.7%
Radix-4	3885	4078	-4.7%
Soft-output unit	Cell area [μm]		
Radix-2	3190	3186	0.1%
Radix-4	10458	5268	**49.6%**
Sum	Cell area [μm]		
Radix-2	4829	4963	-2.7%
Radix-4	14343	9346	**34.8%**

Table 4.1: Post place & route cell area comparison for the computational units of Max-Log-MAP and Local-SOVA in 28nm FDSOI technology @ 800MHz target frequency.

Our preliminary, still unpublished implementation results for radix 4 confirm that this new algorithm provides a significant complexity reduction. In fact, we even achieved an area reduction of around 50% for the soft output unit and total area savings of approximately 35% in comparison to the overall area for the respective Max-Log-MAP units (see Table 4.1), exceeding the projections of [235]. Larger area savings in comparison to Max-Log-MAP are expected when increasing the radix order to 8 and beyond. Confirming this tendency to exceed complexity reductions predicted by [235] is of high interest and is therefore at the heart of the currently performed work. Indeed thanks to its path-based extrinsic computation, Local SOVA has the potential to efficiently manage parallel trellis paths seen for high radix orders by avoiding a large increase in the hardware critical path.

These results suggest that the Local-SOVA algorithm combined with the Unrolled X Maximum A Posteriori (UXMAP) hardware architecture as well as applying an afterburner as we recently proposed in [233] has the potential to raise the achievable throughput to hundreds of Gb/s at an affordable complexity.

4.1.2 FBMC-related: Towards a complete solution for waveform design beyond 5G

The work performed for the proposal of a FBMC/OQAM waveform solution has addressed several previously identified open issues. The aim in the short term is to address remaining open points towards a complete waveform solution supported by a hardware proof of concept.

4.1.2.1 PAPR reduction for FBMC with short ProFs

One of the remaining issues of FBMC concerns its high PAPR. If we assume that an infinite number of FBMC symbols are successively transmitted, the PAPR of the FBMC signal is the same as the one obtained with OFDM, independently of the chosen ProF. In practice, frames have finite duration, and the ramp-up and ramp-down of the FBMC signal, at the beginning and the end of each frame, introduce a slight increase in the PAPR. More concerning, the precoding techniques employed in OFDM to reduce the PAPR, such as the FFT precoder in Single Carrier OFDM (SC-OFDM), cannot be applied in a straightforward manner to FBMC due to the OQAM scheme. When adapted to support FBMC, the obtained PAPR reduction is not as significant as in the OFDM case. In fact, the achieved reduction depends on the overlapping factor K, and it is observed that a short ProF ($K = 1$) can potentially reach higher PAPR reduction than long ProFs ($K = 4$). However, regardless of the filter type, precoded FBMC has higher PAPR than precoded OFDM. In addition, FBMC is more sensitive to high power amplifier non-linearity than OFDM. Particularly, it was observed that FBMC can suffer from spectral regrowth in this case. The spectral confinement is highly degraded, losing one of the main advantage of FBMC over OFDM. For this reason, it is highly important to investigate solutions to reduce the PAPR favoring further the introduction in real world applications.

In a recent article, a FFT-based precoding combined with a low-complexity, Selective Mapping (SLM) technique was proposed for FBMC [242]. The SLM technique [243] consists of transmitting the QAM symbols with C different phase rotations or interleaving schemes. From the C resulting modulated signals, the one having the lowest PAPR is chosen. Then, the index of the chosen signal is separately transmitted as a SI. This technique is typically highly complex and not efficient in terms of data rate. However, the proposed SLM in [242] for FBMC only requires a SI of 2 bits per FBMC symbol. Furthermore, the processing is applied in time domain, after FFT, reducing the complexity. The results show that FBMC with the MMB4 can achieve lower PAPR than OFDM. Since the simple use of short ProFs generally enables to further reduce the PAPR when compared to long ProFs, adapting such technique for short ProFs is expected to largely solve this issue.

4.1.2.2 Enrichment of the proof-of-concept waveform platform

The current platform simulates 5G scenarios where Line-of-Sight (LoS) propagation is considered. A possible improvement consists in integrating a dedicated real-time channel emulator in the platform. Initial work towards the development of such an emulator has been already started. It is based on the technique presented in [47], which consists of using an OS algorithm (based on FFTs) to generate in real-time and at low memory cost the channel coefficients (Rayleigh sequences correlated with Doppler).

In our previous works, we focused on the hardware implementation of the waveform transmitter, since this is the most critical component in terms of complexity and energy-consumption for uplink communication. At the receiver side, only typical FBMC receivers have been implemented. However, we have proposed novel OS-FBMC and OSB-FBMC receiver techniques. These receivers use typical processing units such as FFT and FIR filters. Therefore, the design and implementation of an optimized hardware architecture for these receivers are considered in the short term.

Finally, the current platform only supports single channel point-to-point communication. Since MIMO techniques are widely investigated for 5G and beyond, a considerable improvement of the platform could be to integrate the support of this technology.

4.1.3 NOMA-related: Drone-assisted communications

The use of Unmanned Aerial Vehicles (UAV) as flying base stations in wireless communication systems has received a lot of attention in recent literature [244]. Indeed, the major capabilities of UAVs reside in their fast and cost-effective setup and their virtually unconstrained mobility in the aerial space, largely improving the probability of LoS communication. Unlike terrestrial mobile base stations that are bound by road maps and traffic light constraints for circulation, UAVs can move freely through space to cope with the evolving demand for service or network reconfiguration. Owing to their mobility, flexibility and low cost, UAV-BSs can help increase the throughput and coverage of traditional communication systems [245].

Many applications require such key capabilities, ranging from natural disaster scenarios like floods, hurricanes and tornadoes, to public safety communication, and temporary crowded events like concerts in football stadiums or large festivals. They can surely help alleviate traffic congestion in hotspot areas, as well as establish communication links in remote and disaster areas where the existing communication infrastructure is either non-existent or damaged [246]. Deploying additional small cells especially for that matter equates to large expenditure costs for small periods of time, hence the inefficiency of such approaches. Relying on UAVs for these systems is an appealing feature thanks to their on-demand service capabilities, their adjustable position in real time, and their cost-effective deployment.

4.1.3.1 In-band full-duplex and backhaul-constrained drone-enabled networks using NOMA

Accounting for the limited on-board energy of the UAV, the work in [247] investigated the optimal location of the UAV to minimize its transmit power. The authors in [248] evaluated the optimal UAV altitude that maximizes its coverage region. In [249], the authors built on the results of [248] and found the 3D location of the UAV that maximizes the coverage for users having different QoS requirements.

However, none of the works in [247, 248, 249] accounted for the backhaul link of UAVs. Contrary to most terrestrial BSs, UAVs are connected to the core network through a wireless backhaul link [246]. To be able to reap the benefits promised by the use of UAVs in communication systems, there is a need to dynamically manage this backhaul link according to the traffic state of the network [244]. In fact, if not configured properly, the backhaul link may introduce interference, thus limiting the throughput provided by the UAV in the access link. To increase the spectral efficiency and reduce the latency of systems relying on a wireless backhaul, In-Band Full-Duplex (IBFD) communications were recently investigated [250]. IBFD allows the simultaneous transmission and reception of backhaul and access information in the same frequency band, at the expense of a Self-Interference (SeI), caused by the transmitter to its own receiver. That said, SeI cancellation schemes have progressed significantly [251], allowing an efficient application of IBFD for wireless backhauling.

Few works have addressed the wireless backhaul link in the context of UAV-enabled networks. The authors in [246] investigated the 3D placement problem of the UAV for the sake of maximizing the number of served users while considering a backhaul link with constant transmission rate. Others assumed that access and backhaul transmissions take place on different and sufficiently spaced frequency bands to avoid SeI.

In this new work in progress, we consider a scenario where the traditional wireless infrastructure is missing, e.g. in remote areas or due to a disaster or BS failure. A UAV is dispatched to serve users having QoS requirements in that area, and an in-band wireless backhaul link is established between the UAV and a macro base station to provide the needed backhaul capacity as seen in Fig. 4.1. For a given UAV altitude H, $C_k(H)$ represents the maximum 2D distance between the UAV and user k guaranteeing the required user rate R_k^{req},

i.e. $C_k(H) = r|_{L_{(H,r)}=L_k^{\text{th}}}$. G terms in Fig. 4.1 represent channel gains, specifically, $G_{k,s}$ is the channel gain between the Master BS (MBS) and each user k over subband s, consisting of both small-scale and large-scale fading.

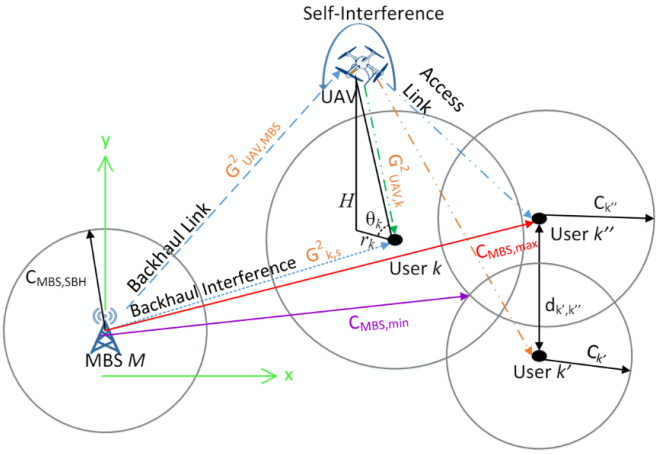

Figure 4.1: System model for IBFD backhaul-constrained UAV assisted networks.

To minimize the UAV transmit power, an optimization problem that finds the assignment of subbands in the backhaul link, the 3D position of the UAV as well as the power levels in the access and backhaul links is described and currently being solved. In fact, the proposed solution is intended to minimize the UAV transmit power necessary to meet the rate requirements of the users, while respecting the backhaul capacity and the power budgets of the UAV and the BS. Initial results have shown that by adopting the proposed approach, the needed power significantly decreases, compared to the case of a UAV-enabled network that separates between the frequency used in the access and the backhaul link, as well as a traditional network.

An extension of this work is planned for the case where the UAV power budget is insufficient to fulfil rate requirements by conducting NOMA pairing to enhance system performance. By using this extension, both the achieved sum rate and the percentage of satisfied users are expected to significantly increase when compared to a strategy that uses separate frequency bands in the access and backhaul links, as well as to the above-mentioned proposed OMA-based method.

4.1.3.2 Drone placement for mutual SIC optimization in two-cell NOMA CoMP systems

The integration of UAVs as aerial base stations supporting the ground network will require a better management of the system resources in time and frequency, since the backhaul link between the UAV and the network needs to be established and the hand-off procedures as well as low latency control need to be guaranteed. CoMP systems [221, 222] provide such a framework of cooperation between adjacent cells. In CoMP, cells can share the channel state information of users when performing joint scheduling.

In the planned study, we will consider JT-CoMP where signals are transmitted to each user from two transmission points. In a previous work, we studied the combination of NOMA with CoMP for a two-cell system [223]. A full JT system over NOMA clusters of two and three users was studied showing significant advantages over partial JT (where JT is only used for cell-edge users). Sending the NOMA signals from different transmission points enabled mutual SIC between users, i.e. all users canceling the signals of each other at the same time. This led to defining the conditions of Dual Mutual SIC (DMSIC) and Triple Mutual SIC

(TMSIC) for two or three-user clusters respectively. The obtained interference-free NOMA clusters provided significantly better performance results than classical NOMA schemes in terms of spectral efficiency as well as fairness among users.

Therefore, in the following, UAV positioning is done to favor TMSIC application. The considered system is shown in Fig. 4.2. UAV positioning procedures will be proposed to best alleviate the load on the congested cell. We particularly aim at enhancing system spectral efficiency through a fairer serving of cell-edge users as well as cell-centered users of the two adjacent cells. The goal is to place the UAV such that the TMSIC conditions are satisfied, thus optimizing both throughput and fairness.

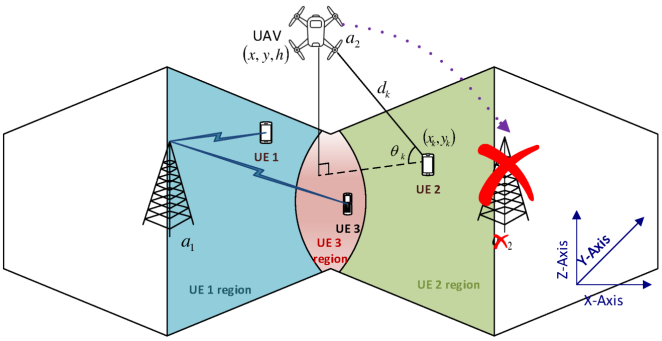

Figure 4.2: Illustration of the two-cell JT system with the functional base station a_1, the saturated BS in cell 2, the UAV working as MBS a_2, and the three colored user regions.

The planned contributions can be summarized as follows:

- The study of the UAV positioning problem while taking into account the specificity of LoS/NLoS propagation between users and the UAV, instead of the mean path loss model.
- The elaboration of a probabilistic framework that enables the calculation of the TMSIC probability associated to the UAV position. This enables the formulation of a UAV positioning problem to maximize the chances of TMSIC between users.
- The proposal of several positioning techniques with different optimization criteria.
- The comparison of the proposals to positioning techniques based on traditional mean path loss consideration, in terms of achieved throughput and fairness.

4.2 Long term future work

4.2.1 Towards efficient Tb/s turbo decoders

Building on the recent advancements obtained in H2020 project EPIC, future works target the improvement of hardware efficiency in terms of chip area and power consumption. Indeed, the first step currently being achieved is the ability to reach these high throughput levels. Then, efforts should be made to allow for such high throughput schemes to be sufficiently appealing for adoption in standards/applications through an efficient support of available resources in terms of chip area and power consumption. This goes through an additional reduction in the number of required operations per decoded bit through algorithmic simplifications at the cost of performance penalty on one side or flexibility on the other side.

Up to now, the different parameters determining the area efficiency for UXMAP decoders have been investigated separately. A joint framework will be set up for a future exploration

based on the architecture of Fig. 4.3. Table 4.2 lists the corresponding main parameters of the UXMAP architecture and their prime trade-offs. In order to achieve this goal, their trade-offs have to be considered jointly to make the leap across the throughput gap. This framework will set the pace of a long future exploration in collaboration with Stefan Weithoffer. A young researcher french national project was jointly submitted in this regard.

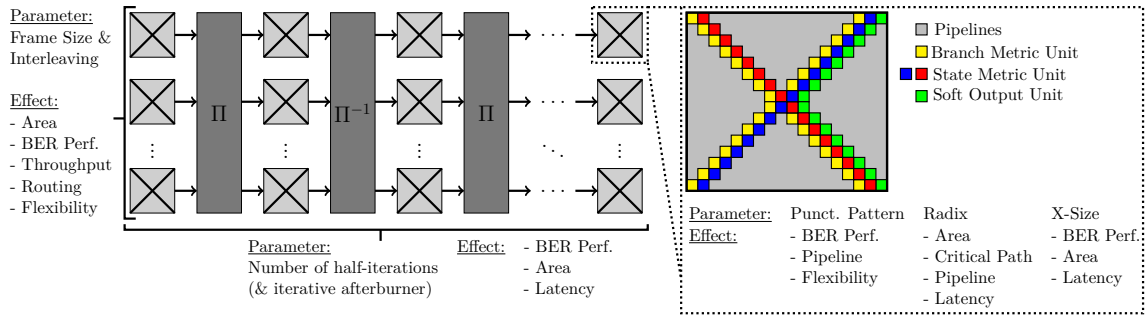

Figure 4.3: UXMAP architecture framework, prime parameters and their effects.

Part of the future work will focus on the interplay of using high-radix computations, reduced number of iterations and reduced X-sizes to achieve improvements in area efficiency. Since it is well known that for a MAP-based Turbo decoder, the critical path lies in the (ACS) operations of the state metric computation, state-of-the-art Turbo decoders typically employ radix orders lower than 8. Moreover, increasing the radix order of the computations will in itself not increase the decoder throughput of a pipelined architecture. The size and length of the local pipelines within each window nevertheless vary with the radix order and significant area savings in the pipelines will allow larger frame sizes, which will in turn increase the decoder throughput since complete frames are processed while progressing through the pipeline (see also [102]).

Parameter	Main Trade-offs
Radix	Area / Frequency (= Throughput), (Pipeline-)Area / Power
Number of iterations	Power / BER Perf., Area / BER Perf.
Window-size	Area / BER Perf.
Frame size	Throughput / BER Perf., Area / BER Perf.
Interleaving	Frame size flexibility, Area (through routing) / BER Perf.
Puncturing Pattern	Code rate flexibility / (Pipeline-)Area
Coupling depth	Num. of iterations / coupling depth, Area / BER Perf.

Table 4.2: Main parameters and trade-offs for the proposed framework.

Achieving a high-radix-order computation without substantially increasing the critical path (i.e. via employing the Local-SOVA [235]) will therefore lead to a higher throughput, especially since, for the fully-pipelined UXMAP, there is a linear relation between frequency and throughput. A higher operating frequency, on the other hand, will increase the power consumption significantly. Another route towards improving the area efficiency goes through limiting the level of code rate flexibility, i.e. introducing a limitation to certain (high) code rates, in connection with the path-based Local-SOVA algorithm and/or varying the size of the windows (i.e. the number of processed trellis steps). In both cases, a loss in BER performance can be expected, but also a reduction in area consumption through reduced pipeline sizes and complexity-reduced high-radix decoding. The BER performance / area trade-off can then again be alleviated by balancing it with the number of instantiated half-iteration pipeline stages.

From this example, it becomes clear that the optimal trade-offs can only be found if parameters related to algorithm (i.e. window-size, radix order), code design (i.e. code rate and puncturing patterns) and hardware implementation are investigated and optimized jointly. Finding optimal trade-offs represent a long term research axis.

4.2.2 FEC code construction using genetic and AI-based algorithms

FEC code construction generally relies on well-identified performance indicators of coding theory such as Hamming distance, performance at low SNR, etc. Tuning these indicators has a large impact on code performance. Therefore, the code design problem can be translated into a problem of optimizing the corresponding performance indicators.

Recently, Artificial Intelligence (AI) techniques have been widely applied to many industry and research domains, thanks to advances in algorithms, an abundance of data, and improvements in computational capabilities. In fact, in the field of communication systems, transceivers built by AI algorithms have been investigated. Without applying particular channel coding or modulation related techniques, [252] proposed to optimize an entire transceiver given a channel model. In [253], a particular encoding/decoding was proposed through the application of recurrent Neural Network (NN) for the case of AWGN channel with feedback. It was reported that NN-based decoding could approach MAP performance for short codes [254] by regarding a channel decoder as a classifier. Even successful decoding of some untrained codewords was reported for highly structured codes. However, the classification complexity is proportional to the number of codewords. Since the code space expands exponentially with the code length, the NN-based decoder is still far from satisfying complexity and latency constraints of nowadays physical layer.

Differently, the planned future work relies on using AI techniques to design codes rather than to directly encode and decode signals. One major advantage is that code design can be done offline where the latency constraint is not an issue. Moreover, we can continue to use legacy encoding and decoding algorithms as they already apply efficient and flexible hardware and software implementations. Thanks to our expertise in designing turbo codes, we will focus first on this family of codes. In particular, interleaver definition remains one of the appealing applications for such an approach. The introduced structuring and periodicity through the incremental ARP design method that we proposed in [82] represents a good fit. Several innovative algorithms can be used in this context. However, we will mainly focus on Reinforcement Learning (RL) and genetic algorithms. Specifically, I think that the multiplayer Multi-Armed Bandits (MAB) framework [255] can be particularly useful. By applying a 2-step incremental MAB approach, the first being the definition of the inter-layer shifts and the second being the intra-layer shifts [82], the complete interleaver parameters can be defined through the evaluation of a MAB "reward" function defined for the bit positions before/after interleaving.

4.2.3 Massive MIMO FBMC-OQAM

As a promising technology for future communication systems, massive MIMO techniques are currently widely investigated in the literature. In a typical massive MIMO scenario, each UE has a few number of antennas (between one and four), while the BS disposes of a larger number of antennas, generally between 32 and 256. This large number of antennas offers diversity gain and can serve multiple users occupying the same time and frequency resources, which increases the channel capacity.

Its association with FBMC is starting to be investigated [256][257]. Massive MIMO's so-called self-equalization property leading to a channel flattening effect was reported through simulations in [258, 259] for their association with FBMC. According to this property, the

effects of channel distortions (i.e., intersymbol interference and intercarrier interference) will diminish by increasing the number of BS antennas. However, it was shown in [260] that the self-equalization property shown through simulations and claimed in [258, 259] is not very accurate. More specifically, by increasing the number of BS antennas, the channel distortions average out only up to a certain extent, but not completely. Thus, the Signal-to-interference-plus-noise ratio (SINR) saturates at a certain deterministic level. This determines an upper bound for the SINR performance of the system. Indeed, in [260] the authors derive an analytical expression for this saturation level, and propose a long prototype filter design method to resolve the problem. With the proposed long prototype filter in place, SINR grows without a bound by increasing the BS array size, and arbitrarily large SINR values are achievable. However, these studies focus on a FBMC system using a long ProF.

Therefore, it is still an open question how short ProFs can perform (in terms of BER, latency, etc.) when compared to long ProFs for massive MIMO. If it is possible to achieve the self-equalization property of massive MIMO for such short filters is still to be answered. To achieve that, it is likely that specific constraints should also be applied on short filters. This is of high importance since short ProFs can provide several advantages in this context: Particularly, Time-Division Duplex (TDD) transmission being privileged for massive MIMO, the reduced frame duration when using a short ProF may be advantageous for such applications. Moreover, similarly to the SISO case, BER performance gain is obtained when using a FS-FBMC receiver compared to a typical PPN-FBMC receiver [261]. This type of receiver becomes viable with such short ProF filters. Also, the multi-tap equalization of [259] can be used to improve the equalization accuracy compared to the single-tap equalization per subcarrier at the expense of a higher computational complexity, now affordable thanks to the reduced complexity of the short filter.

For all of these reasons, a study targeting the extension of all obtained results to the case of massive MIMO is scheduled for the long run.

4.2.4 D2D communications underlaying cellular networks

The growth of the number of connected devices has hit unprecedented highs in the last few years. Indeed, their number is expected to be more than three times the world population by 2023. The corresponding network densification, coupled with the expected increase in data traffic and the limited available spectrum, will require novel efficient solutions to supply the ever increasing demand. Full-Duplex (FD) communication combined with Device-to-Device (D2D) communication represent an attractive solution to leverage the challenges of future generation networks.

D2D enables direct communication between nearby devices with little to no information transiting through the network BSs. The D2D communication rate, in this regard, is alleviated from the network which can use the freed capacity to serve other users, hence increasing the number of accommodated devices. FD communication enables a node to send and receive simultaneously using the same frequency resource. In theory, the achieved gain is a two-fold increase in spectral efficiency compared to half-duplex send-then-receive systems. However, a self interference is incurred due to the transmitted signal looping back into the receiver, thus limiting its appeal compared to half-duplex to the point where this latter may even outperform FD in some cases. Nonetheless, the improvement in antenna architecture and in SeI cancellation circuitry dramatically reduces the residual SeI [262, 263], largely improving their appeal for adoption in future standards.

At the same time, the same need in increasing demand for connected devices pushed research into the direction of NOMA techniques. Indeed, multiple devices can share the same time and frequency resource but are differentiated in a non-orthogonal dimension, e.g. power-domain for PD-NOMA [183].

In our previous works [214, 213, 223], we introduced the concept of mutual SIC, where we showed that the signals of two or more users multiplexed in NOMA, and powered by distributed antennas, can be decoded and removed at the level of every user in the NOMA cluster. This opens a new perspective in the use and usefulness of NOMA. In fact in addition to the sharing of system resources, NOMA can now be used to manage interference between user cluster or different type of users.

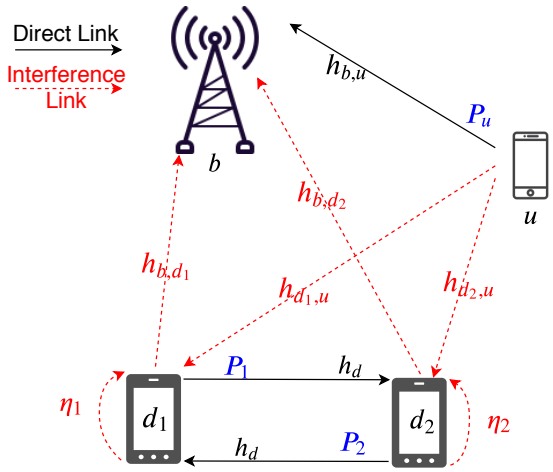

Figure 4.4: FD inband underlay communication sharing the uplink resource of a cellular user.

NOMA has not been applied between cellular and D2D users; and even less for the case of FD-D2D underlay. We mean by NOMA between D2D and cellular users, the intervention of the BS in signalling and power control to enable the interference cancellation of D2D signals at the level of the BS, and the cancellation of the intereference of the cellular user's message at the level of the D2D pair. This can be done by applying mutual SIC between the D2D pair and the BS. The system to be studied is shown in Fig. 4.4. The necessary SIC constraints in terms of power multiplexing conditions and rate conditions would need to be identified and derived. Also, the power allocation needs to be formulated and solved for the cases of half and FD transmissions, as well as for SIC-enabled and disabled scenarios. This is a first step in a long term study where I intend to extend the concept of mutual SIC to all possible applications or real-world scenarios that are interference limited.

4.2.5 Support of grant-free or uncoordinated multiple access through learning algorithms and/or NOMA

With the introduction of the internet of Things, wireless communication networks are faced with an increasingly growing number of Machine-Type-Devices (MTD) [264]. This type of traffic presents specificities in contrast with traditional human user traffic. In this latter case, the focus is on increasing the data rates of the downlink with a "fair" distribution of available frequency and power. However, MTD applications (e.g. smart meters, e-health, etc.) generally result in mobile traffic that mostly relies on the uplink transmission of short packet messages. Compared to the small packet sizes of useful information, the signalling overhead resulting from acquiring the channel state information at MTDs and sending scheduling requests to a central unit is large. Therefore, optimizing the uplink scheduling of MTDs for an efficient spectrum use is of utmost importance. Indeed, to ensure the successful support of MTDs, cellular networks must be developed with the new MTD traffic characteristics in mind.

Uncoordinated spectrum access have received significant interest in recent literature [265, 266, 267, 268, 269, 270, 271]. In a system relying on uncoordinated spectrum access, a

user chooses a channel and transmits whenever it has data to send, without formulating any scheduling request to the receiver or to a control unit. By doing so, the handshake required to receive a scheduling slot is avoided, reducing the transmission latency and the signalling overhead. Because of the distributed nature and the lack of coordination in the resulting spectrum access, the problem of collisions arises. A collision occurs when multiple users choose the same channel for transmission. In this case, the receiver cannot distinguish between the collided messages, leading to a failed reception of all colliding transmissions. To avoid collisions, two techniques can be leveraged. One is to apply novel multiple access techniques, such as NOMA [268] which allows the successful scheduling of multiple users on the same channel by exploiting the power domain for example. The other is to exploit learning algorithms so users can distributively adjust their transmissions, minimizing the number of collisions.

The long-term research will focus first on the latter technique, then on the use of NOMA, leaving the study of the combination of both solutions at last.

As a starting step, the exploration of existing state-of-the-art on the subject shows that the use of RL for uncoordinated spectrum access has recently gathered a lot of attention. To maximize the accumulated data rate and the number of successful transmissions, [266] and [267] adopt Q-learning, while [268] considers a NOMA system and applies deep RL. Moreover, the multi-player MAB framework [255] has been widely used to study uncoordinated spectrum access. In this framework, users learn how to dynamically adjust their transmissions on the available channels to optimize system performance. The work in [272] and [273] uses the MAB model to study the opportunistic spectrum access problem in cognitive radio networks where secondary users compete to access the part of the spectrum not occupied by primary users. In contrast, the authors of [269] and [270] employ MAB to study the uncoordinated spectrum access problem without distinguishing between the users.

Most of the previous MAB related studies assumed that the reward distribution for each channel is the same across users [269, 274, 272]. However, in wireless networks, this assumption may not hold since users perceive the channels differently. Moreover, all previous work employing MAB for uncoordinated spectrum access have restricted each user to transmit on one channel. In addition, only few studies [275, 276] consider the MAB problem with multiple arm plays, but are restricted to the single-player case. In wireless networks, allowing users to choose multiple channels for transmission enhances the achieved performance and increases the probability of a successful transmission.

To round-up this first step, we have seen that the proposal of solutions based on learning algorithms is still in its starting phases. Indeed in general, we can say that system-based assumptions are made in a way to simplify the studied problem regardless from its applicability to real-world scenarios and/or applications. This is where our planned future work should make its largest impact. Indeed, we intend to study realistic scenarios starting from the uplink of an uncoordinated spectrum access wireless system, where users aim to dynamically adjust their transmissions, without communicating with each other, to avoid collisions and optimize system performance. In addition to considering varying channel conditions between users, we intend to study the case where each user can choose multiple channels at each timeslot. This would be the first work that studies the problem of multi-player MAB with multiple plays and varying channel conditions across users. It is a necessary step towards a fully functional realistic solution.

4.3 Conclusions

Some of the short term future works are currently being conducted through the still-running PhD theses of Marie-Josepha Youssef, Antoine Kilzi, Vinh Hoang Son Le and Titouan Gen-

dron. In order to cover long term research, I have recently acquired some funding from the *Institut Carnot* for supporting a 1 year Postdoctoral fellowship for Rami Klaimi to work on coding/decoding aspects. In addition, a collaboration is currently being set into motion with Stefan Weithoffer via his submission of a young researcher grant to finance a PhD and a Postdoctoral fellow on the topic of efficient high-throughput decoding. If successful, in addition to the acquired funding through the ANR QCSP project still running for more than 2 years, these actions would secure the planned actions in coding/decoding. Planned resource allocation/NOMA/ uncoordinated spectrum access work is currently the subject of potential collaborations with industrial and collaborative projects.

List of publications

Patents

[P1] Rami Klaimi, Charbel Abdel Nour, and Catherine Douillard. Procédé de codage d'un signal numérique d'entrée, 2020. Patent number FR2003223.

[P2] Marie Rita Hojeij, Charbel Abdel Nour, Joumana Farah, and Catherine Douillard. User distribution to sub-bands in multiple access communications systems, March 2018. Patent number EP18305353.

[P3] Marie Rita Hojeij, Charbel Abdel Nour, Joumana Farah, and Catherine Douillard. Method and apparatus for user distribution to sub-bands in multiple access communications systems, March 2018. Patent number EP18305352.

[P4] Marie Rita Hojeij, Charbel Abdel Nour, Joumana Farah, and Catherine Douillard. Method and apparatus for power distribution to sub-bands in multiple access communications systems, March 2018. Patent number EP18305355.

[P5] Marie Rita Hojeij, Charbel Abdel Nour, Joumana Farah, and Catherine Douillard. Method and apparatus for user distribution to sub-bands in multiple access communications systems, March 2018. Patent number EP18305354.

[P6] Rami Klaimi, Charbel Abdel Nour, and Catherine Douillard. Procédé de génération d'un signal mettant en oeuvre un turbo-codeur, dispositif et programme d'ordinateur correspondant, December 2018. Patent number FR1873615.

[P7] Jérémy Nadal, Charbel Abdel Nour, and Amer Baghdadi. Pseudo-guard intervals insertion in an FBMC transmitter, March 2018. Patent number EP18305251.

[P8] Ronald Garzón Bohórquez, Charbel Abdel Nour, and Catherine Douillard. Procédés et dispositifs de codage à rendement compatible, March 2017. Patent number FR1752273.

[P9] Jérémy Nadal, Charbel Abdel Nour, and Amer Baghdadi. Overlap-Save FBMC receiver, October 2017. Patent number EP17306395.

[P10] Marie Rita Hojeij, Charbel Abdel Nour, Joumana Farah, and Catherine Douillard. Method and apparatus for power and user distribution to sub-bands in NOMA systems, July 2016. Patent number EP16305929.

[P11] Ronald Garzon Bohorquez, Charbel Abdel Nour, and Catherine Douillard. Procédé de codage d'un message numérique d'entrée mettant en oeuvre un turbo-encodeur, programme d'ordinateur et turbo-encodeur correspondants, December 2016. Patent number WO2016203039.

[P12] Naila Lahbabi, Hao Lin, Charbel Abdel Nour, and Catherine Douillard. Procédé de génération d'un signal multiporteuse, dispositif et programme d'ordinateur correspondant, October 2016. Patent number FR1659988.

[P13] Jérémy Nadal, Charbel Abdel Nour, and Amer Baghdadi. Receiver architecture for linear modulation based communication systems, June 2016. Patent number EP16305752.

[P14] Jérémy Nadal, Charbel Abdel Nour, and Amer Baghdadi. Digital encoder and method of encoding, August 2016. Patent number EP16306056.

[P15] Jérémy Nadal, Charbel Abdel Nour, and Amer Baghdadi. Filter for linear modulation based communication systems, April 2016. Patent number EP16305462.

[P16] Marie Rita Hojeij, Charbel Abdel Nour, Joumana Farah, and Catherine Douillard. Method and apparatus for user distribution to sub-bands in NOMA systems, December 2016. Patent number EP16306722.

[P17] Charbel Abdel Nour and Catherine Douillard. Method and device for Space-Time encoding, September 2011. Patent number WO2011104377.

[P18] Charbel Abdel Nour and Catherine Douillard. Modulation codée avec entrelacement des voies I et Q et rotation optimisée, February 2008. Patent number WO2009103746.

Book chapters

[B1] Frank Schaich, Catherine Douillard, Charbel Abdel Nour, Malte Schellmann, Tommy Svensson, Hao Lin, Honglei Miao, Hua Wang, Jian Luo, Milos Tesanovic, Nuno Pratas, Sandra Roger, and Thorsten Wild. Antenna, PHY and MAC Design. In *5G System Design: Architectural and Functional Considerations and Long Term Research*. April 2018.

[B2] Catherine Douillard and Charbel Abdel Nour. Chapter 11. Bit interleaved coding and modulation in next generation DVB-NGH. In *Next Generation Mobile Broadcasting*, pages 321 – 354. CRC Press, 2013.

Journal publications

[J1] Jeremy Nadal, Francois Leduc-Primeau, Charbel Abdel Nour, and Amer Baghdadi. Overlap-save FBMC receivers. *IEEE Transactions on Wireless Communications*, 2020.

[J2] Rami Klaimi, Charbel Abdel Nour, Catherine Douillard, and Joumana Farah. Union bound evaluation for non-binary turbo coded modulations. *IEEE Communications Letters*, 2020.

[J3] Vinh Hoang Son Le, Charbel Abdel Nour, Emmanuel Boutillon, and Catherine Douillard. Revisiting the Max-Log-Map algorithm with SOVA updates rules: new simplifications for high-radix SISO decoders. *IEEE Transactions on Communications*, 68(4):1991–2004, 2020.

[J4] Marie-Josépha Youssef, Joumana Farah, Charbel Abdel Nour, and Catherine Douillard. Resource Allocation in NOMA Systems for Centralized and Distributed Antennas with Mixed Traffic using Matching Theory. *IEEE Transactions on Communications*, 68(1):414–428, January 2020.

[J5] Antoine Kilzi, Joumana Farah, Charbel Abdel Nour, and Catherine Douillard. Mutual Successive Interference Cancellation Strategies in NOMA for Enhancing the Spectral Efficiency of CoMP Systems. *IEEE Transactions on Communications*, 68(2):1213–1226, October 2019.

[J6] Jon Barrueco Gutierrez, Jon Montalban, Pablo Angueira, Charbel Abdel Nour, and Catherine Douillard. Low Complexity Adaptive Demapper for 2-D Non-Uniform Constellations. *IEEE Transactions on Broadcasting*, 65(1):10–19, March 2019.

[J7] Antoine Kilzi, Joumana Farah, Charbel Abdel Nour, and Catherine Douillard. New Power Minimization Techniques in Hybrid Distributed Antenna Systems with Orthogonal and Non Orthogonal Multiple Access. *IEEE Transactions on Green Communications and Networking*, 3(3):679–690, May 2019.

[J8] Jérémy Nadal, Charbel Abdel Nour, and Amer Baghdadi. Design and Evaluation of a Novel Short Prototype Filter for FBMC/OQAM Modulation. *IEEE access*, 6:19610–19625, March 2018.

[J9] Tarak Arbi, Benoit Geller, Jianxiao Yang, Charbel Abdel Nour, and Olivier Rioul. Uniformly Projected RCQD QAM: A Low-Complexity Signal Space Diversity Solution over Fading Channels With or Without Erasures. *IEEE Transactions on Broadcasting*, 64(4):803–815, 2018.

[J10] Marie Rita Hojeij, Charbel Abdel Nour, Joumana Farah, and Catherine Douillard. Weighted Proportional Fair Scheduling for Downlink Non-Orthogonal Multiple Access. *Wireless Communications and Mobile Computing*, 2018.

[J11] Jérémy Nadal, Charbel Abdel Nour, and Amer Baghdadi. Flexible and efficient hardware platform and architectures for waveform design and proof-of-concept in the context of 5G. *AEÜ - International Journal of Electronics and Communications / Archiv für Elektronik und Übertragungstechnik*, September 2018.

[J12] Joumana Farah, Antoine Kilzi, Charbel Abdel Nour, and Catherine Douillard. Power Minimization in Distributed Antenna Systems using Non-Orthogonal Multiple Access and Mutual Successive Interference Cancellation. *IEEE Transactions on Vehicular Technology*, 67(12):11873 – 11885, 2018.

[J13] Ronald Garzon Bohorquez, Charbel Abdel Nour, and Catherine Douillard. Protograph-based interleavers for punctured turbo codes. *IEEE Transactions on Communications*, 66(5):1833–1844, 5 2018.

[J14] Marie Rita Hojeij, Charbel Abdel Nour, Joumana Farah, and Catherine Douillard. Waterfilling-based Proportional Fairness Scheduler for Downlink Non-Orthogonal Multiple Access. *IEEE Wireless Communications Letters*, 6(2):230 – 233, April 2017.

[J15] Jérémy Nadal, Charbel Abdel Nour, and Amer Baghdadi. Novel UF-OFDM transmitter: significant complexity reduction without signal approximation. *IEEE Transactions on Vehicular Technology*, 67(3):2141–2154, October 2017.

[J16] Marie Rita Hojeij, Joumana Farah, Charbel Abdel Nour, and Catherine Douillard. New Optimal and Suboptimal Resource Allocation Techniques for Downlink Non-orthogonal Multiple Access (NOMA). *Wireless Personal Communications*, 87(3):837 – 867, April 2016.

[J17] Jérémy Nadal, Charbel Abdel Nour, and Amer Baghdadi. Low-complexity pipelined architecture for FBMC/OQAM transmitter. *IEEE Transactions on Circuits and Systems II: Express Briefs*, 63(1):19 – 23, January 2016.

[J18] Ali Haroun, Charbel Abdel Nour, Matthieu Arzel, and Christophe Jego. Low-Complexity Soft Detection of QAM demapper for a MIMO System. *IEEE Communications Letters*, 20(4):732 – 735, April 2016.

[J19] Ronald Garzon Bohorquez, Charbel Abdel Nour, and Catherine Douillard. On the Equivalence of Interleavers for Turbo Codes. *IEEE Wireless Communications Letters*, 4(1):58 – 61, February 2015.

[J20] Ronald Garzon Bohorquez, Charbel Abdel Nour, and Catherine Douillard. Channel Interleavers for Terrestrial Broadcast: Analysis and Design. *IEEE Transactions on Broadcasting*, 60(4):679 – 692, December 2014.

[J21] Hartmut Brandt, Charbel Abdel Nour, Nader ALAGHA, and Hans Peter LEXOW. Digital video broadcasting-return channel via satellite linear modulation with turbo coding. *International Journal of Satellite Communications and Networking*, Special Issue, March 2013.

[J22] Jianxiao Yang, Charbel Abdel Nour, and Charlotte Langlais. Correlated fading channel simulator based on the overlap-save method. *IEEE Transactions on Wireless Communications*, 12(6):3060 – 3071, June 2013.

[J23] Ammar El Falou, Walaa Hamouda, Charlotte Langlais, Charbel Abdel Nour, and Catherine Douillard. Finite-SNR diversity-multiplexing tradeoff for Rayleigh MIMO channels. *IEEE Communications Letters*, 17(4):753 – 756, April 2013.

[J24] A. Graell i Amat, Charbel Abdel Nour, and Catherine Douillard. Serially concatenated continuous phase modulation for satellite communications. *IEEE Transactions on Wireless Communications*, 8(6):3260 – 3269, June 2009.

Invited talks

[I1] Charbel Abdel Nour and Catherine Douillard. Channel coding for Tb/s wireless communications: insights into code design and implementation. In *The International Symposium on Ubiquitous Networking UNet*, Limoges, France, Nov. 2019.

[I2] Rami Klaimi, Charbel Abdel Nour, and Catherine Douillard. Non-binary turbo codes: design, simplified decoding and comparison with SoA codes. In *GdR ISIS day: Coding Theory and Its Applications to Data Storage, Communications and Security*, Paris, France, November 2019.

[I3] Charbel Abdel Nour and Catherine Douillard. Channel coding for Tb/s wireless communications: insights into code design and implementation. In *GdR ISIS workshop on Enabling Technologies for sub-TeraHertz and TeraHertz communications*, Maisons-Alfort, France, Sept. 2019.

[I4] Charbel Abdel Nour, Catherine Douillard, and Stefan Weithoffer. Turbo codes for Tb/s communications: code design and hardware architecture. In *Oberpfaffenhofen Workshop on High Throughput Coding (OWHTC)*, Munich, Germany, Feb. 2019.

[I5] Charbel Abdel Nour and Catherine Douillard. Designing practical diversity schemes for next generation broadcasting applications. In *6th International Symposium on Turbo Codes & Iterative Information Processing*, Brest, France, September 2010.

Conferences

[C1] Stefan Weithoffer, Rami Klaimi, Charbel Abdel Nour, Norbert Wehn, and Catherine Douillard. Fully Pipelined Iteration Unrolled Decoders -The Road to Tb/s Turbo Decoding. In *ICASSP 2020 : 45th International Conference on Acoustics, Speech, and Signal Processing*, Barcelona, Spain, May 2020.

[C2] Stefan Weithoffer, Oliver Griebel, Rami Klaimi, Charbel Abdel Nour, and Norbert Wehn. Advanced Hardware Architectures for Turbo Code Decoding Beyond 100 Gb/s. In *WCNC 2020 : IEEE Wireless Communications and Networking Conference*, Seoul, South Korea, April 2020.

[C3] Vinh Hoang Son Le, Charbel Abdel Nour, Catherine Douillard, and Emmanuel Boutillon. A low-complexity dual trellis decoding algorithm for high-rate convolutional codes. In *WCNC 2020 : IEEE Wireless Communications and Networking Conference*, Seoul, South Korea, April 2020.

[C4] Vinh Hoang Son Le, Charbel Abdel Nour, Emmanuel Boutillon, and Catherine Douillard. Dual Trellis Construction for High-Rate Punctured Convolutional Codes. In *2019 IEEE 30th Annual International Symposium on Personal, Indoor and Mobile Radio Communications (PIMRC) Workshops - W3: First Int. Workshop on Enabling Technologies for TeraHertz Communications*, Istanbul, Turkey, September 2019.

[C5] Marie-Joséph a Youssef, Joumana Farah, Catherine Douillard, and Charbel Abdel Nour. Backhaul-Constrained Resource Allocation and 3D Placement for UAV-Enabled Networks. In *IEEE 90th Vehicular Technology Conference, VTC2019-Fall,*, Honolulu, Hawaii, United States, September 2019.

[C6] Marie-Joséph a Youssef, Joumana Farah, Charbel Abdel Nour, and Catherine Douillard. Resource Allocation for Mixed Traffic Types in Distributed Antenna Systems Using NOMA. In *IEEE 88th Vehicular Technology Conference, VTC2018-Fall*, Chicago, United States, August 2018.

[C7] Stefan Weithoffer, Charbel Abdel Nour, Norbert Wehn, Catherine Douillard, and Claude Berrou. 25 Years of Turbo Codes: From Mb/s to beyond 100 Gb/s. In *10th International Symposium on Turbo Codes & Iterative Information Processing (ISTC 2018)*, Hong Kong, Hong Kong SAR China, December 2018.

[C8] Rami Klaimi, Charbel Abdel Nour, Catherine Douillard, and Joumana Farah. Low-complexity decoders for non-binary turbo codes. In *10th International Symposium on Turbo Codes & Iterative Information Processing (ISTC 2018)*, Hong Kong, Hong Kong SAR China, December 2018.

[C9] Marie-Rita Hojeij, Charbel Abdel Nour, Joumana Farah, and Catherine Douillard. Advanced Resource Allocation Technique for a Fair Downlink Non-Orthogonal Multiple Access System. In *25th International Conference on Telecommunications, ICT 2018*, Saint Malo, France, June 2018.

[C10] Ronald Garzón-Bohórquez, Rami Klaimi, Charbel Abdel Nour, and Catherine Douillard. Mitigating Correlation Problems in Turbo Decoders. In *10th International Symposium on Turbo Codes & Iterative Information Processing (ISTC 2018)*, Hong Kong, Hong Kong SAR China, December 2018.

[C11] Rami Klaimi, Charbel Abdel Nour, Catherine Douillard, and Joumana Farah. Design of Low-Complexity Convolutional Codes over GF(q). In *IEEE Global Communications Conference (GLOBECOM 2018)*, Abu Dhabi, United Arab Emirates, December 2018.

[C12] Jon Barrueco Gutierrez, Jon Montalban, Pablo Angueira, Charbel Abdel Nour, and Catherine Douillard. Low-Complexity Lattice Reduction Demapper for Massive Order One-Dimensional Non-Uniform Constellations. In *BMSB2018: IEEE International Symposium on Broadband Multimedia Systems and Broadcasting*, Valencia, Spain, June 2018.

[C13] Marie-Rita Hojeij, Charbel Abdel Nour, Joumana Farah, and Catherine Douillard. Joint Resource and Power Allocation Technique for Downlink Power-Domain Non-Orthogonal Multiple Access. In *2018 IEEE CAMA - International Conference on Antenna Measurement and Application*, Västerås, Sweden, September 2018.

[C14] Jérémy Nadal, François Leduc-Primeau, Charbel Abdel Nour, and Amer Baghdadi. A Block FBMC Receiver Designed For Short Filters. In *ICC 2018 : IEEE International Conference on Communications*, Kansas City, United States, May 2018.

[C15] Marie-Joséph a Youssef, Joumana Farah, Charbel Abdel Nour, and Catherine Douillard. Waterfilling-based Resource Allocation Techniques in Downlink Non-Orthogonal Multiple Access (NOMA) with Single-User MIMO. In *ISCC 2017 : The 22nd IEEE Symposium on Computers and Communications*, pages 499 – 506, Crete, Greece, July 2017.

[C16] Naila Lahbabi, Lin Hao, Charbel Abdel Nour, Catherine Douillard, and Pierre Siohan. An Enhanced Coding Strategy for FTN-OFDM/OQAM Transceiver Design. In *ICC 2017 : IEEE International Conference on Communications*, Paris, France, May 2017.

[C17] Ronald Garzon Bohorquez, Charbel Abdel Nour, and Catherine Douillard. Amélioration des turbocodes pour la 5G. In *GRETSI 2017 : 26ème colloque du Groupement de Recherche en Traitement du Signal et des Images*, Juan Les Pins, France, September 2017.

[C18] Joumana Farah, Elie Sfeir, Charbel Abdel Nour, and Catherine Douillard. New Resource Allocation Techniques for Base Station Power Reduction in Orthogonal and Non-Orthogonal Multiplexing Systems. In *ICC Workshops 2017: WT02 - 3rd International Workshop on 5G RAN Design*, pages 618 – 624, Paris, France, May 2017.

[C19] Joumana Farah, Elie Sfeir, Charbel Abdel Nour, and Catherine Douillard. New Efficient Energy-Saving Techniques for Resource Allocation in Downlink OFDMA Transmission Systems. In *ISCC 2017 : The 22nd IEEE Symposium on Computers and Communications*, pages 1056 – 1062, Crete, Greece, July 2017.

[C20] Saïd Medjkouh, Jérémy Nadal, Charbel Abdel Nour, and Amer Baghdadi. Reduced Complexity FPGA Implementation for UF-OFDM Frequency Domain Transmitter. In *SIPS 2017: IEEE Workshop on Signal Processing Systems*, pages 1 – 6, Lorient, France, October 2017.

[C21] Jérémy Nadal, Charbel Abdel Nour, and Amer Baghdadi. Proof-of-concept for post-OFDM waveforms as candidates for 5G. In *SIPS 2017: IEEE International Workshop on Signal Processing Systems*, page ., Lorient, France, October 2017.

[C22] Jérémy Nadal, Charbel Abdel Nour, and Amer Baghdadi. Flexible hardware platform for demonstrating new 5G waveform candidates. In *ICM 2017 : 29th IEEE International Conference on Microelectronics*, Beirut, Lebanon, December 2017.

[C23] Jérémy Nadal, Charbel Abdel Nour, and Amer Baghdadi. Hardware demonstration of post-OFDM waveforms. In *EuCNC 2017: European Conference on Networks and Communications*, Oulu, Finland, June 2017.

[C24] Ali Haroun, Charbel Abdel Nour, Matthieu Arzel, and Christophe Jego. Architecture de détecteur MIMO-BP itératif associé à un décodeur LDPC non binaire. In *GRETSI 2017 : 26ème colloque du Groupement de Recherche en Traitement du Signal et des Images*, Juan Les Pins, France, September 2017.

[C25] Tarak Arbi, Jianxiao Yang, Charbel Abdel Nour, Olivier Rioul, and Benoit Geller. Performance et simplicité d'implantation des constellations tournées: une approche pragmatique. In *26ème colloque du Groupement de Recherche en Traitement du Signal et des Images (GRETSI 2017)*, Juan Les Pins, France, September 2017.

[C26] Zeina Eddo, Marie Rita Hojeij, Charbel Abdel Nour, Joumana Farah, and Catherine Douillard. Evaluation of Intra-Subband Power Allocation for a Downlink Non-Orthogonal Multiple Access (NOMA) System. In *GLOBECOM 2016 : IEEE Global Communications Conference: 2nd International Workshop on 5G RAN Design*, page ., Washington, United States, December 2016.

[C27] Ahmed Abdmouleh, Emmanuel Boutillon, Laura Conde-Canencia, Charbel Abdel Nour, and Catherine Douillard. On Signal Space Diversity for non binary coded modulation schemes. In *23rd International Conference on Telecommunications*, Telecommunications (ICT), 2016 23rd International Conference on, pages 1 – 5, Thessaloniki, Greece, May 2016.

[C28] Ahmed Abdmouleh, Emmanuel Boutillon, Laura Conde-Canencia, Charbel Abdel Nour, and Catherine Douillard. A new approach to optimise Non-Binary LDPC codes for Coded Modulations. In *ISTC 2016 : 9th International Symposium on Turbo Codes & Iterative Information Processing*, pages 295–299, Brest, France, September 2016.

[C29] Naila Lahbabi, Hao Lin, Charbel Abdel Nour, Catherine Douillard, and Pierre Siohan. Sparse Interference Pre-Cancellation for FTN-OQAM Systems. In *EW 2016 : 22nd European Wireless Conference*, pages 1 – 6, Oulu, Finland, May 2016.

[C30] Ronald Garzon Bohorquez, Charbel Abdel Nour, and Catherine Douillard. Improving Turbo Codes for 5G with Parity Puncture-Constrained Interleavers. In *ISTC 2016 : 9th International Symposium on Turbo Codes & Iterative Information Processing*, pages 151 – 155, Brest, France, September 2016.

[C31] Ali Haroun, Charbel Abdel Nour, Matthieu Arzel, and Christophe Jego. Soft detector architecture based on Belief Propagation for MIMO systems. In *DASIP 2016 : Conference on Design and Architectures for Signal and Image Processing*, pages 1 – 4, Rennes, France, October 2016.

[C32] Ronald Garzon Bohorquez, Charbel Abdel Nour, and Catherine Douillard. Precoding Techniques for Turbo Codes. In *EW 2015 : 21nd European Wireless 2015 : 5G and Beyond*, pages 1 – 6, Budapest, Hungary, May 2015.

[C33] Ronald Garzon Bohorquez, Charbel Abdel Nour, and Catherine Douillard. Etude de techniques de précodage pour les turbocodes. In *GRETSI 2015 : 25ème colloque du Groupement de Recherche en Traitement du Signal et des Images*, Lyon, France, September 2015.

[C34] Ali Haroun, Charbel Abdel Nour, Matthieu Arzel, and Christophe Jego. Algorithme de détection à très faible complexité pour des systèmes MIMO basés sur la propagation de croyance. In *GRETSI 2015 : 25ème colloque du Groupement de Recherche en Traitement du Signal et des Images*, Lyon, France, September 2015.

[C35] Jianxiao Yang, Wan Kai, Benoit Geller, Charbel Abdel Nour, Olivier Rioul, and Catherine Douillard. A low-complexity 2D signal space diversity solution for future broadcasting systems. In *IEEE International Conference on Communications (ICC 2015)*, volume 63, pages 2762–2767, Londre, France, June 2015.

[C36] Jianxiao Yang, Meng Li, Min Li, Charbel Abdel Nour, Catherine Douillard, and Benoit Geller. Max-log demapper architecture design for DVB-T2 rotated QAM constellations. In *2015 IEEE Workshop on Signal Processing Systems (SiPS)* , Hangzhou, China, 2015.

[C37] Marie Rita Hojeij, Joumana Farah, Charbel Abdel Nour, and Catherine Douillard. Resource Allocation in Downlink Non-orthogonal Multiple Access (NOMA) for Future Radio Access. In *VTC 2015 spring : IEEE 81st Vehicular Technology Conference*, pages 1 – 6, Glasgow, United Kingdom, May 2015.

[C38] Ammar El Falou, Charlotte Langlais, Walaa Hamouda, Charbel Abdel Nour, and Catherine Douillard. Transmit Antenna Selection for Coded Multiple-Input Dual-Output Systems. In *ISTC 2014 : 8th International Symposium on Turbo Codes and Iterative Information Processing*, pages 269 – 273, Bremen, Germany, August 2014.

[C39] Ammar El Falou, Charlotte Langlais, Walaa Hamouda, Charbel Abdel Nour, and Catherine Douillard. Finite-SNR Diversity-Multiplexing Tradeoff for Spatially Correlated Rayleigh MIMO Channels. In *ICC 2014 : IEEE International Conference on Communications*, pages 5604–5609, Sidney, Australia, June 2014.

[C40] Benjamin Ros, Frédéric Lacoste, Kévin Burgi, and Charbel Abdel Nour. Rotated Constellations for a Satellite Communication Link in a DVB-T2 context. In *VEHICULAR 2014 : the Third International Conference on Advances in Vehicular Systems, Technologies and Applications*, pages 1 – 5, Seville, Spain, June 2014.

[C41] Jérémy Nadal, Charbel Abdel Nour, Amer Baghdadi, and Hao Lin. Hardware prototyping of FBMC/OQAM baseband for 5G mobile communication systems. In *RSP 2014 : IEEE International Symposium on Rapid System Prototyping*, pages 135 – 141, New Delhi, India, October 2014.

[C42] Jérémy Nadal, Charbel Abdel Nour, Amer Baghdadi, and Hao Lin. FBMC/OQAM-related new waveform. In *EuCNC 2015 : 24th European Conference on Networks and Communications*, Bologna, Italy, June 2014.

[C43] Ali Haroun, Charbel Abdel Nour, Matthieu Arzel, and Christophe Jégo. Symbol-based BP Detection for MIMO Systems associated with Non-Binary LDPC Codes. In *WCNC 2014 : IEEE Wireless Communications and Networking Conference*, pages 212 – 217, Istanbul, Turkey, April 2014.

[C44] Ali Haroun, Charbel Abdel Nour, Matthieu Arzel, and Christophe Jego. Low-Complexity LDPC-coded Iterative MIMO Receiver Based on Belief Propagation algorithm for Detection. In *ISTC 2014 : 8th International Symposium on Turbo Codes and Iterative Information Processing*, pages 213 – 217, Bremen, Germany, August 2014.

[C45] Ali Haroun, Charbel Abdel Nour, Matthieu Arzel, and Christophe Jégo. Low-Complexity layered BP-based Detection and Decoding for a NB-LDPC Coded MIMO System. In *ICC 2014 : IEEE International Conference on Communications*, pages 5107 – 5112, Sydney, Australia, June 2014.

[C46] Ronald Garzon Bohorquez, Charbel Abdel Nour, and Catherine Douillard. Etude de structures d'entrelacement canal adaptées à la diffusion vidéo par voie terrestre. In *GRETSI 2013 : 24ème colloque du Groupement de Recherche en Traitement du Signal et des Images*, Brest, France, September 2013.

[C47] Ammar El Falou, Charlotte Langlais, Charbel Abdel Nour, and Catherine Douillard. Codage spatio-temporel adaptatif pour les systèmes MIMO utilisant un codage de canal à fort pouvoir de correction. In *GRETSI 2013 : 24ème colloque du Groupement de Recherche en Traitement du Signal et des Images*, Brest, France, September 2013.

[C48] Ali Haroun, Charbel Abdel Nour, Matthieu Arzel, and Christophe Jego. Réception itérative MIMO basée sur la propagation de croyance et des codes LDPC non-binaires. In *GRETSI 2013 : 24ème colloque du Groupement de Recherche en Traitement du Signal et des Images*, Brest, France, September 2013.

[C49] Catherine Douillard and Charbel Abdel Nour. The bit interleaved coded modulation module for DVB-NGH: enhanced features for mobile reception. In *ICT 2012: 19th International Conference on Telecommunications*, pages 1 – 6, Jounieh, Lebanon, April 2012.

[C50] Ammar El Falou, Charlotte Langlais, Charbel Abdel Nour, and Catherine Douillard. Adaptive trace-orthonormal STBC for MIMO system with capacity approaching FEC codes. In *VTC2012-Fall 2012: 76th IEEE Vehicular Technology Conference*, Québec, Canada, September 2012.

[C51] Charbel Abdel Nour and Catherine Douillard. High diversity multi-block space-time code for broadcasting applications. In *ICT 2012 : 19th International Conference on Telecommunications*, Jounieh, Lebanon, April 2012.

[C52] Ammar El Falou, Charlotte Langlais, Charbel Abdel Nour, and Catherine Douillard. Low ML-detection complexity, adaptive 2x2 STBC, with powerful FEC codes. In *7th International Symposium on Turbo Codes & Iterative Information Processing*, Gothenburg, Sweden, August 2012.

[C53] Meng Li, Charbel Abdel Nour, Christophe Jego, Jianxiao Yang, and Catherine Douillard. Etude d'un récepteur itératif dédié à un système de modulation codée à bits entrelacés pour le standard DVB-T2. In *23ème colloque GRETSI*, Bordeaux, France, September 2011.

[C54] Ammar El Falou, Charbel Abdel Nour, Charlotte Langlais, and Catherine Douillard. Low decoding complexity STBC design for turbo coded broadcast transmission. In *IEEE International Symposium on Broadband Multimedia Systems and Broadcasting*, Erlangen, Germany, June 2011.

[C55] Meng Li, Charbel Abdel Nour, Christophe Jego, Jianxiao Yang, and Catherine Douillard. Efficient iterative receiver for Bit-Interleaved Coded Modulation according to the DVB-T2 standard. In *ICASSP 2011 IEEE 36th international Conference on Acoustics, Speech and Signal Processing*, pages 3168 – 3171, Prague, Czech Republic, May 2011.

[C56] Meng Li, Charbel Abdel Nour, Christophe Jego, Jianxiao Yang, and Catherine Douillard. A shuffled iterative bit-interleaved coded modulation receiver for the DVB-T2 standard: Design, implementation and FPGA prototyping. In *Signal Processing Systems (SiPS), 2011 IEEE Workshop on*, pages 55 –60, Beirut, Lebanon, October 2011.

[C57] Meng Li, Charbel Abdel Nour, Christophe Jego, and Catherine Douillard. Design and FPGA prototyping of a bit-interleaved coded modulation receiver for the DVB-T2 standard. In *Signal Processing Systems (SIPS), 2010 IEEE Workshop on*, pages 162 –167, San Francisco, United States, October 2010.

[C58] Jianxiao Yang, Charlotte Langlais, and Charbel Abdel Nour. Joint factor graph detector for LDPC and STBC coded MIMO systems: a new framework. In *6th International Symposium on Turbo Codes & Iterative Information Processing*, Brest, France, September 2010.

[C59] Meng Li, Charbel Abdel Nour, Christophe Jego, and Catherine Douillard. Design of rotated QAM mapper/demapper for the DVB-T2 standard. In *SiPS 2009 : IEEE workshop on Signal Processing Systems*, pages 18 – 23, Tampere, Finland, October 2009.

[C60] Charbel Abdel Nour and Catherine Douillard. Rotated QAM Constellations to Improve BICM Performance for DVB-T2. In *2008 IEEE 10th International Symposium on Spread Spectrum Techniques and Applications (ISSSTA)*, pages 354–359, Bologna, France, August 2008.

[C61] Charbel Abdel Nour and Catherine Douillard. Improving BICM performance of QAM constellations for broadcasting applications. In *2008 5th International Symposium on Turbo Codes and Related Topics*, pages 55–60, Lausanne, France, September 2008.

[C62] Alexandre Graell i Amat, Charbel Abdel Nour, and Catherine Douillard. Serially Concatenated Continuous Phase Modulation with Extended BCH Codes. In *2007 IEEE Information Theory Workshop on Information Theory for Wireless Networks*, pages 1–5, Bergen, Norway, July 2007.

[C63] Charbel Abdel Nour and Catherine Douillard. On Lowering the Error Floor of High Order Turbo BICM Schemes Over Fading Channels. In *IEEE Global Communications Conference*, pages 1–5, San Francisco, United States, November 2006.

[C64] Sylvain S. Chaillou, Joseph J. Boutros, and Charbel Abdel Nour. Efficient iterative decoding of impulse radio based on energy detection. In *International Workshop on UWB Technologies*, Yokosuka, Japan, December 2005.

[C65] Charbel Abdel Nour and Catherine Douillard. Performance improvement using turbo coded BICM-ID with 16 QAM over Gaussian and flat fading Rayleih channels. In *14th IST Mobile & Wireless Communications Summit*, Dresden, Germany, June 2005.

Demonstrations/Exhibitions/Talks/Other publications

[D1] Jérémy Nadal, Charbel Abdel Nour, and Amer Baghdadi. Flexible PoC for Post-OFDM waveforms. In *G5-PPP 2016 : 2nd Global 5G Infrastructure public private partnership event*, Rome, Italy, November 2016.

[D2] Jérémy Nadal, Charbel Abdel Nour, and Amer Baghdadi. Enabling 5G new services – Post-OFDM waveforms, September 2016. Exhibition of a hardware prototype for post-OFDM waveforms at the European researchers night in Brest.

[D3] Ali Haroun, Charbel Abdel Nour, Matthieu Arzel, and Christophe Jego. Architecture d'un détecteur MIMO souple basé sur l'algorithme de propagation de croyance. In *GDR SoC-SiP 2016 : colloque National du Groupe de Recherche System on Chip -System in Package*, Nantes, France, June 2016.

[D4] Jérémy Nadal, Charbel Abdel Nour, Amer Baghdadi, Hao Lin, Bruno Jahan, and Pierre Siohan. New candidate waveform for 5G, November 2015. Proof of concept demonstration at Orange Labs Research Fair.

[D5] Jérémy Nadal, Charbel Abdel Nour, and Amer Baghdadi. FBMC-OQAM, a candidate waveform for 5G, September 2015. Exhibition of FBMC-OQAM waveform candidate for 5G at the European researcher's night in Brest.

[D6] Jérémy Nadal, Charbel Abdel Nour, Amer Baghdadi, Pierre Siohan, Lin Hao, and Bruno Jahan. Flexible FBMC air interface for 5G. MWC 2015 : Mobile World Congress, March 2015. Poster.

[D7] Jérémy Nadal, Charbel Abdel Nour, Amer Baghdadi, Hao Lin, Bruno Jahan, and Pierre Siohan. Flexible FBMC air interface for 5G, 2015. Proof of concept demonstartion at the 3rd International MiWEBA workshop – Green 5G networks.

[D8] Jérémy Nadal, Charbel Abdel Nour, Amer Baghdadi, and Hao Lin. FBMC/OQAM baseband for 5G mobile communication systems: hardware design and on-board prototyping. In *GDR ISIS workshop 2014 : 5G & Beyond: Promises and Challenges*, Paris, France, October 2014.

[D9] Ali Haroun, Charbel Abdel Nour, Matthieu Arzel, and Christophe Jego. An efficient MIMO receiver based on BP algorithm with truncated message-passing. GDR SoC-SiP 2014 : 9ème colloque national du GDR SoC-SiP du CNRS, June 2014. Poster.

[D10] Ali Haroun, Charbel Abdel Nour, Matthieu Arzel, and Christophe Jego. Low-Complexity LDPC-coded Iterative MIMO Receiver Based on Belief Propagation algorithm for Detection. In *GDR SoCSiP-ISIS 2014 : journée thématique Architectures de Codes Correcteurs d'Erreurs*, Plouzané, France, November 2014.

[D11] Ronald Garzon Bohorquez, Charbel Abdel Nour, and Catherine Douillard. Analysis and design of channel interleavers for terrestrial broadcast. M3 Open Event : projet ANR Mobile MultiMedia, May 2013. Poster.

[D12] Ammar El Falou, Charlotte Langlais, Charbel Abdel Nour, and Catherine Douillard. Design of adaptive 2x2 space-time block codes for broadcasting applications. M3 Open Event : projet ANR Mobile MultiMedia, May 2013. Poster.

[D13] Meng Li, Charbel Abdel Nour, Christophe Jego, Jianxiao Yang, and Catherine Douillard. FPGA implementation of a shuffled iterative bit-interleaved coded modulation receiver. In *SOC-SIP : journée du groupe de recherche System On Chip - System In Package*, Lyon, France, June 2011.

[D14] Meng Li, Christophe Jego, Charbel Abdel Nour, and Catherine Douillard. Design of an efficient LDPC decoder for bit-interleaved coded modulation receivers. In *SOC-SIP 2010 : Colloque national du groupe de recherches "System On Chip - System In Package"*, Paris, France, June 2010.

[D15] Charbel Abdel Nour. *Spectrally efficient coded transmissions for wireless and satellite applications*. Phd thesis, Enst-bretagne, January 2008.

References

[1] Digital Video Broadcasting (DVB): Frame Structure Channel Coding and Modulation for a Second Generation Digital Terrestrial Television Broadcasting System (DVB-T2), Apr. 2012.

[2] Digital Video Broadcasting (DVB): Next Generation broadcasting system to Handheld (NGH), physical layer specifications, 2013.

[3] ETSI. Digital Video Broadcasting (DVB), Second Generation Framing Structure, Channel Coding and Modulation Systems for Broadcasting, Interactive Services, News Gathering and Other Broadband Satellite Application, EN 302 307 V1.1.1, 2004.

[4] R.G. Gallager. *Low-Density Parity-Check Codes*. Cambridge, MIT Press, 1963.

[5] R.C. Bose and D.K. Ray-Chaudhuri. On a class of error correcting binary group codes. *Information and Control*, 3(1):68–79, mar 1960.

[6] S.M. Alamouti. A simple transmit diversity technique for wireless communications. *IEEE Journal on Selected Areas in Communications*, 16(8):1451–1458, 1998.

[7] G. Caire, G. Taricco, and E. Biglieri. Bit-interleaved coded modulation. *IEEE Transactions on Information Theory*, 44(3):927–946, may 1998.

[8] E. Zehavi. 8-PSK trellis codes for a rayleigh channel. *IEEE Transactions on Communications*, 40(5):873–884, may 1992.

[9] Xiaodong Li and J.A. Ritcey. Bit-interleaved coded modulation with iterative decoding. *IEEE Communications Letters*, 1(6):169–171, nov 1997.

[10] A. Chindapol and J.A. Ritcey. Design, analysis, and performance evaluation for BICM-ID with square QAM constellations in rayleigh fading channels. *IEEE Journal on Selected Areas in Communications*, 19(5):944–957, may 2001.

[11] Ilan Abramovici and Shlomo Shamai. On turbo encoded BICM. *Annales Des Télécommunications*, 54:225–234, 1999.

[12] X. Giraud, E. Boutillon, and J.C. Belfiore. Algebraic tools to build modulation schemes for fading channels. *IEEE Transactions on Information Theory*, 43(3):938–952, may 1997.

[13] J. Boutros and E. Viterbo. Signal space diversity: a power- and bandwidth-efficient diversity technique for the rayleigh fading channel. *IEEE Transactions on Information Theory*, 44(4):1453–1467, jul 1998.

[14] Charbel Abdel Nour and Catherine Douillard. Improving BICM performance of QAM constellations for broadcasting applications. In *2008 5th International Symposium on Turbo Codes and Related Topics*, pages 55–60, Lausanne, France, September 2008.

[15] Chengshan Xiao, Yahong Zheng, and Norman Beaulieu. Novel sum-of-sinusoids simulation models for rayleigh and rician fading channels. *IEEE Transactions on Wireless Communications*, 5(12):3667–3679, dec 2006.

[16] Y.R. Zheng and Chengshan Xiao. Simulation models with correct statistical properties for rayleigh fading channels. *IEEE Transactions on Communications*, 51(6):920–928, jun 2003.

[17] Florian Kaltenberger, Thomas Zemen, and Christoph W. Ueberhuber. Low-complexity geometry-based MIMO channel simulation. *EURASIP Journal on Advances in Signal Processing*, 2007(1), jul 2007.

[18] Michel C. Jeruchim, Philip Balaban, and K. Sam Shanmugan. *Simulation of Communication Systems*. Springer US, 2000.

[19] K.E. Baddour and N.C. Beaulieu. Autoregressive modeling for fading channel simulation. *IEEE Transactions on Wireless Communications*, 4(4):1650–1662, jul 2005.

[20] J.I. Smith. A computer generated multipath fading simulation for mobile radio. *IEEE Transactions on Vehicular Technology*, 24(3):39–40, aug 1975.

[21] D.J. Young and N.C. Beaulieu. The generation of correlated rayleigh random variates by inverse discrete fourier transform. *IEEE Transactions on Communications*, 48(7):1114–1127, jul 2000.

[22] Jon Barrueco, Jon Montalban, Cristina Regueiro, Manuel Velez, Juan Luis Ordiales, Heung-Mook Kim, Sung-Ik Park, and Sunhyoung Kwon. Constellation design for bit-interleaved coded modulation (BICM) systems in advanced broadcast standards. *IEEE Transactions on Broadcasting*, 63(4):603–614, dec 2017.

[23] J. Zoellner and N. Loghin. Optimization of high-order non-uniform QAM constellations. In *2013 IEEE International Symposium on Broadband Multimedia Systems and Broadcasting (BMSB)*. IEEE, jun 2013.

[24] Belkacem Mouhouche, Daniel Ansorregui, and Alain Mourad. High order non-uniform constellations for broadcasting UHDTV. In *2014 IEEE Wireless Communications and Networking Conference (WCNC)*. IEEE, apr 2014.

[25] J. Barrueco, C. Regueiro, J. Montalban, M. Velez, P. Angueira, Heung-Mook Kim, Sung-Ik Park, and Jae-Young Lee. Combining advanced constellations and SSD techniques for optimal BICM capacity. In *2015 IEEE International Symposium on Broadband Multimedia Systems and Broadcasting*. IEEE, jun 2015.

[26] David Gomez-Barquero, Catherine Douillard, Peter Moss, and Vittoria Mignone. DVB-NGH: The next generation of digital broadcast services to handheld devices. *IEEE Transactions on Broadcasting*, 60(2):246–257, jun 2014.

[27] Manuel Fuentes, David Vargas, and David Gomez-Barquero. Low-complexity demapping algorithm for two-dimensional non-uniform constellations. *IEEE Transactions on Broadcasting*, 62(2):375–383, jun 2016.

[28] Tung-Jung Hsieh and Wern-Ho Sheen. A lattice-reduction-aided max-log list demapper for coded MIMO receivers. *IEEE Transactions on Vehicular Technology*, 63(2):664–673, feb 2014.

[29] Edward C. Y. Peh and Ying-Chang Liang. Power and modulo loss tradeoff with expanded soft demapper for LDPC coded GMD-THP MIMO systems. *IEEE Transactions on Wireless Communications*, 8(2):714–724, feb 2009.

[30] Xiao-Feng Qi and Keith Holt. A lattice-reduction-aided soft demapper for high-rate coded MIMO-OFDM systems. *IEEE Signal Processing Letters*, 14(5):305–308, may 2007.

[31] Stefano Tomasin and Matteo Butussi. Low complexity demapping of rotated and cyclic q delayed constellations for DVB-t2. *IEEE Wireless Communications Letters*, 1(2):81–84, apr 2012.

[32] A. R. Jafri, A. Baghdadi, M. Waqas, and M. Najam Ul Islam. High-Throughput and Area-Efficient Rotated and Cyclic Q Delayed Constellations Demapper for Future Wireless Standards. *IEEE access*, 5(1):3077–3084, Jan 2017.

[33] Meng Li, Charbel Abdel Nour, Christophe Jego, and Catherine Douillard. Design and FPGA prototyping of a bit-interleaved coded modulation receiver for the DVB-T2 standard. In *Signal Processing Systems (SIPS), 2010 IEEE Workshop on*, pages 162 –167, San Francisco, United States, October 2010.

[34] Meng Li, Charbel Abdel Nour, Christophe Jego, and Catherine Douillard. Design of rotated QAM mapper/demapper for the DVB-T2 standard. In *SiPS 2009 : IEEE workshop on Signal Processing Systems*, pages 18 – 23, Tampere, Finland, October 2009.

[35] D.J. Costello, J. Hagenauer, H. Imai, and S.B. Wicker. Applications of error-control coding. *IEEE Transactions on Information Theory*, 44(6):2531–2560, 1998.

[36] John B. Anderson and Seshadri Mohan. Error control coding. In *Source and Channel Coding*, pages 77–197. Springer US, 1991.

[37] L. Vangelista, N. Benvenuto, S. Tomasin, C. Nokes, J. Stott, A. Filippi, M. Vlot, V. Mignone, and A. Morello. Key technologies for next-generation terrestrial digital television standard DVB-t2. *IEEE Communications Magazine*, 47(10):146–153, oct 2009.

[38] David Gozalvez, David Vargas, David Gomez-Barquero, and Narcis Cardona. Performance evaluation of DVB-t2 time interleaving in mobile environments. In *2010 IEEE 72nd Vehicular Technology Conference - Fall*. IEEE, sep 2010.

[39] J. Salz. Digital transmission over cross-coupled linear channels. *AT&T Technical Journal*, 64(6):1147–1159, jul 1985.

[40] Charbel Abdel Nour and Catherine Douillard. Rotated QAM Constellations to Improve BICM Performance for DVB-T2. In *2008 IEEE 10th International Symposium on Spread Spectrum Techniques and Applications (ISSSTA)*, pages 354–359, Bologna, France, August 2008.

[41] Charbel Abdel Nour and Catherine Douillard. Modulation codée avec entrelacement des voies I et Q et rotation optimisée, February 2008.

[42] Meng Li, Christophe Jego, Charbel Abdel Nour, and Catherine Douillard. Design of an efficient LDPC decoder for bit-interleaved coded modulation receivers. In *SOC-SIP 2010 : Colloque national du groupe de recherches "System On Chip - System In Package"*, Paris, France, June 2010.

[43] Meng Li, Charbel Abdel Nour, Christophe Jego, Jianxiao Yang, and Catherine Douillard. Etude d'un récepteur itératif dédié à un système de modulation codée à bits entrelacés pour le standard DVB-T2. In *23ème colloque GRETSI*, Bordeaux, France, September 2011.

[44] Meng Li, Charbel Abdel Nour, Christophe Jego, Jianxiao Yang, and Catherine Douillard. FPGA implementation of a shuffled iterative bit-interleaved coded modulation receiver. In *SOC-SIP : journée du groupe de recherche System On Chip - System In Package*, Lyon, France, June 2011.

[45] Meng Li, Charbel Abdel Nour, Christophe Jego, Jianxiao Yang, and Catherine Douillard. Efficient iterative receiver for Bit-Interleaved Coded Modulation according to the DVB-T2 standard. In *ICASSP 2011 IEEE 36th international Conference on Acoustics, Speech and Signal Processing*, pages 3168 – 3171, Prague, Czech Republic, May 2011.

[46] Meng Li, Charbel Abdel Nour, Christophe Jego, Jianxiao Yang, and Catherine Douillard. A shuffled iterative bit-interleaved coded modulation receiver for the DVB-T2 standard: Design, implementation and FPGA prototyping. In *Signal Processing Systems (SiPS), 2011 IEEE Workshop on*, pages 55 –60, Beirut, Lebanon, October 2011.

[47] Jianxiao Yang, Charbel Abdel Nour, and Charlotte Langlais. Correlated fading channel simulator based on the overlap-save method. *IEEE Transactions on Wireless Communications*, 12(6):3060 – 3071, June 2013.

[48] Jon Barrueco Gutierrez, Jon Montalban, Pablo Angueira, Charbel Abdel Nour, and Catherine Douillard. Low-Complexity Lattice Reduction Demapper for Massive Order One-Dimensional Non-Uniform Constellations. In *BMSB2018: IEEE International Symposium on Broadband Multimedia Systems and Broadcasting*, Valencia, Spain, June 2018.

[49] Jon Barrueco Gutierrez, Jon Montalban, Pablo Angueira, Charbel Abdel Nour, and Catherine Douillard. Low Complexity Adaptive Demapper for 2-D Non-Uniform Constellations. *IEEE Transactions on Broadcasting*, 65(1):10–19, March 2019.

[50] Ronald Garzon Bohorquez, Charbel Abdel Nour, and Catherine Douillard. Etude de structures d'entrelacement canal adaptées à la diffusion vidéo par voie terrestre. In *GRETSI 2013 : 24ème colloque du Groupement de Recherche en Traitement du Signal et des Images*, Brest, France, September 2013.

[51] Ronald Garzon Bohorquez, Charbel Abdel Nour, and Catherine Douillard. Channel Interleavers for Terrestrial Broadcast: Analysis and Design. *IEEE Transactions on Broadcasting*, 60(4):679 – 692, December 2014.

[52] Ronald Garzon Bohorquez, Charbel Abdel Nour, and Catherine Douillard. Analysis and design of channel interleavers for terrestrial broadcast. M3 Open Event : projet ANR Mobile MultiMedia, May 2013. Poster.

[53] Lizhong Zheng and D.N.C. Tse. Diversity and multiplexing: a fundamental tradeoff in multiple-antenna channels. *IEEE Transactions on Information Theory*, 49(5):1073–1096, may 2003.

[54] V. Tarokh, N. Seshadri, and A.R. Calderbank. Space-time codes for high data rate wireless communication: performance criterion and code construction. *IEEE Transactions on Information Theory*, 44(2):744–765, mar 1998.

[55] M.-Z. Win and J.-H. Winters. Analysis of hybrid selection/maximal-ratio combining in rayleigh fading. In *IEEE International Conference on Communications (Cat. No. 99CH36311)*. IEEE, 1999.

[56] Ammar El Falou, Charbel Abdel Nour, Charlotte Langlais, and Catherine Douillard. Low decoding complexity STBC design for turbo coded broadcast transmission. In *IEEE International Symposium on Broadband Multimedia Systems and Broadcasting*, Erlangen, Germany, June 2011.

[57] Ammar El Falou, Charlotte Langlais, Charbel Abdel Nour, and Catherine Douillard. Low ML-detection complexity, adaptive 2x2 STBC, with powerful FEC codes. In *7th International Symposium on Turbo Codes & Iterative Information Processing*, Gothenburg, Sweden, August 2012.

[58] Ammar El Falou, Charlotte Langlais, Charbel Abdel Nour, and Catherine Douillard. Adaptive trace-orthonormal STBC for MIMO system with capacity approaching FEC codes. In *VTC2012-Fall 2012: 76th IEEE Vehicular Technology Conference*, Québec, Canada, September 2012.

[59] Ammar El Falou, Charlotte Langlais, Charbel Abdel Nour, and Catherine Douillard. Codage spatio-temporel adaptatif pour les systèmes MIMO utilisant un codage de canal à fort pouvoir de correction. In *GRETSI 2013 : 24ème colloque du Groupement de Recherche en Traitement du Signal et des Images*, Brest, France, September 2013.

[60] Ammar El Falou, Charlotte Langlais, Walaa Hamouda, Charbel Abdel Nour, and Catherine Douillard. Transmit Antenna Selection for Coded Multiple-Input Dual-Output Systems. In *ISTC 2014 : 8th International Symposium on Turbo Codes and Iterative Information Processing*, pages 269 – 273, Bremen, Germany, August 2014.

[61] Ammar El Falou, Walaa Hamouda, Charlotte Langlais, Charbel Abdel Nour, and Catherine Douillard. Finite-SNR diversity-multiplexing tradeoff for Rayleigh MIMO channels. *IEEE Communications Letters*, 17(4):753 – 756, April 2013.

[62] Ammar El Falou, Charlotte Langlais, Walaa Hamouda, Charbel Abdel Nour, and Catherine Douillard. Finite-SNR Diversity-Multiplexing Tradeoff for Spatially Correlated Rayleigh MIMO Channels. In *ICC 2014 : IEEE International Conference on Communications*, pages 5604–5609, Sidney, Australia, June 2014.

[63] E. Dahlman, G. Mildh, S. Parkvall, J. Peisa, J. Sachs, and Y. Selen. 5g radio access. Technical report, Ericsson Review, 2014.

[64] China Datang Wireless Mobile Innov. Center Datang Telecom Technol. Ind. Group, Beijing. Evolution, convergence, and innovation. Technical report, 5G White Paper, Dec. 2013.

[65] Lte envolved universal terrestrial radio access (e-utra): Multiplexing and channel coding, Jan. 2011.

[66] Jung-Fu Cheng, Ajit Nimbalker, Yufei Blankenship, B. Classon, and T. Keith Blankenship. Analysis of circular buffer rate matching for LTE turbo code. In *2008 IEEE 68th Vehicular Technology Conference*. IEEE, sep 2008.

[67] C. Berrou, A. Glavieux, and P. Thitimajshima. Near Shannon limit error-correcting coding and decoding: Turbo-codes. In *Proc. of the IEEE International Conference on Communications (ICC 93)*, volume 2, pages 1064 –1070, May 1993.

[68] C. Berrou and A. Glavieux. Near optimum error correcting coding and decoding: turbo-codes. *IEEE Transactions on Communications*, 44(10):1261–1271, 1996.

[69] J. Hokfelt, O. Edfors, and T. Maseng. Interleaver design for turbo codes based on the performance of iterative decoding. In *IEEE International Conference on Communications*. IEEE, 1999.

[70] Stewart Crozier and Paul Guinand. Distance upper bounds and true minimum distance results for turbo-codes designed with drp interleavers. *Annales des Télécommunications*, 60:10–28, 01 2005.

[71] Jing Sun and O.Y. Takeshita. Interleavers for turbo codes using permutation polynomials over integer rings. *IEEE Transactions on Information Theory*, 51(1):101–119, jan 2005.

[72] C. Berrou, Y. Saouter, C. Douillard, S. Kerouedan, and M. Jezequel. Designing good permutations for turbo codes: towards a single model. In *Communications, 2004 IEEE International Conference on*, volume 1, pages 341–345, 2004.

[73] Catherine Douillard, Michel Jezequel, Claude Berrou, Jacky Tousch, N. Pham, and N. Brengarth. The Turbo Code Standard for DVB-RCS. In *Proc. of the 2nd International Symposium on Turbo Codes & Related Topics, Brest, France*, pages 535 – 538, 2000.

[74] S. Benedetto, Guido Montorsi, Dariush Divsalar, and F. Pollara. A soft-input soft-output maximum a posteriori (map) module to decode parallel and serial concatenated codes. *Telecommunications and Data Acquisition Progress Report*, 42, 07 1996.

[75] J. Zhang and M.P.C. Fossorier. Shuffled iterative decoding. *IEEE Transactions on Communications*, 53(2):209–213, feb 2005.

[76] O. Muller, A. Baghdadi, and M. Jezequel. Exploring parallel processing levels for convolutional turbo decoding. In *2006 2nd International Conference on Information & Communication Technologies*. IEEE, 2006.

[77] Robert G. Maunder. A fully-parallel turbo decoding algorithm. *IEEE Transactions on Communications*, 63(8):2762–2775, aug 2015.

[78] G. Fettweis and H. Meyr. Parallel viterbi algorithm implementation: breaking the ACS-bottleneck. *IEEE Transactions on Communications*, 37(8):785–790, 1989.

[79] Cheng-Hao Tang, Cheng-Chi Wong, Chih-Lung Chen, Chien-Ching Lin, and Hsie-Chia Chang. A 952ms/s max-log MAP decoder chip using radix-4 x 4 ACS architecture. In *2006 IEEE Asian Solid-State Circuits Conference*. IEEE, nov 2006.

[80] Kai-Ting Shr, Yu-Cheng Chang, Chu-Yi Lin, and Yuan-Hao Huang. A 6.6pj/bit/iter radix-16 modified log-MAP decoder using two-stage ACS architecture. In *IEEE Asian Solid-State Circuits Conference 2011*. IEEE, nov 2011.

[81] Oscar Sanchez, Christophe Jegoy, Michel Jezequel, and Yannick Saouter. High speed low complexity radix-16 max-log-MAP SISO decoder. In *2012 19th IEEE International Conference on Electronics, Circuits, and Systems (ICECS 2012)*. IEEE, dec 2012.

[82] Ronald Garzon Bohorquez, Charbel Abdel Nour, and Catherine Douillard. Protograph-based interleavers for punctured turbo codes. *IEEE Transactions on Communications*, 66(5):1833–1844, 5 2018.

[83] Ronald Garzon Bohorquez, Charbel Abdel Nour, and Catherine Douillard. Improving Turbo Codes for 5G with Parity Puncture-Constrained Interleavers. In *ISTC 2016 : 9th International Symposium on Turbo Codes & Iterative Information Processing*, pages 151 – 155, Brest, France, September 2016.

[84] Ronald Garzon Bohorquez, Charbel Abdel Nour, and Catherine Douillard. On the Equivalence of Interleavers for Turbo Codes. *IEEE Wireless Communications Letters*, 4(1):58 – 61, February 2015.

[85] S. Tong, H. Zheng, and B. Bai. Precoded turbo code within 0.1 dB of shannon limit. *Electronics Letters*, 47(8):521, 2011.

[86] Ronald Garzon Bohorquez, Charbel Abdel Nour, and Catherine Douillard. Precoding Techniques for Turbo Codes. In *EW 2015 : 21nd European Wireless 2015 : 5G and Beyond*, pages 1 – 6, Budapest, Hungary, May 2015.

[87] Ronald Garzon Bohorquez, Charbel Abdel Nour, and Catherine Douillard. Amélioration des turbocodes pour la 5G. In *GRETSI 2017 : 26ème colloque du Groupement de Recherche en Traitement du Signal et des Images*, Juan Les Pins, France, September 2017.

[88] Ronald Garzon Bohorquez, Charbel Abdel Nour, and Catherine Douillard. Procédé de codage d'un message numérique d'entrée mettant en oeuvre un turbo-encodeur, programme d'ordinateur et turbo-encodeur correspondants, December 2016.

[89] Ronald Garzón Bohórquez, Charbel Abdel Nour, and Catherine Douillard. Procédés et dispositifs de codage à rendement compatible, March 2017.

[90] IMT and Orange Labs. R1-164635: Improved LTE turbo codes for NR. Technical report, 3GPP RAN1 meeting number 85, May, 2016.

[91] IMT and Orange Labs. R1-167413: Enhanced Turbo Codes for NR: Implementation Details. Technical report, 3GPP RAN1 meeting number 86, August 2016.

[92] IMT and Orange Labs. R1-167414: Enhanced Turbo Codes for NR: Performance Evaluation. Technical report, 3GPP RAN1 meeting number 86, August 2016.

[93] IMT and Orange Labs. R1-1610314: FEC performance comparison for short frame sizes for NR. Technical report, 3GPP RAN1 meeting number 86bis, Oct. 2016.

[94] Qualcomm. R1-164698: LDPC - Performance evaluation. Technical report, 3GPP RAN1 meeting number 85, May 2016.

[95] IMT and Orange Labs. R1-1613029: Enhanced Turbo Codes for NR: Performance Evaluation for eMBB and URLLC. Technical report, 3GPP RAN1 meeting number 87, Nov. 2016.

[96] AccelerComm; Ericsson; Orange Labs; IMT; LG Electronics and NEC. R1-1613347: WF on channel codes for NR short block length eMBB data. Technical report, 3GPP RAN1 meeting number 87, Nov. 2016.

[97] IMT and Orange Labs. R1-1703331: Enhanced Turbo Codes for URLLC. Technical report, 3GPP RAN1 meeting number number 88, Feb. 2017.

[98] Nokia. R1-1610878: Chairman's notes of AI 8.1.3 on channel coding and modulation for NR. Technical report, 3GPP RAN1 meeting number 86bis, Oct. 2016.

[99] Interdigital. R1-1610600: Updated Summary of Channel Coding Simulation Data Sharing for eMBB Data Channel. Technical report, 3GPP RAN1 meeting number 86bis, Oct. 2016.

[100] Huawei and Hisilicon. R1-1611260: Observations on LDPC decoders. Technical report, 3GPP RAN1 meeting number 87, Nov. 2016.

[101] AccelerComm. R1-1612306: On the hardware implementation of channel decoders for short block lengths. Technical report, 3GPP RAN1 meeting number 87, Nov. 2016.

[102] Stefan Weithoffer, Charbel Abdel Nour, Norbert Wehn, Catherine Douillard, and Claude Berrou. 25 Years of Turbo Codes: From Mb/s to beyond 100 Gb/s. In *10th International Symposium on Turbo Codes & Iterative Information Processing (ISTC 2018)*, Hong Kong, Hong Kong SAR China, December 2018.

[103] P. Robertson, E. Villebrun, and P. Hoeher. A comparison of optimal and sub-optimal MAP decoding algorithms operating in the log domain. In *Proc. of the IEEE International Conf. on Communications*, volume 2, pages 1009 –1013, jun 1995.

[104] Vinh Hoang Son Le, Charbel Abdel Nour, Emmanuel Boutillon, and Catherine Douillard. Dual Trellis Construction for High-Rate Punctured Convolutional Codes. In *2019 IEEE 30th Annual International Symposium on Personal, Indoor and Mobile Radio Communications (PIMRC) Workshops - W3: First Int. Workshop on Enabling Technologies for TeraHertz Communications*, Istanbul, Turkey, September 2019.

[105] Chen-Yang Lin, Cheng-Chi Wong, and Hsie-Chia Chang. A 40 nm 535 mbps multiple code-rate turbo decoder chip using reciprocal dual trellis. *IEEE Journal of Solid-State Circuits*, 48(11):2662–2670, nov 2013.

[106] Vinh Hoang Son Le, Charbel Abdel Nour, Catherine Douillard, and Emmanuel Boutillon. A low-complexity dual trellis decoding algorithm for high-rate convolutional codes. In *IEEE Wireless Communications and Networking Conference (WCNC)*, Seoul, South Korea, April 2020.

[107] G. Liva, E. Paolini, B. Matuz, S. Scalise, and M. Chiani. Short Turbo Codes over High Order Fields. *IEEE Transactions on Communications*, 61(6):2201–2211, jun 2013.

[108] Lara Dolecek, Dariush Divsalar, Yizeng Sun, and Behzad Amiri. Non-binary protograph-based LDPC codes: Enumerators, analysis, and designs. *IEEE Transactions on Information Theory*, 60(7):3913–3941, jul 2014.

[109] Giuseppe Durisi, Tobias Koch, and Petar Popovski. Toward massive, ultrareliable, and low-latency wireless communication with short packets. *Proceedings of the IEEE*, 104(9):1711–1726, sep 2016.

[110] Georg Bocherer, Fabian Steiner, and Patrick Schulte. Bandwidth efficient and rate-matched low-density parity-check coded modulation. *IEEE Transactions on Communications*, 63(12):4651–4665, dec 2015.

[111] Joseph J. Boutros, Fanny Jardel, and Cyril Measson. Probabilistic shaping and non-binary codes. In *2017 IEEE International Symposium on Information Theory (ISIT)*. IEEE, jun 2017.

[112] Fabian Steiner, Gianluigi Liva, and Georg Boecherer. Ultra-sparse non-binary LDPC codes for probabilistic amplitude shaping. In *GLOBECOM 2017 - 2017 IEEE Global Communications Conference*. IEEE, dec 2017.

[113] M.C. Davey and D. MacKay. Low-density parity check codes over GF(q). *IEEE Communications Letters*, 2(6):165–167, jun 1998.

[114] Feng Guo and L. Hanzo. Low complexity non-binary LDPC and modulation schemes communicating over MIMO channels. In *IEEE 60th Vehicular Technology Conference, 2004. VTC2004-Fall.* IEEE, 2004.

[115] Xueqin Jiang, Yier Yan, Xiang gen Xia, and Moon Ho Lee. Application of nonbinary LDPC codes based on euclidean geometries to MIMO systems. In *2009 International Conference on Wireless Communications & Signal Processing*. IEEE, nov 2009.

[116] Ali Haroun, Charbel Abdel Nour, Matthieu Arzel, and Christophe Jego. Low-Complexity LDPC-coded Iterative MIMO Receiver Based on Belief Propagation algorithm for Detection. In *ISTC 2014 : 8th International Symposium on Turbo Codes and Iterative Information Processing*, pages 213 – 217, Bremen, Germany, August 2014.

[117] W. Chen, C. Poulliat, D. Declercq, L. Conde-Canencia, A. Al-Ghouwayel, and E. Boutillon. Non-binary LDPC codes defined over the general linear group: Finite length design and practical implementation issues. In *VTC Spring 2009 - IEEE 69th Vehicular Technology Conference*. IEEE, apr 2009.

[118] David Declercq and Marc Fossorier. Decoding algorithms for nonbinary LDPC codes over GF(q). *IEEE Transactions on Communications*, 55(4):633–643, apr 2007.

[119] P. Robertson and T. Worz. Bandwidth-efficient turbo trellis-coded modulation using punctured component codes. *IEEE Journal on Selected Areas in Communications*, 16(2):206–218, 1998.

[120] Toshiki Matsumine and Hideki Ochiai. Capacity-approaching non-binary turbo codes: A hybrid design based on EXIT charts and union bounds. *IEEE Access*, 6:70952–70963, 2018.

[121] Charly Poulliat, Marc Fossorier, and David Declercq. Design of regular (2,d/sub c/)-LDPC codes over GF(q) using their binary images. *IEEE Transactions on Communications*, 56(10):1626–1635, oct 2008.

[122] Xiao-Yu Hu, E. Eleftheriou, and D.M. Arnold. Regular and irregular progressive edge-growth tanner graphs. *IEEE Transactions on Information Theory*, 51(1):386–398, jan 2005.

[123] Ahmed Abdmouleh, Emmanuel Boutillon, Laura Conde-Canencia, Charbel Abdel Nour, and Catherine Douillard. A new approach to optimise Non-Binary LDPC codes for Coded Modulations. In *ISTC 2016 : 9th International Symposium on Turbo Codes & Iterative Information Processing*, pages 295–299, Brest, France, September 2016.

[124] Ahmed Abdmouleh, Emmanuel Boutillon, Laura Conde-Canencia, Charbel Abdel Nour, and Catherine Douillard. On Signal Space Diversity for non binary coded modulation schemes. In *23rd International Conference on Telecommunications*, Telecommunications (ICT), 2016 23rd International Conference on, pages 1 – 5, Thessaloniki, Greece, May 2016.

[125] Jianxiao Yang, Charlotte Langlais, and Charbel Abdel Nour. Joint factor graph detector for LDPC and STBC coded MIMO systems: a new framework. In *6th International Symposium on Turbo Codes & Iterative Information Processing*, Brest, France, September 2010.

[126] Ali Haroun, Charbel Abdel Nour, Matthieu Arzel, and Christophe Jego. An efficient MIMO receiver based on BP algorithm with truncated message-passing. GDR SoC-SiP 2014 : 9ème colloque national du GDR SoC-SiP du CNRS, June 2014. Poster.

[127] Ali Haroun, Charbel Abdel Nour, Matthieu Arzel, and Christophe Jégo. Symbol-based BP Detection for MIMO Systems associated with Non-Binary LDPC Codes. In *WCNC 2014 : IEEE Wireless Communications and Networking Conference*, pages 212 – 217, Istanbul, Turkey, April 2014.

[128] Ali Haroun, Charbel Abdel Nour, Matthieu Arzel, and Christophe Jégo. Low-Complexity layered BP-based Detection and Decoding for a NB-LDPC Coded MIMO System. In *ICC 2014 : IEEE International Conference on Communications*, pages 5107 – 5112, Sydney, Australia, June 2014.

[129] Ali Haroun, Charbel Abdel Nour, Matthieu Arzel, and Christophe Jego. Low-Complexity LDPC-coded Iterative MIMO Receiver Based on Belief Propagation algorithm for Detection. In *GDR SoCSiP-ISIS 2014 : journée thématique Architectures de Codes Correcteurs d'Erreurs*, Plouzané, France, November 2014.

[130] Ali Haroun, Charbel Abdel Nour, Matthieu Arzel, and Christophe Jego. Réception itérative MIMO basée sur la propagation de croyance et des codes LDPC non-binaires. In *GRETSI 2013 : 24ème colloque du Groupement de Recherche en Traitement du Signal et des Images*, Brest, France, September 2013.

[131] Ali Haroun, Charbel Abdel Nour, Matthieu Arzel, and Christophe Jego. Algorithme de détection à très faible complexité pour des systèmes MIMO basés sur la propagation de croyance. In *GRETSI 2015 : 25ème colloque du Groupement de Recherche en Traitement du Signal et des Images*, Lyon, France, September 2015.

[132] Ali Haroun, Charbel Abdel Nour, Matthieu Arzel, and Christophe Jego. Low-Complexity Soft Detection of QAM demapper for a MIMO System. *IEEE Communications Letters*, 20(4):732 – 735, April 2016.

[133] E. Viterbo and J. Bouros. A universal lattice code decoder for fading channels. *IEEE Transactions on Information Theory*, 45(5):1639–1642, jul 1999.

[134] A. Burg, M. Borgmann, M. Wenk, M. Zellweger, W. Fichtner, and H. Bolcskei. VLSI implementation of MIMO detection using the sphere decoding algorithm. *IEEE Journal of Solid-State Circuits*, 40(7):1566–1577, jul 2005.

[135] Ali Al Ghouwayel and Emmanuel Boutillon. A systolic LLR generation architecture for non-binary LDPC decoders. *IEEE Communications Letters*, 15(8):851–853, aug 2011.

[136] Emmanuel Boutillon, Laura Conde-Canencia, and Ali Al Ghouwayel. Design of a GF(64)-LDPC decoder based on the EMS algorithm. *IEEE Transactions on Circuits and Systems I: Regular Papers*, 60(10):2644–2656, oct 2013.

[137] Rami Klaimi, Charbel Abdel Nour, Catherine Douillard, and Joumana Farah. Design of Low-Complexity Convolutional Codes over GF(q). In *IEEE Global Communications Conference (GLOBECOM 2018)*, Abu Dhabi, United Arab Emirates, December 2018.

[138] Ronald Garzón-Bohórquez, Rami Klaimi, Charbel Abdel Nour, and Catherine Douillard. Mitigating Correlation Problems in Turbo Decoders. In *10th International Symposium on Turbo Codes & Iterative Information Processing (ISTC 2018)*, Hong Kong, Hong Kong SAR China, December 2018.

[139] Rami Klaimi, Charbel Abdel Nour, Catherine Douillard, and Joumana Farah. Union bound evaluation for non-binary turbo coded modulations. *IEEE Communications Letters*, 2020.

[140] Rami Klaimi, Charbel Abdel Nour, and Catherine Douillard. Procédé de génération d'un signal mettant en oeuvre un turbo-codeur, dispositif et programme d'ordinateur correspondant, December 2018.

[141] Rami Klaimi, Charbel Abdel Nour, Catherine Douillard, and Joumana Farah. Low-complexity decoders for non-binary turbo codes. In *10th International Symposium on Turbo Codes & Iterative Information Processing (ISTC 2018)*, Hong Kong, Hong Kong SAR China, December 2018.

[142] Taewon Hwang et al. OFDM and Its Wireless Applications: A Survey. *IEEE Trans. on Veh. Technology*, 58(4):1673–1694, May 2009.

[143] B. Saltzberg. Performance of an efficient parallel data transmission system. *IEEE Trans. on Commun. Tech.*, 15(6):805–811, dec 1967.

[144] Vida Vakilian, Thorsten Wild, Frank Schaich, Stephan ten Brink, and Jean-Francois Frigon. Universal-filtered multi-carrier technique for wireless systems beyond LTE. In *IEEE Globecom Workshops*. IEEE, dec 2013.

[145] Javad Abdoli, Ming Jia, and Jianglei Ma. Filtered OFDM: A new waveform for future wireless systems. In *IEEE 16th Inter. Workshop on Sig. Proc. Advances in Wireless Commun. (SPAWC)*. IEEE, jun 2015.

[146] Hao Lin. Flexible configured OFDM for 5G air interface. *IEEE Access*, 3:1861–1870, 2015.

[147] Gilberto Berardinelli, Fernando M. L. Tavares, Troels B. Sorensen, Preben Mogensen, and Kari Pajukoski. Zero-tail DFT-spread-OFDM signals. In *IEEE Globecom Workshops*, dec 2013.

[148] Gerhard Fettweis, Marco Krondorf, and Steffen Bittner. GFDM - generalized frequency division multiplexing. In *IEEE 69th Veh. Tech. Conf. VTC Spring*. IEEE, 4 2009.

[149] David Demmer, Robin Gerzaguet, Jean-Baptiste Dore, Didier Le Ruyet, and Dimitri Ktenas. Block-filtered OFDM: A novel waveform for future wireless technologies. In *IEEE Inter. Conf. on Commun. (ICC)*. IEEE, 5 2017.

[150] T. Wild and F. Schaich. A Reduced Complexity Transmitter for UF-OFDM. In *2015 IEEE 81st Vehicular Technology Conference (VTC Spring)*, pages 1–6, May 2015.

[151] M. Matthe, D. Zhang, F. Schaich, T. Wild, R. Ahmed, and G. Fettweis. A Reduced Complexity Time-Domain Transmitter for UF-OFDM. In *2016 IEEE 83rd Vehicular Technology Conference (VTC Spring)*, pages 1–5, May 2016.

[152] H.J. Landau. Sampling, data transmission, and the Nyquist rate. *Proceedings of the IEEE*, 55(10):1701–1706, 1967.

[153] B. Saltzberg. Intersymbol interference error bounds with application to ideal bandlimited signaling. *IEEE Transactions on Information Theory*, 14(4):563–568, jul 1968.

[154] J. Salz. Optimum Mean-Square Decision Feedback Equalization. *Bell System Technical Journal*, 52(8):1341–1373, oct 1973.

[155] Gordon E. Moore. Cramming more components onto integrated circuits, Reprinted from Electronics, volume 38, number 8, April 19, 1965, pp.114 ff. *IEEE Solid-State Circuits Society Newsletter*, 11(3):33–35, sep 2006.

[156] Chip Walter. Kryder's Law. *Scientific American*, 293(2):32–33, aug 2005.

[157] Fredrik Rusek and John Anderson. Multistream Faster than Nyquist Signaling. *IEEE Transactions on Communications*, 57(5):1329–1340, may 2009.

[158] P. Siohan, C. Siclet, and N. Lacaille. Analysis and design of OFDM/OQAM systems based on filterbank theory. *IEEE Trans. on Signal Process.*, 50(5):1170–1183, May 2002.

[159] J. E. Mazo. Faster-Than-Nyquist Signaling. *Bell System Technical Journal*, 54(8):1451–1462, oct 1975.

[160] F. Rusek and J.B. Anderson. The two dimensional Mazo limit. In *Proceedings. International Symposium on Information Theory, 2005. ISIT 2005.* IEEE, 2005.

[161] Adnan Prlja, John B. Anderson, and Fredrik Rusek. Receivers for Faster-than-Nyquist signaling with and without turbo equalization. In *2008 IEEE International Symposium on Information Theory*. IEEE, jul 2008.

[162] D. Dasalukunte, F. Rusek, and V. Owall. An Iterative Decoder for Multicarrier Faster-Than-Nyquist Signaling Systems. In *2010 IEEE International Conference on Communications*. IEEE, may 2010.

[163] M.G. Bellanger. Specification and design of a prototype filter for filter bank based multicarrier transmission. In *IEEE Inter. Conf. on Acoustics, Speech, and Sig. Proc.*. IEEE.

[164] Jérémy Nadal, Charbel Abdel Nour, and Amer Baghdadi. Design and Evaluation of a Novel Short Prototype Filter for FBMC/OQAM Modulation. *IEEE access*, 6:19610–19625, March 2018.

[165] D. Pinchon and P. Siohan. Derivation of analytical expressions for flexible PR low complexity FBMC systems. In *Signal Process. Conf. (EUSIPCO), 2013 proc. of the 21st European*, pages 1–5, September 2013.

[166] M. Bellanger, D. Mattera, and M. Tanda. Lapped-OFDM as an Alternative to CP-OFDM For 5g Asynchronous Access and Cognitive Radio. In *Veh. Technology Conf. (VTC Spring), 2015 IEEE 81st*, pages 1–5, May 2015.

[167] Jeremy Nadal, Francois Leduc-Primeau, Charbel Abdel Nour, and Amer Baghdadi. Overlap-save FBMC receivers. *IEEE Transactions on Wireless Communications*, 2020.

[168] Jérémy Nadal, Charbel Abdel Nour, Amer Baghdadi, and Hao Lin. Hardware prototyping of FBMC/OQAM baseband for 5G mobile communication systems. In *RSP 2014 : IEEE International Symposium on Rapid System Prototyping*, pages 135 – 141, New Delhi, India, October 2014.

[169] Jérémy Nadal, Charbel Abdel Nour, and Amer Baghdadi. Low-complexity pipelined architecture for FBMC/OQAM transmitter. *IEEE Transactions on Circuits and Systems II: Express Briefs*, 63(1):19 – 23, January 2016.

[170] Thorsten Wild and Frank Schaich. A reduced complexity transmitter for UF-OFDM. In *2015 IEEE 81st Vehicular Technology Conference (VTC Spring)*. IEEE, may 2015.

[171] Saïd Medjkouh, Jérémy Nadal, Charbel Abdel Nour, and Amer Baghdadi. Reduced Complexity FPGA Implementation for UF-OFDM Frequency Domain Transmitter. In *SIPS 2017: IEEE Workshop on Signal Processing Systems*, pages 1 – 6, Lorient, France, October 2017.

[172] Jérémy Nadal, Charbel Abdel Nour, and Amer Baghdadi. Novel UF-OFDM transmitter: significant complexity reduction without signal approximation. *IEEE Transactions on Vehicular Technology*, 67(3):2141–2154, October 2017.

[173] Jérémy Nadal, Charbel Abdel Nour, and Amer Baghdadi. Flexible hardware platform for demonstrating new 5G waveform candidates. In *ICM 2017 : 29th IEEE International Conference on Microelectronics*, Beirut, Lebanon, December 2017.

[174] Jérémy Nadal, Charbel Abdel Nour, and Amer Baghdadi. Flexible and efficient hardware platform and architectures for waveform design and proof-of-concept in the context of 5G. *AEÜ - International Journal of Electronics and Communications / Archiv für Elektronik und Übertragungstechnik*, September 2018.

[175] Deepak Dasalukunte, Fredrik Rusek, John B. Anderson, and Viktor Owall. Transmitter architecture for faster-than-nyquist signaling systems. In *2009 IEEE International Symposium on Circuits and Systems*. IEEE, may 2009.

[176] Naila Lahbabi, Hao Lin, Charbel Abdel Nour, Catherine Douillard, and Pierre Siohan. Sparse Interference Pre-Cancellation for FTN-OQAM Systems. In *EW 2016 : 22nd European Wireless Conference*, pages 1 – 6, Oulu, Finland, May 2016.

[177] Naila Lahbabi, Lin Hao, Charbel Abdel Nour, Catherine Douillard, and Pierre Siohan. An Enhanced Coding Strategy for FTN-OFDM/OQAM Transceiver Design. In *ICC 2017 : IEEE International Conference on Communications*, Paris, France, May 2017.

[178] Cisco Visual Networking Index: Global Mobile Data Traffic Forecast Update, 2016-2021 White Paper, 2017.

[179] 3GPP. Study on downlink multiuser superposition transmission (MUST) for LTE.

[180] Hosein Nikopour, Eric Yi, Alireza Bayesteh, Kelvin Au, Mark Hawryluck, Hadi Baligh, and Jianglei Ma. SCMA for downlink multiple access of 5g wireless networks. In *2014 IEEE Global Communications Conference*. IEEE, dec 2014.

[181] Liang Zhang, Wei Li, Yiyan Wu, Xianbin Wang, Sung-Ik Park, Heung Mook Kim, Jae-Young Lee, Pablo Angueira, and Jon Montalban. Layered-division-multiplexing: Theory and practice. *IEEE Transactions on Broadcasting*, 62(1):216–232, mar 2016.

[182] Anass Benjebbour, Yuya Saito, Yoshihisa Kishiyama, Anxin Li, Atsushi Harada, and Takehiro Nakamura. Concept and practical considerations of non-orthogonal multiple access (NOMA) for future radio access. In *2013 International Symposium on Intelligent Signal Processing and Communication Systems*. IEEE, nov 2013.

[183] Yuya Saito, Yoshihisa Kishiyama, Anass Benjebbour, Takehiro Nakamura, Anxin Li, and Kenichi Higuchi. Non-orthogonal multiple access (NOMA) for cellular future radio access. In *2013 IEEE 77th Vehicular Technology Conference (VTC Spring)*. IEEE, jun 2013.

[184] Yuya Saito, Anass Benjebbour, Yoshihisa Kishiyama, and Takehiro Nakamura. System-level performance evaluation of downlink non-orthogonal multiple access (NOMA). In *2013 IEEE 24th Annual International Symposium on Personal, Indoor, and Mobile Radio Communications (PIMRC)*. IEEE, sep 2013.

[185] Gerhard Wunder, Martin Kasparick, Stephan Ten Brink, Frank Schaich, Thorsten Wild, Yejian Chen, Ivan Gaspar, Nicola Michailow, Gerhard Fettweis, Dimitri Ktenas, Nicolas Cassiau, Marcin Dryjanski, Kamil Sorokosz, Slawomir Pietrzyk, and Bertalan Eged. System-level interfaces and performance evaluation methodology for 5g physical layer based on non-orthogonal waveforms. In *2013 Asilomar Conference on Signals, Systems and Computers*. IEEE, nov 2013.

[186] Yuanwei Liu, Zhijin Qin, Maged Elkashlan, Zhiguo Ding, Arumugam Nallanathan, and Lajos Hanzo. Nonorthogonal multiple access for 5g and beyond. *Proceedings of the IEEE*, 105(12):2347–2381, dec 2017.

[187] W. Yu, W. Rhee, S. Boyd, and J. M. Ciofli. Iterative water-filling for gaussian vector multiple access channels. In *IEEE International Symposium on Information Theory (IEEE Cat. No.01CH37252)*. IEEE.

[188] Jiho Jang and Kwang Bok Lee. Transmit power adaptation for multiuser OFDM systems. *IEEE Journal on Selected Areas in Communications*, 21(2):171–178, feb 2003.

[189] D. Kivanc, Guoqing Li, and Hui Liu. Computationally efficient bandwidth allocation and power control for ofdma. *IEEE Transactions on Wireless Communications*, 2(6):1150–1158, nov 2003.

[190] D. Kivanc and Hui Liu. Subcarrier allocation and power control for OFDMA. In *Conference Record of the Thirty-Fourth Asilomar Conference on Signals, Systems and Computers (Cat. No.00CH37154)*. IEEE.

[191] W. Rhee and J. M. Cioffi. Increase in capacity of multiuser OFDM system using dynamic subchannel allocation. In *IEEE 51st Vehicular Technology Conference Proceedings (Cat. No.00CH37026)*. IEEE.

[192] Zukang Shen, J. G. Andrews, and B. L. Evans. Adaptive resource allocation in multiuser OFDM systems with proportional rate constraints. *IEEE Transactions on Wireless Communications*, 4(6):2726–2737, nov 2005.

[193] Lei Lei, Di Yuan, Chin Keong Ho, and Sumei Sun. Joint optimization of power and channel allocation with non-orthogonal multiple access for 5g cellular systems. In *IEEE Global Communications Conference (GLOBECOM)*. IEEE, dec 2015.

[194] F. P. Kelly, A. K. Maulloo, and D. K. H. Tan. Rate control for communication networks: shadow prices, proportional fairness and stability. *Journal of the Operational Research Society*, 49(3):237–252, mar 1998.

[195] P. Viswanath, D. N. C. Tse, and R. Laroia. Opportunistic beamforming using dumb antennas. In *Proceedings IEEE International Symposium on Information Theory,*. IEEE.

[196] Nagisa Otao, Yoshihisa Kishiyama, and Kenichi Higuchi. Performance of non-orthogonal access with SIC in cellular downlink using proportional fair-based resource allocation. In *International Symposium on Wireless Communication Systems (ISWCS)*. IEEE, aug 2012.

[197] Anass Benjebbour, Anxin Li, Yuya Saito, Yoshihisa Kishiyama, Atsushi Harada, and Takehiro Nakamura. System-level performance of downlink NOMA for future LTE enhancements. In *IEEE Globecom Workshops (GC Wkshps)*. IEEE, dec 2013.

[198] Yuya Saito, Anass Benjebbour, Yoshihisa Kishiyama, and Takehiro Nakamura. System-level performance of downlink non-orthogonal multiple access (NOMA) under various environments. In *IEEE 81st Vehicular Technology Conference (VTC Spring)*. IEEE, may 2015.

[199] Yuta Hayashi, Yoshihisa Kishiyama, and Kenichi Higuchi. Investigations on power allocation among beams in non-orthogonal access with random beamforming and intra-beam SIC for cellular MIMO downlink. In *IEEE 78th Vehicular Technology Conference (VTC Fall)*. IEEE, sep 2013.

[200] Marie Rita Hojeij, Joumana Farah, Charbel Abdel Nour, and Catherine Douillard. Resource Allocation in Downlink Non-orthogonal Multiple Access (NOMA) for Future Radio Access. In *VTC 2015 spring : IEEE 81st Vehicular Technology Conference*, pages 1 – 6, Glasgow, United Kingdom, May 2015.

[201] Marie Rita Hojeij, Joumana Farah, Charbel Abdel Nour, and Catherine Douillard. New Optimal and Suboptimal Resource Allocation Techniques for Downlink Non-orthogonal Multiple Access (NOMA). *Wireless Personal Communications*, 87(3):837 – 867, April 2016.

[202] Marie Rita Hojeij, Charbel Abdel Nour, Joumana Farah, and Catherine Douillard. Weighted Proportional Fair Scheduling for Downlink Non-Orthogonal Multiple Access. *Wireless Communications and Mobile Computing*, 2018.

[203] Marie Rita Hojeij, Charbel Abdel Nour, Joumana Farah, and Catherine Douillard. Waterfilling-based Proportional Fairness Scheduler for Downlink Non-Orthogonal Multiple Access. *IEEE Wireless Communications Letters*, 6(2):230 – 233, April 2017.

[204] Zeina Eddo, Marie Rita Hojeij, Charbel Abdel Nour, Joumana Farah, and Catherine Douillard. Evaluation of Intra-Subband Power Allocation for a Downlink Non-Orthogonal Multiple Access (NOMA) System. In *GLOBECOM 2016 : IEEE Global Communications Conference: 2nd International Workshop on 5G RAN Design*, page ., Washington, United States, December 2016.

[205] Marie-Rita Hojeij, Charbel Abdel Nour, Joumana Farah, and Catherine Douillard. Advanced Resource Allocation Technique for a Fair Downlink Non-Orthogonal Multiple Access System. In *25th International Conference on Telecommunications, ICT 2018*, Saint Malo, France, June 2018.

[206] Marie-Rita Hojeij, Charbel Abdel Nour, Joumana Farah, and Catherine Douillard. Joint Resource and Power Allocation Technique for Downlink Power-Domain Non-Orthogonal Multiple Access. In *2018 IEEE CAMA - International Conference on Antenna Measurement and Application*, Västerås, Sweden, September 2018.

[207] Marie-Josépha Youssef, Joumana Farah, Charbel Abdel Nour, and Catherine Douillard. Waterfilling-based Resource Allocation Techniques in Downlink Non-Orthogonal Multiple Access (NOMA) with Single-User MIMO. In *ISCC 2017 : The 22nd IEEE Symposium on Computers and Communications*, pages 499 – 506, Crete, Greece, July 2017.

[208] Joumana Farah, Elie Sfeir, Charbel Abdel Nour, and Catherine Douillard. New Efficient Energy-Saving Techniques for Resource Allocation in Downlink OFDMA Transmission Systems. In *ISCC 2017 : The 22nd IEEE Symposium on Computers and Communications*, pages 1056 – 1062, Crete, Greece, July 2017.

[209] Joumana Farah, Elie Sfeir, Charbel Abdel Nour, and Catherine Douillard. New Resource Allocation Techniques for Base Station Power Reduction in Orthogonal and Non-Orthogonal Multiplexing Systems. In *ICC Workshops 2017: WT02 - 3rd International Workshop on 5G RAN Design*, pages 618 – 624, Paris, France, May 2017.

[210] Marie Rita HOJEIJ. *Resource allocation techniques for non-orthogonal multiple access systems*. Theses, Ecole nationale supérieure Mines-Télécom Atlantique, May 2018.

[211] Robert Heath, Steven Peters, Yi Wang, and Jiayin Zhang. A current perspective on distributed antenna systems for the downlink of cellular systems. *IEEE Communications Magazine*, 51(4):161–167, apr 2013.

[212] Zhiyang Liu and Lin Dai. A comparative study of downlink MIMO cellular networks with co-located and distributed base-station antennas. *IEEE Transactions on Wireless Communications*, 13(11):6259–6274, nov 2014.

[213] Joumana Farah, Antoine Kilzi, Charbel Abdel Nour, and Catherine Douillard. Power Minimization in Distributed Antenna Systems using Non-Orthogonal Multiple Access and Mutual Successive Interference Cancellation. *IEEE Transactions on Vehicular Technology*, 67(12):11873 – 11885, 2018.

[214] Antoine Kilzi, Joumana Farah, Charbel Abdel Nour, and Catherine Douillard. New Power Minimization Techniques in Hybrid Distributed Antenna Systems with Orthogonal and Non Orthogonal Multiple Access. *IEEE Transactions on Green Communications and Networking*, 3(3):679–690, May 2019.

[215] Lingyang Song, Yonghui Li, Zhiguo Ding, and H. Vincent Poor. Resource management in non-orthogonal multiple access networks for 5g and beyond. *IEEE Network*, 31(4):8–14, jul 2017.

[216] Marie-Joséph a Youssef, Joumana Farah, Charbel Abdel Nour, and Catherine Douillard. Resource Allocation for Mixed Traffic Types in Distributed Antenna Systems Using NOMA. In *IEEE 88th Vehicular Technology Conference, VTC2018-Fall*, Chicago, United States, August 2018.

[217] D. Gale and L. S. Shapley. College admissions and the stability of marriage. *The American Mathematical Monthly*, 69(1):9, jan 1962.

[218] Marie-Joséph a Youssef, Joumana Farah, Charbel Abdel Nour, and Catherine Douillard. Resource Allocation in NOMA Systems for Centralized and Distributed Antennas with Mixed Traffic using Matching Theory. *IEEE Transactions on Communications*, 68(1):414–428, January 2020.

[219] 3GPP. Mobile Broadband Innovation path to 4G: Release 9, 10 and Beyond. Technical report.

[220] 3GPP. 3GPP TR 36.819 Technical Specification Group Radio AccessNetwork; Coordinated Multi-Point Operation for LTE Physical LayerAspects. Technical report.

[221] M. D. Michelle and J. S. Harrison. CoMP (1): CoMP Types- CS, CB, JT and DPS.

[222] Emmanouil Pateromichelakis, Mehrdad Shariat, Atta ul Quddus, and Rahim Tafazolli. On the evolution of multi-cell scheduling in 3gpp LTE / LTE-a. *IEEE Communications Surveys & Tutorials*, 15(2):701–717, 2013.

[223] Antoine Kilzi, Joumana Farah, Charbel Abdel Nour, and Catherine Douillard. Mutual Successive Interference Cancellation Strategies in NOMA for Enhancing the Spectral Efficiency of CoMP Systems. *IEEE Transactions on Communications*, 68(2):1213–1226, October 2019.

[224] IEEE. IEEE 5G and Beyond Technology Roadmap White Paper, 2017. `https://futurenetworks.ieee.org/images/files/pdf/ieee-5g-roadmap-white-paper.pdf`, Accessed 2019-10-22.

[225] Rysavy Research. Global 5G: Implications of a transformational technology, 2019. `https://www.5gamericas.org/global-5g-implications-of-a-transformational-technology/`, Accessed 2019-10-22.

[226] C. Berrou, A. Glavieux, and P. Thitimajshima. Near shannon limit error-correcting coding and decoding: Turbo-codes. In *IEEE International Conference on Communications (ICC).*, volume 2, pages 1064–1070, 1993.

[227] D.J.C. MacKay. Good error-correcting codes based on very sparse matrices. In *Proc. of the IEEE International Symposium on Information Theory*, page 113, jun 1997.

[228] E. Arıkan. Channel polarization: A method for constructing capacity-achieving codes for symmetric binary-input memoryless channels. *IEEE Trans. on Inf. Theory*, 55(7):3051–3073, July 2009.

[229] C. Kestel, M. Herrmann, and N. Wehn. When channel coding hits the implementation wall. In *2018 IEEE 10th Int. Symp. on Turbo Codes Iterative Information Processing (ISTC)*, pages 1–6, Dec 2018.

[230] A. Balatsoukas-Stimming, M. Meidlinger, R. Ghanaatian, G. Matz, and A. Burg. A fully-unrolled LDPC decoder based on quantized message passing. In *IEEE Inter. Worksh. on Sig. Proc. (SiPS)*, pages 1–6, Oct 2015.

[231] P. Giard, G. Sarkis, C. Thibeault, and W. J. Gross. 237 Gbit/s unrolled hardware polar decoder. *Electronics Letters*, 51(10):762–763, 2015.

[232] A. GrÃ¶vlen W. Yong. Draft LTI on 3GPP 5G initial description template, 2017. `https://www.3gpp.org/ftp/PCG/PCG_40/docs/PCG40_11.zip`.

[233] Stefan Weithoffer, Oliver Griebel, Rami Klaimi, Charbel Abdel Nour, and Norbert Wehn. Advanced Hardware Architectures for Turbo Code Decoding Beyond 100 Gb/s. In *WCNC 2020 : IEEE Wireless Communications and Networking Conference*, Seoul, South Korea, April 2020.

[234] L. Bahl, J. Cocke, F. Jelinek, and J. Raviv. Optimal decoding of linear codes for minimizing symbol error rate (Corresp.). *IEEE Transactions on Information Theory*, pages 284 – 287, Mar. 1974.

[235] Vinh Hoang Son Le, Charbel Abdel Nour, Emmanuel Boutillon, and Catherine Douillard. Revisiting the Max-Log-Map algorithm with SOVA updates rules: new simplifications for high-radix SISO decoders. *IEEE Transactions on Communications*, 68(4):1991–2004, 2020.

[236] F. Guilloud, E. Boutillon, and J. L. Danger. λ-Min decoding algorithm of regular and irregular LDPC codes. In *Proc. 3nd Int. Symp. on Turbo Codes & Related Topics*, pages 451–454, Brest, France, September 2003.

[237] E. Boutillon, J. Castura, and F. R. Kschischang. Decoder-first code design. In *Proc. 2nd Int. Symp. on Turbo Codes & Related Topics*, pages 459–462, Brest, France, September 2000.

[238] M. P. C. Fossorier, M. Mihaljevic, and H. Imai. Reduced complexity iterative decoding of low-density parity check codes based on belief propagation. *IEEE Trans. on Comm.*, 47(5):673–680, May 1999.

[239] I. Tal and A. Vardy. List decoding of polar codes. In *2011 IEEE International Symposium on Information Theory Proceedings*, pages 1–5, July 2011.

[240] B. Li, H. Shen, and D. Tse. An adaptive successive cancellation list decoder for polar codes with cyclic redundancy check. *IEEE Communications Letters*, 16(12):2044–2047, December 2012.

[241] Stefan Weithoffer, Rami Klaimi, Charbel Abdel Nour, Norbert Wehn, and Catherine Douillard. Fully Pipelined Iteration Unrolled Decoders -The Road to Tb/s Turbo Decoding. In *ICASSP 2020 : 45th International Conference on Acoustics, Speech, and Signal Processing*, Barcelona, Spain, May 2020.

[242] D. Na and K. Choi. Low papr fbmc. *IEEE Transactions on Wireless Communications*, PP(99):1–1, 2017.

[243] R. W. Bauml, R. F. H. Fischer, and J. B. Huber. Reducing the peak-to-average power ratio of multicarrier modulation by selected mapping. *Electronics Letters*, 32(22):2056–2057, Oct 1996.

[244] Mohammad Mozaffari, Walid Saad, Mehdi Bennis, Young-Han Nam, and Merouane Debbah. A tutorial on UAVs for wireless networks: Applications, challenges, and open problems. *IEEE Communications Surveys & Tutorials*, 21(3):2334–2360, 2019.

[245] Yong Zeng, Rui Zhang, and Teng Joon Lim. Wireless communications with unmanned aerial vehicles: opportunities and challenges. *IEEE Communications Magazine*, 54(5):36–42, may 2016.

[246] Elham Kalantari, Muhammad Zeeshan Shakir, Halim Yanikomeroglu, and Abbas Yongacoglu. Backhaul-aware robust 3D drone placement in 5G+ wireless networks. In *2017 IEEE International Conference on Communications Workshops (ICC Workshops)*. IEEE, may 2017.

[247] Lei Wang, Bo Hu, and Shanzhi Chen. Energy efficient placement of a drone base station for minimum required transmit power. *IEEE Wireless Communications Letters*, pages 1–1, 2018.

[248] Akram Al-Hourani, Sithamparanathan Kandeepan, and Simon Lardner. Optimal LAP altitude for maximum coverage. *IEEE Wireless Communications Letters*, 3(6):569–572, dec 2014.

[249] Mohamed Alzenad, Amr El-Keyi, and Halim Yanikomeroglu. 3-d placement of an unmanned aerial vehicle base station for maximum coverage of users with different QoS requirements. *IEEE Wireless Communications Letters*, 7(1):38–41, feb 2018.

[250] Mikko Heino, Dani Korpi, Timo Huusari, Emilio Antonio-Rodriguez, Sathya Venkatasubramanian, Taneli Riihonen, Lauri Anttila, Clemens Icheln, Katsuyuki Haneda, Risto Wichman, and Mikko Valkama. Recent advances in antenna design and interference cancellation algorithms for in-band full duplex relays. *IEEE Communications Magazine*, 53(5):91–101, may 2015.

[251] Yang-Seok Choi and Hooman Shirani-Mehr. Simultaneous transmission and reception: Algorithm, design and system level performance. *IEEE Transactions on Wireless Communications*, 12(12):5992–6010, dec 2013.

[252] Timothy O'Shea and Jakob Hoydis. An introduction to deep learning for the physical layer. *IEEE Transactions on Cognitive Communications and Networking*, 3(4):563–575, dec 2017.

[253] Hyeji Kim, Yihan Jiang, Sreeram Kannan, Sewoong Oh, and Pramod Viswanath. Deepcode: Feedback Codes via Deep Learning. In S. Bengio, H. Wallach, H. Larochelle, K. Grauman, N. Cesa-Bianchi, and R. Garnett, editors, *Advances in Neural Information Processing Systems 31*, pages 9436–9446. Curran Associates, Inc., 2018.

[254] Tobias Gruber, Sebastian Cammerer, Jakob Hoydis, and Stephan ten Brink. On deep learning-based channel decoding. In *2017 51st Annual Conference on Information Sciences and Systems (CISS)*. IEEE, mar 2017.

[255] Tor Lattimore and Csaba Szepesvári. *Bandit Algorithms*. Cambridge Univ. Press, 2020.

[256] N. E. Tunali, M. Wu, C. Dick, and C. Studer. Linear large-scale mimo data detection for 5g multi-carrier waveform candidates. In *2015 49th Asilomar Conference on Signals, Systems and Computers*, pages 1149–1153, Nov 2015.

[257] P. Sabeti, A. Farhang, N. Marchetti, and L. Doyle. Performance analysis of fbmc-pam in massive mimo. In *2016 IEEE Globecom Workshops (GC Wkshps)*, pages 1–7, Dec 2016.

[258] Arman Farhang, Nicola Marchetti, Linda E. Doyle, and Behrouz Farhang-Boroujeny. Filter bank multicarrier for massive MIMO. In *2014 IEEE 80th Vehicular Technology Conference (VTC2014-Fall)*. IEEE, sep 2014.

[259] Arman Farhang, Amir Aminjavaheri, Nicola Marchetti, Linda E. Doyle, and Behrouz Farhang-Boroujeny. Pilot decontamination in CMT-based massive MIMO networks. In *2014 11th International Symposium on Wireless Communications Systems (ISWCS)*. IEEE, aug 2014.

[260] Amir Aminjavaheri, Arman Farhang, Linda E. Doyle, and Behrouz Farhang-Boroujeny. Prototype filter design for FBMC in massive MIMO channels. In *2017 IEEE International Conference on Communications (ICC)*. IEEE, may 2017.

[261] A. Aminjavaheri, A. Farhang, N. Marchetti, L. E. Doyle, and B. Farhang-Boroujeny. Frequency spreading equalization in multicarrier massive mimo. In *2015 IEEE International Conference on Communication Workshop (ICCW)*, pages 1292–1297, June 2015.

[262] K. E. Kolodziej, J. G. McMichael, and B. T. Perry. Multitap RF Canceller for In-Band Full-Duplex Wireless Communications. *IEEE Trans. on Wireless Commun.*, 15(6):4321–4334, June 2016.

[263] L. Laughlin, C. Zhang, M. A. Beach, K. A. Morris, and J. Haine. A Widely Tunable Full Duplex Transceiver Combining Electrical Balance Isolation and Active Analog Cancellation. In *2015 IEEE 81st Veh. Technol. Conf. (VTC Spring)*, pages 1–5, May 2015.

[264] T. Taleb and A. Kunz. Machine type communications in 3GPP networks: potential, challenges, and solutions. *IEEE Commun. Magazine*, 50(3):178–184, Mar. 2012.

[265] A. Azari, P. Popovski, G. Miao, and C. Stefanovic. Grant-free radio access for short-packet communications over 5G networks. In *IEEE Global Commun. Conf. GLOBECOM*, pages 1–7, Dec. 2017.

[266] S. K. Sharma and X. Wang. Collaborative distributed Q-learning for RACH congestion minimization in cellular IoT networks. *IEEE Communications Letters*, 23(4):600–603, Apr. 2019.

[267] O. Naparstek and K. Cohen. Deep multi-user reinforcement learning for distributed dynamic spectrum access. *IEEE Transactions on Wireless Communications*, 18(1):310–323, Jan. 2019.

[268] J. Zhang, X. Tao, H. Wu, N. Zhang, and X. Zhang. Deep reinforcement learning for throughput improvement of uplink grant-free NOMA system. *IEEE Internet Things J., Early Access*, pages 1–11, Feb. 2020.

[269] Meghana Bande and Venugopal V. Veeravalli. Multi-user multi-armed bandits for uncoordinated spectrum access, 2018.

[270] Akshayaa Magesh and Venugopal V. Veeravalli. Multi-player multi-armed bandits with non-zero rewards on collisions for uncoordinated spectrum access, 2019.

[271] Ilai Bistritz and Amir Leshem. Distributed multi-player bandits - a game of thrones approach. In *32nd Proc. Int. Conf. on Neural Inf. Process. Syst.*, NIPS'18, pages 7222–7232, Montreal, Canada, 2018.

[272] H. Liu, B. Krishnamachari, and Q. Zhao. Cooperation and learning in multiuser opportunistic spectrum access. In *IEEE Int. Conf. on Commun. Workshops*, pages 487–492, May 2008.

[273] K. Liu and Q. Zhao. Distributed learning in multi-armed bandit with multiple players. *IEEE Transactions on Signal Processing*, 58(11):5667–5681, Nov. 2010.

[274] Jonathan Rosenski, Ohad Shamir, and Liran Szlak. Multi-player bandits-a musical chairs approach. In *Int. Conf. on Mach. Learn.*, pages 155–163, 2016.

[275] Y. Gai, B. Krishnamachari, and R. Jain. Combinatorial network optimization with unknown variables: Multi-armed bandits with linear rewards and individual observations. *IEEE/ACM Transactions on Networking*, 20(5):1466–1478, Oct. 2012.

[276] Y. Xia, T. Qin, W. Ma, N. Yu, and T. Y. Liu. Budgeted multi-armed bandits with multiple plays. *25th Proc. Int. Joint Conf. on Artif. Intell.*, pages 2210–2216, July 2016.